Finanziato dall'Unione europea NextGenerationEU
Ministero dell'Università e della Ricerca
Italiadomani PIANO NAZIONALE DI RIPRESA E RESILIENZA
UNIVERSITÀ DEGLI STUDI DI BARI ALDO MORO

UNIVERSITY OF BARI ALDO MORO

DEPARTMENT OF PHARMACY- PHARMACEUTICAL SCIENCES

PhD COURSE IN

PHARMACEUTICAL SCIENCES

XXXVIII CYCLE

Disciplinary sector CHIM-07/A

Development of Novel ^{18}F-Labeled Positron Emission Tomography Radiotracers for Imaging P-Glycoprotein, Sigma Receptors and Cannabinoid subtype 2 receptors in the Central Nervous System

PhD candidate:

Dott. Francesco Mastropasqua

Coordinator:

Chiar. Prof. Renzo Luisi

Tutors:

Chiar. Prof. Nicola Antonio Colabufo

Chiar.ma Prof.ssa Carmen Abate

FINAL EXAM 2026

Table of Contents

ABSTRACT

Positron emission tomography (PET) is a highly sensitive and noninvasive imaging technique that enables the detection and quantification of receptors and enzymes through the use of radioligands labeled with positron-emitting radionuclides, most commonly carbon-11 and fluorine-18. In the context of central nervous system (CNS) disorders, several molecular targets have emerged as potential biomarkers for early diagnosis and therapeutic monitoring, including P-glycoprotein (P-gp), Sigma-1 (S1R) and Sigma-2 (S2R) receptors, and the endocannabinoid receptor subtype 2 (CB2R).

With the exception of P-gp, structure–affinity relationship (SAfiR) studies were conducted for each target to identify novel PET candidates. For S1R, these efforts led to the identification of **CF31** as a promising radiotracer. Following radiolabeling with fluorine-18, *in vitro* autoradiography studies demonstrated high specific binding and a distribution pattern consistent with known S1R expression in the CNS. In the case of S2R, a tetralin-based radiotracer (**LC2**) was developed, radiolabeled with fluorine-18, and evaluated both *in vitro* and *in vivo* in mice. Although **LC2** exhibited rapid brain uptake, this was followed by equally rapid washout, limiting its suitability as a PET tracer. An additional strategy for S2R focused on the development of indole-based derivatives. However, the corresponding SAfiR study did not yield a suitable PET candidate. The most promising compound (**CF7**) displayed dual S1R/S2R affinity and emerged as a potential neuroprotective agent rather than a PET radiotracer.

For CB2R, SAfiR investigations identified two promising PET candidates, **FM10** and **GR106**, characterized by closely related structures but opposing functional activity profiles. Both compounds were radiolabeled with fluorine-18 with the aim of developing, for the first time, two CB2R PET radiotracers with similar scaffolds yet divergent pharmacological activity. The preliminary *in vitro* autoradiography results indicate higher CB2R-specific binding for **[^{18}F]FM10** compared to **[^{18}F]GR106**. In contrast to the other targets, no novel PET tracers were developed for P-gp. Instead, **MC225** and its corresponding phenolic precursor **MC226** were synthesized, and approval was obtained from AIFA to initiate a Phase II clinical trial in collaboration with the Fondazione Policlinico Universitario A. Gemelli IRCCS in Rome. The study investigates the role of P-gp in treatment-resistant major depression and is currently ongoing; therefore, preliminary clinical results cannot yet be disclosed.

PREFACE

This thesis work was carried out at the laboratory of Prof. Nicola Antonio Colabufo at the University of Bari "Aldo Moro", under the supervision of Prof. Colabufo, Carmen Abate, and Marialessandra Contino, and at the laboratories of Prof. Rares Moldovan-Petru and Friedrich-Alexander Ludwig at the Helmholtz-Zentrum Dresden-Rossendorf (HZDR) in Leipzig.

This research was funded by #NEXTGENERATIONEU (NGEU), the Ministry of University and Research (MUR), and the National Recovery and Resilience Plan (NRRP), within the framework of the MNESYS project (PE0000006)—*A Multiscale Integrated Approach to the Study of the Nervous System in Health and Disease* (DN.1553, 11 November 2022). Additional support was provided by the National Research Council (CNR-Italy) under the program "PROGETTI di RICERCA @CNR" (acronym DATIAMO). The project also received funding from COST (European Cooperation in Science and Technology) Action CA23156 SIGMA-1EUROPE, *European Network for Sigma-1 Receptor as a Therapeutic Opportunity* (www.sigma1europe.eu; www.cost.eu). Through the Short-Term Scientific Mission (STSM) program, this funding enabled a three-month research stay at HZDR in Leipzig, where the radiolabeling studies were performed.

The main objective of this thesis was the development of novel PET radiotracers for the diagnosis of CNS diseases, focusing on P-glycoprotein, Sigma-1 and Sigma-2 receptors, and the endocannabinoid receptor subtype 2 as potential biomarkers.

The thesis is organized into chapters dedicated to each of these targets, preceded by a general introduction and followed by general conclusions. In addition, the final section includes all bibliographic references, a list of abbreviations, a list of scientific articles (published or submitted) for which I am first author, co-author, or corresponding author, and a list of national and international conferences where I participated as a presenting author.

Each chapter is structured as a stand-alone scientific article describing the research conducted on a specific receptor or efflux pump. Specifically, each chapter begins with an introduction to the target, including its structure, localization, function, and role in CNS diseases, followed by an overview of the state of the art and a review of previously reported PET radiotracers. In the case of P-glycoprotein and Sigma-1 receptors, the state-of-the-art sections are adapted from relevant review articles published by our research group. The introduction is followed by the background and aims of the specific project, and subsequently by the results, discussion, conclusions, and materials and methods sections. Each chapter concludes with a supporting information section containing additional images and graphs that complement the work without overloading the main text.

Regarding Sigma-2 receptors, the thesis includes a general introduction and a single background and aim section, followed by two distinct chapters (Part 1 and Part 2 of the broader Chapter 4), reflecting two independent and unrelated research projects.

Since each chapter is written as an independent scientific article, compound numbering restarts from 1 in each chapter rather than following a continuous sequence throughout the thesis. The main and lead compounds are identified using their laboratory acronyms.

CHAPTER 1

General introduction

Overview of Neuroinflammation, CNS Diseases and PET-Based Molecular Imaging

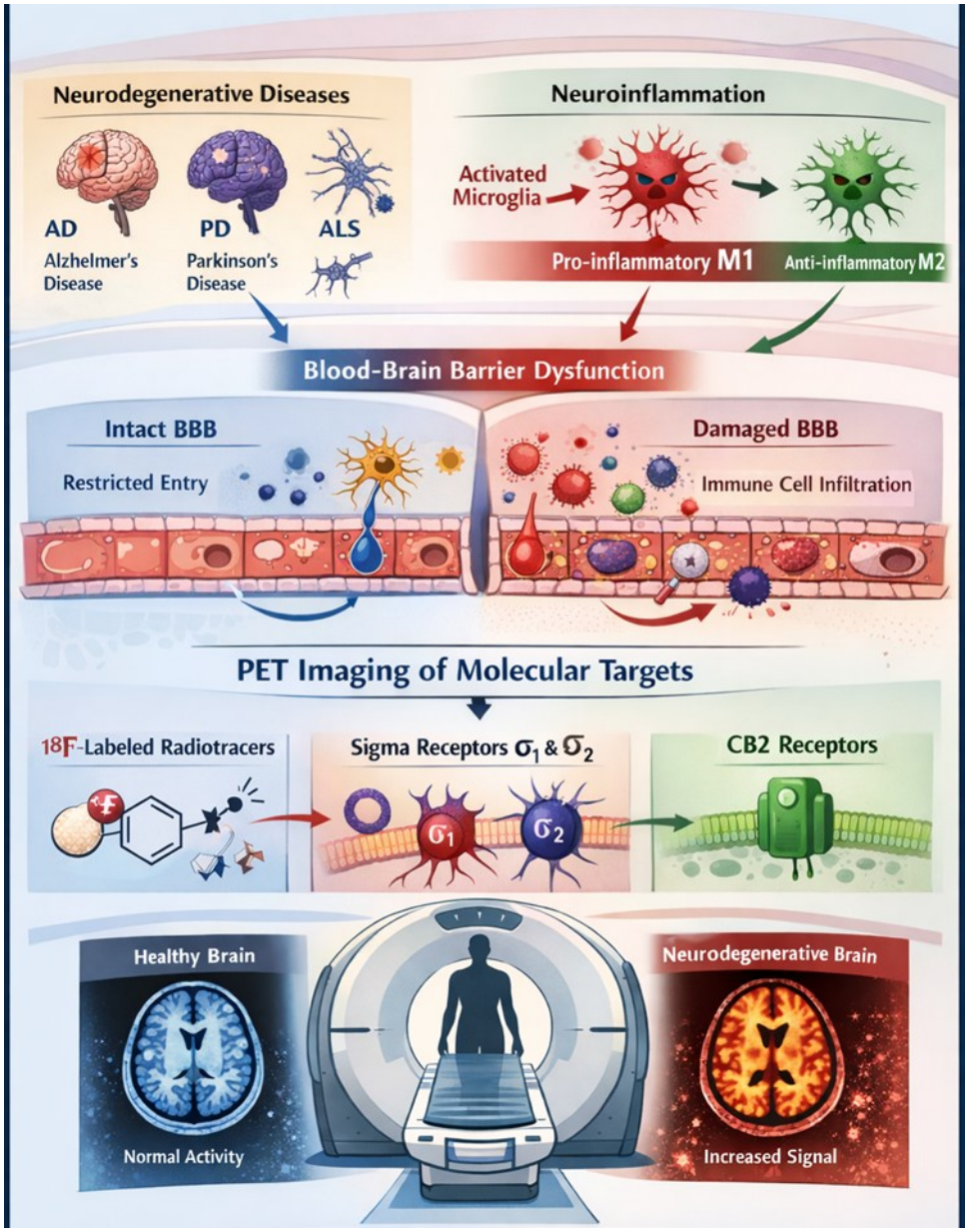

1. General introduction

Neurological disorders represent a major cause of morbidity and disability worldwide. According to a study published in *The Lancet Neurology*, approximately 3.4 billion individuals, corresponding to nearly 43% of the global population, were affected by a neurological condition in 2021 [1]. Collectively, these disorders constitute the second leading cause of mortality globally [2]. Within this broad category, neurodegenerative diseases represent a particularly significant subset, characterized by the chronic and progressive loss of neuronal integrity and function, typically resulting in brain atrophy [3]. Epidemiological projections indicate that the prevalence of these disorders is expected to double over the next two decades [4].

As with many other chronic pathological conditions, neurodegeneration is associated with persistent and unresolved neuroinflammatory processes. Given the high prevalence of neurodegenerative diseases and the absence of curative therapies for the most common forms, such as Alzheimer's disease (AD) and Parkinson's disease (PD), early and accurate diagnosis is considered crucial to delay disease progression and mitigate the onset of cognitive impairment. In this context, several molecular systems emerged as promising diagnostic and therapeutic targets. Among them, P-glycoprotein (P-gp), sigma receptors (classified into sigma-1 and sigma-2 subtypes), and the endocannabinoid receptor type 2 (CB2R) were of particular interest. These proteins were shown to be either overexpressed (as in the case of sigma receptors and CB2R) or dysregulated (as observed for P-glycoprotein) during neurodegenerative processes.

Accordingly, this doctoral research focused on the rational design, synthesis, and biological evaluation of novel ^{18}F-labeled small molecules intended for the *in vivo* visualization of these molecular targets. The overarching goal was to develop innovative tools to support the early diagnosis and characterization of neurodegenerative diseases, thereby contributing to improved understanding and management of these complex conditions.

1.1. Correlation between neuroinflammation and neurodegeneration

1.1.1. Neurodegeneration

Neurodegeneration is defined as a pathological process characterized by the gradual loss of neuronal structure and/or function, ultimately leading to cellular atrophy and death. This neuronal degeneration occurrs in both the CNS and the peripheral nervous system (PNS). Depending on the specific regions affected, distinct pathological conditions are developed, each associated with characteristic cognitive and/or motor impairments [5]. Neurodegenerative diseases (NDs) encompass a broad spectrum of disorders, including AD, PD, amyotrophic lateral sclerosis (ALS), Huntington's disease (HD), and multiple sclerosis (MS) [6]. A variety of factors contribute to the onset and progression of NDs, among which aging has been widely recognized as the predominant risk factor. Nevertheless, genetic predisposition and environmental influences also play significant roles in modulating susceptibility to neurodegenerative processes [7]. A hallmark frequently shared among these disorders is the presence of chronic neuroinflammation, which contribute to neuronal damage and exacerbate disease progression [8].

1.1.2. Inflammation

According to Baker D.L. et al., inflammation is defined as the physiological process through which circulating leukocytes and plasma proteins migrate to sites of tissue infection or injury, where they become activated to eliminate the causative agents. Beyond its role in host defense, inflammation also represents the primary biological response to the accumulation of abnormal substances as well as to cellular damage and death. Consequently, the inflammatory process constitutes a highly coordinated and multifactorial event involving a broad spectrum of molecular mediators and cellular populations [9]. When tissue injury or infection occurs, the associated stimuli are recognized by pattern-recognition receptors, including Toll-like receptors (TLRs) and NOD-like receptors (NLRs), which are predominantly expressed by cells of the innate immune system and by resident immune cells within specific tissues. Engagement of these receptors initiates intracellular pro-inflammatory signaling cascades that culminate in the release of numerous inflammatory mediators, such as cytokines, chemokines, vasoactive amines, eicosanoids, and proteolytic cascade products, through the activation of cellular metabolic pathways, thereby triggering the inflammatory response (Figure 1.1). As a result, an inflammatory exudate is generated, composed primarily of plasma proteins and leukocytes, chiefly polymorphonuclear neutrophils (PMNs), which, by exploiting increased vascular permeability, reach the inflamed site. Upon arrival, PMNs undergo activation, a process that can be induced either by direct contact with pathogens or by exposure to cytokines secreted by tissue-resident immune cells [10,11].

The ultimate goal of PMN activation is the elimination of invading pathogens or endogenous harmful stimuli through the release of granule contents, including reactive oxygen species (ROS), reactive nitrogen species (RNS), and proteolytic enzymes. However, these effector molecules lack selectivity and frequently cause collateral damage to surrounding healthy tissues [10,11].

Following the clearance of pathogens and harmful agents, the “resolution of inflammation” phase is initiated, primarily mediated by resident and infiltrating macrophages. During this stage, macrophages undergo a metabolic reprogramming that results in the acquisition of a pro-resolving phenotype. This specialized phenotype is responsible for the synthesis and release of anti-inflammatory and pro-resolving mediators that restore tissue morphology and function potentially impaired by either the initial insult or the inflammatory response itself [10,11].

Among these mediators, a class of highly potent lipid molecules collectively referred to as “Specialized Pro-Resolving Mediators” (SPMs), including lipoxins, resolvins, and protectins, play a pivotal role. Their principal biological actions comprehendised the inhibition of neutrophil recruitment and activation, alongside the promotion of monocyte recruitment to facilitate apoptotic cell clearance and initiate tissue remodeling [10,11].

A failure in the initiation, regulation, or resolution of the inflammatory process can ultimately result in chronic, unresolved inflammation, a condition that underpins the pathogenesis of several long-term disorders, including neurodegenerative diseases.

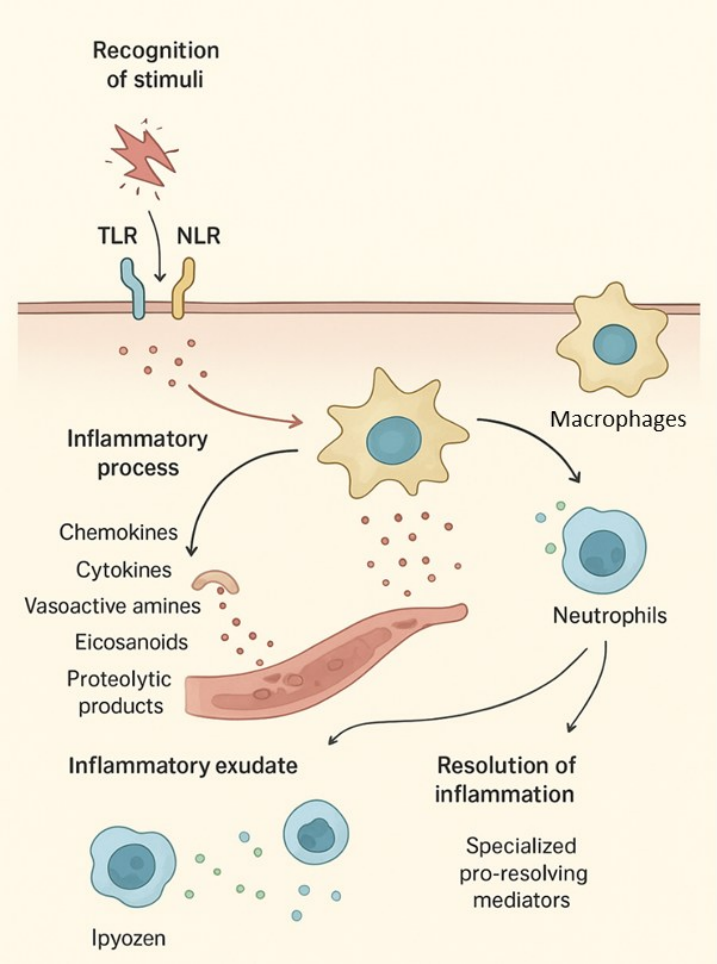

Figure 1.1: Schematic representation of the inflammatory process: stimulus recognition, activation of the inflammatory response, and subsequent resolution.

1.1.3. Neuroinflammation

Neuroinflammation is defined as the inflammatory response occurring within the CNS, particularly in the brain and spinal cord, and is triggered by various pathological stimuli, including infections, trauma, ischemia, or exposure to neurotoxic agents [12,13]. This process is tightly regulated and characterized by the production and release of pro-inflammatory cytokines such as Interleukin-1β (IL-1β), IL-6, IL-18, and tumor necrosis factor (TNF), together with chemokines including CCL1, CCL5, and CXCL1. Other small molecular mediators, such as prostaglandins, nitric oxide (NO), and ROS, also contribute to the amplification of the neuroinflammatory response [12]. These mediators are produced by resident glial cells within the CNS, mainly microglia and astrocytes, as well as by endothelial cells and infiltrating peripheral immune cells [13].

The resolution phase of neuroinflammation is marked by the release of anti-inflammatory cytokines such as IL-1, IL-4, IL-10, and IL-11, which act to suppress pro-inflammatory signaling and restore tissue homeostasis [12]. The release of these cytokines is regulated, among other factors, by SPMs, which play a key role in the termination of neuroinflammation, similar to their function in peripheral inflammation. SPMs modulate the microenvironment of affected neural tissues, promoting the cessation of the inflammatory response, facilitating debris clearance, and stimulating regenerative and repair processes [14].

1.1.3.1. The role of microglia in neuroinflammation

Microglial cells are morphologically, phenotypically, and functionally related to macrophages and are specifically distributed throughout the brain, spinal cord, and retina [15,16]. Like all macrophage-like cells, microglia can acquire different phenotypes depending on the nature and intensity of specific activating stimuli [16].

Two major functional states of microglia are described: “resting” and “activated” (Figure 1.2). Upon activation, microglial cells undergo a process known as reactive gliosis or reactive microgliosis. The transition from the resting to the activated state is triggered by various cytokines or extracellular factors such as lipids or lipopolysaccharides (LPS) [17,18].

The resting state, referred to as M0, represents the quiescent phenotype typical of physiological conditions, in which microglia continuously monitor and patrol the nervous tissue while releasing neurotrophic factors such as NFG, TGF-β, IGF-1, and BDNF. Conversely, the activated state, known as M1, is a pro-inflammatory phenotype acquired in response to harmful or pro-inflammatory stimuli, including IFN, LPS, and TLR4 activation. M1 microglia display phagocytic, cytolytic, and antigen-presenting functions, and produce high levels of pro-inflammatory cytokines such as TNF-α, IL-1β, and IL-6, as well as chemokines and NO. The activation process is considered multistep, with resting microglia progressing through “responsive” and “primed” intermediate states before reaching full activation [15,19].

In addition to the pro-inflammatory M1 state, microglia can also assume an alternatively activated M2 phenotype. These two activation states are associated with different stages of neurodegenerative diseases. While the M1 phenotype predominates at the site of injury, contributing to neuronal damage, the M2 phenotype becomes prevalent during subsequent repair processes, exerting anti-inflammatory and neuroprotective effects [17]. Microglia in the M2 state produce and release anti-inflammatory cytokines such as IL-4, IL-10, and IL-12, together with growth factors including TGF-β and IGF-1, and express high levels of arginase-1, an enzyme responsible for the production of L-ornithine, which contributes to tissue repair [20]. Phagocytosis of debris and extracellular matrix remodeling are also key features of this state.

Microglia therefore represent the principal immune effector cells of the CNS, playing a central role in both the initiation of the immune response and in the orchestration of tissue repair mechanisms required to restore homeostasis once the harmful stimulus has been removed. However, when this resolution phase fails to occur, the sustained pro-inflammatory activity of microglia persists over time, ultimately leading to neurotoxicity and neurodegeneration [16].

Neuroinflammation thus emerges as one of the central mechanisms involved in the pathogenesis of several neurodegenerative diseases, including AD, PD, HD, and ALS, in which specific toxic stimuli activate microglia toward the M1 phenotype. This, in turn, exerts cytotoxic effects and perpetuates a self-sustaining vicious cycle that promotes both neurodegeneration and neuroinflammation [21–23].

This key relationship between neuroinflammation and neurodegeneration, and the potential to modulate microglial polarization toward the alternatively activated and anti-inflammatory M2 phenotype, represents a promising conceptual basis for the development of novel therapeutic strategies.

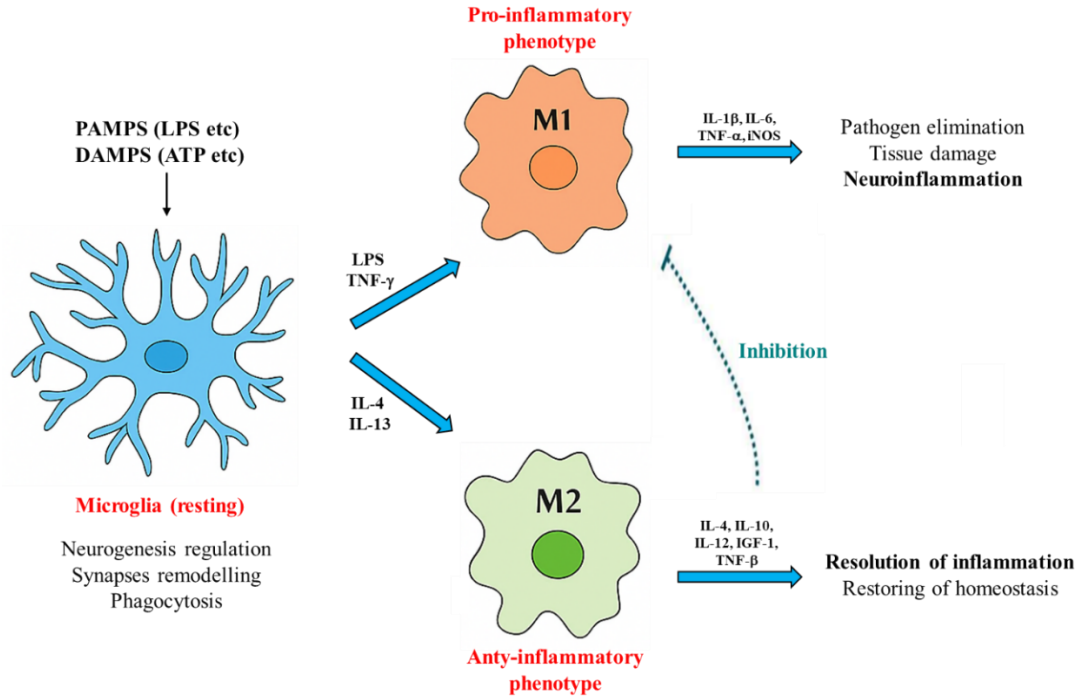

Figure 1.2: Activation and polarization of microglia under resting conditions and during neuroinflammation. Schematic representation of microglial morphology and the phenotypic characteristics associated with distinct functional states. Adapted from Ref. [18].

1.1.3.2. The role of blood-brain barrier in neuroinflammation

The blood–brain barrier (BBB) plays a fundamental role in neuroinflammation and, more broadly, in protecting the CNS. It is formed by brain endothelial cells connected through tight junctions that create a highly selective interface between the brain and the systemic circulation (Figure 1.3). This structure is essential for preserving homeostasis and maintaining brain integrity. A strong correlation between BBB dysfunction and neuroinflammation has been widely demonstrated. When BBB integrity is compromised, peripheral cells such as lymphocytes and macrophages, along with molecules including pro-inflammatory mediators and plasma proteins, can cross from the bloodstream into the brain parenchyma (Figure 1.3). The infiltration of these immune cells triggers microgliosis [24] and promotes neurodegeneration [25].

Structural alterations of the BBB, together with persistent neuroinflammation, have therefore been linked to neurodegenerative disorders such as AD, PD, and MD [26]. Given its crucial role under both physiological and pathological conditions, the BBB has become an important target for the development of new diagnostic and therapeutic strategies for ND.

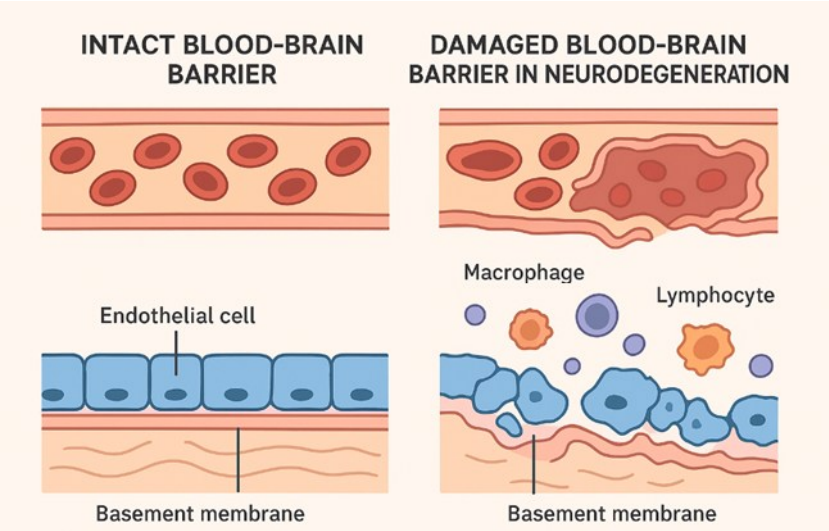

Figure 1.3: Comparison of an intact versus damaged BBB. On the left, tight endothelial junctions and an intact basement membrane maintain CNS protection. On the right, BBB disruption during neurodegeneration allows infiltration of immune cells such as lymphocytes and macrophages, contributing to neuroinflammation.

1.2. Neurodegenerative diseases

1.2.1. Alzheimer's disease

According to the World Health Organization (WHO), AD accounts for 60–80% of all dementia cases and represents the seventh leading cause of death worldwide, making it the most prevalent neurodegenerative disorder. In Europe, AD constitutes approximately 54% of all dementia cases, with a prevalence exceeding 6% among individuals aged over 65 years [27].

AD is characterized by extracellular β-amyloid (Aβ) plaques and intracellular neurofibrillary tangles composed of tau protein. The disease commonly presents with pronounced amnestic cognitive impairment, although non-amnestic forms can also occur. While short-term memory loss is the most frequent clinical presentation, deficits in expressive language, visuospatial abilities, and executive functioning are also observed [28].

Genetic predisposition accounts for approximately 60–80% of AD risk, primarily but not exclusively related to the APOE ε4 allele [29,30]. The amyloid hypothesis posits that Aβ overproduction results from disturbances in the proteolytic processing of amyloid precursor protein (APP). Genetic, environmental, and age-related factors contribute to a metabolic shift favoring the amyloidogenic cleavage pathway of APP at the expense of its non-amyloidogenic route. Aβ peptides are produced by sequential cleavage of APP via beta-secretase (BACE-1) and gamma-secretase, the latter being part of the presenilin complex. Among the various Aβ isoforms, $A\beta_{1-42}$ is considered the most pathogenic, due to its high propensity to aggregate into oligomers and protofibrils that evolve into fibrillar deposits forming senile and neuritic plaques. Impaired Aβ clearance further contributes to extracellular accumulation, triggering neurotoxic cascades that result in cytoskeletal disruption, synaptic dysfunction, and neuronal death [31,32].

Another neuropathological hallmark of AD is the presence of neurofibrillary tangles (NFTs), which consist of abnormally hyperphosphorylated tau protein. These aggregates can form paired helical filaments (PHFs) that accumulate within neuronal soma, axons, and dendrites, leading to microtubule destabilization and loss of tubulin-associated proteins. The progression of NFTs typically follows three stages: (1) the pre-tangle

stage, characterized by the presence of phosphorylated tau in the somatodendritic compartment without PHF formation; (2) the mature NFT stage, involving dense filament aggregation and nuclear displacement; and (3) the extracellular or "ghost" tangle stage, associated with neuronal loss and partially protease-resistant tau filaments [33].

From a diagnostic perspective, early imaging modalities such as computed tomography (CT) and magnetic resonance imaging (MRI) were primarily used to exclude alternative causes of dementia rather than to identify AD in its prodromal phase [34]. PET has emerged as a key tool for assessing molecular pathology. Although Aβ deposition is one of the earliest detectable features of AD, its use as a biomarker of disease progression remains debated due to the uncertain relationship between Aβ burden and clinical symptoms. In contrast, tau accumulation appears to correlate more closely with neurodegeneration and cognitive decline. PET tracers targeting tau have yielded promising results, though large-scale validation is still required to establish their diagnostic reliability. Longitudinal imaging studies have also revealed heterogeneity in tau deposition patterns across different AD phenotypes. Another widely used approach is FDG-PET, which measures cerebral glucose uptake as an indirect indicator of synaptic activity. Reduced glucose metabolism, a feature of AD, reflects synaptic dysfunction; however, similar reductions can occur in other conditions such as stroke or traumatic brain injury. Moreover, recent evidence suggests that glucose uptake in PET imaging may predominantly reflect astrocytic rather than neuronal metabolism [35].

Despite these technological advances, the multifactorial etiology of AD continues to hinder the identification of a single definitive biomarker for diagnosis and stratification. Therefore, current research efforts are focused on identifying specific, sensitive, and early biomarkers capable of accurately diagnosing AD. Early detection is crucial not only for mitigating disease progression and guiding therapeutic interventions but also for reducing the emotional and economic burden on patients and caregivers [36].

1.2.2. Parkinson's disease

PD is the second most prevalent neurodegenerative disorder, affecting approximately 2–3% of individuals aged 65 years or older [37]. PD is a chronic and progressive condition characterized by the selective degeneration of dopaminergic neurons in the substantia nigra (SN) and the accumulation of intracytoplasmic Lewy bodies, which consist of aggregated α-synuclein. In addition to these defining neuropathological features, increasing evidence supports the involvement of the BBB in PD pathogenesis, with several studies reporting structural and functional alterations that may contribute to disease progression [38].

The etiopathogenesis of PD involves a complex interplay between genetic predisposition, environmental exposure, and lifestyle factors. Age remains the strongest risk determinant, with a median onset around 60 years. Epidemiological data indicate a higher incidence in men than in women (male-to-female ratio 1.3–2.0), although differences in factors such as smoking behavior, caffeine consumption, and postmenopausal hormone use may partially explain this disparity. As observed in other neurodegenerative disorders, age-related molecular dysfunctions, including telomere attrition, genomic instability, epigenetic alterations, impairments in the ubiquitin–proteasome and autophagy–lysosomal systems, and mitochondrial defects, may underlie the progressive loss of neuronal viability [39].

Clinically, PD symptoms typically manifest at advanced stages, by which time a substantial proportion of dopaminergic neurons have already been lost. Consequently, identifying reliable early-stage biomarkers

has become a central focus in PD research. Such biomarkers are essential not only for improving diagnostic accuracy but also for monitoring disease progression and evaluating therapeutic efficacy [36].

To achieve clinical utility, PD biomarkers must demonstrate high sensitivity and specificity, allowing discrimination between PD and other neurodegenerative or movement disorders. However, biomarker discovery faces several challenges, including the limited availability of biological samples for large-scale validation. Despite these obstacles, advances in molecular and imaging technologies continue to drive progress in identifying preclinical biomarkers capable of detecting individuals at risk and tracking disease progression with greater precision. The discovery and validation of such biomarkers are expected to play a pivotal role in the early diagnosis, prognosis, and therapeutic management of PD [36].

1.2.3. Other Neurodegenerative diseases

HD is a neurodegenerative disorder that typically manifests between the ages of 30 and 40 years, with a prevalence ranging from 10.6 to 13.7 individuals per 100,000 in Western populations. It is an inherited condition caused by an autosomal dominant CAG trinucleotide repeat expansion in the huntingtin (HTT) gene located on chromosome 4. The mutant huntingtin protein (mHTT) induces neuronal dysfunction and death through several mechanisms, including direct effects of the mHTT exon 1 fragment, the formation of abnormal protein aggregates, and disruption of key cellular processes such as proteostasis, axonal transport, transcription, translation, mitochondrial activity, and synaptic function [40,41]. Regarding diagnosis, MRI and CT are standard techniques for moderate to severe stages of HD but are generally ineffective for detecting early disease. PET and functional MRI studies reveal that structural and metabolic brain alterations occur before the onset of clinical symptoms. In presymptomatic carriers of the HD gene who show no clinical or neuropsychological progression over a two-year period, tensor-based MRI morphometry demonstrates progressive striatal volume loss [42].

MS is the most common non-traumatic neurological disorder causing disability in young adults. Its incidence and prevalence are increasing in both developed and developing countries. Historically, MS is classified as an organ-specific autoimmune disorder primarily mediated by T cells, although substantial evidence also supports the involvement of B cells and the innate immune system. The disease is traditionally viewed as a biphasic condition, early inflammation drives the relapsing-remitting stage, while delayed neurodegeneration leads to non-relapsing progression, namely secondary or primary progressive MS, respectively. The etiology of MS is believed to arise from a complex interplay of genetic susceptibility and environmental triggers [43,44]. Diagnosis of MS requires clinical and/or radiological evidence of lesions in the CNS disseminated in space (DIS) and time (DIT), as determined by MRI. Following a clinically isolated syndrome (CIS), according to the 2010 McDonald criteria, a diagnosis of MS can be made on the basis of a single MRI scan if both DIS and DIT criteria are fulfilled. Nevertheless, MS remains a diagnosis of exclusion, requiring the elimination of alternative explanations for the observed neurological manifestations [43].

ALS is a fatal neurodegenerative disorder of the CNS, with incidence increasing with age and peaking between 60 and 79 years. The incidence varies by sex, with a standardized male-to-female ratio of approximately 1.35, influenced by the age of onset. ALS is a rare disease that is often challenging to diagnose, as its symptoms can mimic those of more common disorders, frequently resulting in diagnostic delays. Despite its rarity, the lifetime risk of developing ALS is about 1 in 350, though its prevalence

remains low due to limited survival time following diagnosis [45,46]. Neuroimaging plays a supportive role in ALS diagnosis, primarily to exclude structural CNS abnormalities that can reproduce ALS-like signs and symptoms. In most patients, MRI of the brain and spinal cord appears as normal or shows only nonspecific findings, such as corticospinal tract hyperintensity or motor cortex hypointensity. PET imaging can provide further insight by detecting regional changes in cerebral metabolism and receptor distribution patterns in affected patients [47].

1.3. Positron Emission Tomography

PET is an imaging modality that enables highly sensitive and non-invasive detection and quantification of receptors, enzymes, and other molecular targets through the use of radiolabeled compounds incorporating positron-emitting radionuclides. PET has become an established tool in both clinical and research settings for investigating the pathophysiology of neurodegenerative and psychiatric disorders, as well as cancer, and for studying normal brain neurophysiology [48,49].

By administering trace amounts of radiopharmaceuticals, PET allows for quantitative three-dimensional imaging of biological processes in vivo, without eliciting physiological or pharmacological effects. In contrast to MRI and CT, which primarily provide structural information, PET offers insight into tissue biochemistry and physiology, detecting molecular alterations that may precede the appearance of anatomical abnormalities. Thus, PET enables the early detection of disease-related changes, offering a powerful tool for assessing molecular and functional dynamics within the body [50].

Given the complementary nature of diagnostic imaging modalities, hybrid systems such as PET–CT and PET–MRI have been developed to combine molecular, functional, and anatomical information within a single scan, thereby improving diagnostic accuracy and clinical interpretation [50,51]. The pivotal role of early and precise diagnosis in the management of disease has consequently driven growing interest in the design and synthesis of novel PET radiotracers, which represent a rapidly expanding frontier in molecular imaging research.

1.3.1. Basic principle of PET

PET imaging is based on the detection of gamma photons generated during the radioactive decay of positron-emitting radionuclides [48]. During this process, a proton within the nucleus is converted into a neutron, emitting a positron (β^+, the electron's antiparticle with equal mass and opposite charge) and an electron neutrino (ν_e), as shown in Equation 1.1. After its emission, the positron travels a short distance through tissue before encountering an electron, leading to an event known as *annihilation*. This interaction produces two gamma photons, each with an energy of 511 keV, which are emitted in nearly opposite directions (Figure 1.4) [48]. PET scanners are equipped with arrays of detectors positioned in a circular configuration around the subject, designed to simultaneously capture these coincident photon pairs [52]. This simultaneous detection, known as *coincidence detection*, enables accurate localization and quantification of positron-emitting isotopes within the body, forming the physical basis of PET's ability to generate three-dimensional maps of radiotracer distribution [52]. Through this mechanism, PET provides highly detailed information on both the spatial distribution and concentration of radionuclides, thereby allowing comprehensive visualization and quantification of physiological and biochemical processes *in vivo* [52].

$$ {}^{A}_{Z}X \rightarrow {}^{A}_{Z-1}Y + \beta^{+} + \nu_{e} $$

Equation 1.1: A is the Atomic mass, Z is the Atomic number, X is the radioactive positron emitter, Y is the resulting daughter nucleus, β^{+} is the positron and ν_e is the neutrino.

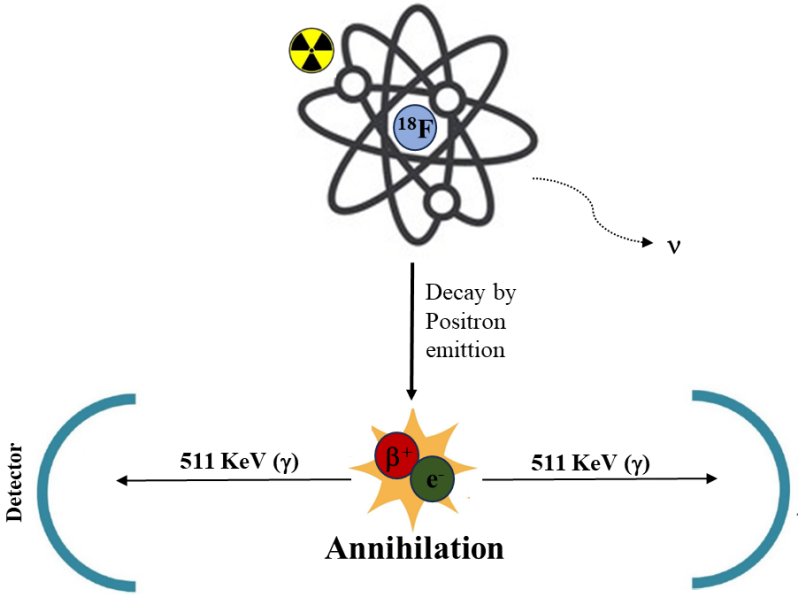

Figure 1.4: Schematic representation of β^{+} decay and consequent annihilation.

1.3.2. Radionuclides commonly used in PET

For a radionuclide to be suitable for PET imaging, it must undergo radioactive decay via positron emission. The most commonly used radionuclides include carbon-11 (^{11}C), fluorine-18 (^{18}F), gallium-68 (^{68}Ga), and nitrogen-13 (^{13}N), among others (Table 1.1) [53]. Among these, ^{18}F is by far the most widely employed radionuclide owing to its favorable physical and chemical properties. Its relatively long half-life (109.8 minutes) allows for complex radiochemical syntheses and enables whole-body imaging protocols [54]. In addition, ^{18}F exhibits a low maximum positron energy (635 keV), corresponding to a short positron range in tissue (~2.3 mm) prior to annihilation. This characteristic results in high spatial resolution and a lower radiation dose to the patient compared to higher-energy positron emitters [48,54]. By contrast, short-lived radionuclides such as ^{11}C (t½ = 20.4 min), ^{13}N (t½ = 9.97 min), and ^{15}O (t½ = 122 s) pose significant logistical challenges, primarily due to their brief half-lives that require on-site cyclotron production and immediate radiochemical synthesis. These isotopes also tend to yield lower image resolution compared to ^{18}F [55–57].

^{68}Ga has also gained increasing relevance in PET imaging in recent years. It is a generator-produced radiometal that can readily be incorporated into a variety of biomolecules. However, compared to ^{18}F, it presents some limitations. Its higher maximum positron energy (1899 keV) leads to a longer positron range and consequently to reduced spatial resolution and image sharpness. Furthermore, its shorter half-life (67.7 minutes) constrains imaging duration and complicates radiotracer logistics, particularly for institutions lacking an on-site generator or requiring long-distance transport of radiopharmaceuticals [58,59].

An unconventional yet valuable long-lived positron emitter is iodine-124 (^{124}I), with a half-life of approximately 4.2 days. Its extended decay time makes it suitable for monitoring slow pharmacokinetics,

especially in large biomolecules. In addition, its versatility in both electrophilic and nucleophilic labeling under mild conditions has established ^{124}I as an important isotope in immunoPET applications [60].
Given the widespread use of ^{18}F in PET imaging and its exclusive application within the scope of this PhD thesis, the following section will focus specifically on radiochemical strategies and methodologies for radiofluorination.

Table 1.1: Physical characteristics of most common PET radionuclides with $t_{1/2}$ (half-life), $E_{\beta+max}$ (positron energy maximum) and R_{max} (maximum range of positron in water).

Radionuclide	$t_{1/2}$	Production	$E_{\beta+ max}$ (keV)	R_{max} (mm)
^{18}F	109.7 min	Cyclotron ^{18}O (p,n)→ ^{18}F	635	2.3
^{11}C	20.4 min	Cyclotron ^{14}N (p,α)→^{11}C, ^{11}B(p,α)→^{11}C	960	3.9
^{68}Ga	67.7 min	Cyclotron ^{68}Zn (p,n)→ ^{68}Ga, Generator ^{68}Ge (e^-,n)→ ^{68}Ga	1880	9.0
^{13}N	9.97 min	Cyclotron ^{16}O (p,α)→^{13}N,	1190	5.1
^{15}O	122 sec	Cyclotron ^{14}N (d,n)→ ^{15}O, ^{15}N (p,n)→ ^{15}O	1720	8.0
^{124}I	4.2 days	Cyclotron ^{124}Te (p,n)→ ^{124}I,	2135	11.7

1.3.3. Production of fluorine-18

Fluorine-18 was typically produced in a cyclotron through proton irradiation of ^{18}O, a stable natural isotope of oxygen, as shown in Equation 1.2. The target material was usually [^{18}O]H_2O, yielding an aqueous solution of fluoride ion ([$^{18}F]^-$). Alternatively, irradiation of [^{18}O]O_2 gas generated gaseous fluorine ([^{18}F]F_2). [^{18}F]F_2 could also be obtained by irradiating neon gas with deuterium [61].
The selected production route depended on the intended chemical use: [^{18}F]fluoride was preferred for nucleophilic substitutions, whereas [^{18}F]F_2 was used for electrophilic labeling reactions [54,62,63]. A key distinction between these two forms lays in their molar activity (A_m). Molar activity was a critical parameter influencing the efficacy and quality of PET imaging. It had to be carefully monitored and optimized during both production and radiotracer synthesis to ensure high-quality imaging performance, particularly for ^{18}F-labeled PET tracers. Am described the amount of radioactivity per mole of compound, typically expressed in Bq/mol or GBq/µmol. Maintaining sufficiently high A_m values was essential to prevent receptor saturation and minimize biological toxicity [61].

$$^{18}_{8}O + p \rightarrow {}^{18}_{9}F + n$$

Equation 1.2: *p* is proton and *n* is neutron.

1.3.3.1. Strategies for radiofluorination

The main strategies for introducing fluorine-18 included electrophilic substitution reactions (using gaseous [^{18}F]F_2), nucleophilic substitution (using aqueous [^{18}F]fluoride), and transition metal-catalyzed radiofluorination (also employing aqueous [^{18}F]fluoride). Formation of carbon–fluorine-18 (C–^{18}F) bonds was generally carried out as the final synthetic step because of the short half-life of ^{18}F and typically

required harsh reaction conditions. However, certain functional groups were incompatible with these conditions, which prompted the development of indirect radiofluorination strategies. In these approaches, ^{18}F was first incorporated into a simpler prosthetic group, which was subsequently conjugated to the target molecule under milder reaction conditions [54,64].

1.3.3.2. Electrophilic radiofluorination

Electrophilic substitution reactions typically employ gaseous $[^{18}F]F_2$. In this approach, the production of $[^{18}F]F_2$ for radiolabeling required the addition of carrier $[^{19}F]$fluorine, which limited the theoretical radiochemical yield (RCY) to approximately 50%. The $[^{18}F]F_2$ gas obtained could be used directly or converted into less reactive and more selective fluorinating agents, such as acetyl hypofluorite ($[^{18}F]CH_3COOF$) [54,65].

An innovative method was developed to increase the A_m of $[^{18}F]F_2$ through a two-step process. In this procedure, $[^{18}F]^-$ was first converted to $[^{18}F]CH_3F$ via nucleophilic substitution on methyl iodide, and the resulting $[^{18}F]CH_3F$ was subsequently transformed into $[^{18}F]F_2$ in an electrical discharge chamber. This method enabled the production of $[^{18}F]F_2$ with high RCY and A_m, although the final outcome still depended on the amount of carrier fluorine and the efficiency of the isotopic exchange reaction [54].

1.3.3.3. Nucleophilic radiofluorination

Nucleophilic radiofluorination (SN_2 for aliphatic substrates, SN_{Ar} for aromatic systems) represents the main method employed for radiolabeling. $[^{18}F]$fluoride is produced in a cyclotron via the $^{18}O(p,n)^{18}F$ reaction, starting from enriched $[^{18}O]H_2O$. Although the fluoride ion is a strong nucleophile, its reactivity in aqueous media decreases significantly due to hydrogen bonding with water molecules. Therefore, before the labeling reaction, it is necessary to dry the $[^{18}F^-]$ by removing residual water, typically through azeotropic distillation with acetonitrile [54,66]. To enhance both solubility and nucleophilicity of the fluoride ion in organic solvents, a phase-transfer catalyst (PTC) such as the cryptand Kryptofix2.2.2 ($K_{2.2.2.}$). complexed with potassium (Figure 1.5) is commonly added. Alternatively, tetraalkylammonium salts, such as tetraethylammonium bicarbonate (TEAF) or tetrabutylammonium bicarbonate (TBAF), are also used as PTCs (Figure 1.5) [64]. After drying, $[^{18}F]$fluoride is typically employed in polar aprotic solvents such as Acetonitrile (CH_3CN), dimethyl sulfoxide (DMSO), or dimethylformamide (DMF) [54,64].

In SN_2 reactions, the choice of leaving group plays a crucial role, following the general reactivity order: trifluoromethanesulfonate (triflate) > 1-nitrobenzenesulfonate (nosylate) > methanesulfonate (mesylate) ≈ 4-methylbenzenesulfonate (tosylate) > I > Br > Cl [54,62,67]. The position and nature of the leaving group also influence substitution efficiency, with the general trend: primary benzyl > primary aliphatic ≫ secondary aliphatic [54].

For SN_{Ar} using $[^{18}F]$fluoride, activation of the aromatic ring by electron-withdrawing groups (EWGs) such as $–NO_2$, –CN, or $–CF_3$ in the ortho- or para-position relative to the leaving group is required [54,64,68]. These reactions generally require high temperatures (around 100 °C or higher), polar aprotic solvents, and suitable leaving groups such as trimethylammonium or nitro moieties. However, this method is limited by the need for electron-deficient aromatic systems [54]. In contrast, heteroarenes such as pyridines are more readily fluorinated without additional activation. The inherent electron deficiency of the 2- and 4-positions in these rings facilitates SN_{Ar} reactions, often leading to higher radiochemical yields [54,64].

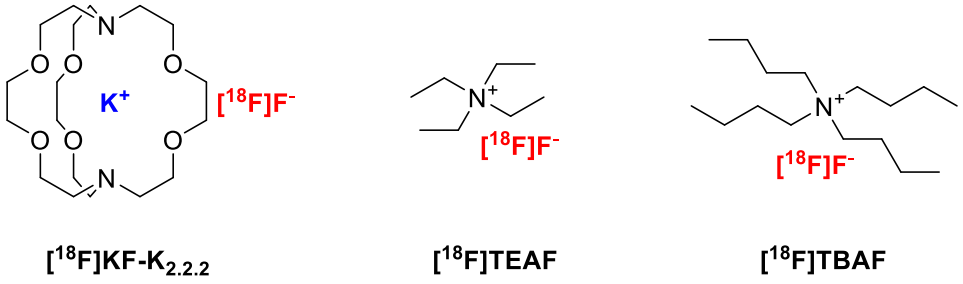

[18F]KF-K2.2.2 [18F]TEAF [18F]TBAF

Figure 1.5: Common phase-transfer catalysts used for nucleophilic ^{18}F-radiolabeling.

1.3.3.4. Other methods of radiofluorination

Another effective approach to radiofluorination was the transition metal-catalyzed cross-coupling reaction. This technique provides broad functional group tolerance, thereby expanding the range of substrates that could be labeled with [^{18}F]fluoride [69]. It was typically employed for systems that were not activated toward direct radiofluorination. Among the transition metals used for this purpose, palladium (Pd), nickel (Ni), and copper (Cu) were the most common, with Cu-based methods proving the most practical and efficient [70–72].

Copper-mediated radiofluorination (CMRF), developed by Gouverneur and co-workers, emerged as a powerful technique in ^{18}F radiochemistry, specifically designed to introduce [^{18}F]fluoride into substrates not activated for SN_{Ar} reactions. This method exploited the reactivity of copper catalysts, typically Cu(II) salts or complexes, to activate aromatic or aliphatic substrates and promote efficient incorporation and transfer of [^{18}F]fluoride [72,73]. In contrast to several other transition metal-mediated processes, CMRF did not require strict exclusion of air or moisture, which simplified handling and minimized the need for specialized equipment [54]. Moreover, late-stage CMRF offered notable advantages in both efficiency and practicality compared with multi-step labeling strategies involving the use of prosthetic groups [72,73].

1.4. A general strategy for the development of new PET radiotracers

The development of a new PET radiotracer is a complex and demanding process, as it requires meeting stringent criteria such as an affinity below 10 nM and a selectivity greater than 100-fold. However, these parameters are not absolute and often depend on the level of target expression within the pathological context [74].

The biological region of interest plays a crucial role in radiotracer design. For instance, when developing a PET radiotracer intended for brain imaging, it is essential to consider chemical and physical properties that facilitate penetration into the CNS. The key physicochemical parameters typically include moderate lipophilicity ($logD_{7.4}$ = 1.5–3.5, logP = 2–4), low molecular weight (< 500 Da), a limited number of hydrogen bond donors (< 3), and a topological polar surface area (TPSA) below 90 Å^2. While exceptions to these guidelines exist, compliance with them generally improves the probability of crossing the BBB [48,75–77].

The position of the radiolabel within the molecule is also a critical factor, both to facilitate the radiosynthetic process and to ensure metabolic stability. In the case of ^{18}F, for example, defluorination can lead to undesired accumulation of radioactivity in bones or to the formation of radioactive metabolites capable of crossing the BBB, thereby complicating image interpretation.

Once synthesized, the radioligand is typically subjected to in vitro evaluations, including cellular uptake assays, assessments of nonspecific binding, and serum stability tests. These are often followed by in vitro or ex vivo autoradiography to determine the localization of tracer binding and to distinguish between specific and nonspecific interactions. If the in vitro findings are promising, in vivo studies are carried out, typically in mice or rats, to assess metabolism, biodistribution, and pharmacokinetics.

Further investigations can be performed using animal models of disease to evaluate whether the radiotracer exhibits appropriate target engagement and specificity under pathological conditions. If the compound demonstrates high on-target accumulation, favorable metabolic stability, minimal off-target effects, and acceptable toxicity, it can then advance to human clinical trials.

CHAPTER 2

P-glycoprotein

Designing a Small Molecule for PET Radiotracing: [^{18}F]MC225 in Human Trials for Early Diagnosis in CNS Pathologies

Introduction adapted from "Mastropasqua, F*., Luurtsema, G., Filosa, C.*, & Colabufo, N. A. "Designing a Small Molecule for PET Radiotracing: [^{18}F]MC225 in Human Trials for Early Diagnosis in CNS Pathologies." *Molecules*, **2025**, *30*(18), 3696. **https://doi.org/10.3390/molecules30183696.**

2. Introduction

P-gp, an ATP-binding cassette transporter (ABC), is a membrane-bound efflux pump that utilizes energy derived from ATP hydrolysis to transport a wide variety of unrelated molecules out of cells, despite their concentration gradient, playing a crucial role in cellular drug absorption and excretion [78,79]. It is a glycoprotein of approximately 170 kDa encoded by the multidrug resistance gene-1 (*mdr1*), highly expressed in various organs, particularly in the luminal membrane of the small intestine and the BBB, as well as in the apical membranes of excretory cells such as hepatocytes and renal cells [80]. Changes in P-gp expression or function could lead to several diseases, both in the CNS and in chemo-resistant morbidities [81].

2.1. Localization, Structure and P-gp Activity

2.1.1. Localization

P-gp shows high expression on the apical surface of the epithelium of intestinal cells, liver bile ducts, and proximal renal tubules. Since all these organs have an excretory role, it was suggested that the pump exerts its physiological role in the elimination of endogenous or xenobiotic metabolites through Phase III-mediated transport. Additionally, it makes the membrane less permeable to drug passage. P-gp is localized in several biological barriers at the apical levels of endothelial cells, both in CNS and in other organs where the flow/transit of xenobiotics needs modulation. This protective role of P-gp is strongly supported by studies performed with knockout transgenic mice lacking one or both genes encoding P-gp transporting drug, Abcb1a and Abcb1b [82,83]. At the intestinal level, P-gp is highly expressed in the epithelial cells of the colon and ileum (apical side), while in the jejunum, duodenum, and stomach, it is relatively reduced compared to the ileum. Here, it plays a key role in drug absorption as it expels the drug and limits its oral bioavailability, reducing its effectiveness *in vivo*. This is a very important aspect to consider because among naturally lipophilic drugs (about 50–60% of new chemical entities and 40–50% of existing ones), it is estimated that more than 25% are P-gp substrates [84,85]. An interesting aspect of P-gp expression in the small intestine is its interaction with metabolizing enzymes, particularly with CYP3A4, a cytochrome P450 isoenzyme, towards which there is considerable overlap in substrate specificity and tissue distribution [86]. P-gp is also expressed throughout the respiratory tract where it plays an important role in protection against the entry of endogenous or exogenous toxic compounds into the lungs. In the human lung, P-gp is expressed on the apical side of ciliated epithelial cells, ciliated and apical collecting ducts, and lateral surfaces of serous cells of bronchial glands but not in mucin-secreting goblet cells. Mutations in the *mdr1* gene affect the natural protection of the respiratory tract by accumulating toxic compounds; however, if P-gp is overexpressed, xenobiotics are metabolized quickly and expelled from the cells, which is particularly important for the treatment of lung cancer. Several studies demonstrated that a number of drugs, usually employed in the treatment of chronic obstructive pulmonary disease (COPD), are P-gp substrates. Following this finding, the concentration of said drugs is lower than expected, and this supports the fact that P-gp can limit the pulmonary absorption of P-gp substrates [87–89]. P-gp is also present in placental tissue of various mammalian species, including humans. It localizes on the apical microvillous surface of syncytiotrophoblasts (STBs), where it participates in the efflux of hydrophobic and cationic drugs into the maternal blood, thus limiting fetal exposure to drugs and xenobiotics. The expression of placental P-gp

during pregnancy is not uniform; in mice and rats, P-gp expression reaches its peak during the second half of pregnancy and then decreases towards term; however, in humans, a decrease in placental expression is observed as gestation progresses. Therefore, placental P-gp seems to be upregulated in the early Phase of human pregnancy, probably to protect the fetus from potentially toxic xenobiotics. Fetal protection has been confirmed by numerous in vivo experiments using genetically modified mice or using in situ perfusion of rat placenta [86,90,91]. Furthermore, it is commonly accepted that P-gp inhibition can affect drug targeting by enhancing the drug toxicity of drugs such as HIV protease inhibitors and antitumor chemotherapeutic agents. Therefore, Eyal S. et al. conducted an experiment on pregnant macaques using [^{11}C]Verapamil as a model substrate of P-gp and Cyclosporin A (CsA) as an inhibitor, testing the feasibility of using non-invasive and simultaneous PET to evaluate P-gp activity and inhibition in maternal organs and placenta. The experiment demonstrated that inhibition of P-gp by CsA resulted in a significant increase in the distribution of [^{11}C]Verapamil radioactivity in tissues most protected by P-gp, namely, the maternal brain and fetus [92]. P-gp is also present at the cardiac level, particularly in arterioles and capillaries of the heart. This is a very important aspect to consider because several drugs employed in the treatment of heart failure are P-gp substrates; therefore, the actual drug concentration is lower than expected when P-gp is over expressed, thus reducing bioavailability, since P-gp is localized between blood and cardiomyocytes (Table 2.1) [93,94].

Table 2.1. Summary table of P-gp localization, expression (high ↑ or low ↓), its physiological and pharmacological roles in different body systems.

Organ/District	Localization	Physiological/Pharmacological Role
Intestine	Epithelial cells of the colon and ileum (↑); jejunum, duodenum, and stomach (↓)	Absorption and bioavailability; interacts with CYP3A4;
Liver	Bile ducts (↑)	Elimination of endogenous and xenobiotic metabolites
Kidneys	Proximal tubules (↑)	Excretion of endogenous and xenobiotic metabolites
CNS	Endothelial cells of BBB (↑)	Protects the CNS by limiting xenobiotic passage
Respiratory system	Ciliated epithelial cells, collecting ducts, lateral surfaces of serous cells in bronchial glands (↑); absent in goblet cells	Modulates pulmonary absorption of P-gp substrates (e.g., COPD drugs)
Placenta	Microvillous surface of syncytiotrophoblasts (↑)	Efflux of hydrophobic/cationic drugs into maternal blood; fetal protection
Heart	Arterioles and cardiac capillaries (↑)	Reduces intracellular drug concentration, lowering bioavailability

2.1.2. Structure and P-gp Activity

P-gp is a plasma membrane protein organized into a single polypeptide of 1280 residues with a molecular weight of 170 kDa. It contains two transmembrane domains (TMDs) consisting of 12 transmembrane α-helices each and two nucleotide-binding cytosolic regions (NBD) that are highly expressed when water is involved in ATP hydrolysis; these two halves are symmetric to each other and are connected by a highly

charged “linker region,” approximately 75 amino acids long and phosphorylated at different sites by protein kinase C (PKC). The two halves of the molecule do not need to be covalently bound to function. The TMDs, representing the hydrophobic portion of P-gp, contain the drug-binding domains (DBSs) and create the pathway through which drug molecules cross the membrane, causing P-gp to shift from an inward-facing to an outward-facing conformation (Figure 2.1). The structure of P-gp transporter displays specific NDB domains, namely, Walker A e Walker B, whereas the TMDs are structurally superimposed to other ABC pumps (sister pumps) [79,82,95–97].

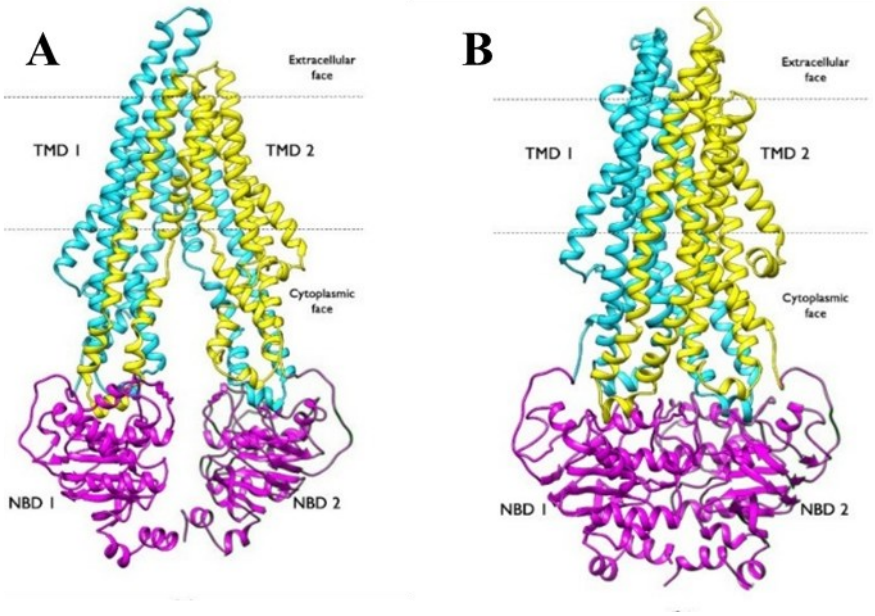

Figure 2.1. Shift in P-gp’s physiological state during its activity. Cryo EM structures of h P-gp. (**A**) Resting state of P-gp, corresponding to the inward-facing conformation (PDB ID: 6QEX); (**B**) outward-facing conformation (PDB ID: 6C0V). Nucleotide-binding domains (NBDs) are shown in magenta, and transmembrane domains (TMDs) are shown in cyan and yellow [95].

An essential aspect to consider is the flexibility of P-gp, which, like any protein in natural conditions, is flexible in an aqueous environment; specifically, it must adapt its specific dimensions to different ligands. P-gp has an unusually broad poly-specificity, allowing it to easily change the size of its internal cavity, thus recognizing hundreds of compounds. X-ray crystallography of the inward-facing conformation of P-gp has revealed the dimensions of the internal cavity (6000 $Å^3$), which are sufficient to accommodate at least two compounds simultaneously. High flexibility is also provided by the tertiary structure of P-gp, allowing for three-dimensional reorientation; in fact, it was demonstrated that P-gp interacts with various stereoisomers of the same compound. In addition to that, molecules displaying an MW between 250 and 4000 Da are also P-gp substrates, especially if they present hydrophobic moieties that interact with the lipid bilayer, where P-gp binds them selectively. Owing to the main binding cavity (MBC) and other binding sites (OBSs), P-gp displays great binding activity, which leads to a pharmaceutical side-effect occurring, determining multidrug resistance (MDR) [98,99]. The flexible structure of P-gp is responsible for its translational and rotational movements during the efflux mechanism. Conformational changes, both local and global, are induced by the entry of a suitable efflux substrate and lead, among other things, to a simultaneous variation in NBD distance. In P-gp, intracellular coupling helices (CHs), each formed by two TMs, mediate physical

connections with the NBDs. In the case of substrate binding, a series of small but significant displacements occurred, mainly in CH2 and CH3, leading to the reorientation of the NBDs towards a pre-dimer configuration. Cross-linking showed that the conformational flexibility of CH2/CH3 and the hydrophobic network at the CH2/CH3/NBD2 transmission interface were critical for P-gp transport activity. A key role in the conformational transition is played by TM4 and TM9, as conformational changes induced by the substrate in TM4 and TM9 may provide allosteric communication with the NBDs through CH2 and CH3. Based on experimental observations, the secondary structure of P-gp does not change during its catalytic function [78,100].

2.2. Role of P-gp in CNS Diseases

CNS pathologies represent a constant challenge in medicine and research as they are steadily increasing, and in most cases, therapeutic responses are poorly effective. ABC transporters play an essential role in many neurodegenerative pathologies because altered expression and functionality of these transporters have been observed in many of them. Additionally, they reduce the efficacy of many drugs since they are substrates for these transporters [101,102]. Within this class of transporters, a particularly important role is played by P-gp because it limits the penetration of many exogenous agents across the BBB and appears to be involved in the etiology of some neurological disorders. Several studies demonstrate that the function of P-gp decreases in the advanced stages of neurodegenerative diseases such as PD and AD. Dysfunction of P-gp may contribute to neuronal damage induced by the increased accumulation of toxins, as seen in PD, or by the reduced ability of the brain to expel accumulating proteins, as in AD [28].

2.2.1. Role of P-gp in Alzheimer's Disease

The P-gp plays a critical role in endothelial efflux of Aβ; indeed, it normally transports Aβ out of the brain. A reduction in P-gp efflux function at the BBB can therefore lead to an accumulation of insoluble proteins involved in neurodegenerative diseases in the brain [103,104]. Several studies demonstrate that a reduction in P-gp expression in brain capillaries at the BBB decreases the clearance of Aβ from the brain into the blood, significantly contributing to the accumulation and burden of Aβ in AD [87,105]. The highest expression of P-gp has been found in the brainstem, where the lowest levels of Aβ plaques have also been detected. This discovery of the highest level of P-gp expression within the brainstem is observed in both normal brains and brain tissue of patients with Alzheimer's disease [106]. Ding Y. et al., using a transgenic mouse model of AD (mice overexpressing the human amyloid precursor protein (hAPP), Tg2576), discovered that hAβ40 causes degradation of P-gp in brain capillaries. Specifically, hAβ40 triggers the degradation of P-gp through the activation of the ubiquitin–proteasome pathway; by preventing the ubiquitination of P-gp, the expression of P-gp protein and its transport activity at the blood–brain barrier can be preserved, leading to lower levels of Aβ in the brain *in vivo* [107].

2.2.2. Role of P-gp in Parkinson's Disease

There is a strong correlation between reduced expression of P-gp and an increased risk of PD. Mice lacking P-gp show a high accumulation of pesticides and other harmful toxic substances in the brain, indicating its importance [108]. However, it has not been possible to confirm a correlation between the reduced function of P-gp at the BBB and the onset of Parkinson's disease [109]. Several studies therefore demonstrate that

the reduced efflux of P-gp is not the main cause in the onset of PD, but rather, the function of P-gp decreases with aging and in the advanced stages of various Parkinsonian diseases [110,111]. Bartels A.L. et al. conducted an in vivo PET study on seventeen healthy volunteers aged between 18 and 86 years old. By using [^{11}C]Verapamil, it was shown that a more profound functional decrease in P-gp was observed in the regions of the white matter of the internal capsule and the corona radiata, as well as in the orbitofrontal regions [112].

2.2.3. Role of P-gp in Major Depressive Disorder

Major depressive disorder (MDD) is the most severe form of depression and the third leading cause of long-term disability. It is estimated that 4% of the population suffers from depression, including 5.9% of adults aged 70 years or older. Approximately 332 million people worldwide are affected by depression. In 2021, an estimated 727,000 people died by suicide.

MDD affects men and women differently. Women are twice as likely as men to develop MDD over the course of their lifetime [113] and are more likely to experience recurrent MDD [114]. Moreover, women and men, among other differences, respond differently to antidepressant treatment, particularly pharmacological therapies [115].

MDD is characterized by high negative affectivity and reduced positive affectivity, and these emotional abnormalities can be partly attributed to emotion dysregulation [116].

An association between MDD and P-gp has been identified. This correlation is due to polymorphisms of the ABCB1 gene, among which the most relevant are single nucleotide polymorphisms (SNPs) at C3435T, G2677T, and C1236. In a study conducted on a Japanese population sample (62 patients and 160 controls), associations between functional ABCB1 polymorphisms and mood disorders, including depression, were reported [117]. This hypothesis was further confirmed by another study conducted on a Japanese cohort. The results suggest that the C3435T polymorphism (one of the functional ABCB1 polymorphisms) plays an important role in the development of major depressive disorder [118].

P-gp also plays an important role in the bioavailability of antidepressants in the CNS. P-gp may lead to insufficient intracerebral concentrations of these drugs and to a poor therapeutic response [119,120]. The three ABCB1 SNPs C3435T, G2677T, and C1236T have been controversially associated with substrates of selective serotonin reuptake inhibitors (SSRIs) and with dose and response to serotonin–norepinephrine reuptake inhibitors (SNRIs) for MDD [118,121–124]. Hui Hua Chang et al. also demonstrated that ABCB1 polymorphisms can influence short-term antidepressant response in patients with MDD, without affecting cortisol levels before and after antidepressant treatment [125].

2.2.4. Role of P-gp in Other Diseases

The P-gp is also involved in the etiopathology of other CNS disorders such as HD. Kao Y.H. et al. demonstrated that the expression of P-gp is upregulated in cerebral capillaries in the cerebral cortex and striatum of human patients with HD; in particular, P-gp expression in the cortex increased with the progression of the disease, and P-gp mRNA levels were higher in a later stage of the disease [126]. The P-gp is also involved in other conditions such as Schizophrenia [127].

2.3. P-gp and Multidrug Resistance (MDR)

MDR is responsible for over 90% of deaths among cancer patients receiving traditional chemotherapeutic agents or new targeted drugs [128]. MDR is the cellular mechanism through which tumor cells develop resistance to various structurally and mechanistically unrelated chemotherapeutic drugs. It can manifest through various mechanisms, with the primary one being the overexpression of P-glycoprotein [129]. It mediates MDR in many tumors such as breast cancer, lung cancer, human colorectal cancer, ovarian cancer, and others. Its expression confers high resistance to chemotherapeutic drugs such as taxanes (Paclitaxel), vinca alkaloids, anthracyclines and camptothecins [130]. The P-gp expels a wide variety of drugs from tumor cells, leading to a decrease in intracellular drug concentration and the MDR phenotype; thus, it limits the therapeutic effect, resulting in low bioavailability [131]. Pettersson M. et al. demonstrated that drugs with a higher molecular weight have a lower risk of efflux by P-gp; specifically, efflux pumps do not affect macromolecules like proteins because they are too large to be expelled [132]. Regarding methodologies to reverse MDR, the strategy of molecular-level P-gp downregulation has proven to be less effective compared to blocking P-gp efflux function. It has been hypothesized that inhibiting P-gp efflux function could represent a potential therapeutic strategy to overcome MDR. Although it has been shown that numerous P-gp inhibitors significantly enhance the efficacy of some antitumor drugs in MDR tumor cells in vitro and *in vivo*, no P-gp inhibitor has been approved for clinical use [133].

2.4. PET Imaging and the Importance of P-gp

PET imaging of P-gp function was first demonstrated in 1998 using verapamil labeled with ^{11}C. The basic idea when using labeled P-gp substrates as PET tracers is that a low brain concentration suggests efficient P-gp function, while a high concentration indicates less efficient P-gp function [134]. Many studies demonstrate that P-gp activity/expression can correlate with the early onset of not only CNS diseases, but also with other pathologies such as chemo-resistant tumors, and HIV encephalopathy [135]. By using radiolabeled P-gp substrates, the contribution of P-gp to the pharmacokinetics of drugs *in vivo* can also be studied. Increased brain uptake in animals or humans of the radiolabeled drug after pre-treatment of a modulator indicates drug transport mediated by P-gp. Increased brain absorption of the drug under examination in P-gp knockout mice compared to wild-type mice can also prove that the drug under examination is actively expelled from the brain [136]. Radiotracers for P-gp measurements are typically administered intravenously. Since the distribution of the PET radiotracer in the brain depends on the arterial concentration entering the brain, arterial blood is also sampled. Once the radioactivity concentration in the brain measure by the PET scan and arteries is obtained, quantification of the data can be performed using two different approaches. Calculated kinetic parameters reflect P-gp function at the BBB. These approaches are called NON-COMPARTMENTAL METHODS and COMPARTMENTAL METHODS [137].

2.5. Current State of PET Radiotracers Targeting the P-gp

The main radiotracers currently used are [^{11}C]Verapamil and (*R*)-[^{11}C]Verapamil, [^{11}C]Loperamide and [^{11}C]-*N*-desmethyl-loperamide, [^{11}C]Metoclopramide and [^{18}F]MC225 (Figure 2.2), a radiotracer developed in an academic setting and currently in Phase II clinical trials.

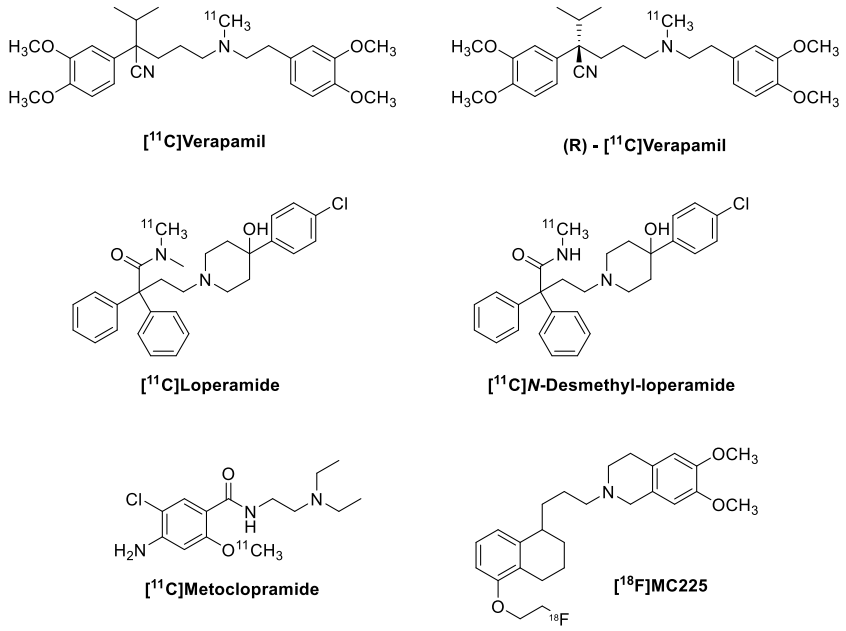

Figure 2.2. Structures of the main radiotracers.

2.5.1. [^{11}C]Verapamil and (*R*)-[^{11}C]Verapamil

Verapamil is a voltage-dependent calcium channel antagonist used to treat hypertension, angina pectoris, and supraventricular tachycardia. It is also the oldest tracer developed for PET imaging of P-gp in humans, and thus has been the subject of the largest number of clinical studies. Verapamil is a P-gp substrate, but at the microdoses used for PET imaging, [^{11}C]Verapamil acts as a strong P-gp substrate [138,139]. [^{11}C]Verapamil has been used to measure P-gp function at BBB *in vivo* based on the fact that its penetration into the brain reflects P-gp function, specifically measuring the decrease in P-gp function as an increase in tissue radioactivity uptake. Using this radioligand, possible changes in P-gp function have been suggested in neurological disorders such as PD, AD, or epilepsy [140,141]. [^{11}C]Verapamil was initially used as a racemic mixture, but it was later discovered that enantiomerically pure (*R*)-[^{11}C]Verapamil is preferable for the kinetic modeling of PET data due to differences in metabolism and plasma protein binding between (*R*)- and (*S*)-Verapamil [142]. Verapamil works a calcium channel blocker in both its enantiomers. Nevertheless, the S-enantiomer displays a much greater efficiency as a blocker, namely, around 10 times more. On the other hand, the R enantiomer is preferably used as a P-gp radiotracer because it acts as a stronger substrate for this protein [143]. Luurtsema G. et al. demonstrated the pharmacodynamic profiles of both Verapamil enantiomers in several animal models, showing that, despite the fact that both enantiomers are P-gp substrates, the R enantiomer is a safer PET tracer for measuring P-gp function *in vivo* [144,145].

2.5.1.1. Metabolism and Kinetic Evaluation of [^{11}C]Verapamil and (*R*)-[^{11}C]Verapamil

Verapamil's main metabolic pathways include *N*-dealkylation (producing **D-617** and **D-717**), *N*-demethylation (producing norverapamil and formaldehyde), and *O*-demethylation (producing **D-703** and **D-702**). The metabolites obtained from *N*-dealkylation are **[^{11}C]D-617** and **[^{11}C]D-717**, and from *O*-demethylation, **[^{11}C]D-702** and **[^{11}C]D-703**, as shown in Figure 2.3. Additionally, small-labeled carbon fragments are formed. It is predicted that [^{11}C]Formaldehyde is the main metabolite, which can be further converted into many other metabolites and eventually into [^{11}C]CO_2. A schematic representation of the main metabolites is shown in Figure 2.3. Thus, the study by Verbeek J. et al. highlights how these [^{11}C]-labeled metabolites may contribute to the measured PET signal. In particular, [^{11}C]D-617 is a P-gp substrate with similar brain kinetics to (*R*)-[^{11}C]Verapamil under basal conditions. P-gp inhibition led to a much smaller increase in brain uptake of **[^{11}C]D-617**, suggesting a lower affinity for P-gp compared to (*R*)-[^{11}C]Verapamil. In contrast, the study conducted by Luurtsema G. et al. shows that aside from [^{11}C] polar metabolites, no other [^{11}C] metabolites of verapamil (such as **[^{11}C]D-617** or **[^{11}C]D-703**) were detected in the rat brain. The formation of [^{11}C] polar metabolites, such as formaldehyde, could lead to levels of [^{11}C] in the brain that are not mediated by P-gp. This could influence the measurements of BBB P-gp function [146–148]. Ikoma Y. et al. conducted a quantitative analysis of [^{11}C]Verapamil transfer from plasma to the brain of healthy volunteers, showing that the amount of not metabolized [^{11}C]Verapamil was approximately 94% at 7 min, 83% at 12 min, 55% at 30 min, and 35% at 60 min. This study also demonstrates that the existence of metabolites modifies BBB permeation, and it suggests the possibility that metabolites contribute to the measured activity [149]. Currently, the preferred model for the kinetic analysis of (*R*)-[^{11}C]Verapamil is a single-input model with a single tissue compartment, using the sum of (*R*)-[^{11}C]Verapamil and *N*-dealkylation metabolites in the plasma as the input function, with V_d serving as a surrogate marker for P-gp function. This model represents the optimal compromise between fit accuracy, precision, and biological plausibility [147].

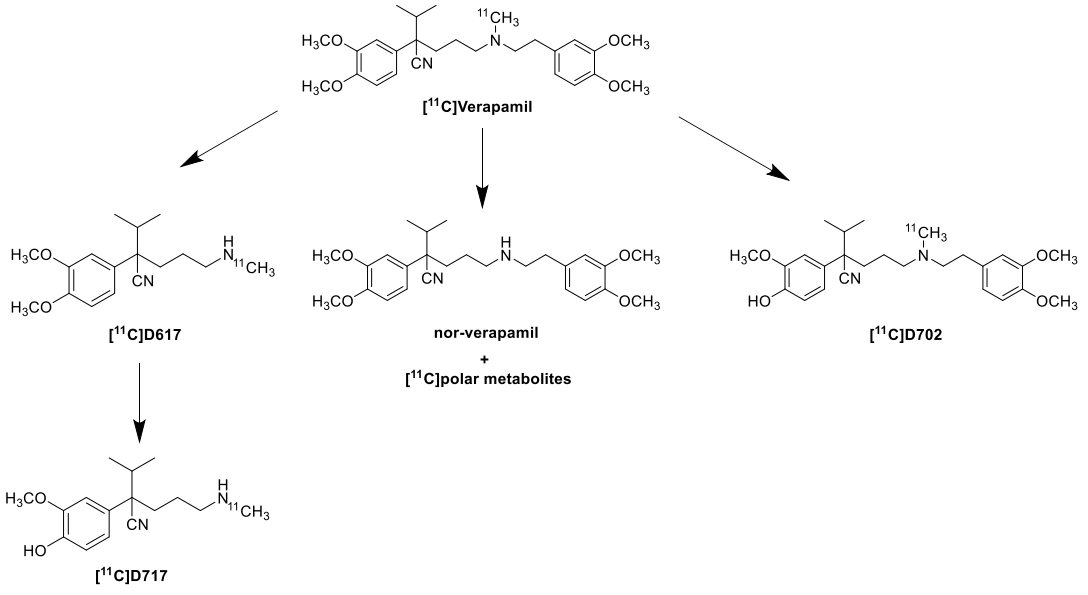

Figure 2.3. Structure of [^{11}C]Verapamil and its major metabolites [146].

This was demonstrated in a study conducted by Lee Y. J. et al. After intravenous administration of [^{11}C]Verapamil, rapid distribution in the brain was observed for a short period, followed by slow elimination. In order to demonstrate the specific binding of the radiotracer to the P-gp site, two groups are compared by measuring the area under the curve$_{cereb}$ (AUC_{cereb}) and $C_{max\ cereb}$; in fact, one of the groups is pre-treated with PSC833 and it shows a stark increase in the values of AUC_{cereb} and $C_{max\ cereb}$ compared to the control group that was not pre-treated [150].

CsA also strongly influences the time-dependent brain uptake of [^{11}C]Verapamil. The combined use of [^{11}C]Verapamil and CsA, respectively, as a P-gp substrate and inhibitor, would be ideal for non-invasive measurement of P-gp transport across the human BBB [151]. The time–activity curves of [^{11}C]Verapamil showed a peak 15 min after injection of [^{11}C]Verapamil, both in the presence and absence of CsA. Both the PSC833 and CsA assays are useful to measure the kinetic profile of [^{11}C]Verapamil as P-gp substrates in vivo at the BBB for quantitatively evaluating P-gp function at the BBB [152–154]. Verapamil shows largely linear PK in plasma and brain at both microdoses and therapeutic doses. It was also found that PET tracers administered at therapeutic doses are metabolized more slowly than at microdose levels [152]. Toornvliet R. et al. conducted a pilot study to assess the role of aging on P-gp function at the BBB using (*R*)-[^{11}C]Verapamil and PET in healthy volunteers [155]. This pilot study shows that the V_d of the specific P-gp substrate (*R*)-[^{11}C]Verapamil in the brain is higher in healthy elderly volunteers compared to healthy young volunteers. Therefore, during aging, the V_d of (*R*)-[^{11}C]Verapamil in the brain increases, which may be associated with BBB dysfunction [156].

2.5.1.2. Fluorinated Verapamil Analogues

One of the problems with [^{11}C]Verapamil, which has led to its slow decline in use over the years, is the short half-life of ^{11}C (20 min) [157]. For this reason, Raaphorst R. M. et al. developed fluorinated analogs such as (*R*)-*N*-[^{18}F]fluoroethylverapamil (**[^{18}F]1**) and (*R*)-*O*-[^{18}F]fluoroethylnorverapamil (**[^{18}F]2**, Figure 2.4), which could be radiolabeled with ^{18}F. **(*R*)-*O*-[^{18}F]2** is more specific for P-gp, despite its rapid metabolism, as well as a poor low metabolic stability [158]. Raaphorst R. M. et al. improved metabolic stability by incorporating deuterium into the tracer molecule. Additionally, greater metabolic stability was observed in methyl-containing analogs **[^{18}F]3-d$_3$** and **[^{18}F]3-d$_7$** (Figure 2.4), which could result from steric hindrance of enzymatic metabolism. **[^{18}F]3-d$_7$** thus showed similar *in vivo* behavior to (*R*)-[^{11}C]Verapamil but with greater metabolic stability [159]. [^{11}C]Verapamil and PET have been used for a long time in *in vivo* studies and human studies to investigate P-gp and the changes that substrates and inhibitors provoke on it [140,160,161].

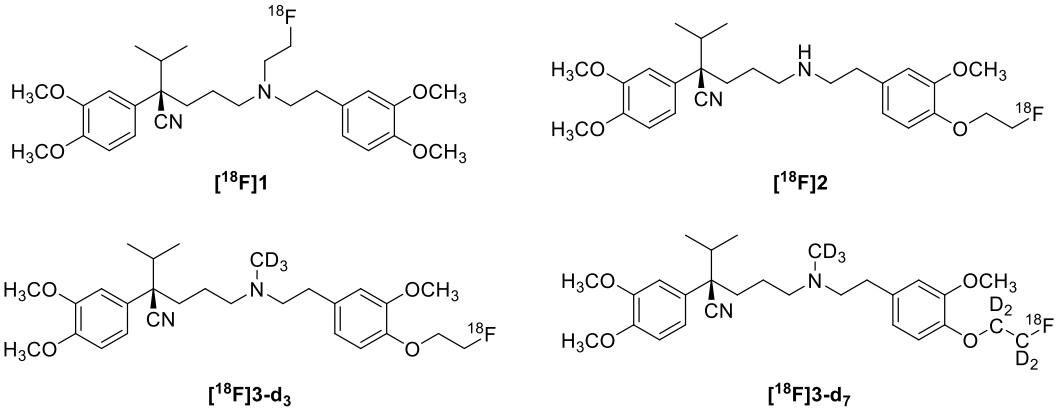

Figure 2.4. Structure of ^{18}F-derivatives of verapamil [158,159].

2.5.2. [^{11}C]Loperamide and [^{11}C]-*N*-Desmethyl-Loperamide

Loperamide and its metabolite *N*-desmethyl-loperamide are potent substrates of P-gp at the BBB, but [^{11}C]-*N*-desmethyl-loperamide ([^{11}C]dLop) is used as a PET radiotracer for imaging P-gp [162,163]. In a study conducted on human hepatic microsomes, it was observed that loperamide undergoes *N*-demethylation catalyzed by multiple cytochrome P450 isoforms, such as CYP2B6, CYP2C8, CYP2D6, and especially CYP3A4 [164]. The co-administration of ketoconazole (an inhibitor of CYP3A4) was partially effective in reducing the metabolism of [^{11}C]Loperamide without showing any appreciable effect on the brain accumulation of [^{11}C]dLop [165]. Zoghbi S. S. et al. demonstrated through in vivo and *ex vivo* studies conducted on wild-type and P-gp knockout mice that [^{11}C]dLop is a better radiotracer than [^{11}C]Loperamide for assessing P-gp function at the BBB, as the former has one fewer contaminating radiometabolite and thus better metabolic stability. Moreover, [^{11}C]dLop presents [^{11}C]CO_2 as its final radiometabolite, which has minimal penetration into the brain [151,166,167]. dLop shows a pK_a of 7.3 [168]; therefore, it is a weak base. This allows for the passive diffusion and subsequent protonation of dLop in acidic environments, such as lysosomes, excluding mitochondria [169].

Liow-San Liowsulle J.-S. et al. analyzed the biodistribution of [^{11}C]dLop in the whole body in monkeys. The highest accumulation of radioactivity was found in the liver, lungs, and kidneys. Despite the high accumulation in the kidneys, little radioactivity was excreted through urine. Instead, most of the radioactivity was likely excreted from the liver into the gastrointestinal tract. Following demethylation, [^{11}C]dLop may be exhaled as [^{11}C]CO_2 [170]. Regarding plasma protein binding, no differences were found in that of [^{11}C]-*N*-desmethyl-loperamide between mice and humans, unlike (*R*)-[^{11}C]Verapamil, for which small but significant differences in the percentages of unbound (*R*)-[^{11}C]Verapamil were observed [171]. Kannan P. et al. demonstrated that dLop acts as a P-gp inhibitor at high concentrations, whereas it behaves as a substrate at low concentrations, making the activity of dLop concentration-dependent. The *in vivo* results displayed that dLop is interesting only at low concentrations because it is a competitive substrate for P-gp [172].

Through a study conducted on WT and KO mice and WT mice pre-treated with cyclosporine, it emerged that the duration of the scan could play an important role in determining the kinetic parameters in the kinetic model. It has been demonstrated that 2 min after the administration of dLop, passive diffusion is the prevalent mechanism [173].

Farwell M. D. et al. studied P-gp activity with [^{11}C]dLop in rat brains. These studies were carried out by pre-treating one group with CsA or Tariquidar (TQ) and leaving the other group untreated. CsA and TQ act as P-gp inhibitors; therefore, a higher uptake of [^{11}C]dLop is observed [174]. The regional cerebral radioactivity uptake after intravenous administration of [^{11}C]dLop, following various doses of DCPQ (0–16 mg/kg, iv), was measured in a monkey. It was found to increase almost linearly with the dose of DCPQ. This strongly indicates that [^{11}C]dLop is sensitive to the degree of P-gp blockade in the brain. [^{11}C]dLop has thus proven to be a strong substrate for brain P-gp in both mice and monkeys, as is [^{11}C]Lop [168]. Kreisl W. C. et al. examined the ability of [^{11}C]dLop to quantify P-gp function in humans after increasing doses of Tariquidar, highlighting that P-gp function can be quantified from a simple measure of brain uptake ($AUC_{10–30}$) or from the brain influx rate constant (K1), both of which are strongly correlated. However, the single-pass extraction fraction (E) of [^{11}C]dLop is sufficiently high that both AUC_{10-30} and K1 should be corrected for regional cerebral blood flow to separately measure the effects of permeability from those of drug administration [173,175]. The baseline $AUC_{10–30}$ value found by Kreisl W. C. et al. [175] in humans was similar to the $AUC_{10–30}$ value measured in baboons by Damont A. et al. (2.94 ± 0.66 SUV·min vs. 3.2 ± 0.5, respectively) [176]. The concomitant administration of the radiotracer allows for the use of lower doses of Tariquidar while producing a similar degree of P-gp inhibition. This method also reduces the amount of time needed to administer Tariquidar and perform the PET scan with [^{11}C]dLop [177]. [^{11}C]Lop has also been used to investigate P-gp modulation induced by antiepileptic drugs (AEDs) at the BBB, observing a small difference in [^{11}C]dLop uptake after pretreatment with AEDs compared to treatment with cyclosporine [173]. In conclusion, [^{11}C]-*N*-desmethyl-loperamide, like (*R*)-[^{11}C]Verapamil, is not a highly sensitive radiopharmaceutical for detecting small (<50%) changes in P-gp expression/function at the BBB when used without the administration of a P-gp inhibitor [171].

2.5.3. [^{11}C]Metoclopramide

Metoclopramide is an antiemetic and gastroprokinetic drug that acts as an antagonist of D_2 receptors. [^{11}C]Metoclopramide, on the other hand, is used as a PET radiotracer to measure P-gp function. It is a weak substrate of P-gp, showing significantly higher brain uptake under conditions of full P-gp functionality compared to previously described avid substrates such as [^{11}C]Verapamil or [^{11}C]dLop. Consequently, [^{11}C]Metoclopramide has better sensitivity for detecting moderate changes in P-gp function at the BBB level compared to avid substrates [178]. Metoclopramide is metabolized by the CYP450 superfamily, particularly by the CYP3A4 and CYP2D6 isoforms. The main metabolites formed are **M3** (a deethylation product) and **M4** (a monooxygenation product), the latter being formed in the form of three different isomers. It has been shown that metoclopramide does not act as an inactivator of CYP2D6 [179]. However, Breuil L. et al. demonstrated that the induction of CYP with CBZ and the inhibition of CYP with RIT have a negligible impact on the plasma kinetics of [^{11}C]Metoclopramide in rats. This supports the use of [^{11}C]Metoclopramide as a PET probe for P-gp function at the BBB in situations where concomitant pharmacological treatment cannot be avoided [180]. The metabolism of metoclopramide can also be regulated independently of the intrinsic activity of metabolizing enzymes. Specifically, saturable transport mediated by a transporter on the sinusoidal plasma membrane of the liver was found to be essential for hepatic clearance, metabolism, and pharmacokinetics of metoclopramide [181]. Pottier G. et al. demonstrated, through studies on rats, that co-injecting [^{11}C]Metoclopramide with non-labeled

metoclopramide at its pharmacological dose (2 mg/kg) slows down the peripheral metabolism of the radiotracer while maintaining its ability to measure P-gp activity in the brain [182]. Alcohol exposure, on the other hand, had no impact on plasma concentrations, metabolism, protein binding, or brain kinetics of [^{11}C]Metoclopramide [183]. From a kinetic perspective, Auvity S. et al. sought simplified parameters for the quantitative estimation of P-gp's role in the brain kinetics of the radiotracer. In fact, $AUC_{30–60}$ min was determined to be a better parameter that displays the impact of P-gp on the overall brain exposure to [^{11}C]Metoclopramide without the need for an arterial input function [184]. The effect of an inhibitor on the kinetics of [^{11}C]Metoclopramide was studied both in NHP and humans, using Tariquidar in the former and CsA in the latter. In both cases, P-gp inhibition led to a significant increase in the V_T of [^{11}C]Metoclopramide. Pharmacokinetic modeling was performed in both cases to rationalize the V_T increase, using the 1-TCM model for NHP and the 1T2K model for humans. An increase in K1 (28.5% vs. 9%) and a concomitant decrease in K2 (36% vs. 15%) emerged [184,185]. Unlike avid P-gp substrates, [^{11}C]Metoclopramide shows rapid and substantial initial brain uptake followed by rapid metabolism and elimination from plasma; therefore, the later part of the cerebral PET signal, which is mainly represented by unmetabolized [^{11}C]Metoclopramide, allows for reliable calculation of $k_{E,brain}$. The advantage of $k_{E,brain}$ over cerebral V_T, which is considered the gold standard for measuring P-gp function, is that it is calculated solely from dynamic cerebral PET data and does not require an arterial input function. However, $k_{E,brain}$ is less sensitive than V_T in detecting maximum P-gp inhibition at the BBB [186]. The feasibility and relevance of $k_{E,brain}$ of [^{11}C]Metoclopramide have been evaluated in rats, non-human primates (NHPs) and humans, showing that $k_{E,brain}$ has adequate sensitivity to measure the impact of pharmacological inhibition of P-gp at the BBB. Given the substantial differences in BBB permeation and peripheral clearance of [^{11}C]Metoclopramide between rats, NHP, and humans, $k_{E,brain}$ values cannot be used to compare P-gp function across species. The main limitation of using $k_{E,brain}$ is that this quantification method cannot be applied to other P-gp radiolabeled substrates that do not share the advantageous pharmacokinetic properties of [^{11}C]Metoclopramide [186,187]. Bauer M. et al. studied *in vivo* the biodistribution of [^{11}C]Metoclopramide in healthy males and females. The results demonstrated that the majority of the radiotracer was accumulated in the liver, with a minimal part of the radiotracer quickly excreted in urine, with very little difference between the male and female volunteers [188]. Apart from a slight accumulation in the basal ganglia (BG), the distribution across different brain regions was quite homogeneous; thus, no predominant accumulation was observed in regions rich in D2 dopamine receptors, such as the striatum [184,185]. In mice, it was demonstrated that the renal and hepatic uptake of [^{11}C]Metoclopramide is partially mediated by transport through OCT1 and OCT2, while MATE transporters contributed to the urinary excretion of [^{11}C]Metoclopramide and its radiolabeled metabolites [189]. As demonstrated by Bauer M. et al., [188] age-related differences in brain exposure to [^{11}C]Metoclopramide were not caused by differences in the peripheral disposition of [^{11}C]Metoclopramide, and reduced clearance of metoclopramide from the brain in elderly subjects may be related to an age-dependent decline in cerebral P-gp.

Mairinger S. et al. evaluated in rats how pulmonary P-gp was affected by exposure to [^{11}C]Metoclopramide (aerosolized model), showing a different behavior compared to other previously studied avid substrates such as (*R*)-[^{11}C]Verapamil and [^{11}C]dLop. Unlike (*R*)-[^{11}C]Verapamil and [^{11}C]dLop, the absence of P-gp activity led to an increase, rather than a decrease, in pulmonary exposure to [^{11}C]Metoclopramide

[88,188,189]. Over the years, [^{11}C]Metoclopramide has also been used to assess both the immediate and delayed impact of BBB disruption induced by focused ultrasound with microbubbles [190]; furthermore, it was used to evaluate the effect of treatment with St. John's Wort extract (SJW) with a high hyperforin content on central and peripheral P-gp activity, as well as peripheral CYP activity, in healthy volunteers [191].

2.5.4. [^{18}F]MC225

[^{18}F]MC225 is a weak P-gp substrate used as a PET tracer for imaging P-gp function in the BBB. This tracer exhibits higher baseline brain uptake, allowing for measurement of both increases and decreases in P-gp function. *In vivo*, **[^{18}F]MC225** has demonstrated good pharmacokinetic properties, a suitable signal-to-noise ratio, high sensitivity towards the target, and low levels of radiometabolites in the brain [192]. It is selective for P-gp, as additional inhibition of Bcrp had a negligible effect on the tracer's brain uptake, as shown by Savolainen et al. [193]. The primary advantage of **[^{18}F]MC225** over [^{11}C]Verapamil is its greater metabolic stability and lower number of metabolites in the brain. Over 96% of the parent radiopharmaceutical **[^{18}F]MC225** remained intact in the brain after 45 min, while radioactive metabolites constituted only 11–24% of total brain radioactivity at 60 min post-injection, compared to over 50% for [^{11}C]Verapamil. The main metabolites of **[^{18}F]MC225** are products of defluoroethylation and demethylation. The [^{18}F]fluoroethane/ethanol formed can likely enter the brain, but the fraction of metabolites observed in the brain after the PET scan was found to be small [194,195]. Garcia-Valera L. et al. studied different kinetic models of **[^{18}F]MC225** in NHP to assess P-gp function across varying scan durations. For short-duration scans, the 1-TCM model was preferred, with K1 being the best parameter for estimating P-gp function. For long-duration scans (>60 min), the 2-TCM model was preferred, where both K1 and V_T could be used to estimate P-gp function at the BBB [196]. **[^{18}F]MC225** has been compared to (*R*)-[^{11}C]Verapamil to determine the best pharmacokinetic parameters to evaluate P-gp interactions for both radioligands. The main difference was the K2 value, which decreased for (*R*)-[^{11}C]Verapamil, but remained unchanged for **[^{18}F]MC225**, in the presence of an inhibitor. In addition, low baseline V_T values of (*R*)-[^{11}C]Verapamil could hinder the quantification of increases in P-gp function, which are associated with further decreases in V_T. This limitation is not present with **[^{18}F]MC225**, making it suitable for measuring increases in P-gp function [196–198]. The difference in V_T between **[^{18}F]MC225** and [^{11}C]Verapamil was also observed in a healthy human subject under both unblocked and blocked P-gp states, with blocking achieved via intravenous infusion of the specific P-gp inhibitor cyclosporine (2.5 mg/kg/h) starting 30 min before the scan. V_T in gray matter increased from 4.38 at baseline to 5.48 after cyclosporine administration, significantly higher than the V_T values previously reported for [^{11}C]Verapamil (1.28 at baseline, 2.00 after P-gp inhibition), verifying **[^{18}F]MC225** as a promising tracer for measuring BBB P-gp function in humans [199,200]. The direct comparison between **[^{18}F]MC225** and (*R*)-[^{11}C]Verapamil led to an initial evaluation of **[^{18}F]MC225** in human subjects as a Phase I study. Toyohara J. et al. validated the radiosynthesis process of **[^{18}F]MC225**, assessing preclinical toxicity and radiation dosimetry based on distribution data in mice. Preclinical toxicology studies indicated that **[^{18}F]MC225** showed acceptable pharmacological safety at tracer concentrations required for adequate PET imaging. Regarding radiation dosimetry, a single intravenous injection of 185 MBq of **[^{18}F]MC225** resulted in an estimated effective dose of 2.9 mSv (with voiding 360 min post-injection) and 3.1 mSv (without voiding), well within the acceptable radiation dose

limits for PET imaging. Cardiovascular toxicity studies further indicated that the cardiovascular activity of **[^{18}F]MC225** is negligible at tissue concentrations sufficient for in vivo quantification of P-gp activity [201,202]. In the Phase I trial conducted by Toyohara et al. with eight healthy subjects, **[^{18}F]MC225** was well tolerated, with no clinically significant adverse pharmacological effects or safety signals observed. Differences in V_T were noted across individuals in gray matter and choroid plexus regions, with interindividual variability (CV) in V_T in the 1-TCM, 2-TCM, and Logan plot models being 26% ± 4%, while intraindividual differences were relatively small (CV of V_T was 11% ± 3%). These large interindividual variances may be due to differences in P-gp density and/or function [203]. Mossel P. et al. analyzed the pharmacokinetics of [^{18}F]**MC225** in healthy volunteers, identifying the 2T4K model as the most accurate for describing its brain kinetics and quantifying P-gp function at the BBB with VB as the model parameter. However, **[^{18}F]MC225** displayed relatively large test retest (TRT) variability (28%) for V_T, higher than the 9% reported for (*R*)-[^{11}C]Verapamil [204]. **[^{18}F]MC225** has also been used to study circadian modulation of P-gp function in the brain. P-gp activity showed daily rhythms independent of sleep, suggesting that it is modulated by circadian rhythms in neurotransmitters, cytokines, or hormones [205]. Furthermore, **[^{18}F]MC225** was tested for its effects on anesthetic exposure in rats, showing significant increases in K2 values and corresponding decreases in V_T after prior anesthesia exposure, without significant changes in K1 [206].

2.5.5. [^{11}C]-Labeled P-gp Inhibitors: Tariquidar, Elacridar, Laniquidar

Tariquidar, Elacridar, and Laniquidar are third-generation inhibitors with high affinity for P-gp. They also cause fewer pharmacokinetic and pharmacodynamic interactions because they only minimally interfere with the cytochrome P-450 system [207]. Bauer F. et al. labeled Tariquidar with carbon-11 to evaluate its ability to measure P-gp function in rats. [^{11}C]Tariquidar (Figure 2.5) does not exhibit selectivity towards P-gp as it also interacts specifically with BCRP at the BBB [208]. Dörner B. et al. labeled Elacridar with carbon-11, highlighting its ability to specifically bind to P-gp at the BBB. [^{11}C]Elacridar (Figure 2.5), analyzed *in vivo* 2h after the injection of unlabeled Elacridar, exhibited behavior comparable to (*R*)-[^{11}C]Verapamil in a similar study setup [209]. The derivative [^{18}F]Elacridar has also been developed, showing in vivo behavior similar to that of [^{11}C]Elacridar. However, the significant degree of defluorination observed with [^{18}F]Elacridar, along with low radiochemical yields, limited its subsequent use [210]. Compared to (*R*)-[^{11}C]Verapamil, [^{11}C]Elacridar and [^{11}C]Tariquidar exhibited greater metabolic stability. The K1 values of [^{11}C]Tariquidar and [^{11}C]Elacridar were up to 10 times lower than those of (*R*)-[^{11}C]Verapamil, suggesting that [^{11}C]Tariquidar and [11C]Elacridar were more effectively effluxed at the BBB than (*R*)-[^{11}C]Verapamil. The washout of [^{11}C]Tariquidar and [^{11}C]Elacridar from the brain was very slow [211]. The brain PET signal of [^{11}C]Elacridar and [^{11}C]Tariquidar was very low in rats, consistent with P-gp-mediated efflux transport. This limits the applicability of these tracers for visualizing brain P-gp density [212]. The tumor uptake of [^{11}C]Tariquidar and [^{11}C]Elacridar, on the other hand, demonstrated an absorption 2 to 3 times higher than the uptake in the brain, suggesting a better suitability of these radiotracers for tumor imaging rather than brain imaging [151]. The total body distribution of [^{11}C]Elacridar and [^{11}C]Tariquidar was studied in healthy men and women. They showed a high concentration of radioactivity in the liver, gallbladder, and intestines, with negligible concentration in the urinary bladder. This suggests that biliary excretion and possibly intestinal secretion are the primary elimination pathways

for these radiotracers [213]. A marked decrease in radioactivity excreted in bile was also observed, in both humans and mice, when a pharmacological dose of unlabeled Tariquidar was co-administered with the radiotracer, suggesting inhibition of canalicular efflux transport activity [213]. Laniquidar was also labeled with ^{11}C by Luurtsema G. et al., but initial preclinical studies on this tracer did not show the expected brain uptake. They highlighted that at PET doses, [^{11}C]Laniquidar (Figure 2.5) behaved as a substrate for P-gp rather than as an inhibitor [214]. [^{11}C]Laniquidar has a K2 close to zero, suggesting that the best model was a single-tissue compartment model with a single parameter (K1), for which 5 min of data collection was sufficient. However, [^{11}C]Laniquidar generates a high number of radioactive metabolites that cross the BBB; so, for the 60 min scan interval, it is better to use a kinetic model consisting of two parallel single-tissue compartment models, one for the parent [^{11}C]Laniquidar and the other for the labeled metabolites [215]. The biodistribution of [^{11}C]Laniquidar showed the highest uptake in the liver, followed by the spleen, kidneys, and lungs. In rats, the highest uptake was observed in the lungs, followed by the liver, spleen, and kidneys [216].

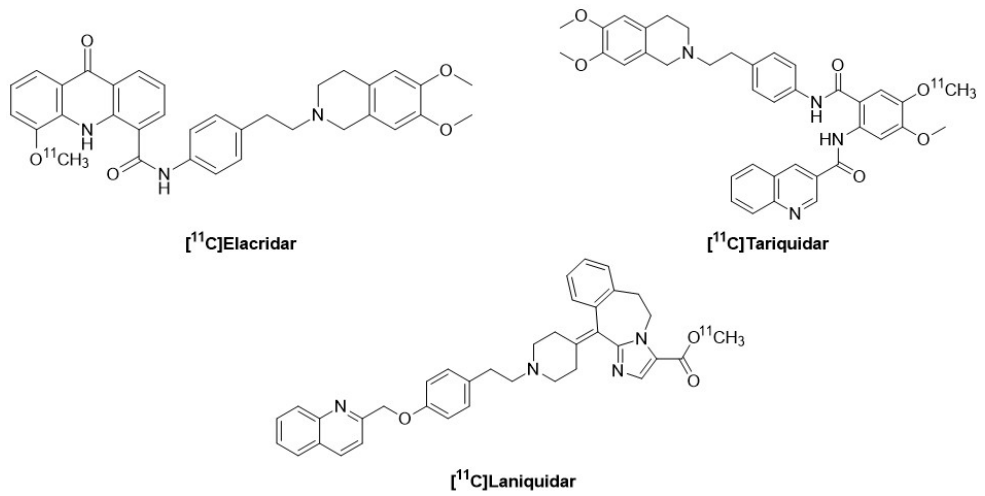

Figure 2.5. Structures of [^{11}C] labeled P-gp inhibitors: Tariquidar, Elacridar, Laniquidar.

2.6. Summary of the Introduction

The sensitivity of PET probes in detecting moderate changes in P-gp function at the BBB has been shown to be different among clinically validated radiolabeled substrates.

[^{11}C]Verapamil was the first radiotracer used for PET imaging of P-gp because it is a selective substrate for it, thus allowing for non-invasive detection. [^{11}C]Verapamil enables the study of P-gp function at the BBB, in normal conditions but also after treatment of inhibitors, and therapeutic drug interactions with P-gp. The racemic [^{11}C]Verapamil has been replaced by its *R*-enantiomer since it has been shown that, despite being transported equally by P-gp, it has a slower metabolism [144]. However, [^{11}C]Verapamil presents several disadvantages, including a rapid metabolism, which reduces the amount of available radiotracer in plasma, as well as being labeled with ^{11}C, which is not preferred for clinical use. Due to these drawbacks, despite still being considered the "gold standard", its use has progressively decreased in favor of better and more specific radiotracers. Among these are [^{11}C]Lop and its metabolite [^{11}C]dLop, which is a more specific substrate, as it does not interact with ion channels. The main advantage of [^{11}C]dLop is its reduced metabolism [166]. Overall, however, [^{11}C]dLop suffers from limitations similar to those of (*R*)-

[^{11}C]Verapamil, as the cerebral PET signal can be compromised by radiolabeled metabolites that are partially transported by P-gp. The baseline brain uptake of [^{11}C]-*N*-desmethyl-loperamide is about two times lower than that of (*R*)-[^{11}C]Verapamil, making it even more difficult to assess regional differences in cerebral P-gp function [155].

[^{11}C]Metoclopramide, in contrast to [^{11}C]Verapamil and [^{11}C]dLop, is a weak substrate for P-gp, allowing better penetration through the BBB even when P-gp is active. It also has a more predictable metabolism, with its metabolites not significantly interfering with PET imaging.

However, the PET radiotracer currently delivering the best results is **[^{18}F]MC225**. Like [^{11}C]Metoclopramide, it is a weak substrate, which is why it shows a higher uptake at the CNS level. Unlike the previously mentioned radiotracers, **[^{18}F]MC225** was designed as a specific substrate for P-gp, thus allowing greater specificity, sensitivity, and providing a more accurate and detailed image of P-gp activity, especially in the brain. **[^{18}F]MC225** also has reduced interaction with other transport proteins. Owing to these characteristics, **[^{18}F]MC225** is currently undergoing three different Phase II clinical trials.

2.7. Background and aim

As previously described, there isn't several PET radiotracer for the imaging of P-gp. Almost everyone used during the years are not born for the P-gp imaging but they were used for other utilities. In fact, verapamil is a calcium-antagonist currently uses for the treatment of hypertension; Loperamide is a weak agonist of oppiod recepters currently uses as antidiarrheal; Metoclopramide is a D2 receptor antagonist used for as antiemetic agent. Among then, only MC225 was drawn as candidate P-gp PET radiotracer.

[^{18}F]MC225 is a weak P-gp substrate and for this reason it can measure both the overexpression of P-gp and the reduced expression.

For this reason, **[^{18}F]MC225** is undergoing two different Phase II clinical trials: (i) [^{18}F]MC225-PET in Neurodegenerative Disease, EudraCT Number: 2021-005024-37 (The Netherlands); (ii) The impact of gender differences in P-glycoprotein function measured with **[^{18}F]MC225** and PET, EudraCT Number: 2022-003664-25 (The Netherlands).

Because several studies show an association between P-gp transporter overexpression and treatment-resistant depression **[^{18}F]MC225**, the aim of this part of PhD project was to synthesize the phenol precursor (**FM4/MC226**) and the corresponding cold compound (**FM5/MC225**) to obtain the AIFA approval to start a new Phase II clinical trial with the nuclear medicine department of the "Gemelli hospital" in Rome. The goal of this new clinical trial is investigate the correlation between P-gp and depression.

To obtain the AIFA approval, **FM4/MC226** and **FM5/MC225** have been syntetized following the Good Laboratory Practice (GLP) and the purity of **FM4/MC226** had to demonstrate by an accredited external laboratory. Furthermore it was also necessary to carry out stability studies on the precursor phenol.

However, nothing related to the ongoing clinical trial will be shown in this chapter because it is the property of the Gemelli Polyclinic.

2.8. Results

2.8.1. Chemistry

The synthesis of the phenolic precursor **FM4/MC226** was performed as previously described by García-Valera et al. [192], with minor modifications.

Commercially available 5-hydroxy-3,4-dihydronaphthalen-1(2*H*)-one was first alkylated under basic conditions using benzyl bromide (BnBr) to protect the phenolic function during subsequent steps, affording intermediate **FM1**. Subsequently, a Grignard reaction with magnesium and cyclopropyl bromide was carried out, followed by dehydration using AcOH/HBr (2:1), yielding intermediate **FM2** as a mixture of positional isomers. Intermediate **FM2** was then reacted with the basic moiety 6,7-dimethoxy-1,2,3,4-tetrahydroisoquinoline under basic conditions to obtain **FM3**, again as a mixture of positional isomers. **FM3** was subjected to catalytic hydrogenation using 10% Pd/C to reduce the double bond and simultaneously remove the benzyl protecting group, affording the final phenolic precursor **FM4/MC226**. To obtain the non-radioactive reference compound **FM5/MC225**, the phenolic group of **FM4** was alkylated with 1-fluoro-2-iodoethane under basic conditions.

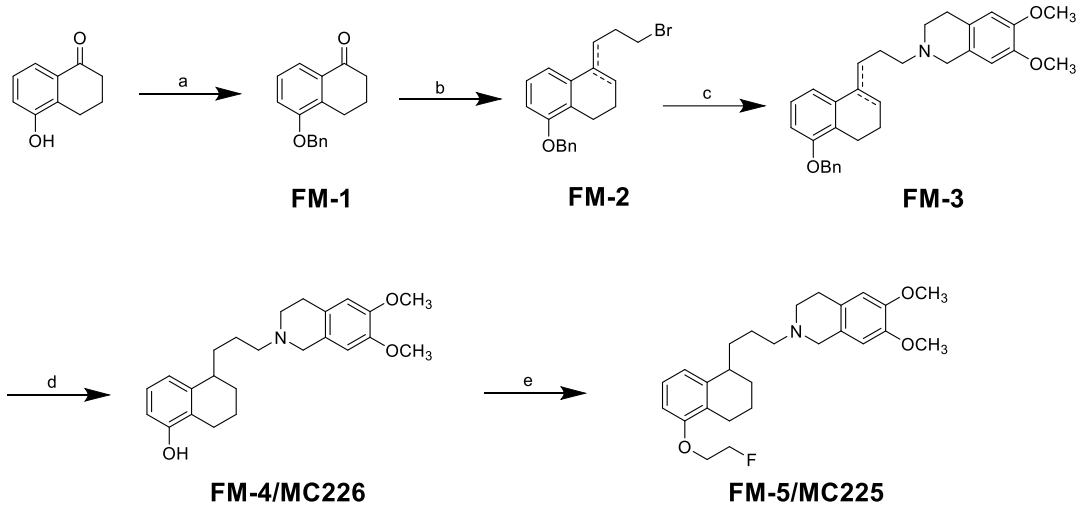

Scheme 2.1 Synthesis of phenol precursor **FM4/MC226** and cold compound **FM5/MC225**. (a) BnBr, K_2CO_3, CH_3CN, reflux, ON; (b) 1) Mg, cyclopropyl bromide, anhydrous THF, RT 4h to reflux ON; 2) AcOH/HBr 3N (2:1), RT, 2h; (c) 6,7-dimethoxy-1,2,3,4-tetrahydroisoquinoline, K_2CO_3, CH_3CN, reflux, ON; (d) Pd/C 10%, H_2, 4.5 bar, MeOH + EtOH 96%, RT, 72h; (f) 1-fluoro-2-iodoethane, K_2CO_3, acetone, reflux, ON.

2.9. Discussion

[^{18}F]MC225 is a PET radiotracer developed in the laboratory where this thesis was conducted and is currently being evaluated in two independent Phase II clinical trials in collaboration with the Department of Nuclear Medicine of the University of Groningen. These studies aim to investigate the potential application of this radiotracer in neurodegenerative disorders such as PD and AD (NCT05853471), as well as to assess the presence of gender-related differences in P-gp expression at the BBB level (NCT05618119).
In parallel, the phenol precursor **FM4/MC226** and the non-radioactive reference compound **FM5/MC225** were synthesized in order to obtain authorization from the Italian Medicines Agency (AIFA) to initiate an additional Phase II clinical trial, in collaboration with the Fondazione Policlinico Universitario Agostino Gemelli IRCCS in Rome, aimed at investigating the correlation between P-gp expression and depression.
FM4/MC226 and **FM5/MC225** were synthesized in three independent batches (202305FM401, 202403FM402, 202407FM403 for **FM4/MC226** and 202305FM501, 202403FM502, 202407FM503 for **FM5/MC225**). The yields obtained for each synthetic step were comparable among the different batches, demonstrating the robustness and reproducibility of the synthetic procedure.
For AIFA approval, it was mandatory to demonstrate the purity of the phenol precursor through analyses performed by an accredited external laboratory. **FM4/MC226** showed a purity >98%, which, according to current regulatory guidelines, made it unnecessary to identify and characterize the individual impurities present. The purity of **FM4/MC226** was assessed by UPLC and quantitative ^{1}H-NMR. In addition, **FM4/MC226** was shown to be free from biological contamination and from palladium residues on Carbone, the catalyst employed during the synthesis. Residual solvent (Toluene, CH_2Cl_2, CH_3OH) levels were also below the established regulatory limits (<5000 ppm), ensuring compliance with applicable legal requirements.
Approval also required the execution of stability studies at the same accredited external laboratory. **FM4/MC226** was found to be stable, although the corresponding data cannot be reported as they are proprietary and belong to the company Biofordrug.
On the basis of the submitted documentation, on 16/04/2025 **[^{18}F]MC225** received authorization from AIFA for a new Phase II clinical study entitled "*Evaluation of P-glycoprotein alterations in treatment-resistant depression: a **[^{18}F]MC225** PET study"* (CTIS ID: IN-1-43738). This clinical trial includes the enrollment of 30 depressive-responsive and 30 depressive-nonresponsive patients and is expected to be completed by April 2027.
The ^{18}F-radiolabeling of **MC225** was carried out at the Gemelli Polyclinic in Rome using a "two-step radiosynthesis". **[^{18}F]MC225** was obtained with a RCY ranging from 8.5% to 12.3% and radiochemical purity >99%
The radiosynthetic procedure employed, the formulation intended for human administration and the preliminary results obtained to date cannot be disclosed, as they are the property of Gemelli Hospital in Rome.

2.10. Other ongoing projects

Despite the impressive results obtained with **[^{18}F]MC225** over the years and the promising outcomes emerging from the ongoing clinical trial, research in this field is continuing.

During this doctoral work, structural modifications of **MC225** were also undertaken with the aim of developing a new PET radiotracer for P-gp characterized by reduced lipophilicity.

As the primary focus of this thesis chapter is the synthesis of **MC225** and its clinical implications, this section will briefly outline (i) the molecular design strategy, (ii) the main results obtained, and (iii) future perspectives. The experimental details are therefore not reported here. The full manuscript is currently under review in *ACS Omega*, entitled: *"From ^{18}F-MC225 to conformationally free derivatives: Potent and promising PET tracers to detect P-glycoprotein at the BBB with aryloxy-(thio)-alkyl fragment"* (Lisi A.T., Mastropasqua F. et al.).

The structural optimization strategy focused on increasing conformational flexibility and, above all, on introducing a heteroatom into the molecular scaffold (Figure 2.6). The incorporation of a heteroatom also enabled the removal of the chiral center present in **MC225**, thereby simplifying the molecular architecture.

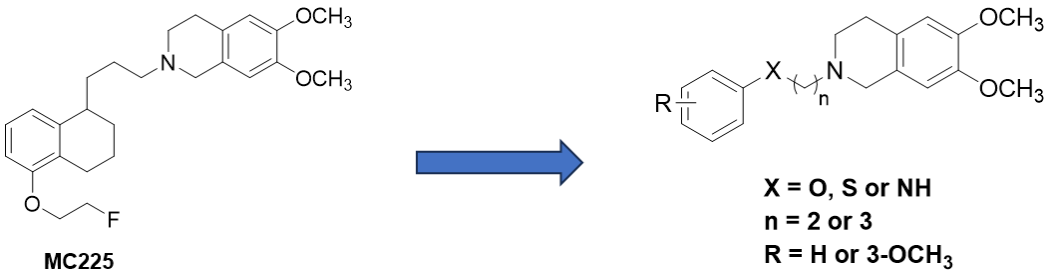

Figure 2.6. From **MC225** to new compounds targeting P-gp: general structure.

A structure–activity relationship (SAR) study was conducted to evaluate the impact of these modifications on P-gp activity, with the goal of identifying new lead compounds suitable for subsequent radiolabeling. A series of derivatives was synthesized and characterized, featuring a single unsubstituted or meta-substituted aromatic ring bearing a methoxy group. This aromatic moiety was linked to the 6,7-dimethoxytetrahydroisoquinoline core through a two- or three-carbon spacer. The connection between the aromatic ring and the linker was established via a heteroatom (O, S, or NH).

All synthesized compounds were evaluated for P-gp interaction using the calcein-AM assay, and their apparent permeability (P_{app}) and BA/AB ratios were determined in Caco-2 cell monolayers. The results, expressed as EC_{50} values, are summarized in Table 2.2.

Table 3.3. Evaluation of the BBB Permeability and P-gp Interaction.

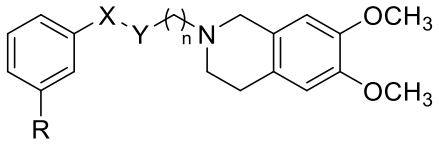

Compound	R	X	Y	n	P-gp activity, EC_{50} μM[a]	P_{app} (BA/AB)[b]
4	H	O	CH_2	2	7.5 ± 0.3	3.2 ± 0.2
5	H	O	CH_2	1	12.6 ± 0.40	3.9 ± 0.1
6 (ATL22)	OCH_3	O	CH_2	2	1.8 ± 0.3	4.7 ± 0.3
7	OCH_3	O	CH_2	1	5.3 ± 0.2	4.5 ± 0.2
8	H	S	CH_2	2	5.6 ± 0.2	3.1 ± 0.1
9	H	S	CH_2	1	8.0 ± 0.5	3.1 ± 0.2
10 (ATL30)	OCH_3	S	CH_2	2	3.3 ± 0.2	3.8 ± 0.4
11	OCH_3	S	CH_2	1	8.4 ± 0.4	3.7 ± 0.1
12	H	NH	CO	0	>100	3.3 ± 0.1
13	OCH_3	NH	CO	0	N.A.	4.5 ± 0.2
14	H	NH	CH_2	1	56.9 ± 1.5	3.8 ± 3
15	OCH_3	NH	CH_2	1	31.7 ± 2.1	4.0 ± 0.1
MC225					6.35	18

[a]The result was obtained by carrying out three independent assays , sample in triplicate; [b]The value has been calculated as mean of two independent experiments, sample in triplicate. N.A. = non active

Among the tested molecules, the most promising candidates were 6,7-dimethoxy-2-(3-(3-methoxyphenoxy)propyl)-1,2,3,4-tetrahydroisoquinoline (**6**, also known as **ATL22**; EC_{50} = 1.8 μM, Figure 2.7) and 6,7-dimethoxy-2-(3-((3-methoxyphenyl)thio)propyl)-1,2,3,4-tetrahydroisoquinoline (**10**, also known as **ATL30**; EC_{50} = 3.3 μM, Figure 2.7). Further in-depth computational studies supported these findings, confirming that **ATL22** and **ATL30** display the most favorable predicted interactions with P-gp (data not shown).

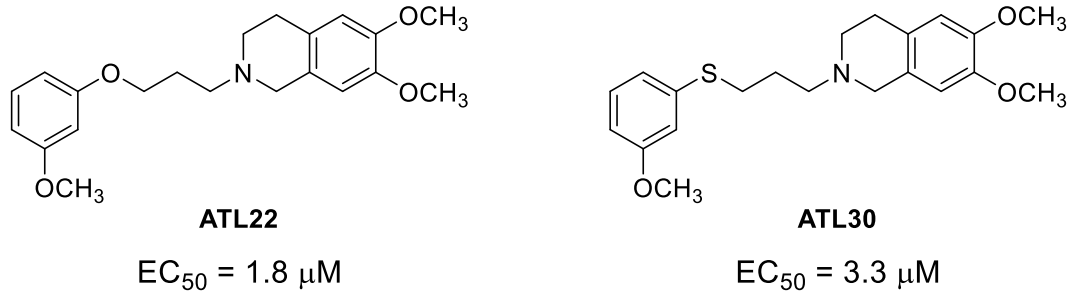

Figure 2.7. Chemical structure and pharmacodynamic profile of new lead compounds.

Starting from **MC225**, the SAR investigation led to the identification of **ATL22** as a new lead compound. **ATL22** will be radiolabeled with ^{11}C (Figure 2.8) in collaboration with the Gemelli Polyclinic. Encouraged by these results, we also synthesized the corresponding fluoroethoxy derivative. Although data regarding its P-gp activity and permeability are not yet available, we anticipate comparable or improved performance. If confirmed, this derivative will be radiolabeled with ^{18}F (Figure 2.8), again in collaboration with the

Gemelli Polyclinic, to enable *in vivo* comparison between the methoxy and fluoroethoxy analogues and to obtain a radiotracer with a longer half-life.

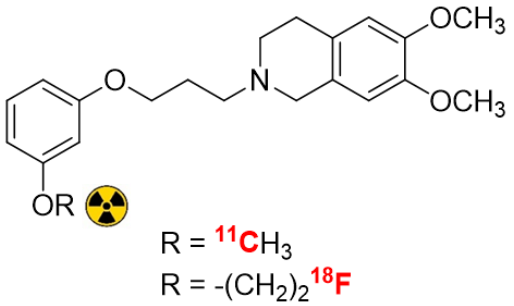

Figure 2.8. Future Perspectives: Radiolabeling with ^{11}C and/or ^{18}F

2.11. Conclusions

[^{18}F]MC225 has received approval from the AIFA for a new Phase II clinical trial, conducted in collaboration with the Fondazione Policlinico Universitario Agostino Gemelli IRCCS in Rome, aimed at investigating the correlation between P-gp expression and depression. Although the human studies are still ongoing, the first qualitative results are highly promising.

Building on **MC225** and informed by SAR studies, a new series of compounds was synthesized in order to have new PET radiotracers for P-gp. Among the tested molecules, compound **ATL30** and, in particular, compound **ATL22** emerged as new lead candidates, suitable for further radiolabeling with both ^{11}C and ^{18}F.

2.12. Materials and Methods

2.12.1. Chemistry

The companies from which the reagents and solvents were purchased, together with their CAS numbers, lot numbers, product codes, purity specifications, and the specific synthetic steps in which they were used, are reported in Table 2.3. This detailed documentation is required by the AIFA to obtain authorization for the Phase II clinical study. Thin layer chromatography (TLC) was performed using plates from Merck (silica gel 60 F_{254}). Column chromatography was performed with Merck silica gel 60 Å (63-200 mm; ratio of crude mixture to silica gel 1:30 w/w, unless otherwise stated) as the stationary phase. ^{1}H-NMR spectra were recorded in the indicated solvent on a Varian Mercury-VX spectrometer (300 MHz) or on an Agilent 500-vnmrs500 spectrometer (499.801MHz). The following data are reported: chemical shift (δ) in ppm, multiplicity (s = singlet, d = doublet, t = triplet, q = quartet, quint = quintet, m = multiplet, dd = doublet of doublets, dt = doublet of triplets, td = triplet of doublets, and br = broad signal), integration, and coupling constant (J) in hertz. Recording of mass spectra was done on an HP6890-5973 MSD gas chromatograph/mass spectrometer; only significant m/z peaks, with their percentage of relative intensity in parentheses, are reported. HRMS-ESI analyses were performed on a Bruker Daltonics MicrOTOF-Q II mass spectrometer. All spectra were in accordance with the assigned structures.

Table 2.3. Complete description of all reagents and solvents used in the synthesis of **FM4/MC226**.

Material	CAS RN	Synthetic step of use	Purity	Code	Company	Lot N°
5-hydroxy-1-tetralone	28315-93-7	**FM1**	>99%	H0614	TCI	P27TC-NN
Benzyl bromide	100-39-0	**FM1**	>98%	B0411	TCI	PVMTC-CJ
K_2CO_3	584-08-7	**FM1-FM3**	≥99%	209619	Sigma-Aldrich	BCCF1997
Acetonitrile	75-05-8	**FM1, FM3**	≥99 %	UN1648	Panreac applichem	0002412013
Dichloromethane	75-09-2	**FM1-FM4**	≥99 %	24233-5L-ALU	Honeywell	N3480
Na2SO4	7755-82-6	**FM1-FM4**	≥99 %	239313-1KG	Honeywell	M0060
Ethyl acetate	141-78-6	**FM1, FM3**	≥99%	23882.321	VWR	24B294033
n-Hexane	110-54-3	**FM1-FM2**	≥98%	UN1208	Carlo Erba	P3H080143I
Bromocyclopropane	4333-56-6	**FM2**	>98%	C1067	TCI	8CUFM-KK
Magnesium	7439-95-4	**FM2**	/	459085	Carlo Erba	23513-6639
Tetrahydrofuran	109-99-9	**FM2**	≥99%	186562-1L	Sigma-Aldrich	STBK8049
Acetic acid	64-19-7	**FM2**	≥99 %	33209-1L	Honeywell	I2280
Hydrobromic acid	10035-10-6	**FM2**	48%	26,800-3	Sigma-Aldrich	S30736-385
Ethyl ether	60-29-7	**FM2**	≥99%	32203-5L	Honeywell	N2690
6,7-dimethoxy-THIC	2328-12-3	**FM3**	>98%	D2472	TCI	82OEF-JH

Methanol	67-56-1	**FM3-FM4**	≥99 %	20847.307	VWR	24A254016
Pd/C 10%	7440-05-3	**FM4**	9.5-10.5%	205699-10G	Sigma-Aldrich	MKCM7616
Ethanol 96%	64-17-5	**FM4**	≥96 %	20824.321	VWR	23E234031
Celite	68855-54-9	**FM4**	/	419931	Sigma-Aldrich	MKCK8774

*5-(benzyloxy)-3,4-dihydronaphthalen-1(2H)-one (**FM1**)*. Benzyl bromide (4.03 mL, 33.91 mmol, 1.1 eq) was added to a solution of 5-Hydroxytetralone (5 g, 30.83 mmol, 1.0 eq) and K_2CO_3 (10 g, 17.07 mmol, 2.5 eq) in MeCN (50 mL). The resulting mixture was refluxed with stirring ON and then was allowed to cool to room temperature. The solvent was removed under vacuum. The residue was taken up with H_2O (30 mL) and extracted with CH_2Cl_2 (3 x 30 mL). The collected organic layers were dried (Na_2SO_4) and evaporated under vacuum to afford a yellow solid crude residue which was purified by column chromatography using n-Ex/AcOEt 1:1 to obtain a 7.2 g of **FM1** as a white solid. Yield, 93%. ^{1}H-NMR (500 MHz, $CDCl_3$) δ 7.68 (1H, dd, J_1 = 7.9 Hz, J_2 = 1.1 Hz), 7.48–7.22 (7H, m), 7.08 (1H, dd, J_1 = 8.1 Hz, J_2 = 1.2 Hz), 5.11 (2H, s), 2.98 (2H, t, J = 6.2 Hz), 2.68-2.60 (2H, m), 2.19–2.07 (2H, m). GC-MS m/z: 252 (M^+, 1), 91 (100).

*8-(benzyloxy)-4-(3-bromopropyl)-1,2-dihydronaphthalene + (E)-5-(benzyloxy)-1-(3-bromopropylidene)-1,2,3,4-tetrahydronaphthalene (**FM2**)*. To a suspension of magnesium chips (635 mg, 26.16 mmol, 1.65 eq) in anhydrous THF (30 mL) under a nitrogen atmosphere a solution of bromocyclopropane (1.89 mL, 23.77 mmol, 1.5 eq) in anhydrous THF (10 mL) is added drop by drop. The mixture is heated under gentle reflux until the disappearance of the magnesium chips is observed. After then, a solution containing cyclopropylmagnesium bromide is obtained and then brought to room temperature under a nitrogen atmosphere. The solution is then cooled to 0 °C in an ice bath, and the intermediate **FM1** (4.0 g, 15.85 mmol, 1.0 eq) dissolved in anhydrous THF (15 mL) is added. The resulting mixture, kept stirring under a nitrogen atmosphere, is heated at reflux ON. Subsequently, the mixture is brought to room temperature, and a saturated aqueous solution of NH_4Cl (80 mL) is added. Then, ethyl ether (100 mL) is added to extract aqueous phase. The ethyl ether extraction is repeated twice (2 × 50 mL). The collected organic layers were concentrated under vacuum to afford a red oil (5.7 g) which is used for the subsequent reaction without further purification.

The red oil is solubilized in a mixture of Acetic acid (52 mL) and hydrobromic acid 3N (26 mL). The reaction mixture is kept under stirring for about 2 hours at room temperature. The residue was taken up with H_2O (50 mL) and extracted with ethyl ether (3 x 50 mL). The collected organic layers were washed with a saturated aqueous solution of K_2CO_3 (1 × 100 mL), dried (Na_2SO_4) and evaporated under vacuum to afford a red oil crude residue which was purified by column chromatography using n-Ex/CH_2Cl_2 8:2 to obtain 2.6 g of **FM2** as a white solid composed by a mixture of the isomers 8-(benzyloxy)-4-(3-bromopropyl)-1,2-dihydronaphthalene and (*E*)-5- (benzyloxy)-1-(3-bromopropylidene)-1,2,3,4-tetrahydronaphthalene. Yield, 46%. ^{1}H-NMR (500 MHz, $CDCl_3$) δ 7.48-7.30 (5H, m), 7.25-7.22, 6.98-6.92 (1H, m + m), 7.19-7.09 (1H, m), 6.89-6.85, 6.83-6.77 (1H, m + m), 6.02-5.91 (1H, m), 5.09, 5.08 (2H, s + s), 3.46 (2H, t, J = 7.3), 2.88-2.75 + 2.66-2.58 (4H, m + m, allylic), 2.52-2.43 + 2.29-2.19 (2H, m + m), 2.13-2.04 + 1.92-1.81 (2H, m + m). Spectrum data correlate with the presence of the geometric isomer

mixture. GC-MS m/z: 358 (M^++2, 1) 356 (M^+, 1), 91 (100). The isomers do not show different fragmentation peaks but different retention times (R_{t1}: 15.741 min; R_{t2} 16.410 min).

*2-(3-(5-(benzyloxy)-3,4-dihydronaphthalen-1-yl)propyl)-6,7-dimethoxy-1,2,3,4-tetrahydroisoquinoline + (E)-2-(3-(5-(benzyloxy)-3,4-dihydronaphthalen-1(2H)-ylidene)propyl)-6,7-dimethoxy-1,2,3,4-tetrahydroisoquinoline (**FM3**)*. The mixture of **FM2** isomers (2.6 g, 7.63 mmol, 1.0 eq) is solubilized in MeCN (40 mL) and added K_2CO_3 (3.2 g, 22.89 mmol, 3.0 eq) and 6,7-dimethoxy-1,2,3 ,4-tetrahydroisoquinoline (2.7 g, 11.64 mmol, 1.5 eq). The resulting mixture was refluxed with stirring ON and then was allowed to cool to room temperature. The solvent was removed under vacuum. The residue was taken up with H_2O (30 mL) and extracted with CH_2Cl_2 (3 x 30 mL). The collected organic layers were dried (Na_2SO_4) and evaporated under vacuum to afford a yellow solid crude residue which was purified by column chromatography using CH_2Cl_2/MeOH 95:5 to obtain 2.7 g of **FM3** as a yellow solid composed by a mixture of the isomers 2-(3-(5-(benzyloxy)-3,4-dihydronaphthalen-1-yl)propyl)-6,7-dimethoxy-1,2,3,4-tetrahydroisoquinoline and (*E*)-2-(3-(5-(benzyloxy)-3,4-dihydronaphthalen-1(2H)-ylidene)propyl)-6,7-dimethoxy-1,2,3,4-tetrahydroisoquinoline. Yield, 80%. ^{1}H-NMR (500 MHz, $CDCl_3$) δ 7.48-7.28 (5H, m), 7.22, 6.97 (1H, d + d, J = 7.5 Hz, J = 7.5 Hz), 7.16-7.07 (1H, m), 6.85, 6.77 (1H, d, + d, J = 8.1 Hz, J = 8.1 Hz), 6.60, 6.59 (1H, s + s), 6.54, 6.51 (1H, s + s), 6.09- 6.02 + 5.93-5.88 (1H, m), 5.09, 5.07 (2H, s + s), 3.85, 3.84, 3.83 (6H, s + s + s), 3.63, 3.56 (2H, s + s), 2.88-2.49 (12H, m), 2.26-2.20 + 1.89-1.70 (2H, m + m). Spectrum data correlate with the presence of the geometric isomer mixture. HRMS-ESI$^+$ for $C_{31}H_{35}NO_3$ (m/z): $[M+Na]^+$ calcd, 492.2515; found 492.2505.

*5-(3-(6,7-dimethoxy-3,4-dihydroisoquinolin-2(1H)-yl)propyl)-5,6,7,8-tetrahydronaphthalen-1-ol (**FM4/MC226**)*. The isomeric mixture of **FM3** (2.7 g, 5.75 mmol, 1.0 eq) is solubilized in ethanol 96% (20 mL) and methanol (20 mL). The solution is kept stirring and under a nitrogen atmosphere for 15 min. After the addition of palladium on carbon (Pd/C 10% w/w, 0.06 g, 0.57 mmol, 0.1 eq), the suspension is kept under stirring for 72 hours at room temperature in an H_2 atmosphere (4.5 bar). Subsequently, the reaction mixture is filtered on celite and the solvent is removed under vacuum. The residue is solubilized in dichloromethane (100 mL) and washed with water (3 × 100 mL). The collected organic layers were dried (Na_2SO_4) and evaporated under vacuum to afford a white solid crude residue which was purified by column chromatography using CH_2Cl_2/MeOH 95:5 to obtain 1.5 g of **FM4/MC226** as a white solid. Yield, 68%. All analyses are reported in Table 2.4 and figure S2.1, S2.2, S2.3.

*2-(3-(5-(2-fluoroethoxy)-1,2,3,4-tetrahydronaphthalen-1-yl)propyl)-6,7-dimethoxy-1,2,3,4-tetrahydroisoquinoline (**FM5/MC225**)*. 1-fluoro-2-iodoethane (0.11 mL, 1.26 mmol, 2.0 eq) was added to a solution of **FM4/MC225** (240 mg, 0.63 mmol, 1.0 eq) and K_2CO_3 (261 mg, 1.89 mmol, 3 eq) in acetone (15 mL). The resulting mixture was refluxed with stirring ON and then was allowed to cool to room temperature. The solvent was removed under vacuum. The residue was taken up with H_2O (30 mL) and extracted with CH_2Cl_2 (3 x 30 mL). The collected organic layers were dried (Na_2SO_4) and evaporated under vacuum to afford a white solid crude residue which was purified by column chromatography using CH_2Cl_2/MeOH 95:5 to obtain 100 mg of **FM5/MC225** as a yellow oil. Yield, 37%. All analyses are reported in Table 2.4 and figure S2.4 and S2.5.

Table 2.4. Analytical data for **FM4/MC226** and **FM5/MC225**.

Parameter	Method	Acceptance criteria	Result	Annex
FM4/MC226				
Appearance	Visual Inspection	white solid	conforms	-
Identification	HRMS-ESI$^+$	*m/z* $(M+23)^+$ 404.2190	conforms	I
	GC-MS	*m/z* :381 (M^+, 16); 206 (100), 192 (43), 164 (29)	conforms	II
	^{1}H-NMR	^{1}H NMR (500 MHz, $CDCl_3$) δ 6.98 (t, J = 7.8 Hz, 1H), 6.77 (d, J = 7.7 Hz, 1H), 6.62–6.49 (m, 3H), 3.84 (s, 3H), 3.83 (s, 3H), 3.57 (s, 2H), 2.88–2.45 (m, 9H), 1.92–1.57 (m, 8H).	conforms	II
Optical rotation	Polarimetry	$[\alpha]_D = \pm 0.10°$ (c = 2–3 in $CHCl_3$)	$[\alpha]_D = +0.05°$	-
FM5/MC225				
Appearance	Visual Inspection	yellow oil	conforms	-
Identification	HRMS-ESI$^+$	*m/z* $(M+23)^+$ 450.2404	conforms	I
	^{1}H-NMR	^{1}H-NMR (500 MHz, $CDCl_3$): δ 1.60-1.87 (7H, m), 2.49-2.89 (10H, m), 3.59 (2H, s) 3.83 (3H, s), 3.84 (3H, s), 4.16-4.21 (2H, m), 4.69-4.79 (2H, m) 6.52 (1H, s), 6.59 (1H, s), 6.62 (1H, d, J = 7.8 Hz), 6.83 (1H, d, J = 7.5 Hz), 7.08 (1H, t, J = 7.9).	conforms	II

2.13. Supporting information

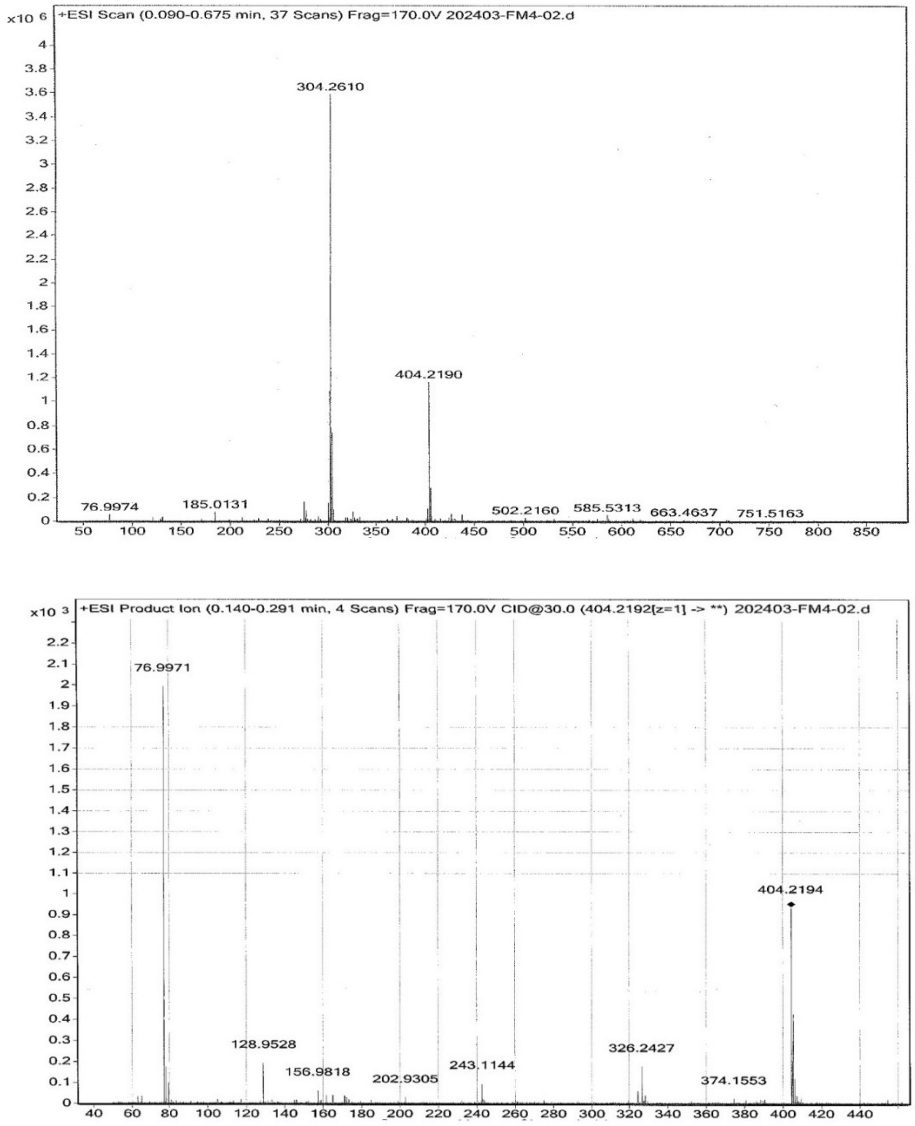

Figure S2.1.: Analytical data for **FM4/MC226**: HRMS-ESI$^+$

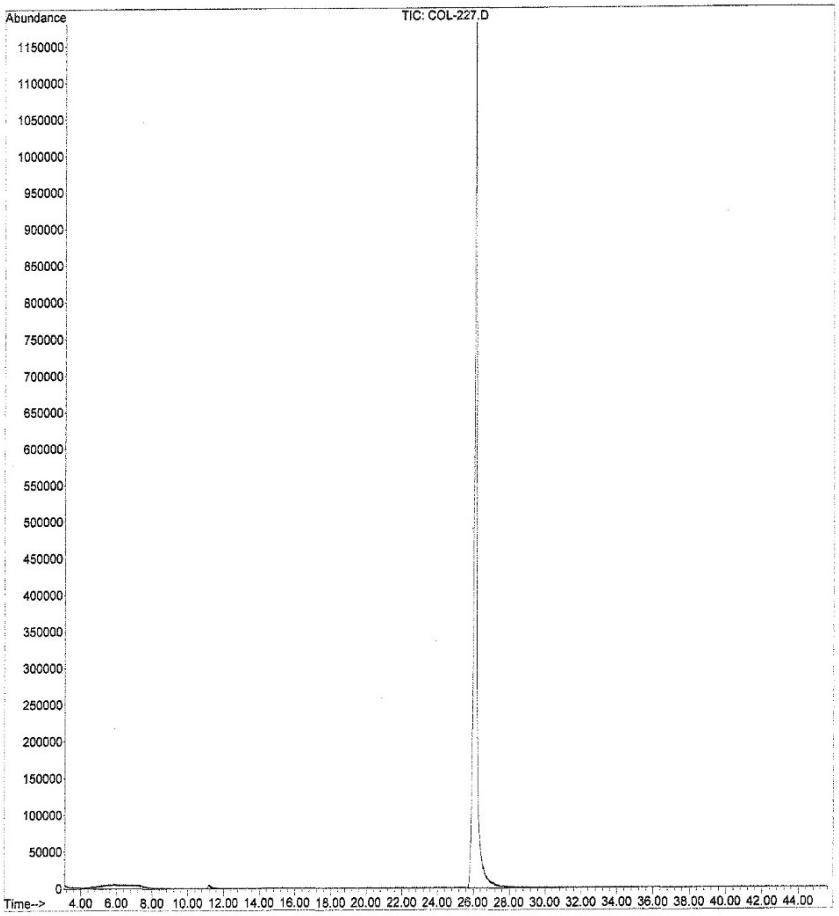
TIC: COL-227.D
Abundance
Time-->

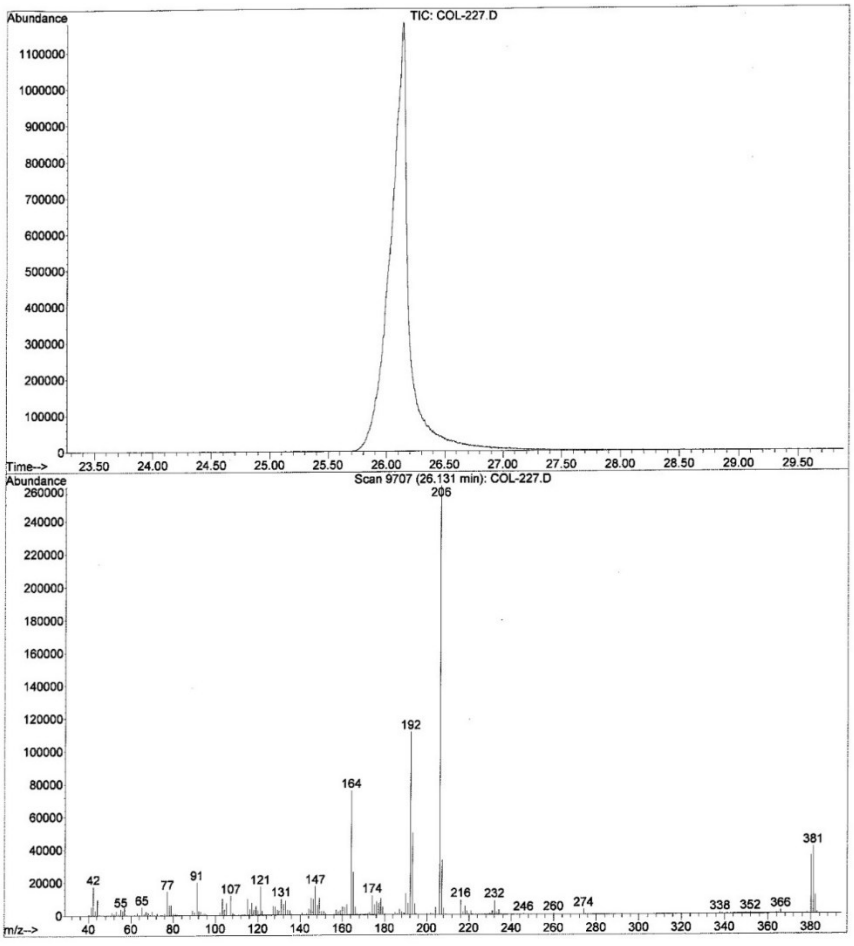
TIC: COL-227.D
Abundance
Time-->
Scan 9707 (26.131 min): COL-227.D
Abundance
m/z-->

Scan 9707 (26.131 min): COL-227.D
202403-FM4-02

m/z	Abundance
40.10	3.0
41.30	20.0
42.20	67.0
43.10	10.0
44.20	37.0
45.10	2.0
50.00	1.0
51.20	7.0
52.10	2.0
53.10	10.0
54.10	2.0
55.20	14.0
56.20	10.0
57.10	18.0
58.10	2.0
59.10	1.0
61.90	1.0
63.10	5.0
64.10	2.0
65.20	18.0
66.10	3.0
67.10	9.0
68.10	5.0
69.10	2.0
70.10	9.0
71.10	1.0
72.50	4.0
74.10	1.0
74.90	1.0
76.00	3.0
77.20	55.0
78.10	23.0
79.10	23.0
80.10	3.0
81.00	3.0
81.80	2.0
83.30	1.0
84.00	1.0
87.10	1.0
89.10	10.0
90.00	6.0
91.20	76.0
92.10	9.0
93.20	7.0
94.10	3.0
95.00	4.0
95.80	2.0
102.10	6.0
103.20	38.0
104.20	13.0
105.10	27.0
107.20	44.0
108.10	5.0
108.80	2.0
113.80	1.0
115.20	38.0
116.10	13.0
117.20	29.0
118.10	12.0
119.10	21.0
120.10	10.0
121.20	66.0
122.10	10.0
122.80	1.0
127.10	21.0
128.10	19.0
129.10	11.0
130.10	10.0
131.10	37.0
132.10	24.0
133.10	33.0
134.10	12.0
135.10	11.0
135.90	3.0
139.90	1.0
141.00	4.0
141.80	2.0
143.10	4.0
144.10	13.0
145.10	39.0
146.10	36.0
147.20	66.0
148.10	23.0
149.10	40.0
150.10	8.0
151.10	10.0
152.00	4.0
152.90	1.0
154.00	1.0
154.70	1.0
156.00	1.0
157.00	12.0
158.00	7.0
159.10	10.0
160.10	19.0
161.10	17.0
162.10	24.0
164.10	290.0
165.10	99.0
166.10	18.0
166.90	4.0
169.80	1.0
170.90	2.0
172.10	2.0
172.90	6.0
174.10	45.0
175.10	23.0
176.10	30.0
177.10	27.0
178.10	38.0
179.10	18.0
180.00	3.0
180.90	1.0
182.80	1.0
184.90	5.0
185.90	3.0
187.10	13.0
188.00	7.0
189.10	5.0
190.10	50.0
191.10	26.0
192.10	426.0
193.10	191.0
194.10	25.0
194.80	2.0
198.90	1.0
200.00	2.0
201.90	3.0
203.00	2.0
204.10	16.0
206.10	1000.0
207.10	128.0
208.10	15.0
209.00	1.0
216.10	34.0
217.00	5.0
218.10	20.0
219.10	8.0
219.90	2.0
221.00	8.0
221.80	1.0
229.90	3.0
231.00	9.0
232.10	33.0
233.00	5.0
234.10	12.0
234.90	1.0
245.80	2.0
246.90	1.0
248.00	1.0
254.90	1.0
257.90	1.0
260.00	3.0
260.90	1.0
274.10	12.0
275.00	1.0
280.80	0.0
337.90	2.0
338.90	1.0
349.90	2.0
352.00	3.0
353.80	1.0
354.80	1.0
363.90	2.0
364.90	2.0
366.00	8.0
367.00	1.0
368.00	1.0
378.10	3.0
380.10	136.0
381.10	157.0
382.10	43.0
382.90	5.0

Area Percent Report

Data Path : D:\DATA\Snapshot\BSB\
Data File : COL-227.D
Acq On : 28 Feb 2024 10:40
Operator :
Sample : 202403-FM4-02
Misc :
ALS Vial : 4 Sample Multiplier: 1

Integration Parameters: EVENTS.E
Integrator: ChemStation

Method : C:\MSDCHEM\1\METHODS\P402028H.M
Title :

Signal : TIC

peak #	R.T. min	first scan	max scan	last scan	PK TY	peak height	corr. area	corr. % max.	% of total
1	26.141	9517	9711	10161	M4	1177980	129143365	100.00%	100.000%

Sum of corrected areas: 129143365

P402028H.M Wed Feb 28 11:26:57 2024

Figure S2.2.: Analytical data for **FM4/MC226**: GC-MS.

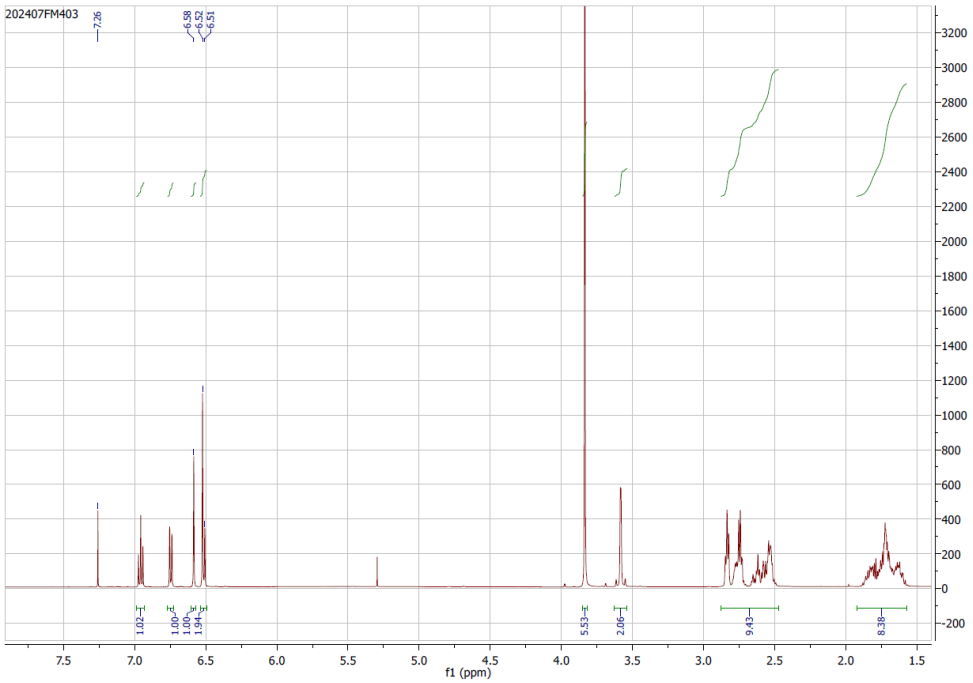

Figure S2.3.: Analytical data for **FM4/MC226**: ^{1}H-NMR.

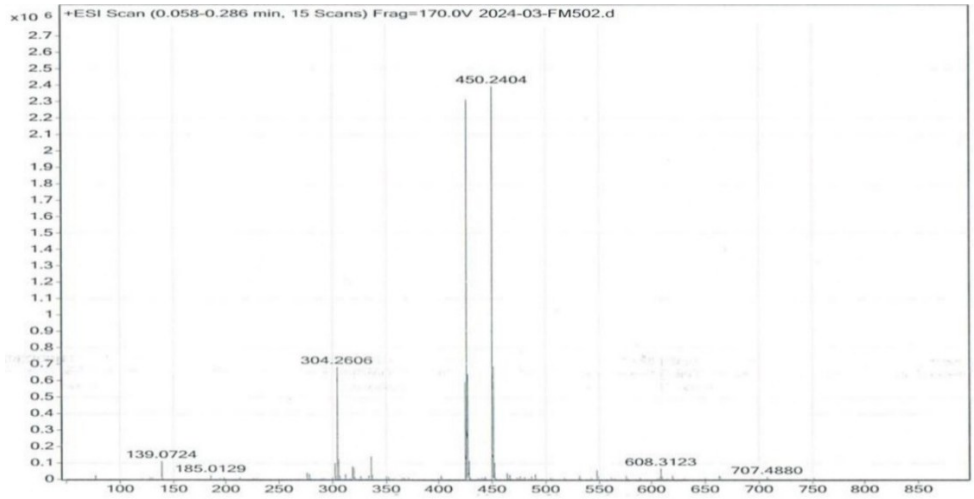

Figure S2.5.: Analytical data for **FM5/MC225**: HRMS-ESI^{+}

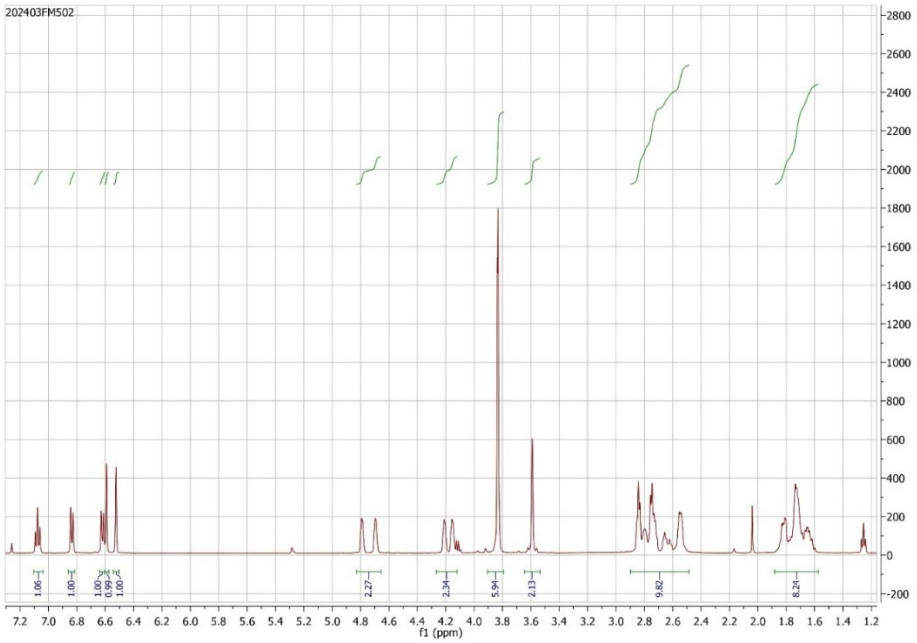

Figure S2.6.: Analytical data for **FM5/MC225**: ^{1}H-NMR.

CHAPTER 3

Sigma-1 receptors

Development and *In Vitro* Evaluation of [^{18}F]CF31 as a Novel Positron Emission Tomography Radiotracer Targeting the Sigma-1 Receptor

Introduction adapted from "Mastropasqua, F.*, Ludwig, F.-A.*, & Abate, C. "A Full-Spectrum Evaluation of Sigma-1 Receptor (S1R) Positron Emission Tomography (PET) Radioligands from Binding Affinity to Clinical Imaging". *Molecules*, **2025**, *30*(21), 4296. https://doi.org/10.3390/molecules30214296".

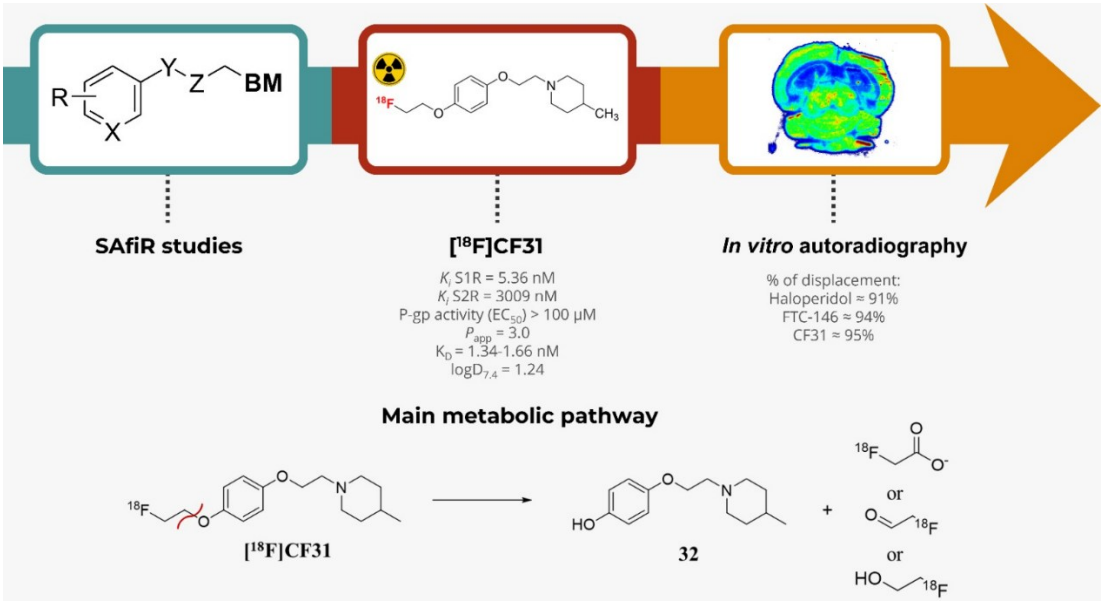

3. Introduction

Sigma receptors (SRs) are classified into two subtypes: the sigma-1 receptor (S1R) and the sigma-2 receptor (S2R, also known as transmembrane protein 97, TMEM97). These subtypes differ in molecular weight, tissue distribution, and drug-binding selectivity [217]. Notably, the primary amino acid sequences of the two proteins show no similarity; their crystal structures reveal completely different folding patterns, although their ligand-binding sites are structurally convergent [218,219].

The S1R is a small transmembrane protein (~25 kDa) [220], encoded by a gene located on chromosome 9, band p13, in both humans and mice, and composed of four exons and three introns [221,222]. The S1R is defined as a "pluripotent chaperone" [223] because it is capable of interacting with several proteins, as reviewed by Schmidt and colleagues [218], although further evidence is required to ascertain the functional relevance of these interactions. This pluripotent nature of the S1R is responsible for a number of complex effects on cellular status. The S1R had been cloned in the early 1990s, and its crystal structure was only recently elucidated.

3.1. Localization, Structure and Function

3.1.1. Localization

The S1R was particularly expressed in the CNS, with high levels in the granular layer of the olfactory bulb, in multiple cortical layers, and in the dentate gyrus, where it exerted its most prominent activities. Slightly lower expression levels were also detected in certain pyramidal layers of the hippocampus, in various hypothalamic nuclei, in the septum, in the central gray matter, in the motor nuclei of the rhombencephalon, and in the dorsal horn of the spinal cord [224]. Overall, the receptor was particularly abundant in regions involved in memory processing, emotional regulation, and sensorimotor functions [218,224].

At the peripheral level, S1R expression was detected in the gastrointestinal tract, vas deferens [225], liver and kidneys [226], heart, adrenal medulla, pituitary gland, testes and ovaries [227].

Subcellularly, the S1R was mainly localized to the endoplasmic reticulum (ER), with a particular enrichment in mitochondria-associated membranes (MAM), specialized ER subdomains in close contact with mitochondria [228,229].

3.1.2. Structure

Structurally, the S1R consisted of a 223–amino acid sequence that was highly conserved among vertebrates but showed no significant similarity to other known proteins. The most closely related protein appeared to be ERG2p, a C8–C7 sterol isomerase expressed in yeast. Both proteins were thought to derive from the same sterol-binding domain-like (SBDL) regions; however, no isomerase activity had been demonstrated for the S1R [230].

The elucidation of the S1R crystal structure (Figure 3.1), published in 2016 [217], represented a pivotal advance. Subsequently, the crystal structures of the S1R in complex with both agonists and antagonists (Figure 3.1) were also determined [231].

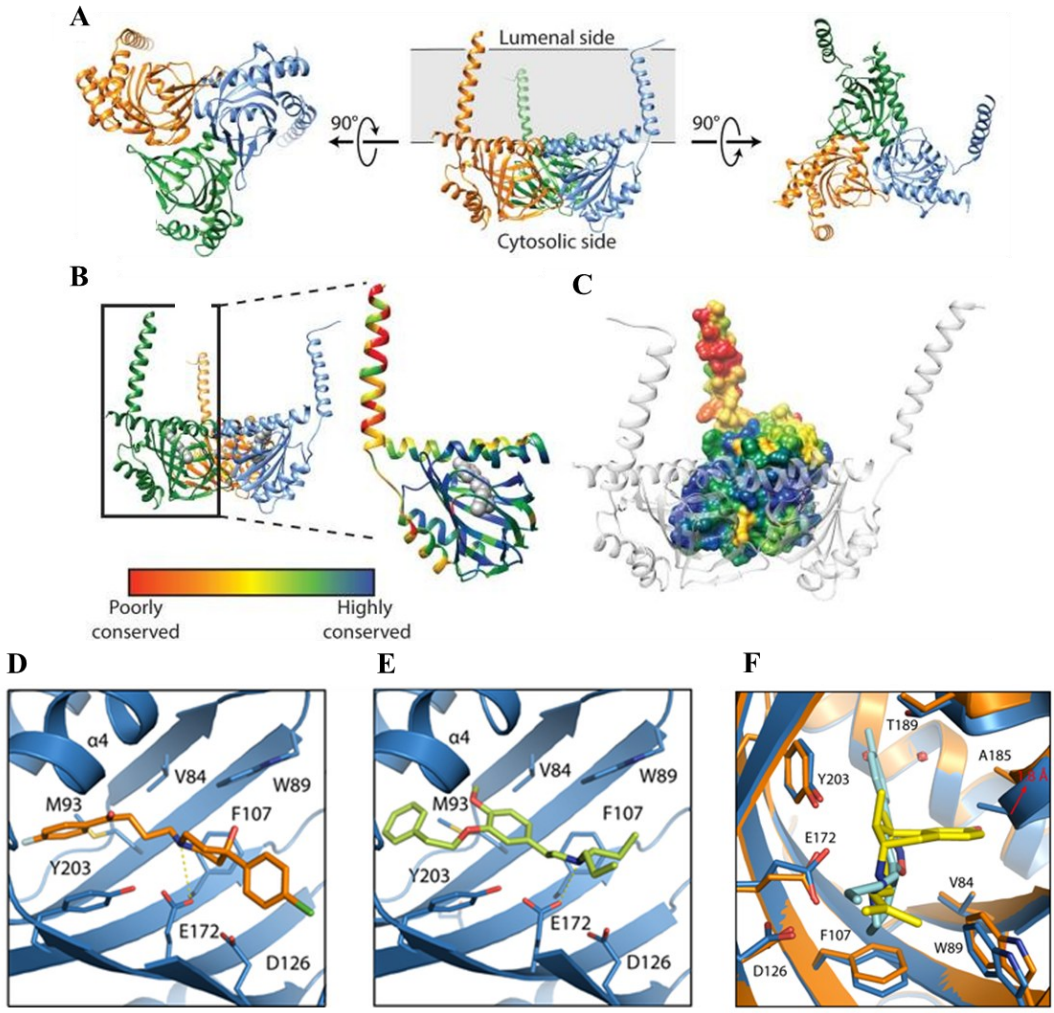

Figure 3.1: Overall structure of the S1R**. A.** View perpendicular to the membrane plane (indicated in gray). The S1R adopted a triangular arrangement composed of three tightly associated protomers, each containing a single transmembrane domain positioned at one vertex of the trimeric complex. When viewed laterally, the receptor displayed a relatively flat surface in contact with the membrane. **B–C.** Architecture of the S1R protomer. **B.** Each protomer exhibited a β-barrel fold reminiscent of cupin-like proteins, flanked by four α-helices, with the ligand (shown in gray) bound at the center of the β-barrel domain. The receptor was color-coded according to sequence conservation, highlighting strong conservation within the ligand-binding domain and lower conservation within the transmembrane helices, which appeared to primarily serve as membrane anchors. **C.** The interface between adjacent protomers within the trimer was also highly conserved, suggesting functional relevance of the oligomeric organization . **D–E.** Crystal structures of the human S1R monomer in complex with the canonical antagonists haloperidol (**D**, orange; PDB ID: 6DJZ) and NE-100 (**E**, light green; PDB ID: 6DK0). The receptor binding pocket is shown in blue. **F.** Binding pocket of the human S1R in complex with the classical agonists (+)-pentazocine (yellow; PDB ID: 6DK1) and PD 144418 (cyan; PDB ID: 5HK1), with the receptor represented in blue . Picture adpapted from Ref. [217,231].

Regarding ligand–receptor interactions, the key feature is an electrostatic bond between a basic amine group, protonatable at physiological pH and present in all high-affinity S1R ligands, and the Glu172 residue of the receptor. The remaining portions of the ligand were accommodated within two distinct hydrophobic pockets positioned at an optimal distance from the basic nitrogen. Together, these interactions defined the so-called “Glennon pharmacophore” (Figure 3.2) [232]. According to this model, the pharmacophore of the S1R comprised a basic amino group capable of bearing a small substituent (typically a hydrogen atom

or a small alkyl group) and two hydrophobic regions: the primary hydrophobic region located 6–10 Å from the amino site, and the secondary hydrophobic region positioned 2.5–3.9 Å from the amine. The robustness of this model was supported by its strong concordance with the crystallographic data [232].

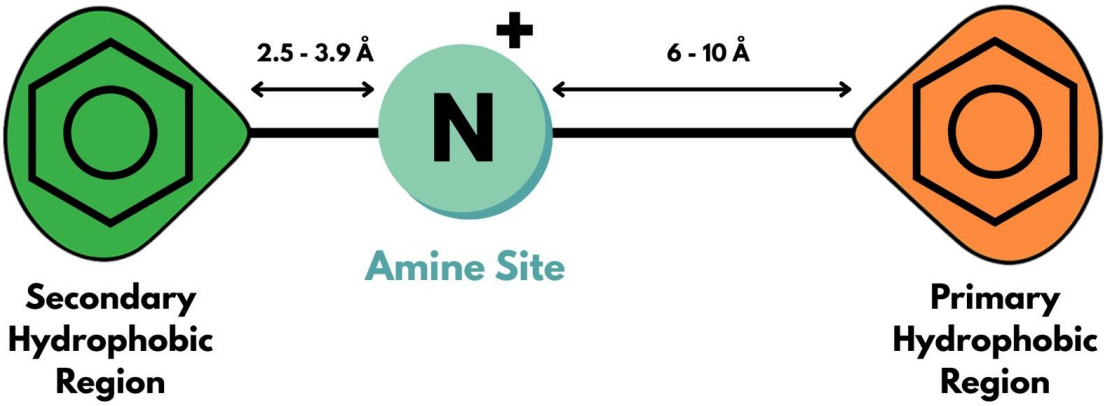

Figure 3.2: Schematic representation of the "Glennon pharmacophore", highlighting the key structural features common to S1R ligands. Adapted from Ref. [232,233].

Crystallization revealed that S1R appears as a trimeric complex, suggesting that the protein acts through polymerization states. Each subunit consists of a single TMD and a large cytosolic region containing the binding pocket for each monomer. The 223 amino acid sequence is organized into five α-helices and ten β-strands: the *N*-terminal end spans the membrane, forms the single TMD, and protrudes into the ER lumen. The *C*-terminal end is a flat, hydrophobic sequence associated with the cytosolic surface of the ER. Within the binding pocket, in addition to the ionic interaction with Glu172, S1R ligands interact with Tyr103 (through hydrogen bonds with hydrophilic residues), which provides a favorable environment for hydrophobic bonds within the primary hydrophobic region (consisting of Val84, Ala86, Trp89, Met93, Leu95, Ala98, Tyr103, Leu105, Phe107, Tyr120, Ile124, Trp164, Met170, Ile178, Thr181, Leu182, Phe184, Ala185, Thr202, and Tyr206). The secondary hydrophobic region (consisting of Trp89, Ser117, Tyr120, Ile124, Asp126, Phe133, Val152, His154, Thr160, Val162, Trp164 and Met170, with Ser117 and His154 showing their hydrophobic side chain in the cavity) tolerates smaller groups than the primary one [232].

3.1.3. Function

Under physiological conditions, the S1R formed calcium-sensitive complexes with the ER chaperone BiP (Binding Immunoglobulin Protein) [217,234]. Upon activation by agonists or in response to ER Ca^{2+} depletion, the S1R dissociated from BiP and translocated to multiple cellular compartments, including mitochondria, the nucleus, and the plasma membrane. Within these locations, the receptor carried out critical functions such as stabilizing the inositol 1,4,5-trisphosphate receptor (IP_3R), promoting calcium transfer from the ER to mitochondria, and sustaining ATP synthesis [223,235].

More recently, S1R activity was proposed to modulate store-operated calcium entry (SOCE). Agonists such as (+)-pentazocine enhanced SOCE-mediated calcium influx, suggesting a regulatory role of S1R in intracellular calcium homeostasis [236]. The receptor also contributed to the protection of the ER against ROS. In particular, S1R prevented ROS-induced activation of the inositol-requiring enzyme 1 (IRE1) at the MAM, thereby stabilizing IRE1 and prolonging activation of the IRE1–XBP1s signaling pathway to

promote cell survival. In addition, S1R interacted with components of the B-cell lymphoma 2 (Bcl-2) and nuclear factor erythroid 2–related factor 2 (Nrf2) pathways, conferring resistance to apoptotic and oxidative stress–induced damage [234]. The neuroprotective effects of S1R agonists were well established and were attributed to several mechanisms, including regulation of intracellular Ca^{2+} dynamics, attenuation of oxidative stress, and anti-apoptotic signaling.

Beyond its neuroprotective functions, S1R was also implicated in viral infections, including severe acute respiratory syndrome coronavirus 2 (SARS-CoV-2) [237]. The receptor was found to interact with the viral non-structural protein NSP6, and S1R knockout (KO) or knockdown (KD) markedly reduced cellular infection by both SARS-CoV-1 and SARS-CoV-2, prompting interest in S1R as a host factor in coronavirus replication. In contrast, depletion of the S2R subtype, which interacted with the viral protein ORF9c, did not affect viral infectivity [238]. For these reasons, S1R was recently proposed as a promising therapeutic target in COVID-19 research [239,240].

3.2. Agonists vs. Antagonists: Key Differences

The crystal structures of the S1R bound to various ligands revealed that agonists, in contrast to antagonists, induced a conformational displacement of the α4 helix. This rearrangement likely interfered with the receptor's oligomeric assembly, supporting the hypothesis that S1R function was mediated through protein–protein interactions (PPIs). Consequently, S1R ligands might act as allosteric modulators of PPIs, and the distinct oligomeric states of the receptor could account for the wide range of cellular effects attributed to S1R activity. In particular, agonists promoted the formation of lower-order oligomers, such as monomers and dimers, whereas antagonists stabilized higher-order oligomeric assemblies [241].

Despite these structural and functional insights, defining S1R activity in terms of classical agonism or antagonism remained challenging. Both classes of ligands demonstrated therapeutic efficacy in similar pathological contexts, including psychotic disorders [242,243]. Moreover, certain compounds, such as BMY 14802 [244], exhibited dual behavior-acting as either agonists or antagonists depending on experimental conditions [245].

To clarify the functional distinctions between agonists and antagonists, several methodological approaches were developed. Gómez-Soler et al. designed a live-cell biosensor utilizing fluorescence resonance energy transfer (FRET) to monitor S1R conformational dynamics in real time [246]. In parallel, Yano et al. established a receptor homomer assay based on bioluminescence resonance energy transfer (BRET), while other studies applied BRET-based systems to investigate heteromeric interactions between S1R and BiP [245]. Collectively, although a definitive classification of S1R ligands remains elusive, these fluorescence-based assays provided valuable insights into the conformational transitions underlying receptor activation and signaling.

3.3. Role of S1R in neurodegenerative diseases

The S1R contributed to the maintenance of protein homeostasis by enhancing neurotrophin receptor signaling and reducing protein aggregation, processes that are critically involved in the onset of neurodegenerative diseases. In addition, the receptor was shown to activate autophagy as a protective response to the accumulation of misfolded proteins. Through these mechanisms, the S1R exerted a pronounced neuroprotective effect and was implicated in the pathophysiology of multiple neurological

disorders. Recent studies demonstrated that the S1R could interact, either directly or indirectly, with several receptors and enzymes central to neurodegenerative processes, particularly in AD [247,248]. A reduction in sigma receptor density was observed in patients with AD [249], and some reports linked this decrease to the ε4 allele of the apolipoprotein E gene (*APOE4*), although this association remained controversial [250]. Beyond AD, alterations in S1R expression or function were also associated with other neurodegenerative disorders, including PD [234], HD [251], ALS [252].

Highlighting the importance of this receptor in neurodegeneration, two S1R-targeting ligands, Blarcamesine (also known as ANAVEX2-73) and Pridopidine, are under clinical investigation for the treatment of AD [NCT03774459; NCT02244541; NCT03790709; NCT02756858] and HD, respectively [NCT02494778; NCT01306929; NCT02006472; NCT03019289; NCT00724048].

3.4. Current State of PET Radiotracers Targeting the Sigma-1 Receptor

PET radiotracers are invaluable tools for advancing our understanding of the pathophysiological role of S1Rs. Moreover, they play a crucial role in supporting the drug development process. The radionuclides most commonly used for PET imaging of S1R are ^{18}F and ^{11}C [74].

In the following sections, a comprehensive analysis of the most relevant PET radiotracers (Figure 3.3) developed for S1Rs since the early 2000s is presented, comparing them according to key parameters essential for radiotracer evaluation. To fully capture the current state of the art, their *in vivo* performance in different animal models is assessed alongside *in vitro* and *ex vivo* autoradiographic data, as well as analyses of metabolic stability and pharmacokinetic properties. This overview concludes with an evaluation of the dosimetric profiles and clinical translation potential of these compounds.

Overall, this synthesis underscores the considerable efforts required to develop optimal PET radiotracers and highlights the importance of achieving a balance between binding affinity and kinetic behavior.

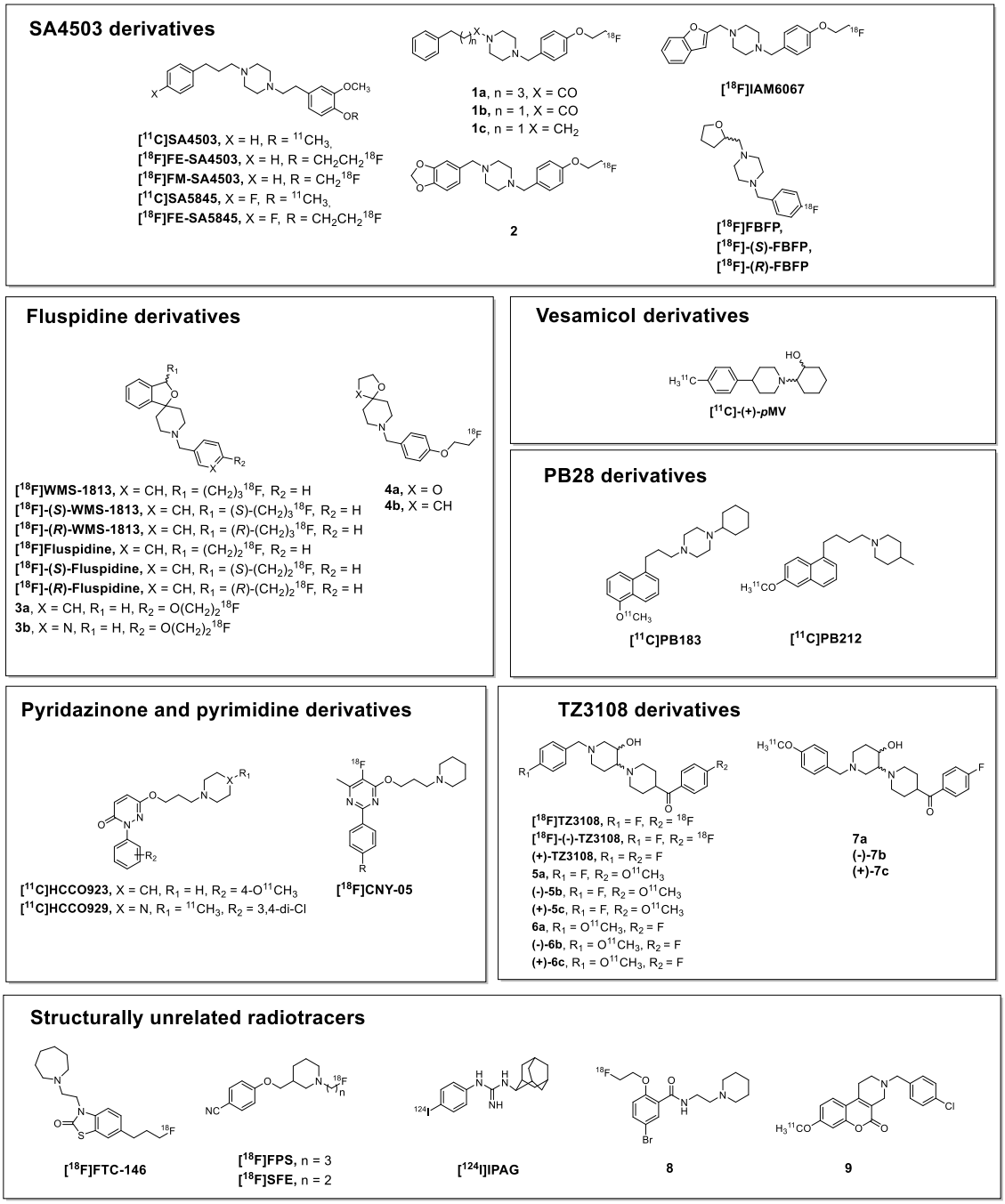

Figure 3.3: Structures of known PET tracers developed for S1R imaging.

3.4.1. Preclinical Biodistribution and Blocking Studies

In vivo biodistribution and blocking studies are key components of PET tracer validation, providing essential data on pharmacokinetics, uptake, target specificity, and off-target binding. These evaluations are critical to confirm tracer suitability before clinical translation [49]. [^{11}C]SA4503 in rat and mice studies, exhibited high initial uptake, followed by a gradual washout over time. Radioactivity in the blood and heart also decreased progressively. Brain uptake was significantly reduced by pre-administration of haloperidol, (+)-pentazocine, or non-labeled SA4503. All three agents showed a substantial blocking effect, up to approximately 80%, indicating a high specific binding to S1R [253,254]. [^{18}F]FE-SA4503 exhibited a regional brain distribution in rats similar to that of [^{11}C]SA4503. However, it showed a higher initial brain

uptake that declined more rapidly, suggesting a lower affinity and more reversible binding to sigma receptors. Additionally, [^{18}F]FE-SA4503 demonstrated a gradual increase in bone accumulation of radioactivity over time. Brain uptake was significantly reduced following pretreatment, co-injection, or displacement with haloperidol, as well as by co-injection of SA4503 [255]. [^{18}F]FM-SA4503 displayed time–activity curves in the brain and peripheral organs of mice that closely resemble those of [^{11}C]SA4503. In the brain, [^{18}F]FM-SA4503 uptake increased over the first 30 min before gradually decreasing, whereas [^{11}C]SA4503 peaks within the first 5 min and then declines. Specific binding of [^{18}F]FM-SA4503, assessed via co-injection with haloperidol, was 68% at 60 min p.i., compared to 60% for [^{11}C]SA4503 at 30 min [256]. [^{18}F]FE-SA4503, [^{18}F]FM-SA4503, and [^{11}C]SA4503 exhibited similar regional distributions in the conscious monkey brain, with high uptake observed in cortical areas, thalamus, striatum, and cerebellum, regions known to be rich in sigma receptors. However, their time–activity curves differed significantly. Blocking studies with haloperidol demonstrated a rapid reduction in tracer uptake for all compounds. Notably, [^{18}F]FM-SA4503 showed higher specific binding compared to [^{11}C]SA4503 (68–83% vs. 50–60% at 60–80 min p.i.) [255–257]. [^{18}F]FE-SA5845 was evaluated in the conscious monkey brain. Compared to [^{18}F]FE-SA4503, it showed lower uptake in the cingulate, temporal, and frontal cortices, but higher uptake in the vermis, thalamus, and occipital cortex [154]. Regarding compounds structurally related to [^{11}C]SA4503, compounds **1a–c** exhibited high brain uptake and specific binding comparable to [^{11}C]SA4503. Among them, compound **1c** showed the most promising profile; however, its brain kinetics in mice were very slow, which is why this compound was not advanced in NHPs [258]. Compound **2** demonstrated a very high initial brain uptake, surpassing that of both [^{11}C]SA4503 and [^{18}F]Fluspidine, followed by a slow clearance phase. It also exhibited strong specific binding [259]. In the mouse model, [^{18}F]IAM6067 showed rapid brain uptake. Blocking studies with haloperidol resulted in approximately 80% reduction in uptake, and co-injection with CM398 confirmed in vivo selectivity against S2R, demonstrating that [^{18}F]IAM6067 is a specific and selective radiotracer [260]. In Papio hamadryas baboons, the tracer displayed high and homogeneous uptake in brain regions known to have high S1R density (cerebral cortex, hippocampus, striatum, amygdala, cerebellum, and brainstem), followed by complete washout. Blocking studies confirmed the results observed in mice [261]. Despite its low $logD_{7.4}$ (0.76), [^{18}F]FBFP showed very high initial brain uptake, followed by gradual washout. Blocking studies with SA4503 revealed a reduction in uptake both in the brain and in peripheral organs rich in S1R [262]. Since FBFP possesses a chiral center, enantiomeric resolution was performed, and both enantiomers were evaluated in rodents. Both the *R*- and *S*-enantiomers exhibited high brain uptake and favorable brain-to-blood ratios. Blocking studies with SA4503 resulted in a marked reduction in the uptake of both enantiomers, consistent with the behavior observed for the racemate. In dynamic micro-PET studies, [^{18}F]-(*S*)-FBFP demonstrated substantially faster clearance from the brain than the *R*-enantiomer, indicating distinct pharmacokinetic profiles between the two [85]. On the other hand, among compounds with a spirocyclic structure, [^{18}F]WMS-1813 exhibited high brain uptake and prolonged retention of radioactivity, indicating favorable brain penetration as well as specific binding. It also showed high initial uptake of radioactivity in most organs known to express S1R. Radioactivity was also observed in the femur, indicating defluorination in vivo. Blocking studies with haloperidol demonstrated a significant reduction in radioactivity uptake in organs with high S1R expression, approximately 80% in the brain, except for the liver [263]. [^{18}F]Fluspidine showed higher initial brain uptake (at 5 min) than [^{18}F]WMS-1813 and [^{11}C]SA4503, and its uptake at 30 min is 40–50% higher

compared to its F-propyl derivative and [^{11}C]SA4503. Its biodistribution pattern is similar to that of [^{18}F]WMS-1813, including radioactivity observed in the femur [264]. Based on [^{18}F]Fluspidine, compounds **3a** and **3b** were synthesized. Compound **3a** exhibited better brain uptake than both [^{11}C]SA4503 and [^{18}F]Fluspidine, with specific binding in the brain and other S1R-rich organs comparable to the two reference radiotracers. However, it is eliminated too slowly from the brain and shows irreversible brain kinetics [265]. In contrast, compound **3b** has lower brain uptake than compound **3a** but displays faster brain clearance. Blocking studies showed a higher reduction in brain uptake, consistent with a decrease in lipophilicity [266]. Baum et al. [267] compared (*R*)-[^{18}F]Fluspidine, (*S*)-[^{18}F]Fluspidine, and compounds **3a** and **3b** in NHPs. All four compounds demonstrated high brain uptake. (*S*)-[^{18}F]Fluspidine and compound **3b** showed rapid washout, whereas (*R*)-[^{18}F]Fluspidine and compound **3a** exhibited much slower clearance from the brain. Notably, compound **3b** displayed a more heterogeneous uptake pattern. The distribution profiles of all four compounds were consistent with that of [^{11}C]SA4503 in humans. Additionally, (*S*)-[^{18}F]Fluspidine and compound **3b** were compared to [^{11}C]SA4503 in monkeys. Both showed high uptake and a distribution similar to [^{11}C]SA4503, although the latter displayed a slower washout. Moreover, [^{11}C]SA4503 exhibited higher nonspecific binding than (*S*)-[^{18}F]Fluspidine and compound **3b,** possibly due to its lower S1R affinity [267]. Compounds **4a** and **4b** exhibited good brain uptake despite their low $logD_{7.4}$ values. Among the two, compound **4b** showed superior initial brain uptake and greater specific binding [268,269]. Regarding [^{18}F]FTC-146, studies in mouse models showed that it rapidly crosses the BBB, reaches peak brain uptake within the first few minutes, and then slowly washes out. This kinetic profile is similar to that of [^{18}F]FM-SA4503 and [^{18}F]Fluspidine. Pre-treatment with haloperidol or the non-labeled reference led to a marked reduction in [^{18}F]FTC-146 binding in the brain, approximately 80% [270]. [^{18}F]FTC-146 was also evaluated in rats and squirrel monkeys, where it demonstrated widespread uptake and distribution throughout the brain, showing a similar behavior to [^{11}C]SA4503 and [^{18}F]FE-SA4503. In squirrel monkeys, high specific binding was confirmed through haloperidol blockade studies; however, accumulation of radioactivity in the skull was also observed, which could pose a problem, as additional radioactivity in the skull may affect PET analysis. However, subsequent studies conducted in humans found no evidence of accumulation into the skull [271]. Regarding [^{18}F]FPS and [^{18}F]SFE, in the rat brain model, both exhibited the highest average radioactivity uptake in the posterior and frontal cortices, with slightly lower uptake observed across all other examined regions, including the striatum, cerebellum, medulla pons, midbrain, hippocampus, and hypothalamus. A key difference between the two compounds lay in their pharmacokinetics: [^{18}F]SFE reached its peak uptake at approximately 5 min p.i. and subsequently showed progressive clearance across all brain regions, whereas [^{18}F]FPS demonstrated no observable decrease in radiotracer concentration within the same timeframe. This clearance behavior was considered an advantage of [^{18}F]SFE over [^{18}F]FPS. Both tracers exhibited high specific binding [272,273]. When comparing [^{18}F]SFE to [^{18}F]FE-SA4503 in the mouse brain, both showed similar uptake levels; however, [^{18}F]FE-SA4503 demonstrated slower clearance. Additionally, [^{18}F]FE-SA4503 displayed slightly higher non-specific binding than [^{18}F]SFE [274]. [^{18}F]TZ3108, evaluated in the rat model, showed uptake patterns consistent with the distribution of S1R in the body, with pronounced accumulation in the lungs and brain. An increase in liver uptake was also observed during imaging, likely indicating hepatobiliary clearance. In NHPs, [^{18}F]TZ3108 readily crossed the BBB and demonstrated high brain uptake with a regional distribution similar to that in rats, enabling excellent anatomical visualization. However, its brain kinetics

were relatively slow, reaching a peak at around 45 min and maintaining stable concentrations for over 120 min. Blocking studies with cold TZ3108 or Yun-122 confirmed specific binding [275]. Additionally, both enantiomers, (−)-[^{18}F]TZ3108 and (+)-[^{18}F]TZ3108, have been investigated in rats and NHPs. Despite its lower S1R affinity, the (−)-enantiomer showed faster brain clearance compared to the racemate, reaching its peak at 30 min versus 45 min. Therefore, (–)-[^{18}F]TZ3108 is considered superior to both the racemic mixture and the eutomer alone in terms of pharmacokinetics. In blocking studies, (−)-[^{18}F]TZ3108 reduced uptake in most brain regions [276]. Among the derivatives of TZ3108, only compounds **5b** and **6b** were studied in vivo in mice. Compound **5b** entered the CNS with a maximum Standardized Uptake Value (SUV) of 2.1 at 5 min p.i., followed by a progressive decrease from 0 to 60 min, whereas compound 6b reached a higher maximum SUV of 4.1. Blocking studies with haloperidol and TZ3108 reduced brain uptake by 5–10% and 30–35%, respectively, confirming specific binding. In macaques, all six radiolabeled compounds were evaluated and successfully entered the brain, displaying distinct uptake and washout profiles. Among them, compound **7c** showed the highest brain uptake, with an SUV greater than 2.0 at 5 min p.i. Compounds **6b** and **6c**, however, failed to reach equilibrium during a 2 h scan, making them the least suitable candidates for further clinical development. In contrast, compounds **5b** and **5c** demonstrated good brain penetration, favorable washout kinetics, and specific uptake in brain regions with high S1R density [277]. In the mouse model, both [^{11}C]HCCO923 and [^{11}C]HCCO929 demonstrated similar brain distribution patterns and exhibited specific and selective binding to S1R. Between the two compounds, [^{11}C]HCCO929 displayed superior kinetic properties and higher specific binding [278]. [^{18}F]CNY-05, in brain imaging studies, successfully crossed the BBB and showed rapid brain uptake with a favorable cerebral clearance profile. However, the blocking studies using SA4503 revealed an unexpected increase in radioactivity levels. In NHPs, the SUV stabilized within the first minutes p.i. and peaked at approximately 40 min. Tracer washout exhibited promising potential for clinical translation. Additionally, [^{18}F]CNY-05 was evaluated in 5xFAD transgenic mice, a model for AD. The tracer uptake in all brain regions of AD mice was significantly lower than that observed in wild-type (WT) controls. Notably, the hypothalamus showed markedly reduced radioactivity accumulation in AD mice. These findings support the potential application of [^{18}F]CNY-05 in the imaging of AD-related pathological changes [279]. Compound **9**, initially designed for the investigation of D_4 receptors, exhibited high brain uptake and a high degree of specific binding in a monkey model, as confirmed by blocking studies [280]. As for vesamicol derivatives, [^{11}C]-(+)-pMV shows a regional distribution pattern in the rat brain similar to [^{11}C]SA4503, but with lower specific binding [281].

The radioiodine compound [^{124}I]IPAG was investigated in an LNCaP xenograft model with regard to possible tumor imaging. It showed specific uptake; however, after a period of 4h, the activity became non-specifically distributed. Tumor visualization became evident after 24h, as radioactivity was cleared from non-target organs with minimal S1R expression, similarly to observations for **5** [282]. [^{11}C]PB183 and [^{11}C]PB212 are unable to cross the BBB and were therefore investigated for imaging prostate cancer or assessing peripheral S1R expression, respectively. In blocking studies using haloperidol, Fluspidine, and SA4503, [^{11}C]PB212 demonstrated specific and reversible binding in the spleen. Moreover, [^{11}C]PB212 is an S1R antagonist, with the potential to provide additional information about S1Rs compared to the agonists, which are more represented among the S1R PET radioligands [283,284]. To the best of our knowledge, however, this aspect has not been investigated further. Compound **8** was intended to provide a dual S1/S2R radiotracer, able to image prostate cancer. In mice bearing PC-3 tumors, increasing tumor

accumulation was shown, reaching a peak at 1.5 h, along with rapid renal and hepatobiliary excretion. Blocking studies with haloperidol demonstrated a reduced accumulation in the tumor, indicating specific binding [285].

3.4.2. *In Vitro* and *Ex Vivo* Autoradiographic Studies

In vivo biodistribution and blocking studies are key components of PET tracer validation, providing essential data on pharmacokinetics, uptake, target specificity, and off-target binding. These evaluations are critical to confirm tracer suitability before clinical translation [49]. Characterization of the radiotracers also in pathological models (preclinical models of cancers and neurodegenerative diseases that involve S1R) is also performed for the most promising radioligands, in the perspective of further validation towards the translation into the clinic.

Many of the compounds discussed in this review have been investigated using *in vivo* assays but have not been evaluated through *in vitro* or *ex vivo* autoradiography (ARG). Although modern dedicated micro-PET scanners achieve spatial resolutions of approximately 1–2 mm and excellent system sensitivity (enabling precise quantification of radiotracer uptake in small brain structures and longitudinal, dynamic studies within the same animal), ARG remains of extreme importance for validating PET findings by providing high-resolution spatial maps of tracer uptake, confirming binding specificity, and revealing microregional distribution patterns that surpass the resolution limits of *in vivo* imaging [286,287]. In addition, ARG aligns with the principles of the 3Rs (reduce, refine, replace) in animal research [287]. For both [^{11}C]SA4503 and [^{18}F]FE-SA4503, *ex vivo* ARG in rats confirmed the *in vivo* biodistribution and revealed highly comparable regional uptake patterns. Notably, high tracer accumulation was observed in the vestibular nucleus, temporal cortex, cingulate cortex, inferior colliculus, thalamus, and frontal cortex. Moderate uptake levels were detected in the parietal cortex and caudate putamen, while the cerebellum and hippocampus exhibited relatively low tracer accumulation [254,255]. Compounds **2** and [^{18}F]FBFP, structurally related to [^{11}C]SA4503, demonstrated a brain distribution pattern consistent with regions known to exhibit high S1R expression, although some differences were observed compared to [^{11}C]SA4503. Blocking studies confirmed its specific binding to S1R [259,262]. For [^{18}F]FBFP, *ex vivo* ARG was also employed to explore its potential application in AD by comparing senescence-accelerated prone (SAMP8) mice with senescence-accelerated resistant (SAMR1) mice. Consistent with the *ex vivo* autoradiography results observed in rats, a high level of [^{18}F]FBFP accumulation was detected in brain regions with known high S1R expression in SAMR1 mice. In contrast, the same regions showed a reduced accumulation of the radiotracer in age-matched SAMP8 mice [259]. For [^{18}F]IAM6067, *in vitro* autoradiography in rats showed strong concordance with *in vivo* PET imaging, further validating its specificity and selectivity as an S1R radiotracer [260]. Regarding the spirocyclic compounds, both [^{18}F]WMS-1813 and [^{18}F]Fluspidine show an *ex vivo* ARG pattern consistent with *in vivo* distribution in brain regions known to be rich in S1R, particularly in the facial nucleus. For [^{18}F]Fluspidine, the lowest concentration of binding sites was observed in the anterior part of the olfactory bulb [263]. Compound **3a** displayed a regional brain distribution similar to that of [^{18}F]Fluspidine; however, unlike [^{18}F]Fluspidine, only moderate accumulation in the facial nucleus was detected [265]. Compound **3b**, in *ex vivo* ARG analysis, displayed high uptake in brain areas rich in S1R, which is consistent with the brain distribution of [^{11}C]SA4503. Similarly to [^{18}F]Fluspidine, it has shown low binding site concentration in the anterior part of the olfactory bulb [266].

For both compounds **4a** and **4b**, *ex vivo* autoradiography confirmed the *in vivo* biodistribution in brain regions with high concentrations of S1R. Blocking studies with haloperidol or SA4503 further supported the specificity of binding [268,269]. As for [^{18}F]FTC-146, administration of the compound resulted in an accumulation in the midbrain, facial nucleus, cortex, and hippocampus. Uptake was also observed in the cerebellum, although to a lesser extent than in the midbrain and cortex, whereas the corpus callosum lacked [^{18}F]FTC-146 binding. Blocking studies demonstrated a marked reduction in tracer uptake throughout the mouse brain. Overall, *ex vivo* autoradiography confirmed the *in vivo* biodistribution in both mice and rats [270,271]. For [^{18}F]CNY-05, *in vitro* autoradiography confirmed its S1R-specific binding. Similarly to the in vivo studies, in vitro ARG performed in the 5xFAD mouse model revealed a heterogeneous distribution of radioactivity across brain regions and a marked reduction in brain uptake in 5xFAD mice compared to WT controls [279]. The regional distribution of (+)-[^{11}C]pMV in the brain was very similar to that of [^{11}C]SA4503 [288]. For [^{11}C]PB212, *in vitro* autoradiography was performed using brain tissues from both WT and S1R KO mice. Specific binding was demonstrated through blocking studies using haloperidol, SA4503, and Fluspidine [284]. For compound **9**, *in vitro* autoradiography was performed to evaluate its binding affinity toward both the D_4 receptor and the S1R. The observed distribution did not correspond to the known brain distribution of the D_4 receptor. Blocking studies with (+)-pentazocine conclusively demonstrated specific binding to S1R [280].

3.4.3. *In Vitro* and *In Vivo* Metabolism

The chemical identification of radiometabolites serves two primary purposes: first, to accurately quantify the proportion of unchanged (parent) radiotracer present in the plasma; second, to identify and correct for any unintended accumulation of radiometabolites in non-target tissues. The formation of radiometabolites can pose significant challenges in PET imaging, as these byproducts often exhibit markedly different pharmacokinetics and biodistribution compared to the original tracer [157]. In the case of brain imaging agents, it is preferable that metabolic breakdown occur outside the CNS, resulting in more polar, less lipophilic compounds that are unlikely to cross the BBB or interfere with the specific binding to the target protein [157]. Regarding [^{11}C]SA4503, its metabolic profile varies significantly across species. In rats, the radiotracer exhibited slow peripheral metabolism, with more than 99% of the intact compound present in the frontal cortex and 77% remaining in plasma 30 min post-injection (p.i.), and no detectable ^{11}C-labeled metabolites in the brain [254]. In contrast, cats showed rapid metabolism: the fraction of unchanged [^{11}C]SA4503 in plasma declined sharply to 21.9% at 30 min, 12.5% at 60 min, and 11.0% at 90 min after administration [289]. In monkeys, the radiotracer underwent intermediate metabolic degradation, with the parent compound accounting for 57%, 42%, and 31% of plasma radioactivity at 30, 60, and 90 min, respectively, under baseline conditions. Under carrier-added conditions, these values slightly decreased to 43%, 32%, and 29% at the corresponding time points. These findings indicate that [^{11}C]SA4503 undergoes peripheral metabolism more rapidly in monkeys than in rats but less rapidly than in cats [257]. As for [^{18}F]FE-SA4503, at 30 min p.i., the percentage of unchanged radiotracer in plasma was 49 ± 9.5% in mice and 55 ± 24% in monkeys. In mice, a small amount of metabolites was detected in brain tissue (the percentage of unchanged radiotracer was 93.4 ± 2.6%), and defluorination was observed. In contrast, in monkeys, neither brain metabolites nor defluorination were observed [154,255]. Instead, the percentage of unchanged [^{18}F]FM-SA4503 in mouse plasma was only 8.4 ± 1.2% at 60 min p.i. In brain tissue, only a

small fraction of metabolites was detected, with 94.1 ± 1.0% of the radiotracer remaining unchanged [256]. Regarding the [^{11}C]SA4503 derivatives, radiotracers 1a and 1b, both containing an amide group, showed parent compound percentages of 33.7% and 75.4%, respectively, in mouse brain at 30 min p.i. In plasma, the intact forms of **1a** and **1b** accounted for 10.1% and 46.9%, respectively, at the same time point. In the liver, the corresponding values were 3.3% for 1a and 49.3% for **1b**. For radiotracer 1c, the parent compound represented 10.6%, 92.4%, and 68.3% of the total radioactivity in mice plasma, brain, and liver, respectively, at 30 min p.i. [258]. In contrast, rapid metabolism in mice was detected for [^{18}F]IAM6067, with only 10.1 ± 8.6% of the intact tracer remaining in plasma at 10 min p.i. However, over 91% of the parent compound was retained in the brain at 10, 20, and 60 min p.i. Two more hydrophilic metabolites were identified as products of [^{18}F]IAM6067 metabolism [260]. For racemic [^{18}F]FBFP and its *R*- and *S*-enantiomers, approximately 95% of the total radioactivity in the mouse brain at 60 min p.i. was attributable to the parent compound [262,290].

Regarding spirocyclic compounds in mice at 60 min p.i., the percentage of unmetabolized [^{18}F]WMS-1813 and [^{18}F]Fluspidine in plasma was over 85% and approximately 50%, respectively. In the brain, the parent compound represented over 95% and ~98% of total radioactivity, respectively. For [^{18}F]Fluspidine, 57% of the intact tracer was detected in liver homogenates of mice at 60 min, along with two main hydrophilic metabolites. For both radiotracers, no radiometabolites were found in the brain; however, unbound [^{18}F]Fluoride was detected in plasma. The findings indicate that [^{18}F]Fluspidine undergoes a metabolic process similar to [^{18}F]WMS-1813, but at a faster rate [263]. The metabolism of the *R*- and *S*-enantiomers of both compounds was also investigated in vitro using rat liver microsomes. In both cases, the (*R*)-enantiomer was metabolized more rapidly than the (*S*)-enantiomer. For [^{18}F]WMS-1813, only 28% of the (*R*)-form remained after 30 min of incubation, compared to 54% of the (*S*)-form [291]. For [^{18}F]Fluspidine, ~72% of both enantiomers remained unchanged after 30 min; however, after 90 min, the (*S*)-enantiomer showed significantly greater stability, with 58% remaining intact versus 33% for the (*R*)-counterpart [292]. The stereospecificity of the metabolism of [^{18}F]Fluspidine was confirmed in a pig model, where at 16 min p.i., 23% of the (*R*)-enantiomer and 45% of the (*S*)-enantiomer remained unmetabolized [293]. In Rhesus monkeys, 60 min p.i., plasma levels of unmetabolized tracer were 37% for the (*R*)-enantiomer and 35% for the (*S*)-enantiomer [267]. In human plasma, 91% of the (*S*)-enantiomer remained intact at 30 min p.i. It was shown that the primary metabolic pathway involves hydroxylation of the fluoroethyl chain followed by glucuronide conjugation. Furthermore, debenzylation has been identified as a secondary metabolic route [294]. For the Fluspdine derivative **3a** investigated in male ICR mice, the percentage of parent tracer in the liver was 40% at 30 min p.i., and no radiometabolites were detected in the brain [265]. For compound **3b**, investigated under similar conditions, the percentages of unchanged radiotracer were 77% in plasma, 49% in the liver, and 93% in the brain [266]. In monkeys, the parent fraction at 60 min p.i. was 18% for compound **3a** and 19% for compound **3b**, indicating a faster metabolic depletion in comparison to both the enantiomers of [^{18}F]Fluspidine [267]. Compound **4a** exhibited very rapid metabolism in mice, with only 6% of the unchanged parent compound remaining 60 min p.i., likely due to its ketal as a vulnerable function [268]. Indeed, compound **4b**, which lacks the ketal group, showed a slower, though still relatively fast, metabolic degradation. At 15 min after radiotracer injection, 13% of the total radioactivity was detected in plasma samples and 84% in brain homogenates of ICR mice, respectively [269]. Regarding [^{18}F]FTC-146, in mouse models, the percentages of intact parent compound in the liver and plasma were 34% and 60% at

30 min, respectively, and 27% and 50% at 60 min, respectively. The percentage of intact tracer in the brain remained at 100% throughout the study duration [270]. In rat models, metabolism was faster than in mice, with 25.3% and 19.5% of the parent compound detected in plasma at 30 and 60 min, respectively. In monkeys, the metabolic profile was comparable to that observed in mice. Similarly to mice, 100% of the parent compound was observed in the brain at all time points analyzed both in mice and monkeys [271]. In humans, 43% and 23% of peak radioactivity remained in circulation at 30 and 120 min p.i., respectively. As seen in preclinical studies, only intact [^{18}F]FTC-146 was detected in the rat brain at 15, 30, and 60 min p.i. [295]. Metabolism studies of [^{18}F]TZ3108 were conducted in both rats and NHPs, revealing similar results across species. The percentages of intact parent compound in plasma of rats and NHPs were 88.5% and 97.9% at 5 min, 86.5% and >86% at 30 min, and 78.2% and ~70% at 60 min, respectively. The major metabolite identified in both species does not cross the BBB [275]. As for vesamicol derivatives, the percentage of unchanged [^{11}C]-(+)-pMV in the brain was 95%, while in plasma at 30 min p.i., 21% was detected [288]. Regarding [^{18}F]CNY-05, in NHPs, more than 50% of the parent compound remained in plasma at 60 min p.i. No radiometabolites were found to cross the BBB [279]. For compound **8**, analysis of radioactivity in tumor and blood samples at 5 min p.i. showed that more than 99% of the extracted radioactivity corresponded to the intact compound. However, by 30 min p.i., the proportions had decreased to 52% in the tumor and 24% in the blood. In contrast, in the liver, intact compound 8 accounted for 46% and 67% of total radioactivity at 5 and 30 min p.i., respectively [285]. Regarding compound **2**, metabolite analysis in monkey plasma indicated that it was considerably stable, with approximately 80% of the total radioactivity corresponding to the intact parent compound even at 90 min p.i. [280].

3.4.4. Kinetic Characterization of PET Radiotracers

Kinetic studies are fundamental in the development of novel PET radiotracers because they provide a time-resolved, quantitative characterization of tracer behavior *in vivo*, encompassing delivery, target engagement, metabolism, and clearance. By acquiring dynamic PET data immediately after tracer injection and applying compartmental models, each compartment representing a distinct physiological or biochemical state, researchers can estimate rate constants (k1, k2, k3, k4) that reflect key processes such as blood–tissue transfer, receptor binding, intracellular trapping, and dissociation [296]. Such analyses not only yield biologically meaningful parameters beyond static SUVs but also guide rational tracer design (e.g., optimizing affinity and lipophilicity), inform selection of optimal imaging time points, and underpin protocol simplification strategies for clinical translation [297]. In this framework, Logan graphical analysis provides a model-independent, linear regression approach for reversible tracer kinetics, enabling the estimation of total distribution volume (V_t) or distribution volume ratio (DVR) from dynamic PET data once a pseudo-equilibrium between tissue and plasma has been achieved [298]. By incorporating Logan analysis into the kinetic evaluation of novel PET tracers, researchers can efficiently screen candidates for favorable reversible binding profiles, optimize scanning protocols, and accelerate the transition of promising compounds toward clinical application [299]. For [^{11}C]SA4503, a three-compartment, two-tissue kinetic model was employed to estimate parameters including k1, k2, k3, k4, and blood–brain delay. In addition, a Logan graphical analysis was applied to assess reversible binding. The brain uptake of [^{11}C]SA4503 exhibited a biphasic pattern, with a rapid initial uptake followed by a slow, progressive accumulation over time. Notably, [^{11}C]SA4503 demonstrated prolonged retention in the brain, consistent

with its target-binding profile [300,301]. For both [^{11}C]SA4503 and [^{18}F]FE-SA4503, a shortened acquisition protocol of 60 min has been shown to provide sufficient kinetic information. In contrast, [^{18}F]FE-SA5845 requires a longer acquisition time of up to 2 h to achieve reliable kinetic modeling results [106,129]. For [^{18}F]WMS-1813, [^{18}F]Fluspidine and [^{18}F]TZ3108, kinetic studies were fundamental to determining which enantiomer was more suitable. For both [^{18}F]WMS-1813 and [^{18}F]Fluspidine, the (*S*)-enantiomer showed more favorable kinetics [291,292]. Both enantiomers of Fluspidine were evaluated in porcine brain using a two-compartment tissue model to determine binding potential (BP_{ND}) and VT, with comparisons made to [^{11}C]SA4503. The (*S*)-enantiomer displayed lower BP_{ND} and V_T values than both [^{11}C]SA4503 and the (*R*)-enantiomer. Additionally, B_{max} values, which represent the maximum amount of radioligand that can bind specifically to receptors when all available binding sites are fully occupied, for the (*R*)-enantiomer were approximately five-fold higher than those of the (*S*)-enantiomer, likely reflecting differences in their respective K_i values. Notably, the (*S*)-enantiomer exhibited faster equilibration kinetics, including a higher k4 value, suggesting more rapid dissociation from the target site. Due to these favorable kinetic properties, specifically shorter scan durations and slower peripheral metabolism, the (*S*)-enantiomer shows greater potential for clinical application in brain imaging [48]. In NHPs, binding potential followed the order: compound **3a** > (*R*)-[^{18}F]Fluspidine > compound **3b** > (*S*)-[^{18}F]Fluspidine, consistent with their K_i values. V_T estimates were also time-dependent: reliable measurements were obtained within 90 min for (*S*)-[^{18}F]Fluspidine and compound **3b**, while longer acquisitions were required for (*R*)-[^{18}F]Fluspidine and compound **3a**. However, due to their very slow kinetics, (*R*)-[^{18}F]Fluspidine and compound **3a** are considered unsuitable for clinical translation [267]. [^{18}F]CNY-05 was also evaluated in NHPs from a kinetic perspective, revealing a lower V_T compared to both enantiomers of [^{18}F]Fluspidine as well as compounds **3a** and **3b**. As for [^{18}F]FTC-146, the V_T was not determined in NHPs, to the best of our knowledge, making it impossible to compare its kinetic profile with that of other radiotracers [279]. Regarding [^{18}F]TZ3108, the (−)-enantiomer, although characterized by lower *in vitro* affinity for the S1R, was shown to exhibit significantly faster clearance kinetics compared to the racemate. Specifically, (−)-[^{18}F]TZ3108 reached its peak brain uptake at approximately 30 min p.i., whereas the racemic mixture peaked at around 45 min. Importantly, (−)-[^{18}F]TZ3108 demonstrated greater *in vivo* imaging ability as an S1R tracer than [^{11}C]SA4503, while simultaneously offering more favorable pharmacokinetic properties. These include improved washout rates and reduced nonspecific binding, making (−)-[^{18}F]TZ3108 a promising candidate for clinical PET imaging of the S1R system [276].

3.4.5. Dosimetric Evaluation and Clinical Translation

In the context of clinical translation of novel PET radiotracers, preclinical dosimetry and toxicity studies are crucial to rule out safety issues at an early stage so that there are no concerns for first-in-human trials. Dosimetric studies allow for the estimation of radiation absorbed doses in organs and tissues following radiotracer administration, typically using animal models. This step is crucial to ensure that exposure levels are consistent with human safety thresholds, as recommended by the International Commission on Radiological Protection [302]. In parallel, preclinical toxicity studies, usually performed in animal models according to the International Conference on Harmonization (ICH) guidelines, are intended to detect non-radiological adverse effects, such as chemical toxicity of the compound or its metabolites. As for the Effective Dose (ED) limits, most European countries follow a general threshold of 10 mSv, in accordance

with ICRP recommendations, while the U.S. Food and Drug Administration (FDA) sets the ED limit at 50 mSv. However, for radiotracers investigated under the authority of a Radioactive Drug Research Committee (RDRC) in the United States, dose constraints are applied both to the whole body and to individual organs. Furthermore, the injected mass must not induce any pharmacologically detectable effect. For most novel ^{18}F-labeled PET radiotracers, the injected mass is maintained within the range of 1 to 5 μg per dose [303]. Human radiation dosimetry studies of [^{11}C]SA4503 have shown that the highest absorbed doses were observed in the liver, kidneys, and pancreas. However, the overall radiation burden remained within acceptable limits for clinical application [254]. Subsequently, [^{11}C]SA4503 was employed together with [^{15}O]H2O in humans to compare the radioligand's brain kinetics with the regional cerebral blood flow (rCBF) in the same subject. Results showed that regional variations in binding potential are due to differences in S1R density and are not likely to reflect perfusion-related artifacts. Therefore, [^{11}C]SA4503 represents a suitable radiotracer for quantifying S1R expression in the human brain [304]. To date, no other compound derived from [^{11}C]SA4503 has been investigated in humans. As for [^{18}F]Fluspidine, both the (*R*)- and (*S*)-enantiomers have been investigated in mouse models to determine radiation dosimetry. The (*S*)-[^{18}F]Fluspidine enantiomer was further evaluated in four human volunteers, revealing an ED of 21.0 ± 1.3 μSv/MBq, which falls within the acceptable range for human studies. The radiotracer exhibited faster elimination from the brain, liver, stomach, and spleen, while clearance was comparatively slower in the bone marrow [305]. As with [^{11}C]SA4503, no other compounds derived from (*S*)-[^{18}F]Fluspidine have been studied in humans. Regarding [^{18}F]FTC146, dosimetric analysis indicated the highest radiation exposure in the spleen, urinary bladder, and, most prominently, bone tissue. Nevertheless, preclinical toxicity studies supported its suitability for human use [306]. In a first-in-human study involving 10 healthy volunteers, [^{18}F]FTC146 showed an effective dose of approximately 11.0 μSv/MBq. No adverse events were reported, and absorbed doses in critical and radiosensitive organs were considered acceptable and safe [295]. In terms of biodistribution, [^{18}F]FTC146 demonstrated a faster brain washout in humans compared to NHPs, though its kinetics remained relatively slow. Clearance was predominantly renal, with elimination via the kidneys and bladder. Unlike in monkeys, no significant skull uptake was observed in humans, but notable thyroid uptake was detected [306]. Other radioligands evaluated in the past through dosimetric tests to assess their potential for clinical translation are [^{18}F]FPS and [^{18}F]SFE. For both compounds, each organ is estimated to receive approximately 0.012–0.015 mGy/MBq, with the adrenal glands identified as the critical organs. Overall, both tracers appear to be safe for human use, with a maximum administered activity of 185 MBq and a mass dose of less than 2.8 μg for [^{18}F]FPS and less than 4 μg for [^{18}F]SFE per injection. However, neither compound has been further investigated in human studies [273,307].

3.4.6. Role of PET Imaging in the Assessment of Pathophysiological Processes

Only the most relevant PET radiotracers have been employed to investigate the role of S1R in pathophysiological processes and receptor occupancy studies. Among them, [^{11}C]SA4503 stands out as one of the earliest and most widely used S1R PET tracers, often considered the gold standard in this field. It has been utilized in a variety of applications. Using [^{11}C]SA4503, it was demonstrated that fluvoxamine and donepezil bind to S1R in the human brain at therapeutic doses following a single oral administration [308,309]. The tracer was also used in receptor occupancy studies in rat brains, where pretreatment with donepezil was shown to increase [^{11}C]SA4503 metabolism in a dose-dependent manner [289]. PET imaging

with [^{11}C]SA4503 has revealed that the iris-ciliary body and retina are rich in S1R expression [310]. Additionally, the tracer has been employed in preclinical *in vivo* drug screening to identify novel S1R agonists [311] and to detect spontaneous pituitary tumors in aged rats, distinguishing them from normal pituitary tissue and brain tumors [289]. Furthermore, [^{11}C]SA4503 has also been demonstrated to be suitable to quantify S1R binding of unlabeled ligands in competitive binding studies [312]. (*S*)-[^{18}F]Fluspidine has been investigated in patients with acute major depressive disorder, and an increased S1R binding in specific brain areas was found, which possibly reflects different depression subtypes. Furthermore, the authors assumed that this, together with a correlation between severity and receptor density, gives an indication for neuroadaptive counter regulation in such disease states [313]. The radioligand has also been used in glioblastoma studies in an orthotopic mouse model, revealing the presence of S1R in the infiltrative tumor margin, highlighting its potential applicability in tumor imaging as well [314]. [^{18}F]Fluspidine was also used in healthy volunteers and in patients with HD to demonstrate that pridopidine acts as a selective ligand for S1R, showing nearly complete S1R occupancy (~90%) and minimal occupancy of S2R/D3R (~3%) [315]. [^{18}F]FTC146 has proven to be a valuable tool in the investigation of pain-related conditions. It has been successfully employed to visualize nerve damage in a rat model of neuropathic pain, enabling non-invasive detection of affected areas. This highlights the potential of [^{18}F]FTC146, in PET/MRI combination, for the study of neuropathic pain [316]. In a clinical context, [^{18}F]FTC146 was used in a pilot study involving five healthy volunteers and five patients with chronic pelvic pain, demonstrating its possible utility as a diagnostic tool in such conditions [317]. Furthermore, [^{18}F]FTC146 has been applied in receptor occupancy studies of blarcamesine in rat models of Fragile X syndrome, where it revealed that blarcamesine binds to S1R in a dose-dependent manner [318]. As for [^{18}F]FPS, it has been used to demonstrate that neuroactive steroids can occupy the S1R in the brain of mice [319]. [^{18}F]TZ3108 has shown potential in detecting changes in the quantity and density of S1Rs in the liver of subjects with metabolic-associated fatty liver disease (MAFLD). Specifically, it enables the assessment of liver function impairment during the early stages of MAFLD, thereby overcoming the limitations associated with the use of [^{18}F]FDG. As such, [^{18}F]TZ3108 may serve as a promising tool for the early diagnosis of MAFLD [320,321].

3.5. Summary of the Introduction

From the analysis of the various PET radiotracers developed for S1R, the most significant compounds identified are [^{11}C]SA4503, one of the first PET ligands targeting S1R, along with [^{18}F]-(*S*)-Fluspidin and [^{18}F]FTC-146, the latter of which has been, and continues to be, evaluated clinically as a diagnostic tool for several pathologies (e.g., chronic pain, sciatica and osteosarcoma). Importantly, these radiotracers have also been employed in receptor occupancy studies to characterize novel S1R-based therapeutics, revealing specific interactions with S1R and thereby supporting their S1R-mediated effects (e.g., Blarcamesin and Pridopidine). Similarly, they have contributed to elucidating the S1R-mediated mechanisms of action of already established drugs such as fluvoxamine and donepezil.

Among the newer radiotracers, [^{18}F]TZ3108 and [^{18}F]CNY-05 appear to be the most promising as diagnostic agents (the former for the study of MAFLD and the latter for investigating the role of S1R in neurodegenerative diseases) although their clinical potential remains to be confirmed in future studies.

Despite ongoing investigations with the currently leading S1R radiotracers, the growing number of available PET agents will likely continue to expand in the pursuit of an optimal S1R imaging tool that overcomes the limitations of existing compounds and enables the full exploration of S1R function in health and disease.

3.6. Background and Aim

The S1R is widely expressed in the CNS, particularly in the cerebral cortex, hippocampus, striatum, amygdala, cerebellum, and brainstem. Its rexpression changes in several neurodegenerative diseases, such as AD [247] and PD [322]. Various molecules targeting S1R are under clinical investigation for the treatment of these pathologies [323]. For this reason, S1R has been proposed as a promising biomarker for the early diagnosis of neurodegenerative disorders, as demonstrated by the development of several PET radiotracers over recent years [233].

The research group in which this thesis was carried out had been active for several years in the study of S1R. During this research activity, 4-methylpiperidine was identified as a key basic moiety for the design of high-affinity S1R ligands. In the first series of compounds developed, 4-methylpiperidine was connected via a 3- or 4-methylene chain to a hydrophobic portion, such as tetralin or naphthalene nuclei [324], or phenoxy rings [325]. In particular, Berardi *et al.* investigated 4-chlorophenoxy-ethyl-4-methylpiperidine and 4-chlorophenoxy-propyl-4-methylpiperidine derivatives to analyze how the introduction of a stereogenic center near the pharmacophoric nitrogen atom affected binding to S1R and S2R. The chiral center was introduced by inserting a methyl group at different positions within the intermediate chain (Figure 3.4). All tested compounds exhibited good affinity for S1R. Among these, the propyl derivative (1-(3-(4-chlorophenoxy)propyl)-4-methylpiperidine, K_i S1R = 1.78 nM, K_i S2R = 38.6 nM) showed one of the highest affinity values, although with limited selectivity (22-fold). The ethyl derivative (1-(2-(4-chlorophenoxy)ethyl)-4-methylpiperidine (**L6**) with a subnanomolar K_i (S1R = 0.86 nM, K_i S2R = 239 nM, Figure 3.5) was also identified as a potent and selective ligand [325].

Building on **L6**, Abatematteo *et al.* [326] developed a new series of phenoxyethyl derivatives bearing para-substituents such as methoxy or chloro groups. The influence of methyl substitution at the α and β positions of the nitrogen atom, and the resulting creation of a stereogenic center, was also investigated (Figure 3.4). Overall, the stereochemistry of the chiral carbon atom appeared to affect selectivity only when the methyl group was adjacent to the basic nitrogen atom. The study further demonstrated that more stringent structural requirements were needed to reduce S2R affinity. Notably, the presence of a shorter and more flexible oxyethylene linker improved S1R affinity and selectivity. Nevertheless, **L6** remained the best-performing compound in this series [326].

Maintaining the phenoxyethylene scaffold, our research group subsequently conducted a new SAfiR and structure–activity relationship (SAR) study (Figure 3.4). The *p*-chloro substituent was replaced with electron-withdrawing, electron-donating, or bulky groups. In addition, different substitution patterns on the aromatic ring, including polysubstitution, were explored. The replacement of the 4-methylpiperidine moiety with alternative basic groups (BMs) was also evaluated. Since the new compounds were tested using different experimental sets, the reference compound **L6** was re-evaluated (K_i S1R = 1.49 nM, K_i S2R = 145.5 nM). All newly synthesized phenoxyethylpiperidines exhibited nanomolar affinity for S1R and varying degrees of selectivity, confirming the promise of the phenoxyethylpiperidine scaffold for S1R targeting. Compounds showing higher affinity and selectivity, together with **L6**, were tested *in vivo* in an AD model and demonstrated significant anti-AD activity [327].

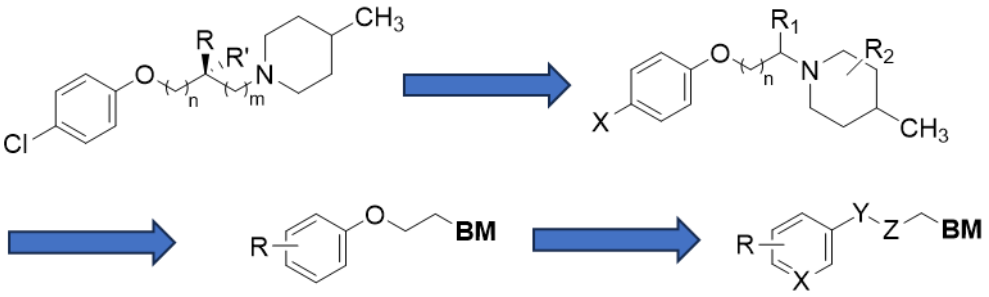

Figure 3.4. Evolution of scaffolding over the years [325–327].

Encouraged by these promising results and the potential of this scaffold in AD pathology, several structural modifications were subsequently carried out to develop a novel PET radiotracer for investigating S1R's role in AD. Among the previously tested compounds, the *p*-NO_2 derivative (4-methyl-1-(2-(4-nitrophenoxy)ethyl)piperidine, **PA9**, K_i S1R = 0.38 nM, K_i S2R = 143 nM, Figure 3.5) and the *p*-F derivative (1-(2-(4-fluorophenoxy)ethyl)-4-methylpiperidine, **LBB121**, K_i S1R = 11.6 nM, K_i S2R = 189 nM, Figure 3.5) [327] were selected as new lead structures. Based on these leads, a new series of phenoxyethylpiperidines incorporating a fluorine atom was synthesized to improve pharmacodynamic and pharmacokinetic properties and to identify the optimal fluorine position for radiolabeling (general structure shown in Figure 3.3). In parallel, isosteric modifications aimed at reducing lipophilicity were explored. Specifically, the aromatic ring was replaced with a pyridine moiety, and the 4-methylpiperidine was substituted with 4-methylpiperazine.

Among the tested compounds, compound **10** (also known as **CF31**), displayed particularly high affinity and selectivity and was therefore selected for radiolabeling and further biological evaluation through autoradiography on rat brain slices.

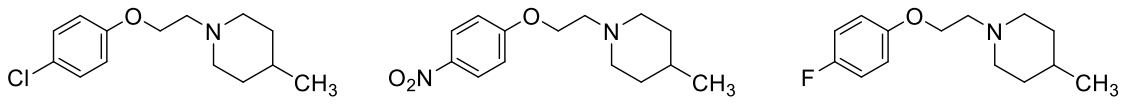

L6
K_i S1R = 1.49 nM
K_i S2R = 145.5 nM

PA9
K_i S1R = 0.38 nM
K_i S2R = 143 nM

LBB121
K_i S1R = 11.6 nM
K_i S2R = 189 nM

Figure 3.5. Chemical structure and pharmacodynamic profile of **L6, PA9** and **LBB12** [327].

3.7. Results

3.7.1. Chemistry

The synthesis of final compounds **10-15** and **17-19** was carried out using a conventional synthetic route previously described for lead compounds **LBB121**, **PA9** [327] and related derivatives (Scheme 3.1). In brief, commercially available phenols were condensed with ethyl 2-bromoacetate, and the resulting already known intermediates **26a-e** [327–329] were hydrolyzed under basic conditions to yield the corresponding already known carboxylic acids **27a-e** [327–329]. Condensation of these acids with either 4-methylpiperidine or 4-methylpiperazine upon activation with 1,1′-carbonyldiimidazole (CDI), afforded the corresponding amides **28a-b**,**e** and **29a-e**, respectively and the already known **28d** [327]. The amides were subsequently reduced to the corresponding final amines **11**–**15**, **18** and the already known **19** [330], as well as to the intermediates **31** and the previously reported compounds **30** [327], using borane–methyl sulfide complex (BMS). The resulting amines were then converted into their corresponding hydrochloride salts. Compounds **30** and **31** were subjected to catalytic hydrogenation using 10% Pd/C to furnish the already known **32** [327] and **33**, respectively. Subsequent alkylation of the phenolic group with 1-fluoro-2-iodoethane under basic conditions provided final compounds **10** (also known as **CF31)** and **17**.

A distinct synthetic route was employed for the preparation of final compounds **16**, **20** and **21** (Scheme 3.2), enabling access to the final amines in only two steps. In this strategy, the appropriate phenol was alkylated with 1,2-dibromoethane to obtain intermediates **34** [331] and **35**, which were then reacted with either 4-methylpiperidine or 4-methylpiperazine under basic conditions to afford the final products **16**, **20** and **21** .

As for compounds **22-25** (Scheme 3.3), the synthesis began with the condensation of 4-fluoroaniline and 2-bromoacetic acid upon activation with 1-ethyl-3-(3-dimethylaminopropyl)carbodiimide (EDC) to form the already known intermediate **36** [332]. This last compound was then coupled with the appropriate basic moiety (i.e. 4-methylpiperidine or 4-methylpiperazine) under basic conditions to afford compounds **22** and **23**, which were subsequently reduced using BMS to yield the final amines **24** and **25**.

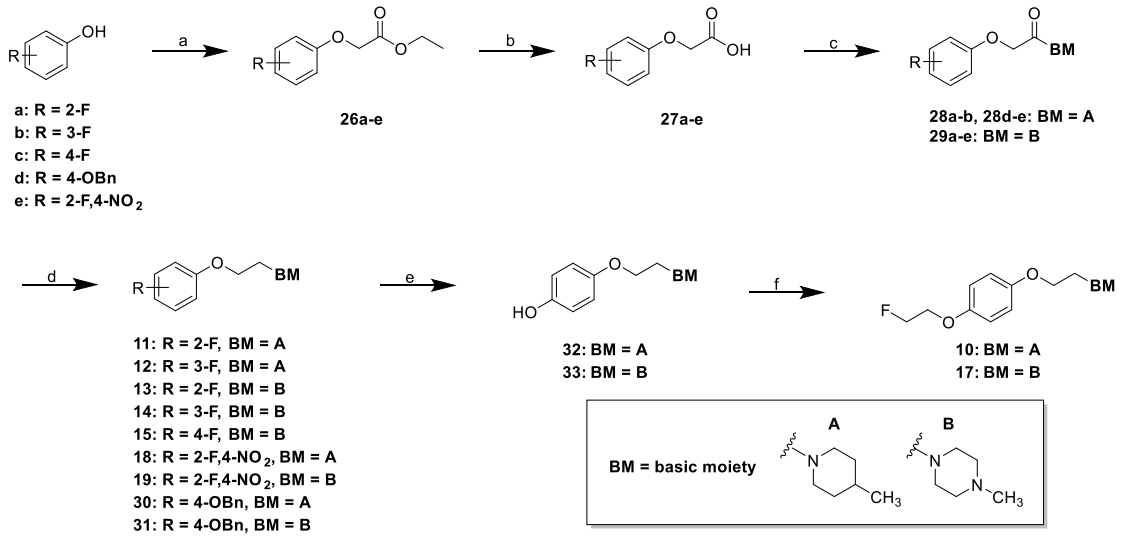

Scheme 3.1 Synthesis of final compounds **10-15** and **17-19**. (a) Ethyl 2-bromoacetate, K_2CO_3, CH_3CN, reflux, ON; (b) NaOH 2N, EtOH, RT, 4h; (c) Appropriate BM, CDI, dry THF, RT, ON; (d) $BH_3 \cdot Me_2S$ 2M, dry THF, reflux, 3h; (e) Pd/C 10%, H_2, 3.5 bar, EtOH 96%, RT, ON; (f) 1-fluoro-2-iodoethane, K_2CO_3, CH_3CN, reflux, ON.

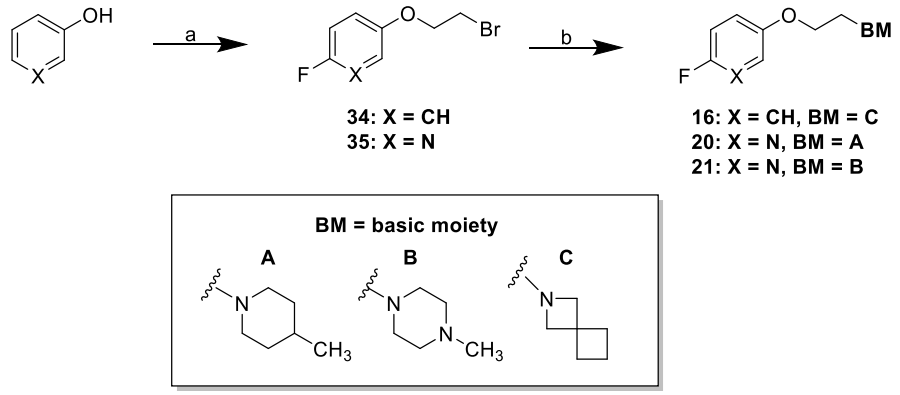

Scheme 3.2 Synthesis of final compounds **16**, **20** and **21**. (a) 1,2-dibromoethane K_2CO_3, CH_3CN, reflux, ON; (b) Appropriate BM, K_2CO_3, CH_3CN, reflux, ON.

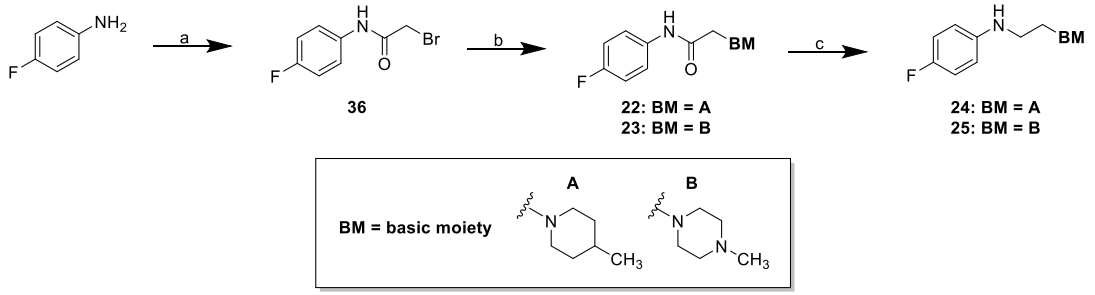

Scheme 3.3 Synthesis of final compounds **22-25**. (a) 2-bromoacetic acid, EDC, CH_2Cl_2, RT, 24h; (b) Appropriate BM, K_2CO_3, CH_3CN, reflux, ON; (c) $BH_3 \cdot Me_2S$ 2M, dry THF, reflux, 3h.

3.7.2. *In vitro* S1R and S2R Binding Affinities

The results of radioligand displacement studies are reported in Tables 3.1 and 3.2. as inhibition constants (K_i values), which were calculated by converting the experimentally determined IC_{50} values using the Cheng–Prusoff equation. Overall, phenoxyalkylpiperidines display low-nanomolar K_i values at S1R, as previously shown in our earlier work [327], confirming this scaffold as an optimal framework for high-affinity S1R binding. Since the lead compound **LBB121** shows good S1R affinity but limited S2R selectivity, we undertook structural modifications in order to obtain higher affinity and selectivity S1R ligands. Thus, we explored different substituents on the aromatic ring where we also inserted isosteric changes and replaced the basic moiety in order to identify a new PET candidate for S1R. We always kept the F-atom in view of the possible development of the ^{18}F-radiolabelled corresponding ligand. We firstshifted the fluorine atom from the *para*- to the *ortho*- and *meta*-positions (**11** and **12**). Although this resulted in slightly improved S1R affinity (K_i = 5.84 nM and 6.47 nM, respectively), the selectivity against the S2R was not improved. Replacing the *p*-fluoro group with a *para*-fluoro-ethoxy substituent (**10**) led to a slight improvement in the S1R affinity (K_i = 5.36 nM) and a marked increase in selectivity (561-fold). Starting from the lead compound **PA9**, we retained the *para*-nitro substitution and introduced an *ortho*-fluorine (**18**). The S1R affinity (K_i = 2.38 nM) which was reduced compared to **PA9** remained in the low-

nanomolar range, , while the affinity at the S2R was in the same range of **PA9** thus considerably decreasing the selectivity that dropped from >300-fold to >40-fold.

Replacement of the 4-methylpiperidine moiety in compounds **11**, **12**, **LBB121**, **10** and **18** with a 4-methylpiperazine one (**13**, **14**, **15**, **17** and **19**) resulted in an approximately 10-fold loss of S1R affinity. However, the marked reduction in S2R affinity led to a substantial increase in selectivity for each piperazine compared to the piperidine analogues and the highest selectivity values reached in the series. The only exception was *o*-F derivative (**13**) the in which the 4-methylpiperazine substituent led to a 24-fold loss in S1R affinity (K_i = 138 nM), so that the selectivity matched the value of the 4-methylpiperidine analogue (**11**). To explore the effect of the rigidification the 4-methylpiperidine was also replaced by the 2-azaspiro[3.3]heptane (**16**) showing an around 2-fold improvement in S1R (K_i = 5.85 nM) and S2R affinity (K_i = 65.6 nM) so that the selectivity profile remained unchanged.

Substitution of the aromatic ring with pyridine (**20**) led to a decrease in S1R affinity (K_i = 46.9 nM) with a parallel decrease in the S2R (K_i = 699 nM). Replacement of the phenoxy group with an aniline one (**24**) gave a comparable S1R affinity (K_i = 19.7 nM) to **LBB121** but improved S2R affinity (K_i = 78.4 nM) and thus reduced selectivity.

Introduction of an acetamide group (**22**) resulted in a dramatic reduction of affinity for both S1R (K_i = 499 nM) and S2R (Ki = 1631 nM), likely due to electron-withdrawing effects impairing the basicity of the piperidine *N*-atom.

The corresponding 4-methylpiperazine derivatives (**21**, **25**, **23**, respectively) exhibited the same trend shown by the phenoxy derivatives: i.e. considerably reduced S1R affinity and loss of S2R affinity with K_i values ranging from 294 nM to 14862 nM for S1R and from 8267 nM to 43020 nM for S2R.

Overall these data while confirming the phenoxy portion combined to a 4-methylpiperidine as the best combination for achieving S1R low nanomolar affinity and appreciable selectivity, provide also indication about the piperazine as a mean to achieve high S1R/S2R selectivity.

Taken all these data together, compound **10** (also known as **CF31)** emerged as the only derivative combining affinity and selectivity values amenable for PET application, prompting the development of [^{18}**F]-CF31** as a PET candidate for S1R.

Table 3.1. S1R and S2R affinities

GENERAL STRUCTURE

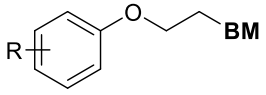

BM =

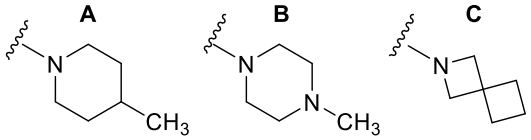

Compound	R	BM	K_i (nM)[a] S1R	K_i (nM)[a] S2R	SI[b] K_i S2R/S1R
11	2-F	A	5.84 ± 0.36	85.1 ± 8.6	14
12	3-F	A	6.47 ± 0.88	129 ± 9	20
LBB121[c]	4-F	A	11.6 ± 0.4	189 ± 69	16
13	2-F	B	138 ± 31	1511 ± 3.5	11
14	3-F	B	79.4 ± 14	9521 ± 204	120
15	4-F	B	59.4 ± 2.35	9648 ± 902	162
16	4-F	C	5.85 ± 0.69	66 ± 9	11
10 (CF31)	4-$O(CH_2)_2F$	A	5.36 ± 0.57	3009 ± 924	561
17	4-$O(CH_2)_2F$	B	65.3 ± 10.4	83285 ± 33015	1275
PA9[c]	4-NO_2	A	0.38 ± 0.14	143 ± 26	376
18	4-NO_2,-2-F	A	2.38 ± 0.30	115.05 ± 34	48
19	4-NO_2,-2-F	B	34.4 ± 2.5	6743 ± 2194	196
Haloperidol[d]			3.53	20.5	6

[a]Values represent the mean of at least two separate experiments in duplicate ± SEM; [b]SI represents selectivity; [c]Data from [327]; [d]Data from [333].

Table 3.2. S1R and S2R affinities

GENERAL STRUCTURE

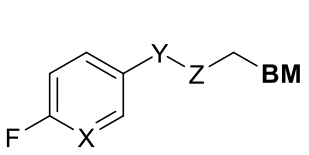

BM =

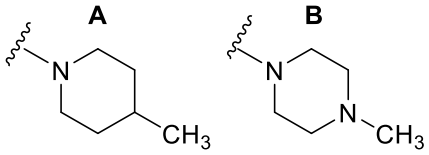

Compound	X	Y	Z	BM	K_i (nM)[a] S1R	K_i (nM)[a] S2R	SI[b] K_i S2R/S1R
LBB121[c]	CH	O	CH_2	A	11.6 ± 0.4	189 ± 69	16
20	N	O	CH_2	A	46.9 ± 6.69	699 ± 24	15
21	N	O	CH_2	B	314 ± 9	43020 ± 12020	137
22	CH	NH	CO	A	499 ± 113	1631 ± 141.5	3
23	CH	NH	CO	B	14862 ± 4129	29227 ± 20002	2
24	CH	NH	CH_2	A	19.7 ± 1.50	78.4 ± 13.5	4
25	CH	NH	CH_2	B	294 ± 180	8267 ± 1221	28

[a]Values represent the mean of at least two separate experiments in duplicate ± SEM; [b]SI represents selectivity; [c]Data from [327].

3.7.3. Blood-Brain Barrier permeability and P-Glycoprotein Interaction Investigation

CF31 was designed as a fluorine-18 PET ligand for imaging the S1R in the CNS with the aim of supporting early diagnosis of neurodegenerative disorders such as AD. The tracer's utility for CNS imaging depends fundamentally on its ability to cross the BBB and to avoid removal by active efflux transporters, notably P-gp. The BBB is a tightly regulated interface that restricts the brain entry of most xenobiotics and small molecules. P-gp, highly expressed at the luminal surface of brain capillary endothelium, is a major determinant of drug distribution to the brain and can substantially limit cerebral exposure of substrate compounds [334]. Consequently, assessing both passive permeability across a validated BBB model and the compound's interaction with P-gp is a critical step in radiotracer development for CNS targets. To evaluate whether **CF31** has favorable brain access we measured bidirectional permeability coefficients (P_{app}AB and P_{app}BA), calculated the BA/AB ratio (P_{app}) across Caco-2 cell monolayers, and quantified P-gp interaction using established protocols previously published by our group [335]. All experimental results are reported in Table 3.3.

Table 3.3. Evaluation of the BBB Permeability and P-gp Interaction of **CF31**

Compound	P_{app}BA (nm/sec)	P_{app}AB (nm/sec)	P_{app}(BA/AB)	P-gp activity EC_{50} μM (% at 100 μM)
CF31	1917	629	3.0	>100 (29%)

The comprehensive evaluation of the experimental findings (Table 3.3) indicates that **CF31** possesses favorable properties as a PET radiotracer for CNS applications, based on its BBB permeability and P-gp interaction profile. **CF31** exhibited appreciable bidirectional membrane permeability, reflecting both passive diffusion (BA flux) and active transport (AB flux). The high P_{app}BA value (1977 nm/s) indicates very high passive permeability of **CF31**, while the relatively good P_{app}AB value (629 nm/s), together with the absence of significant interaction with P-gp (EC_{50} > 100 μM), predicts a lack of efflux at the CNS level. Therefore, **CF31** is expected to cross the BBB effectively and reach its CNS target.

3.7.4. Radiochemistry

Based on its binding affinity and favorable prediction for BBB permeation, **CF31** was identified as the most promising candidate for the development of a novel S1R radioligand and was therefore selected for further biological investigations.

The synthesis of the tosylated precursor **38** (Scheme 3.4) was accomplished in two steps starting from the already known 4-(2-(4-methylpiperidin-1-yl)ethoxy)phenol (**32**) [327]. Initially, compound **32** underwent microwave-assisted alkylation with 2-bromoethan-1-ol to yield intermediate **37**. Subsequent conversion of the hydroxyl group into the corresponding tosylate, using tosyl chloride (TsCl), afforded the key intermediate **38**, as the precursor required for radiolabeling.

The radiosynthesis of **[^{18}F]CF31** (Scheme 3.4) was optimized employing a [^{18}F]fluoride-kryptofix complex and K_2CO_3 as base. The used activity ([^{18}F]fluoride) was in the range of 6-8 GBq. Various amounts of the key intermediate **38** (0.5–2 mg) were tested under thermal conditions using either CH_3CN (70–90 °C) or DMSO (100–140 °C) as solvents. The formation of **[^{18}F]CF31** was monitored by radio-HPLC analysis using both short (8 min of run, Method C) and long gradient method (15 min of run, Method B). The radiochemical yields (non-isolated) were in the range of 52–83% and 36–58% for CH_3CN and DMSO, respectively. Complementary radio-TLC analyses (AcOEt/MeOH 1:1, Figure S3.1) were performed to further assess the efficiency of each condition.

The optimized protocol was subsequently transferred to an automated module (Synthra RNplus Research, Hamburg, Figure S3.2 and Figure S3.3). In the final procedure, compound **38** (2 mg) dissolved in 1 mL of CH_3CN was combined with the [^{18}F]fluoride-kryptofix complex, and the reaction mixture was heated at 90 °C for 20 min. The reaction was quenched by addition of 3.5 mL of water, and the crude product was purified by semi-preparative RP-HPLC (Rt: ~41–42 min, Figure S3.4). Fractions containing **[^{18}F]CF31** were concentrated using a preconditioned reversed-phase SPE (RP-SPE) cartridge, followed by elution with 1.5 mL of absolute ethanol.

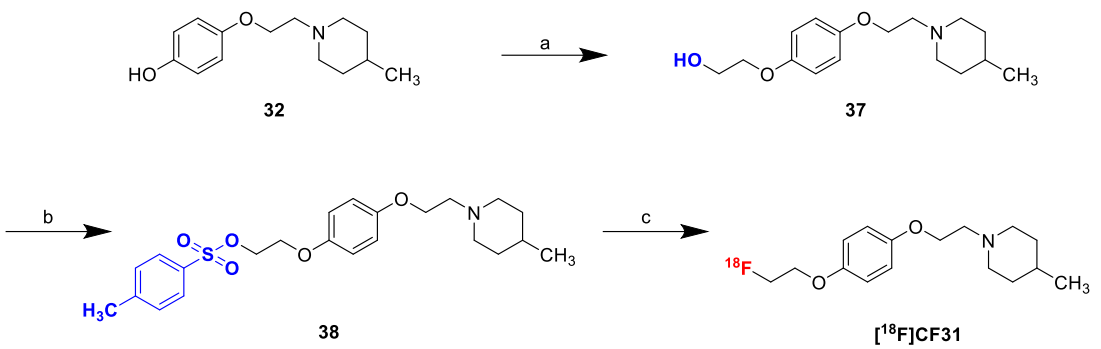

Scheme 3.4. Synthesis of tosylate precursor **38** and radiofluorination of final compound **[^{18}F]CF31**: (a) 2-bromoethan-1-ol, K_2CO_3, CH_3CN, MW, 120 °C, 40 min; (b) TsCl, Et_3N, dry CH_2Cl_2, 0 °C, 4h; (c) [^{18}F]fluoride-K_{222}/K_2CO_3, CH_3CN, 90 °C, 20 min.

For subsequent biological studies, ethanol was removed under a gentle stream of helium at 40 °C, and the final formulation was prepared in phosphate-buffered saline (PBS). The overall synthesis time was approximately 108 min. **[^{18}F]CF31** was obtained in 12–22% decay-corrected radiochemical yield (RCY, based on end of bombardment, *n = 6*), with radiochemical purity >99% and high molar activity (A_m: 118–194 GBq/µmol at the end of synthesis, *n = 6*).

Product identity was confirmed by analytical HPLC through co-injection with the non-radioactive reference standard using a ReproSil-Pur 120 C_{18}-AQ column (3 µm, 150 × 3 mm; Dr. Maisch GmbH), applying the long elution method B (Figure 3.6 and Figure S3.5).

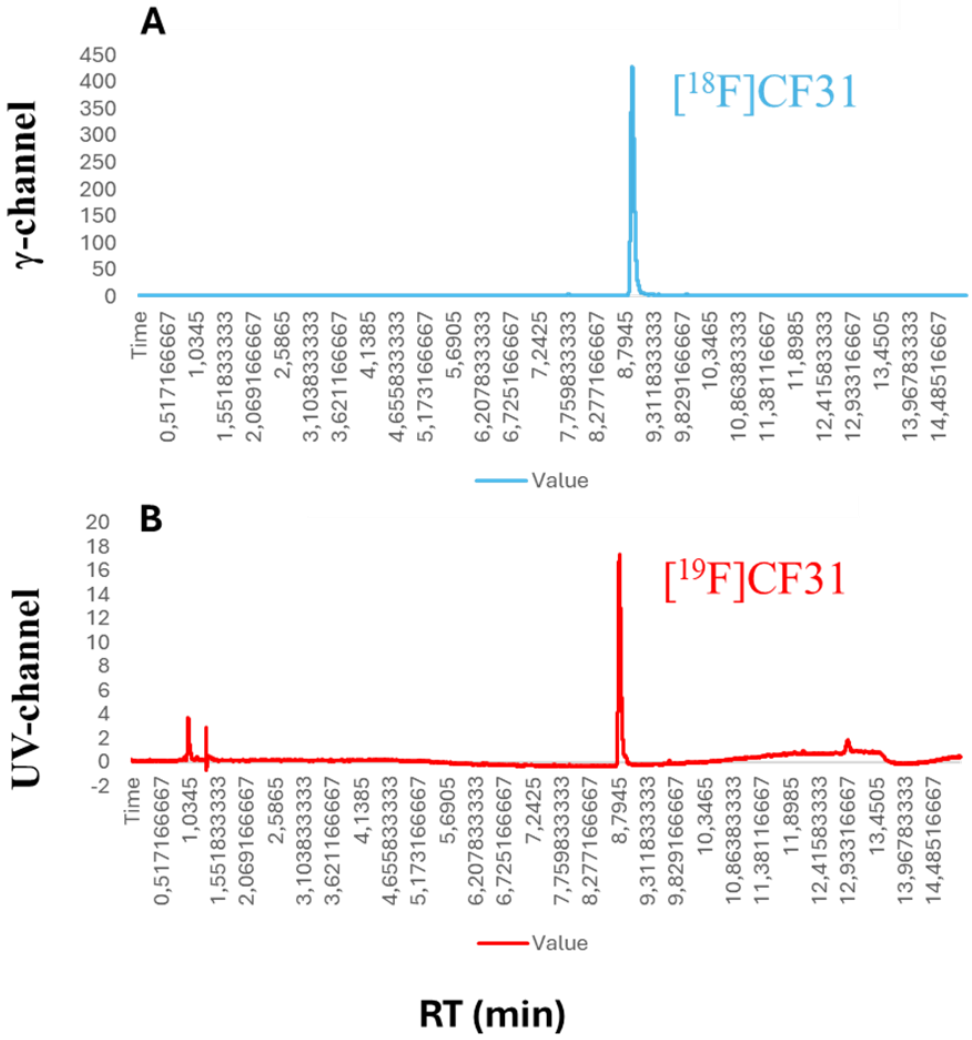

Figure 3.6. Radio- (light blue line, **A**) and UV- (red line, **B**) HPLC chromatograms of the identity confirmation of **[^{18}F]CF31** co-injected with the reference standard **CF31** (ReproSil-Pur 120 C_{18}-AQ, 3 µm, 150 x 3 mm (Dr. Maisch GmbH); Elution method B).

3.7.5. *In Vitro* Evaluation of [^{18}F]CF31.

3.7.5.1. Chemical Stability Evaluation

The *in vitro* stability of **[^{18}F]CF31** was evaluated by incubation in saline solution and PBS at 25 °C and in mouse plasma at 37 °C. Aliquots were collected at five time points (0–120 min) and analyzed by radio-HPLC (Figure 3.7). For stability studies in murine plasma, the aliquots were subjected to protein precipitation by the addition of cold acetonitrile, followed by vortex mixing and centrifugation. The recovery of radioactivity after protein precipitation was found to be 91.8 ± 3.1 %. In all cases, the proportion of intact **[^{18}F]CF31** was > 98% after 120 min of incubation, which corresponds to high stability throughout the entire incubation period.

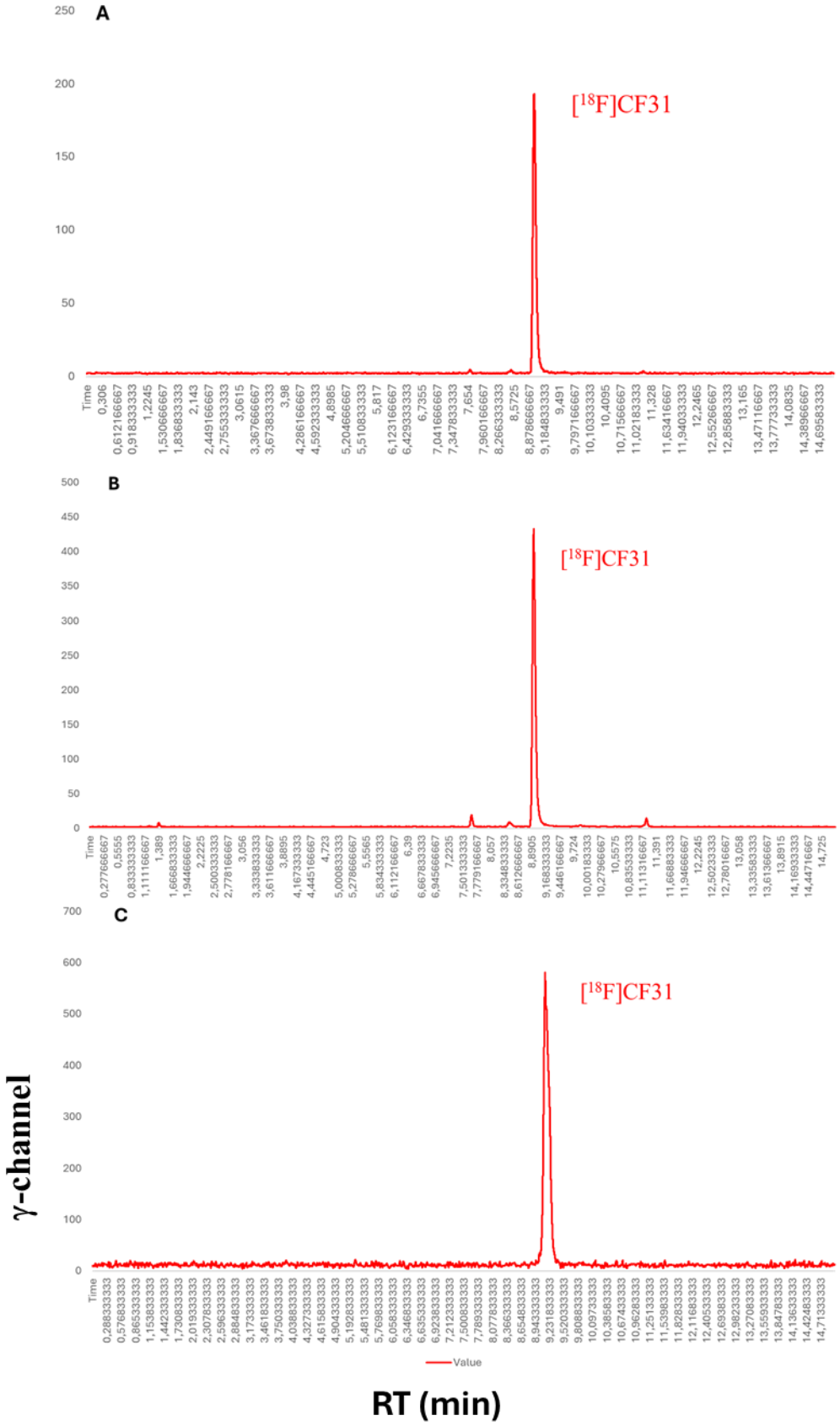

Figure 3.6. Radio-HPLC chromatograms (ReproSil-Pur 120 C_{18}-AQ, 3 µm, 150 × 3 mm; Dr. Maisch GmbH; elution method B) illustrating the *in vitro* chemical stability of **[^{18}F]CF31** after 120 min of incubation in (**A**) saline, (**B**) PBS and (**C**) mouse plasma. In all cases, the proportion of intact **[^{18}F]CF31** is > 98%,

3.7.5.2. Experimental determination of lipophilicity

The lipophilicity of **[^{18}F]CF31** was experimentally determined at physiological pH using the shake-flask method [77], yielding a $logD_{7.4}$ value of 1.24 ± 0.01 (*n = 4*). This is markedly lower than predicted by computational methods (clogP = 4.123 with ChemDraw and clogP = 3.29 with SwissADME). Although the measured $logD_{7.4}$ falls below the recommended range (1.5–3.0) for central nervous system–oriented radiotracers [77], **[^{18}F]CF31** does not interact with P-gp (Table 3.3). Therefore, it is still expected to penetrate the BBB, as has been demonstrated for other S1R PET tracers such as **[^{18}F]FTC146** and **[^{18}F]FBFP** with similar or lower $logD_{7.4}$ value ($logD_{7.4}$ = 1.45 and 0.76, respectiviy) [233].

3.7.5.3. Experimental determination of K_D and B_{max}

The radioligand binding assay demonstrated a high affinity of **[^{18}F]CF31** for *h*S1R. In membrane preparations from *h*S1R-HEK293 cells, homologous competition with unlabeled **CF31** yielded an apparent dissociation constant (K_D) of 1.66 nM and an apparent maximal binding capacity (i.e., the total number of available receptor sites in the preparation) B_{max} of approximately 1.41×10^{-10} mol/mg protein (≈ 0.14 pmol/mg protein). In intact *h*S1R-HEK293 cells, **[^{18}F]CF31** exhibited comparable affinity, with an estimated apparent K_D of 1.34 nM. Conversely, towards wildtype HEK293 cells, expressing the *h*S1R at physiological levels, **[^{18}F]CF31** displayed lower affinity (apparent K_D = 45.7 nM,).

In summary, **[^{18}F]CF31** displayed higher apparent affinity in cells transfected with the target receptor compared to cells expressing the receptor at physiological levels. This difference is likely attributable to the higher receptor density in transfected cells, which increases the proportion of specific binding relative to non-specific binding and improves ligand-receptor interaction efficiency. Additional factors such as receptor localization, accessibility at the cell surface, and reduced ligand depletion in high-B_{max} systems may also contribute to the observed increase in apparent affinity. All data are resumed in Table 3.4. and the curves for the determination of K_D are shown in Figure S3.6.

Furthermore, radioligand binding experiments confirmed the high target specificity of **[^{18}F]CF31**, as binding was completely abolished by co-incubation with 1 µM of the S1R ligands haloperidol or **FTC-146**. Together, these findings demonstrate that **[^{18}F]CF31** is a nanomolar-affinity radioligand for the *h*S1R, exhibiting robust and reproducible binding parameters across independent experiments and experimental systems.

Table 3.4. Experimental values of K_D and B_{max} obtained from a single binding assay performed with different HEK293-based cell systems.

Material	K_D (nM)	B_{max} (mol/mg protein)
*h*S1R-HEK293 membrane preparation	1.66	1.41×10^{-10}
*h*S1R-HEK293 whole cells	1.34	Not determined
Wild type HEK-293 cells	45.7	Not determined

3.7.5.4. *In Vitro* Metabolism

[^{18}F]CF31 was incubated with mouse liver microsomes (MLM) in PBS in the presence of nicotinamide adenine dinucleotide phosphate (NADPH) for 30 min at 37 °C under gentle shaking at 350 rpm (*n = 3*), following a published protocol [336,337]. The samples were subjected to protein precipitation by the addition of ice-cold CH_3CN, followed by vortex mixing and centrifugation, as previously described for the murine plasma stability studies. The resulting supernatants were collected and analyzed by radio-HPLC (Figure 3.7). The recovery of radioactivity after protein precipitation was determined using a gamma counter and was found to be 98.4%. The validity of the assay was verified by observing complete conversion of testosterone under identical conditions. Control experiments lacking either NADPH or both NADPH and MLM were also carried out for each test compound. After 30 min of incubation, only 5% of the parent compound, **[^{18}F]CF31**, remained. The predominant metabolite, designated **[^{18}F]M1**, accounted for approximately 94% of the total signal. Its retention time (Rt = 1.24 min) indicates high polarity. Based on previous investigations of radiotracers containing a [^{18}F]fluoroethoxy group [338], **[^{18}F]M1** is most likely 2-[^{18}F]fluoroethanol or its oxidized derivatives, 2-[^{18}F]fluoroacetaldehyde and 2-[^{18}F]fluoroacetate, formed through CYP450-mediated metabolism [339,340], all of which are capable of crossing the BBB.

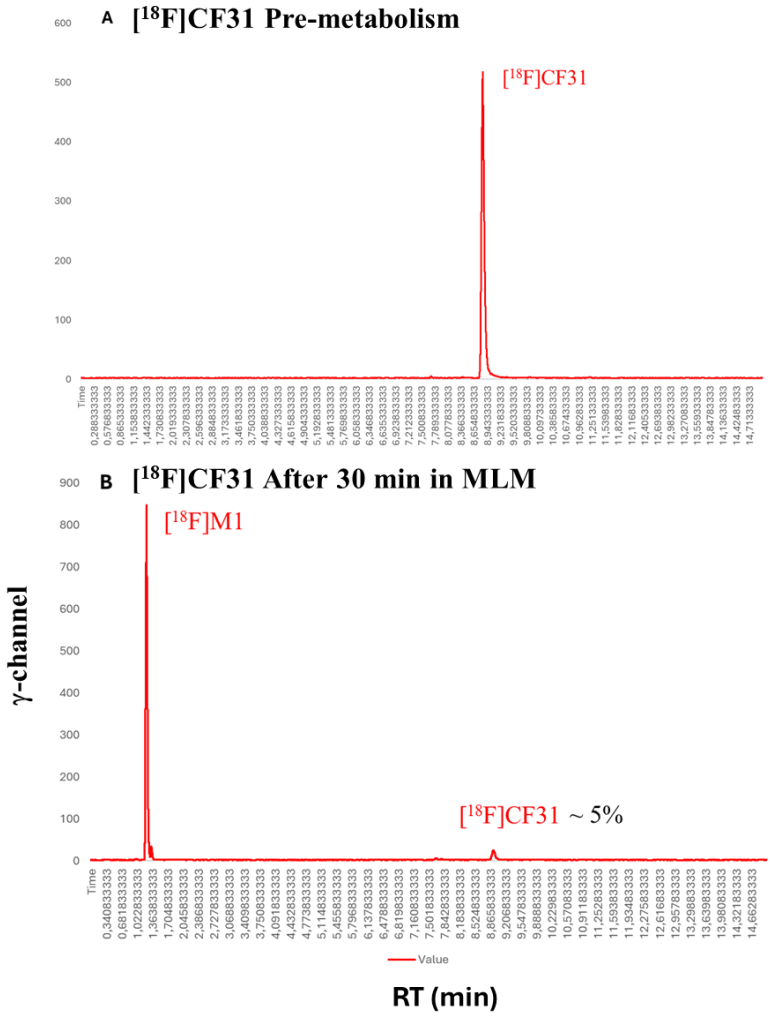

Figure 3.7. Radio-HPLC chromatograms (ReproSil-Pur 120 C_{18}-AQ, 3 µm, 150 × 3 mm; Dr. Maisch GmbH; elution method B) showing **[^{18}F]CF31** before metabolic studies (**A**) and after 30 min of incubation in MLM (**B**). After 30 min, only 5% of unchanged **[^{18}F]CF31** remained; the major metabolite was identified as **[^{18}F]M1**.

To verify whether the main metabolite corresponded to the hypothesized structure, the *in vitro* metabolism of the non-radioactive analogue (**[^{19}F]-CF31**) was investigated using compounds **32** and **37** as reference. The study was conducted as previously described, employing two concentrations of the cold compound (20 and 100 µM, $n = 3$ for each). The HPLC method was modified (Elution method D), as under the chromatographic conditions established for **[^{18}F]CF31**, compounds **32** and **37** exhibited identical retention times, hindering the identification of potential metabolic pathways.

At 20 µM of **CF31**, no parent compound was detectable after 30 min of incubation. Conversely, at 100 µM, **CF31** was still present, possibly due to the higher substrate concentration or the relatively high acetonitrile content in the incubation medium (approximately 1.5%). Nevertheless, at 100 µM a greater amount of one metabolite was observed.

To determine the predominant metabolite between **32** and **37**, the 100 µM **CF31** MLM incubation sample was analyzed after sequential spiking with **32** and **37**. In the chromatogram of **CF31** spiked with **37**, two distinct metabolite peaks were observed (Figure S3.7). In contrast, the chromatogram of **CF31** spiked with **32** showed an increased intensity of metabolite peaks (Figure 3.8).

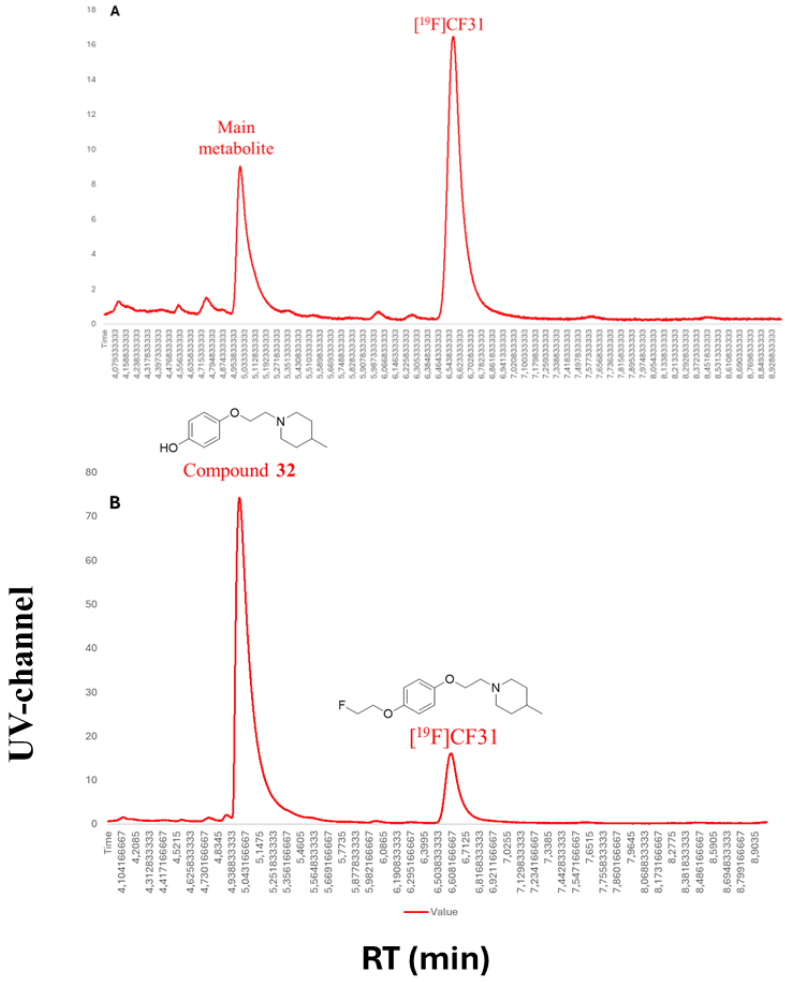

Figure 3.8. Radio-HPLC chromatograms (ReproSil-Pur 120 C_{18}-AQ, 3 µm, 150 × 3 mm; Dr. Maisch GmbH; elution method D) showing **[^{19}F]CF31** before spiking with compound **32** (**A**) and after spiking with compound **32** (**B**). The increased metabolite signal after spiking confirms its assignment to compound **32**. For clarity, only the 4–9 min retention time window is shown in both chromatograms to improve peak visibility.

These findings identified compound **32** as the primary metabolite, confirming that the main metabolic pathway involves cleavage of the fluoroethyl group (Figure 3.9).

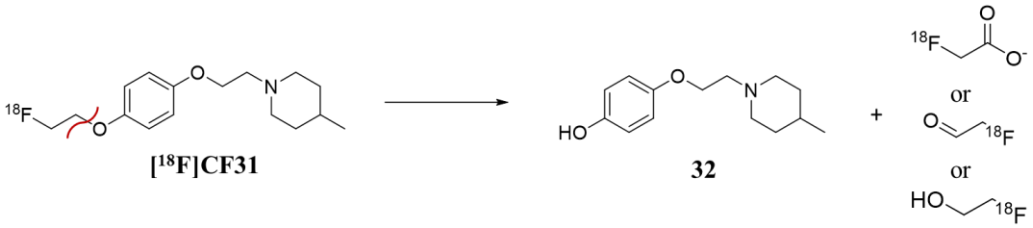

Figure 3.9. Schematic representation of the cleavage of the fluororethoxy moiety, which represents the principal metabolic pathway observed in the *in vitro* MLM experiment.

3.7.5.5. *In vitro* autoradiography

In vitro autoradiography of **[^{18}F]CF31** (3.35 nM; A_m=194 GBq/µmol at start of the incubation) with cryosections of mouse brain (*n = 2*) revealed a well-defined binding pattern with intense labeling in regions known to express high levels of the S1R. The autoradiographic images (Figure 3.10) showed particularly high signal in the caudate–putamen, followed by the cerebral cortex and hippocampus, with additional pronounced binding in the superior colliculus. This distribution closely mirrors the S1R expression map reported by Phan et al. [341], which highlights strong immunoreactivity in the same areas, supporting the conclusion that **[^{18}F]CF31** selectively targets S1R. Low non-specific binding of **[^{18}F]CF31** is indicated by the low signal displayed in white-matter structures. Blocking studies (Figure S3.8) further confirmed the target specificity of **[^{18}F]CF31**: haloperidol, **FTC-146**, and **CF31** at 1 µM displaced > 90% of the total binding.

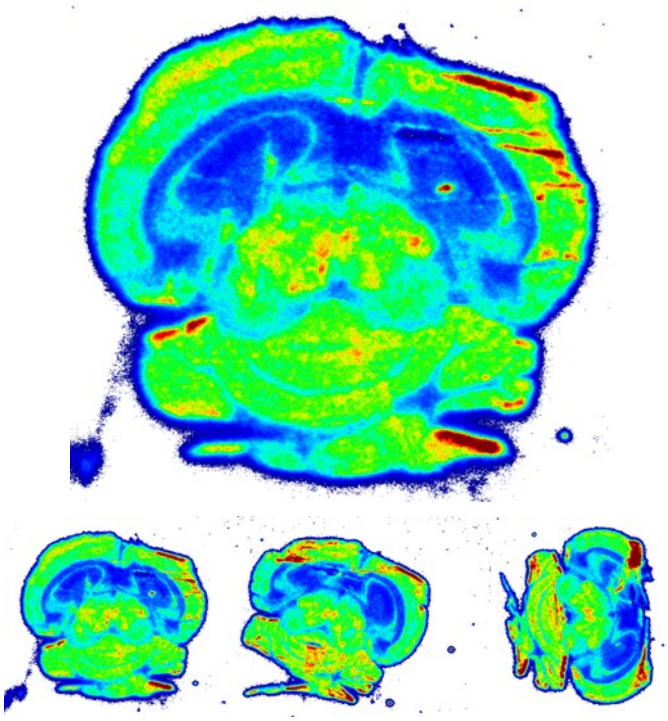

Figure 3.10. Examples for total binding; showing the heterogeneous distribution of binding sites of **[^{18}F]CF31** in mouse brain with high density in regions known to express sigma1 receptor; low binding in white matter regions indicates low non-specific binding (corresponding to the comparably low lipophilicity) (quantum level 4000 – 50972).

3.8. Discussion

Starting from the lead compounds **L6** [326], **PA9** and **LB121** [327], a new series of phenoxyethylpiperidines and their isosteres was developed. SAfiR studies revealed that the phenoxyethylpiperidine scaffold outperforms the corresponding isosteric derivatives (Tables 3.1 and 3.2).

Among the synthesized compounds, **CF31** emerged as a promising new PET candidate, displaying high S1R affinity (K_i = 5.36 nM) and excellent selectivity against the S2R (approximately 560-fold). Its lack of interaction with the P-gp (EC_{50} > 100 μM) and the appreciable bidirectional membrane permeability, suggested its ability to cross the BBB, supported by the experimental $logD_{7.4}$ of 1.24.

Radiolabeling has successfully been performed using $K_{2.2.2.}$ and K_2CO_3 sol. (20 mg/mL) in CH_3CN at 90 °C for 20 min, yielding the corresponding ^{18}F-labeled compound with good RCY (12–22%), high molar activity (118–194 GBq/μmol), and excellent radiochemical purity (>99%, *n = 6*).

[^{18}F]CF31 exhibits high chemical stability in PBS, saline solution, and mouse plasma (>98% after 2h). *In vitro* metabolism studies in mouse liver microsomes however show extensive degradation, with only ~5% of unchanged parent compound remaining after 30 min of incubation. Parent-compound control experiments have confirmed cleavage of the fluoroethoxy group as the main metabolic pathway.

Determination of K_D values for **[^{18}F]CF31**, with and without blocking agents, demonstrates clear target specificity. Notably, the measured K_D is consistent with the K_i of the cold compound (2–5 nM vs. 5.36 nM, respectively).

In vitro autoradiography clearly demonstrate that **[^{18}F]CF31** possesses a highly specific binding profile, an excellent match with the known S1R distribution, and overall characteristics that support its potential application as a selective PET radiotracer for the S1R.

The promising results obtained through *in vitro* autoradiography, both in the presence and absence of a blocker, allow for a comparison with the main PET radiotracers for S1R as discussed in the current literature. This comparison is, however, limited to autoradiographic data, as *in vivo* information is not yet available.

The autoradiographic distribution of **[^{18}F]CF31** is consistent with previously reported S1R radioligands, such as [^{18}F]Fluspidine and **[^{18}F]FTC146**. Similarly to these tracers, **[^{18}F]CF31** shows high uptake in S1R-rich regions, including the cortex and hippocampus, and low binding in white matter structures, indicative of minimal nonspecific binding. While [^{18}F]Fluspidine exhibits particularly strong accumulation in the facial nucleus, **[^{18}F]CF31** displays a distinct yet consistent S1R-specific pattern, further supported by effective blockade of tracer uptake. Unlike **FTC-146**, **CF31** exhibits a lower K_i, which may be advantageous in avoiding irreversible kinetics *in vivo*. Metabolically, however, **CF31** performs less favourably than the other reported radiotracers, showing poor metabolic stability, although these data are currently limited to *in vitro* predictions and require *in vivo* confirmation.

Given that lead compounds belonging to the same structural class as **CF31**, previously reported in our earlier work [327], have demonstrated strong anti-AD activity *in vivo*, ongoing studies are investigating **[^{18}F]CF31** using human brain slices from AD patients and healthy controls to explore its potential utility in early AD diagnosis. Data from these studies are not yet available.

3.9. Future perspectives

Regarding future directions, **[^{18}F]CF31** will be evaluated *in vivo* (rats and/or mice) to determine its ability to cross the BBB and to analyze its biodistribution. These experiments will also provide insights into its actual metabolic stability and the potential for any metabolites to cross the BBB and influence imaging results.

If poor metabolic stability is confirmed *in vivo*, structural modifications may be warranted, as the metabolically labile site has been precisely identified: metabolism occurs specifically at the fluoroethoxy moiety. The Ar–O–CH_2 group represents the weakest metabolic site due to its high conformational accessibility and the ability of the ether oxygen to stabilize the α-carbon radical/carbocation formed during CYP-mediated oxidation, resulting in an unstable hemiacetal that rapidly collapses to the corresponding phenol.

Several strategies could be considered to improve metabolic stability. One option is the isosteric replacement of the ether oxygen with a carbon (Option A, Figure 3.11), which would abolish the *O*-dealkylation pathway, prevent hemiacetal formation, and reduce stabilization of oxidative intermediates. Alternatively, introducing an electron-withdrawing substituent on the aromatic ring, such as F, Cl, or CF_3 (Option B, Figure 3.11), could decrease CYP-mediated oxidation by lowering the electron density of the ring and sterically shielding the ether bond. This approach is unlikely to compromise S1R affinity or selectivity, as such substituents have been well-tolerated in this scaffold, as demonstrated in the SAfiR studies reported in this chapter and in our previous work [327]. Another strategy could be the introduction of a gem-dimethyl group along the side chain (Option C, Figure 3.11) increases metabolic stability by imposing steric hindrance that limits access of oxidative enzymes, while simultaneously eliminating α-hydrogens at the substituted carbon, thereby reducing susceptibility to oxidative metabolism. However, this strategy may significantly affect both affinity and selectivity. Finally, deuteration of the ethoxy chain (Option D, Figure 3.11) could be employed, as commonly done in PET radiotracer development. The presence of deuterium would slow CYP-mediated *O*-dealkylation via a primary kinetic isotope effect, reducing the rate of the C–H bond cleavage at the rate-limiting step without affecting receptor binding.

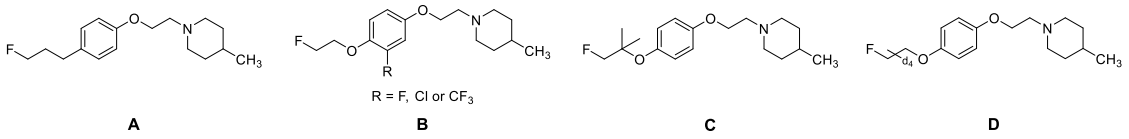

Figure 3.11. Possible strategies to improve metabolic stability include: **A**) isosteric replacement of the ether oxygen with carbon; **B**) introduction of an electron-withdrawing substituent on the aromatic ring; **C**) introduction of a gem-dimethyl group chain **D**) incorporation of a deuterated ethoxy chain.

3.10. Conclusions

[^{18}F]CF31 is a novel PET radiotracer targeting the S1R. Belonging to the phenoxyethylpiperidine class, it has demonstrated high affinity and exceptional selectivity for S1R *in vitro*. Its low interaction with P-gp, combined with a favorable $logD_{7.4}$, suggests efficient penetration into the central nervous system. The observed K_D values, together with autoradiographic studies conducted in the presence and absence of a blocker, confirm the tracer's high specificity and support its further evaluation in *in vivo* studies.

3.11. Materials and Methods

3.11.1. Chemistry

All chemicals were purchased from Sigma-Aldrich, TCI Chemicals, Ambeed, or Angene. Thin layer chromatography (TLC) was performed using plates from Merck (silica gel 60 F_{254}). Column chromatography was performed with Merck silica gel 60 Å (63-200 mm; ratio of crude mixture to silica gel 1:30 w/w, unless otherwise stated) as the stationary phase. Melting points (mp) were determined with a capillary apparatus (Büchi 540). ^{1}H-NMR spectra were recorded in the indicated solvent on a Varian Mercury-VX spectrometer (300 MHz) or on an Agilent 500-vnmrs500 spectrometer (499.801MHz). The following data are reported: chemical shift (δ) in ppm, multiplicity (s = singlet, d = doublet, t = triplet, q = quartet, quint = quintet, m = multiplet, dd = doublet of doublets, dt = doublet of triplets, td = triplet of doublets, and br = broad signal), integration, and coupling constant (J) in hertz. Recording of mass spectra was done on an HP6890-5973 MSD gas chromatograph/mass spectrometer; only significant m/z peaks, with their percentage of relative intensity in parentheses, are reported. HRMS-ESI analyses were performed on a Bruker Daltonics MicrOTOF-Q II mass spectrometer. All spectra were in accordance with the assigned structures. The purity of target compounds was assessed by HPLC. Analytical HPLC analyses were performed on final compounds using a Thermo Fisher Scientific Vanquish HPLC with Thermo Fischer Scientific Accucore aQ Column, 2.6 µm, 2.1 X 100 mm at a flow rate of 0.3 mL/min. Isocratic elution of the compounds **10**, **16**, **18**-**19** and **21**-**22** was carried out with 60:40 (v/v) (pH = 3.00), whereas compounds **11**-**15**, **17**, **20** and **23**-**24** were eluted using 70:30 (v/v) NH_4OAc /MeOH (pH = 3). Finally, elution of the compound **25** was carried out with 90:10 (v/v) NH_4OAc /MeOH (pH = 3). UV signals were detected at 254 nm and 280 nm. All compounds are >95% pure by HPLC.

*General procedure for the synthesis of esters **26a-e**.* To a solution of the appropriate phenol (1 mol, 1 eq) in CH_3CN (15 mL), K_2CO_3 (2 mol, 2 eq) and ethyl 2-bromoacetate (1.2 mol, 1.2 eq) are added. The resulting mixture was refluxed with stirring ON and then was allowed to cool to room temperature. The solvent was removed under vacuum. The residue was taken up with H_2O (20 mL) and extracted with CH_2Cl_2 (3 x 20 mL). The combined organic layers were dried (Na_2SO_4) and evaporated under vacuum to afford a crude residue which was purified by column chromatography. The GC-MS and NMR analyses are consistent with those previously reported.

*ethyl 2-(2-fluorophenoxy)acetate (**26a**)* [329].

*ethyl 2-(3-fluorophenoxy)acetate (**26b**)* [329].

*ethyl 2-(4-fluorophenoxy)acetate (**26c**)* [327].

*ethyl 2-(4-(benzyloxy)phenoxy)acetate (**26d**)* [327].

*ethyl 2-(2-fluoro-4-nitrophenoxy)acetate (**26e**)* [328].

*General procedure for the synthesis of acids **27a-e**.* The ethyl esters ***26a-e*** were dissolved in a mixture 1:1 of NaOH 2N (15 mL) and EtOH 96% (15 mL) and the reaction mixture was stirred at room temperature for 4 h. The solvent was removed under vacuum. The solution was acidified (HCl 3N) and extracted with AcOEt (3 x 20 mL). The combined organic layers were dried (Na_2SO_4) and evaporated under vacuum to afford a desired carboxylic acid, which was used without further purification.

*2-(2-fluorophenoxy)acetic acid (**27a**)* [329].

*2-(3-fluorophenoxy)acetic acid (**27b**)* [329].

*2-(4-fluorophenoxy)acetic acid (**27c**)* [327].

*2-(4-(benzyloxy)phenoxy)acetic acid (**27d**)* [327].

*2-(2-fluoro-4-nitrophenoxy)acetic acid (**27e**)* [328].

*General procedure for the synthesis of amides **28a-b, 28d-e** and **29a-e***. The acids **27a-e** (1 mol, 1 eq) were dissolved in dry THF (8 mL) and CDI (1.3 mmol, 1.3 eq) were added. The reaction mixture was stirred at room temperature for 2 h to activate the acid. The appropriate BM (1.3 mol, 1.3 eq) was added to the solution and the mixture was stirred at room temperature for 18 h under argon atmosphere. The mixture was taken up with H_2O (20 mL) and extracted with Et_2O (2 x 20 mL) and AcOEt (2 x 20 mL). The collected organic layers were dried (Na_2SO_4) and evaporated under vacuum to afford a crude residue which was purified by column chromatography.

*2-(2-fluorophenoxy)-1-(4-methylpiperidin-1-yl)ethan-1-one **(28a)***. The crude residue was purified by column chromatography using CH_2Cl_2/AcOEt 6:4 to obtain a yellow oil. Yield, 83%. ^{1}H-NMR ($CDCl_3$, 300 MHz) δ: 0.93 (3H, d, J = 6.6 Hz), 1.01-1.19 (2H, m), 1.56-1.73 (3H, m), 2.57-2.66 (1H, m), 3.00-3.09 (1H, m), 3.95-4.01 (1H, m), 4.48-4.54 (1H, m), 4.74 (2H, s), 6.89-6.96 (1H, m, Ar), 7.01-7.11 (3H, m, Ar). GC-MS m/z: 251 (M^+, 49), 140 (89), 126 (100), 112 (20), 98 (42), 83 (36), 55 (51).

*2-(3-fluorophenoxy)-1-(4-methylpiperidin-1-yl)ethan-1-one **(28b)***. The crude residue was purified by column chromatography using CH_2Cl_2/AcOEt 6:4 to obtain a yellow oil. Yield, 88%. ^{1}H-NMR ($CDCl_3$, 300 MHz) δ: 0.94 (3H, d, J = 6.6 Hz), 1.01-1.18 (2H, m), 1.55-1.72 (3H, m), 2.57-2.66 (1H, m), 2.99-3.08 (1H, m), 3.85-3.91 (1H, m), 4.49-4.54 (1H, m), 4.66 (2H, s), 6.64-6.75 (3H, m, Ar), 7.16-7.24 (1H, m, Ar). GC-MS m/z: 251 (M^+, 29), 140 (43), 126 (100), 95 (29), 83 (31), 55 (48).

*2-(4-(benzyloxy)phenoxy)-1-(4-methylpiperidin-1-yl)ethan-1-one **(28d)*** [327]**.**

*2-(2-fluoro-4-nitrophenoxy)-1-(4-methylpiperidin-1-yl)ethan-1-one **(28e)***. The crude residue was purified by column chromatography using CH_2Cl_2/AcOEt 6:4 to obtain a yellow solid. Yield, 61%. ^{1}H-NMR ($CDCl_3$, 300 MHz) δ: 0.95 (3H, d, J = 6.3 Hz), 1.05-1.18 (2H, m), 1.63-1.77 (3H, m), 2.57-2.66 (1H, m), 3.04-3.12 (1H, m), 3.83-3.87 (1H, m), 4.45-4.50 (1H, m), 4.88 (2H, s), 7.11 (1H, t, J = 8.7 Hz), 7.97-8.04 (2H, m, Ar). GC-MS m/z: 296 (M^+, 12), 140 (55), 126 (100), 83 (21), 55 (40).

*2-(2-fluorophenoxy)-1-(4-methylpiperazin-1-yl)ethan-1-one **(29a)***. The crude residue was purified by column chromatography using CH_2Cl_2/MeOH 95:5 to obtain a yellow oil. Yield, 58%. ^{1}H-NMR ($CDCl_3$, 500 MHz) δ: 2.28 (3H, s), 2.36-2.42 (4H, m), 3.60-3.69 (4H, m), 4.75 (2H, s), 6.91-6.97 (1H, m, Ar), 7.01-7.12 (3H, m, Ar). GC-MS m/z: 252 (M^+, 10), 99 (54), 70 (100), 56 (34), 42 (27).

*2-(3-fluorophenoxy)-1-(4-methylpiperazin-1-yl)ethan-1-one **(29b)***. The crude residue was purified by column chromatography using CH_2Cl_2/MeOH 95:5 to obtain a trasparent oil. Yield, 90%. ^{1}H-NMR ($CDCl_3$, 500 MHz) δ: 2.28 (3H, s), 2.37-2.40 (4H, m), 3.55-3.63 (4H, m), 4.67 (2H, s), 6.64-6.73 (3H, m, Ar), 7.20-7.24 (1H, m, Ar). GC-MS m/z: 252 (M^+, 24), 99 (50), 70 (100), 56 (32), 42 (25).

*2-(4-fluorophenoxy)-1-(4-methylpiperazin-1-yl)ethan-1-one **(29c)***. The crude residue was purified by column chromatography using CH_2Cl_2/MeOH 95:5 to obtain a trasparent oil. Yield, 83%. ^{1}H-NMR ($CDCl_3$, 500 MHz) δ: 2.30 (3H, s), 2.35-2.39 (4H, m), 3.56-3.64 (4H, m), 4.68 (2H, s), 6.88 (2H, dd, J = 8.3 Hz, J_F = 4.5 Hz, Ar), 6.95 (2H, t, J = 8.0 Hz, Ar). GC-MS m/z: 252 (M^+, 28), 99 (52), 70 (100), 56 (30), 42 (22).

2-(4-(benzyloxy)phenoxy)-1-(4-methylpiperazin-1-yl)ethan-1-one ***(29d)***. The crude residue was purified by column chromatography using CH_2Cl_2/MeOH 95:5 to obtain a yellow solid. Yield, 98%. ^{1}H-NMR ($CDCl_3$, 500 MHz) δ: 2.28 (3H, s), 2.36-2.38 (4H, m), 3.58-3.63 (4H, m), 4.63 (2H, s), 5.01 (2H, s), 6.87-6.91 (4H, m, Ar), 7.30-7.33 (1H, m, Ar), 7.36-7.39 (2H, m, Ar), 7.41-7.42 (2H, m, Ar). GC-MS m/z: 340 (M^+, 40), 141 (29), 91 (100), 70 (37).

2-(2-fluoro-4-nitrophenoxy)-1-(4-methylpiperazin-1-yl)ethan-1-one ***(29e)***. The crude residue was purified by column chromatography using CH_2Cl_2/MeOH 95:5 to obtain a yellow solid. Yield, 76%. ^{1}H-NMR ($CDCl_3$, 500 MHz) δ: 2.30 (3H, s), 2.37-2.43 (4H, m), 3.56-3.63 (4H, m), 4.89 (2H, s), 7.12 (1H, t, J = 8.2 Hz), 7.99-8.04 (2H, m, Ar). GC-MS m/z: 297 (M^+, 13), 141 (18), 99 (52), 70 (100), 56 (38), 42 (29).

General procedure for the synthesis of final amines **11-15**, **18-19**, **24-25** and **30-31**. A solution of $BH_3 \cdot Me_2S$ 2M (3 mol, 3 eq) in dry THF (10 mL) was carefully added dropwise to a stirred and ice bath cooled solution of the appropriate amides **28a-b**, **28d-e** and **29a-e** (1 eq, 1 mol) in dry THF (5 mL). The reaction mixture was refluxed with stirring for 3h, cooled to 0 °C and carefully added with MeOH (10 mL) to destroy the excess of boran complex. Then, HCl 3N (10 mL) was added and the resulting mixture was refluxed with stirring for 1h. The mixture was allowed to cool at room temperature and alkalized with NaOH 2M. The residue was extracted with CH_2Cl_2 (3 x 20 mL). The collected organic layers were dried (Na_2SO_4) and evaporated under vacuum to afford a crude residue which was purified by column chromatography using CH_2Cl_2/MeOH 95:5. The corresponding hydrochloride salts were prepared by adding a HCl saturated ethereal solution to a solution of the amine. The hydrochloride salt was purified by crystallization in MeOH/Et_2O.

1-(2-(2-fluorophenoxy)ethyl)-4-methylpiperidine ***(11)***. The title compound was obtained as a transparent oil as free base and as white crystalline solid as hydrochloride salt. Yield, 64%. m.p.$_{(HCl)}$ 150-153 °C. ^{1}H-NMR ($CDCl_3$, 300 MHz) δ: 0.92 (3H, d, J = 6.0 Hz), 1.19-1.43 (3H, m), 1.60-1.65 (2H, m), 2.04-2.16 (2H, m), 2.81 (2H, t, J = 6.2 Hz), 2.94-2.98 (2H, m), 4.16 (2H, t, J = 6.3 Hz), 6.84-7.09 (4H, m, Ar). GC-MS m/z: 237 (M^+, 2), 112 (100).

1-(2-(3-fluorophenoxy)ethyl)-4-methylpiperidine ***(12)***. The title compound was obtained as a white solid as free base and as white crystalline solid as hydrochloride salt. Yield, 65%. m.p.$_{(HCl)}$ 169-172 °C. ^{1}H-NMR ($CDCl_3$, 300 MHz) δ: 0.92 (3H, d, J = 6.0 Hz), 1.20-1.43 (3H, m), 1.60-1.65 (2H, m), 2.03-2.12 (2H, m), 2.77 (2H, t, J = 6.1 Hz), 2.92-2.97 (2H, m), 4.08 (2H, t, J = 6.1 Hz), 6.59-6.70 (3H, m, Ar), 7.16-7.24 (1H, m, Ar). GC-MS m/z: 237 (M^+, 1), 112 (100).

1-(2-(2-fluorophenoxy)ethyl)-4-methylpiperazine ***(13)***. The title compound was obtained as a transparent oil as free base and as white crystalline solid as hydrochloride salt. Yield, 82%. ^{1}H-NMR ($CDCl_3$, 500 MHz) δ: 2.28 (3H, s), 2.36-2.73 (8H, m), 2.83 (2H, t, J = 6.0 Hz), 4.16 (2H, t, J = 6.0 Hz), 6.86-6.90 (1H, m, Ar), 6.94-6.97 (1H, m, Ar), 7.01-7.07 (2H, m, Ar). GC-MS m/z: 238 (M^+, 1), 127 (73), 113 (100), 70 (95), 42 (35).

1-(2-(3-fluorophenoxy)ethyl)-4-methylpiperazine ***(14)***. The title compound was obtained as a transparent oil as free base and as white crystalline solid as hydrochloride salt. Yield, 50%. m.p.$_{(HCl)}$ 234-237 °C. ^{1}H-NMR ($CDCl_3$, 500 MHz) δ: 2.28 (3H, s), 2.41-2.72 (8H, m), 2.80 (2H, t, J = 5.7 Hz), 4.07 (2H, t, J = 5.7 Hz), 6.59-6.67 (3H, m, Ar), 7.17-7.21 (1H, m, Ar). GC-MS m/z: 238 (M^+, 1), 127 (54), 113 (100), 70 (79), 42 (26).

1-(2-(4-fluorophenoxy)ethyl)-4-methylpiperidine ***(15)***. The title compound was obtained as a yellow oil as free base and as white crystalline solid as hydrochloride salt. Yield, 70%. m.p.$_{(HCl)}$ 224-226 °C. ^{1}H-NMR ($CDCl_3$, 500 MHz) δ: 2.29 (3H, s), 2.43-2.62 (8H, m), 2.79 (2H, t, J = 5.7 Hz), 4.05 (2H, t, J = 5.7 Hz), 6.83 (2H, dd, J = 8.7 Hz, J_F = 4.2 Hz, Ar), 6.95 (2H, t, J = 8.7 Hz). GC-MS m/z: 238 (M^+, 1), 127 (48), 113 (100), 70 (77), 42 (22).

1-(2-(2-fluoro-4-nitrophenoxy)ethyl)-4-methylpiperidine ***(18)***. The title compound was obtained as a yellow solid as free base and as white crystalline solid as hydrochloride salt. Yield, 59%. m.p.$_{(HCl)}$ 198-201 °C. ^{1}H-NMR ($CDCl_3$, 300 MHz) δ: 0.92 (3H, d, J = 6.0 Hz), 1.17-1.44 (3H, m), 1.61-1.66 (2H, m), 2.08-2.16 (2H, m), 2.84 (2H, t, J = 6.0 Hz), 2.91-2.97 (2H, m), 4.26 (2H, t, J = 6.0 Hz), 7.04 (1H, t, J = 8.5 Hz), 7.98 (1H, dd, J_1 = 8.5 Hz, J_2 = 2.7 Hz Ar), 8.02-8.06 (1H, m, Ar). GC-MS m/z: 282 (M^+, 1), 112 (100).

1-(2-(2-fluoro-4-nitrophenoxy)ethyl)-4-methylpiperazine ***(19)*** Matthew W. Martin, John Newcomb et al.

4-fluoro-N-(2-(4-methylpiperidin-1-yl)ethyl)aniline ***(24)***. The title compound was obtained as a red oil as free base and as white crystalline solid as hydrochloride salt. Yield, 46%. m.p.$_{(HCl)}$ 184-187 °C. ^{1}H-NMR ($CDCl_3$, 300 MHz) δ: 0.93 (3H, d, J = 6.3 Hz), 1.15-1.43 (3H, m), 1.59-1.64 (2H, m), 1.92-2.00 (2H, m), 2.58 (2H, t, J = 6.0 Hz), 2.83-2.88 (2H, m), 3.10 (2H, t, J = 6.0 Hz), 4.21 (1H, br s), 6.54-6.59 (2H, m, Ar), 6.85-6.91 (2H, m, Ar). GC-MS m/z: 236 (M^+, 5), 112 (100).

4-fluoro-N-(2-(4-methylpiperazin-1-yl)ethyl)aniline ***(25)***. The title compound was obtained as a pink oil as free base and as white crystalline solid as hydrochloride salt. Yield, 52%. ^{1}H-NMR ($CDCl_3$, 500 MHz) δ: 2.29 (3H, s), 2.43-2.50 (8H, m), 2.62 (2H, t, J = 5.7 Hz), 3.10 (2H, t, J = 5.7 Hz), 4.19 (1H, br s), 6.56 (2H, dd, J = 8.5 Hz, J_F = 4.2 Hz, Ar), 6.88 (2H, t, J = 8.5 Hz, Ar). GC-MS m/z: 237 (M^+, 5), 113 (100), 70 (81).

1-(2-(4-(benzyloxy)phenoxy)ethyl)-4-methylpiperidine ***(30)*** [327].

1-(2-(4-(benzyloxy)phenoxy)ethyl)-4-methylpiperazine ***(31)***. The title compound was obtained as a white solid. Yield, 76%. ^{1}H-NMR ($CDCl_3$, 500 MHz) δ: 2.28 (3H, s), 2.45-2.66 (8H, m), 2.79 (2H, t, J = 5.9 Hz), 4.05 (2H, t, J = 5.8 Hz), 5.19 (2H, s), 6.84-6.88 (4H, m, Ar), 7.29-7.38 (5H, m, Ar). GC-MS m/z: 326 (M^+, 5), 113 (100).

General procedure for the synthesis of compounds ***32-33***. Compounds **30** and **31** (1 mol, 1 eq) were dissolved in EtOH 96% (8 mL) and put to react under H_2 atmosphere at 4.5 bar pressure and in presence of 10% Pd on activated carbon at room temperature ON. Subsequently, the mixture was filtered on a Celite® pad and the filtrate was concentrated under reduced pressure to obtain a crude residue which was purified by column chromatography using CH_2Cl_2/MeOH 95:5.

4-(2-(4-methylpiperidin-1-yl)ethoxy)phenol ***(32)*** [327].

4-(2-(4-methylpiperazin-1-yl)ethoxy)phenol ***(33)***. The title compound was obtained as a pink oil. Yield, 70%. ^{1}H-NMR ($CDCl_3$, 500 MHz) δ: 2.30 (3H, s), 2.45-2.74 (8H, m), 2.81 (2H, t, J = 5.7 Hz), 3.70 (1H, br s), 4.01 (2H, t, J = 5.7 Hz) 6.69 (4H, br s, Ar). GC-MS m/z: 236 (M^+, 1), 127 (54), 113 (100), 70 (69).

General procedure for the synthesis of fluoroethoxy derivatives ***CF31*** *and* ***17***. To a solution of the appropriate phenol (**32** or **33**) (1 mol, 1 eq) in CH_3CN (15 mL), K_2CO_3 (2 mol, 2 eq) and 1-fluoro-2-iodoethane (2 mol, 2 eq) are added. The resulting mixture was refluxed with stirring ON and then was allowed to cool to room temperature. The solvent was removed under vacuum. The residue was extracted with CH_2Cl_2 (3 x 15 mL). The collected organic layers were dried (Na_2SO_4) and evaporated under vacuum

to afford a crude residue which was purified by column chromatography using CH_2Cl_2/MeOH 95:5. The corresponding hydrochloride salts were prepared by adding a HCl saturated ethereal solution to a solution of the amine. The hydrochloride salt was purified by crystallization in MeOH/Et_2O.

*1-(2-(4-(2-fluoroethoxy)phenoxy)ethyl)-4-methylpiperidine (**CF31**).* The title compound was obtained as a white solid as free base and as white crystalline solid as hydrochloride salt. Yield, 60%. m.p.$_{(HCl)}$ 147-149 °C. ^{1}H-NMR ($CDCl_3$, 500 MHz) δ: 0.92 (3H, d, J = 6.0 Hz), 1.20-1.43 (3H, m), 1.60-1.65 (2H, m), 2.07-2.16 (2H, m), 2.76 (2H, t, J = 6.0 Hz), 2.93-2.98 (2H, m), 4.05 (2H, t, J = 6.2 Hz), 4.09-4.22 (2H, m), 4.63-4.81 (2H, m), 6.83-6.86 (4H, m, Ar) (The NMR spectrum is shown in Figure S3.9.). GC-MS m/z: 281 (M^+, 2), 126 (5), 112 (100) (The GC–MS and HPLC chromatograms are shown in Figures S3.10 and S3.11, respectively).

*1-(2-(4-(2-fluoroethoxy)phenoxy)ethyl)-4-methylpiperazine (**17**).* The title compound was obtained as a white solid as free base and as white crystalline solid as hydrochloride salt. Yield, 49%. m.p.$_{(HCl)}$ 229-231 °C. ^{1}H-NMR ($CDCl_3$, 500 MHz) δ: 2.31 (3H, s), 2.43-2.71 (8H, m), 2.80 (2H, t, J = 5.7 Hz), 4.06 (2H, t, J = 5.7 Hz), 4.12-4.20 (2H, m), 4.67-4.78 (2H, m), 6.83-6.87 (4H, m, Ar). GC-MS m/z: 282 (M^+, 1), 127 (28), 113 (100), 70 (80), 56 (27), 42 (21).

*General procedure for the synthesis of ethyl bromide **34** and **35**.* To a solution of the appropriate phenol (1 mol, 1 eq) in CH_3CN (20 mL), K_2CO_3 (2 mol, 2 eq) and 1,2-dibromoethane (3 mol, 3 eq) are added. The resulting mixture was refluxed with stirring ON and then was allowed to cool to room temperature. The solvent was removed under vacuum. The residue was taken up with H_2O (20 mL) and extracted with CH_2Cl_2 (3 x 20 mL). The combined organic layers were washed with brine, dried (Na_2SO_4) and evaporated under vacuum to afford a crude residue which was purified by column chromatography.

*1-(2-bromoethoxy)-4-fluorobenzene (**34**)* [331].

*5-(2-bromoethoxy)-2-fluoropyridine (**35**).* The crude residue was purified by column chromatography using n-Ex/AcOEt 7:3 to obtain a white solid. Yield, 32%. ^{1}H-NMR ($CDCl_3$, 500 MHz) δ: 3.62 (2H, t, J = 6.2 Hz), 4.25 (2H, t, J = 6.0 Hz), 6.83-6.87 (2H, m, Ar), 6.98 (1H, t, J = 8.5 Hz, Ar). GC-MS m/z: 218 (M^+, 49), 220 (M^++2, 48), 109 (100), 83 (57), 57 (28).

*General procedure for the synthesis of final amines **16** and **20-23**.* The appropriate BM (1.2 mol, 1.2 eq) was added to a solution of the appropriate bromine derivative **34-36** (1 mol, 1 eq) in CH_3CN (10 mL) and K_2CO_3 (1.2 mol, 1.2 eq). The resulting mixture was refluxed with stirring ON and then was allowed to cool to room temperature. The solvent was removed under vacuum. The residue was taken up with H_2O (20 mL) and extracted with CH_2Cl_2 (3 x 20 mL). The collected organic layers were dried (Na_2SO_4) and evaporated under vacuum to afford a crude residue which was purified by column chromatography using CH_2Cl_2/MeOH 95:5. The corresponding hydrochloride salts were prepared by adding a HCl saturated ethereal solution to a solution of the amine. The hydrochloride salt was purified by crystallization in MeOH/Et_2O.

*2-(2-(4-fluorophenoxy)ethyl)-2-azaspiro[3.3]heptane (**16**).* The title compound was obtained as a trasparent oil as free base and as white crystalline solid as hydrochloride salt. Yield, 77%. m.p.$_{(HCl)}$ 142-145 °C. ^{1}H-NMR ($CDCl_3$, 500 MHz) δ: 1.80 (2H, quint, J = 7.7 Hz), 2.11 (4H, t, J = 7.7 Hz), 2.80 (2H, t, J = 5.7 Hz), 3.31 (4H, s), 3.92 (2H, t, J = 5.7 Hz), 6.82 (2H, dd, J = 8.7 Hz, J_F = 4.2 Hz, Ar), 6.95 (2H, t, J = 8.7 Hz, Ar). GC-MS m/z: 235 (M^+, 2), 110 (100), 56 (24), 42 (27).

*2-fluoro-5-(2-(4-methylpiperidin-1-yl)ethoxy)pyridine (**20**).* The title compound was obtained as a trasparent oil as free base and as white crystalline solid as hydrochloride salt. Yield, 82%. m.p.$_{(HCl)}$ 171-174 °C. ^{1}H-NMR ($CDCl_3$, 300 MHz) δ: 0.91 (3H, d, J = 6.3 Hz), 1.19-1.38 (3H, m), 1.59-1.64 (2H, m), 2.03-2.11 (2H, m), 2.76 (2H, t, J = 5.8 Hz), 2.91-2.96 (2H, m), 4.10 (2H, t, J = 5.8 Hz), 6.83 (1H, dd, J_F = 9.0 Hz, J = 3.6 Hz, Ar), 7.29-7.35 (1H, m, Ar), 7.81 (1H, dd, J_1 = 3.3 Hz, J_2 = 1.9 Hz, Ar). GC-MS m/z: 238 (M^+, 1), 112 (100).

*1-(2-((6-fluoropyridin-3-yl)oxy)ethyl)-4-methylpiperazine (**21**).* The title compound was obtained as a yellow oil as free base and as white crystalline solid as hydrochloride salt. Yield, 67%. ^{1}H-NMR ($CDCl_3$, 500 MHz) δ: 2.26 (3H, s), 2.39-2.65 (8H, m), 2.78 (2H, t, J = 5.7 Hz), 4.07 (2H, t, J = 5.7 Hz), 6.80 (1H, dd, J = 8.7 Hz, J_F = 4.0 Hz, Ar), 7.27-7.31 (1H, m, Ar), 7.80 (1H, dd, J_1 = 2.5 Hz, J_2 = 2.0 Hz, Ar). GC-MS m/z: 239 (M^+, 1), 127 (66) 113 (100), 70 (83), 42 (28).

*N-(4-fluorophenyl)-2-(4-methylpiperidin-1-yl)acetamide (**22**).* The title compound was obtained as a red solid as free base and as white crystalline solid as hydrochloride salt. Yield, 52%. m.p.$_{(HCl)}$ 218-221 °C. ^{1}H-NMR ($CDCl_3$, 300 MHz) δ: 0.96 (3H, d, J = 6.3 Hz), 1.46-1.99 (3H, m), 1.66-1.71 (2H, m), 2.20-2.28 (2H, m), 2.83-2.89 (2H, m), 3.08 (2H, s), 6.99-7.05 (2H, m, Ar), 7.51-7.55 (2H, m, Ar), 9.23 (1H, br s). GC-MS m/z: 250 (M^+, 1), 112 (100).

*N-(4-fluorophenyl)-2-(4-methylpiperazin-1-yl)acetamide (**23**).* The title compound was obtained as a pink solid as free base and as white crystalline solid as hydrochloride salt. Yield, 73%. m.p.$_{(HCl)}$ 215-219 °C. ^{1}H-NMR ($CDCl_3$, 500 MHz) δ: 2.32 (3H, s), 2.45-2.65 (8H, m), 3.13 (2H, s), 7.02 (2H, t, J = 8.5 Hz, Ar), 7.52 (2H, dd, J = 8.7 Hz, J_F = 4.7 Hz), 9.09 (1H, br s). GC-MS m/z: 251 (M^+, 7), 113 (100), 70 (81), 42 (25).

*2-bromo-N-(4-fluorophenyl)acetamide (**36**)* [332].

*2-(4-(2-(4-methylpiperidin-1-yl)ethoxy)phenoxy)ethan-1-ol (**37**).* Compound **32** (1 mmol, 1 eq), 2-bromoethan-1-ol (2 eq, 2 mmol), and K_2CO_3 (2 mmol, 2 eq) were weighted altogether in a 2-5 mL microwave vial and CH_3CN (4 mL) was added. The vial was sealed, shaken vigorously, and heated at the microwave irradiator at 120°C for 40 min. After cooling, the solvent was removed under reduced pressure and the corresponding residue was taken up with H_2O (20 mL) and extracted with CH_2Cl_2 (3 x 20 mL). The collected organic layers were dried (Na_2SO_4) and evaporated under vacuum to afford a crude residue which was purified by column chromatography using CH_2Cl_2/MeOH 95:5 to obtain the title compound as a white crystalline solid. Yield, 55%. ^{1}H-NMR ($CDCl_3$, 500 MHz) δ: 0.91 (3H, d, J = 6.5 Hz), 1.20-1.29 (2H, m), 1.30-1.40 (1H, m), 1.55-1.72 (2H, m), 2.03-2.08 (2H, m), 2.74 (2H, t, J = 6.2 Hz), 2.90-2.98 (2H, m), 3.91 (2H, t, J = 4.5 Hz), 4.01 (2H, t, J = 4.5 Hz), 4.04 (2H, t, J = 6.0 Hz), 4.78 (1H, br s, exchange with D_2O), 6.82 (4H, br s). GC-MS m/z: 279 (M^+, 1), 112 (100).

*2-(4-(2-(4-methylpiperidin-1-yl)ethoxy)phenoxy)ethyl 4-methylbenzenesulfonate (**38**).* To a solution of compound **37** (1 mmol, 1 eq) in CH_2Cl_2 (15 mL), TsCl (1.3 eq, 1.3 mmol), and Et_3N (1.3 mmol, 1.3 eq) were added. The resulting mixture was stirred at 0 °C for 4h. The residue mixture was taken up with H_2O (20 mL) and extracted with CH_2Cl_2 (3 x 20 mL). The collected organic layers were dried (Na_2SO_4) and evaporated under vacuum to afford a crude residue which was purified by column chromatography using CH_2Cl_2/MeOH 95:5 to obtain the title compound as a yellow solid. Yield, 80%. ^{1}H-NMR ($CDCl_3$, 500 MHz) δ: 0.92 (3H, d, J = 6.5 Hz), 1.22-1.30 (2H, m), 1.32-1.41 (1H, m), 1.58-1.65 (2H, m), 2.02-2.10 (2H,

m), 2.44 (3H, s), 2.74 (2H, t, J = 6.0 Hz), 2.91-2.97 (2H, m), 4.03 (2H, t, J = 6.0 Hz), 4.09 (2H, t, J = 5.0 Hz), 4.33 (2H, t, J = 4.7 Hz), 6.69-6.72 (2H, m, Ar), 6.77-6.81 (2H, m, Ar), 7.33 (2H, d, J = 8.0 Hz, Ar), 7.81 (2H, d, J = 8.5 Hz, Ar). HRMS-ESI for $C_{23}H_{31}NO_5S$ (m/z): $[M+H]^+$ calcd, 434.2003; found, 434.2010 $[M+Na]^+$ calcd, 456.1821; found 456.1822.

3.11.2. Biological studies

3.11.2.1. Cell cultures

HEK-293 cells, stably transfected with human sigma1 receptor (hS1R-HEK293; obtained from Olivier Soriani, Inserm/CNRS, Institut de Biologie Valrose, Université de Nice, Nice, France) were cultivated in selective medium (RPMI, supplemented with 10 % FCS, 100 U/ml penicillin, 100 µg/ml streptomycin, and 100 µg/ml G-418 in a humidified incubator at 37 °C with a 5 % CO_2 atmosphere.

Caco-2 and MDCK-MDR1 cells were grown in Dulbecco's high-glucose modified eagle medium, composed of 10% fetal bovine serum, 2 mM of glutamine, 100 U/mL of penicillin, and 0.1 mg/mL of streptomycin (all components purchased from Euroclone, Milan, Italy) in a humidified incubator at 37 °C with a 5 % CO2 atmosphere.

3.11.2.2. *In vitro* competition binding assays

The affinity for S1R and S2R was determined by *in vitro* radioligand displacement experiments as published [327].

In brief, S1R affinity was determined with [^{3}H]-(+)-pentazocine (A_m = 995 GBq/µmol; Revvity) and the membrane preparation of hS1R-HEK293 cells with serial dilutions of the test compound. Incubation was performed in 50 mM TRIS-HCl, pH 7.4 at 21°C, supplemented with 120 mM NaCl, 5 mM KCl, 2 mM $CaCl_2$, and 1mM $MgCl_2$ for 120 min at ambient temperature.

S2R affinity was determined with [^{3}H]DTG (A_m=1850 GBq/mmol; ARC) and the membrane preparation of liver obtained from Wistar rats with 100 nM FTC-146 to mask S1R receptors, and serial dilutions of the test compound. Incubation was performed in 50 mM TRIS-HCL, pH 7.4 at 21°C, for 120 min at ambient temperature.

For S1R and S2R assays, non-specific binding of the respective radioligand was determined by co-incubation with 10 µM haloperidol. Free and bound radioligand were separated by filtration on GF/B glass-fibre filters (Hahnemühle FineArt GmbH, Dassel, Germany) pre-soaked in 0.3% polyethyleneimine using a Brandel Cell Harvester and rapidly washed four times with pre-chilled 50 mM TRIS-HCl, pH 7.4 at 4°C. Filters were isolated, transferred to scintillation vials, and incubated with scintillation cocktail (Ultima Gold™, Revvity) at 300 rpm for two hours at room temperature. The vials were counted in a liquid scintillation counter (Hidex 600 SL; Hidex Oy, Turku, Finland) to determine activity as Becquerel per vial. Data were expressed as percentage of specifically bound activity versus concentration of the respective test compound and analysed by non-linear curve analysis using GraphPad Prism software to calculate IC_{50} values. Inhibitory constant values (K_i) were calculated using the Cheng-Prusoff equation with dissociation constants of K_D = 33 nM for [^{3}H]-(+)-Pentazocine and K_D = 50 nM for [^{3}H]DTG. All experiments were performed at least two times with two technical replicates.

3.11.2.3. Calcein-AM experiment

These experiments were carried out as described by Contino *et al.* [335] with minor modifications.
Briefly, the MDCK-MDR1 cell line (30,000 cells per well) was seeded into a 96-well black culture plate with 100 µL medium and allowed to become confluent overnight. 100 µl of test compounds were solubilized in culture medium and added to monolayers, with final concentrations ranging from 0.1 to 100 µM. 96/wells plate was incubated for 30 min. Calcein-AM was added in 100 µl of Phosphate Buffered Saline (PBS) to yield a final concentration of 2.5 µM, and the plate was incubated for 30 min. Each well was washed 3 times with ice-cold PBS. A saline buffer was added to each well, and the plate was read with Victor3 (PerkinElmer) at excitation and emission wavelengths of 485 nm and 535 nm, respectively. In these experimental conditions, Calcein cell accumulation in the absence and in the presence of tested compounds was evaluated, and the fluorescence basal level was estimated with untreated cells. In treated wells, the fluorescence increase with respect to basal level was measured. EC_{50} values were determined by fitting the fluorescence increase percentage versus log[dose].

3.11.2.4. Caco-2 monolayer preparation

For permeability and drug transport assays, to prepare the Caco-2 monolayer, *in vitro* model of BBB barrier, cells were seeded into a Merck Millicell™ Cell Culture Insert Plates assay system (Millipore, Bedford, MA), where a cell monolayer is set in between a filter cell and a receiver plate, at a density of 20,000 cells/well. The culture medium was replaced every 48h and the cells were kept for 21 days in culture. The TransEpithelial Electrical Resistance (TEER) of the monolayers was measured daily, before and after the experiment, using an epithelial voltohmmeter (Millicell® -ERS, Millipore). Generally, TEER values greater than 1000 Ω for a 21 day culture are considered optimal.

3.11.2.5. Permeability Experiments

After 21 days of Caco-2 cell growth, the medium was removed from filter wells and from the receiver plate, which was filled with fresh HBSS buffer (Invitrogen). This procedure was repeated twice, and the plates were incubated at 37 °C for 30 min. After incubation, the HBSS buffer was removed and drug solutions and reference compounds were added to the filter well at a concentration of 100µM, while fresh HBSS was added to the receiver plate. The plates were incubated at 37 °C for 120 min. Afterwards, samples were removed from the apical (filter well) and basolateral (receiver plate) side of the monolayer to measure the permeability.
The apparent permeability (P_{app}), in units of nm/second, was calculated using the following equation:

$$P_{app} = \left(\frac{V_A}{Area\ x\ time}\right) \times \left(\frac{[drug]_{acceptor}}{[drug]_{initial}}\right)$$

Where VA is the volume (in mL) in the acceptor well, area is the surface area of the membrane (0.11 cm^2 of the well), time is the total transport time (7200 s), $[drug]_{acceptor}$ is the concentration of the drug measured by UV spectroscopy, and $[drug]_{initial}$ is the initial drug concentration (1 x 10^{-4} M) in the apical or basolateral wells.

3.11.3. Radiochemistry

Anhydrous Acetonitrile used for radiosynthesis Kryptofix® $K_{2.2.2}$ were purchased from Sigma-Aldrich Chemie GmbH, part of merck, Taufkirchen, Germany. Anhydrous acetonitrile used for radiosynthesis and K_2CO_3 were purchased from VWR Life Science, part of avantor, Darmstadt, Germany).

Radio thin layer chromatography (radio-TLC) was performed on silica gel (POLYGRAM® SIL G/UV_{254} from Machery-Nagel, Düren, Germany) pre-coated plates with a mixture of ethyl acetate/MeOH 1/1 (v/v) as eluent. The plates were exposed to storage phosphor screens (BAS-IP MS 2025, Fujifilm Co., Tokyo, Japan), recorded using an CR-25 Bio image plate scanner, and images were evaluated using AIDA software (both Elysia s.a., Angieur, Belgium).

^{18}F Separation Cartridges" (45 mg, PS-HCO_3^-, Synthra GmbH, Hamburg, Germany) were used without preconditioning. Preconditioning of Sep-Pak® C_{18} light and plus cartridges (Waters GmbH, Eschborn, Germany) was done using 5 ml of EtOH and 20 ml of water.

Mouse plasma for determination of *in vitro* stability was kindly provided by University of Leipzig, Medical Faculty Rudolf-Boehm-Institute for Pharmacology and Toxicology, Leipzig, Germany).

For determination of metabolic stability in vitro, GIBCO liver microsomes, pooled from CD-1 mice (MLM), were purchased from Thermo Fisher Scientific GmbH (Dreieich, Germany). ß-Nicotinamide adenine dinucleotide 2'-phosphate reduced tetrasodium salt (NADPH) and testosterone were purchased from Sigma-Aldrich Chemie GmbH, part of merck, Taufkirchen, Germany.

For evaluation of stability the thermo shaker BioShake iQ (QUANTIFOIL Instruments, Jena, Germany) was used.

For centrifugation a Centrifuge 5424 (Eppendorf, Hamburg, Germany) was used, unless otherwise stated.

3.11.3.1. [^{18}F]Fluoride production

No-carrier-added [^{18}F]Fluoride was produced via the [^{18}O(p,n)^{18}F] nuclear reaction by irradiation of an [^{18}O]H_2O target (Hyox 18 enriched water, Rotem Industries Ltd, Israel) on a Cyclone 18/9 (iba RadioPharma Solutions, Belgium) with fixed energy proton beam using Nirta [^{18}F]Fluoride XL target.

3.11.3.2. Manual Radiosynthesis of [^{18}F]CF31

The manual synthesis of **[^{18}F]CF31** began with the provision of azeotropically dried [^{18}F]fluoride, dissolved in CH_3CN or DMSO. Using the synthesis module Synthra RNplus Research (Synthra GmbH, Hamburg, Germany), cyclotron-produced [^{18}F]fluoride (6-8 GBq) was fixated on an PS-HCO_3^- cartridge and eluted by a mixture of $K_{2.2.2}$ (11.4 mg); K_2CO_3 (sol., 20 mg/mL, 89 µL) in 1 mL CH_3CN and 0.3 mL H_2O. After addition of 1.8 mL CH_3CN, the [^{18}F]fluoride-Kryptofix complex solution was obtained by azeotropic drying by heating for 15 min and final addition of CH_3CN and DMSO.

For the labeling, aliquots of the [^{18}F]fluoride–Kryptofix complex were added to a vials containing the tosylate precursor (**38**) previously dissolved in the reaction solvent (CH_3CN or DMSO). The reactions were carried out in CH_3CN at 70-90 °C and in DMSO at 100-140 °C. To monitor the labeling progress, aliquots were withdrawn at 5, 10, 15 and 20 min and analyzed by radio-HPLC and, randomly, by radio-TLC (Figure S3.1).

Radio-HPLC was performed on a JASCO X-LC system (JASCO Labor- und Datentechnik GmbH, Pfungstadt, Germany) equipped with a UV/vis detector UV-2070 (monitoring at 285 nm) and a

radioactivity flow detector GABI Star (raytest Isotopenmessgeräte, Straubenhardt, Germany) including NaI detector (2" × 2" pinhole, 16 mm × 30 mm).

Analyses were performed using a ReproSil-Pur 120 C_{18}-AQ, 3 µm, 150 x 3 mm (Dr. Maisch GmbH) and a solvent system consisting of CH_3CN and 20 mM aqueous NH_4OAc.

Two distinct linear gradient elution methods, one short and one long, along with one isocratic method, were employed: (Method A, Isocratic method) 40% CH_3CN for a 15-min run; (Method B, Long gradient method) isocratic elution at 5% CH_3CN from 0 to 1.5 min, followed by a linear gradient from 5% to 80% CH_3CN between 1.5 and 10.0 min, isocratic elution at 80% CH_3CN from 10.1 to 12.0 min, and re-equilibration at 5% CH_3CN from 12.1 to 15.0 min; (Method C, Short gradient method) isocratic elution at 5% CH_3CN from 0 to 0.5 min, followed by isocratic elution at 80% CH_3CN from 0.51 to 5.0 min, and re-equilibration at 5% CH_3CN from 5.1 to 8.0 min. For all methods, the flow rate was set at 0.7 mL/min, and detection was carried out at 285 nm.

Optimized manual procedure for **[^{18}F]CF31**: the azeotropically dried [^{18}F]fluoride–Kryptofix complex was dissolved in CH_3CN (1 mL) and **38** (2 mg) dissolved in CH_3CN (1 mL) was added. The resulting reaction mixture was stirred at 90 °C for 20 min.

3.11.3.3. Automated Radiosynthesis of [^{18}F]CF31

The optimized manual labeling procedure was transferred to the remote-controlled synthesis module Synthra RNplus Research (Synthra GmbH, Hamburg, Germany Figure S3.2 and S3.3), installed in a hot-cell. The [^{18}F]fluoride was trapped on a PS-HCO_3^- cartridge, entry 1, Figure S3.3). The trapped [^{18}F]fluoride was eluted with Kryptofix/K_2CO_3, as described for the manual synthesis (entry A_1, Figure S3.3) into reactor 1 (entry 2, Figure S3.3) and was dried by azeotropic distillation with CH_3CN (entry A_2, Figure S3.3) for 15 min. Then 2 mg of **38** in 1 mL of CH_3CN (entry A_3, Figure S3.3) was added into reactor 1 (entry 2, Figure S3.3) and stirring for 20 min at 90 °C. The reaction mixture was diluted with 3.5 mL of H_2O (entry A_5, Figure S3.3) to terminate the reaction, followed by eluted in reactor 2 (entry 3, Figure S3.3).

The resulting mixture containing **[^{18}F]CF31** was injected through the injector (entry 4.1, Figure S3.3) and the loop (entry 4.2, Figure S3.3) on the RP-HPLC column (ReproSil Gold C18 10µm, 50 x 10 mm, Dr Maisch GmbH, Ammerbuch, Germany; entry 5, Figure S3.3) and eluted with a mobile phase of 15% CH_3CN (20 mM NH_4OAc) with flow rate of 3 mL/min.

The radiolabeled product (**[^{18}F]CF31**) was collected (R_t = 41-42 min) and directed to a collection vial (entry 6, Figure S3.3) that was previously loaded with 25 mL of water. After loading on a SPE Sep-Pak C_{18} light cartridge (entry 7, Figure S3.3) and washing with 5 mL water (entry C_3, Figure S3.3), the radiotracer was eluted with 1.5 mL of EtOH (entry C_2, Figure S3.3) into the target product vial (entry 8, Figure S3.3). EtOH was evaporated under a gentle Helium stream at 40 °C to a final volume of 10-25 µL. The radiotracer was formulated by addition of PBS to obtain a final product solution containing < 10 % EtOH (*v/v*).

For quality control, the final product of the radiotracer was inspected by analytical radio- and UV-HPLC with and without co-injection of the reference compound in isocratic (Method A) or gradient method (long and short, Method B and C, respectively) with RP-HPLC (ReproSil-Pur 120 C_{18}-AQ, 3 µm, 150 x 3 mm (Dr. Maisch GmbH).

For the determination of A_m, an aliquot of the **[^{18}F]CF31** solution (50 µL, 62–216 MBq) was analyzed by HPLC under isocratic conditions (40% CH_3CN, Method A), using chromatograms recorded at 285 nm, the wavelength of maximum absorbance.
The amount of non-radioactive **CF31** was calculated from calibration curves (Figure S3.12) obtained using different solutions of **CF31** (50 µL), analyzed under the same isocratic conditions as described.

3.11.4. Determination of *In Vitro* Stability

[^{18}F]CF31 (10 µL ≈ 35 MBq) was added to saline solution and PBS (250 µL for both) and shaken gently (350 rpm) at 25°C for 2 h (*n = 2*). The radiotracer was incubated smililarly with mouse plasma and shaken gently at 37°C (*n = 3*).
Aliquots of 25 µL were withdrawn every 30 min. Samples from saline and PBS were diluted and analyzed by radio-HPLC. Aliquots from mouse plasma were added to 100 µL of ice-cold CH_3CN, vortexed for 5 min, and placed on ice for 3 min, followed by centrifugation at 14,000 rpm for 10 min. The supernatant was separated from the pellet and analyzed by radio-HPLC. Efficiencies of the extractions were calculated after activity measurement of aliquots of the supernatants and the corresponding residues by gamma counter using the following equation:

$$\text{Extraction Efficiency (\%)} = \frac{\text{activity}_{\text{supernatant}}}{\text{activity}_{\text{residue}} + \text{activity}_{\text{supernatant}}} \times 100\%$$

Radio-HPLC analysis of samples from saline solution, PBS, and mouse plasma was performed using the same radio-HPLC method as for quality control after automated synthesis (Method B and C).

3.11.5. Determination of Lipophilicity ($LogD_{7.4}$)

The apparent distribution coefficient ($logD_{7.4}$) value of **[^{18}F]CF31** was determined using a shake-flask method by measuring the distribution of the radiotracer between *n*-octanol and PBS (0.05 mol/L, pH = 7.4) following a previously published protocol [77]. The two phases were pre-saturated with each other. A solution of the radiotracer (10 µL, 0.5 MBq) was added to a 15 mL plastic centrifuge tube containing *n*-octanol (3 mL) and PBS (3 mL). The tube was vortexed for 3 min and centrifuged at 3,500 rpm for 5 min (UNIVERSAL 320 R, Hettich, Germany). About 50 µL of the *n*-octanol layer and 500 µL of the buffer layer were pipetted in two tared tubes and the activity was measured in an automatic γ-counter (Wallac 1480 Wizard, PerkinElmer, USA). The $logD_{7.4}$ was determined as the ratio of cpm/mL of the *n*-octanol layer to that of the buffer layer. Samples from the *n*-octanol layer were redistributed until consistent distribution coefficient values were obtained. The measurement was carried out in triplicate and repeated three times.

3.11.6. Determination of Binding Affinities by Homogenate Assays

Briefly, the S1R affinity of **[^{18}F]CF31** was determined by homologous radioligand displacement using *h*S1R-HEK293 membrane preparations as well as intact hS1R-HEK293 and HEK293wt cells. Serial dilutions of **CF31** (0.01 nM–1 µM) were used for displacement. Non-specific binding was determined in the presence of haloperidol or **FTC-146** (1 µM). Cells/membranes were incubated with 1.3 nM **[^{18}F]CF31** (1.31 MBq/mL; A_m = 101 GBq/µmol at incubation) in PBS for 120 min at room temperature.

3.11.7. *In Vitro* Autoradiography

In vitro autoradiography was performed as described previously. Briefly, mouse brain (courtesy of Dr. Birgit Belter, Institute of Radiopharmaceutical Cancer Research, HZDR, Germany) cryosections mounted on glass slides were incubated with 3.35 nM **[^{18}F]CF31** in PBS for 90 min at room temperature. For competition/blocking experiments, sections were co-incubated with vehicle or haloperidol, **FTC146**, or **CF31** (each 1 µM) to assess total and non-specific binding and binding saturability. Slides were then washed twice in ice-cold 50 mM Tris-HCl (pH 7.4; 2 min each, 4°C), briefly dipped in cold demineralized water (5 s), dried in a cold air stream, and exposed to a phosphor imaging plate. Plates were scanned in a phosphorimager and images were analyzed using AIDA software (Elysia, Straubenhardt, Germany).

3.11.8. *In Vitro* Metabolism

[^{18}F]CF31 was incubated with MLM in PBS in the presence of NADPH for 30 min at 37 °C with gentle shaking at 350 rpm (*n = 3*), following a previously published protocol [337] with minor modifications. For all incubation mixtures the total volume was 250 µL. 12.5 µL of MLM (1 mg/mL) was added to 187.5 µL of PBS, followed by 25 µL of **[^{18}F]CF31** (10–20 MBq). The mixture was pre-incubated at 37 °C with gentle shaking at 350 rpm for 5 min. Subsequently, 25 µL of pre-incubated NADPH (2 mM) was added, and the reaction was incubated at 37 °C with gentle shaking at 350 rpm for 30 min (*n = 3*). Positive control experiments were performed using testosterone as substrate, both in the presence and absence of NADPH (25 µL of testosterone, 12.5 µL of MLM at 1 mg/mL, and either 0 or 25 µL of 2 mM NADPH in 212.5 µL or 187.5 µL of PBS, respectively). In these experiments, incubation was carried out at 37 °C with gentle shaking at 350 rpm for 60 min, corresponding to the time required for complete conversion of testosterone. Negative control experiments were conducted by incubating **[^{18}F]CF31** either without NADPH (25 µL of **[^{18}F]CF31** and 12.5 µL of MLM at 1 mg/mL in 212.5 µL of PBS) or in the absence of both MLM and NADPH (25 µL of **[^{18}F]CF31** in 225 µL of PBS). All negative control incubations were performed at 37 °C with gentle shaking at 350 rpm for 30 min. After incubation, samples were subjected to protein precipitation. An aliquot of 25 µL from each reaction mixture was added to 100 µL of ice-cold CH_3CN, vortexed for 5 min, and placed on ice for 3 min, followed by centrifugation at 14,000 rpm for 10 min. The supernatant was separated from the pellet and analyzed by radio-HPLC. Efficiencies of the extractions were calculated after activity measurement of aliquots of the supernatants and the corresponding residues by gamma counter using the following equation:

$$\text{Extraction Efficiency (\%)} = \frac{\text{activity}_{\text{supernatant}}}{\text{activity}_{\text{residue}} + \text{activity}_{\text{supernatant}}} \times 100\%$$

Radio-HPLC analysis of **[^{18}F]CF31** metabolism was performed using the same radio-HPLC method as for quality control after automated synthesis (B and C). For the analysis of testosterone metabolism in the positive control experiments, HPLC was performed using an appropriate gradient method and UV detection (λ = 245 nM). Incubations of non-labeled **CF31** were performed at two different substrate concentrations (20 and 100 µM, *n = 3* for each) instead of using **[^{18}F]CF31**. HPLC analysis was conducted based on the method used for quality control after automated synthesis, monitoring at 285 nm, with the following changes (Method D): 1.5-8.0 min 40-60 % CH_3CN, 8.0-10.0 min 60-80 % CH_3CN. For the purpose of metabolite identification, the references **32** and **37** were added to samples from incubation of **CF31**.

3.12. Supporting information

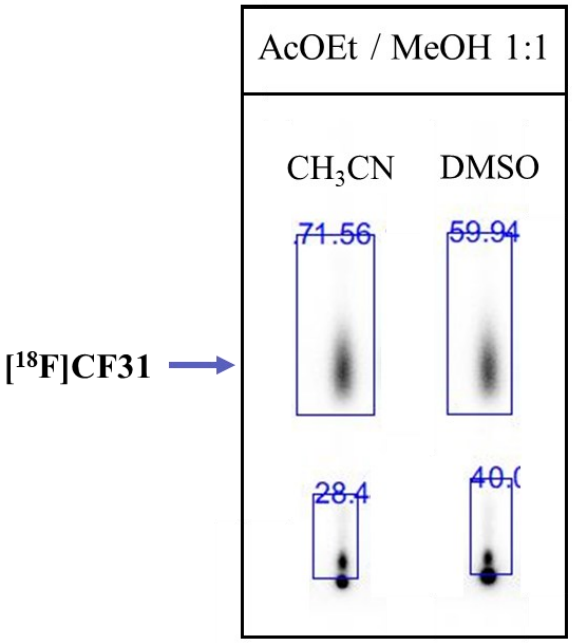

Figure S3.1. Radio-TLC monitoring of the manual synthesis after 20 min of reaction in AcOEt/MeOH 1:1. The percentage of product formation is shown in blue.

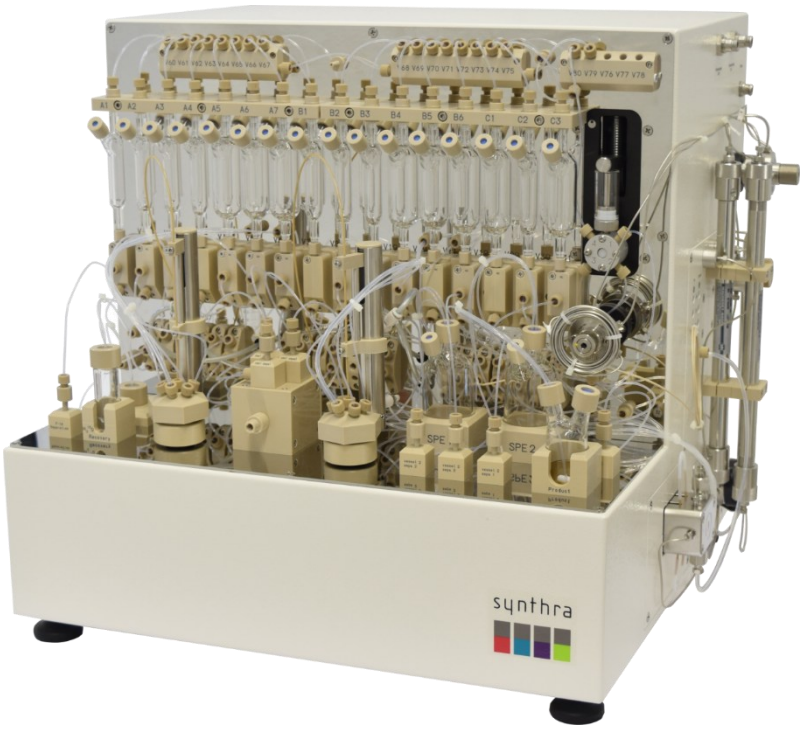

Figure S3.2. Synthra RNplus Research radiosynthesizer GmbH, Hamburg, Germany.

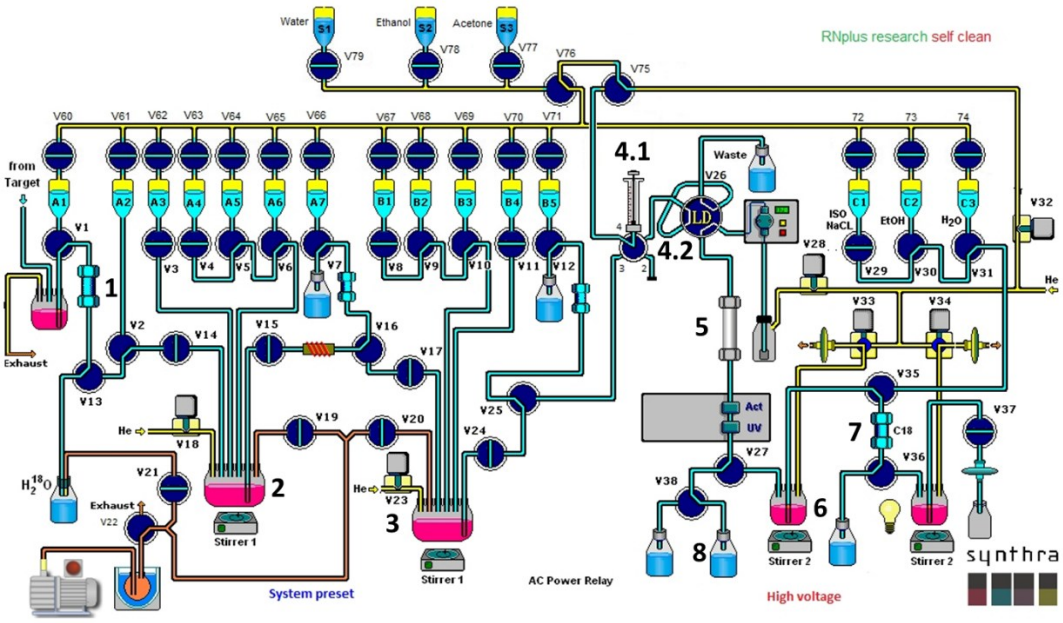

Figure S3.3. Scheme of Synthra Graphical User Interface for the automated radiosynthesis of the **[^{18}F]CF31** with A_1) Kryptofix complex ($K_{2.2.2}$, 11.4 mg; CH_3CN, 1 mL; H_2O, 300 µL; K_2CO_3 sol. (20 mg/mL), 89 µL); A_2) 1.8 mL of CH_3CN; A_3) 2 mg of **38** in 1 mL of CH_3CN; A_4) Empty; A_5) 3.5 mL of water; A_6-A_7) empty; B_1-B_6) empty; C_1) empty; C_2) 1.5 mL of EtOH; C_3) 5 mL of water; 1) "shorty" (Chromafix 30-PS-HCO_3^- Content of sorbent = 45 mg from Synthra GmBH); 2) Reactor 1; 3) Reactor 2; 4.1) Injector; 4.2) Loop; 5) ReproSil Gold (SHORT) C_{18}, 50 x 10 mm, 10 µm from Dr Maisch GmBH; 15% ACN (20 mM NH_4OAc), flow 400 mV (3.05 mL/min); 6) Collection vial (25 mL of water); 7) SPE (Sep-Pak C_{18} light, 3 mL EtOH, 20 ml water) 8) Target product vial.

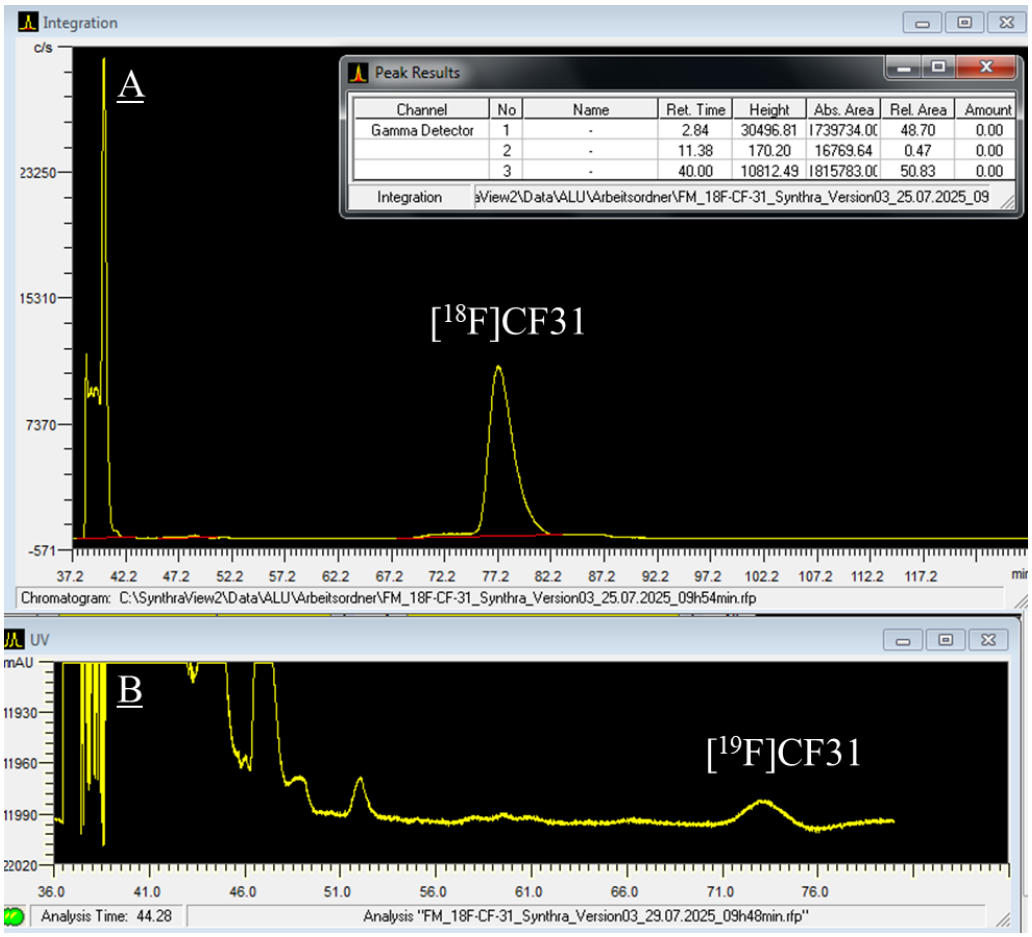

Figure S3.4. Representation of the graphical interface during purification by semi-preparative HPLC (ReproSil Gold C_{18}, 10 µm, 50 × 10 mm, Dr. Maisch GmbH, Ammerbuch, Germany), eluted with a mobile phase of 15% CH_3CN (20 mM NH_4OAc) at a flow rate of 3 mL/min (Rt ≈ 41–42 min). (**A**) Gamma channel; (**B**) UV channel.

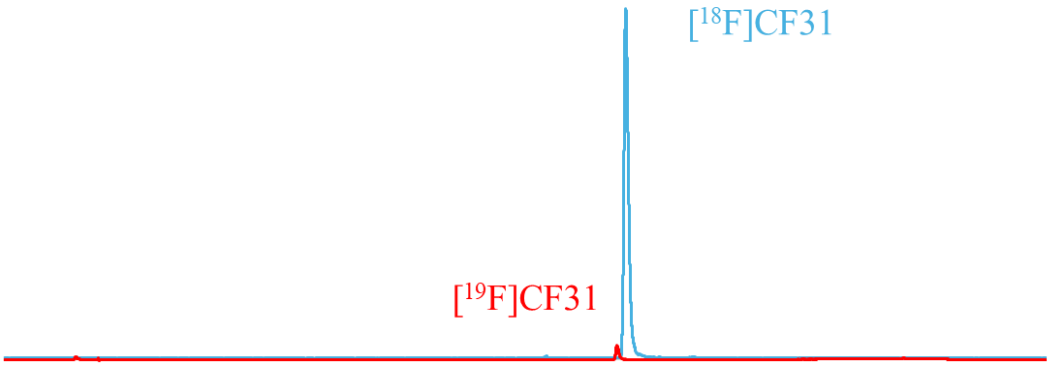

Figure S3.5. Radio- (light blue line) and UV- (red line) HPLC chromatograms of the identity confirmation of **[^{18}F]CF31** co-injected with the reference standard **CF31** (ReproSil-Pur 120 C_{18}-AQ, 3 µm, 150 x 3 mm (Dr. Maisch GmbH); Elution method B).

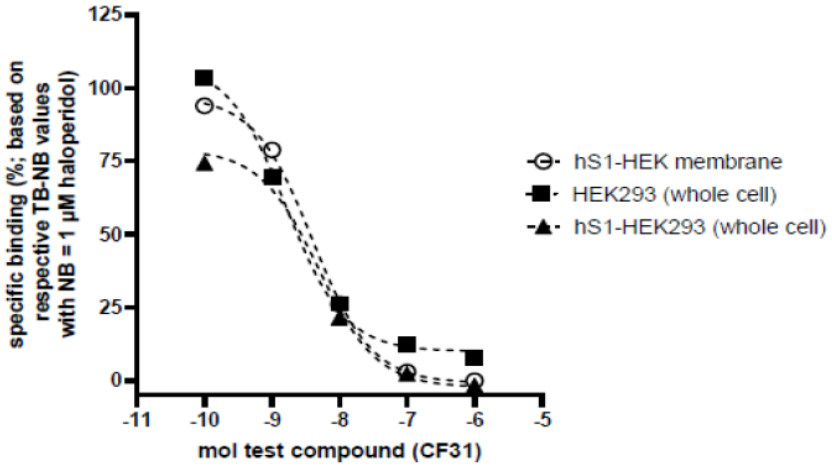

Figure S3.6. Homologous competition binding assays of **CF31** versus **[^{18}F]CF31** in different biological matrices for determination of the K_D.

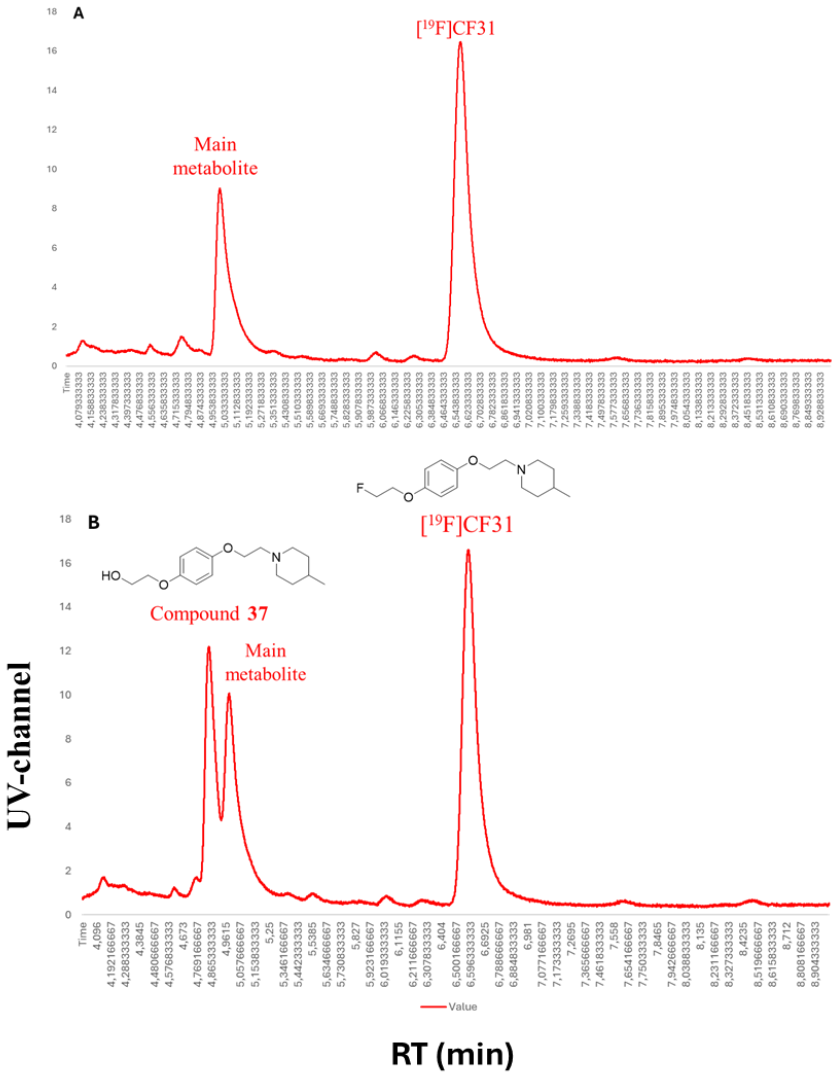

Figure S3.7. Radio-HPLC chromatograms (ReproSil-Pur 120 C18-AQ, 3 µm, 150 × 3 mm; Dr. Maisch GmbH; elution method C) showing **[^{19}F]CF31** before spiking with compound **37** (**A**) and after spiking with compound **37** (**B**). The presence of two distinct peaks indicates that compound **37** does not correspond to the major metabolite. For clarity, only the 4–9 min retention time window is shown in both chromatograms to enhance peak visibility.

Figure S3.8. **A**) example for self blocking; range (quantum level 0 – 50972) identical to the above example of total binding; **B**) Example for blocking with FTC146; range (quantum level 0 – 50972) identical to the above example of total binding.

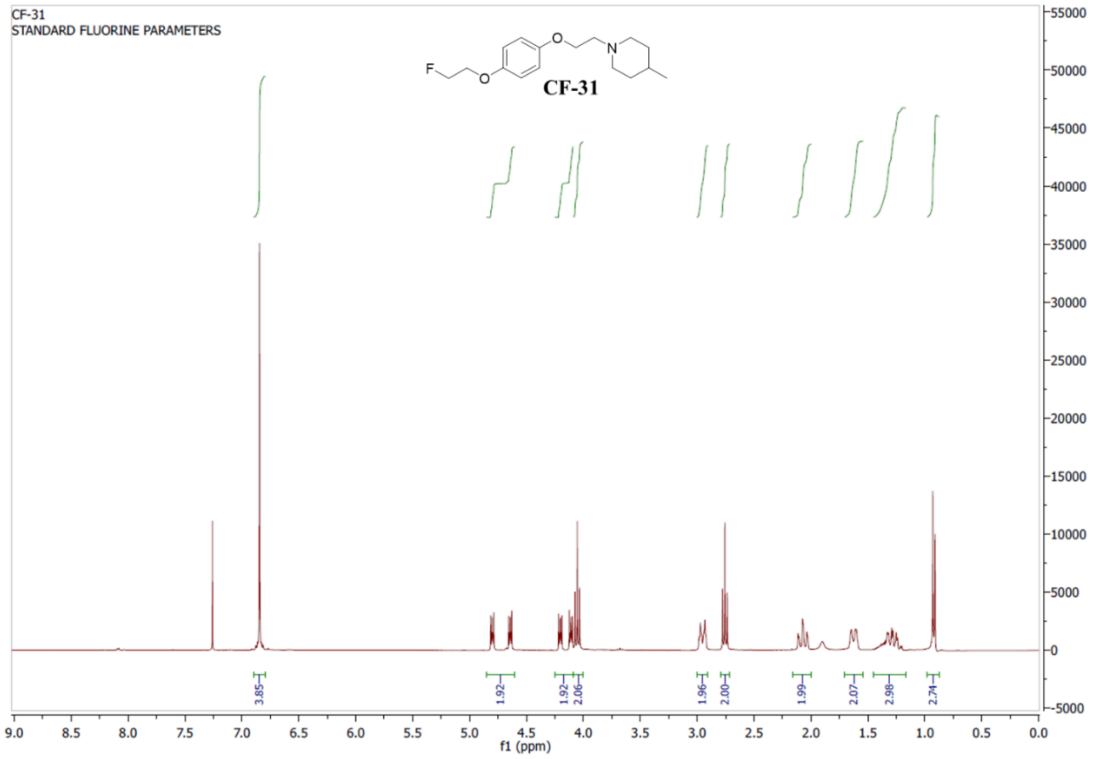

Figure S3.9. ^{1}H-NMR spectrum of **CF31**. $CDCl_3$, 300 MHz, 25 °C.

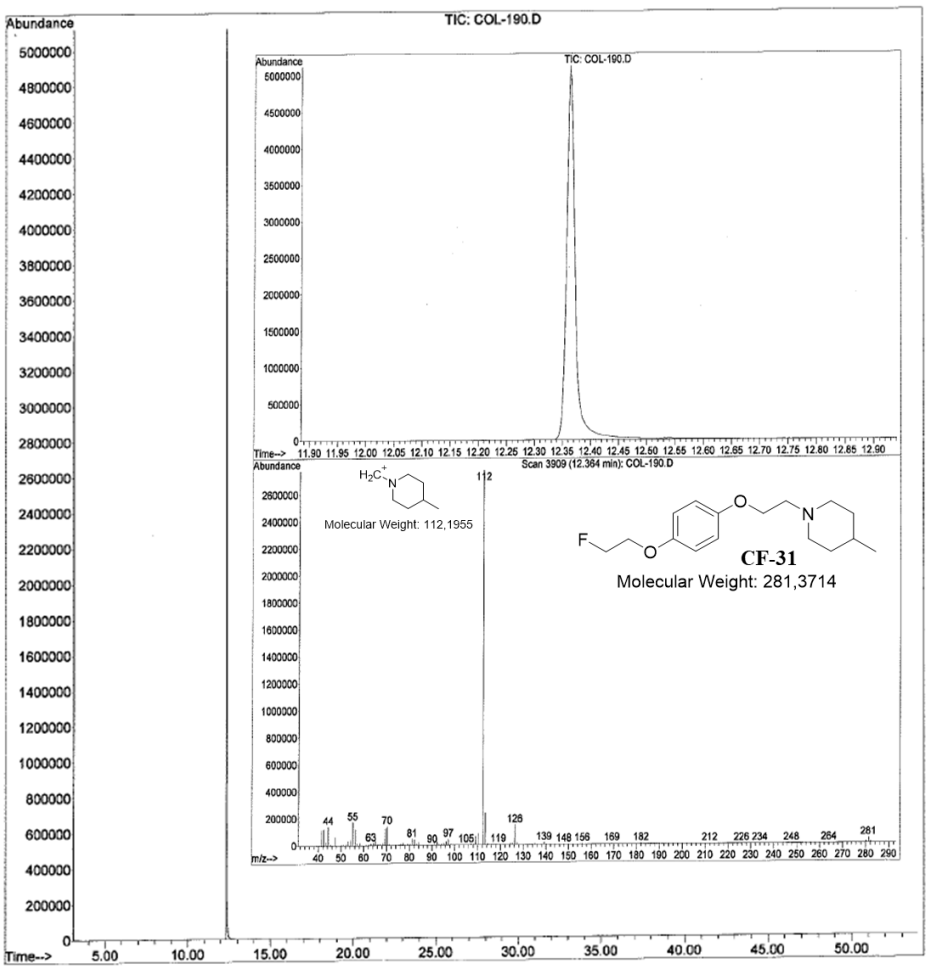

Figure S3.10. GC-MS analysis of **CF31**.

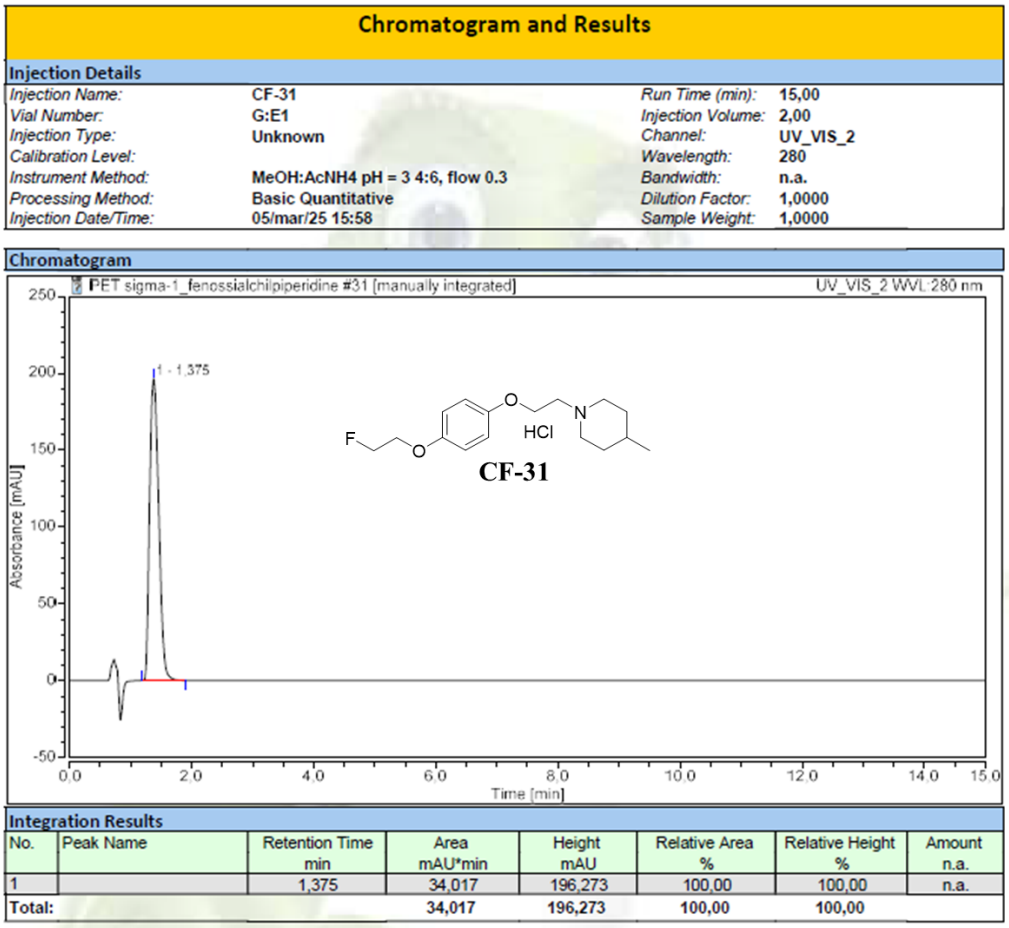

Figure S3.11: HPLC analysis of **CF31**. MeOH-NH_4OAc (pH = 3.0) 4:6, flow 0.3 mL/min. Wavelength, 280 nM.

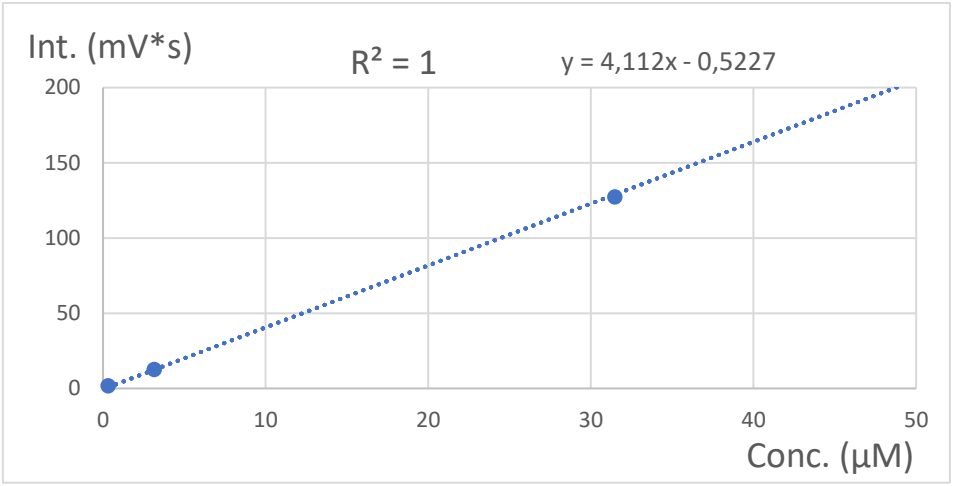

Figure S.12. Calibration curve for the determination of A_m.

CHAPTER 4

Sigma-2 receptors

Introduction, background and Aim

4. Introduction

As mentioned in Chapter 3, the S2R belongs to the sigma receptor family but is pharmacologically and structurally distinct from the S1R.

The S2R was first identified by Hellewell et al., who demonstrated that [^{3}H]-DTG specifically bound to two proteins in rat liver: a 25 kDa protein corresponding to the S1R and a 21.5 kDa protein corresponding to the S2R. The definitive distinction between these two receptors was made using Dextralorphan (DXA, Figure 4.1), which blocked radioligand binding to the S1R but not to the 21.5 kDa protein. The latter was therefore designated as the S2R [342].

In 2011, it was proposed that S2R was part of the progesterone receptor membrane component 1 (PGRMC1) complex. This hypothesis was based on observed similarities between PGRMC1 expression and S2R density in tumor cells and normal tissues. Moreover, the S2R ligand SW120 was found to bind to the PGRMC1 protein complex. These findings led to the suggestion that the S2R binding site might be associated with PGRMC1 [343].

However, subsequent studies by Abate C. et al. demonstrated that S2R and PGRMC1 are distinct entities. Their results indicated that S2R ligands such as DTG and PB28 (Figure 4.1) do not bind to the PGRMC1 monomer but instead to the heme-mediated dimeric form of PGRMC1 with micromolar affinity. These findings supported the view that S2R and PGRMC1 are separate proteins [344,345].

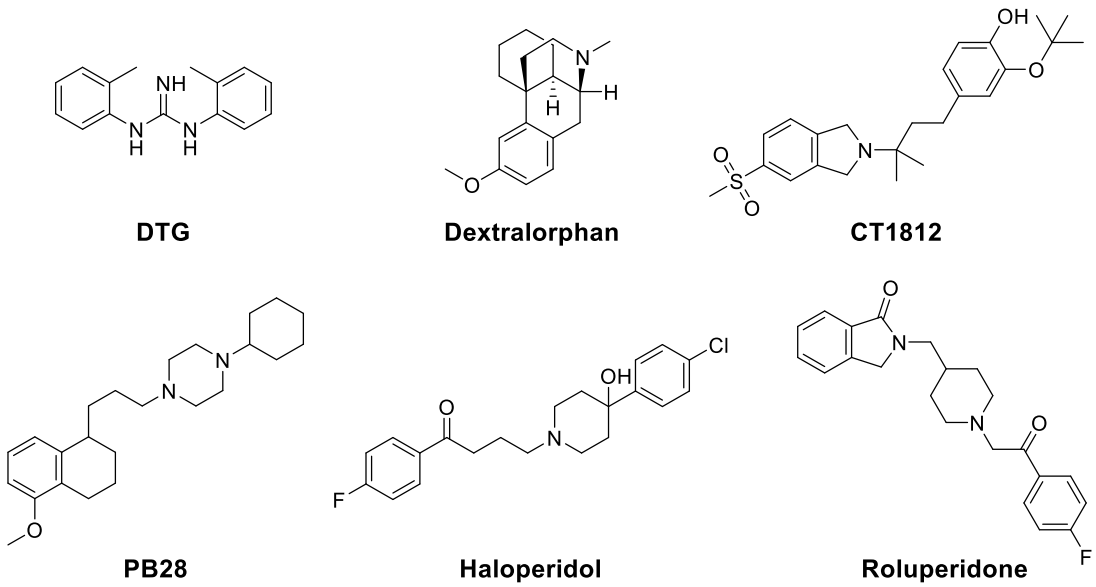

Figure 4.1: Structures of the main S2R ligands.

The most recent and widely accepted hypothesis regarding the molecular identity of S2R was proposed by Alon et al. in 2017, who identified S2R as TMEM97 (also known as MAC-30). TMEM97 is an integral membrane protein localized to the ER and comprises four transmembrane domains, with both *N*- and *C*-termini oriented toward the cytoplasm (Figure 4.2). It has a molecular weight of approximately 21.5 kDa and plays a role in cholesterol homeostasis [346].

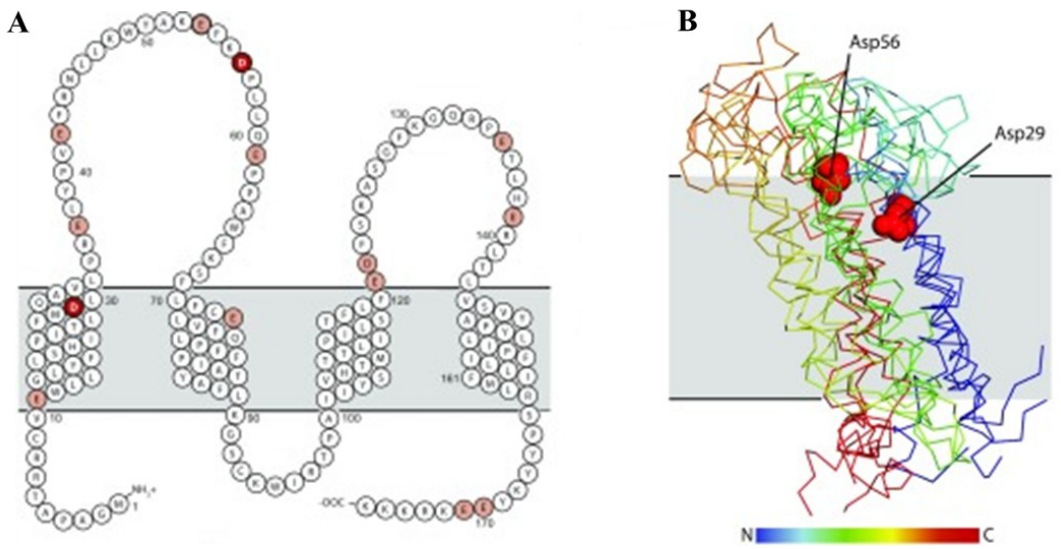

Figure 4.2: Structural analysis of TMEM97 and mapping of the ligand binding site. (**A**) Schematic of TMEM97 in the membrane. The acidic residues chosen for mutagenesis are colored light red, with Asp29 and Asp56 highlighted in dark red. (**B**) Molecular models of TMEM97; the top four ranked models are shown. Models are colored with rainbow colors from the N-terminus to the C-terminus, as indicated. The position of the membrane plane is shown in gray, Asp29 and Asp56 are shown as red spheres Picture adpapted from Ref. [346].

Alon et al. performed affinity chromatography purification of calf liver homogenates and isolated proteins interacting with the piperazine-based S2R ligand JVW-1625. Binding studies using [^{3}H]-DTG were subsequently conducted on membrane proteins overexpressed in HEK293 cells, revealing TMEM97 as the most likely candidate. Several lines of experimental evidence supported this identification: (i) knockdown of TMEM97 in PC-12 cells resulted in reduced S2R expression; (ii) in Sf9 insect cells engineered to overexpress human TMEM97, [^{3}H]-DTG binding affinities were consistent with reported S2R values; (iii) S2R ligands from diverse chemical classes displayed affinities for TMEM97 matching previously reported S2R affinities; (iv) the Ki values of two TMEM97 ligands, Elacridar and Ro 48-8071, in TMEM97-overexpressing Sf9 membranes were identical to those measured in MCF7 cells, which endogenously overexpress S2Rs; and (v) site-directed mutagenesis of glutamate (E) and aspartate (D) residues showed that D29 and D56 are essential for ligand binding, in a manner analogous to the S1R binding site (Figure 4.2) [346].

Furthermore, the same group that identified TMEM97 as S2R subsequently resolved the crystal structure of the protein in complex with roluperidone and PB28, marking a major milestone in S2R research (Figure 4.3) [347].

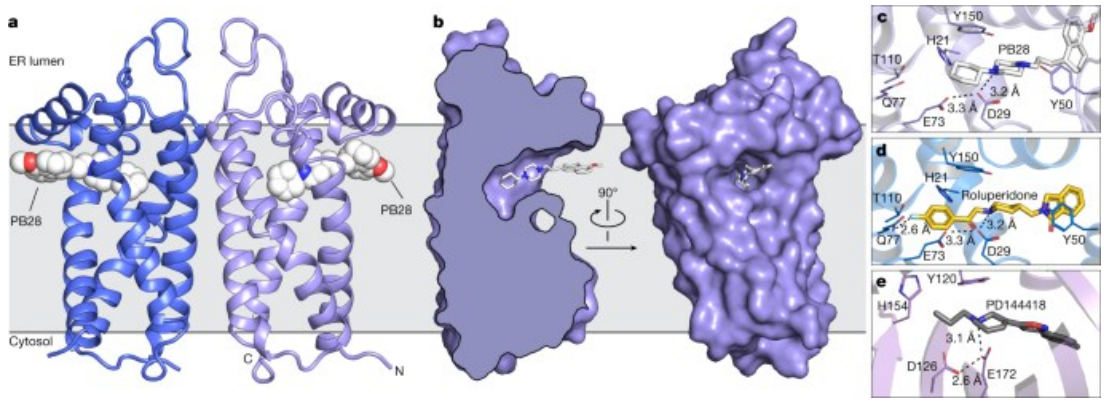

Figure 4.3: First determination of the crystal structure of S2R in complex with roluperidone and PB28 (structures shown in Figure 4.1). (**a**) Crystal structure of the S2R in complex with PB28, with the N- and C-terminal ends labeled. (**b**) A sectional view of the S2R ligand-binding pocket (left) and a view of the pocket entrance from the membrane side (right). (**c**) Orientation of PB28 within the binding site, highlighting the electrostatic interaction with Asp29 (black dashed line) as well as additional contacts with surrounding residues. (**d**) Corresponding depiction of the binding pose of roluperidone. (**e**) Structure of the S1R bound to PD144418 (PDB ID: 5HK1), with residues marked that adopt roles and orientations analogous to those observed in S2R. Picture adpapted from Ref. [347].

4.1. Function

Like S1R, S2Rs are involved in the regulation of intracellular calcium homeostasis. Several studies have identified two distinct calcium responses mediated by S2R ligands. The first is a rapid, dose-dependent response characterized by a transient increase in intracellular calcium released from the ER, even in the absence of extracellular calcium. This effect is abolished by pretreatment with thapsigargin. The second response is slower and more sustained, originating from mitochondrial calcium stores after prolonged exposure to S2R ligands, and remains unaffected by thapsigargin pretreatment [348].

In the intracardiac and cervical ganglia of neonatal rats, S2Rs have been shown to rapidly inhibit calcium influx through ion channels, suggesting that these receptors can block multiple types of calcium channels present in excitable cells [349].

PB28, a potent S2R agonist in SK-N-SH cells, has been reported to inhibit calcium release from the ER, a process typically enhanced by physiological agonists such as IP_3 or caffeine. This effect occurs rapidly, indicating that it does not require de novo protein synthesis [350]. These findings reinforce the concept that S2R can negatively modulate intracellular calcium levels, counteracting the calcium increases mediated by S1R. It has also been proposed that S2R activation may trigger a calcium-dependent cascade in PC12 cells, contributing to dopamine release via the Ca^{2+}/calmodulin-dependent protein kinase II pathway, particularly under amphetamine stimulation. This points to a possible interplay between the two sigma receptor subtypes in regulating intracellular signaling [351].

Multiple lines of evidence indicate that S2R can induce cell death through distinct mechanisms. Specifically, S2R agonists have been shown to promote cytotoxicity via lysosomal dysfunction and the production of ROS [352,353]. In addition, S2R appears to modulate ER stress [354], likely through regulation of Ca^{2+} release mediated by direct or indirect interactions with IP_3 receptors, ryanodine receptors, and the sarcoplasmic/endoplasmic reticulum calcium ATPase (SERCA) [355]. Further evidence links S2R ligand-induced cytotoxicity with the downregulation of SOCE [356], activation of caspases and

mitochondrial superoxide generation [357], and the initiation of p53- and caspase-independent apoptotic pathways [358].

However, Mach et al. demonstrated that the cytotoxicity induced by S2R agonists such as PB28 and SW43 is independent of both TMEM97 and PGRMC1. Knockout of TMEM97, PGRMC1, or both proteins in HeLa cells did not alter the cytotoxic effects of these ligands, suggesting that their antiproliferative activity is not mediated by either protein [359]. Nevertheless, the specific roles of TMEM97 and PGRMC1 in modulating these cytotoxic pathways in the presence of S2R ligands remain to be clarified.

Several molecules, including PB28, haloperidol (Figure 4.1), and the cyclohexanediamine derivative BD614, along with various neuroleptics active at sigma receptors, exhibit cytotoxic effects, underscoring the involvement of sigma receptors in mechanisms of programmed cell death and proliferation [243]. Prolonged exposure to sigma ligands induces cell death in a dose-dependent manner, with high concentrations producing rapid morphological alterations and subsequent cell death. Because S2Rs are overexpressed in rapidly proliferating cells and S2R agonists can trigger apoptosis, these compounds have emerged as promising anticancer agents [244,245]. Owing to this strong association with tumor proliferation, S2R has also been proposed as a potential molecular target for PET imaging to assess the proliferative state of solid tumors *in vivo* [360].

Beyond its role in calcium regulation and cytotoxicity, S2R is also involved in cholesterol synthesis and regulation. S2R shares a functional domain with cholesterol-associated genes such as TM6SF and EBP and has been identified as a regulator of cholesterol homeostasis. In response to progesterone, S2R and cholesterol biosynthesis genes are co-upregulated in ovarian epithelial cells. Conversely, reduction of S2R expression results in decreased cholesterol content and diminished internalization of the low-density lipoprotein receptor (LDLR) [137].

4.2. Role of S2R in Alzheimer's disease

S2Rs are well known for their involvement in cellular proliferation. More recently, compelling evidence has demonstrated a role for S2R in neurodegenerative disorders such as AD [361]. In 2014, it was proposed that S2R mediates the binding of Aβ42 oligomers and contributes to synaptotoxicity [362]. Subsequently, in 2017, researchers reported that S2R ligands exert neuroprotective effects capable of mitigating cognitive deficits and neuroinflammation [363].

Modulation of S2R, and thereby interference with oligomer binding at neuronal synapses, offers a traditional pharmacological strategy to counteract amyloid-β oligomer toxicity. S2R modulators have the potential to act directly at the synapse by blocking the binding of toxic amyloid-β oligomers and preventing oligomer-induced synaptotoxicity [220]. Independent groups have shown that S2R modulators possess neuroprotective and synaptoprotective properties: they prevent toxic amyloid-β oligomers from binding to neuronal synapses and restore neuronal function and cognitive performance in a variety of preclinical AD models, ranging from cultured neurons to in vivo systems including *C. elegans* and rodent models [220].

Supporting the strong connection between S2R and AD, the small molecule **CT1812** (also known as Elayta; Figure 4.1) is currently being developed by Cognition Therapeutics and is under evaluation in multiple phase 2 clinical trials for Alzheimer's disease (NCT03507790, NCT04735536, NCT05531656). **CT1812** is administered orally, crosses the BBB, and binds selectively to S2R, exerting a novel mechanism of action that is fundamentally distinct from that of most existing Alzheimer's therapeutics. By engaging S2R,

CT1812 displaces Aβ oligomers from neuronal receptors, thereby reducing Aβ-induced synaptic toxicity. In preclinical studies, **CT1812** also slows oligomer-induced synapse loss and restores synaptic activity [364].

These preclinical findings have begun to be supported by completed clinical studies evaluating safety as well as pharmacokinetic and pharmacodynamic outcomes [364–366]. Ongoing phase 2 clinical trials will further assess the therapeutic efficacy of **CT1812** in patients with AD.

4.3. Current State of PET Radiotracers Targeting the Sigma-2 Receptor

Over the years, several PET radiotracers have been developed for S2R imaging (Figure 4.4). From a structural perspective, these compounds can be broadly categorized into benzamide derivatives, indole derivatives, and a set of additional molecules that do not cluster into defined structural classes. The radionuclides most commonly employed for S2R imaging are ^{18}F and ^{11}C, although ^{76}Br has also been used in some cases.

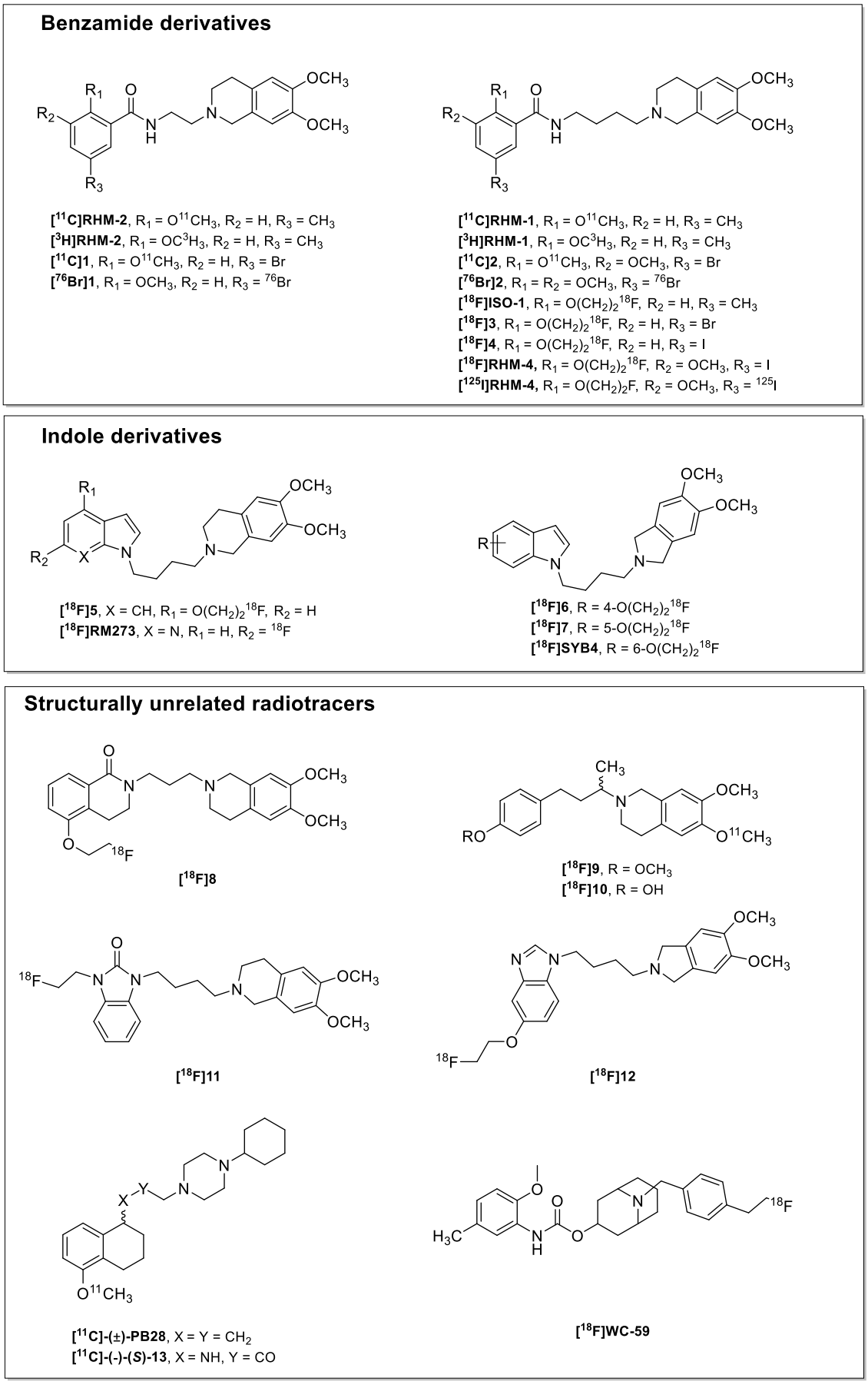

Figure 4.4: Structures of known PET tracers developed for S2R imaging.

4.3.1. Benzamide derivatives

Benzamide derivatives (Figure 4.4) represent the most significant class of PET radiotracers developed for S2R imaging. The scaffold introduced by Mach R.H. and colleagues consists of a benzamide core bearing various aromatic substitutions, linked to 6,7-dimethoxytetrahydroisoquinoline through either a two- or four-carbon linker. These compounds were originally designed for tumor imaging.

The first series of compounds incorporated the radioisotope ^{11}C. Although **[^{11}C]RHM-2**, **[^{11}C]RHM-1**, **[^{11}C]1**, and **[^{11}C]2** exhibit comparable affinity for S2R, *in vivo* biodistribution studies demonstrated that [^{11}C]RHM-1 achieved the highest tumor uptake at all time points in BALB/c mice bearing EMT-6 mammary tumors, as well as the most favorable tumor-to-organ ratios. This difference is likely attributable to variations in lipophilicity. Blockade studies with YUN143 showed an 18–46% reduction in tumor-to-organ ratios for **[^{11}C]RHM-1** [367].

Compounds **1** and **2** were also radiolabeled with ^{76}Br to evaluate their suitability for breast tumor imaging in a murine breast adenocarcinoma model. Both ^{76}Br derivatives exhibited rapid clearance from non-target tissues and good tumor retention, with fast hepatic and renal washout over the first 2 hours. Because both liver and kidney express high levels of S2R, the prolonged retention of **[^{76}Br]1** and **[^{76}Br]2** in these organs likely reflects S2R-mediated binding, as confirmed by blockade experiments. The pronounced uptake of **[^{76}Br]2** in liver and kidneys limits its usefulness for imaging tumors in the abdominal cavity. The longer half-life of ^{76}Br compared with ^{11}C also enabled Scatchard analyses, which indicated that **[^{76}Br]2** has low nonspecific binding [368].

RHM-1 was additionally labeled with ^{3}H. Owing to its subnanomolar affinity and >4000-fold selectivity for S2R, **[^{3}H]RHM-1** proved superior to **[^{3}H]DTG** for quantifying S2R density and function in *in vitro* binding assays [369].

Overall, these studies indicate that benzamide derivatives containing a four-carbon linker outperform their two-carbon counterparts. On this basis, Mach's group synthesized a second generation of benzamides labeled with ^{18}F, all incorporating the four-carbon linker **([^{18}F]ISO-1**, **[^{18}F]3**, **[^{18}F]4**, **[^{18}F]RHM-4**).

Evaluation in female BALB/c mice bearing EMT-6 tumors showed that all four radiotracers exhibited excellent tumor uptake at 5 min p.i. Tumor uptake remained elevated at 1 and 2 hours relative to normal tissues, fat, and muscle. Among them, **[^{18}F]RHM-4** achieved the highest tumor-to-muscle ratio. Although tumor uptake of **[^{18}F]3** and **[^{18}F]4** exceeded that of **[^{18}F]ISO-1**, these radiotracers displayed slower blood clearance, reducing their suitability for PET imaging. Blockade studies with YUN-143 confirmed selective S2R binding by **[^{18}F]ISO-1** and **[^{18}F]RHM-4**, identifying these two compounds as the most promising candidates [370]. **RHM-4** was also labeled with ^{125}I for potential Single Photon Emission Computed Tomography (SPECT) imaging **([^{125}I]RHM-4**). Its *in vivo* behavior closely matched that of **[^{18}F]RHM-4**, except for modest iodine retention in the thyroid [371].

Regarding **[^{18}F]ISO-1**, Dehdashti et al. conducted the first clinical study in humans and demonstrated its feasibility for imaging solid tumors, including lymphoma, breast cancer, and head and neck cancer. Tumor SUV_{max} and tumor-to-muscle ratios correlated with Ki-67, the gold-standard marker of cellular proliferation. The strong correlation between **[^{18}F]ISO-1** uptake and Ki-67 highlights its potential for assessing tumor proliferative status. The study also reported extensive plasma protein binding (free fraction ~1%) and high metabolic stability [372].

McDonald et al. evaluated **[^{18}F]ISO-1** in 29 women with primary breast cancer and found a modest but significant correlation between SUV_{max} and Ki-67, supporting its use as an in vivo biomarker of proliferative activity [373].

Shoghi et al. further demonstrated a strong linear relationship between **[^{18}F]ISO-1** uptake and the ratio of proliferating to quiescent cells in mouse mammary tumor xenografts, confirming its utility for visualizing proliferative status. **[^{18}F]ISO-1** has also been used to monitor therapeutic response in *N*-methyl-*N*-nitrosourea (MNU)-induced tumors treated with bexarotene or vorozole, with PET-derived uptake values correlating with tumor regression or progression [374].

In summary, benzamide derivatives have proven to be effective PET radiotracers for tumor imaging. Among them, **[^{18}F]ISO-1** emerges as the most promising and is currently under clinical evaluation (NCT00968656; NCT02284919).

4.3.2. Indole derivatives

Unlike the benzamide derivatives described above, which were primarily designed for tumor imaging, indole derivatives (Figure 4.4) were developed as brain-penetrant radiotracers suitable for applications in the CNS.

Among the first indole-based radiotracers reported **[^{18}F]5** and **[^{18}F]SYB4** are included**.**, They differ in the position of the fluoroethoxy substituent and, more importantly, in their BM, with **[^{18}F]SYB4** incorporating 5,6-dimethoxyisoindoline. In mouse biodistribution studies, both **[^{18}F]5** and **[^{18}F]SYB4** exhibited higher initial brain uptake than **[^{18}F]ISO-1**, as well as elevated brain-to-blood ratios at 15 min p.i. Pretreatment with haloperidol significantly reduced tracer accumulation in both brain and liver, confirming the specific in vivo binding of **[^{18}F]5** and **[^{18}F]SYB4** to S2R. Between the two, **[^{18}F]SYB4** showed superior brain uptake and brain-to-blood ratios. *Ex vivo* experiments with cyclosporine A (a P-gp inhibitor) increased brain uptake of both tracers while leaving blood activity unchanged, suggesting that these radiotracers may serve as P-gp substrates, which could account for their relatively modest initial brain penetration. Neither radiometabolite was able to cross the BBB [375].

These comparisons appear to indicate that 5,6-dimethoxyisoindoline provides more favorable properties than 6,7-dimethoxytetrahydroisoquinoline as a BM moiety for this series. This was further supported by direct comparison of **[^{18}F]5** and **[^{18}F]6**, which differ only in their BM group. *In vivo* biodistribution studies showed that **[^{18}F]6** achieved higher initial brain uptake and higher brain-to-blood ratios than **[^{18}F]5** [375,376].

To determine the optimal aromatic position for the fluoroethoxy substituent**,** **[^{18}F]6**, **[^{18}F]7**, and **[^{18}F]SYB4** were compared in vivo. **[^{18}F]6** and **[^{18}F]SYB4** displayed higher initial brain uptake at 2 min p.i. than **[^{18}F]7**, with all three outperforming **[^{18}F]ISO-1**. At 30 min, brain uptake was similar for **[^{18}F]7** and **[^{18}F]SYB4**, but markedly higher for **[^{18}F]6**, consistent with its superior affinity. **[^{18}F]6** also produced the highest brain-to-blood ratios. Blocking studies with the unlabeled ligand or CM-398 demonstrated the greatest reduction in radioactivity for **[^{18}F]6** in brain, heart, spleen, lungs, and kidneys, confirming its highest level of specific S2R binding. All three compounds exhibited minimal *in vivo* defluorination [376].

Pretreatment with cyclosporine A increased **[^{18}F]6** uptake in both brain and blood, indicating that **[^{18}F]6** is a moderate P-gp substrate. Similar results were obtained for **[^{18}F]7** and **[^{18}F]SYB4**. *Ex vivo* autoradiography of **[^{18}F]6** showed robust accumulation in cortex, cerebellum, and olfactory bulb, consistent with findings

for other S2R radioligands, along with higher uptake in the midbrain and lateral ventricles and lower uptake in hippocampus and thalamus, confirming selective S2R binding. Pharmacokinetic analysis revealed that **[^{18}F]6** entered the brain rapidly and was subsequently washed out slowly from rat brain regions. Metabolite analysis showed that **[^{18}F]6** remained the predominant radioactive species in the brain, with negligible radiometabolite contribution, consistent with its high specific binding [376].

The encouraging rodent data prompted evaluation of **[^{18}F]SYB4** in NHPs to assess translational potential. In monkey brain, **[^{18}F]SYB4** exhibited highest uptake in the cerebellum (which showed the highest V_T values), followed by putamen and hippocampus, with the lowest levels in white matter. This distribution pattern is consistent with S2R expression reported in rodents. Specific binding was demonstrated using CM-398 as a blocker. Metabolism of **[^{18}F]SYB4** was rapid, with ~36% parent fraction at 30 min. The resulting radiometabolites were more polar and therefore unlikely to cross the BBB or interfere with quantitative PET analysis [377].

A variation on this theme is **[^{18}F]RM273**, in which the indole scaffold is replaced by an aza-indole framework. **[^{18}F]RM273** showed good brain penetration, entering the CNS rapidly and clearing quickly, indicative of low nonspecific binding *in vivo*. Metabolite studies showed that, under conditions of an intact BBB, PET images obtained with **[^{18}F]RM273** were unaffected by radiometabolites. Autoradiography revealed strong binding in cortical and hippocampal regions, overlapping well with the distribution of established S2R ligands such as ISO-1, PB28, and siramesine, indicating a high degree of S2R specificity. **[^{18}F]RM273** was also evaluated in a rat glioblastoma model, where it exhibited an exceptionally high B_{max} value (3600 fmol/mg tissue), consistent with previous reports of elevated S2R density in glioblastoma cell lines such as U-138MG and C6 [378].

4.3.3. Structurally unrelated radiotracers

In addition to the categories described above, several research groups have developed a number of PET radiotracers that do not fall within the main structural classes (Figure 4.4).

[^{18}F]8 features a 3,4-dihydroisoquinolinone scaffold linked through a three-carbon linker to 6,7-dimethoxytetrahydroisoquinoline. Autoradiographic studies showed maximal binding of **[^{18}F]8** in the cerebral cortex and hippocampus, along with high accumulation in the cerebellum. Time–activity curves (CT scans) revealed elevated levels of radioactivity in the cortex, olfactory bulb, and cerebellum, consistent with autoradiographic findings; however, hippocampal radioactivity was not higher than in other regions, contradicting autoradiography. PET imaging demonstrated rapid washout of **[^{18}F]8** from rat brain. Overall, **[^{18}F]8** was unsuccessful for in vivo S2R imaging in rat brain, likely due to hindered BBB penetration resulting from P-gp–mediated efflux [379].

Regarding compounds **9** and **10**, both containing a chiral center, radiolabeling was carried out on the racemic mixtures. **[^{11}C]-(±)-9** exhibited widespread brain distribution with particularly high uptake in the cerebral cortex and hypothalamus, whereas **[^{11}C]-(±)-10** showed no region-specific distribution. This contrast likely reflects differences in affinity and lipophilicity. CT scans confirmed that **[^{11}C]-(±)-9** reached a high peak uptake in the whole brain at 3 min p.i., whereas **[^{11}C]-(±)-10** displayed lower uptake, suggesting that the higher lipophilicity of **[^{11}C]-(±)-9** enables more efficient BBB penetration. The washout rate of **[^{11}C]-(±)-9** was slower than that of **[^{11}C]-(±)-10**, consistent with its higher S2R affinity and slower receptor dissociation. Blockade studies further supported the superiority of **[^{11}C]-(±)-9** over **[^{11}C]-(±)-10** [380]**.**

[^{18}F]11 and **[^{18}F]12** bear some resemblance to indole-based radiotracers, incorporating benzimidazole and benzoxazole scaffolds, respectively, with **[^{18}F]12** also employing 5,6-dimethoxyisoindoline as the BM. In mouse biodistribution studies, **[^{18}F]11** showed higher brain uptake than **[^{18}F]ISO-1**. Pretreatment with CM398 markedly reduced **[^{18}F]11** uptake in S2R-rich organs, confirming high specific binding. In contrast, uptake reduction for **[^{18}F]12** was observed only in the pancreas, suggesting that this moderate-affinity ligand yields measurable S2R-specific binding only in tissues with high receptor density. Pre-injection of cyclosporine A significantly increased brain accumulation of both **[^{18}F]11** and **[^{18}F]12**, indicating that both are P-gp substrates [381].

Compound **11** was further evaluated as a potential diagnostic tool for glioblastoma. Small-animal PET/CT imaging with **[^{18}F]11** demonstrated high uptake and clear visualization of U87MG glioma xenografts in nude mice, with superior tumor retention and higher tumor-to-muscle ratios compared with **[^{18}F]ISO-1** [381].

The radiotracers **[^{11}C]-(±)-PB28**, **[^{11}C]-(-)-(S)-13**, and **[^{11}C]WC-59** are unique in that they do not contain 6,7-dimethoxytetrahydroisoquinoline or its lower homologue as the BM.

Instead, **[^{11}C]-(±)-PB28** and **[^{11}C]-(-)-(*S*)-13** incorporate cyclohexylpiperazine, while **[^{11}C]WC-59** contains 9-azabicyclo[3.3.1]nonane. PB28 is a well-established reference S2R ligand and has been crystallized in complex with the receptor [219]. *In vivo* biodistribution of **[^{11}C]-(±)-PB28** in mice showed high uptake in posterior cortex, temporal cortex, cerebellum, and, to a lesser extent, frontal cortex, thalamus, and striatum. Uptake increased over the first 60 minutes and remained comparable at 90 min. However, blockade studies using unlabeled **PB28** or the selective S2R ligand SM-21 failed to reduce tracer uptake, instead yielding increased uptake in all brain regions, likely due to displacement of tracer from peripheral reservoirs. These findings indicate that the observed brain uptake of **[^{11}C]-(±)-PB28** represents nonspecific binding, leading to discontinuation of its development [382].

[^{11}C]-(-)-(*S*)-13 represents a further structural variation, with the propyl linker replaced by an acetamide and radiolabeling performed on the *S*-enantiomer. PET imaging showed very low brain accumulation in rats, with haloperidol producing only minor reductions. These data suggest predominantly nonspecific uptake. Clearance from blood was slower under blocked conditions, possibly due to haloperidol interfering with radiotracer metabolism. When tested in mice bearing EMT-6 breast cancer, C6 glioma, or PC-3 prostate cancer xenografts, **[^{11}C]-(-)-(*S*)-13** exhibited no uptake in PC-3 or EMT-6 tumors and only moderate uptake in C6 tumors, which was only slightly reduced by haloperidol co-administration. Consequently, this radiotracer was also not pursued further [383].

[^{18}F]WC-59, a carbamate analogue structurally reminiscent of benzamide radiotracers, was evaluated in BALB/c mice with EMT-6 tumors. Its biodistribution did not show any advantage over existing PET tracers for assessing proliferative status, and thus development was not continued [384].

Taken together, these findings indicate that radiotracers lacking 6,7-dimethoxytetrahydroisoquinoline, or its lower homologue, as the BM moiety generally fail to provide adequate PET imaging performance. This strongly supports the conclusion that 6,7-dimethoxytetrahydroisoquinoline is a critical structural component for high-quality S2R radioligands.

4.4. Summary of the Introduction

Compared to S1R, the number of PET radiotracers reported for S2R remains limited. Among the available compounds, structural diversity is relatively narrow, both in the hydrophobic domain and in the BM. With respect to the hydrophobic portion, most radiotracers fall into the benzamide or indole classes; regarding the BM, 6,7-dimethoxytetrahydroisoquinoline is predominantly used, with 5,6-dimethoxyisoindoline occasionally serving as a lower homologous substitute. Only a few compounds deviate from this framework, namely **[^{11}C]-(±)-PB28**, **[^{11}C]-(-)-(S)-13**, and **[^{11}C]WC-59**, and these are also the radiotracers that showed the poorest performance.

Indole-based radiotracers generally show adequate brain penetration and are therefore applied in CNS imaging, whereas benzamide derivatives were primarily designed for tumor imaging. Many S2R radiotracers interact with P-gp, likely due to similarities between the S2R pharmacophore and that of P-gp, the major efflux transporter at the BBB. As a consequence, these agents have limited use in neurodegenerative disorders.

Because of their interaction with P-gp and the high expression of S2R in tumors, most S2R PET radiotracers have been applied predominantly in oncology. Among these, **[^{18}F]ISO-1** is notable; it is a clinically advanced S2R PET tracer and is currently under evaluation in ongoing clinical trials (NCT00968656, NCT02284919).

4.5. Background and Aim

The research group in which this PhD thesis was carried out has been studying the S2R for many years. Several molecular scaffolds have been explored as potential therapeutic tools, including tetrahydronaphthalene derivatives and 2-aminopyridine derivatives bearing cyclohexylpiperazine as a BM [385,386], as well as thiosemicarbazone derivatives incorporating 3*H*-spiro[isobenzofuran-1,4'-piperidine] as BM, which have shown promise as strategies against pancreatic cancer [387].

S2R has also been investigated as a promising diagnostic target, using fluorescent compounds such as tetrahydroisoquinoline derivatives featuring 6,7-dimethoxy-3,4-dihydroisoquinoline as BM [388], or tetrahydronaphthalene derivatives containing cyclohexylpiperazine as BM [389,390]. Moreover, PET radiotracers for S2R have been developed based on the tetrahydroisoquinoline scaffold and 6,7-dimethoxy-3,4-dihydroisoquinoline as BM [379].

Among these compounds, PB28 stood out and was co-crystallized with the S2R crystal structure by Alon *et al.* [347].

Within the framework of S2R research, we attempted to develop two different PET radiotracers featuring completely distinct scaffolds and BMs.

In the first case, we retained the rigid conformers of benzamides linked through a three-carbon spacer to 6,7-dimethoxy-3,4-dihydroisoquinoline as the BM. In the second case, we aimed to design an innovative PET radiotracer incorporating an indole or aza-indole scaffold connected via a four-carbon linker to 3*H*-spiro[isobenzofuran-1,4'-piperidine] as the BM.

For the development of the new rigid benzamide-based PET radiotracer, we started from 2-(3-(6,7-dimethoxy-3,4-dihydroisoquinolin-2(1*H*)-yl)propyl)-5-(2-fluoroethoxy)-3,4-dihydroisoquinolin-1(2*H*)-one (**8**, Figure 4.5) [379], whose properties were thoroughly discussed in the introductory section of this chapter. Compound **8** exhibited high affinity for S2R (K_i = 9.24 nM) and high selectivity over S1R (K_i = 3095 nM). Moreover, the presence of fluorine in the fluoroethoxy chain facilitates the radiolabeling step.

These compounds, prompted the development of their isomeric tetrahydroquinolines, whose investigation led to another reference lead compound, i.e. 1-(3-(6,7-dimethoxy-3,4-dihydroisoquinolin-2(1*H*)-yl)propyl)-5-methoxy-1,2,3,4-tetrahydroquinoline (**FA10**, Figure 4.5) [391], which showed high affinity for S2R (K_i = 1.42 nM) and high selectivity over S1R (K_i = 3987 nM).

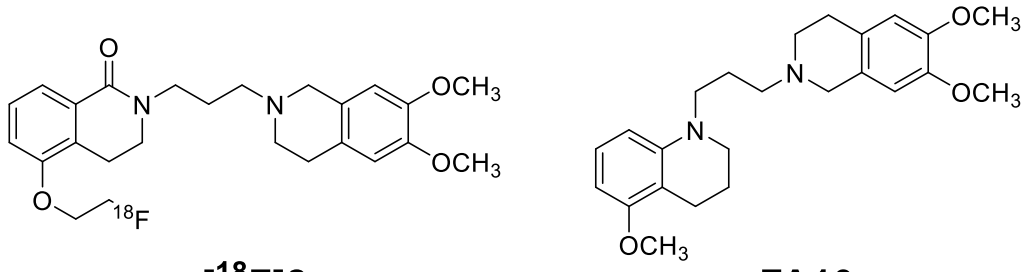

[^{18}F]8

K_i S1R = 3095 nM
K_i S2R = 9.24 nM

FA10

K_i S1R = 3987 nM
K_i S2R = 1.42 nM

Figure 4.5. Chemical structure and pharmacodynamic profile of lead compounds **[^{18}F]8** [379] and **FA10** [391].

The promising properties of **FA10** inspired the replacement of the methoxy group with a fluoroethoxy one, yielding 1-(3-(6,7-dimethoxy-3,4-dihydroisoquinolin-2(1*H*)-yl)propyl)-5-(2-fluoroethoxy)-1,2,3,4 tetrahydroquinoline (**14**, also known as **LC2**, Figure 4.6).

LC2 demonstrated low nanomolar affinity and moderate selectivity toward sigma-2 receptor and, more broadly, high selectivity against major CNS targets, including common GPCRs, enzymes, ion channels, and transporters. Based on the promising results obtained, the corresponding PET radiotracer radiolabelled with ^{18}F. , was obtained and subjected to *in vitro* autoradiography studies on rat brain slices and *in vivo* PET imaging in female CD-1 mice, with analysis of time–activity curves (TACs). These preliminary data will be likely confirmed in due course at the Emory University in Atlanta (USA).

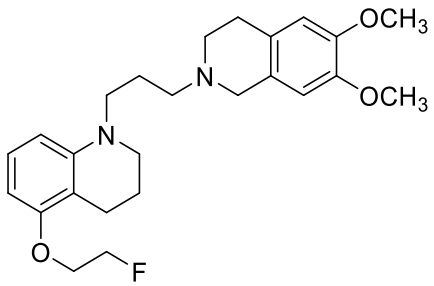

LC2

Figure 4.6. Chemical structure of PET candidate **LC2**.

To develop a new PET radiotracer for the S2R, we built upon the work of Moldovan et al., who synthesized a series of indole and azaindole derivatives bearing fluorine substituents at different positions. In agreement with the findings of Alon et al. [347], the most promising compound was the azaindole substituted at position 6 with an F-atom, namely **[^{18}F]RM273** (Figure 4.7). This innovative brain-penetrant PET radiotracer exhibits high affinity for S2R (K_i = 1.6 nM) and marked selectivity over the S1R (K_i = 691 nM) [378]. This study follows the work of Linkens et al., who employed a "*scaffold-hopping*" approach to design tetrahydroisoquinoline-substituted isoindolines that demonstrated significantly higher affinity for S2R compared to S1R [392].

A major advantage of **[^{18}F]RM273** is its ability to effectively cross the BBB, an important feature given that S2R ligands share a key pharmacophore, 6,7-dimethoxytetrahydroisoquinoline, with P-gp, the major efflux transporter at the BBB [334].

Since 6,7-dimethoxytetrahydroisoquinoline represents both a common pharmacophore with P-gp and a core scaffold in many PET radiotracers for S2R (as discussed in the previous section), we sought to replace it with a different BM to design a novel, structurally distinct PET radiotracer. To achieve this, we drew inspiration from the work of Anobile et al. [393], in which the structure of the S2R ligand Siramesine, an indole-based structure incorporating a 3*H*-spiro[isobenzofuran-1,4-piperidine] as the basic moiety was slightly modified [394], leading to compound **MT8** (Figure 4.7). that demonstrated remarkable affinity for S2R (K_i = 0.43 nM) and good selectivity over S1R (K_i = 27.3 nM) [393].

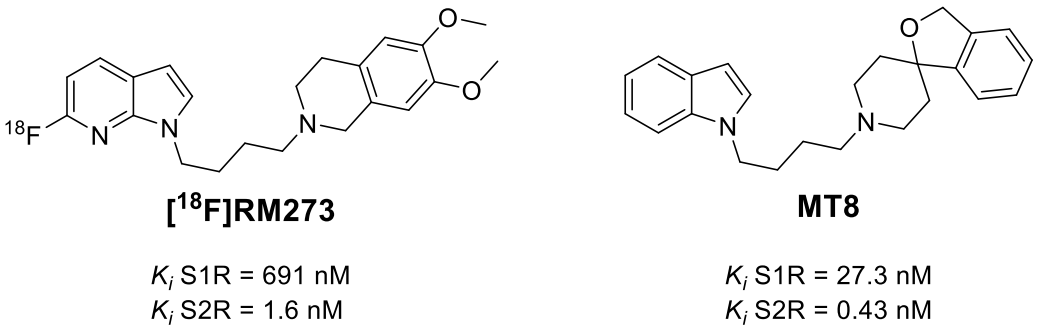

Figure 4.7. Chemical structure and pharmacodynamic profile of lead compounds **[¹⁸F]RM273** [378] and **MT8** [393].

Building upon the promising characteristics of **[¹⁸F]RM273** and **MT8**, we designed a new series of indole and azaindole derivatives substituted at the 5- or 6-position with either a fluorine atom or a fluoroethoxy group (Figure 4.8) for potential PET ligands development, incorporating the 3*H*-spiro[isobenzofuran-1,4-piperidine] unit as the BM.

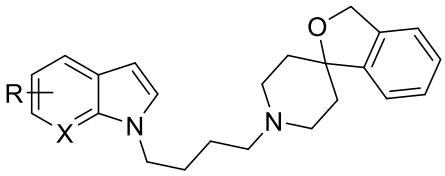

Figure 4.8. General structure of PET candidates for S2R.

Sigma-2 receptors part 1

Synthesis and *In Vivo* Evaluation of 1-(3-(6,7-Dimethoxy-3,4-dihydroisoquinolin-2(1*H*)-yl)propyl)-5-(2-fluoroethoxy)-1,2,3,4-tetrahydroquinoline for Positron Emission Tomography Imaging of Sigma-2 Receptors

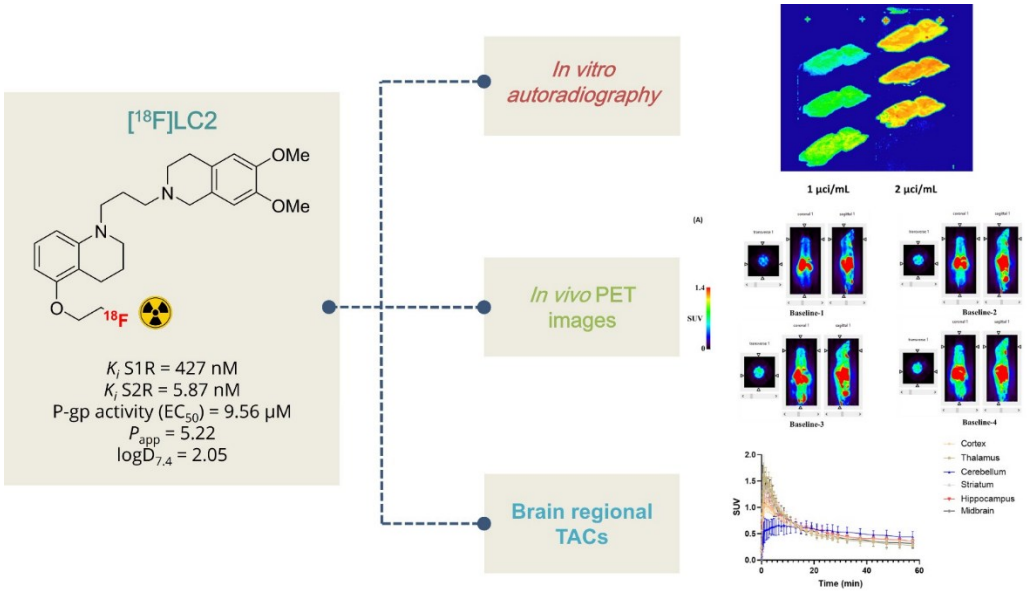

4.6. Results

4.6.1. Chemistry

The synthesis of the phenol precursor **20** and the final compound **14** (also known as **LC2**) was carried out following a synthetic route previously described for the lead compounds **FA10** [391] and **8** [379], with minor modifications (Scheme 4.1).

Commercially available 4-hydroxy-2,3-dihydro-1*H*-inden-1-one underwent a Schmidt rearrangement using NaN_3 in CH_2Cl_2/methanesulfonic acid (1:1) to afford the already known compound **15** [395]. The phenolic group was first protected by benzylation with benzyl bromide, yielding compound **16**, which was subsequently alkylated with 1-bromo-3-chloropropane in the presence of NaH to obtain the chloride derivative **17**. Nucleophilic substitution with 6,7-dimethoxy-1,2,3,4-tetrahydroisoquinoline afforded intermediate **18**, and the amide group was then reduced using BMS in dry THF to give the corresponding amine **19**. This compound was subjected to catalytic debenzylation over 10% Pd/C to furnish the phenol precursor **20**. Finally, alkylation of the phenolic group with 1-fluoro-2-iodoethane under basic conditions afforded the final compound **LC2** which was converted to oxalate salt via treatment with oxalic acid in Et_2O, followed by recrystallization from MeOH/Et_2O.

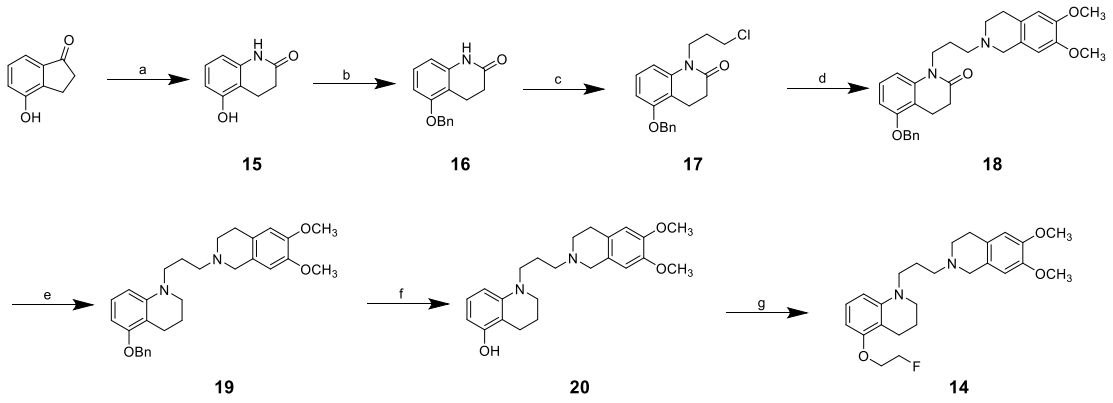

Scheme 4.1. Synthesis of phenol precursor **20** and final compound **LC2**. (a) NaN_3, CH_2Cl_2/methanesulfonic acid (1:1), 0 °C, 2h; (b) BnBr, K_2CO_3, acetone, reflux, 4h; (c) 1-Bromo-3-chloropropane, NaH, dry DMF, RT, 3h; (d) 6,7-Dimethoxy-1,2,3,4-tetrahydroisoquinoline, K_2CO_3, CH_3CN, reflux, ON; (e) $BH_3{\cdot}Me_2S$ 2M, dry THF, reflux, ON; (f) Pd/C 10%, H_2, 4.5 bar, EtOH 96%, RT, 72h; (g) 1-Fluoro-2-iodoethane, K_2CO_3, acetone, reflux, ON.

4.6.2. *In vitro* Binding Affinities

The results of radioligand displacement studies are reported in Tables 4.1. as K_i values, which were calculated by converting the experimentally determined IC_{50} values using the Cheng–Prusoff equation.

LC2 exhibits high affinity for the S2R receptor along with good selectivity compared with the methoxy analogue (**FA10**) [391], the introduction of a fluoroethoxy group in **LC2** results in reduced affinity for S2R (K_i = 5.87 nM vs 1.42 nM, respectively) and, more importantly, a marked decrease in selectivity due to increased affinity for S1R (K_i = 427 nM vs 3987 nM, respectively). However, these data were obtained using two different binding protocols. Therefore, the binding assay for **FA10** was repeated using the same protocol applied to **LC2**, and the new results were comparable to those obtained for **LC2** (K_i S1R = 427

nM; K_i S2R = 8.25 nM). Based on these updated data, replacing the methoxy group with a fluoroethoxy group leads to similar affinity and selectivity profiles.

When compared to compound **8** [379], a lead compound with a dihydroisoquinolinone scaffold, the use of a tetrahydroquinoline core in **LC2** leads to increased affinity for S2R (K_i = 5.87 nM vs. 9.24 nM, respectively), but at the cost of reduced selectivity, as **LC2** shows considerably higher affinity for S1R than compound **8** (K_i = 427 nM vs. 3095 nM, respectively).

Table 4.1. S1R and S2R affinities.

Compound	Structure	K_i S1R (nM)	K_i S2R (nM)	SI[a] K_i S1R/S2R
LC2	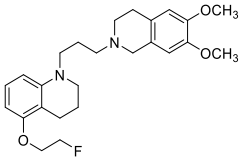	427	5.87	73
FA10	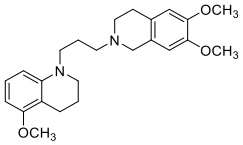	3987[b] 482[c]	1.42[b] 8.25[c]	2807[b] 58[c]
8[d]	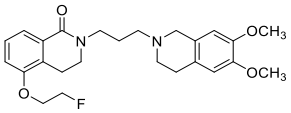	3095	9.24	330

[a]SI represents selectivity; [b]Data from [391]; [c]Data were obtained using the same binding protocol employed for **LC2**, as reported in the experimental section; [d]Data from [379].

Given its favorable affinity and selectivity profile for potential PET imaging of S2R in the CNS, **LC2** was further evaluated against 56 major CNS targets, including common GPCRs, enzymes, ion channels, and transporters. Initial screening was performed by measuring the percentage inhibition of target activity (Figure S4.1). For targets showing >50% inhibition in the primary screen, secondary radioligand binding assays were conducted (Table 4.2).

Across all tested targets, **LC2** demonstrated selectivity at least 70-fold over S2R, with the exceptions of 5-HT_{1A} (50-fold), 5-HT_{2B} (38-fold), α_{1A} (35-fold), α_{2B} (58-fold), and SERT (28-fold).

Overall, these results indicate that **LC2** is a highly selective S2R ligand at the brain level with minimal off-target activity, supporting its potential as a promising PET radiotracer candidate.

Table 4.2. Secondary radioligand binding assays for the targets with >50% of inhibition on primary screening.

Target	K_i (nM)[a]	SI[b] K_i target/S2R
5-HT$_{1A}$	303	50
5-HT$_{1B}$	2731	455
5-HT$_{1D}$	9856	1643
5-HT$_{2B}$	227	38
5-HT$_{7A}$	913	152
α_{1A}	212	35
α_{2A}	618	103
α_{2B}	350	58
D_3	433	72
D4	>10000	>1667
MOR	8800	1467
PBR	>2000	>333
SERT	167	28
NR$_{2B}$	857	143
HERG	1782	297

[a]All assays were conducted following established PDSP protocols [396]. [b]SI represents selectivity.

4.6.3. Blood-Brain Barrier permeability and P-Glycoprotein Interaction Investigation

LC2 has been selected as a promising PET candidate for brain imaging of S2R. For effective CNS application, it is essential that the compound crosses the BBB. One of the primary defense mechanisms of the BBB is P-gp [334].

To evaluate the brain penetration potential of **LC2**, bidirectional permeability coefficients (P_{app}AB and P_{app}BA) were measured across Caco-2 cell monolayers, and the efflux ratio (P_{app}BA/P_{app}AB) was calculated. In addition, **LC2**'s interaction with P-gp was assessed using established protocols previously reported by our group [335]. All experimental results are summarized in Table 4.3.

Table 4.3. Evaluation of the BBB Permeability and P-gp Interaction of **LC2**

Compound	P_{app}BA (nm/sec)	P_{app}AB (nm/sec)	P_{app}(BA/AB)	P-gp activity EC_{50} μM
LC2	2063	395	5.22	9.56
FA10[a]	/	/	/	2.13
8[b]	/	/	2.58	5.00
MC225[c]	/	/	18	6.35

[a]Data from Ref [391]; [b]Data from Ref [379]; [c]Data from Ref [397].

The relatively low P_{app}AB value indicates that passive permeability of **LC2** from the apical to the

basolateral side is limited, whereas the substantially higher P_{app}BA value suggests active transport from the basolateral to the apical side. The efflux ratio (P_{app}BA / P_{app}AB) of 5.22 confirms that **LC2** is a substrate of P-gp, a conclusion further supported by the measured P-gp activity EC_{50} of 9.56 µM. These findings are consistent with expectations, as **LC2** is an isostere of **MC225**, a weak P-gp substrate currently undergoing several phase II clinical trials to investigate P-gp involvement in various CNS pathologies [334]. Notably, the lower P_{app} ratio observed for **LC2** compared to **MC225** (5.22 vs. 18) [397] indicates that **LC2** is a stronger substrate for P-gp.

Overall, these results suggest that while **LC2** is capable of crossing cellular barriers, its brain penetration *in vivo* may be significantly modulated by P-gp–mediated efflux at the BBB, which could limit its CNS exposure.

4.6.4. Radiochemistry

Based on its binding affinity and selectivity toward the main CNS targets, **LC2** was advanced to obtain its corresponding radiolabeled version with Fluorine-18.

Radiolabeling was carried out using a two-step radiosynthesis approach, as illustrated in Scheme 4.2. This method, developed by Schoultz B.W. et al. [398], enables the direct introduction of a [^{18}F]fluoroethoxy group onto a phenolic moiety via the preliminary synthesis of [^{18}F]fluoroethyltosylate ([^{18}F]FETos) and has been widely employed in the literature.

The synthesis of the phenolic precursor (**20**) is shown in Scheme 4.1. For the preparation of [^{18}F]FETos, ethane-1,2-diyl bis(4-methylbenzenesulfonate) (3 mg) was reacted with [^{18}F]fluoride (1.1 GBq), $K_{2.2.2}$ (10 mg), and K_2CO_3 (2 mg) in CH_3CN (0.5 mL) at 85 °C for 15 min. The resulting [^{18}F]FETos was then reacted with compound **20** (2 mg) in the presence of $K_{2.2.2}$ (10 mg) and K_2CO_3 (2 mg) in CH_3CN (0.5 mL) at 85 °C for 15 min.

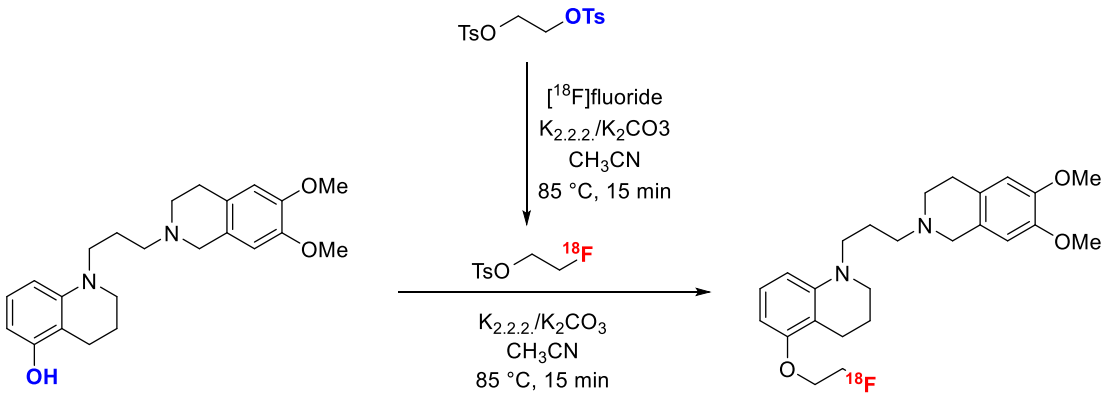

Scheme 4.2. Radiosynthesis of final compound **[^{18}F]LC2**.

[^{18}F]LC2 was purified by semi-preparative HPLC using a Phenomenex Luna C_{18} (2) column (5 µm, 10 × 250 mm) with MeCN/H_2O (40:60, v/v, 0.1% Et_3N) as the mobile phase.

[^{18}F]LC2 was obtained with a RCY of 7%. The reaction was performed only once to produce material for biological assays, while determination of the A_m is still ongoing.

Identification of **[^{18}F]LC2** was achieved by analytical HPLC through co-injection with the non-radioactive reference compound (Figure 4.9) using a Luna 5 µm C_{18} (2) 100 Å LC column (100 × 4.6 mm), with a mobile phase consisting of 60% CH_3CN and 0.1% TEA in H_2O at a flow rate of 1 mL/min.

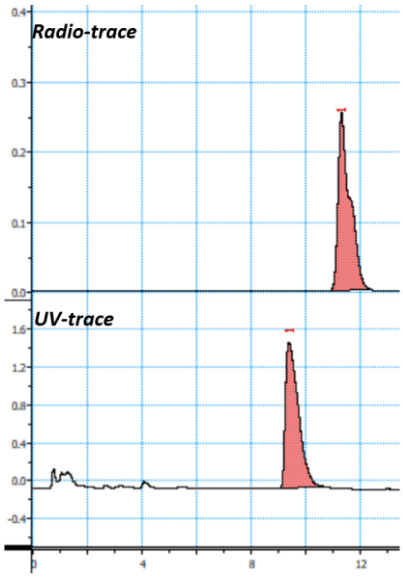

Figure 4.9. HPLC chromatography of co-injection of **[^{18}F]LC2** with cold reference compound. HPLC conditions: Luna 5 µ C18(2) 100 Å LC column (100 × 4.6 mm), mobile phase: 60% acetonitrile-0.1% TEA in H_2O, flow rate: 1 mL/min.

The lipophilicity of **[^{18}F]LC2** was experimentally determined at physiological pH using the shake-flask method, as previously described [399], yielding a $logD_{7.4}$ value of 2.05 ± 0.01 (*n* = *3*). This value falls within the recommended range (1.5–3.0) for CNS-targeted radiotracers [77].

4.6.5. *In vitro* autoradiography

To validate the specificity and selectivity of the radiotracer, in vitro autoradiography experiments with **[^{18}F]LC2** were performed on rat brain sections, using two radiotracer concentrations (1 µCi/mL and 2 µCi/mL).

The autoradiography images (Figure 4.10) reveal a heterogeneous distribution of **[^{18}F]LC2** across different anatomical regions, suggesting differential regional uptake of the tracer within the tissue. Comparison between the two concentrations shows an increase in signal intensity at 2 µCi/mL relative to 1 µCi/mL. This increase corresponds to higher detectable binding in the same brain regions already positive at the lower concentration, without altering the overall pattern of regional localization within the sections.

These data are preliminary, and further studies are required to precisely map the CNS regions where the radiotracer binds and to perform blockade experiments to determine whether the observed binding is specific.

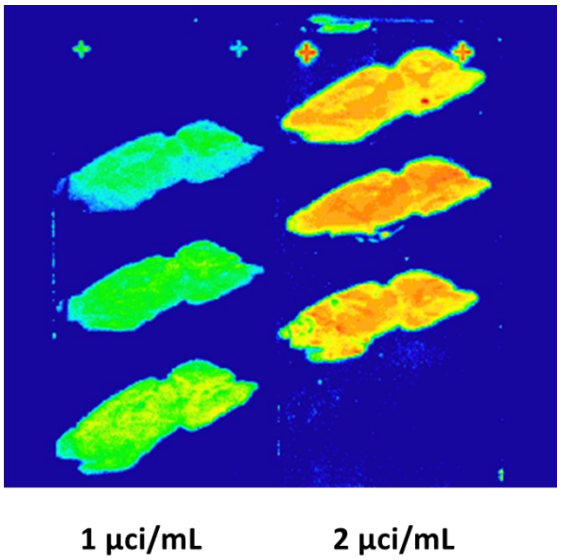

Figure 4.10. *In vitro* autoradiography of S2R PET radiotracer **[^{18}F]LC2** in rat brain sections.

4.6.6. *In vivo* PET imaging in mice

In the next step, we evaluated the *in vivo* PET imaging performance of **[^{18}F]LC2** in female CD-1 mice, with the results summarized in Figure 4.11.

Analysis of TACs (Figure 4.11B) shows that **[^{18}F]LC2** exhibits rapid cerebral uptake, reaching an early peak SUV of approximately 1.4, followed by a progressive decrease in activity over time, indicative of relatively fast washout. Cerebral distribution appears generally diffuse, with a consistent spatial pattern throughout the acquisition period, suggesting that initial accumulation and subsequent clearance occur without substantial changes in regional localization. Notably, **[^{18}F]LC2** binds homogeneously across the CNS regions examined, except for the cerebellum, where lower binding is detected.

Quantitatively, the observed SUV values are moderate, indicating that the tracer crosses the BBB and reaches the brain parenchyma, though it does not show particularly high accumulation. This may be influenced by P-gp activity, and experiments with CsA are planned to assess whether inhibition of P-gp increases cerebral SUV.

The combination of rapid initial uptake and pronounced washout suggests favorable kinetics for dynamic imaging studies but may be limiting for static acquisitions, as rapid clearance could reduce the time window available for accurate quantification of specific binding.

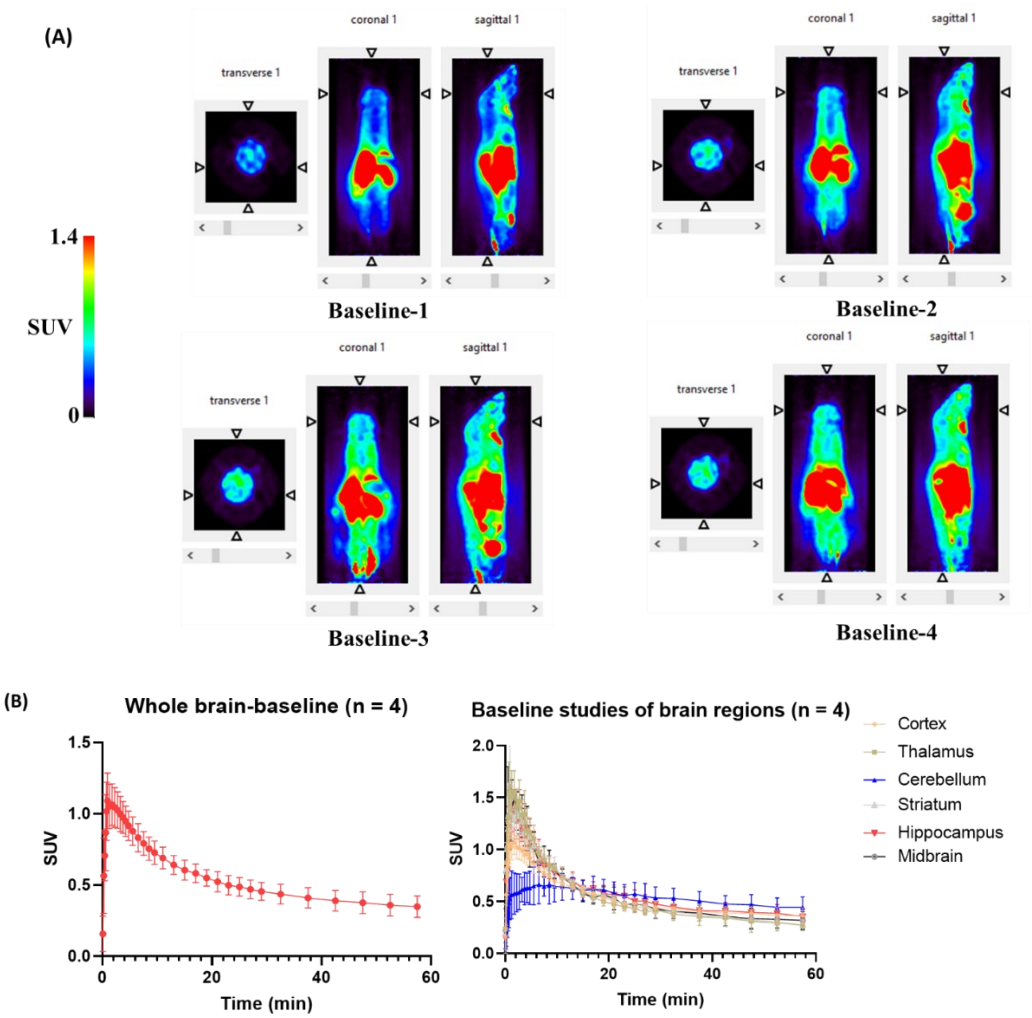

Figure 4.11: *In vivo* brain distribution in CD-1 mice female of **[^{18}F]LC2**. **(A)** Representative PET images; **(B)** whole-brain and regional TACs of selected brain regions under baseline conditions.

4.7. Discussion

LC2 was developed as a novel PET radiotracer for brain imaging of the S2R. *In vitro* pharmacological evaluation demonstrated high affinity for the S2R (K_i = 5.87 nM) and good selectivity over the S1R (K_i = 427 nM). Screening against 56 major CNS targets revealed minimal off-target interactions, supporting its potential as a selective PET radiotracer. A measured $logD_{7.4}$ of 2.05 is in line with the ability of LC2 to cross the BBB. However, bidirectional permeability studies and P-gp assays indicated that **LC2** is a substrate of P-gp, suggesting that although it is capable of crossing cellular barriers, its *in vivo* brain penetration may be significantly influenced by P-gp–mediated efflux.

Radiolabeling of **LC2** was successfully achieved using a two-step radiosynthesis approach. [^{18}F]FETos was first produced and subsequently reacted with the phenolic precursor **20** in CH_3CN at 85 °C for 15 min in the presence of $K_{2.2.2}$ and K_2CO_3, yielding **[^{18}F]LC2** with a RCY of 7%.

In vitro autoradiography on rat brain slices revealed a relatively uniform uptake of **[^{18}F]LC2** across CNS regions in a dose-dependent manner. Increasing the concentration enhanced binding in already positive regions without inducing additional regional binding, indicating a conserved distribution pattern.

In vivo PET imaging in female CD-1 mice showed rapid CNS uptake, with a peak SUV of approximately 1.4. This uptake was observed in all CNS regions except the cerebellum, demonstrating a homogeneous binding pattern and absence of cerebellar binding. A rapid washout of **[^{18}F]LC2** was also observed. The moderate overall CNS uptake is likely influenced by P-gp–mediated efflux, consistent with the in vitro permeability data.

Compared with other PET radiotracers for S2R reported in the literature, which often suffer from poor brain penetration or high nonspecific binding, the measurable and dynamic brain signal observed with **[^{18}F]LC2** represents a positive advancement. Nonetheless, the moderate SUV values and rapid washout suggest a limited residence time in the CNS relative to other preclinical S2R ligands, where higher accumulation and more stable kinetics often correlate with improved target quantification.

4.8. Future perspectives

The investigation of **LC2** as a PET radiotracer for S2R is still in its early stages. Future studies will focus on repeating radiosynthesis to optimize the radiochemical yield, evaluating *in vitro* stability, and performing autoradiography and *in vivo* experiments in the presence of structurally unrelated S2R-specific blockers to confirm binding specificity. Additional *in vivo* studies will include P-gp inhibition using cyclosporine A to determine whether moderate CNS uptake is indeed due to efflux, and metabolic studies to characterize the *in vivo* fate of **[^{18}F]LC2**.

4.9. Conclusions

[^{18}F]LC2 exhibits rapid cerebral uptake and well-defined kinetics, overall characteristics that make it a promising radiotracer for CNS imaging. However, further studies, including kinetic modeling, binding specificity assessments, and metabolic stability evaluations, are required to determine whether the observed profile is optimal for quantitative PET imaging of S2R in the CNS.

4.10. Materials and Methods

4.10.1. Chemistry

All chemicals were purchased from Sigma-Aldrich, TCI Chemicals, Ambeed, or Angene. Thin layer chromatography (TLC) was performed using plates from Merck (silica gel 60 F_{254}). Column chromatography was performed with Merck silica gel 60 Å (63-200 mm; ratio of crude mixture to silica gel 1:30 w/w, unless otherwise stated) as the stationary phase. Melting points (mp) were determined with a capillary apparatus (Büchi 540). ^{1}H-NMR spectra were recorded in the indicated solvent on a Varian Mercury-VX spectrometer (300 MHz) or on an Agilent 500-vnmrs500 spectrometer (499.801MHz). The following data are reported: chemical shift (δ) in ppm, multiplicity (s = singlet, d = doublet, t = triplet, q = quartet, quint = quintet, m = multiplet, dd = doublet of doublets, dt = doublet of triplets, td = triplet of doublets, and br = broad signal), integration, and coupling constant (J) in hertz. Recording of mass spectra was done on an HP6890-5973 MSD gas chromatograph/mass spectrometer; only significant m/z peaks, with their percentage of relative intensity in parentheses, are reported. HRMS-ESI analyses were performed on a Bruker Daltonics MicrOTOF-Q II mass spectrometer. All spectra were in accordance with the assigned structures. The purity of target compounds was assessed by HPLC. Analytical HPLC analyses were performed on final compounds using a Thermo Fisher Scientific Vanquish HPLC with Thermo Fischer Scientific Accucore aQ Column, 2.6 µm, 2.1 X 100 mm at a flow rate of 0.4 mL/min. Isocratic elution of **LC2** was carried out with 50:50 (v/v) (pH = 3.00). UV signals were detected at 254 nm and 280 nm. The compounds is >95% pure by HPLC.

*5-Hydroxy-3,4-dihydroquinolin-2(1H)-one (**15**)* [395].

*5-(Benzyloxy)-3,4-dihydroquinolin-2(1H)-one (**16**).* To a solution of compound **15** (1 mol, 1 eq) in acetone (20 mL), K_2CO_3 (3 mol, 3 eq) and BnBr (2 mol, 2 eq) are added. The resulting mixture was refluxed with stirring 4h and then was allowed to cool to room temperature. The solvent was removed under vacuum. The residue was taken up with H_2O (20 mL) and extracted with CH_2Cl_2 (3 x 20 mL). The combined organic layers were dried (Na_2SO_4) and evaporated under reduced pressure to afford a crude residue, which was purified by column chromatography using CH_2Cl_2/AcOEt 95:5 to give a white solid. Yield, 87%. ^{1}H-NMR ($CDCl_3$, 300 MHz) δ: 2.61 (2H, t, J = 7.6 Hz), 3.02 (2H, t, J = 7.6 Hz), 5.09 (2H, s), 6.45 (1H, d, J = 8.1 Hz, Ar), 6.65 (1H, d, J = 7.8 Hz, Ar), 7.11 (1H, t, J = 8.1 Hz, Ar), 7.30-7.45 (5H, m, Ar), 8.45 (1H, br s).

*5-(Benzyloxy)-1-(3-chloropropyl)-3,4-dihydroquinolin-2(1H)-one (**17**).* To a suspension of NaH (2.0 mmol, 2 eq) in dry DMF (1 mL), a solution in dry DMF (3 mL) of **16** (1.0 mmol, 1 eq), was added in a dropwise manner, at 0 °C under a stream of N_2. After 30 min, 1-bromo-3-chloropropane (1.3 mmol, 1.3 eq) was added in a dropwise manner and the mixture was allowed to warm to room temperature and was kept under stirring for 3 h. After cooling to 0 °C, H_2O was added and the solvent was removed under reduced pressure. The residue was taken up with water and extracted with CH_2Cl_2 (3 × 20 mL). The combined organic layers were dried (Na_2SO_4) and evaporated under reduced pressure to afford a crude residue, which was purified by column chromatography using CH_2Cl_2/AcOEt 95:5 to give a white solid. Yield, 92%. ^{1}H-NMR ($CDCl_3$, 300 MHz) δ: 2.09-2.19 (2H, m), 2.61 (2H, t, J = 7.5 Hz), 2.95 (2H, t, J = 7.5 Hz), 3.62 (2H,

t, *J* = 6.4 Hz), 4.06-4.11 (2H, m), 5.09 (2H, s), 6.71-6.74 (2H, m, Ar), 7.20 (1H, t, *J* = 8.2 Hz, Ar), 7.33-7.45 (5H, m, Ar). HRMS-ESI for $C_{19}H_{20}ClNO_2$ (m/z): $[M+Na]^+$ calcd, 352.1075; found, 352.1084.

*5-(benzyloxy)-1-(3-(6,7-dimethoxy-3,4-dihydroisoquinolin-2(1H)-yl)propyl)-3,4-dihydroquinolin-2(1H)-one (**18**)*. To a solution of **17** (1 mmol, 1 eq) in CH_3CN (15 mL), 6,7-dimethoxy-1,2,3,4-tetrahydroisoquinoline (1.3 mmol, 1.3 eq) and K_2CO_3 (3 mmol, 3 eq) were added. The mixture was heated to reflux overnight. After cooling to room temperature, the solvent was removed under reduced pressure. The residue was treated with H_2O and extracted with CH_2Cl_2 (3 × 10 mL).
The combined organic layers were dried (Na_2SO_4) and evaporated under reduced pressure to afford a crude residue, which was purified by column chromatography using CH_2Cl_2/MeOH 98:2 to give a yellow solid. Yield, 48%. ^{1}H-NMR ($CDCl_3$, 300 MHz) δ: 1.93 (2H, quint, *J* = 7.3 Hz), 2.56-2.62 (4H, m), 2.72 (2H, t, *J* = 5.8 Hz), 2.82 (2H, t, *J* = 5.5 Hz), 2.94 (2H, t, *J* = 7.5 Hz), 3.55 (2H, s), 3.83 (3H, s), 3.84 (3H, s), 4.02 (2H, t, *J* = 7.5 Hz), 5.08 (2H, s), 6.51 (1H, s), 6.59 (1H, s), 6.68 (1H, d, *J* = 8.4 Hz), 6.78 (1H, d, *J* = 8.1 Hz), 7.14 (1H, t, *J* = 8.2 Hz), 7.30-7.45 (5H, m). HRMS-ESI for $C_{30}H_{34}N_2O_4$ (m/z): $[M+Na]^+$ calcd, 509.2417; found, 509.2418.

*5-(benzyloxy)-1-(3-(6,7-dimethoxy-3,4-dihydroisoquinolin-2(1H)-yl)propyl)-1,2,3,4-tetrahydroquinoline (**19**)*. A solution of $BH_3{\cdot}Me_2S$ 2M (3 mol, 3 eq) in dry THF (10 mL) was carefully added dropwise to a stirred and ice bath cooled solution of **18** (1 eq, 1 mol) in dry THF (5 mL). The reaction mixture was refluxed with stirring for ON, cooled to 0 °C and carefully added with MeOH (10 mL) to destroy the excess of boran complex. Then, HCl 3N (10 mL) was added and the resulting mixture was refluxed with stirring for 1h. The mixture was allowed to cool at room temperature and alkalized with NaOH 2M. The residue was extracted with CH_2Cl_2 (3 x 20 mL). The collected organic layers were dried (Na_2SO_4) and evaporated under vacuum to afford a crude residue which was purified by column chromatography using CH_2Cl_2/MeOH 95:5. 2 to give a trasparent oil. Yield, 80%. ^{1}H-NMR ($CDCl_3$, 300 MHz) δ: 1.83-1.99 (4H, m), 2.56 (2H, t, *J* = 7.1 Hz), 2.70-2.80 (4H, m), 2.85 (2H, t, *J* = 5.7 Hz), 3.26 (2H, t, *J* = 5.5 Hz), 3.37 (2H, t, *J* = 7.2 Hz), 3.57 (2H, s), 3.85 (3H, s), 3.86 (3H, s), 5.05 (2H, s), 6.29 (1H, d, *J* = 7.9 Hz), 6.39 (1H, d, *J* = 8.4 Hz), 6.53 (1H, s), 6.61 (1H, s), 7.00 (1H, t, *J* = 8.2 Hz), 7.32-7.47 (5H, m). HRMS-ESI for $C_{30}H_{36}N_2O_3$ (m/z): $[M+Na]^+$ calcd, 495.2618; found, 495.2629; $[M+H]^+$ calcd, 473.2799; found, 473.2798.

*1-(3-(6,7-dimethoxy-3,4-dihydroisoquinolin-2(1H)-yl)propyl)-1,2,3,4-tetrahydroquinolin-5-ol (**20**)*. Compound **19** (1 mol, 1 eq) was dissolved in EtOH 96% (8 mL) and put to react under H_2 atmosphere at 4.5 bar pressure and in presence of 10% Pd on activated carbon at room temperature for 72h. Subsequently, the mixture was filtered on a Celite® pad and the filtrate was concentrated under reduced pressure to obtain a crude residue which was purified by column chromatography using CH_2Cl_2/MeOH 95:5 to give a pink oil. Yield, 54%. ^{1}H-NMR ($CDCl_3$, 300 MHz) δ: 1.83-1.98 (4H, m), 2.55 (2H, t, *J* = 7.2 Hz), 2.65 (2H, t, *J* = 6.6 Hz), 2.73 (2H, t, *J* = 5.6 Hz), 2.84 (2H, t, *J* = 5.6 Hz), 3.24 (2H, t, *J* = 5.4 Hz), 3.33 (2H, t, *J* = 7.2 Hz), 3.57 (2H, s), 3.83 (3H, s), 3.85 (3H, s), 6.06 (1H, d, *J* = 7.8 Hz, Ar), 6.26 (1H, d, *J* = 8.4 Hz, Ar), 6.52 (1H, s, Ar), 6.60 (1H, s, Ar), 6.87 (1H, t, *J* = 8.1 Hz, Ar). HRMS-ESI for $C_{23}H_{30}N_2O_3$ (m/z): $[M+Na]^+$ calcd, 495.2618; found, 495.2629; $[M+H]^+$ calcd, 405.2154; found, 405.2156.

*1-(3-(6,7-dimethoxy-3,4-dihydroisoquinolin-2(1H)-yl)propyl)-5-(2-fluoroethoxy)-1,2,3,4-tetrahydroquinoline (**LC2**)*. To a solution of **20** (1 mol, 1 eq) in acetone (20 mL), K_2CO_3 (3 mol, 3 eq) and

1-fluoro-2-iodoethane (2 mol, 2 eq) are added. The resulting mixture was refluxed with stirring ON and then was allowed to cool to room temperature. The solvent was removed under vacuum. The residue was taken up with H_2O (20 mL) and extracted with CH_2Cl_2 (3 x 20 mL). The combined organic layers were washed with brine, dried (Na_2SO_4) and evaporated under vacuum to afford a crude residue which was purified by column chromatography using CH_2Cl_2/MeOH 95:5 to give a grey solid. The corresponding oxalate salt was prepared by adding an ethereal solution of oxalic acid to a solution of the amine. The oxalate salt was purified by crystallization from MeOH/Et_2O. Yield, 80%. ^{1}H-NMR ($CDCl_3$, 500 MHz) δ: 1.83-1.94 (4H, m), 2.54 (2H, t, J = 7.2 Hz), 2.69-2.72 (4H, m), 2.83 (2H, t, J = 5.7 Hz), 3.24 (2H, t, J = 5.5 Hz), 3.34 (2H, t, J = 7.2 Hz), 3.55 (2H, s), 3.83 (3H, s), 3.84 (3H, s), 4.18 (2H, dt, J_F = 47.5 Hz, J = 4.0 Hz), 4.73 (2H, dt, J_F= 28 Hz, J = 4.5 Hz), 6.16 (1H, d, J = 8.0 Hz, Ar), 6.37 (1H, d, J = 8.5 Hz, Ar), 6.52 (1H, s, Ar), 6.60 (1H, s, Ar), 6.97 (1H, t, J = 8.2 Hz, Ar) (The NMR spectrum is shown in Figure S4.2.). HRMS-ESI for $C_{25}H_{33}FN_2O_3$ (m/z): $[M+Na]^+$ calcd, 451.2373; found, 451.2372; $[M+H]^+$ calcd, 429.2553; found, 429.2564 (HRMS-ESI and HPLC chromatogram are shown in Figures S4.3 and S4.4, respectively).

4.10.2. Biological studies

4.10.2.1. *In vitro* competition binding assays

The affinity for S1R and S2R was determined by *in vitro* radioligand displacement experiments as published [327].

In brief, S1R affinity was determined with [^{3}H]-(+)-pentazocine (A_m = 995 GBq/µmol; Revvity) and the membrane preparation of hS1R-HEK293 cells with serial dilutions of the test compound. Incubation was performed in 50 mM TRIS-HCl, pH 7.4 at 21°C, supplemented with 120 mM NaCl, 5 mM KCl, 2 mM $CaCl_2$, and 1mM $MgCl_2$ for 120 min at ambient temperature. S2R affinity was determined with [^{3}H]DTG (A_m=1850 GBq/mmol; ARC) and the membrane preparation of liver obtained from Wistar rats with 100 nM FTC-146 to mask S1R receptors, and serial dilutions of the test compound. Incubation was performed in 50 mM TRIS-HCL, pH 7.4 at 21°C, for 120 min at ambient temperature.

For S1R and S2R assays, non-specific binding of the respective radioligand was determined by co-incubation with 10 µM haloperidol. Free and bound radioligand were separated by filtration on GF/B glass-fibre filters (Hahnemühle FineArt GmbH, Dassel, Germany) pre-soaked in 0.3% polyethyleneimine using a Brandel Cell Harvester and rapidly washed four times with pre-chilled 50 mM TRIS-HCl, pH 7.4 at 4°C. Filters were isolated, transferred to scintillation vials, and incubated with scintillation cocktail (Ultima Gold™, Revvity) at 300 rpm for two hours at room temperature. The vials were counted in a liquid scintillation counter (Hidex 600 SL; Hidex Oy, Turku, Finland) to determine activity as Becquerel per vial. Data were expressed as percentage of specifically bound activity versus concentration of the respective test compound and analysed by non-linear curve analysis using GraphPad Prism software to calculate IC_{50} values. Inhibitory constant values (K_i) were calculated using the Cheng-Prusoff equation with dissociation constants of K_D = 33 nM for [^{3}H]-(+)-Pentazocine and K_D = 50 nM for [^{3}H]DTG. All experiments were performed at least two times with two technical replicates.

To assess potential off-target interactions in the CNS, receptor binding and functional assays were performed through the Psychoactive Drug Screening Program (PDSP, National Institute of Mental Health, USA), which offers standardized in vitro evaluation of compounds across a broad range of CNS targets,

including G protein-coupled receptors, ion channels, transporters, and enzymes. All assays were conducted following established PDSP protocols [396].

4.10.2.2. Calcein-AM experiment

These experiments were carried out as described by Contino *et al.* [335] with minor modifications.
Briefly, the MDCK-MDR1 cell line (30,000 cells per well) was seeded into a 96-well black culture plate with 100 µL medium and allowed to become confluent overnight. 100 µl of test compounds were solubilized in culture medium and added to monolayers, with final concentrations ranging from 0.1 to 100 µM. 96/wells plate was incubated for 30 min. Calcein-AM was added in 100 µl of PBS to yield a final concentration of 2.5 µM, and the plate was incubated for 30 min. Each well was washed 3 times with ice-cold PBS. A saline buffer was added to each well, and the plate was read with Victor3 (PerkinElmer) at excitation and emission wavelengths of 485 nm and 535 nm, respectively. In these experimental conditions, Calcein cell accumulation in the absence and in the presence of tested compounds was evaluated, and the fluorescence basal level was estimated with untreated cells. In treated wells, the fluorescence increase with respect to basal level was measured. EC_{50} values were determined by fitting the fluorescence increase percentage versus log[dose].

4.10.2.3. Caco-2 monolayer preparation

For permeability and drug transport assays, to prepare the Caco-2 monolayer, *in vitro* model of BBB barrier, cells were seeded into a Merck Millicell™ Cell Culture Insert Plates assay system (Millipore, Bedford, MA), where a cell monolayer is set in between a filter cell and a receiver plate, at a density of 20,000 cells/well. The culture medium was replaced every 48h and the cells were kept for 21 days in culture. The TransEpithelial Electrical Resistance (TEER) of the monolayers was measured daily, before and after the experiment, using an epithelial voltohmmeter (Millicell® -ERS, Millipore). Generally, TEER values greater than 1000 Ω for a 21 day culture are considered optimal.

4.10.2.4. Permeability Experiments

After 21 days of Caco-2 cell growth, the medium was removed from filter wells and from the receiver plate, which was filled with fresh HBSS buffer (Invitrogen). This procedure was repeated twice, and the plates were incubated at 37 °C for 30 min. After incubation, the HBSS buffer was removed and drug solutions and reference compounds were added to the filter well at a concentration of 100µM, while fresh HBSS was added to the receiver plate. The plates were incubated at 37 °C for 120 min. Afterwards, samples were removed from the apical (filter well) and basolateral (receiver plate) side of the monolayer to measure the permeability.
The apparent permeability (P_{app}), in units of nm/second, was calculated using the following equation:

$$P_{app} = \left(\frac{V_A}{Area\ x\ time}\right) \times \left(\frac{[drug]_{acceptor}}{[drug]_{initial}}\right)$$

Where V_A is the volume (mL) in the acceptor well, area is the surface area of the membrane (0.11 cm^2 of the well), time is the total transport time (7200 s), $[drug]_{acceptor}$ is the concentration of the drug measured by UV spectroscopy, and $[drug]_{initial}$ is the initial drug concentration (1 x 10^{-4} M) in the apical or basolateral wells.

4.10.3. Radiochemistry

[^{18}F]Fluoride was trapped from [^{18}O]H_2O target water on a Sep-Pak QMA Plus Light cartridge (Waters, cat. no. 186004540) and eluted in the reverse direction using a solution of Kryptofix 2.2.2 (10 mg) and K_2CO_3 (2 mg) in H_2O/MeOH (1:9 v/v, 1.0 mL). The resulting [^{18}F]fluoride solution was azeotropically dried at 110 °C under a nitrogen stream with three sequential additions of anhydrous CH_3CN (1.0 mL each). Ethane-1,2-diyl bis(4-methylbenzenesulfonate) (3 mg) in CH_3CN (0.5 mL) was then added, and the mixture was heated at 85 °C for 15 min. To separate the ^{18}F-prosthetic group [^{18}F]FETos from ethane-1,2-diyl bis(4-methylbenzenesulfonate), the differential solubility of these compounds in water was exploited. The poor aqueous solubility of ethane-1,2-diyl bis(4-methylbenzenesulfonate), combined with the sufficient solubility of [^{18}F]FETs at trace concentrations and its chemical stability toward hydrolysis, enabled selective separation. The reaction mixture was diluted with 20 mL of water, causing precipitation of ethane-1,2-diyl bis(4-methylbenzenesulfonate). The precipitate was removed by filtration through a 22 µm filter, and the dissolved [^{18}F]FETos was trapped on a Sep-Pak C_{18} Plus Light cartridge. The cartridge was dried with air using a 24 mL syringe and eluted with 500 µL of MeCN.

Compound **20** (2 mg) in the presence of Kryptofix 2.2.2 (10 mg) and K_2CO_3 (2 mg) in CH_3CN (0.5 mL) was added to the vial, and the mixture was heated at 85 °C for 15 min. The crude product was diluted with HPLC mobile phase and purified by semi-preparative HPLC using a Phenomenex Luna C_{18} (2) column (5 µm, 10 × 250 mm) with MeCN/H_2O (40:60 v/v, 0.1% NEt_3) as the mobile phase.

4.10.3.1. Determination of Lipophilicity ($LogD_{7.4}$)

The lipophilicity of **[^{18}F]LC2** was experimentally determined at physiological pH using the shake-flask method, as previously described [399]. In brief, PBS and *n*-octanol were pre-saturated with each other prior to the experiment. A solution containing 0.2 MBq of **[^{18}F]LC2** in PBS (3 mL) and *n*-octanol (3 mL) was prepared in a vial and vortexed for 5 min. The PBS and *n*-octanol layers were separated and transferred into a centrifuge tube, then centrifuged at 12,000 rpm for 5 min. Aliquots of PBS (0.5 mL) and *n*-octanol (0.5 mL) were weighed, and radioactivity was measured using a gamma counter (PerkinElmer Wizard). The $logD_{7.4}$ value of **[^{18}F]LC2** was calculated using the following formula:

$$\mathrm{logD} = \log \frac{\frac{\mathrm{Radioactivity_{n-octanol}}}{\mathrm{weight_{n-octanol}}}}{\frac{\mathrm{Radioactivity_{PBS}}}{\mathrm{weight_{PBS}}}}$$

4.10.4. *In Vitro* Autoradiography

In vitro autoradiography was performed on 20 µm cryosectioned rat brain tissues embedded in Tissue-Tek® O.C.T. and stored at -80 °C until use. Briefly, brain sections were pre-equilibrated in buffer 1 (50 mM Tris, 0.1% BSA, 200 mL) for 10 min at room temperature, then incubated for 30 min in buffer 1 containing **[^{18}F]LC2** (1 or 2 µCi/mL). Following incubation, sections were washed sequentially in buffer 1 (1 × 5 min) and buffer 2 (50 mM Tris without BSA; 2 × 2 min), then briefly dipped twice in distilled water (5 s each) and air-dried. Sections were exposed to a phosphor imaging plate (BAS-MS2025, GE Healthcare) for 12 h and scanned using an Amersham Typhoon system (Cytiva, USA).

4.10.5. *In vivo* PET imaging in mice

PET imaging was performed in anesthetized CD-1 mice using a Genisys G8 PET scanner (Sofie Biosciences, USA). Following intravenous tail-vein administration of **[^{18}F]LC2** (1.5–3.0 MBq), dynamic PET images were acquired for 60 min. Image reconstruction and quantitative analysis were performed using PMOD software (version 4.3, PMOD Technologies, Switzerland).

4.11. Supporting information

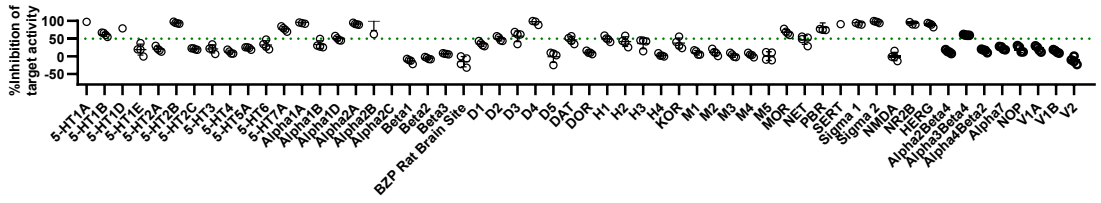

Figure S4.1. Off-target pharmacological evaluation of LC2 at a concentration of 10 μM against 56 major CNS targets, including common GPCRs, enzymes, ion channels and transporters.

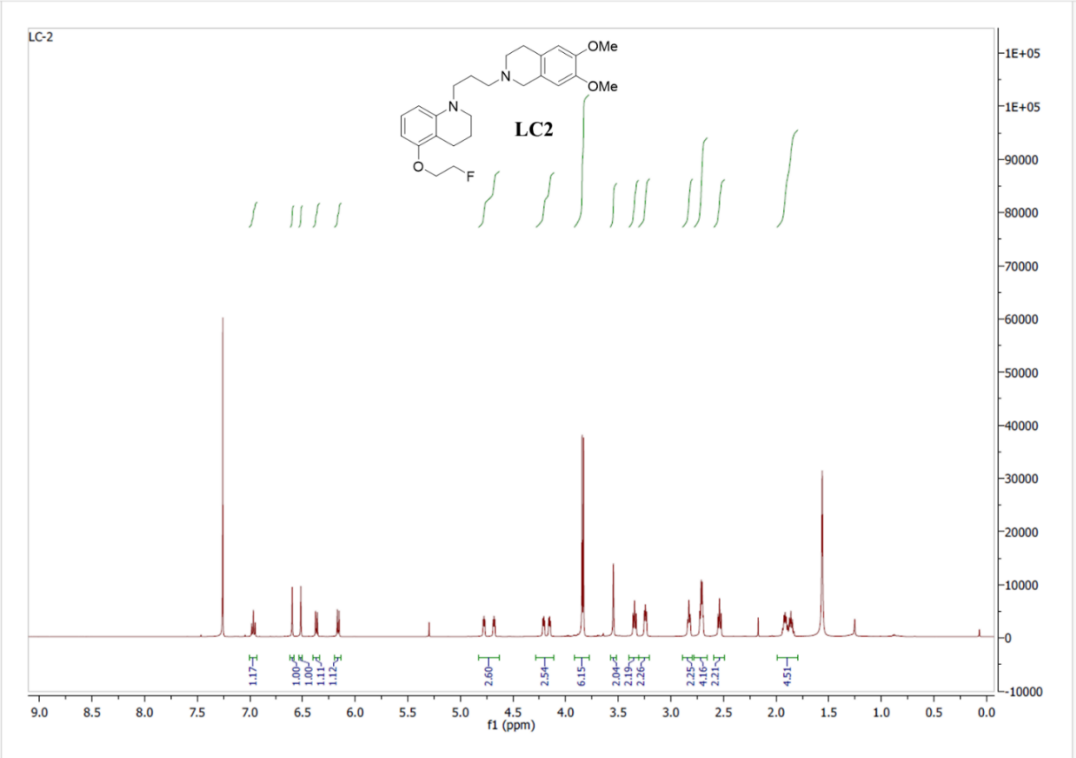

Figure S4.2. ^{1}H-NMR spectrum of **LC2**. $CDCl_3$, 500 MHz, 25 °C.

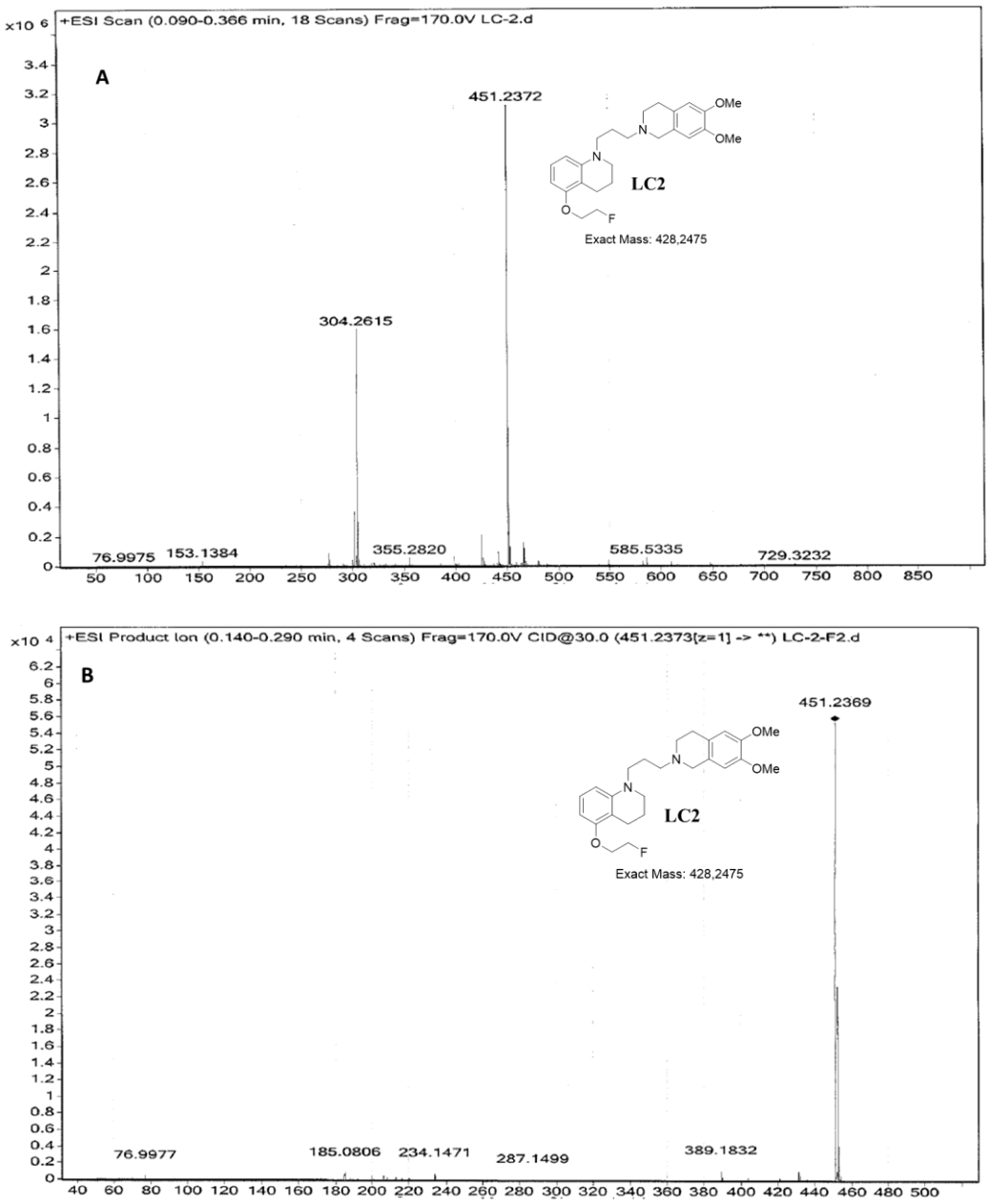

Figure S4.3. HRMS-ESI analysis of **LC2**. **A)** HRMS-ESI$^+$ spectrum; **B)** HRMS-ESI$^+$ spectrum MS-MS fragmentation.

Chromatogram and Results

Injection Details

Injection Name:	LC2	*Run Time (min):*	15,00
Vial Number:	B:F4	*Injection Volume:*	2,00
Injection Type:	Unknown	*Channel:*	UV_VIS_1
Calibration Level:		*Wavelength:*	254
Instrument Method:	MeOH/AcNH4 (pH = 3.0) 1:1	*Bandwidth:*	n.a.
Processing Method:	Basic Quantitative	*Dilution Factor:*	1,0000
Injection Date/Time:	15/dic/25 14:44	*Sample Weight:*	1,0000

Chromatogram

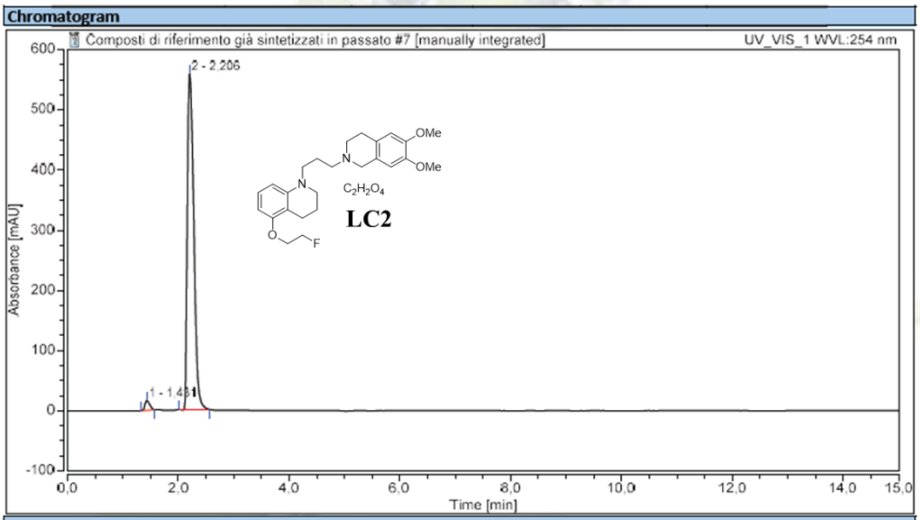

Integration Results

No.	Peak Name	Retention Time min	Area mAU*min	Height mAU	Relative Area %	Relative Height %	Amount n.a.
1		1,431	1,597	16,610	2,08	2,89	n.a.
2		2,206	75,210	559,036	97,92	97,11	n.a.
Total:			**76,807**	**575,646**	**100,00**	**100,00**	

Figure S4.4. HPLC analysis of **LC2**. MeOH-$AcNH_4$ (pH = 3.0) 1:1, flow 0.4 mL/min. Wavelength, 254 nM.

Sigma-2 receptors part 2

Design and Synthesis of Indole- and Azaindole-Substituted 3*H*-Spiro[isobenzofuran-1,4'-piperidine] Derivatives: From PET Imaging Candidates to Dual Sigma-1/Sigma-2 Receptor Ligands

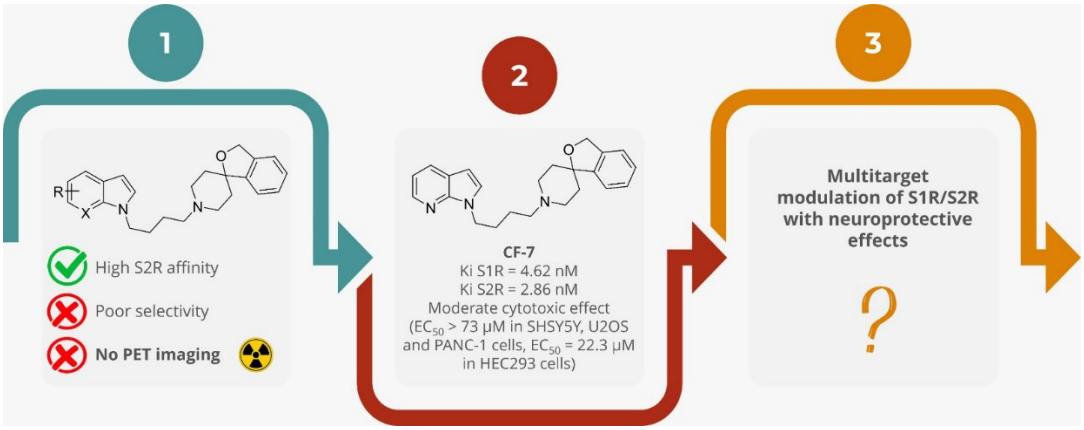

4.12. Results

4.12.1. Chemistry

Scheme 4.3 summarizes the synthesis of final compounds **21-28**. The appropriate commercially available hydroxyindole or hydroxyazaindole was first *O*-alkylated using 1-fluoro-2-iodoethane in the presence of a weak base (Cs_2CO_3), affording the already known intermediates **29b**, **29d** [375] and **29g**. These intermediates, along with commercially available indoles and azaindoles, were subsequently *N*-alkylated under phase-transfer conditions using tetrabutylammonium bromide (TBABr) and KOH to yield the corresponding chlorinated derivatives **30a-h**. Nucleophilic substitution of these intermediates with BM commercially available 3*H*-spiro[isobenzofuran-1,4′-piperidine] provided the target compounds **21-28**. Final products were converted to their oxalate salts via treatment with oxalic acid in Et_2O, followed by recrystallization from MeOH/Et_2O.

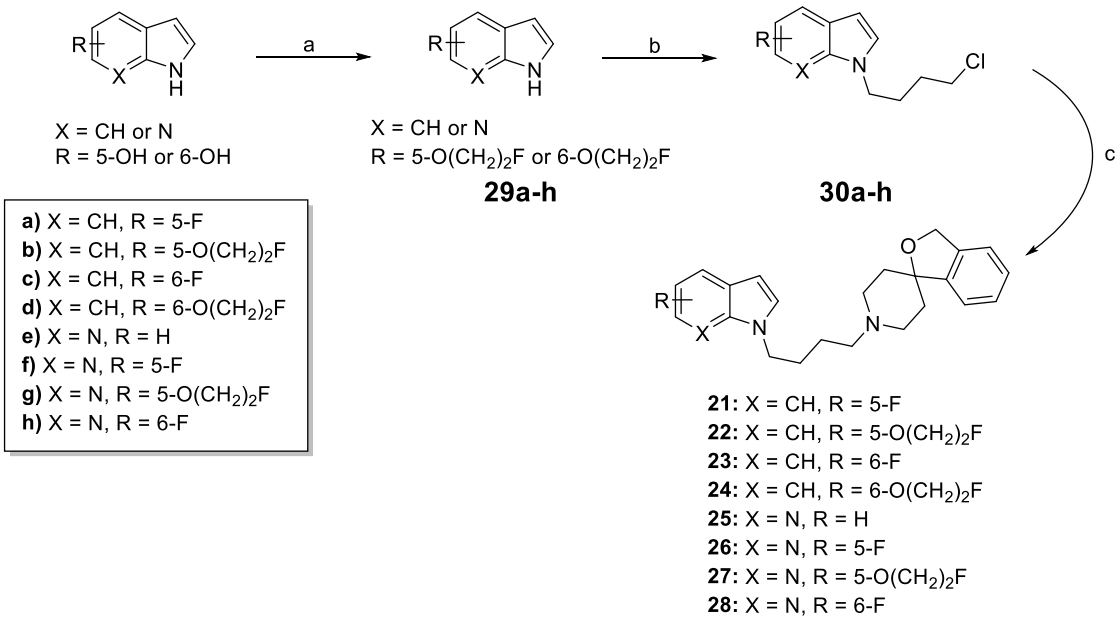

Scheme 4.3. Synthesis of final compounds **21-28**. (a) 1-fluoro-2-iodoethane, Cs_2CO_3, acetone, reflux, ON. (b) 1-bromo-4-chlorobutane, TBABr, KOH, dry DMF, RT, 2h; (c) 3*H*-spiro[isobenzofuran-1,4'-piperidine], K_2CO_3, CH_3CN, reflux, ON.

4.12.2. *In Vitro* S1R and S2R Receptor Binding Affinities

Table 4.4 shows the results from the radioligand binding assays as K_i values (nM).

All synthesized compounds display high affinity (low nanomolar range) for both S2R and S1R, indicating limited selectivity. This behavior contrasts with that of the lead compound **MT8**, which shows subnanomolar affinity for S2R (K_i = 0.43 nM) and good selectivity (~63-fold) [393]. Overall, the new series exhibits reduced affinity for S2R and increased affinity for S1R relative to **MT8**. However, it is important to note that **MT8** was evaluated using different binding protocols for both sigma receptor subtypes, which complicates direct comparison of the data.

Neither the position of the fluorine or fluoroethoxy substituent nor the use of an indole vs. azaindole scaffold significantly affects affinity or selectivity, suggesting that these hydrophobic substituents engage similarly with sigma receptors. This indicates that simple variation of these structural elements is

insufficient to achieve the desired pharmacological profile; improving selectivity may instead require modifications to the basic moiety. It must also be highlighted that also the S2R reference compound Siramesine, that has inspired the development of this series, upon re-investigation with binding assays appears to lack selectivity for S2R as well (see Table 4.4).

Table 4.4. S1R and S2R affinities.

Comp.	X	R	K_i (nM) ± SEM[a]	
			S1R	S2R
MT8[b]	CH	H	27.3	0.43
21	CH	5-F	2.07 ± 0.03	3.43 ± 0.22
22	CH	5-O$(CH_2)_2$F	3.13 ± 0.14	5.02 ± 2.12
23	CH	6-F	1.88 ± 0.23	3.03 ± 0.52
24	CH	6-O$(CH_2)_2$F	3.30 ± 1.28	3.46 ± 0.20
25 (CF7)	N	H	4.62 ± 0.02	2.86 ± 0.25
26	N	5-F	4.24 ± 0.86	3.35 ± 0.56
27	N	5-O$(CH_2)_2$F	5.12 ± 1.01	3.08 ± 1.14
28	N	6-F	2.87 ± 0.99	3.31 ± 0.27
Siramesine[c]			10.5	12.6
RM273[d]			691	1.6

[a]Values represent the mean of at least two separate experiments in duplicate ± SEM; [b]Data from Ref [393].The reference compound **MT8** was evaluated using a different binding protocol for both S1R and S2R; [c]Data from Ref [394]; [d]Data from Ref [378].

4.12.3. *In Vitro* Cytotoxicity Evaluation

As reported in Table 4.4, all compounds exhibit high affinity for both sigma receptors, showing no selectivity between S1R and S2R. For this reason, they are not suitable for use as PET radiotracers. However, their nearly identical affinities for S1R and S2R, in the low nanomolar range, suggest that they could be exploited as dual modulators with potential neuroprotective effects or antitumor effects. In this context, Loraine et al. recently reported a dual S1R/S2R modulator as a promising therapeutic strategy for the treatment of AD [400], supporting this hypothesis.

To further evaluate their neuroprotective potential, it is essential that these compounds display low cytotoxicity. Therefore, cytotoxic activity was assessed in different cell lines, and the results are summarized in Table 4.5 (EC_{50}, μM). In MCF7wt cells, indole derivatives were consistently more cytotoxic (3- to 15-fold) than their corresponding azaindole analogues. In this assay, the position of the substituent did not significantly influence cytotoxicity, whereas the nature of the substituent had a measurable effect. In both indole and azaindole series, the fluoroethoxy substituent reduced cytotoxicity compared with fluorine. Among the compounds tested in MCF7wt cells, compounds **25** (also known as **CF7)** and **27** were the least cytotoxic (EC_{50} = 92.9 μM and 94.9 μM, respectively), whereas **MT8** was the most potent (EC_{50} = 6.02 μM) [393].

All compounds were also evaluated in SH-SY5Y cells. In this cell line, a similar trend was observed, with indole derivatives again showing higher cytotoxicity (3- to 11-fold) than azaindoles. The EC_{50} values obtained in SH-SY5Y cells were generally comparable to those measured in MCF7wt cells. However, in SH-SY5Y cells, the influence of substituent type and position differed between indole and azaindole derivatives. In the indole series, the position of the substituent did not affect cytotoxicity, whereas the nature of the substituent did; specifically, fluoroethoxy-substituted compounds were less cytotoxic than their fluorinated counterparts. In contrast, for azaindole derivatives, the position of the substituent played a significant role: the 6-F derivative **28** was approximately threefold less cytotoxic than the 5-F derivative **26** (EC_{50} = 81.0 μM vs 25.6 μM). Moreover, within the azaindole series, fluorinated compounds were less cytotoxic than fluoroethoxy-substituted analogues. Overall, in SH-SY5Y cells, compound **21** was the most cytotoxic compound (EC_{50} = 3.10 μM), whereas **CF7** and compound **28** were the least cytotoxic (EC_{50} = 73.1 μM and 81.0 μM, respectively).

A comparison between MCF7wt and SH-SY5Y data indicates that **CF7** is the only compound exhibiting low cytotoxicity in both cell lines.

To further confirm its suitability as a neuroprotective candidate, **CF7** was evaluated in additional cell lines, including U2OS, PANC-1, and HEK293. In U2OS and PANC-1 cells (Figure S4.5), **CF7** was confirmed to be non-cytotoxic (EC_{50} = 100 μM and 86.9 μM, respectively), except for HEK293 cells where it displayed higher cytotoxicity (EC_{50} = 22.3 μM).

Overall, the cytotoxic effects observed for dual indole compounds may arise from S1R antagonism combined with S2R agonism, while the weak cytotoxicity of azaindoles could be associated with S2R antagonism and S1R agonism. On this basis, azaindole derivatives, particularly **CF7**, which shows minimal cytotoxicity across most of the tested cell lines, emerge as promising dual S1R/S2R modulators with potential neuroprotective effects. Consequently, functional activity assays, especially at S1R, are necessary before further evaluation of their neuroprotective properties.

Table 4.5. *In vitro* cytotoxicity evaluation in different cell lines.

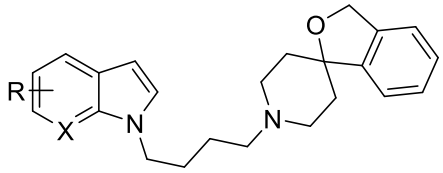

Comp.	X	R	EC_{50} (μM) ± SEM[a]				
			MCF7wt	SHSY5Y	HEK293	U2OS	PANC-1
MT8[b]	CH	H	6.02	6.82 ± 0.5			
21	CH	5-F	11.3 ± 1.5	3.10 ± 0.4			
22	CH	5-$O(CH_2)_2F$	37.1 ± 0.9	14.6 ± 1.2			
23	CH	6-F	13.6 ± 2.4	7.15 ± 1.0			
24	CH	6-$O(CH_2)_2F$	21.3 ± 1.9	13.5 ± 2.1			
CF7	N	H	92.9 ± 1.6	73.1 ± 7.5	22.3 ± 3.1	100 ± 9.5	86.9 ± 6.8
26	N	5-F	33.9 ± 1.0	25.6 ± 3.1			
27	N	5-$O(CH_2)_2F$	94.9 ± 0.9	41.1 ± 3.5			
28	N	6-F	48.0 ± 2.2	81.0 ± 6.2			

[a]Data are expressed as the mean ± SEM of at least two independent experiments in duplicate (SH-SY5Y human neuroblastoma cells, HEK293 human embryonic kidney cells, U2OS human osteosarcoma cells, and PANC-1 human pancreatic ductal adenocarcinoma cells). [b]Data from Ref [393].

4.13. Discussion

Starting from the lead compound **MT8** [393], and with the aim of developing the first PET radiotracer for S2R bearing a basic moiety different from 6,7-dimethoxytetrahydroisoquinoline, a series of fluorine- or fluoroethoxy-substituted indole and azaindole derivatives incorporating a 3*H*-spiro[isobenzofuran-1,4-piperidine] core was synthesized.

All compounds exhibited high affinity in the low nanomolar range for both S2R and S1R, reflecting a marked decline in both S2R affinity and selectivity compared with **MT8**. The observation that neither the position of the fluorine/fluoroethoxy substituent nor the choice between an indole and an azaindole scaffold significantly affected affinity or selectivity suggests that these hydrophobic regions interact in a similar manner with both sigma receptor subtypes, at least when affinity is considered as there are not proofs of functional activity, yet. Consequently, simple variation of these substituents is insufficient to produce the desired pharmacological profile

For this reason, we attempted to modify the basic moiety 3*H*-spiro[isobenzofuran-1,4-piperidine] by introducing two methoxy substituents at different positions on the aromatic ring (Figure 4.12), mimicking the interaction profile of 6,7-dimethoxytetrahydroisoquinoline at S1R and S2R in an effort to recover selectivity without compromising affinity. However, synthetic challenges encountered during the preparation of this modified scaffold prevented us from completing this strategy prior to the submission of this doctoral thesis.

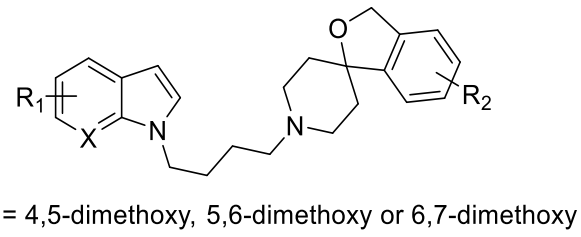

Figure 4.12. General structure of second generation PET candidates for S2R.

Given their nearly equivalent affinity for both sigma receptors, the compounds described herein are not suitable as PET radiotracers. Nonetheless, their dual S1R/S2R binding profile may be of interest within a multitarget therapeutic strategy (Multi-Target Directed Agents, MTDAs) for the treatment of multifactorial oncological or neurodegenerative disorders. In this context, Loraine et al. recently reported a dual S1R/S2R modulator as a promising therapeutic strategy for AD [400] thereby supporting this hypothesis.

Accordingly, the cytotoxic effects of all compounds were evaluated in MCF7wt human breast adenocarcinoma cells and SH-SY5Y human neuroblastoma cells. In both cell lines, azaindole derivatives consistently exhibited lower cytotoxicity than the corresponding indole derivatives. A comparison between MCF7 wt and SH-SY5Y data revealed that **CF7** was the only compound showing low cytotoxicity in both cell lines (EC_{50} = 92.9 μM and 73.1 μM, respectively). For this reason, **CF7** was further evaluated in additional cell lines, including U2OS human osteosarcoma cells, PANC-1 human pancreatic ductal adenocarcinoma cells, and HEK293 human embryonic kidney cells. In U2OS and PANC-1 cells, **CF7** was confirmed to be non-cytotoxic (EC_{50} = 100 μM and 86.9 μM, respectively), whereas in HEK293 cells it displayed higher cytotoxicity (EC_{50} = 22.3 μM).

The different behavior observed between indole and azaindole derivatives may be attributed to distinct functional profiles at S1R and S2R. Indole derivatives exhibiting cytotoxic effects may act as S1R antagonists and/or S2R agonists, whereas azaindole derivatives may preferentially behave as S1R agonists and/or S2R antagonists. This latter activity profile could result in synergistic neuroprotective effects.
Therefore, azaindole derivatives, owing to their low-nanomolar affinity for both sigma receptors combined with low cytotoxicity, may represent promising candidates for neuroprotective (anti-AD) and anti-amnesic applications. Among this series, **CF7** emerged as the least cytotoxic compound across almost all tested cell lines and was thus selected for further biological evaluation focused in particular to the functional activity at S1R and S2R to confirm whether it indeed acts as a S2R antagonist and S1R agonist.
Overall, the dual receptor profile described herein represents a promising starting point for the development of new multitarget agents.

4.14. Conclusions

The indolic–azaindolic scaffold did not prove to be a promising framework for PET imaging of S2R, as all compounds exhibited high affinity but poor selectivity. Owing to its high affinity for both S1R and S2R, together with its low cytotoxicity, **CF7** may represent a promising dual-target S1R/S2R neuroprotective agent. However, further studies, first and foremost the evaluation of its activity at S1R, are required to confirm this hypothesis.

4.15. Materials and Methods

4.15.1. Chemistry

All chemicals were purchased from Sigma-Aldrich, TCI Chemicals, Ambeed, or Angene. Thin layer chromatography (TLC) was performed using plates from Merck (silica gel 60 F_{254}). Column chromatography was performed with Merck silica gel 60 Å (63-200 mm; ratio of crude mixture to silica gel 1:30 w/w, unless otherwise stated) as the stationary phase. ^{1}H-NMR spectra were recorded in the indicated solvent on a Varian Mercury-VX spectrometer (300 MHz) or on an Agilent 500-vnmrs500 spectrometer (499.801MHz). The following data are reported: chemical shift (δ) in ppm, multiplicity (s = singlet, d = doublet, t = triplet, q = quartet, quint = quintet, m = multiplet, dd = doublet of doublets, dt = doublet of triplets, td = triplet of doublets, and br = broad signal), integration, and coupling constant (J) in hertz. Recording of mass spectra was done on an HP6890-5973 MSD gas chromatograph/mass spectrometer; only significant *m/z* peaks, with their percentage of relative intensity in parentheses, are reported. HRMS-ESI analyses were performed on a Bruker Daltonics MicrOTOF-Q II mass spectrometer. All spectra were in accordance with the assigned structures. The purity of target compounds was assessed by HPLC. Analytical HPLC analyses were performed on final compounds using a Thermo Fisher Scientific Vanquish HPLC with Thermo Fischer Scientific Accucore HILIC Column, 2.6 µm, 3 X 150 mm at a flow rate of 0.4 mL/min. Isocratic elution of the compounds **21-28** as their oxalate salts was performed using CH_3CN-CH_3COONH_4 30:70 (v/v) (pH = 3.00). UV signals were detected at 254 nm and 280 nm. All compounds are >95% pure by HPLC.

*General procedure for the synthesis of fluoroethoxy derivatives **29b, 29d** and **29g**.* To a solution of the appropriate hydroxyindole or hydroxyazaindole (1 mol, 1 eq) in acetone (15 mL), Ce_2CO_3 (1.2 mol, 1.2 eq) and 1-fluoro-2-iodoethane (1.2 mol, 1.2 eq) were added. The resulting mixture was refluxed with stirring ON and then was allowed to cool to room temperature. The solvent was removed under vacuum. The residue was taken up with H_2O (20 mL) and extracted with CH_2Cl_2 (3 x 20 mL). The combined organic layers were dried (Na_2SO_4) and evaporated under vacuum to afford a crude residue which was purified by column chromatography using n-Ex/AcOEt 1:1.

*5-(2-fluoroethoxy)-1H-indole (**29b**)* [375].

*6-(2-fluoroethoxy)-1H-indole (**29d**)* [375].

*5-(2-fluoroethoxy)-1H-pyrrolo[2,3-b]pyridine (**29g**)*. The title compound was obtained as a white solid. Yield, 61%. ^{1}H-NMR ($CDCl_3$, 300 MHz) δ: 4.23-4.35 (2H, m), 4.70-4.88 (2H, m), 6.44 (1H, dd, J_1 = 3.3 Hz, J_2 = 1.9 Hz), 7.32 (1H, t, J = 3.0 Hz), 7.50 (1H, d, J = 2.7 Hz), 8.14 (1H, d, J = 2.7 Hz), 9.44 (1H, br s). GC-MS (*m/z*): 180 (M^+, 85), 134 (45), 105 (100), 78 (17), 51 (16).

*General procedure for the synthesis of chloride derivatives **30a-h**.* To a solution of the appropriate indole or azaindole (1 mol, 1 eq) in dry DMF (5 mL), TBABr (0.03 mol, 0.03 eq) and KOH (1.5 mol, 1.5 eq) were added. The mixture was stirred at RT for 45 min, after which 1-bromo-4-chlorobutane was added at 0 °C. The reaction was stirred at this temperature for 15 min, then warmed to room temperature and stirred for an additional 1 hour.. The solvent was removed under vacuum. The residue was taken up with H_2O (20 mL) and extracted with CH_2Cl_2 (3 x 20 mL). The combined organic layers were dried (Na_2SO_4) and evaporated under vacuum to afford a crude residue which was purified by column chromatography.

1-(4-chlorobutyl)-5-fluoro-1H-indole ***(30a)***. The crude residue was purified by column chromatography using *n*-Ex/CH_2Cl_2 6:4 to obtain a trasparent oil. Yield, 71%. ^{1}H-NMR ($CDCl_3$, 300 MHz) δ: 1.72-1.81 (2H, m), 1.97-2.06 (2H, m), 3.51 (2H, t, J = 6.4 Hz), 4.15 (2H, t, J = 6.9 Hz), 6.46 (1H, dd, J_1 = 3.1 Hz, J_2 = 0.7 Hz), 6.96 (1H, td, J_1 = 9.0 Hz, J_2 = 2.4 Hz), 7.12 (1H, d, J = 3.0 Hz), 7.22-7.29 (2H, m, Ar). GC-MS (*m/z*): 225 (M^+, 27), 227 (M^+ + 2, 9), 190 (8), 148 (100).

1-(4-chlorobutyl)-5-(2-fluoroethoxy)-1H-indole ***(30b)***. The crude residue was purified by column chromatography using *n*-Ex/AcOEt 7:3 to obtain a green oil. Yield, 70%. ^{1}H-NMR ($CDCl_3$, 300 MHz) δ: 1.71-1.80 (2H, m), 1.95-2.05 (2H, m), 3.51 (2H, t, J = 6.4 Hz), 4.13 (2H, t, J = 6.9 Hz), 4.22-4.36 (2H, m), 4.69-4.88 (2H, m), 6.41 (1H, dd, J_1 = 3.0 Hz, J_2 = 0.6 Hz), 6.93 (1H, dd, J_1 = 8.7 Hz, J_2 = 2.4 Hz), 7.07 (1H, d, J = 3.0 Hz), 7.11 (1H, d, J = 2.4 Hz), 7.24 (1H, d, J = 8.7 Hz). GC-MS (*m/z*): 269 (M^+, 73), 271 (M^+ + 2, 24), 234 (10), 222 (53), 192 (100), 146 (17).

1-(4-chlorobutyl)-6-fluoro-1H-indole ***(30c)***. The crude residue was purified by column chromatography using *n*-Ex/CH_2Cl_2 1:1 to obtain a yellow oil. Yield, 85%. ^{1}H-NMR ($CDCl_3$, 300 MHz) δ: 1.72-1.82 (2H, m), 1.95-2.05 (2H, m), 3.52 (2H, t, J = 6.6 Hz), 4.11 (2H, t, J = 6.9 Hz), 6.48 (1H, dd, J_1 = 3.3 Hz, J_2 = 0.9 Hz), 6.85-6.91 (1H, m), 7.01 (1H, dd, J_F = 10.2 Hz, J = 2.2 Hz, Ar), 7.07 (1H, d, J = 3.3 Hz), 7.53 (1H, dd, J = 8.7 Hz, J_F = 5.4 Hz). GC-MS (*m/z*): 225 (M^+, 33), 227 (M^+ + 2, 11), 190 (21), 148 (100).

1-(4-chlorobutyl)-6-(2-fluoroethoxy)-1H-indole ***(30d)***. The crude residue was purified by column chromatography using *n*-Ex/AcOEt 7:3 to obtain a green oil. Yield, 61%. ^{1}H-NMR ($CDCl_3$, 300 MHz) δ: 1.73-1.82 (2H, m), 1.95- 2.05 (2H, m), 3.52 (2H, t, J = 6.3 Hz), 4.10 (2H, t, J = 6.9 Hz), 4.22-4.36 (2H, m), 4.69-4.89 (2H, m), 6.43 (1H, dd, J_1 = 3.3 Hz, J_2 = 0.9 Hz), 6.82 (1H, dd, J_1 = 8.7 Hz, J_2 = 2.2 Hz), 6.85 (1H, d, J = 2.1 Hz), 7.00 (1H, d, J = 3.0 Hz), 7.51 (1H, dd, J_1 = 8.5 Hz, J_2 = 0.4 Hz). GC-MS (*m/z*): 269 (M+, 100), 271 (M+2, 33), 234 (48), 222 (74), 192 (70), 146 (23), 132 (46), 55 (21).

1-(4-chlorobutyl)-1H-pyrrolo[2,3-b]pyridine ***(30e)***. The crude residue was purified by column chromatography using *n*-Ex/AcOEt 7:3 to obtain a green oil. Yield, 87%. ^{1}H-NMR ($CDCl_3$, 300 MHz) δ: 1.72-1.82 (2H, m), 1.99-2.08 (2H, m), 3.53 (2H, t, J = 6.6 Hz), 4.33 (2H, t, J = 7.0 Hz), 6.46 (1H, d, J = 3.6 Hz), 7.02-7.06 (1H, m), 7.20 (1H, d, J = 3.6 Hz), 7.89 (1H, dd, J_1 = 7.7 Hz, J_2 = 1.5 Hz), 8.31 (1H, dd, J_1 = 4.6 Hz, J_2 = 1.6 Hz). GC-MS (*m/z*): 208 (M^+, 30), 210 (M^+ + 2, 10), 173 (91), 159 (23), 131 (99), 118 (100).

1-(4-chlorobutyl)-5-fluoro-1H-pyrrolo[2,3-b]pyridine ***(30f)***. The crude residue was purified by column chromatography using *n*-Ex/AcOEt 8:2 to obtain a yellow oil. Yield, 86%. ^{1}H-NMR ($CDCl_3$, 300 MHz) δ: 1.71-1.81 (2H, m), 1.98-2.08 (2H, m), 3.54 (2H, t, J = 6.3 Hz), 4.31 (2H, t, J = 6.9 Hz), 6.43 (1H, d, J = 3.6 Hz), 7.26 (1H, d, J = 3.3 Hz), 7.58 (1H, dd, J_F = 9.0 Hz, J = 2.7 Hz), 8.17-8.19 (1H, m, Ar). GC-MS (*m/z*): 226 (M^+, 24), 228 (M^+ + 2, 9), 191 (73), 149 (100), 136 (68).

1-(4-chlorobutyl)-5-(2-fluoroethoxy)-1H-pyrrolo[2,3-b]pyridine ***(30g)***. The crude residue was purified by column chromatography using *n*-Ex/AcOEt 1:1 to obtain a green oil. Yield, 71%. ^{1}H-NMR ($CDCl_3$, 300 MHz) δ: 1.72-1.81 (2H, m), 1.98-2.07 (2H, m), 3.53 (2H, t, J = 6.4 Hz) 4.21-4.33 (4H, m), 4.70-4.89 (2H, m), 6.38 (1H, d, J = 3.3 Hz), 7.20 (1H, d, J = 3.6 Hz), 7.45 (1H, d, J = 2.7 Hz), 8.13 (1H, d, J = 2.7 Hz). GC-MS (*m/z*): 270 (M^+, 29), 272 (M^+ + 2, 10), 235 (100), 193 (58), 180 (57), 105 (16).

1-(4-chlorobutyl)-6-fluoro-1H-pyrrolo[2,3-b]pyridine ***(30h)***. The crude residue was purified by column chromatography using *n*-Ex/AcOEt 7:3 to obtain a green oil. Yield, 85%. ^{1}H-NMR ($CDCl_3$, 300 MHz) δ: 1.71-1.81 (2H, m), 1.97-2.06 (2H, m), 3.54 (2H, t, J = 6.6 Hz), 4.25 (2H, t, J = 6.9 Hz), 6.47 (1H, d, J = 3.6

Hz), 6.69 (1H, dd, J = 8.4 Hz, J_F = 1.2 Hz), 7.14 (1H, d, J = 3.6 Hz), 7.93 (1H, t, J = 8.1 Hz). GC-MS (*m/z*): 226 (M^+, 26), 228 (M^+ + 2, 8), 191 (52), 149 (100), 136 (38).

General procedure for the synthesis of final compounds ***21-28***. To a solution of the appropriate chloride derivative (1 mol, 1 eq) in MeCN (15 mL), K_2CO_3 (3 mol, 3 eq) and 3*H*-spiro[isobenzofuran-1,4'-piperidine] hydrochloride (1.2 mol, 1.2 eq) were added. The resulting mixture was refluxed with stirring ON and then was allowed to cool to room temperature. The solvent was removed under vacuum. The residue was taken up with H_2O (20 mL) and extracted with CH_2Cl_2 (3 x 20 mL). The combined organic layers were dried (Na_2SO_4) and evaporated under vacuum to afford a crude residue which was purified by column chromatography using CH_2Cl_2/MeOH 95:5.

1'-(4-(5-fluoro-1H-indol-1-yl)butyl)-3H-spiro[isobenzofuran-1,4'-piperidine] ***(21)***. The title compound was obtained as a transparent oil as free base and as white crystalline solid as oxalate salt. Yield, 18%. $m.p._{.(C2H2O4)}$ 222-226 °C. ^{1}H-NMR ($CDCl_3$, 300 MHz) δ: 1.57-1.67 (2H, m), 1.74-1.79 (2H, m), 1.85-1.94 (2H, m), 2.01-2.12 (2H, m), 2.41-2.50 (4H, m), 2.87-2.90 (2H, m), 4.15 (2H, t, J = 7.0 Hz), 5.06 (2H, s), 6.44 (1H, d, J = 3.0 Hz), 6.95 (1H, td, J_1 = 9.1 Hz, J_2 = 2.4 Hz), 7.13-7.25 (5H, m), 7.27-7.29 (2H, m). HRMS-ESI for $C_{24}H_{27}FN_2O$ (*m/z*): $[M+Na]^+$ calcd, 401.2005; found, 401.2006; $[M+H]^+$ calcd, 379.2185; found, 379.2190.

1'-(4-(5-(2-fluoroethoxy)-1H-indol-1-yl)butyl)-3H-spiro[isobenzofuran-1,4'-piperidine] ***(22)***. The title compound was obtained as a transparent oil as free base and as needle-like white solid as oxalate salt. Yield, 18%. ^{1}H-NMR ($CDCl_3$, 300 MHz) δ: 1.55-1.65 (2H, m), 1.73-1.79 (2H, m), 1.89 (2H, quint, J = 7.2 Hz), 1.99-2.01 (2H, m), 2.38-2.48 (4H, m), 2.84-2.89 (2H, m), 4.13 (2H, t, J = 6.9 Hz), 4.22-4.37 (2H, m), 4.69-4.88 (2H, m), 5.06 (2H, s), 6.40 (1H, dd, J_1 = 4.0 Hz, J_2 = 0.9 Hz), 6.92 (1H, dd, J_1 = 8.7 Hz, J_2 = 2.4 Hz), 7.09-7.21 (4H, m), 7.24-7.25 (1H, m), 7.26-7.28 (2H, m). HRMS-ESI for $C_{26}H_{31}FN_2O_2$ (*m/z*): $[M+Na]^+$ calcd, 445.2268; found, 445.2258; $[M+H]^+$ calcd, 423.2448; found, 423.2438.

1'-(4-(6-fluoro-1H-indol-1-yl)butyl)-3H-spiro[isobenzofuran-1,4'-piperidine] ***(23)***. The title compound was obtained as a yellow oil as free base and as white crystalline solid as oxalate salt. Yield, 27%. $m.p._{.(C2H2O4)}$ 152-154 °C. ^{1}H-NMR ($CDCl_3$, 300 MHz) δ: 1.55-1.65 (2H, m), 1.74-1.80 (2H, m), 1.84-1.94 (2H, m), 2.01-2.12 (2H, m), 2.36-2.48 (4H, m), 2.83-2.87 (2H, m), 4.10 (2H, t, J = 7.0 Hz), 5.07 (2H, s), 6.47 (1H, dd, J_1 = 3.1 Hz, J_2 = 0.7 Hz), 6.83-6.90 (1H, m), 7.05 (1H, dd, J_F = 10.0 Hz, J = 2.2 Hz), 7.08 (1H, d, J = 3.3 Hz), 7.14-7.24 (2H, m), 7.26-7.28 (2H, m), 7.52 (1H, dd, J = 8.7 Hz, J_F = 5.4 Hz). HRMS-ESI for $C_{24}H_{27}FN_2O$ (*m/z*): $[M+Na]^+$ calcd, 401.2005; found, 401.2015; $[M+H]^+$ calcd, 379.2185; found, 379.2200.

1'-(4-(6-(2-fluoroethoxy)-1H-indol-1-yl)butyl)-3H-spiro[isobenzofuran-1,4'-piperidine] ***(24)***. The title compound was obtained as a transparent oil as free base and as white crystalline solid as oxalate salt. Yield, 35%. ^{1}H-NMR ($CDCl_3$, 300 MHz) δ: 1.55-1.65 (2H, m), 1.73-1.79 (2H, m), 1.88 (2H, quint, J = 7.2 Hz), 1.96-2.06 (2H, m), 2.35-2.47 (4H, m), 2.83-2.86 (2H, m), 4.09 (2H, t, J = 6.9 Hz), 4.22-4.34 (2H, m), 4.69-4.89 (2H, m), 5.06 (2H, s), 6.42 (1H, dd, J_1 = 3.3 Hz, J_2 = 0.9 Hz), 6.80 (1H, dd, J_1 = 8.4 Hz, J_2 = 2.1 Hz), 6.87 (1H, d, J = 2.1 Hz), 7.02 (1H, d, J = 3.3 Hz), 7.13-7.25 (2H, m), 7.26-7.30 (2H, m), 7.50 (1H, d, J = 8.4 Hz). HRMS-ESI for $C_{26}H_{31}FN_2O_2$ (*m/z*): $[M+Na]^+$ calcd, 445.2268; found, 445.2258; $[M+H]^+$ calcd, 423.2448; found, 423.2434.

1'-(4-(1H-pyrrolo[2,3-b]pyridin-1-yl)butyl)-3H-spiro[isobenzofuran-1,4'-piperidine] ***(CF7)***. The title compound was obtained as a brown oil as free base and as brown crystalline solid as oxalate salt. Yield,

20%. m.p.$_{(C2H2O4)}$ 94-96 °C. ^{1}H-NMR ($CDCl_3$, 300 MHz) δ: 1.58-1.68 (2H, m), 1.73-1.78 (2H, m), 1.88-1.98 (2H, m), 2.01-2.11 (2H, m), 2.40-2.53 (4H, m), 2.87-2.90 (2H, m), 4.24 (2H, t, J = 7.2 Hz), 5.05 (2H, s), 6.44 (1H, d, J = 3.6 Hz), 7.02-7.06 (1H, m), 7.13-7.25 (4H, m, Ar), 7.26-7.27 (1H, m), 7.89 (1H, dd, J_1 = 7.9 Hz, J_2 = 1.7 Hz), 8.31 (1H, dd, J_1 = 4.6 Hz, J_2 = 1.8 Hz). (The NMR spectrum is shown in Figure S4.6.). HRMS-ESI for $C_{23}H_{27}N_3O$ (*m/z*): $[M+Na]^+$ calcd 384.2052; found, 384.2051; $[M+H]^+$ calcd, 362.2232; found, 362.2229 (The HRMS-ESI and HPLC chromatograms are shown in Figures S4.7 and S4.8, respectively).

1'-(4-(5-fluoro-1H-pyrrolo[2,3-b]pyridin-1-yl)butyl)-3H-spiro[isobenzofuran-1,4'-piperidine] ***(26)***. The title compound was obtained as a brown oil as free base and as yellow crystalline solid as oxalate salt. Yield, 33%. m.p.$_{(C2H2O4)}$ 91-94 °C. ^{1}H-NMR ($CDCl_3$, 300 MHz) δ: 1.55-1.65 (2H, m), 1.72-1.77 (2H, m), 1.86-1.96 (2H, m), 1.98-2.09 (2H, m), 2.38-2.51 (4H, m), 2.84- 2.88 (2H, m), 4.29 (2H, t, J = 7.2 Hz), 5.04 (2H, s), 6.40 (1H, dd, J_1 = 3.0 Hz, J_2 = 1.2 Hz), 7.11-7.25 (4H, m, Ar), 7.26-7.27 (1H, m), 7.56 (1H, ddd, J_F = 9.0 Hz, J_1 = 2.7 Hz, J_2 = 1.2 Hz), 8.16-8.18 (1H, m). HRMS-ESI for $C_{23}H_{26}FN_3O$ (*m/z*): $[M+Na]^+$ calcd, 402.1958; found, 402.1962; $[M+H]^+$ calcd, 380.2138; found, 380.2138.

1'-(4-(5-(2-fluoroethoxy)-1H-pyrrolo[2,3-b]pyridin-1-yl)butyl)-3H-spiro[isobenzofuran-1,4'-piperidine] ***(27)***. The title compound was obtained as a brown oil as free base and as brown crystalline solid as oxalate salt. Yield, 32%. ^{1}H-NMR ($CDCl_3$, 300 MHz) δ: 1.56-1.66 (2H, m), 1.73-1.79 (2H, m), 1.92 (2H, quint, J = 7.2 Hz), 2.00-2.10 (2H, m), 2.39-2.52 (4H, m), 2.86-2.90 (2H, m), 4.21-4.33 (4H, m), 4.70-4.89 (2H, m), 5.06 (2H, s), 6.37 (1H, d, J = 3.6 Hz), 7.12-7.25 (4H, m), 7.27 (1H, d, J = 3.0 Hz), 7.45 (1H, d, J = 2.7 Hz), 8.13 (1H, d, J = 2.7 Hz). HRMS-ESI for $C_{25}H_{30}FN_3O_2$ (*m/z*): $[M+Na]^+$ calcd, 446.2220; found, 446.2203; $[M+H]^+$ calcd, 424.2400; found, 424.2382.

1'-(4-(6-fluoro-1H-pyrrolo[2,3-b]pyridin-1-yl)butyl)-3H-spiro[isobenzofuran-1,4'-piperidine] ***(28)***. The title compound was obtained as a yellow oil as free base and as yellow crystalline solid as oxalate salt. Yield, 35%. m.p.$_{(C2H2O4)}$ 139-142 °C. ^{1}H-NMR ($CDCl_3$, 300 MHz) δ: 1.56-1.66 (2H, m), 1.73-1.79 (2H, m), 1.86-1.97 (2H, m), 2.00-2.11 (2H, m), 2.41-2.53 (4H, m), 2.90-2.91 (2H, m), 4.24 (2H, t, J = 7.0 Hz), 5.06 (2H, s), 6.45 (1H, d, J = 3.3 Hz), 6.68 (1H, dd, J = 8.4 Hz, J_F = 0.9 Hz, Ar), 7.13-7.25 (4H, m, Ar), 7.26-7.27 (1H, m), 7.92 (1H, t, J = 8.0 Hz). HRMS-ESI for $C_{23}H_{26}FN_3O$ (*m/z*): $[M+Na]^+$ calcd, 402.1958; found, 402.1959; $[M+H]^+$ calcd, 380.2138; found, 380.2139.

4.15.2. Biological studies

4.15.2.1. *In vitro* competition binding assays

The affinity for S1R and S2R was determined by *in vitro* radioligand displacement experiments as published [327].

In brief, S1R affinity was determined with [^{3}H]-(+)-pentazocine (A_m = 995 GBq/μmol; Revvity) and the membrane preparation of hS1R-HEK293 cells with serial dilutions of the test compound. Incubation was performed in 50 mM TRIS-HCl, pH 7.4 at 21°C, supplemented with 120 mM NaCl, 5 mM KCl, 2 mM $CaCl_2$, and 1mM $MgCl_2$ for 120 min at ambient temperature.

S2R affinity was determined with [^{3}H]DTG (A_m=1850 GBq/mmol; ARC) and the membrane preparation of liver obtained from Wistar rats with 100 nM FTC-146 to mask S1R receptors, and serial dilutions of the test compound. Incubation was performed in 50 mM TRIS-HCL, pH 7.4 at 21°C, for 120 min at ambient temperature.

For S1R and S2R assays, non-specific binding of the respective radioligand was determined by co-incubation with 10 µM haloperidol. Free and bound radioligand were separated by filtration on GF/B glass-fibre filters (Hahnemühle FineArt GmbH, Dassel, Germany) pre-soaked in 0.3% polyethyleneimine using a Brandel Cell Harvester and rapidly washed four times with pre-chilled 50 mM TRIS-HCl, pH 7.4 at 4°C. Filters were isolated, transferred to scintillation vials, and incubated with scintillation cocktail (Ultima Gold™, Revvity) at 300 rpm for two hours at room temperature. The vials were counted in a liquid scintillation counter (Hidex 600 SL; Hidex Oy, Turku, Finland) to determine activity as Becquerel per vial. Data were expressed as percentage of specifically bound activity versus concentration of the respective test compound and analysed by non-linear curve analysis using GraphPad Prism software to calculate IC_{50} values. Inhibitory constant values (K_i) were calculated using the Cheng-Prusoff equation with dissociation constants of K_D = 33 nM for [^{3}H]-(+)-Pentazocine and K_D = 50 nM for [^{3}H]DTG. All experiments were performed at least two times with two technical replicates.

4.15.2.2. Cytotoxicity assays

Materials: All cell culture reagents were purchased from S.I.A.L. S.r.l. (Rome, Italy). MTT (3-[4,5-dimethylthiazol-2-yl]-2,5-diphenyltetrazoliumbromide), was obtained from Sigma-Aldrich (Milan, Italy).

Cell Culture: MCF7wt, human breast adenocarcinoma, PANC-1, human pancreas adenocarcinoma cells, HEK-293, human embryonic kidney cells, U2OS, human osteosarcoma cells, and SH-SY5Y, human neuroblastoma cells were obtained from American Type Culture Collection (ATCC, Bethesda, MD). MCF7wt, PANC-1 and HEK-293 cells were cultured in high-glucose DMEM supplemented with 10% fetal bovine serum, 2 mM L-glutamine, 100 U/mL penicillin, and 100 µg/mL streptomycin. U2OS cells were growth in McCoy's 5a Medium Modified supplemented with 10% fetal bovine serum, 2 mM L-glutamine, 100 U/mL penicillin, and 100 µg/mL streptomycin. SH-SY5Y cells were cultured in DMEM/F12 supplemented with 10% fetal bovine serum, 2 mM L-glutamine, 100 U/mL penicillin, and 100 µg/mL streptomycin. Cells were maintained at 37 °C in a humidified 5% CO_2 atmosphere.

Cytotoxicity Assay (MTT): Antiproliferative activity was assessed using the MTT assay after 48 h of drug exposure. On day 1, 1 × 10^4 cells/well were seeded in 96-well plates in 100 µL of complete medium. On day 2, test compounds were added at final concentrations ranging from 0.1 to 100 µM. Vehicle controls (EtOH, DMSO) were included at the same final concentration used in treated wells to account for solvent effects. After 48 h of incubation, 0.5 mg/mL MTT solution was added to each well and plates were incubated for 3 h at 37 °C. The medium was then removed and formazan crystals were dissolved in 100 µL DMSO. Absorbance was measured at 570 nm (reference wavelength: 630 nm) using a Victor microplate reader.

4.16. Supporting information

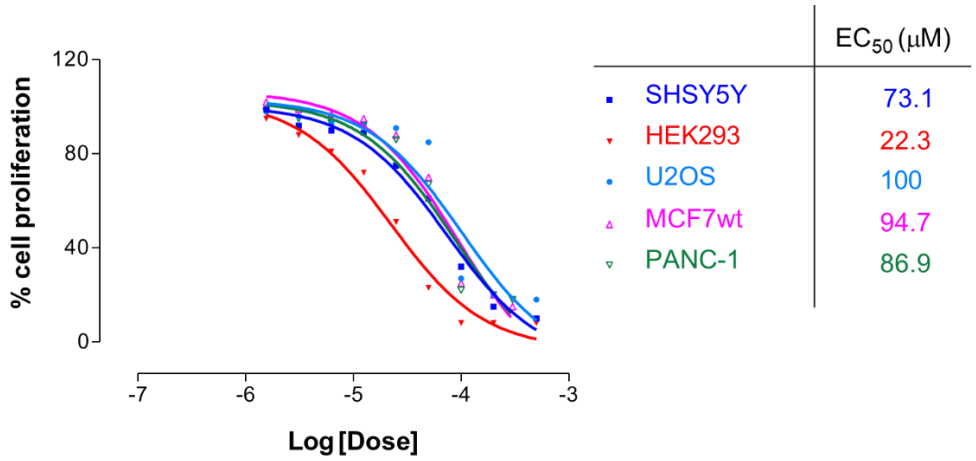

Figure S4.5. Cytotoxicity of **CF7** evaluated by MTT assay after 48 h in different cell lines.

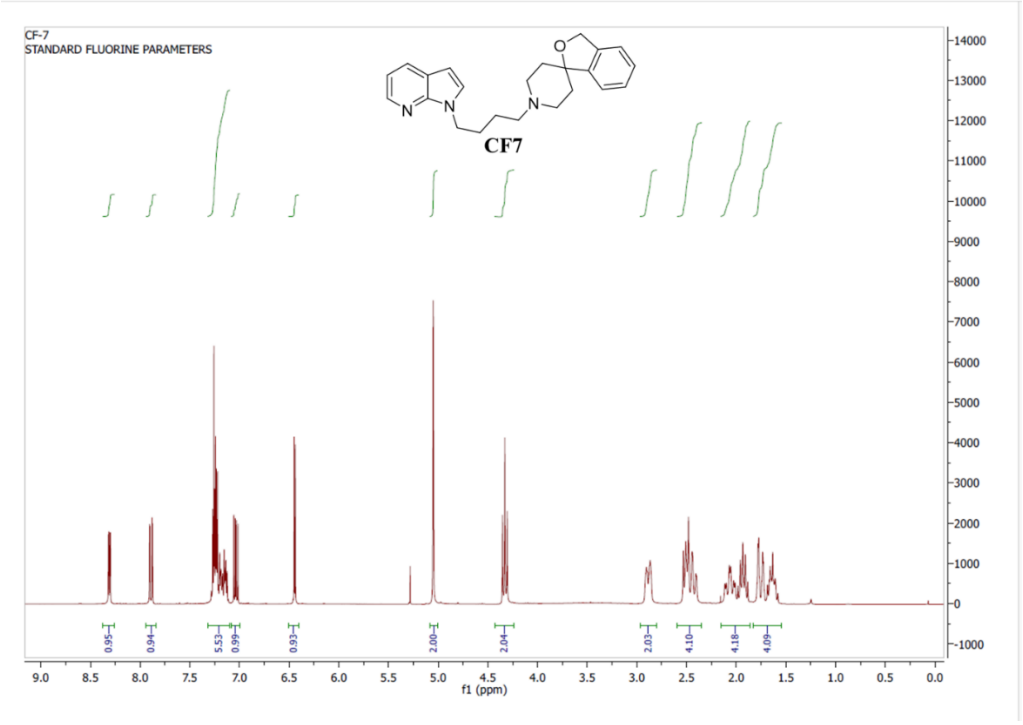

Figure S4.6. ^{1}H-NMR spectrum of **CF7**. $CDCl_3$, 500 MHz, 25 °C.

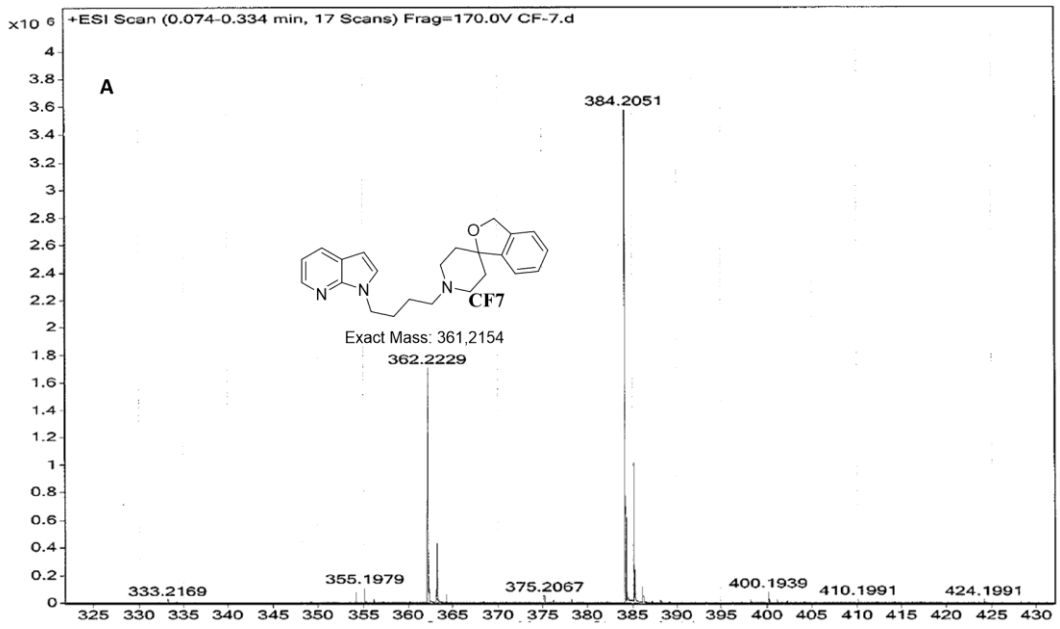
x10 6
+ESI Scan (0.074-0.334 min, 17 Scans) Frag=170.0V CF-7.d
A
384.2051
CF7
Exact Mass: 361,2154
362.2229
333.2169
355.1979
375.2067
400.1939
410.1991
424.1991

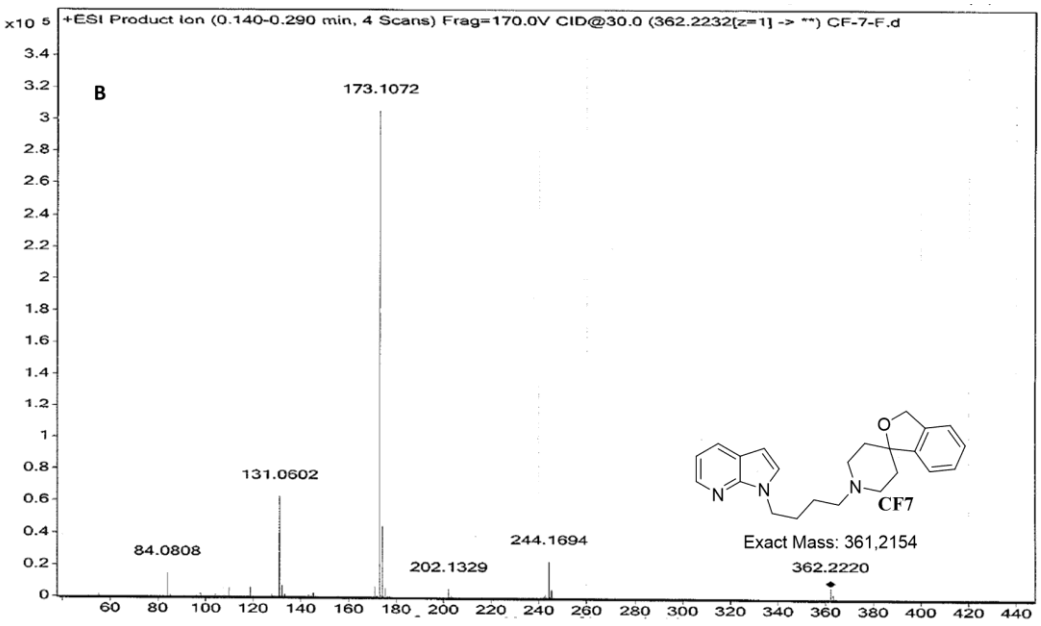
x10 5
+ESI Product Ion (0.140-0.290 min, 4 Scans) Frag=170.0V CID@30.0 (362.2232[z=1] -> **) CF-7-F.d
B
173.1072
131.0602
84.0808
202.1329
244.1694
CF7
Exact Mass: 361,2154
362.2220

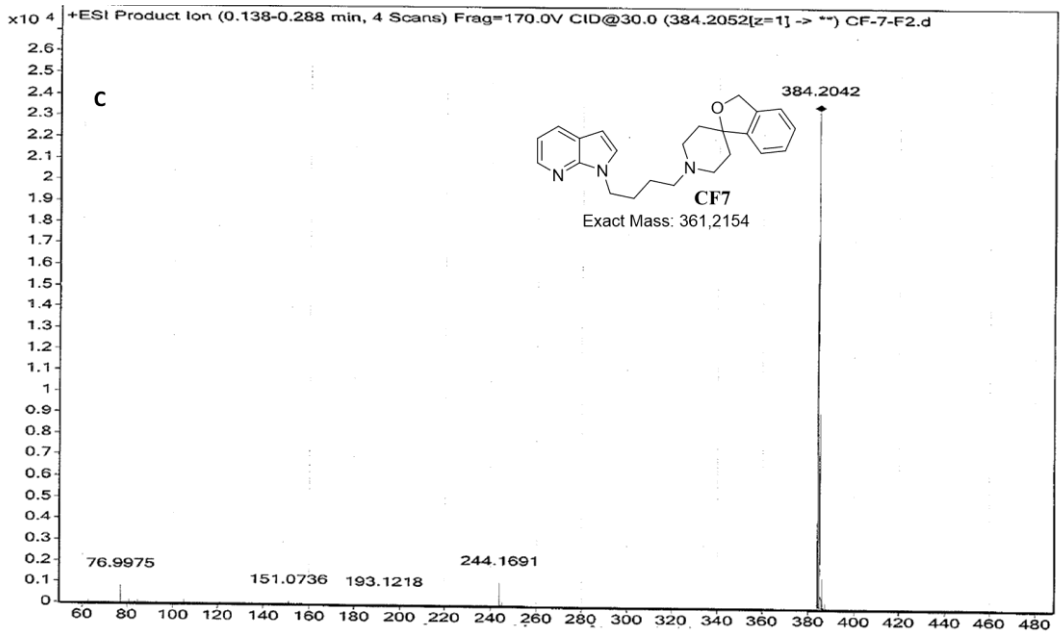

Figure S4.7. HRMS-ESI analysis of **CF7**. **A)** HRMS-ESI$^+$ spectrum; **B** and **C)** HRMS-ESI$^+$ spectrum MS-MS fragmentation.

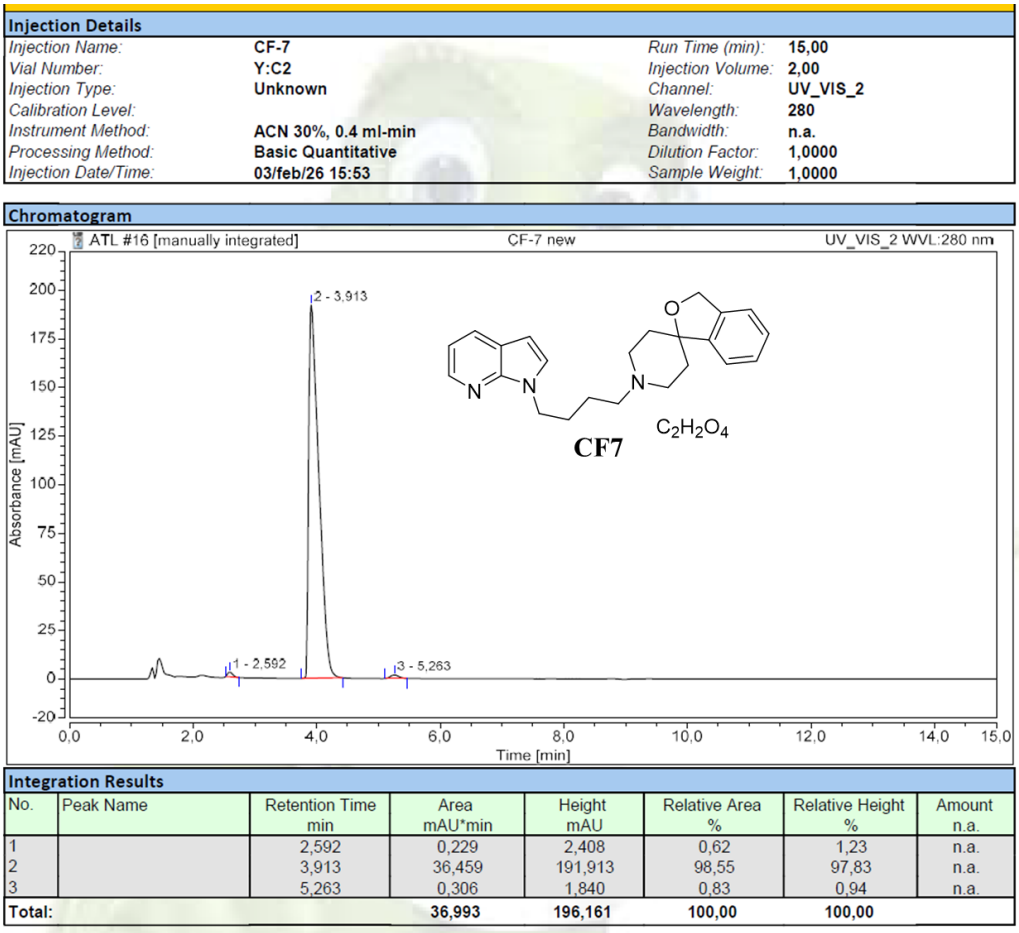

Integration Results

No.	Peak Name	Retention Time min	Area mAU*min	Height mAU	Relative Area %	Relative Height %	Amount n.a.
1		2,592	0,229	2,408	0,62	1,23	n.a.
2		3,913	36,459	191,913	98,55	97,83	n.a.
3		5,263	0,306	1,840	0,83	0,94	n.a.
Total:			**36,993**	**196,161**	**100,00**	**100,00**	

Figure S4.8. HPLC analysis of **CF7**. CH_3CN-$AcNH_4$ (pH = 3.0) 3:7, flow 0.4 mL/min. Wavelength, 280 nM.

CHAPTER 5

Cannabinoid subtype 2 receptors

Design, synthesis, radiolabeling and *in vitro* evaluation of two structurally related Positron Emission Tomography radiotracers targeting cannabinoid subtype 2 receptors with distinct activity profiles

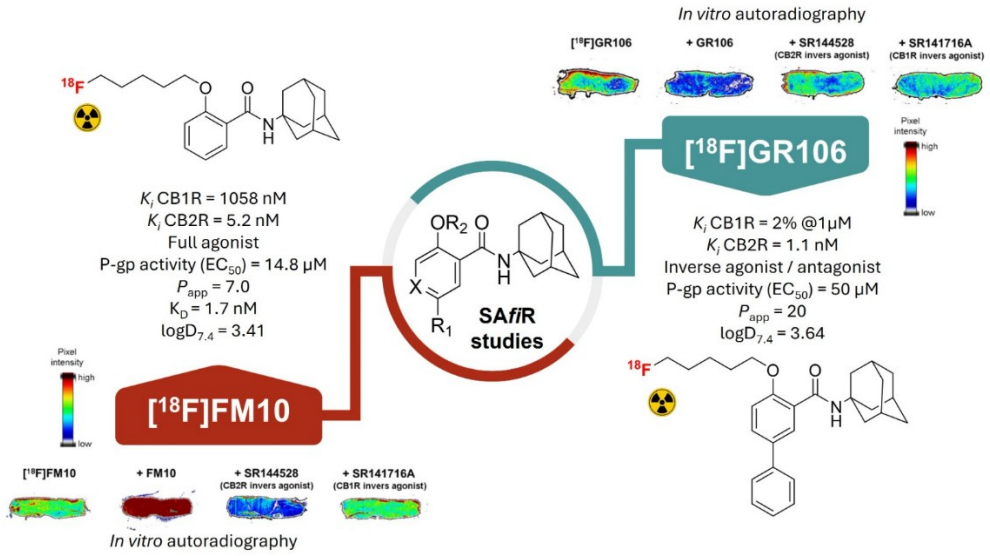

5. Introduction

The CB1R and CB2R are key components of the endocannabinoid system (ECS) [401]. The ECS was identified in 1988 by Howlett and Devane and was subsequently recognized as a complex molecular and biological network that played essential roles in numerous physiological processes. It influenced anxiety, appetite regulation, mood, cognitive performance, learning, memory, nociception, and motor function. Moreover, the ECS is implicated in the pathophysiology of several disorders, including cancer, cardiovascular dysfunction, and neurodegenerative diseases [402].

In addition to CB1R and CB2R, the ECS includes other receptors, such as G protein–coupled receptors (GPR18, GPR55, GPR119, etc.), transient receptor potential (TRP) channels (e.g., TRPV1, TRPV2), and peroxisome proliferator-activated receptors (PPARs), including PPARα and PPARγ [403].

Endocannabinoids are endogenous lipid mediators that activate cannabinoid receptors embedded in lipid membranes. They are synthesized "on demand" and released into the extracellular space when specific cellular stimuli occur. Arachidonoyl ethanolamide (anandamide, AEA, Figure 5.1), and 2-arachidonoyl glycerol (2-AG, Figure 5.1) are the most studied endocannabinoids, and both are produced in response to physiological stimuli, stored within intracellular vesicles, and enzymatically released from membrane phospholipids [404]. Recent findings have identified AEA storage "depots" in adipose tissue [405].

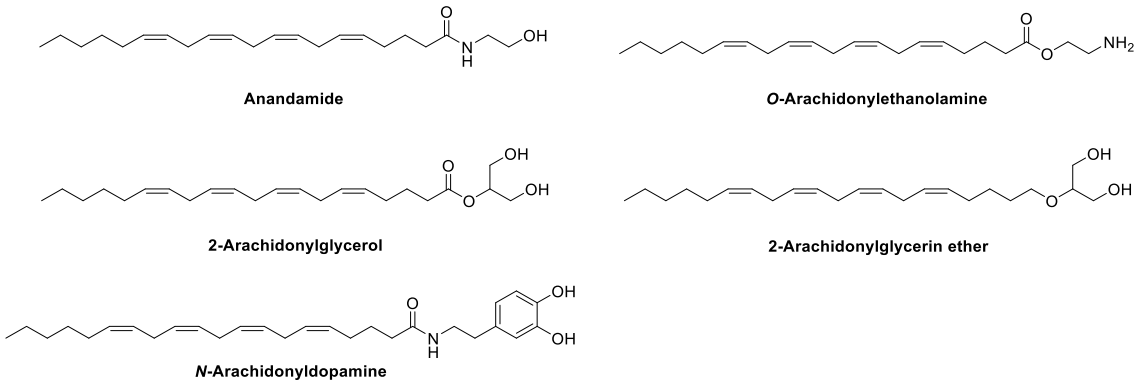

Figure 5.1. Structure of major endocannabinoids.

Once released from postsynaptic neurons, endocannabinoids act as retrograde messengers (Figure 5.2), traveling across the synaptic cleft to activate CB1R located on presynaptic terminals. Following their release, these ligands are rapidly cleared from the synaptic space through selective reuptake mechanisms mediated by a membrane transporter or, alternatively, by passive diffusion [405].

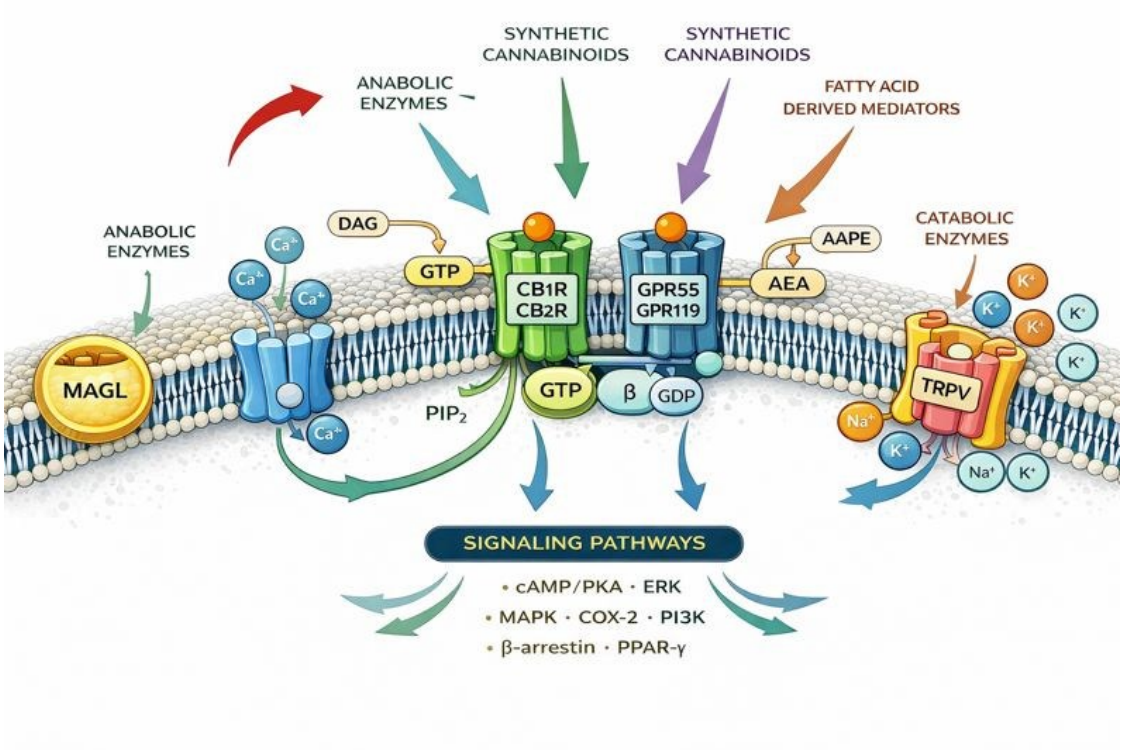

Figure 5.2. Retrograde mechanism of the endocannabinoid system.

Pharmacologically, AEA acts as partial agonist at both CB1 and CB2 receptors and binds to Transient Receptor Potential Vanilloid 1 (TRPV1) and G protein-coupled receptor 55 (GPR55).

2-AG serves as a full agonist at CB1 and CB2 receptors, interacts with GABA receptors, and is able to activate PPAR-α and PPAR-γ nuclear receptors.

Other identified endocannabinoids included 2-arachidonylglyceryl ether (noladin ether, 2-AGE), *N*-arachidonoyl dopamine (NADA), *O*-arachidonoyl ethanolamine (virodhamine, *O*-AEA, Figure 5.1), and hemopressin [406,407].

5.1. Cannabinoid receptors

CB1R and CB2R belong to the family of G protein–coupled receptors (GPCRs) associated with Gi/o proteins. These receptors are part of a broader family of membrane proteins characterized by an extracellular amino-terminal domain, seven conserved transmembrane α-helices connected by three extracellular and three intracellular loops, and an intracellular carboxy-terminal domain [408].

CB1R and CB2R share approximately 44% amino acid sequence homology, with most of their sequence divergence localized to the *N*-terminal region, the second extracellular loop (ECL2), and the *C*-terminal domain. Despite their structural similarities, the two receptors display distinct tissue distribution patterns (Figure 5.3) [409].

Upon activation, both receptors inhibit adenylate cyclase activity, resulting in a decrease in intracellular cyclic adenosine monophosphate (cAMP) levels and, consequently, a reduction in protein kinase A (PKA)-mediated phosphorylation. Beyond this classical signalling pathway, stimulation of CB1R and CB2R also activate mitogen-activated protein kinases (MAPKs), which regulate the activity of various transcription

factors and modulate key cellular processes, including gene expression, differentiation, proliferation, mitosis, survival, and apoptosis [409,410].

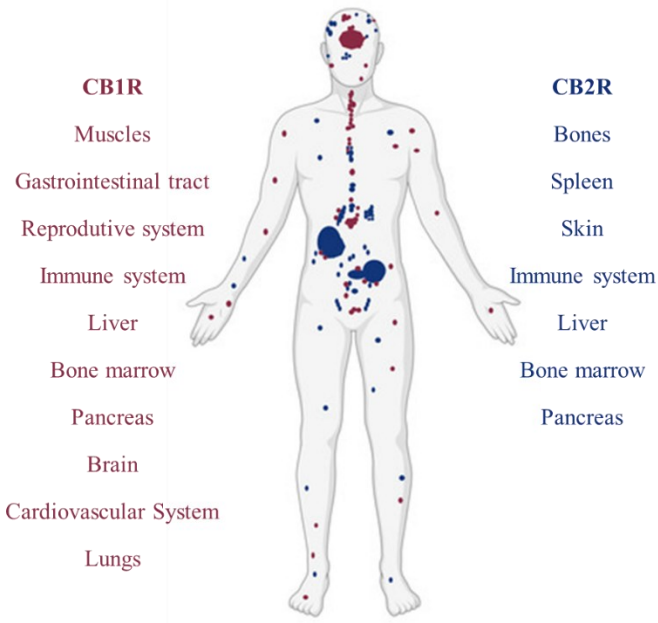

Figure 5.3. CB1R and CB2R and their relative distribution in the human body. Adapted for Ref [409].

5.2. Cannabinoid receptor subtype 1 (CB1R)

CB1R is composed of 472 amino acids and, in humans, is encoded by the *CNR1* gene, which is located on chromosome 6q14–15. CB1R represents the most abundant metabotropic receptor in the CNS, with particularly high expression levels in the cerebellum, hippocampus, basal ganglia, astrocytes, microglia, and presynaptic terminals. Within these regions, CB1R is critically involved in regulating appetite, learning, and memory processes [411].

Although CB1R is primarily localized at presynaptic terminals, a smaller population has also been detected at postsynaptic sites, where it mediates the slow autoinhibition of neocortical interneurons and modulates the expression of neuropeptide precursors regulating appetite within the hypothalamic arcuate nucleus. Additionally, mitochondrial CB1Rs (mtCB1Rs) have been identified on neuronal mitochondria, where they suppress electron transport chain activity, thereby modulating energy metabolism and memory-related processes [412].

CB1R is also expressed in the peripheral nervous system and several peripheral organs, including the gastrointestinal tract, liver, kidneys, and lungs, where it contributes to the regulation of energy metabolism, nociception, and reproductive functions. While its hepatic expression is normally low, CB1R upregulation has been observed under pathological conditions such as obesity and liver disease, promoting insulin resistance, fibrosis, and lipogenesis. Similarly, enhanced CB1R expression in the cardiovascular system has been associated with cardiac dysfunction [408].

Upon activation, CB1R triggers multiple intracellular signaling cascades, including the MAPK, c-Jun *N*-terminal kinase (JNK), and p38 pathways, which collectively regulate cell proliferation, differentiation, and apoptosis. At the synaptic level, CB1R inhibits the release of GABA and glutamate from presynaptic terminals, a mechanism that underlies its neuroprotective effects against excitotoxicity. This

neuroprotection also involves the inhibition of nitric oxide synthesis, the attenuation of zinc mobilization, and the upregulation of brain-derived neurotrophic factor (BDNF) expression [401].

Increased CB1R expression has been documented in several neurodegenerative disorders, including AD, PD, and HD [413]. More recently, CB1R has been shown to be implicated in nociception, opening the possibility of targeting this receptor for the development of non-opioid analgesics for chronic pain management, including cancer-related pain. Furthermore, CB1R has emerged as a potential target in oncology, as its activation can inhibit tumor proliferation, induce apoptosis, and suppress angiogenesis, thereby limiting tumor growth and metastasis [410].

5.3. Cannabinoid receptor subtype 2 (CB2R)

Similar to CB1R, the CB2R is also coupled to Gi/o proteins, and its activation leads to inhibition of adenylate cyclase, resulting in a decrease in intracellular cAMP levels. This signaling cascade triggers the activation of MAPK pathways and promotes an increase in intracellular calcium concentration.

The CB2R gene was first cloned in 1993 by *Munro et al.* from a human promyelocytic leukemia cell line (HL-60). The resulting protein, initially referred to as CX5, exhibited specific binding affinity for a range of synthetic cannabinoids (such as WIN55,212-2 and CP55,940), phytocannabinoids (including Δ^9-tetrahydrocannabinol (THC) and cannabinol), and the endogenous ligand 2-AG [414].

5.3.1. Structure, Localization and Function

5.3.1.1. Structure

Recent structural studies provided the three-dimensional cryo-electron microscopy (cryo-EM) structure of the CB2R (Figure 5.4), offering valuable insights for the rational design of high-affinity and high-selectivity CB2R ligands. These investigations were performed with on the CB1R/CB2R agonist WIN 55,212-2 (K_i = 62.3 nM for CB1R and 3.3 nM for CB2R), a compound known for its efficacy in the treatment of several pathological conditions, including pain and cancer [415].

The resolved structure revealed that WIN 55,212-2 (Figure 5.4) occupies the orthosteric binding pocket of CB2R, overlapping with the binding site of the antagonist AM10257. The agonist stabilizes the CB2R–Gi complex in its active conformation through interaction with the conserved “toggle switch” residue W2586.48 (tryptophan), a key determinant in distinguishing agonists from antagonists. In addition, the ECL2 and residues within transmembrane helices 2, 3, and 6 were shown to play crucial roles in ligand recognition and receptor selectivity [415].

Importantly, the distinct conformation adopted by W2586.48 in CB1R compared with CB2R was associated with specific rearrangements in the intracellular regions of TM5, TM6, and TM7, defining a unique activation and signaling mechanism for CB2R. Despite the high degree of structural homology between CB1R and CB2R, their interactions with the α5 helix of the G-protein exhibit significant differences. Collectively, these findings provide an advanced structural framework for the structure-based design of selective CB2R agonists, optimizing both receptor selectivity and functional activity [415].

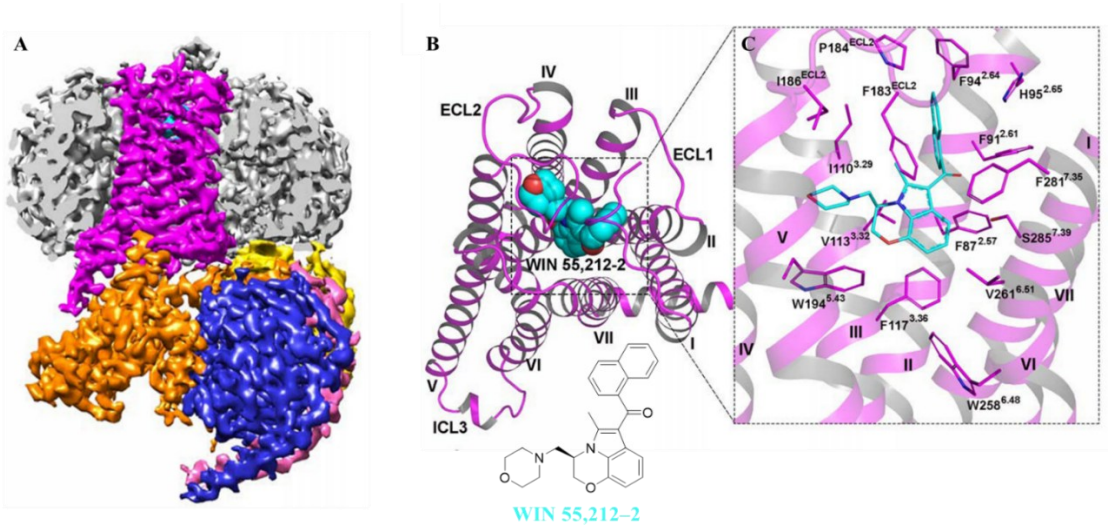

Figure 5.4. CB2R Cryo-EM Structure**. A,** Cross-sectional view of the cryo-EM density map of the CB2–WIN 55,212–2–Gi–scFv16 complex. **B,** Overall structure of the CB2–WIN 55,212–2 complex. The WIN 55,212–2 molecule is shown in cyan, while the CB2 cryo-EM structure is shown in magenta. **C,** Detailed view of the interactions between WIN 55,212–2 (cyan) and CB2 (magenta). The residues forming the CB2 binding pocket are mainly hydrophobic (magenta sticks) and are located within TM2–TM3, TM5–TM7, and ECL2. Picture Adapted form Ref [415].

5.3.1.2. Localization and Function

For many years, CB2R expression was believed to be restricted to peripheral immune tissues (thymus, tonsils, spleen) and cells (macrophages, T lymphocytes, B lymphocytes, natural killer cells, monocytes, etc.) [416]. However, macrophage-derived immune cells, the so-called microglia, are present in the CNS, and many studies have questioned the absence of CB2R expression at this level. Indeed, although the lack of CB2R expression in the CNS under physiological conditions suggests that resting microglia do not express this receptor, several reports have demonstrated its marked up-regulation and overexpression in activated microglia upon pathological conditions [411]. In fact, CB2R was found to be overexpressed in activated microglial cells in animal models of AD, HD, HIV-induced encephalitis, and multiple sclerosis [417]. In addition, further studies demonstrated the expression of CB2Rs in the brain also to some extent under physiological conditions [416]. The presence of CB2 mRNA was first found in cultured cerebellar cells and in mouse cerebellum [418]. Later, CB2R expression was confirmed in neurons of different brain regions, such as the cerebellum [419], hippocampus [420], brainstem [421], and midbrain [422].

The functions of these physiologically expressed brain CB2Rs are still under investigation, but a role has been postulated in dopamine-related behaviours [422], cocaine's action [423], and synaptic plasticity [424]. Experimental evidence has also correlated the increased expression of the receptor, primarily in the spinal cord. In addition to neurons, CB2R has also been found in other tissues such as pulmonary endothelial cells, male and female reproductive tissues, bone, gastrointestinal system, eyes, and adipocytes [415].

In pulmonary endothelial cells, CB2R activation results in phospholipase C-mediated calcium release from the smooth endoplasmic reticulum, resulting in increased mitochondrial calcium [425]. The CB2R may influence meiosis in spermatogonia [426] but more generally the activation of CB2Rs can act in different aspects of mammalian reproduction [427].

In bone, particularly in osteocytes, osteoblasts, and osteoclasts, CB2R modulates bone formation and turnover. CB2R deficiency has also been associated with osteoporosis [426].

The presence of CB2R mRNA was demonstrated in the stomach where cannabinoids modulate excitatory cholinergic and inhibitory NANC neurotransmission in the gastric fundus [428]. CB2Rs expressed on enteric neurons are present in the gut under physiological conditions but do not appear to be functionally active under normal conditions. Activation of either enteric neurons (directly) or glia (indirectly) in response to a neuroimmune challenge leads to a reduction in neurotransmitter release, thereby reducing muscle contractility [429].

In the eye, it has been shown that trabecular meshwork cells exhibit functional CB2Rs and that these are involved in improving outflow facility [430].

Finally, regarding CB2R expression on human adipose tissue adipocytes, it has been shown that both mature adipocytes and pre-adipocytes express CB1R and CB2R on their plasma membranes. While CB1R activation increases intracytoplasmic cyclic AMP, CB2R activation leads to a decrease in cyclic AMP [431].

However, the main localization remains in the immune tissues and, although a certain expression of CB1R has been also found, several studies have indicated that the modulation of the majority of immune responses is CB2R-dependent [432,433].

The activation of CB2Rs by endocannabinoids (2-AG and AEA) or exogenous ligands (THC and synthetic cannabinoids) has been associated with both direct and indirect regulation of immune cells [433]. This latter consists in the regulation of the expression of chemokines and cytokines, key mediators secreted by immune cells that regulate the activity of other immune cells toward either a pro-inflammatory or an anti-inflammatory phenotype [433]. However, some studies suggested that the CB2R regulatory role in inflammation remains controversial [433]. Nevertheless, CB2R has emerged as an attractive therapeutic target, due to its anti-inflammatory and neuroprotective effects in the absence of psychotropic actions [434].

Table 5.1. Summary table of CB2R localization, expression and its physiological and pharmacological roles in different body systems.

Tissue/Cell Type	Expression Level	Physiological/Pathological Role
Immune cells (macrophages, lymphocytes)	High	Immune modulation, cytokine regulation
Microglia (activated)	Upregulated (pathological)	Neuroinflammation, neuroprotection
Neurons (hippocampus, cerebellum, midbrain)	Moderate	Dopaminergic signaling, synaptic plasticity
Pulmonary endothelial cells	Moderate	Calcium signaling, mitochondrial regulation
Reproductive tissues	Moderate	Regulation of meiosis and fertility
Bone (osteocytes, osteoclasts)	Moderate	Bone turnover, anti-osteoporotic role
Gastrointestinal tract	Moderate	Neuroimmune signaling, motility regulation
Eye (trabecular meshwork)	Low–moderate	Regulation of aqueous humor outflow
Adipocytes	Low	cAMP modulation, metabolic regulation

5.4. Role of CB2R In CNS diseases

The neuroprotective effects of the ECS have been recognized for several years [435]. Overall, the ECS exerts its neuroprotective action through a heterogeneous set of mechanisms involving neurons, glial cells, and critical brain structures such as the BBB [436–438].

CB1R agonists contribute to neuroprotection through several complementary mechanisms, including the reduction of glutamate excitotoxicity and Ca^{2+} influx [439], attenuation of pro-inflammatory cytokine production [440], and preservation of cerebral blood flow [441].

However, the psychotropic effects typically associated with CB1R activation have significantly limited the therapeutic potential of CB1R agonists, redirecting research interest toward the CB2R. As previously discussed, CB2R is physiologically expressed in neurons in several brain regions, but its expression levels are extremely low, making its detection technically challenging [416].

Under pathological conditions associated with CNS disorders, CB2R expression becomes markedly upregulated, particularly in microglial cells [416]. For instance, CB2R overexpression has been identified in postmortem brain tissue from AD patients, where it localizes predominantly in glial cells surrounding senile plaques and correlates with $A\beta_{42}$ levels and plaque burden [411,442,443].

Similarly, enhanced CB2R expression has been reported in microglial cells of animal models of PD [444–446], HD [447,448], MS, and ALS [449,450]. Increased CB2R levels have also been observed in postmortem tissue from human patients affected by PD [451] and ALS [452].

5.4.1. Role of CB2R in Alzheimer's Disease

CB2R is closely associated with AD. Postmortem analyses of AD patients' brain have shown markedly elevated CB2R levels, particularly in microglial cells surrounding Aβ plaques [453]. Both *in vitro* and *in vivo* studies have demonstrated that CB2R agonists are capable of reducing the formation of new Aβ plaques as well as promoting the clearance of pre-existing ones, ultimately leading to improvements in memory performance [453–455].

In contrast, activation of CB1R does not appear to influence the production, aggregation, or clearance of Aβ protein [453]. Interestingly, recent findings indicate that Δ^9-tetrahydrocannabinol (Δ^9-THC) can significantly enhance the expression of neprilysin, a key endopeptidase responsible for Aβ degradation; however, the precise contribution of CB1 and CB2 receptors to this mechanism remains uncertain [456].

Beyond its effects on Aβ metabolism, CB2R activation also appears to mitigate tau protein hyperphosphorylation, another major pathological hallmark of AD [453]. Thus, the therapeutic potential of CB2R agonists in AD is two-fold: on one hand, they can modulate the pathological accumulation of both Aβ and tau proteins; on the other, they exert potent anti-inflammatory effects [453].

Neuroinflammation plays a central role in the progressive neuronal damage characteristic of AD. Activation of CB2Rs has been shown to inhibit microglia-mediated neurotoxicity by reducing the release of pro-inflammatory molecules and promoting the phenotypic shift of microglial cells from the neurotoxic M1 state to the neuroprotective M2 phenotype. This effect has been consistently demonstrated in vitro using selective CB2R agonists such as JWH-015, JWH-133, and HU-308, as well as mixed CB1R/CB2R agonists including WIN55,212-2 and HU-210 [457].

5.4.2. Role of CB2R in Parkinson's Disease

From an enteropathogenic perspective, the involvement of the ECS in PD has been extensively investigated. CB2R expression has been identified in nigrostriatal dopaminergic neurons, supporting the hypothesis of a direct modulatory role of the ECS on dopaminergic transmission. Generally, in hyperkinetic disorders, a reduced ECS tone accompanies elevated dopaminergic activity, whereas in hypokinetic movement disorders, the opposite condition occurs, increased endocannabinoid activity suppresses dopaminergic signaling [458].

Multiple studies have confirmed the capacity of CB2R to attenuate neuroinflammation and counteract the progressive degeneration of nigrostriatal dopaminergic neurons characteristic of PD. Notably, treatment with β-caryophyllene, a natural CB2R agonist, has been shown to reduce dopaminergic neuronal loss, pro-inflammatory cytokine levels, and iNOS expression [459]. Furthermore, upregulation of CB2R has been demonstrated in microglial cells in animal models of PD as well as in the substantia nigra of human PD patients [460].

Several preclinical studies employing diverse experimental paradigms have indicated that CB2R modulation could be beneficial in alleviating motor symptoms associated with PD, including levodopa-induced dyskinesias (LID) [458]. Clinical investigations have also reported that oral cannabis administration can improve both motor and non-motor symptoms in PD patients. In contrast, results with inhaled cannabis are more variable: while some patients experienced no improvement in tremor or motor spasms after a single dose of phytocannabinoids, others reported notable reductions in tremor, rigidity, bradykinesia, pain, and sleep disturbances within 30 min of intake [461].

Recent findings, regarding Δ⁹-THC, have revealed its antioxidant properties and dual pharmacological action, activation of CB2R concomitant with CB1R blockade, suggesting its potential to mitigate symptoms and delay neurodegeneration without inducing the psychotropic effects typically associated with cannabis use [462].

In neurodegenerative diseases characterized by impaired neurogenesis, the generation of new neurons is crucial to maintaining proper neuronal function. Elevated endocannabinoid concentrations or inhibition of fatty acid amide hydrolase (FAAH) have been shown to promote the proliferation of neural stem cells in various brain regions. Moreover, the CB2R agonist WIN-55,212-2 has been demonstrated to stimulate neural stem cell proliferation and neurogenesis, further supporting the potential therapeutic role of CB2R agonists in counteracting age-related neurogenic decline associated with PD [459].

5.4.3. Role of CB2R in other diseases

As previously mentioned, CB2R is also implicated in other neurodegenerative disorders, including HD, MS, and ALS. In HD, CB2R is emerging as a promising therapeutic target for both treatment and early diagnosis. CB2Rs expressed in microglial cells exert neuroprotective effects against HD-related excitotoxicity by attenuating neuroinflammation, cerebral edema, striatal neuronal loss, and motor dysfunction. In the R6/2 transgenic mouse model of HD, CB2R expression is elevated in the hippocampus, cortex, striatum, and cerebellum. Upregulation of CB2R has also been observed in microglial cells in the striatum of HD models, as well as in the caudate nucleus of HD patients [463].

Pharmacological studies have shown that treatment with CB2R agonists increases survival and mitigates motor deficits, whereas administration of a peripherally acting CB2R antagonist abolishes these beneficial effects. These findings have led to the hypothesis of a communication mechanism between the periphery and the CNS, in which CB2Rs regulate plasma levels of IL-6, potentially mediating the observed central effects. Supporting this hypothesis, neutralizing antibodies against IL-6 have demonstrated protective effects against motor deficits and weight loss [464].

In MS, postmortem studies have revealed CB2R overexpression in spinal cord lesions of patients [465]. Furthermore, a significant genetic association has been identified between the CB2R polymorphism rs35761398 (Q63R) and MS, confirming the involvement of the CB2 gene in the pathogenesis of this disorder [463]. While cannabinoids have demonstrated analgesic efficacy in MS-related pain, CB1R-mediated psychotropic effects substantially limit their clinical use. Notably, preclinical studies in mouse models of MS have shown that the CB2R agonist JWH-133 provides analgesic effects independently of CB1R activation, adding a further therapeutic dimension to the anti-inflammatory and immunomodulatory properties of CB2R [463].

Finally, the role of CB2R in ALS has been investigated using SOD1 transgenic mice. Administration of the CB2R agonist AM1241 via intraperitoneal injection, at the onset of symptoms, improved motor performance and increased overall survival in two independent studies [449]. These results further support the potential of CB2R-targeted therapies in modulating neurodegenerative disease progression.

5.4.4. Role of CB2R in cancer

The antitumor effects of cannabis were first identified over 40 years ago, when THC and other cannabinoids were shown to inhibit the growth of lung adenocarcinoma cells both *in vitro* and *in vivo* [466]. The ECS plays a significant role in cancer pathogenesis, with numerous studies reporting increased levels of all its components, including endocannabinoids, classical and non-classical cannabinoid receptors, and metabolic enzymes, in tumor cell lines and tumor tissues [467,468].

Activation of cannabinoid receptors, whether through selective or non-selective CB1R/CB2R agonists, exerts antitumor effects via multiple mechanisms [467,468]. In particular, CB2R activation, but not CB1R, has demonstrated antiproliferative effects in breast (N202.1A) and prostate (PC3) cancer cell lines [469,470]. The well-known CB2R-selective agonist JWH-133 has been shown to induce antiproliferative, antiangiogenic, and antimetastatic effects in *in vivo* models of breast cancer [469,471], glioma [472], and skin cancer [473]. The mechanisms by which cannabinoid receptor activation produces antitumor effects are multifaceted and typically result in apoptosis, cell cycle arrest, and inhibition of cell growth, adhesion, and migration. Key events include the activation of ceramide synthase, leading to ceramide production; inhibition of adenylate cyclase; and induction of p53 expression. Ceramide generation triggers downstream activation of extracellular signal-regulated kinase (ERK) and p38/MAPK pathways, culminating in apoptosis and cell cycle arrest via mechanisms such as caspase activation and cytochrome C release from mitochondria. Similarly, inhibition of adenylate cyclase and reduction of intracellular cAMP levels promotes apoptosis by ERK pathway activation and modulation of gene transcription. Upregulation of p53 also induces caspase activation, enhancing apoptosis through the positive regulation of the pro-apoptotic protein Bax and the negative regulation of the anti-apoptotic protein Bcl2 [462,467].

Conversely, CB2R activation has also been associated with anti-apoptotic and pro-tumorigenic effects mediated by the PI3K/PKB signaling pathway [462,474]. In this context, the expression of cannabinoid receptors may contribute to the development of certain cancers, including skin cancer, leukemia, and breast cancer [475]. These divergent findings highlight the controversial and tumor type–dependent role of the ECS in cancer etiopathogenesis.

Importantly, several clinical trials have been conducted or are ongoing to evaluate THC and other cannabinoids as potential anticancer therapies (NCT01812603; NCT01812616) [476,477].

5.5. Current State of PET Radiotracers Targeting the CB2R

CB2R PET radiotracers represent an important tool for the diagnosis of neuroinflammatory states, as these receptors are not expressed in the CNS under physiological conditions but are overexpressed under pathological conditions. However, the development of new CNS PET radiotracers is challenging because CB2R ligands are usually highly lipophilic and besides being characterized by high nonspecific binding they hardly cross the BBB. Demonstrating the relevance of this target, several reviews and perspectives analyzing CB2R PET radiotracers have been published over the years [478–480]. Of particular importance is the review published by Basagni F. et al., who analyzed, among other aspects, the main CB2R PET radiotracers reported up to 2020, dividing them into structural classes [480]. This work therefore served as the inspiration for the present analysis of the state of the art of CB2R PET radiotracers, which is likewise divided into structural classes (Figure 5.5).

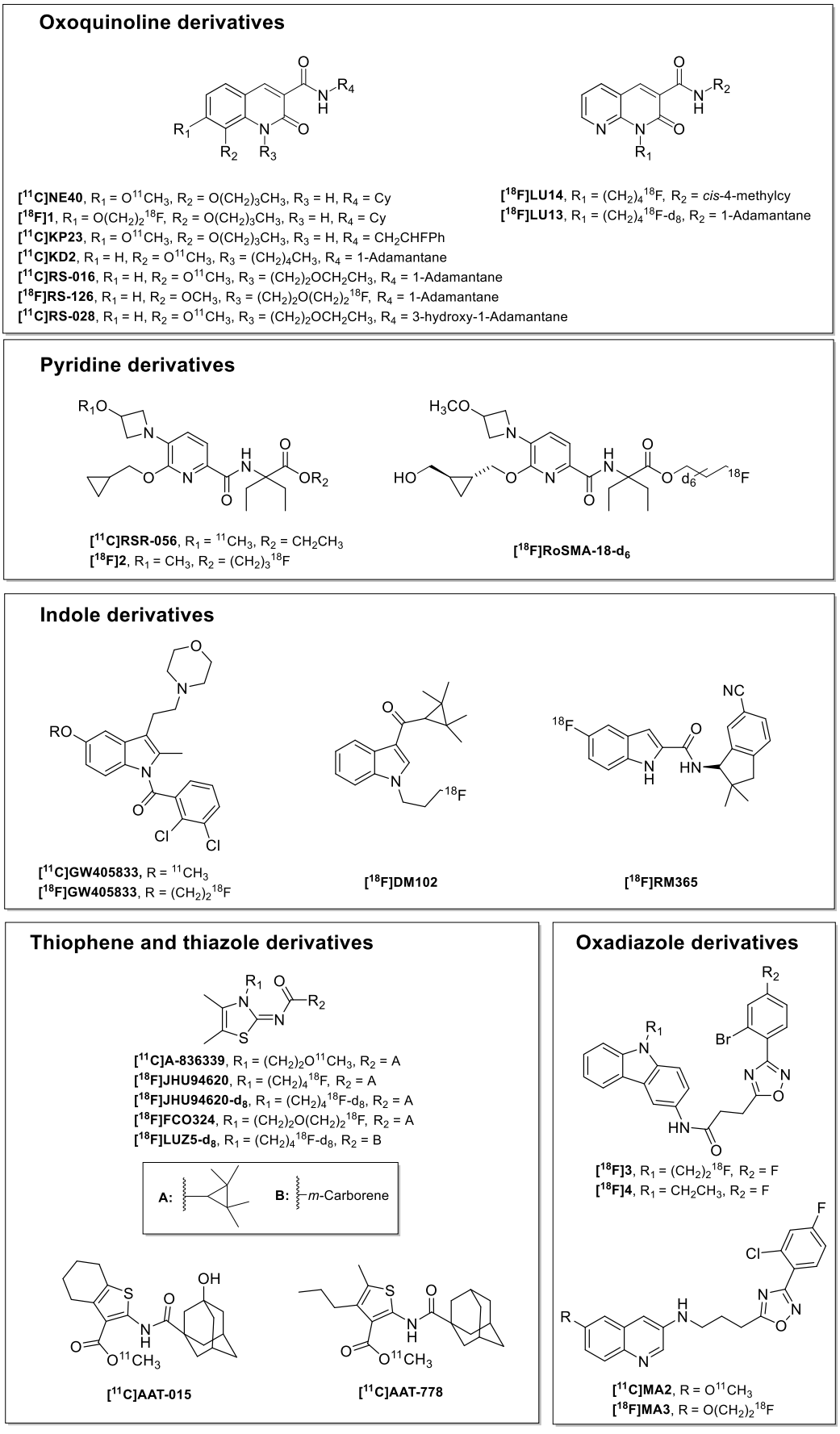

Figure 5.5: Structures of known PET tracers developed for CB2R imaging.

5.5.1. Oxoquinoline derivatives

The oxoquinoline scaffold is widely used for CB2R ligands, not only for the development of PET radiotracers but also for the design of fluorescent probes and therapeutic molecules.

The first PET radiotracers developed within this class were **[^{11}C]NE40** and **[^{18}F]1**. Both molecules were evaluated in mice and were found to cross the BBB and to exhibit persistent and specific accumulation in the spleen. Both compounds were cleared from plasma via the hepatobiliary system and underwent rapid metabolism. Of the two, **[^{18}F]1** showed a more rapid brain washout than **[^{11}C]NE40** and exhibited *in vivo* defluorination, indicating that **[^{11}C]NE40**, despite the short half-life of ^{11}C, is more promising for brain PET imaging [481].

[^{11}C]NE40 was also studied in Wistar rats, in which splenic CB2R-specific retention was even more pronounced than in biodistribution studies in mice. To further confirm the promising *in vivo* characteristics of **NE40**, biodistribution and autoradiography studies were performed in Wistar rats. Brain time-activity curves (CT scans) over time in rats and mice were quite similar and relatively homogeneous across brain regions. MicroPET studies were also conducted in rhesus monkeys, showing brain uptake in the cerebellum comparable to that in the frontal cortex and a similarly rapid washout. Finally, **[^{11}C]NE40** was evaluated in a rat model with local overexpression of *h*CB2R in the right striatum and using a structurally unrelated partial agonist such as GW405833; **[^{11}C]NE40** was demonstrated to bind reversibly to *h*CB2Rs [482].

The favorable characteristics of **[^{11}C]NE40** for PET neuroimaging enabled a human study to evaluate its biodistribution and safety. No subjective effects or adverse events were observed. The mean effective radiation dose of **[^{11}C]NE40** was determined to be 3.64 μSv/MBq, which was below the mean tolerable dose. Biodistribution with uptake in the spleen and the absence of brain uptake under healthy conditions make this tracer promising for further studies under pathological conditions [483].

[^{11}C]NE40 has also been used as an experimental marker of activated microglia, and its kinetic modeling in the brains of HD and AD patients has been investigated. AD patients did not show increased CB2R availability compared to HD. In contrast, AD patients exhibited significantly lower overall CB2R availability throughout the brain, in both cortical and subcortical regions. Furthermore, no correlation was found between regional amyloid deposition and homologous CB2R availability in AD patients. Regarding kinetic modeling, the best results were obtained with a reversible two-tissue compartment (2T) model. **[^{11}C]NE40** showed relatively slow kinetics; the tracer accumulated and dissipated slowly in the bound compartment, allowing appropriate quantification over a 90-min period [484].

Given the excellent results obtained with **[^{11}C]NE40**, a series of PET radiotracers was developed starting from this scaffold, in which small structural modifications were introduced with the aim of improving affinity, reducing lipophilicity, or increasing half-life, as already analyzed by Basagni F. et al. [480].

The first derivatives developed were **[^{11}C]KP23** and **[^{11}C]KD2**, designed to increase affinity and specific binding. **[^{11}C]KP23** showed high binding in autoradiographic studies with rat and mouse spleen slices. However, splenic binding was found to be largely nonspecific [485]. *In vitro* autoradiography with rat and mouse spleen slices conducted with [^{11}C]**KD2** instead demonstrated highly specific and selective reversible binding [486]. For both radiotracers, brain CT scans in healthy rats showed low uptake, consistent with the low level of CB2R expression [485,486]. *In vitro* autoradiography was also performed for **[^{11}C]KD2** using spinal cord tissue from ALS patients, showing specific accumulation of the tracer, an encouraging result for noninvasive imaging of CB2R levels in the spinal cord [486].

One possible cause of the nonspecific binding of **[^{11}C]KD2** is its high lipophilicity. For this reason, [^{11}C]**RS-016** was designed by introducing an oxygen atom into the pentyl chain to reduce lipophilicity. In vitro autoradiography showed that **[^{11}C]RS-016** exhibited lower nonspecific binding than **[^{11}C]KD2**. *Ex vivo* biodistribution studies revealed low accumulation of radioactivity in the healthy rat brain, consistent with the low levels of CB2R expression under physiological conditions. This low accumulation may also reflect limited BBB penetration of [^{11}C]**RS-016**. Using a mouse model of LPS-induced neuroinflammation, increased brain uptake was observed [487].

Maintaining low lipophilicity, **[^{18}F]RS-126** was designed to increase half-life by radiolabeling with ^{18}F rather than ^{11}C. Autoradiographic studies with **[^{18}F]RS-126** showed high specific binding to CB2R-positive rat spleen tissue sections. *In vivo* displacement studies confirmed selective binding to CB2R in rat spleen. Biodistribution studies in rats revealed 79% specific binding of **[^{18}F]RS-126** to splenic tissue. In contrast to **[^{11}C]RS-016**, **[^{18}F]RS-126** did not enable detection of CB2R expression in the brains of LPS-treated mice. Another disadvantage of **[^{18}F]RS-126** compared to **[^{11}C]RS-016** is *in vivo* defluorination, indicating metabolic instability [488].

[^{18}F]RS-126 was also evaluated *in vivo* in the R6/2 neuroinflammatory mouse model. However, no difference in CB2R expression between R6/2 and wild-type mice was detected by PET imaging with **[^{18}F]RS-126**, regardless of brain region or age [448].

To further reduce the lipophilicity of [^{11}C]**RS-016**, a hydroxyl group was introduced onto the adamantane moiety to yield **[^{11}C]RS-028**. In vitro autoradiography of **[^{11}C]RS-028** revealed significantly reduced nonspecific tissue binding. **[^{11}C]RS-028** was shown to be stable in brain, plasma, and spleen tissue in *ex vivo* metabolite studies using Wistar rats. However, splenic uptake was rather low compared to previously described CB2R radioligands, and a rapid washout was observed, likely due to the high polarity of the tracer. Therefore, preliminary animal studies with **[^{11}C]RS-028** do not support its use for *in vivo* CNS imaging [448].

More extensive structural modifications, conducted by different research groups, led to the development of **[^{18}F]LU14** and **[^{18}F]LU13-d$_8$**.

In autoradiographic studies of the spleen, **[^{18}F]LU14** showed no or only low specific binding. CT scans revealed rather low uptake in the spleen, comparable to that in muscle tissue used as a reference, in agreement with autoradiographic findings. To evaluate BBB penetration and the potential to visualize *h*CB2R under pathological conditions, PET imaging experiments with **[^{18}F]LU14** were performed in a rat model with local overexpression of hCB2 receptors in the right striatum. CT analysis revealed significantly higher uptake in the hCB2R-overexpressing striatal region (D80N) compared to the contralateral region and cerebellum after intravenous injection of **[^{18}F]LU14**. Initial uptake was followed by washout with a significantly longer mean residence time (MRT) in the target region than in nontarget regions. Strong metabolic conversion of **[^{18}F]LU14** to more polar metabolites was observed; in plasma, only 17% of unchanged **[^{18}F]LU14** was detected, whereas in the brain, 82 ± 5% of intact [^{18}F]**LU14** was measured. Dynamic small-animal PET/MR scans with [^{18}F]**LU14** were performed under control and blocked conditions in healthy male Wistar rats [489].

For **[^{18}F]LU13**, autoradiographic results were comparable to those obtained for **[^{18}F]LU14**. The main novelty of [^{18}F]**LU13** is the use of a deuterated chain to increase metabolic stability; indeed, a smaller fraction of radiometabolites was detected compared to the structural analogue **[^{18}F]LU14**. In the brain, 85

± 3% of the activity corresponded to intact **[^{18}F]LU13**. Brain uptake and specific binding of **[^{18}F]LU13** were also investigated in PET imaging experiments using a D80N rat model in the right striatum. CT analysis revealed significantly higher uptake in the *h*CB2R-overexpressing striatal region. **[^{18}F]LU13** therefore crosses the BBB and binds specifically and reversibly to *h*CB2R [490].

5.5.2. Pyridine derivatives

The pyridine scaffold has received less attention, from a PET imaging perspective, than the oxoquinoline scaffold; indeed, only three PET radiotracers, based on this structure, have been reported to date.

[^{11}C]RSR-056 has proven to be particularly suitable for brain imaging of neuroinflammatory states; indeed, brain radioactivity was significantly higher in LPS-treated mice than in control mice. *In vivo* PET and biodistribution studies also confirmed its specificity for splenic tissue. Regarding metabolic stability, the percentage of intact parent tracer in plasma decreased over time to 51% after 5 min, 37% after 10 min, and 21% after 20 min [491].

Compared to the previous radiotracer, **[^{18}F]2** has a longer alkyl chain linked to the ester group and, importantly, it is radiolabeled with ^{18}F rather than ^{11}C. *In vitro* autoradiography using CB2R-positive rat spleen tissue showed that **[^{18}F]2** exhibited high specific binding to the spleen under basal conditions. In CB2R-negative brain slices from healthy Wistar rats, tracer binding was not reduced by the addition of GW-405833, confirming the absence of displaceable CB2R binding in healthy brains. CT scan time-activity curves calculated for the spleen indicated that **[^{18}F]2** binds specifically and reversibly to CB2R *in vivo* [492].

[^{18}F]RoSMA-18-d$_6$ has a structure very similar to that of the previous radiotracer but it is characterized by the presence of a deuterated propyl chain to increase metabolic stability. **[^{18}F]RoSMA-18-d$_6$** was evaluated by imaging a subacute tMCAO mouse model, concomitant with reduced CMRglc levels and structural lesion formation. Dynamic microPET scanning with **[^{18}F]RoSMA-18-d$_6$** indicated reduced perfusion in the lesioned brain regions during the first time interval of 1-3 min. The in vivo specificity of **[^{18}F]RoSMA-18-d$_6$** toward CB2R was demonstrated by a 58% reduction in splenic radioactivity under blocked conditions in ex vivo biodistribution studies. CT scans of **[^{18}F]RoSMA-18-d$_6$** in healthy brain showed poor binding specificity, whereas those acquired in the tMCAO mouse model showed significantly higher initial brain uptake under blocked conditions compared to baseline in both hemispheres of the mouse brain [493].

5.5.3. Indole derivatives

The indole scaffold is highly versatile and has been used for ligands targeting several receptors. The first PET radiotracer in this category was the reference CB2R agonist GW-405833, which was radiolabeled with ^{11}C. **[^{11}C]GW405833** showed high brain uptake in rats and did not bind specifically to the spleen. It exhibited hepatobiliary excretion and rapid metabolism, with only 15% of intact tracer remaining in plasma 30 min after injection in mice. PET studies in primates confirmed the high brain uptake of **[^{11}C]GW405833**, but brain washout was slower than that observed in rats [494].

Starting from **[^{11}C]GW405833**, its fluoroethoxy analogue **[^{18}F]FE-GW405833** was also developed. In mice, this tracer showed moderate brain uptake, a rather slow washout, and hepatobiliary-type excretion [340]. Spleen binding was comparable to that of **[^{11}C]GW405833**. Metabolism was also comparable to that of **[^{11}C]GW405833**, with only 12% of intact tracer remaining in plasma at 30 min p.i. [340,494]. CT scans

of the left striatum showed an initial peak followed by slow clearance until approximately 60 min, after which activity levels remained constant, consistent with biodistribution data in mice. CT scans of the right striatum showed a similar pattern but with slower clearance, resulting in a 1.6-fold higher concentration than in the contralateral striatum at 60 min p.i., a ratio comparable to that observed for **[^{11}C]GW405833** [340,494].

Regarding **[^{18}F]DM102**, autoradiography of rat splenic tissue sections revealed binding, with a degree of nonspecific binding within acceptable limits [495].

[^{18}F]RM365 showed a comparable biodistribution in the spleen between mice and rats, with a constant SUV value of 0.7 ± 0.1. Regarding metabolism, approximately 90% of the radioactivity detected in brain samples corresponded to the intact radioligand. Using the D80N model in the right striatum, both blood–brain barrier permeability and high specific binding to the CB2R were demonstrated [496].

5.5.4. Thiophene and thiazole derivatives

The first compound in the thiazole series to be developed was **[^{11}C]A-836339**, which served as a model for the development of subsequent radiotracers.

The whole-body and brain distribution of **[^{11}C]A-836339** in mice was assessed, and the radiotracer was found to exhibit specific binding in both the spleen and the brain. **[^{11}C]A-836339** also showed high brain-specific uptake in a mouse model of LPS-induced neuroinflammation, and comparison of SUV values between this model and control mice highlighted the applicability of this radiotracer for PET imaging of neuroinflammation [497]. In a mouse model of AD, **[^{11}C]A-836339** showed significant specific binding in various brain regions [497,498]. **[^{11}C]A-836339** was also evaluated in a mouse model of cerebral ischemia; however, the lack of radiotracer uptake after stroke demonstrated the limitations of this compound in this pathological condition [499].

[^{18}F]JHU94620 was developed from **[^{11}C]A-836339** by lengthening the alkyl chain linked to the nitrogen atom and eliminating the oxygen atom. Autoradiographic experiments on rat spleen slices demonstrated the specificity of this radiotracer. PET/MR experiments in healthy female CD-1 mice revealed high uptake in the liver, kidney, intestine, urinary bladder, and gallbladder, confirming a predominantly hepatic excretion pathway. Clear and marked uptake was also observed in the spleen as a specific target tissue. When compared with CD-1 mice in a mouse model of LPS-induced neuroinflammation, higher uptake of **[^{18}F]JHU94620** was observed in the brains of LPS-treated mice. Rapid metabolism was observed, with only 7% of intact **[^{18}F]JHU94620** detected in plasma and approximately 36% in brain samples [500].

To increase metabolic stability, the alkyl chain of **[^{18}F]JHU94620** was replaced with its deuterated analogue. In this way, the formation of more hydrophilic radiometabolites, presumably hydroxylated species capable of crossing the blood–brain barrier, was reduced. Although a low fP of **[^{18}F]JHU94620-d8** was determined, which is common for lipophilic radiotracers, sufficiently high brain uptake was observed. In particular, brain CT scans in a rat model with high *h*CB2R (D80N) expression demonstrated reversible and CB2R-specific binding of **[^{18}F]JHU94620-d8** in the brain [501].

To reduce lipophilicity, an oxygen atom was introduced into the alkyl chain of **[^{18}F]JHU94620**, yielding **[^{18}F]FC0324**. Biodistribution studies in healthy rats showed similar distribution and elimination patterns across most organs, except for the spleen, where marked accumulation was observed, suggesting specific binding of the radiotracer. Blockade experiments in rat spleen confirmed the specificity and selectivity of

[^{18}F]FC0324. With respect to metabolism, the percentage of unmetabolized **[^{18}F]FC0324** decreased exponentially as a function of time, accounting for 53% at 5 min and 25% at 30 min after injection. Over the same time period, the percentage of the major polar radiometabolite increased and reached 50% of total plasma radioactivity [502].

[^{18}F]FC0324 was also evaluated in NHPs. CT scans showed rapid and homogeneous brain distribution followed by rapid washout, consistent with the low abundance of CB2R in the healthy brain. Whole-body PET–CT suggested high and specific uptake of the radiotracer in the spleen and in organs involved in metabolism and excretion, with low bone uptake. Regarding metabolism, the main radiometabolite was likely the result of further oxidation of hydroxylated compounds, and the parent **[^{18}F]FC0324** accounted for only 8% of plasma radioactivity [503].

Further structural modifications of previous radiotracers led to the development of **[^{18}F]LUZ5-d$_8$**, in which the 1,1,2,2-tetramethylcyclopropane moiety was replaced with a meta-carborane unit, while retaining the deuterated alkyl chain to increase metabolic stability. Dynamic PET scans in rats with and without the blocking agent GW405833 revealed rapid uptake into the spleen and liver, rapid hepatic clearance, and non-displaceable binding in the spleen. Brain uptake of the radiotracer was low. Regarding metabolic stability, only a small fraction of intact tracer was found in mouse plasma at 30 min p.i., whereas the percentage of intact radioligand in mouse brain and spleen was high and higher than that observed for **[^{18}F]JHU94620**. The metabolic stability of **[^{18}F]LUZ5-d$_8$** in rats exceeded that in mice [504].

The only thiophene-based CB2R PET radiotracers reported to date are **[^{11}C]AAT-015** and **[^{11}C]AAT-778**. Both radiotracers showed poor splenic specificity in both autoradiographic and PET studies. They also exhibited rapid metabolism, likely mediated by plasma esterases [505].

5.5.5. Oxadiazole derivatives

The oxadiazole scaffold has been only marginally explored to date; indeed, only four compounds belonging to this category have been reported.

Regarding the compounds **[^{18}F]3** and **[^{18}F]4**, the structures are identical, differing only in the position of the fluorine atom selected for radiolabeling. Biodistribution analysis showed that the highest uptake for both radiotracers was detected at 5 min p.i. in the spleen. Comparable kinetics were observed in the brain and in most other organs, such as the lung, liver, kidney, thymus, and adrenal glands. No defluorination was observed *in vivo*. The main difference between the two radiotracers lies in the fact that radioactivity levels measured for **[^{18}F]4** were higher in organs that natively express CB2R. This relationship was reversed in organs associated with excretion. This behavior is likely related to the much faster metabolism of **[^{18}F]4** compared to that of **[^{18}F]3**. In both cases, radiometabolites generated in the periphery penetrated the BBB, leading to pronounced accumulation of the main radiometabolites in the brain and thereby hindering the application of **[^{18}F]3** and **[^{18}F]4** for CB2R imaging in the brain [506].

As for **[^{11}C]MA2** and [^{18}F]**MA3**, the structural differences are again minimal; in the first case, a methoxy group is present, whereas in the second case a fluoroethoxy group is present. Both compounds crossed the BBB efficiently, and washout from the brain was rapid. Brain uptake of **[^{11}C]MA2** was similar to that of **[^{11}C]NE40**. Biodistribution studies also showed that both **[^{11}C]MA2** and **[^{18}F]MA3** were eliminated from the blood via the hepatobiliary system. No accumulation of either **[^{11}C]MA2** or **[^{18}F]MA3** was observed in the spleen [507].

[^{18}F]MA3 (agonist) was compared with [^{11}C]**NE40** (inverse agonist) in a rat model overexpressing an inactive mutant of the *h*CB2 receptors. A similar BP_{ND} was found for the two compounds. **[^{18}F]MA3** was also evaluated in a healthy NHP model and showed moderate brain uptake with homogeneous distribution and rapid washout. The appearance of radiometabolites in monkey plasma was rather rapid. Again, no defluorination was observed *in vivo*. Contrary to expectations, pretreatment with the **NE40** inverse agonist increased the concentration of radioactivity in monkey brain [508].

5.6. Summury of introduction

Over the past two decades, a wide variety of CB2R PET radiotracers has been developed across multiple structural scaffolds, reflecting sustained interest in CB2R as a biomarker of neuroinflammation. Among the investigated classes, oxoquinoline derivatives, particularly **[^{11}C]NE40**, remain the most extensively validated, with demonstrated BBB penetration, favorable kinetic behavior, and translation to human studies. Nonetheless, even within this class, metabolic instability, lipophilicity, and nonspecific binding continue to limit quantitative accuracy and clinical applicability.

Pyridine and indole scaffolds have yielded promising candidates capable of BBB penetration and CB2R-specific binding under pathological conditions; however, both classes suffer from limited metabolic stability and suboptimal specificity in healthy brain. Thiazole derivatives have shown strong splenic binding and sensitivity to neuroinflammatory states, but rapid metabolism and inconsistent brain uptake have restricted their broader utility. Oxadiazole-based tracers, although structurally appealing, have so far underperformed due to extensive peripheral metabolism and the formation of BBB-penetrating radiometabolites.

Collectively, these studies highlight that achieving the optimal balance among affinity, lipophilicity, metabolic stability, BBB permeability, and specific binding remains the central challenge in CB2R radiotracer development. While several tracers demonstrate encouraging properties in preclinical models, particularly under conditions of CB2R overexpression or neuroinflammation, no single compound has yet emerged as a fully satisfactory clinical PET tracer for CB2R imaging in the CNS.

Future efforts should focus on rational scaffold optimization, strategic isotopic labeling, and systematic evaluation in disease-relevant models to enable the translation of CB2R PET imaging into routine clinical and research applications.

5.7. Background and Aim

CB2R is involved in the neuroinflammatory processes underlying neurodegenerative diseases such as AD [509] and PD [445]. CB2Rs are minimally expressed in the CNS under physiological conditions but become markedly upregulated during neuroinflammation and in pathological states. For this reason, they have been identified as promising biomarkers for the early diagnosis of neurodegenerative disorders such as PD and AD.

The research group, where this thesis was carried out, has been active over the last years in the development of CB2R ligands, pursuing both single-target and multi-target approaches (MTDL – multi-target directed ligand design strategies). From a MTDL perspective, the FAAH enzyme has been identified as a complementary target capable of enhancing the overall therapeutic effect [454] induced by CB2R stimulation. FAAH, as above mentioned, is the enzyme responsible for the metabolism of endocannabinoids and thus, the proposed dual-strategy (CB2R activation and FAAH inhibition) may lead to the increase of the endocannabinoid tone exerting a final anti-inflammatory effect.

The choice of this strategy was supported by a principal component analysis (PCA) study that identified a shared chemical space between CB2R ligands and FAAH inhibitors reported in the ChEMBL database (IC_{50} or $K_i \leq 1$ μM for both targets under study). The analysis provided excellent results, as illustrated in Figure 5.6, clearly highlighting an overlapping chemical space between ligands active on CB2R and those active on FAAH [510].

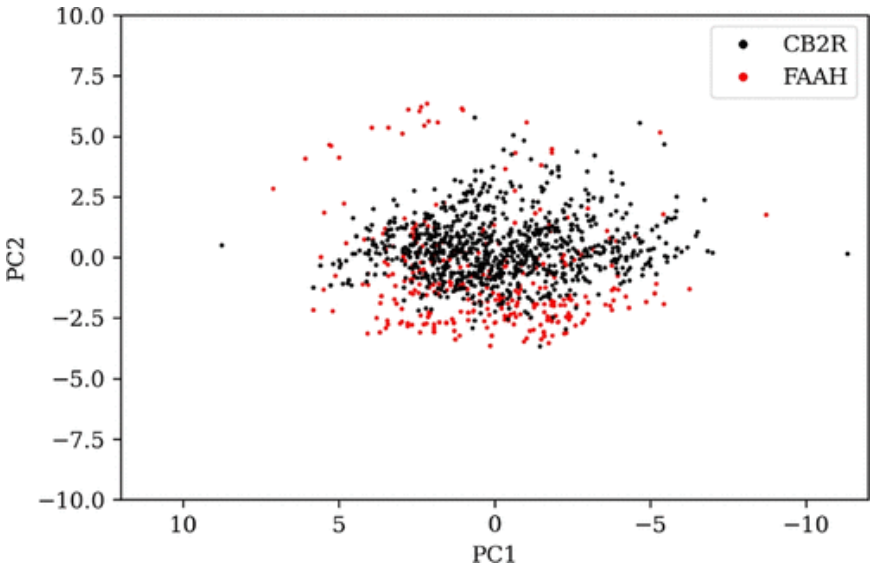

Figure 5.6. Projection of CB2R (black points) and FAAH (red points) high affinity (IC_{50} or $K_i \leq 1$ μM) compounds into the top two PCs obtained from 16 physicochemical descriptors. Note that PC1 and PC2 are plotted accounting for 70% of the total variance [510].

The starting point was the series of pyridine-3-carboxamide derivatives developed by Lucchesi *et al.* as highly potent and selective CB2R ligands (general formula in Figure 5.7.A) [511]. The pyridine-3-carboxamide core was isosterically replaced with a salicylamide, and the adamantane tricycle was introduced in place of the cycloalkanes, in line with previous and robust SAfiR studies that identified the adamantyl fragment as responsible for the high CB2R affinity [454]. This scaffold led to a new series of dual CB2R agonists-FAAH inhibitors (general formula in Figure 5.6.B) [510] among which emerged the

dual compounds *N*-((3s,5s,7s)-adamantan-1-yl)-2-(pentyloxy)benzamide (**FI8,** Figure 5.8) and *N*-((3s,5s,7s)-adamantan-1-yl)-2-(benzyloxy)benzamide (**CC48**, Figure 5.8), endowing with high CB2R affinity, good (even if not high) selectivity towards the CB1R subtype, moderate activity at the FAAH and not optimal lipophilicity.

FI8 and **CC48** have proven to be very promising since experimental studies further demonstrated that both exert antitumor activity in an *in vivo* model of gastric cancer [512] as well as neuroprotective effects in an *in vivo* model of AD [513].

In parallel, my research group developed a similar series of CB2R single target agents, bearing an antranilic scaffold, leading to compounds with lower affinity toward CB2R but higher selectivity against the CB1R (general formula in Figure 5.7.C) [514].

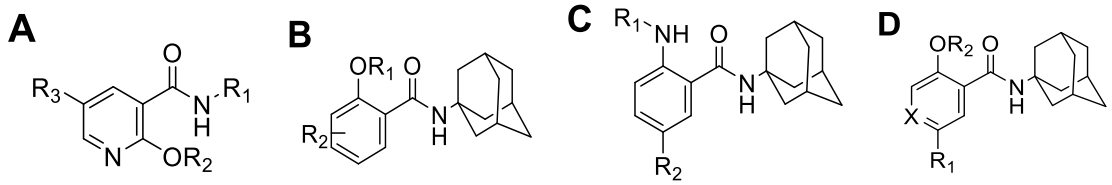

Figure 5.7. Generale formula of **A.** Pyridine-3-carboxamide-derivatives [511]; **B.** Salicylamide-derivatives [510]; **C.** Antranil-derivatives [514]; **D.** PET candidates for CB2R.

Then, with the aim to improve the limitations of compounds **FI8** and **CC48** (the selectivity towards the CB1R subtype, the moderate activity at the second target FAAH and the not optimal lipophilicity), we performed structural modifications by introducing, several substituents such as bromine, phenyl and naphthyl groups, on both the salicylic and anthranilic core, always retaining the adamantyl-benzamide function.

Among the newly synthesised derivatives, *N*-((3s,5s,7s)-adamantan-1-yl)-4-(pentyloxy)-[1,1'-biphenyl]-3-carboxamide (**GR75**, Figure 5.8) emerged for its high CB2R affinity and selectivity and antagonist activity [515]. This antagonism was expected, considering our previous SAR studies carried out on both antranilic and salicylic scaffolds [514,515]. Indeed, we observed that the introduction of a second phenyl ring as R_1 in the above reported general formula (Figure 5.7.D.), shifted the activity from agonism to inverse agonism/antagonism.

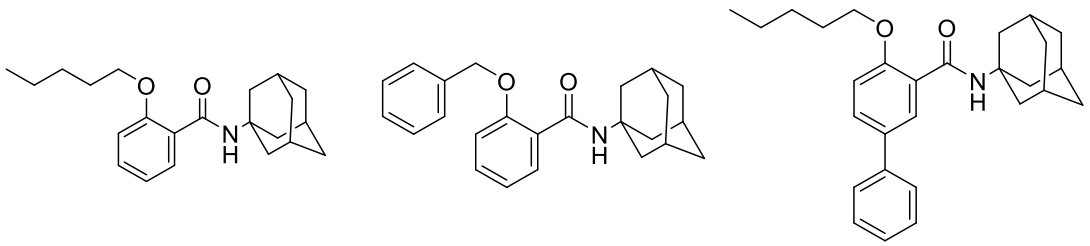

FI8
K_i CB1R = 152.9 nM
K_i CB2R = 10.8 nM

CC48
K_i CB1R = 241.3 nM
K_i CB2R = 14.8 nM

GR75
K_i CB1R = 8% @1μM
K_i CB2R = 7.9 nM

Figure 5.8. Chemical structure and pharmacodynamic profile of **FI8** [510], **CC48** [510] and **GR75** [515].

Therefore, with the aim to produce highly potent and selective radiotracers to image CB2R, mainly in pathological conditions we modified the two CB2R agonists **FI8** and **CC48** and the CB2R antagonist **GR75** as depicted in figure 5.7.D.

A series of *N*-adamantyl-salicylamides bearing a fluorine atom was synthesized to improve the pharmacodynamic and pharmacokinetic profile, as well as to identify the optimal position for a F-atom insertion in order to develop the corresponding radiolabeled counterpart (general structure shown in Figure 5.7.D). In parallel, to reduce lipophilicity, isosteric modifications were explored. Specifically, the aromatic ring was replaced with a pyridine one and an oxygen atom was incorporated into the alkyl chain.

Among the synthesized compounds, compounds **5** and **6** (also known as **FM10** and **GR106**, respectively) emerged for their high CB2R affinity, selectivity towards the CB1R (Table 5.2) and different activity profile (Table 5.4).

Thus, the two ligands were selected for the development of the corresponding ^{18}F-labeled radiotracers and were subsequently biologically evaluated, enabling a direct comparison of the two structurally closely related CB2R PET tracers with different functional profile. This approach provides, for the first time, a unique opportunity to investigate whether ligands sharing a similar scaffold but differing in intrinsic activity exhibit distinct diagnostic behavior toward the CB2R target.

5.8. Results

5.8.1. Chemistry

The synthesis of the final compounds **5-21** was carried out following a conventional synthetic route previously described for compounds **FI8**, **CC48** [510] and **GR75** [515], as well as related derivatives (Scheme 5.1).

Briefly, commercially available benzoic acid or isonicotinic acid was first activated with *O*-benzotriazol-1-yl-*N*,*N*,*N*′,*N*′-tetramethyluronium hexafluorophosphate (HBTU) in the presence of diisopropylethylamine (DIPEA), and then condensed with 1-adamantylamine to afford the corresponding adamantylamides (**22** [510], **23** [515] and **24-25**). The phenolic group was subsequently alkylated under basic conditions with the appropriate alkyl or aryl bromide to yield final compounds **5** and **8-19** as well as intermediate **26** and the already known **27** [515]. The final bicyclic derivatives **6** and **20-21** were obtained from the bromo derivatives (**16** and **27**, respectively) by Suzuki–Miyaura coupling with the appropriate boronic acids, catalyzed by tetrakis(triphenylphosphine)palladium(0) [$Pd(PPh_3)_4$]. For final compound **7**, the hydroxyl group of intermediate **26** was first converted into the corresponding tosylate (**28**) using tosyl chloride (TsCl), followed by nucleophilic substitution under basic conditions in the presence of 4,7,13,16,21,24-hexaoxa-1,10-diazabicyclo[8.8.8]hexacosane ($K_{2.2.2}$).

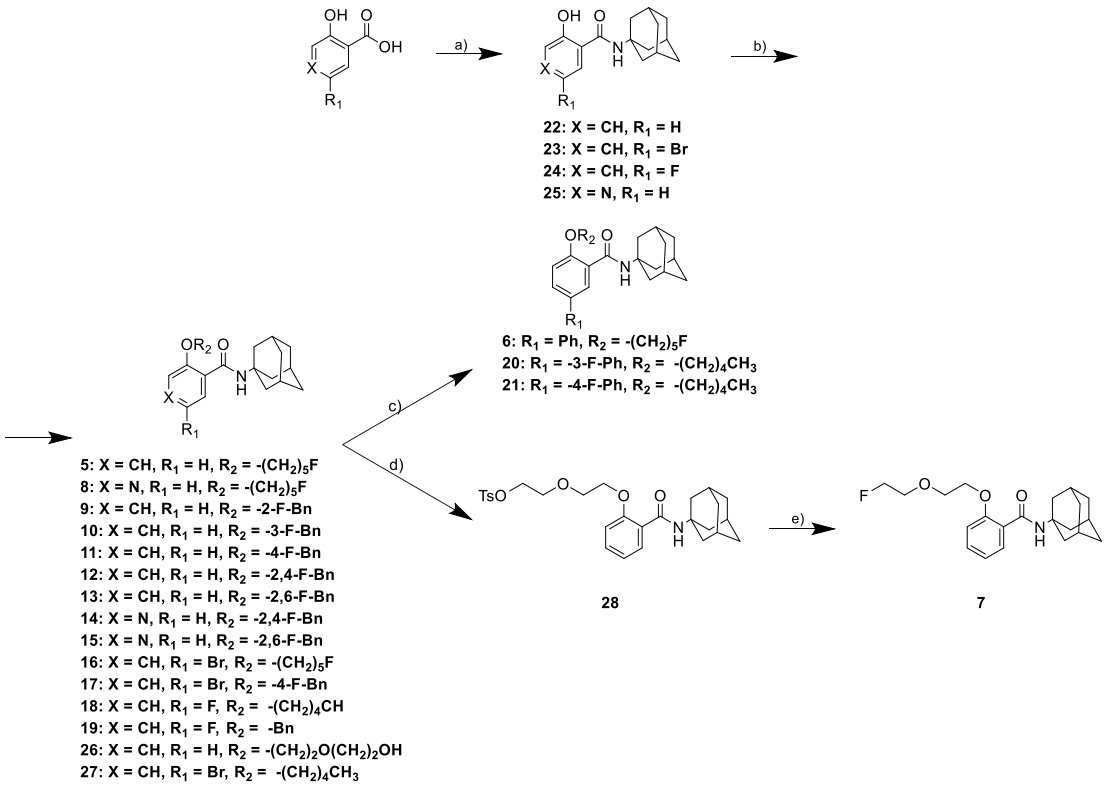

Scheme 5.1. Synthesis of final compounds **5-21**. (a) HBTU, DIPEA, 1-adamantylamine, dry DMF, from 0°C to RT, ON; (b) Appropriate alkyl/aryl bromide, K_2CO_3, acetone, reflux, 4h; (c) appropriate boronic acid, $Pd(PPh_3)_4$, dioxane/K_2CO_3 (2M), reflux, 2–4h; (d) TsCl, Et_3N, dry CH_2Cl_2, 0 °C, 4h; (e) KF, K_{222}, K_2CO_3, dry CH_3CN, reflux, ON.

5.8.2. *In vitro* CB1R and CB2R Binding Affinities

The results from the radioligand competition binding assays were reported as K_i values in Table 5.2. Overall, the salicylamide derivatives displayed nanomolar affinity values at CB2R, as previously demonstrated in our earlier studies [510,515], confirming this scaffold as an optimal framework for high-affinity CB2R binding.

The lead compound **FI8** showed good CB2R affinity but only moderate selectivity (K_i CB1R = 152.9 nM, K_i CB2R = 10.8 nM) [510]. Compared to the lead compound **FI8**, the introduction of a F-atom into the pentyl chain (compound **5**) resulted in an increased affinity for CB2R (K_i = 5.2 nM) and, more importantly, a marked enhancement in CB2R selectivity towards the CB1R subtype (from 14-fold to 200-fold). To reduce lipophilicity, various isosteric substitutions were explored. The replacement of the F-pentyl chain with a 2-(fluoroethoxy)ethoxy moiety (compound **7**) and the substitution of the phenyl ring with a pyridine ring (compound **8**) led to a slightly decrease in CB2R affinity (K_i = 26.8 nM, K_i = 19.5 nM, respectively) but an increase in CB2R selectivity over the CB1R (CB1R: 32%@1μM, 43%@1μM, respectively). Starting from compound **5**, the introduction of an additional lipophilic group, such as a bromo atom at position 5 of the aromatic ring (compound **16**), produced a 10-fold reduction in CB2R affinity (K_i = 58.0 nM). Conversely, the addition of a phenyl group (compound **6**) increased both the CB2R affinity (K_i = 1.1 nM) and selectivity over the CB1R subtype (CB1R: 2%@1 μM). A similar trend was observed when comparing the two lead compounds **FI8** and **GR75**, where the addition of an aromatic ring led to the improvement in both parameters [515]. Maintaining the pentyl chain, as in **FI8**, but introducing either a 3-F-phenyl (compound **20**) or 4-F-phenyl (compound **21**) substituents at position 5 of the aromatic ring, resulted in a comparable CB2R affinity for compound **20** (*Ki* = 11.6 nM) and a 4-fold lower CB2R affinity for compound **21** (K_i = 39.9 nM); both compounds exhibited enhanced CB2R selectivity over the CB1R subtype (CB1R: 14%@1 μM, 11%@1 μM, respectively). Comparing compound **21** to the lead compound **GR75**, it is evident that the presence of a fluorine atom on the second phenyl ring caused a 5-fold reduction in CB2R affinity (*Ki* = 39.9 nM, *Ki* = 7.9 nM, respectively). In compound **18**, where a F-atom was introduced at position 5 of the aromatic ring, the CB2R affinity remained similar (*Ki* = 8.6 nM) to that of the lead compound **FI8** and of compound **5**, whereas the selectivity towards the CB1R increased compared to both compounds (**18**, CB1R = 41%@1 μM; **FI8**, K_i CB1R = 152.9 nM and **5**, K_i CB1R = 1058 nM).

A series of compounds was also developed starting from **CC48**, which had shown good CB2R affinity but moderate selectivity towards the CB1R subtype [510]. In the **CC48** scaffold a single F-atom was introduced at the *ortho*- (compound **9**), *meta*- (compound **10**) and *para*-position (compound **11**) of the benzyl ring. Compounds **9** and **11** exhibited higher CB2R affinity (K_i = 4.1 nM and K_i = 0.7 nM, respectively), reaching sub-nanomolar affinity in the case of compound **11**, along with an improved selectivity towards the CB1R (K_i = 222.7 nM and K_i = 48.2 nM, respectively). In contrast, compound **10** showed reduced CB2R affinity (K_i = 28.7 nM) but increased selectivity towards the CB1R (CB1R: 39%@1 μM).

Encouraged by the favourable results obtained through fluorine substitution on the benzyl ring, difluorinated derivatives were synthesized. Both the 2,4-F (compound **12**) and 2,6-F (compound **13**) derivatives retained sub-nanomolar affinity for CB2R (K_i = 0.7 nM, K_i = 1.4 nM, respectively) but displayed only moderate selectivity over the CB1R (CB1R: K_i = 22.3 nM, K_i = 77.3 nM, respectively). As for compound **5**, a strategy to reduce lipophilicity was attempted by replacing the aromatic ring of compounds

12 and **13** with a pyridine moiety, yielding compounds **14** and **15**, respectively. This modification led to compounds with negligible affinity for CB2R. Starting from compound **11**, the benzyl-derived compound with the highest CB2R affinity, the introduction of a Br-atom at position 5 of the aromatic ring yielded compound **17**, which showed a 40-fold decrease in CB2R affinity (K_i = 27.9 nM) and selectivity towards the CB1R subtype (K_i = 198.4 nM). Similarly, replacing the benzene ring with a F-atom at position 5 of the aromatic ring produced compound **19** with a lower CB2R affinity (K_i = 41.6 nM) but higher selectivity vs the CB1R compared to the lead compound **CC48** (45%@1 μM and K_i = 241.3 nM, respectively) [510].

In conclusion, the presence of a pentyl chain led to more potent compounds than benzyl derivatives for PET purposes. The introduction of a F-atom generally increased both CB2R affinity and selectivity towards the CB1R subtype, particularly when positioned on the chain rather than on the aromatic or benzyl ring. Less lipophilic compounds exhibited reduced CB2R affinity.

Among all tested ligands, compounds **5** and **6** (also known as **FM10** and **GR106**, respectively) emerged as the most promising candidates, due to their high CB2R affinity and selectivity and were therefore selected as potential PET tracers for CB2R imaging.

Compounds **7**, **8**, **10**, and **18** (also known as **FM13**, **FM15**, **FM24**, and **FM26**, respectively) demonstrated high affinity and selectivity. However, they were not selected for radiolabeling because they did not meet the predefined criteria for suitable CB2R PET radiotracers (K_i for CB2R < 6.0 nM and ≥100-fold selectivity).

Table 5.2. CB1R and CB2R affinities.

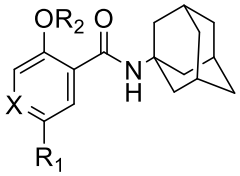

Compound	X	R_1	R_2	*h*CB1R, K_i %@1μM or nM[a]	*h*CB2R, K_i %@1μM or nM[a]
FI8[b]	CH	H	-$(CH_2)_4CH_3$	152.9	10.8
5 (FM10)	CH	H	-$(CH_2)_5F$	1058 ± 102.1	5.2 ± 0.6
7 (FM13)	CH	H	-$(CH_2)_2O(CH_2)_2F$	32 ± 2%	26.8 ± 3.8
8 (FM15)	N	H	-$(CH_2)_5F$	43 ± 6%	19.5 ± 3.0
CC48[b]	CH	H	-Bn	241.3	14.8
9	CH	H	2-F-Bn	222.7 ± 32.9	4.1 ± 0.5
10 (FM24)	CH	H	3-F-Bn	39 ± 1%	28.7 ± 2.4
11	CH	H	4-F-Bn	48.2 ± 3.8	0.7 ± 0.08
12	CH	H	2,4-F-Bn	23.4 ± 2.1	0.7 ± 0.07
13	CH	H	2,6-F-Bn	77.3 ± 6.8	1.4 ± 0.2
14	N	H	2,4-F-Bn	2 ± 3%	14 ± 2%
15	N	H	2,6-F-Bn	11 ± 4%	47 ± 5%
16	CH	Br	-$(CH_2)_5F$	4 ± 2%	58.0 ± 7.4
17	CH	Br	4-F-Bn	198.4 ± 9.5	27.9 ± 1.7
18 (FM26)	CH	F	-$(CH_2)_4CH_3$	41 ± 1%	8.6 ± 0.1
19	CH	F	-Bn	45 ± 3%	41.6 ± 5.2
GR75[c]	CH	Ph	-$(CH_2)_4CH_3$	8%	7.9
6 (GR106)	CH	Ph	-$(CH_2)_5F$	2 ± 2%	1.1 ± 0.09
20	CH	3-F-Ph	-$(CH_2)_4CH_3$	14 ± 2%	11.6 ± 1.3
21	CH	4-F-Ph	-$(CH_2)_4CH_3$	11 ± 4%	39.9 ± 6.5
GW405833					3.8
Rimonabant				17.5	

[a]Values represent the mean of at least two separate experiments in duplicate ± SEM; %@1μM represents percentage of displacement at 1 μM.; [b]Data from ref [510]; [c]Data from ref [515].

5.8.3. Binding kinetics at the human CB2R

The two PET candidates **FM10** and **GR106** were evaluated for their kinetic profiles at the CB2R through competitive binding experiments using [^{3}H]RO6957022 [516] (Table 5.3, Figure S5.1). Both **FM10** and **GR106** showed an activation rate (k_{on} = 36.0 and 46.2 $\mu M^{-1}min^{-1}$, respectively) on CB2R that was approximately 2-3 times slower than the reference agonist CP55,940 (k_{on} = 105 $\mu M^{-1}min^{-1}$) [517]. Nevertheless, the values indicated that binding to the receptor was essentially instantaneous at the tested concentrations. When compared with their corresponding parent compounds, an increase in k_{on} was observed both when moving from **FI8** [513] to **FM10** and from **GR75** [515] to **GR106**. Thus, the simple addition of a fluorine atom to the pentyl chain resulted in faster binding to CB2R.

About the dissociation rate from the receptor (k_{off}), **FM10** exhibited a k_{off} approximately 12-fold higher (k_{off} = 0.37 min^{-1}) than the reference agonist CP55,940 (k_{off} = 0.03 min^{-1}), whereas for **GR106** the increase was approximately 3-fold (k_{off} = 0.11 min^{-1}). Consequently, **FM10** displayed a residence time (RT) approximately 12 times shorter than the reference agonist **FI8**, while for **GR106** the decrease in RT was less evident, being only 3-fold lower than the reference antagonist **GR75**. Comparison with the lead compounds showed that, in this case, the fluorine substitution led to a clear increase in RT only for the monophenyl derivative (2.73 min for **FM10** vs too fast rate for **FI8** [513], whereas in the biphenyl derivatives the trend was reversed, with fluorination decreasing the RT (9.00 min for **GR106** vs 15 min for **GR75**) [515].

Overall, comparison of **FM10** and **GR106** with their respective lead compounds **FI8** and **GR75**, showed that the fluorine addition increased the rate at which the molecules binds to CB2R. In contrast, the effect of a fluorine on the duration of receptor engagement was structure-dependent: RT increased only in the monophenyl derivative, while it decreased in the biphenyl derivative. The increase in RT was likely associated with increased lipophilicity; indeed, the compounds with the highest RT values were the biphenyl derivatives **GR75** and **GR106**. This behaviour may have arisen from deeper hydrophobic interactions within the binding pocket promoted by the second phenyl ring.

The kinetic K_D values obtained from these competitive binding experiments were in good agreement with the K_i values from the equilibrium shift assays in the case of **GR106** (K_D = 2.41 nM vs K_i = 1.37 nM). For **FM10**, however, a two-fold difference was observed (K_D = 10.1 nM vs K_i = 5.28 nM).

It is important to note that the K_i values described here were comparable to those reported in Table 5.2 (5.2 nM vs 5.3 nM for **FM10**; 1.1 nM vs 1.4 nM for **GR106**). This consistency supported the reliability of the data, as they were obtained using different methods in different laboratories.

Table 5.3. Kinetic parameters.

	Competition association assay					Displacement assay
Compound	**k_{on} ± S.E.M ($\mu M^{-1}min^{-1}$)**	**ET (min at 1 µM)**	**k_{off} ± S.E.M (min^{-1})**	**RT (min)**	**Kinetic K_D (nM)**	**pK_i ± S.E.M. (K_i (nM))**
CP55,940[a]	105 ± 24	0.01	0.03 ± 0.01	32	0.29	8.9 ± 0.1 (1.4)
FM10	36.0 ± 23.4	0.03	0.37 ± 0.17	2.73	10.1	8.28 ± 0.18 (5.3)
GR106	46.2 ± 30.6	0.02	0.11 ± 0.04	9.00	2.41	8.86 ± 0.25 (1.4)
FI8[b]	Too fast					
GR75[c]	8.36 ± 5.61	0.12	0.07 ± 0.04	15	7.87	8.82 ± 0.08 (1.5)

[a]Reference compound; data converted to minutes for comparison [517]. [b]Data from ref [513]. [c]Data from ref [515]. Data from the competition association experiments are presented as mean ± S.E.M. of three independent experiments performed in duplicate. ET is the engagement time at 1 µM in minutes (reciprocal of k_{on}). RT is the residence time in minutes (reciprocal of k_{off}). The kinetic K_D values were calculated using the formula: $K_D = k_{off}/k_{on}$. Data from the displacement assays are presented as mean ± S.E.M. of three independent experiments performed in duplicate. Within parentheses, the K_i in nM is shown.

5.8.4. Functional selectivity studies

FM10 and **GR106** were evaluated for their CB2R functional selectivity by assessing their ability to inhibit cAMP production via $G_{\alpha i}$ signaling and to promote β-arrestin-2 recruitment (Table 5.4, Figure 5.9).

In both assays, the two compounds preserved the functional profiles of their corresponding lead compounds. **FM10** behaved as a CB2R full agonist in both pathways, similarly to **FI8** [513], whereas **GR106** was confirmed as an inverse agonist in the cAMP assay and as an antagonist in the β-arrestin2 recruitment assay, consistently to what observed for the corresponding lead compound **GR75** [515]. Therefore, both ligands were CB2R unbiased ligands since able to activate or block the two studied CB2R pathways (cAMP and β-arrestin2 recruitment).

A detailed analysis revealed that the full agonist profile of **FM10** is comparable to that of **FI8** in terms of efficacy, with similar E_{max} values in both assays (107% vs 95% in the cAMP assay and 97% vs 92% in the β-arrestin2 recruitment assay for **FM10** and **FI8** [513], respectively).

Notably, **FM10** displayed an improved potency in comparison to to its lead compound **FI8**, with a pEC_{50} values of 8.10 in the cAMP assay and 7.84 in the β-arrestin2 assay, compared to 7.67 and 7.29 for **FI8** [513]. This corresponds to an approximately three-fold increase in potency, which could be due to the higher CB2R affinity of **FM10** for the CB2R with respect to **FI8**.

In the case of **GR106**, the compound exhibited a reduced inverse agonist efficacy in the cAMP inhibition assay compared to **GR75** (E_{max} −57% vs −77%) [515]. As observed for **FM10**, this increase in potency may be attributed to enhanced receptor affinity. Despite these differences in efficacy and potency in the cAMP pathway, **GR106** and **GR75** displayed indistinguishable antagonist profiles in the β-arrestin2 recruitment assay, indicating that the introduction of a fluorine atom on the pentyl chain does not significantly affect this signalling route.

Overall, the data clearly indicate that the introduction of a second phenyl ring induces a marked shift in functional activity, converting full agonists (**FI8** and **FM10**) into inverse agonist/antagonist ligands (**GR75** and **GR106**), in agreement with our previous findings [515].

In both chemical series, fluorination of the pentyl chain does not alter the qualitative activity profile but modulates its magnitude. This observation suggests that the pentyl chain occupies a receptor region that is not critically involved in receptor activation or blockade. Consistently, fluorine substitution does not induce a signalling bias between $G_{\alpha i}$-mediated cAMP inhibition and β-arrestin2 recruitment.

Thus, **FM10** and **GR106**, although belonging to the same structural class, display markedly different functional activity profiles at the CB2R, in line with the W258 interaction of the latter compound that confers a CB2R antagonist profile. Radiolabeling these two compounds and performing subsequent autoradiographic studies would therefore provide a unique opportunity to investigate, for the first time, whether structurally closely related CB2R ligands with opposing functional activities exhibit distinct diagnostic behaviours toward CB2R.

Table 5.4. CB2R activity profile.

Compounds	cAMP signaling			β-arrestin2 recruitment		
	pEC_{50} ± SEM	E_{max} ± SEM (%)	Activity profile	pEC_{50} ± SEM	E_{max} ± SEM (%)	Activity profile
CP55,940[a]	9.07 ± 0.14	98 ± 3	Full agonist	8.65 ± 0.07	102 ± 1	Full agonist
FM10	8.10 ± 0.09	107 ± 9	Full agonist	7.84 ± 0.08	97 ± 5	Full agonist
GR106	6.04 ± 0.39	-57 ± 15	Inverse agonist	N.d.	4.0 ± 0	Antagonist
FI8[b]	7.67 ± 0.09	95 ± 5	Full agonist	7.29 ± 0.05	92 ± 2	Full agonist
GR75[c]	5.84 ± 0.23	-77 ± 22	Inverse agonist	N.d.	3.0 ± 2	Antagonist

[a]Previously published data for reference [517]. [b]Data from ref [513]. [c]Data from ref [515]. N.d. = Not determinate. cAMP signaling and β-arrestin2 recruitment data represent pEC_{50} and E_{max} values ± SEM of three independent experiments performed in duplicate. The E_{max} values are normalized to the effect of 1 μM CP55,940. For both experiment, the activity profile is reported in the last column of table.

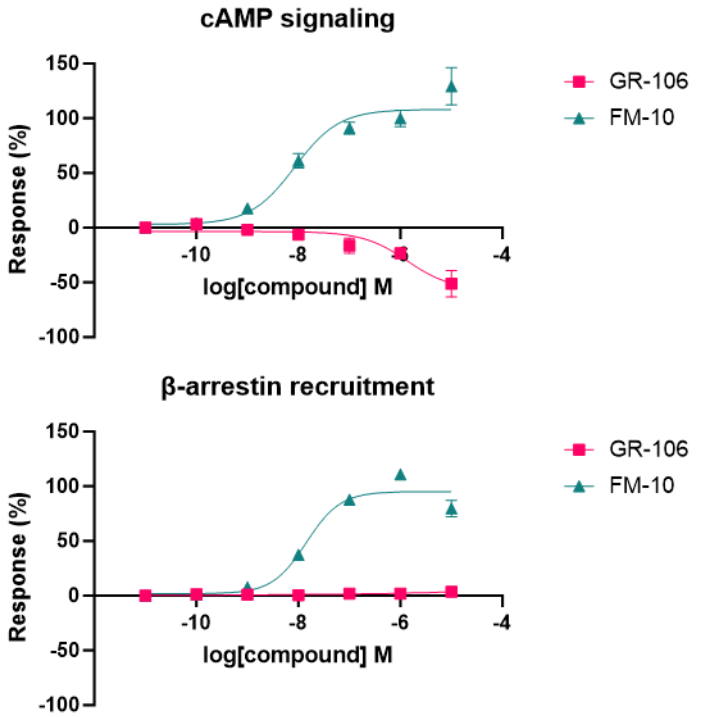

Figure 5.9. cAMP signaling and β-arrestin2 recruitment data represent mean ± SEM of three independent experiments performed in duplicate. The maximum response is normalized to the effect of 1 μM CP55,940.

5.8.5. Blood-Brain-Barrier permeability and P-Glycoprotein Interaction Investigation

To assess the suitability of **FM10** and **GR106** for brain imaging applications, their interaction with P-gp, the major efflux transporter at the BBB level [334], as well as their in vitro BBB permeability profiles, were investigated (Table 5.5).

P-gp interaction was evaluated in cell lines overexpressing the transporter using as probe the P-gp substrate, calcein-AM, and evaluating the ability of each compound to inhibit it transport P-gp-mediated.

Both **FM10** and **GR106** showed moderate/very low interaction with the pump, showing an EC_{50} of 14.8 μM and 50 μM, for **FM10** and **GR106**, respectively. Notably, the introduction of a fluorine atom on the pentyl chain in **FM10**, significantly enhances the interaction with P-gp in comparison with the parent compound **FI8** (EC_{50} > 100 μM) [513].

The permeability assay was assessed using Caco-2 cell monolayer to evaluate transcellular transport via passive diffusion (basolateral-to-apical, BA, flux) and active efflux mediated by P-gp (apical-to-basolateral, AB, flux). Both compounds exhibited moderate passive diffusion (BA permeability), with higher values observed for **GR106** compared to **FM10** (537 vs 353 nm/s, respectively), whereas AB transport was markedly lower (50 nm/s for **FM10** and negligible for **GR106**), consistent with active efflux at the apical membrane. The resulting BA/AB ratios (7 for **FM10** and 20 for **GR106**) indicate that passive diffusion is the predominant transport mechanism although some influence of efflux processes cannot be excluded.

It should be noted that the apparent permeability coefficients (P_{app}) may be affected by the high lipophilicity of these compounds, particularly in the case of **GR106**, which may promote non-specific binding to the cellular membranes and lead to an underestimation of true permeability. Consequently, the in vivo BBB permeability profile may differ from that observed *in vitro*.

Comparison between **FM10** and **FI8** [513] further reveals that fluorination of the pentyl chain substantially reduces both passive diffusion from the BA side (approximately 7-fold decrease for **FM10**) and transport in the AB direction (approximately 9-fold decrease), indicating a significant impact of this modification on membrane transport properties.

Overall, despite moderate/low interaction with P-gp, both **FM10** and **GR106** are expected to retain at least partial ability to cross the BBB, supporting their potential applicability as brain imaging agents.

Table 5.5. Evaluation of the BBB permeability and P-gp interaction.

Compound	P_{app}BA (nm/sec)	P_{app}AB (nm/sec)	P_{app}(BA/AB)	P-gp activity (EC_{50}, μM)
Verapamil[a]	687	591	1.2	0.55
FM10	353	50	7	14.8
GR106	537	0	20	50
FI8[b]	2456	467	5.25	>100

[a]Previously published data for reference [397]. [b]Data from ref [513].

5.8.6. Computational studies

Docking studies were performed to support the experimental data and to further rationalize why **FM10** and **GR106**, despite their structural similarity, display distinct activity profiles.

Figures 5.10.A and 5.9.B illustrate the top-scoring docking poses obtained for **FM10** and **GR106** within the binding cavity of the protein complexed with an agonist and antagonist, respectively.

FM10 adopts a pose consistent with its agonist activity; the molecular recognition aligns with the conformation of residue W258, which, based on available crystallographic data, is essential for receptor activation. The interactions are predominantly hydrophobic, and the binding is driven by shape complementarity. The energetic profile also supports its agonist behavior, yielding a docking score of –9.580 kcal/mol in the agonist-bound crystal structure, compared to –8.422 kcal/mol in the antagonist-bound structure, which features a cavity typically associated with antagonist recognition.

Conversely, and in agreement with the experimental data, **GR106** shows a preference for the pose obtained in the antagonist-bound crystal structure (docking score: –10.010 kcal/mol – Figure 5.10.B) over the agonist-bound one (docking score: –8.120 kcal/mol). Notably, its alkyl chain extends into a region of the cavity that is formed only through a conformational rearrangement of W258, a configuration that, according to current literature, is incompatible with receptor activation.

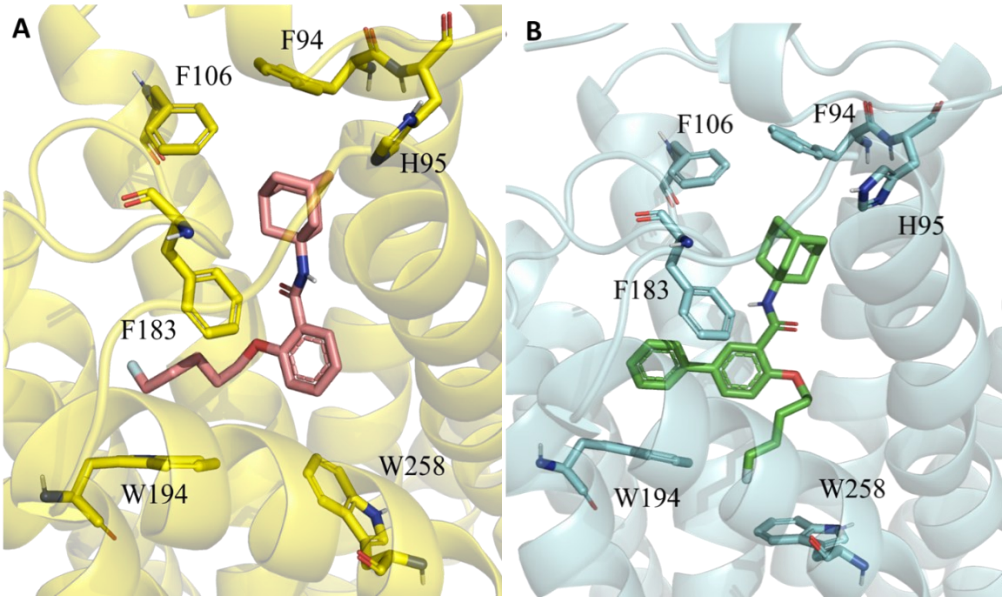

Figure 5.10. Top-scored docking poses returned by docking simulations performed on compounds **FM10** and **GR106** in the CB2R agonist crystal structure (**A**, **FM10** in red, PDB: 6KPC) and in the CB2R antagonist crystal structure (**B**, **GR106** in green; PDB: 5ZTY).

5.8.7. Radiochemistry

Based on their binding affinity and divergent pharmacological profiles despite belonging to the same structural class, **FM10** and **GR106** were identified as the most suitable candidates for the development of novel CB2R radioligands. Consequently, they were selected for further biological evaluation.

The synthesis of the tosylated precursors **32** and **33** was achieved following analogous procedures, starting from compounds **22** [510] and **23** [515], respectively (Scheme 5.1). In the first step, compounds **22** and **23** underwent alkylation with 5-bromopentan-1-ol, affording intermediates **29** and **30**. The latter was then subjected to a Suzuki–Miyaura coupling with phenylboronic acid, following previously reported

conditions, to yield **31**. Conversion of both **29** and **31** into the corresponding tosylates using TsCl afforded the key intermediates **32** and **33**, which served as precursors for radiolabeling.

The radiosynthesis of **[^{18}F]FM10** and **[^{18}F]GR106** was optimized using a kryptofix-based complex (10 mg $K_{2.2.2}$, 15 µL K_2CO_3 solution at 20 mg/mL, 200 µL H_2O, and 800 µL CH_3CN), activated by microwave (MW) heating. For **[^{18}F]FM10**, the tosylated precursor **32** (1–2 mg) was tested under thermal conditions in different solvents: CH_3CN (90 °C), DMSO (130 °C), and DMF (130 °C). Radio-HPLC analysis revealed radiochemical conversions (RCC) of 75-94% in CH_3CN, 14% in DMSO and 70% in DMF (non-isolated). For **[^{18}F]GR106**, precursor **33** (1–2 mg) only CH_3CN was tested as solvent using 90 °C, yielding approximately 79-95% (non-isolated). In both cases, additional confirmation of labeling efficiency was obtained by radio-TLC (*n*-Ex/AcOEt, 7:3).

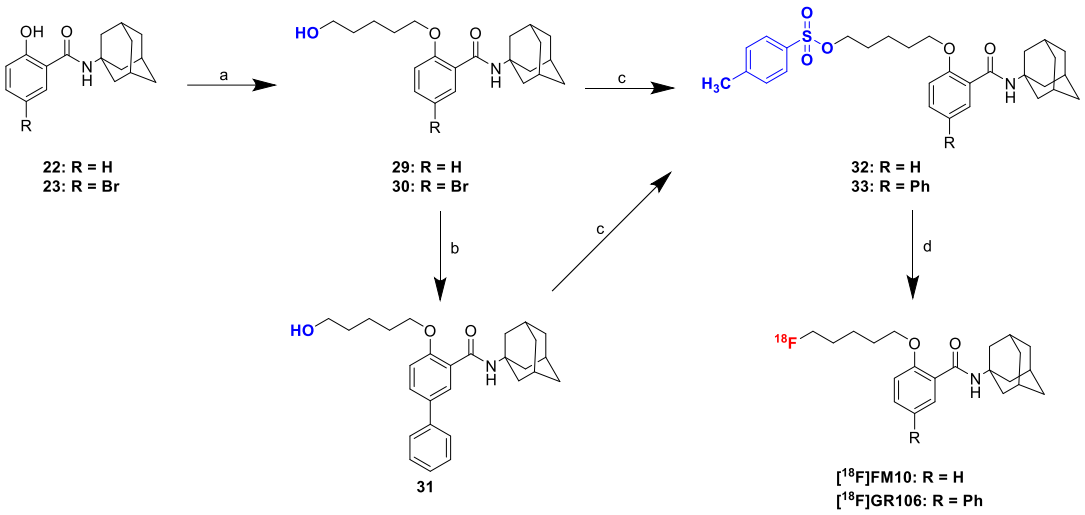

Scheme 5.2. Synthesis of tosylate precursor **32** and **33** and radiofluorination of final compounds **[^{18}F]FM10** and **[^{18}F]GR106**: (a) 5-bromopentan-1-ol, K_2CO_3, acetone, reflux, 4h; (b) Compound **31**, phenylboronic acid, $Pd(PPh_3)_4$, dioxane/K_2CO_3 (2M), reflux, 4h; (c) TsCl, Et_3N, dry CH_2Cl_2, 0 °C, 4h; (d) [^{18}F]K_{222}/K_2CO_3, CH_3CN, 90 °C, 10 min

The optimized methodology was subsequently transferred to an automated radiosynthesizer (SynChrom R&D from Elysia-Raytest GmbH, Hamburg, Germany Figure S5.2). In the final automated protocol, 1 mg of compound **32** or 2 mg of compound **33** dissolved in CH_3CN was reacted with the ^{18}F-kryptofix complex at 90 °C for 10 min. The reaction mixture was quenched by the addition of 4.1 mL of CH_3CN/H_2O (1:1), and the crude product was purified by HPLC (retention times ~21–22 min for **[^{18}F]FM10** and ~24–25 min for **[^{18}F]GR106**, Figure S5.3 and Figure S5.4, respectively). Product-containing fractions were collected and concentrated on preconditioned RP-SPE cartridges, followed by elution with 1.2 mL absolute ethanol.

For subsequent biological studies, ethanol was removed under a gentle stream of Argon at 70 °C, and the final product was formulated using 10% EtOH saline solution.

The overall synthesis time was approximately 86 min for both **[^{18}F]FM10** and **[^{18}F]GR106**. **[^{18}F]FM10** was obtained in 32–35% decay-corrected radiochemical yield and **[^{18}F]GR106** in 7-17% (RCY, based on end of bombardment). Both compounds have been obtained with radiochemical purity >99% and high molar activity calculated at the end of the synthesis (79-81 GBq/µmol for **[^{18}F]FM10**, $n = 2$ and 45-61 GBq/µmol for **[^{18}F]GR106**, $n = 2$). Product identity was confirmed by analytical HPLC through co-injection with the non-radioactive reference standard using iscoratic method of elution (Figure 5.11).

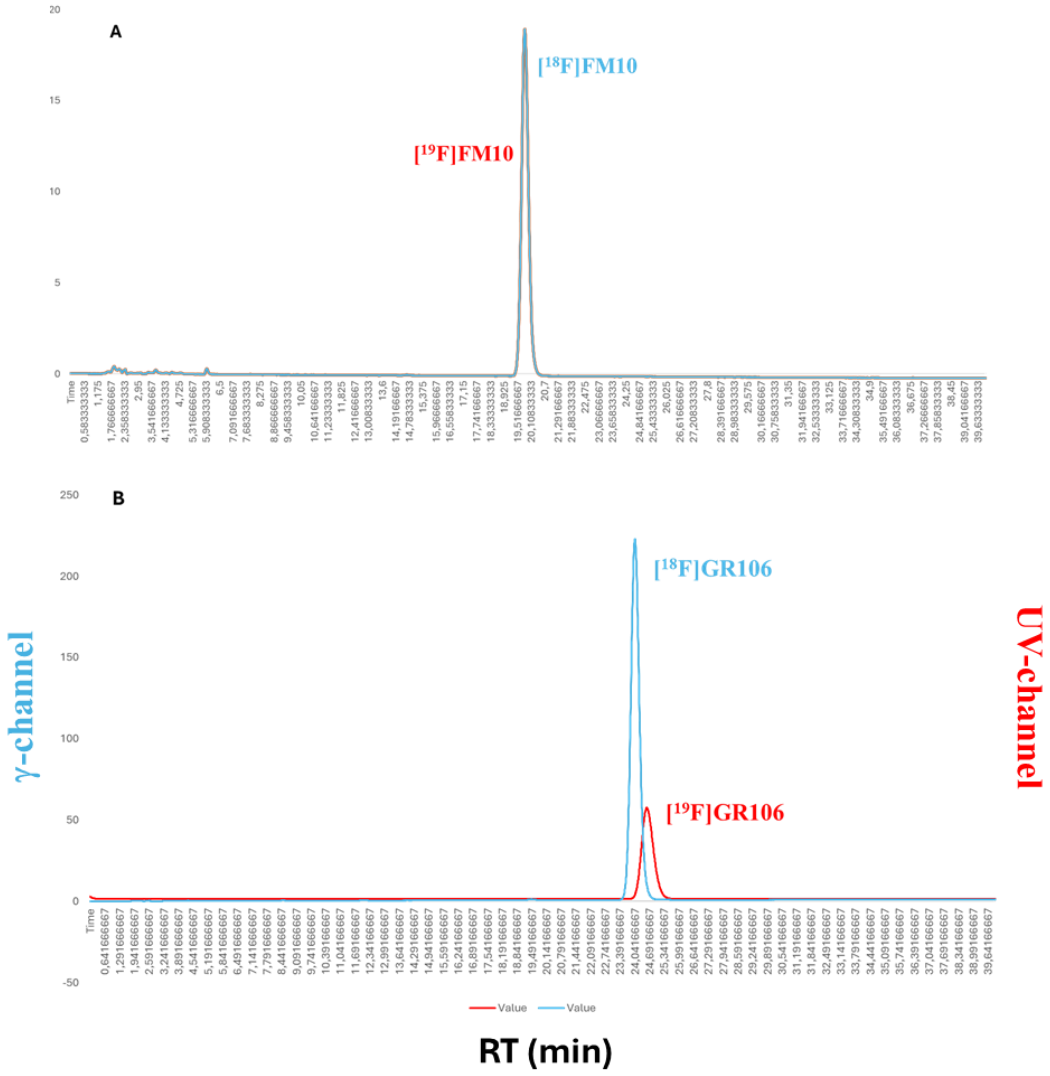

Figure 5.11. Radio- (light blue line) and UV- (red line) HPLC chromatograms of the identity confirmation of **[^{18}F]FM10** (**A**) or **[^{18}F]GR106** (**B**) co-injected with the reference standard **FM10** or **GR106** (Reprosil-Pur C_{18}-Aq, 10 mm, 250 x 10 mm column from Dr. Maisch GmbH). An isocratic elution method was used for both compounds. The mobile phase was composed of 70% MeCN/20 mM NH_4OAc (aq) for **[^{18}F]FM10** (**A**) and 80% MeCN/20 mM NH_4OAc (aq) for **[^{18}F]GR106** (**B**), with a flow rate of 1 mL/min. UV detection was carried out at 286 nm for **[^{18}F]FM10** and 260 nm for **[^{18}F]GR106**.

5.8.8. *In Vitro* Evaluation of [^{18}F]FM10 and [^{18}F]GR106

5.8.8.1. Experimental determination of lipofilicity

The lipophilicity of **[^{18}F]FM10** and **[^{18}F]GR106** at physiological pH was experimentally determined using the shake-flask method [77], yielding $logD_{7.4}$ values of 3.41 ± 0.15 and 3.64 ± 0.12 (n = 4), respectively. For both compounds, the experimentally determined $logD_{7.4}$ values were markedly lower than those predicted by computational methods (cLogP = 5.04 with ChemDraw and 4.72 with SwissADME for **FM10**; cLogP = 6.93 with ChemDraw and 6.05 with SwissADME for **GR106**). The measured $logD_{7.4}$ values fall outside the recommended range (1.5–3.0) for central nervous system–oriented radiotracers [77]. However, *in vivo* studies are required to determine whether these compounds are capable of crossing the BBB.

5.8.8.2. Experimental determination of K_D

A K_D of 1.7 nM for **[^{18}F]FM10** (63 GBq/µmol, 3.7 nM at start of the binding experiment) to the *h*CB2R was determined by a homologous competition assay using crude cell homogenates of CHO(hCB2) (Figure 5.12.A). An optimized formulation of **[^{18}F]FM10** in a 2:1 DMSO:Kolliphor EL solution was used to reduce the unspecific binding due to an precipitation of the radiotracer at higher concentrations of the reference compound (< 10^{-7} M). The homologous competition assay for [^{18}F]**GR106** (41.2 GBq/µmol, 1.8nM at start of the binding experiment) showed low CB2R-specific binding of the radiotracer and needs further optimization (Figure 5.12.B).

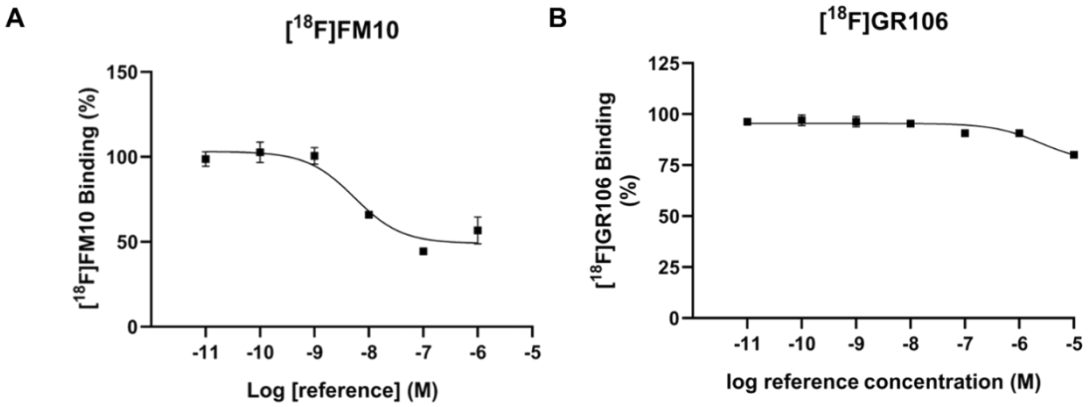

Figure 5.12. Determination of the binding affinity and specifity of **[^{18}F]FM10** (**A**) and **[^{18}F]GR106** (**B**) to human and rat CB2R (preliminary results). Homologous competition assays using crude cell membrane extracts of CHO(hCB2R) cells for the determination of the dissociation constant (K_D = 1.7 nM for **[^{18}F]FM10**) determined by the Cheng-Prussoff equation integrated into GraühPag Prism software.

5.8.8.3. *In Vitro* Metabolism

Both **[^{18}F]FM10** and **[^{18}F]GR106** were incubated with MLMs in PBS in the presence of NADPH for 30 min at 37 °C under gentle shaking at 350 rpm (*n = 2*), following a previously published protocol [337,501]. The samples were subjected to protein precipitation by the addition of ice-cold CH_3CN, followed by vortex mixing and centrifugation. The resulting supernatants were collected at five time points (0–30 min) and analyzed by radio-HPLC (Figure 5.13). The recovery of radioactivity after protein precipitation was determined using a gamma counter and was found to be 99% for **[^{18}F]FM10** and 97% for **[^{18}F]GR106**. The validity of the assay was verified by observing complete conversion of testosterone under identical conditions. Control experiments lacking either NADPH or both NADPH and MLM were also carried out for each test compound. After 30 min of incubation, less than 1% of the parent compound remained for **[^{18}F]FM10** and only 14% for **[^{18}F]GR106**. The *in vitro* half-life ($t_{1/2}$) was determined to be ≤ 0.68 ± 0.02 min for **[^{18}F]FM10** and 9.2 ± 0.1 min for **[^{18}F]GR106**, indicating that **[^{18}F]GR106** is more metabolically stable than **[^{18}F]FM10** over the 30 min incubation period. Nevertheless, both compounds exhibited poor metabolic stability, with **[^{18}F]FM10** showing particularly rapid *in vitro* metabolism.

After 30 min of incubation, **[^{18}F]FM10** produced three main metabolites (**[^{18}F]M1**, Rt = 0.998 min, 16%; **[^{18}F]M2**, Rt = 5.348 min, 25%; **[^{18}F]M3**, Rt = 5.849 min, 30%), whereas **[^{18}F]GR106** generated two main metabolites (**[^{18}F]M4**, Rt = 1.108 min, 39%; **[^{18}F]M5**, Rt = 5.950 min, 16%). In both cases, a highly polar metabolite (**[^{18}F]M1** and **[^{18}F]M4**) was observed, which was hypothesized to correspond to free

[^{18}F]fluoride. To investigate this hypothesis, radio-TLC analysis (MeOH / AcOEt / aqAcNH$_4$ (20 mM) 1:1:1) was performed using a reference spot of [^{18}F]fluoride (Figure S5.5). Under these conditions, [^{18}F]fluoride, **[^{18}F]M1**, and **[^{18}F]M4** exhibited identical retention factor (R_f) values. Furthermore, the relative percentages of these metabolites determined by radio-TLC and radio-HPLC were in good agreement (17% vs 16%, respectively, for **[^{18}F]M1**, and 36% vs 39%, respectively, for **[^{18}F]M4**). These results strongly suggest that the major polar metabolite observed for both radiotracers corresponds to free [^{18}F]fluoride, which represents the predominant metabolite for **[^{18}F]GR106**.

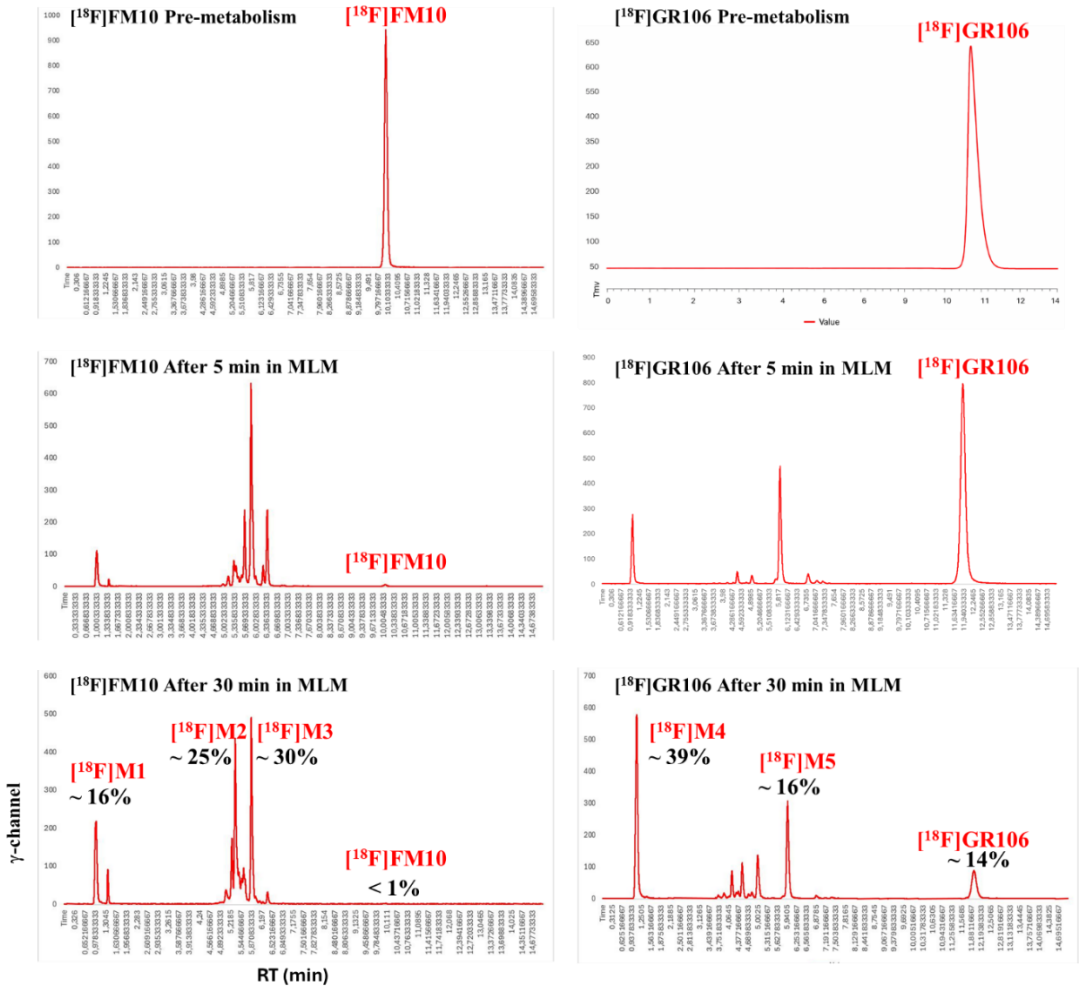

Figure 5.13. Radio-HPLC chromatograms (ReproSil-Pur 120 C$_{18}$-AQ, 3 µm, 150 × 3 mm; Dr. Maisch GmbH) of **[^{18}F]FM10** (left panel) and **[^{18}F]GR106** (right panel). From top to bottom: before metabolic studies, after 5 min incubation in MLM, and after 30 min incubation in MLM. After 30 min, less than 1% of unchanged **[^{18}F]FM10** and approximately 14% of unchanged **[^{18}F]GR106** remained. For both compounds, the same gradient program was applied: isocratic elution at 5% CH$_3$CN from 0 to 1.5 min, followed by a linear gradient from 5% to 80% CH$_3$CN between 1.5 and 10.0 min, isocratic elution at 80% CH$_3$CN from 10.1 to 12.0 min, and re-equilibration at 5% CH$_3$CN from 12.1 to 15.0 min. The Rt were 10.0 min for **[^{18}F]FM10** and 11.9 min for **[^{18}F]GR106**.

5.8.8.4. *In vitro* autoradiography

In order to validate the CB2R-specific binding, cryo sections (10 µm) of rodent spleen were used as a positive control tissue for *in vitro* autoradiography studies. To compare the signal intensity of bound radiotracers, both in the absence of and co-incubation with the reference compounds and target-specific inhibitors in competition studies were used (Figure 5.14). In particular, SR144528 CB2R is an inverse agonist, with a K_i value of 0.6 nM and a selectivity of approximately 700-fold over CB1R (K_i = 400 nM) [518] and SR141716A functions as an CB1R inervs agonist (K_i = 2 nM) and a selectivity ratio of approximately 1000-fold over CB2R [519].

It is noteworthy that a higher concentration of **FM10** (greater than 10^{-7} M) without being dissolved in Kolliphor El resulted in an increased binding signal in homologous competition studies (data not shown). This phenomenon is further substantiated by the enhanced binding signal observed in micrographs using 10^{-6} M **FM10** (Figure 5.14.A). In the event of aggregation, there is a possibility of precipitation and binding of the radiotracer-reference compound precipitates in an unspecific manner. It should be noted that, owing to the fact that the detergent was not included in the preliminary autoradiography studies presented herein, these experiments require validation under optimal conditions. However, a decrease of approximately 30 % in signal observed in the competition assay with SR144528, and the comparable signal detected in the competition assay with SR141716A (approximately -7 %), estimate a CB2R-specific binding of **[^{18}F]FM10**.

Although, in preliminary homologous binding assay a low specific binding **of [^{18}F]GR106** towards the human CB2R was found, a signal intensity reduction by 25 % in the homologous competition on rat spleen cryosections could be determined, whereas the signal intensity reduction in competition assays with SR144528 and S141716A approximately 15% (Figure 5.14.B).

Based on the current autoradiographic data, **[^{18}F]FM10** displays a binding pattern more consistent with a CB2R-specific component, whereas **[^{18}F]GR106** exhibits a comparatively lower or less clearly distinguishable specific binding under the present experimental conditions.

These differences may relate to their distinct intrinsic activities (**FM10** is a full agonist and **GR106** is an inverse agonist/antagonist; Table 5.4), potentially reflecting differential stabilization of receptor conformations and consequent variations in the detectable receptor-bound fraction. However, methodological limitations, particularly the absence of detergent in the incubation buffer and the potential for compound aggregation or nonspecific deposition, preclude a definitive attribution of these differences solely to pharmacological properties.

Further optimization of the *in vitro* evaluation protocol, including improved control of nonspecific binding, will be required to substantiate these preliminary findings and clarify the contribution of intrinsic activity to CB2R-specific binding.

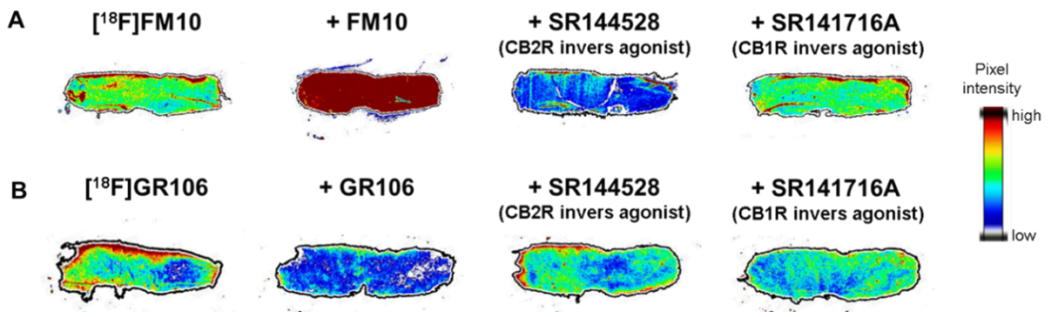

Figure 5.14. Autoradiographic micrographs of 4 µm rat spleen cryosections incubated with radiotracer **[^{18}F]FM10** (**A**) or **[^{18}F]GR106** (**B**) alone or with the indicated competitors.

5.9. Discussion

With the aim of developing new PET radiotracers for cerebral CB2R imaging, primarily under pathological conditions, a novel series of *N*-adamantyl-salicylamide derivatives was synthesized starting from three lead compounds: the CB2R agonists **CC48** and **FI8** [510,513] and the CB2R antagonist **GR75** [515].

Based on the aforementioned lead compounds, one or more fluorine atoms were introduced at different positions to improve both pharmacodynamics (enhancing CB2R selectivity towards the CB1R subtype in comparison to the lead compounds **CC48** and **FI8**) and to facilitate an efficient and straightforward radiolabeling process. The series of these new fluorinated salicylamides remains highly promising, as all compounds exhibited nanomolar (and in some case sub-nanomolar) affinity for the CB2R along with varying degrees of selectivity over the CB1R. Efforts were also made to reduce lipophilicity by replacing the aromatic ring with a pyridinyl ring or introducing an *O*-atom into the pentyl chain. However, these modifications led to decreased affinity, rendering them unsuitable for PET imaging.

Among the synthesized compounds, **FM10** and **GR106** emerged as the most promising candidates, showing high affinity for the CB2R (K_i = 5.2 nM for **FM10** and K_i = 1.1 nM for **GR106**) and strong selectivity over the CB1R, as well as the presence of a fluorine atom in a molecular region easily accessible for radiolabeling. Both compounds demonstrated moderate interaction with P-gp, suggesting their potential capability to cross the BBB.

For both ligands, kinetic parameters were evaluated, revealing rapid receptor binding and residence times of 2.73 min for **FM10** and 9.00 min for **GR106**. Functional activity profiles were assessed using two complementary assays: inhibition of cAMP production via Gαi signaling and promotion of β-arrestin-2 recruitment. **FM10** acted as CB2R full unbiased agonist, whereas **GR106** behaved as a CB2R agonist/inverse antagonist, consistently with our previous results [515]. Experimental data were further supported by molecular docking studies. **FM10** adopted a binding pose consistent with its agonist activity, with docking scores corroborating this behavior (DS = -9.580 kcal/mol in the agonist-bound crystal structure). **GR106** preferentially adopted the pose observed in the antagonist-bound crystal structure (DS = -10.010 kcal/mol). The key difference between the two ligands lies in the orientation of the alkyl chain relative to residue W258, which plays a crucial role in receptor activation.

Based on these findings, **FM10** and **GR106** were selected for ^{18}F radiolabeling, as labeling two structurally similar compounds with opposing functional profiles offers a unique opportunity to investigate, for the first time, whether closely related ligands with divergent activity exhibit distinct diagnostic behaviors toward CB2R. To date, no PET radiotracers for CB2R belonging to the same structural class with opposing activities are reported in the literature.

For both compounds, the tosylate was selected as the leaving group, and radiolabeling was successfully performed in CH_3CN at 90 °C for 10 min using a kryptofix-complex as catalyst. Both radiotracers were obtained with good RCY and A_m, and radiochemical purity exceeded 99%.

Experimental $logD_{7.4}$ values were determined (3.41 ± 0.15 for **[^{18}F]FM10** and 3.64 ± 0.12 for **[^{18}F]GR106**), supporting their BBB permeability. For **[^{18}F]FM10**, the K_D was determined to be 1.7 nM, confirming its high affinity at CB2R, which is very similar to the *in vitro* K_i of the cold compound. For **[^{18}F]GR106**, K_D has not yet been determined, as experimental protocols are still being optimized.

Preliminary *in vitro* autoradiography experiments on rat spleen slices are ongoing. Preliminary results indicate that **[^{18}F]FM10** exhibits higher CB2R-specific binding compared to **[^{18}F]GR106**. Specifically

[^{18}F]FM10 shows approximately 30% signal reduction in the presence of a selective CB2R blocker, whereas **[^{18}F]GR106** shows a modest decrease. These differences may be related to the ligands' intrinsic activity (full agonist vs inverse agonist/antagonist), potentially reflecting differential stabilization of receptor conformational states. However, experimental challenges, particularly in sample formulation, represent significant methodological limitations that prevent definitive attribution of the observed differences solely to pharmacological properties. Further experimental optimization is therefore necessary to confirm the actual extent of specific CB2R binding.

In vitro metabolism studies using rat liver microsomes have revealed poor metabolic stability after 30 min incubation for both compounds (1% of parent radiotracer intact for **[^{18}F]FM10** and 14% for **[^{18}F]FM10**). The retention times of two metabolites (**[^{18}F]M1** and **[^{18}F]M4**, respectively), together with TLC confirmation using [^{18}F]fluoride, indicate that a possible metabolic pathway is defluorination, which appears to be the main route for **[^{18}F]GR106**.

5.10. Future perspectives

Future perspectives will likely depend on the definitive *in vitro* autoradiography results. If these results are promising, the goal will be to evaluate both radiotracers *in vivo*, particularly to assess whether differing activity profiles affect PET imaging, and to verify whether poor metabolic stability is confirmed. If low *in vivo* metabolic stability is observed, a potential strategy could involve substituting the pentyl chain with the corresponding deuterated chain, a strategy widely employed for PET radiotracers targeting CB2R in the literature. This approach may reduce defluorination, the primary metabolic pathway for both radiotracers, particularly for **[^{18}F]GR106**.

Among the compounds developed, in addition to the two PET candidates, other compounds (**FM13**, **FM15**, **FM24**, and **FM26**, Table 5.2) displayed high affinity and selectivity but were not selected for radiolabeling for various reasons.

The cytotoxic effects of these compounds were evaluated using the MTT assay in different cell lines (HGC27-S, HGC27-R, HMC-3, PANC-1, and MCF-7 wt) at multiple time points (24, 48, and 72 h). Overall, the data indicate a clear time- and cell line-dependent response for all four compounds. At 24 h, the activity was generally modest in HGC27-S and HGC27-R cells, with reductions in cell viability mainly observed only at the highest tested concentration (100 μM), while the effect in HMC-3 cells was limited or absent (e.g., **FM13** showed no cytotoxicity). After 48 h, an increase in antiproliferative activity became evident, particularly for **FM15** and **FM24** in HGC27-S/R cells ($IC_{50} \approx 25–30$ μM), and for **FM24** and **FM26** in PANC-1 cells (IC_{50} = 9.3 μM and 4.3 μM, respectively), suggesting a higher sensitivity of this cell line. At 72 h, the effect was further enhanced for some compounds (e.g., **FM15** in MCF-7 cells, IC_{50} = 27 μM), whereas others maintained moderate activity (e.g., **FM26** in HGC27-S cells, $IC_{50} > 70$ μM).

Overall, **FM15** and **FM24** exhibited the most consistent and progressive cytotoxic profile over time in gastric tumor cell lines, while **FM26** demonstrated marked selective activity in PANC-1 cells. The low toxicity observed in HMC-3 cells suggests a potentially favorable therapeutic window.

Detailed data are not presented here, as the experiments are still ongoing and the therapeutic implications of these compounds fall beyond the scope of this thesis. Nevertheless, their excellent affinity and selectivity, together with the preliminary cytotoxicity findings, support further investigation of these molecules as potential anticancer or neuroprotective agents

5.11. Conclusions

[^{18}F]FM10 and **[^{18}F]GR106** are two novel CB2R PET radiotracers belonging to the *N*-adamantyl-salicylamide class. They exhibit high affinity and exceptional selectivity for CB2R towards the CB1R subtype, along with different functional profiles, making them unique within this class. Their moderate interaction with P-gp, together with favorable $logD_{7.4}$ values, suggests potential CNS penetration. *In vitro* autoradiography is still at a preliminary stage; thus, subsequent *in vivo* evaluation has not started yet.

5.12. Materials and Methods

5.12.1. Chemistry

All chemicals were purchased from Sigma-Aldrich, TCI Chemicals, Ambeed, or Angene. Thin layer chromatography (TLC) was performed using plates from Merck (silica gel 60 F_{254}). Column chromatography was performed with Merck silica gel 60 Å (63-200 mm; ratio of crude mixture to silica gel 1:30 w/w, unless otherwise stated) as the stationary phase. Melting points (mp) were determined with a capillary apparatus (Büchi 540). ^{1}H-NMR spectra were recorded in the indicated solvent on a Varian Mercury-VX spectrometer (300 MHz) or on an Agilent 500-vnmrs500 spectrometer (499.801MHz). The following data are reported: chemical shift (δ) in ppm, multiplicity (s = singlet, d = doublet, t = triplet, q = quartet, quint = quintet, m = multiplet, dd = doublet of doublets, dt = doublet of triplets, td = triplet of doublets, and br = broad signal), integration, and coupling constant (J) in hertz. Recording of mass spectra was done on an HP6890-5973 MSD gas chromatograph/mass spectrometer; only significant m/z peaks, with their percentage of relative intensity in parentheses, are reported. HRMS-ESI analyses were performed on a Bruker Daltonics MicrOTOF-Q II mass spectrometer. All spectra were in accordance with the assigned structures. The purity of target compounds was assessed by HPLC. Analytical HPLC analyses were performed on final compounds using a Thermo Fisher Scientific Vanquish HPLC with Thermo Fischer Scientific Accucore aQ Column, 2.6 µm, 2.1 X 100 mm at a flow rate of 0.4 mL/min. Isocratic elution of the compounds **5-21** was carried out with 20:80 (v/v) H_2O/MeOH. UV signals were detected at 254 nm and 280 nm. All compounds are >95% pure by HPLC.

*General procedure for the synthesis of amides **22-25**.* One of the appropriate carboxylic acids (1.0 mmol, 1.0 eq) was dissolved in dry DMF (5 mL), DIPEA (3.0 mmol, 3.0 eq) was added at 0° C, and the solution was stirred at 0°C for 10 min under inert atmosphere. HBTU (1.5 mmol, 1.5 eq) was added to the solution and the reaction mixture was stirred at room temperature for 2 h. 1-Adamantanamine (1.5 mmol, 1.5 eq) was added to the solution and the mixture was stirred at room temperature for 18 h under inert atmosphere. The solvent was removed under vacuum. The residue was taken up with H_2O (20 mL) and extracted with CH_2Cl_2 (3 x 20 mL). The collected organic layers were dried (Na_2SO_4) and evaporated under vacuum to afford a crude residue which was purified by column chromatography to afford the relative adamantylamide.

*N-((3s,5s,7s)-adamantan-1-yl)-2-hydroxybenzamide (**22**)* [510].

*N-((3s,5s,7s)-adamantan-1-yl)-5-bromo-2-hydroxybenzamide (**23**)* [515].

*N-((3s,5s,7s)-adamantan-1-yl)-5-fluoro-2-hydroxybenzamide (**24**).* The crude residue was purified by column chromatography using n-Ex/AcOEt 8:2 to obtain a white solid. Yield, 60%. ^{1}H-NMR ($CDCl_3$, 500 MHz) δ: 1.71-1.76 (6H, m, Ad), 2.09-2.13 (6H, m, Ad), 2.15 (3H, br s, Ad), 5.81 (1H, br s), 6.91 (1H, dd, J_1 = 9.0 Hz, J_2 = 4.5 Hz, Ar), 6.96 (1H, dd, J_F = 9.7 Hz, J = 3.4 Hz, Ar), 7.06-7.12 (1H, m, Ar), 12.13 (1H, br s). GC-MS m/z: 289 (M^+, 5), 135 (100).

*N-((3s,5s,7s)-adamantan-1-yl)-3-hydroxyisonicotinamide (**25**).* The crude residue was purified by column chromatography using AcOEt 100% to obtain a white solid. Yield, 50%. ^{1}H-NMR ($CDCl_3$, 500 MHz) δ: 1.72-1.74 (6H, m, Ad), 2.11-2.16 (9H, m, Ad), 6.10 (1H, br s), 7.10 (1H, d, J = 5.0 Hz), 8.12 (1H, d, J = 5.0 Hz, Ar), 8.42 (1H, s, Ar). GC-MS m/z: 272 (M^+, 5), 135 (100).

General procedure for the synthesis of compounds **FM10, 8-19**, **26-27** and **29-30**. To a solution of the appropriate phenol among compounds **22-25** (1 mol, 1 eq) in acetone (10 mL), K_2CO_3 (3 mol, 3 eq) and appropriate alkyl/aryl bromide (3 mol, 3 eq) are added. The resulting mixture was refluxed with stirring 4h and then was allowed to cool to room temperature. The solvent was removed under vacuum. The residue was taken up with H_2O (20 mL) and extracted with CH_2Cl_2 (3 x 20 mL). The combined organic layers were dried (Na_2SO_4) and evaporated under vacuum to afford a crude residue which was purified by column chromatography.

*N-((3s,5s,7s)-adamantan-1-yl)-2-((5-fluoropentyl)oxy)benzamide (**FM10**).* The crude residue was purified by column chromatography using n-Ex/AcOEt 8:2 to obtain a white solid. Yield, 75%. m.p. 80-82 °C. ^{1}H-NMR ($CDCl_3$, 300 MHz) δ: 1.60-1.65 (2H, m), 1.66-1.69 (6H, m, Ad), 1.76-1.94 (4H, m), 2.08-2.10 (9H, m, Ad), 4.07 (2H, t, J = 6.3 Hz), 4.45 (2H, dt, J_F = 47.4 Hz, J = 5.8 Hz), 6.88 (1H, d, J = 8.1 Hz), 6.98-7.03 (1H, m, Ar), 7.31-7.37 (1H, m, Ar), 7.82 (1H, br s), 8.13 (1H, dd, J_1 = 7.8 Hz, J_2 = 1.8 Hz, Ar) (The NMR spectrum is shown in Figure S5.6). HRMS-ESI for $C_{22}H_{30}FNO_2$ (m/z): $[M+Na]^+$ calcd, 382.2159; found, 382.2173; $[2M+Na]^+$ calcd, 741.4420; found, 741.4545; $[M-H]^-$ calcd, 358.2183; found, 358.2220. The HPLC chromatogram is shown in Figure S5.7.

*N-((3s,5s,7s)-adamantan-1-yl)-3-((5-fluoropentyl)oxy)isonicotinamide (**8**).* The crude residue was purified by column chromatography using CH_2Cl_2/AcOEt 1:1 to obtain a white solid. Yield, 46%. m.p. 105-107 °C. ^{1}H-NMR ($CDCl_3$, 500 MHz) δ: 1.65-1.70 (2H, m), 1.72-1.76 (6H, m, Ad), 1.77-1.86 (2H, m), 1.93-1.98 (2H, m), 2.11-2.15 (9H, m, Ad), 4.25 (2H, t, J = 6.0 Hz), 4.49 (2H, dt, J_F = 47.5 Hz, J = 5.7 Hz), 7.69 (1H, br s), 7.96 (1H, d, J = 4.5 Hz), 8.37 (1H, d, J = 5.0 Hz, Ar), 8.38 (1H, s, Ar). HRMS-ESI for $C_{21}H_{29}FN_2O_2$ (m/z): $[M+Na]^+$ calcd, 383.2111; found, 383.2112; $[2M+Na]^+$ calcd, 743.4324; found, 743.4331; $[M-H]^-$ calcd, 359.2133; found, 359.2148.

*N-((3r)-adamantan-1-yl)-2-((2-fluorobenzyl)oxy)benzamide (**9**).* The crude residue was purified by column chromatography using n-Ex/AcOEt 7:3 to obtain a white solid. Yield, 91%. m.p. 94-96 °C. ^{1}H-NMR ($CDCl_3$, 500 MHz) δ: 1.60-1.64 (6H, m, Ad), 1.89-1.90 (6H, m, Ad), 1.99 (3H, br s, Ad), 5.20 (2H, s) 7.05 (1H, d, J = 8.0 Hz, Ar), 7.09 (1H, td, J_1 = 7.7 Hz, J_2 = 1.0 Hz, Ar), 7.12-7.16 (1H, m, Ar), 7.20 (1H, td, J_1 = 7.5 Hz, J_2 = 1.0 Hz, Ar), 7.37-7.44 (2H, m), 7.49 (1H, td, J_1 = 7.5 Hz, J_2 = 1.5 Hz, Ar), 7.59 (1H, br s), 8.15 (1H, dd, J_1 = 7.7 Hz, J_2 = 1.7 Hz, Ar). HRMS-ESI for $C_{24}H_{26}FNO_2$ (m/z): $[M+Na]^+$ calcd, 402.1846; found, 402.1845; $[2M+Na]^+$ calcd, 781.3794; found, 781.3791; $[M-H]^-$ calcd, 378.1868; found, 378.1897.

*N-((3r)-adamantan-1-yl)-2-((3-fluorobenzyl)oxy)benzamide (**10**).* The crude residue was purified by column chromatography using n-Ex/AcOEt 7:3 to obtain a white solid. Yield, 98%. m.p. 135-137 °C. ^{1}H-NMR ($CDCl_3$, 500 MHz) δ: 1.62-1.67 (6H, m, Ad), 1.90-1.95 (6H, m, Ad), 2.01 (3H, br s, Ad), 5.12 (2H, s) 7.00 (1H, d, J = 8.5 Hz, Ar), 7.07-7.11 (2H, m, Ar), 7.20 (1H, d, J = 9.0 Hz, Ar), 7.24 (1H, d, J = 8.0 Hz, Ar), 7.38-7.43 (2H, m Ar), 7.56 (1H, br s), 8.16 (1H, dd, J_1 = 7.7 Hz, J_2 = 1.7 Hz, Ar). HRMS-ESI for $C_{24}H_{26}FNO_2$ (m/z): $[M+Na]^+$ calcd, 402.1846; found, 402.1841; $[2M+Na]^+$ calcd, 781.3794; found, 781.3795; $[M-H]^-$ calcd, 378.1868; found, 378.1880.

N-((3r)-adamantan-1-yl)-2-((4-fluorobenzyl)oxy)benzamide ***(11)***. The crude residue was purified by column chromatography using n-Ex/AcOEt 7:3 to obtain a white solid. Yield, 88%. m.p. 137-139 °C. ^{1}H-NMR ($CDCl_3$, 500 MHz) δ: 1.66-1.69 (6H, m, Ad), 1.86-1.87 (6H, m, Ad), 2.00 (3H, br s, Ad), 5.09 (2H, s) 7.02 (1H, dd, J_1 = 8.0 Hz, J_2 = 0.5 Hz, Ar), 7.08-7.10 (1H, m), 7.11-7.15 (2H, m, Ar), 7.40-7.44 (1H, m), 7.45-7.47 (2H, m), 7.61 (1H, br s), 8.17 (1H, dd, J_1 = 7.7 Hz, J_2 = 1.7 Hz, Ar). HRMS-ESI for $C_{24}H_{26}FNO_2$ (m/z): $[M+Na]^+$ calcd, 402.1846; found, 402.1843; $[2M+Na]^+$ calcd, 781.3794; found, 781.3793; $[M-H]^-$ calcd, 378.1868; found, 378.1893.

N-((3r)-adamantan-1-yl)-2-((2,4-difluorobenzyl)oxy)benzamide ***(12)***. The crude residue was purified by column chromatography using n-Ex/AcOEt 7:3 to obtain a white solid. Yield, 82%. m.p. 107-109 °C. ^{1}H-NMR ($CDCl_3$, 500 MHz) δ: 1.64-1.68 (6H, m, Ad), 1.90-1.92 (6H, m, Ad), 2.00 (3H, br s, Ad), 5.16 (2H, s), 6.89-6.97 (2H, m, Ar), 7.02-7.05 (1H, m), 7.10 (1H, td, J_1 = 7.5 Hz, J_2 = 1.0 Hz, Ar), 7.41-7.44 (1H, m), 7.46-7.49 (1H, m), 7.52 (1H, br s), 8.15 (1H, dd, J_1 = 7.7 Hz, J_2 = 1.7 Hz, Ar). HRMS-ESI for $C_{24}H_{25}F_2NO_2$ (m/z): $[M+Na]^+$ calcd, 420.1751; found, 420.1747; $[2M+Na]^+$ calcd, 817.3604; found, 817.3613; $[M-H]^-$ calcd, 396.1773; found, 396.1775.

N-((3r)-adamantan-1-yl)-2-((2,6-difluorobenzyl)oxy)benzamide ***(13)***. The crude residue was purified by column chromatography using n-Ex/AcOEt 9:1 to obtain a white solid. Yield, 95%. m.p. 110-112 °C. ^{1}H-NMR ($CDCl_3$, 500 MHz) δ: 1.56-1.58 (1H, m, Ad), 1.61-1.66 (5H, m, Ad), 1.87-1.92 (6H, m, Ad), 1.97-2.02 (3H, m, Ad), 5.25 (2H, s), 6.95-7.01 (2H, m, Ar), 7.07-7.11 (2H, m), 7.36-7.40 (1H, m, Ar), 7.41-7.45 (1H, m, Ar), 7.58 (1H, br s), 8.15 (1H, dd, J_1 = 7.5 Hz, J_2 = 1.5 Hz, Ar). HRMS-ESI for $C_{24}H_{25}F_2NO_2$ (m/z): $[M+Na]^+$ calcd, 420.1751; found, 420.1754; $[2M+Na]^+$ calcd, 817.3604; found, 817.3622; $[M-H]^-$ calcd, 396.1789; found, 396.1775.

N-((3r)-adamantan-1-yl)-3-((2,4-difluorobenzyl)oxy)isonicotinamide ***(14)***. The crude residue was purified by column chromatography using CH_2Cl_2/AcOEt 1:1 to obtain a brown solid. Yield, 42%. m.p. 214-216 °C. ^{1}H-NMR ($CDCl_3$, 500 MHz) δ: 1.64-1.67 (6H, m, Ad), 2.05-2.12 (3H, m, Ad), 2.14-2.17 (6H, m, Ad), 5.25 (2H, s), 6.91-6.98 (2H, m, Ar), 7.18 (1H, dd, J_1 = 6.0 Hz, J_2 = 2.0 Hz, Ar), 7.27-7.31 (1H, m, Ar), 7.65 (1H, d, J = 1.0 Hz, Ar), 8.17 (1H, d, J = 6.0 Hz, Ar), 10.88 (1H, br s). HRMS-ESI for $C_{23}H_{24}F_2N_2O_2$ (m/z): $[M+Na]^+$ calcd, 421.1704; found, 421.1708; $[2M+Na]^+$ calcd, 819.3510; found, 819.3520; $[M-H]^-$ calcd, 397.1726; found, 397.1728.

N-((3r)-adamantan-1-yl)-3-((2,6-difluorobenzyl)oxy)isonicotinamide ***(15)***. The crude residue was purified by column chromatography using CH_2Cl_2/AcOEt 1:1 to obtain a brown solid. Yield, 45%. m.p. 218-220 °C. ^{1}H-NMR ($CDCl_3$, 500 MHz) δ: 1.56-1.58 (1H, m, Ad), 1.62-1.65 (5H, m, Ad), 1.87-1.91 (6H, m, Ad), 1.97-2.02 (3H, m, Ad), 5.34 (2H, s), 7.00-7.05 (2H, m, Ar), 7.25-7.27 (1H, m), 7.41-7.48 (1H, m, Ar), 7.74 (1H, d, J = 1.5 Hz, Ar), 8.16 (1H, d, J = 6.0 Hz, Ar), 10.92 (1H, br s). HRMS-ESI for $C_{23}H_{24}F_2N_2O_2$ (m/z): $[M+Na]^+$ calcd, 421.1704; found, 421.1710; $[2M+Na]^+$ calcd, 819.3510; found, 819.3524; $[M-H]^-$ calcd, 397.1726; found, 397.1729.

*N-((3s,5s,7s)-adamantan-1-yl)-5-bromo-2-((5-fluoropentyl)oxy)benzamide (**16**)*. The crude residue was purified by column chromatography using n-Ex/AcOEt 8:2 to obtain a white solid. Yield, 60%. m.p. 110-112 °C. ^{1}H-NMR ($CDCl_3$, 500 MHz) δ: 1.61-1.86 (10H, m), 1.92 (2H, quint, J = 7.0 Hz), 2.05-2.16 (9H, m, Ad), 4.09 (2H, t, J = 6.0 Hz), 4.88 (2H, dt, J_F = 47.0 Hz, J = 5.7 Hz), 6.80 (1H, d, J = 9.0 Hz, Ar), 7.46 (1H, dd, J_1 = 8.7 Hz, J_2 = 2.7 Hz, Ar), 7.72 (1H, br s), 8.26 (1H, d, J = 3.0 Hz, Ar). HRMS-ESI for $C_{22}H_{29}BrFNO_2$ (m/z): $[M+Na]^+$ calcd, 460.1264; found, 460.1258; $[M-H]^-$ calcd, 436.1286; found, 436.1342.

*N-((3r)-adamantan-1-yl)-5-bromo-2-((4-fluorobenzyl)oxy)benzamide (**17**)*. The crude residue was purified by column chromatography using n-Ex/AcOEt 8:2 to obtain a white solid. Yield, 65%. m.p. 178-180 °C. ^{1}H-NMR ($CDCl_3$, 500 MHz) δ: 1.60-1.66 (6H, m, Ad), 1.83-1.87 (6H, m, Ad), 2.00 (3H, br s, Ad), 5.06 (2H, s), 6.89 (1H, d, J = 9.0 Hz), 7.09-7.16 (2H, m, Ar), 7.41-7.47 (2H, m, Ar), 7.49-7.51 (2H, m, Ar), 8.27 (1H, d, J = 2.5 Hz). HRMS-ESI for $C_{24}H_{25}BrFNO_2$ (m/z): $[M+Na]^+$ calcd, 480.0951; found, 480.0940; $[M-H]^-$ calcd, 456.0973; found, 456.1008.

*N-((3r)-adamantan-1-yl)-2-(benzyloxy)-5-fluorobenzamide (**18**)*. The crude residue was purified by column chromatography using n-Ex/AcOEt 8:2 to obtain a white solid. Yield, 62%. m.p. 72-74 °C. ^{1}H-NMR ($CDCl_3$, 500 MHz) δ: 0.95 (3H, t, J = 6.7 Hz), 1.37-1.45 (2H, m), 1.47-1.53 (2H, m), 1.67-1.78 (6H, m, Ad), 1.82-1.90 (2H, m), 2.05-2.17 (9H, m, Ad), 4.06 (2H, t, J = 6.3 Hz), 6.85 (1H, dd, J_1 = 9.0 Hz, J_2 = 4.0 Hz, Ar), 7.03-7.09 (1H, m, Ar), 7.87 (1H, dd, J_F = 9.7 Hz, J = 3.2 Hz, Ar), 7.92 (1H, br s). HRMS-ESI for $C_{22}H_{30}FNO_2$ (m/z): $[M+Na]^+$ calcd, 382.2159; found, 382.2164; $[2M+Na]^+$ calcd, 741.4420; found, 741.4430; $[M-H]^-$ calcd, 358.2181; found, 358.2183.

*N-((3s,5s,7s)-adamantan-1-yl)-5-fluoro-2-(pentyloxy)benzamide (**19**)*. The crude residue was purified by column chromatography using n-Ex/AcOEt 8:2 to obtain a white solid. Yield, 65%. m.p. 133-135. ^{1}H-NMR ($CDCl_3$, 500 MHz) δ: 1.60-1.65 (6H, m, Ad), 1.82-1.87 (6H, m, Ad), 1.93 (3H, br s, Ad), 5.09 (2H, s), 6.98 (1H, dd, J_1 = 8.5 Hz, J_2 = 4.5 Hz, Ar), 7.07-7.13 (1H, m, Ar), 7.22 (1H, br s), 7.37-7.48 (5H, m, Ar), 7.88 (1H, dd, J_F = 9.7 Hz, J = 3.0 Hz, Ar). HRMS-ESI for $C_{24}H_{26}FNO_2$ (m/z): $[M+Na]^+$ calcd, 402.1846; found, 402.1847; $[2M+Na]^+$ calcd, 781.3794; found, 781.3785; $[M-H]^-$ calcd, 378.1868; found, 378.1868.

*N-((3s,5s,7s)-adamantan-1-yl)-2-(2-(2-hydroxyethoxy)ethoxy)benzamide (**26**)*. The crude residue was purified by column chromatography using CH_2Cl_2/AcOEt 7:3 to obtain a white solid. Yield, 60%. ^{1}H-NMR ($CDCl_3$, 500 MHz) δ: 1.69-1.75 (6H, m, Ad), 2.01 (1H, t, J = 6.2 Hz), 2.10-2.14 (9H, m, Ad), 3.64-3.66 (2H, m), 3.76-7.79 (2H, m), 3.90-3.92 (2H, m), 4.26-4.27 (2H, m), 6.91 (1H, dd, J_1 = 8.5 Hz, J_2 = 0.5 Hz), 7.05-7.08 (1H, m), 7.37-7.40 (1H, m), 7.81 (1H, br s), 8.15 (1H, dd, J_1 = 7.7 Hz, J_2 = 1.7 Hz, Ar). HRMS-ESI for $C_{21}H_{29}NO_4$ (m/z): $[M+Na]^+$ calcd, 382.1995; found, 382.1976; $[M-H]^-$ calcd, 358.2017; found, 358.1977.

*N-((3s,5s,7s)-adamantan-1-yl)-5-bromo-2-(pentyloxy)benzamide (**27**)* [515].

*N-((3s,5s,7s)-adamantan-1-yl)-2-((5-hydroxypentyl)oxy)benzamide (**29**).* The crude residue was purified by column chromatography using n-Ex/AcOEt 7:3 to obtain a white solid. Yield, 68%. ^{1}H-NMR ($CDCl_3$, 500 MHz) δ: 1.44-1.49 (1H, m) 1.59-1.69 (4H, m), 1.70-1.77 (6H, m, Ad), 1.91 (2H, quint, J = 7.0 Hz), 2.08-2.13 (9H, m, Ad), 3.68-3.71 (2H, m), 4.10 (2H, t, J = 6.5 Hz), 6.91 (1H, d, J = 8.5 Hz), 7.04 (1H, td, J_1 = 7.5 Hz, J_2 = 1.0 Hz, Ar), 7.36-7.39 (1H, m, Ar), 7.86 (1H, br s), 8.15 (1H, dd, J_1 = 7.7 Hz, J_2 = 1.7 Hz, Ar). HRMS-ESI for $C_{22}H_{31}NO_3$ (m/z): $[M+Na]^+$ calcd, 380.2202; found, 380.2196; $[2M+Na]^+$ calcd, 737.4506; found, 737.4508; $[M-H]^-$ calcd, 356.2224; found, 356.2265.

*N-((3s,5s,7s)-adamantan-1-yl)-5-bromo-2-((5-hydroxypentyl)oxy)benzamide (**30**).* The crude residue was purified by column chromatography using n-Ex/AcOEt 1:1 to obtain a white solid. Yield, 80%. ^{1}H-NMR ($CDCl_3$, 500 MHz) δ: 1.36-1.38 (1H, m) 1.57-1.67 (4H, m), 1.68-1.74 (6H, m, Ad), 1.91 (2H, quint, J = 6.9 Hz), 2.03-2.17 (9H, m, Ad), 3.68-3.71 (2H, m), 4.08 (2H, t, J = 6.2 Hz), 6.78 (1H, d, J = 8.5 Hz), 7.46 (1H, dd, J_1 = 8.7 Hz, J_2 = 2.7 Hz, Ar), 7.75 (1H, br s), 8.26 (1H, d, J = 3.0 Hz, Ar). HRMS-ESI for $C_{22}H_{30}BrNO_3$ (m/z): $[M+Na]^+$ calcd, 458.1320; found, 458.1307; $[M-H]^-$ calcd, 434.1329; found, 434.1373.

General procedure for the synthesis of final byciclic compounds **GR106, 20-21** and **31**. Appropriate Bromo derivatives among compounds **16**, **27** and **30** (1 eq, 1 mmol) and the appropriate boronic acid (1.5 eq, 1.5 mmol) were suspended in a solution of dioxane (2.4 mL) and a solution of K_2CO_3 2M (0.6 mL). After purging the solution with argon, $Pd(PPh_3)_4$ (0.1 eq, 0.1 mmol) was added, and the mixture was refluxed for 3 hours. The solvent was removed under vacuum. The residue was taken up with H_2O (10 mL) and extracted with CH_2Cl_2 (3 x 10 mL). The combined organic layers were dried (Na_2SO_4) and evaporated under vacuum to afford a crude residue which was purified by column chromatography.

*N-((3s,5s,7s)-adamantan-1-yl)-4-((5-fluoropentyl)oxy)-[1,1'-biphenyl]-3-carboxamide (**GR106**).* The crude residue was purified by column chromatography using n-Ex/AcOEt 8:2 to obtain a white solid. Yield, 67%. m.p. 106-108 °C. ^{1}H-NMR (DMSO-d_6, 300 MHz) δ 1.52-1.62 (2H, m), 1.63-1.70 (6H, m, Ad), 1.72-1.91 (4H, m), 1.99-2.11 (9H, m, Ad), 4.15 (2H, t, J = 6.2 Hz), 4.46 (2H, dt, J_F = 47.4 Hz, J = 6.2 Hz), 7.20 (1H, d, J = 8.7 Hz, Ar), 7.28-7.36 (1H, m, Ar), 7.40-7.47 (2H, m, Ar), 7.58-7.64 (2H, m, Ar), 7.72 (1H, dd, J_1 = 8.7 Hz, J_1 = 2.7 Hz, Ar), 7.85 (1H, br s), 8.02 (1H, d, J = 2.7 Hz, Ar) (The NMR spectrum is shown in Figure S5.8). HRMS-ESI for $C_{28}H_{34}FNO_2$ (m/z): $[M+Na]^+$ calcd, 458.2472; found, 458.2473; $[2M+Na]^+$ calcd, 893.5046; found, 893.5046; $[M-H]^-$ calcd, 434.2494; found, 434.2492. The HPLC chromatogram is shown in Figure S5.9.

*N-((3s,5s,7s)-adamantan-1-yl)-3'-fluoro-4-(pentyloxy)-[1,1'-biphenyl]-3-carboxamide (**20**).* The crude residue was purified by column chromatography using n-Ex/AcOEt 8:2 to obtain a white solid. Yield, 62%. ^{1}H-NMR (DMSO-d_6, 300 MHz) δ 0.90 (3H, t, J = 7.2 Hz), 1.28-1.53 (4H, m), 1.61-1.71 (6H, m, Ad), 1.73-1.86 (2H, m), 2.00-2.11 (9H, m, Ad), 4.13 (2H, t, J = 6.0 Hz), 7.10-7.23 (2H, m, Ar), 7.40-7.54 (3H, m, Ar), 7.77 (1H, dd, J_1 = 8.7 Hz, J_2 = 2.7 Hz, Ar), 7.85 (1H, br s), 8.03 (1H, d, J = 2.4 Hz, Ar). HRMS-ESI for $C_{28}H_{34}FNO_2$ (m/z): $[M+Na]^+$ calcd, 458.2472; found, 458.2476; $[2M+Na]^+$ calcd, 893.5046; found, 893.5042; $[M-H]^-$ calcd, 434.2494; found, 434.2494.

*N-((3s,5s,7s)-adamantan-1-yl)-4'-fluoro-4-(pentyloxy)-[1,1'-biphenyl]-3-carboxamide (**21**).* The crude residue was purified by column chromatography using n-Ex/AcOEt 8:2 to obtain a white solid. Yield, 65%. ^{1}H-NMR (DMSO-d_6, 300 MHz) δ 0.90 (3H, t, J = 7.2 Hz), 1.30-1.56 (4H, m), 1.61-1.70 (6H, m, Ad), 1.78 (2H, quint, J = 6.0 Hz), 2.01-2.09 (9H, m, Ad), 4.13 (2H, t, J = 6.0 Hz), 7.19 (1H, d, J = 8.7 Hz, Ar), 7.22-7.28 (2H, m, Ar), 7.60-7.66 (2H, m, Ar) 7.74 (1H, dd, J_1 = 8.7 Hz, J_2 = 2.7 Hz, Ar), 7.87 (1H, br s), 7.99 (1H, d, J = 2.7 Hz, Ar). HRMS-ESI for $C_{28}H_{34}FNO_2$ (m/z): $[M+Na]^+$ calcd, 458.2472; found, 458.2473; $[2M+Na]^+$ calcd, 893.5046; found, 893.5040; $[M-H]^-$ calcd, 434.2494; found, 434.2493.

*N-((3s,5s,7s)-adamantan-1-yl)-4-((5-hydroxypentyl)oxy)-[1,1'-biphenyl]-3-carboxamide (**31**).* The crude residue was purified by column chromatography using n-Ex/AcOEt 1:1 to obtain a white solid. Yield, 45%. ^{1}H-NMR (DMSO-d_6, 500 MHz) δ 1.63-1.68 (4H, m), 1.71-1.80 (6H, m, Ad), 1.97 (2H, quint, J = 7.0 Hz), 2.08-2.13 (3H, m, Ad), 2.18-2.21 (6H, m, Ad), 3.59-3.64 (2H, m), 4.26 (2H, t, J = 6.5 Hz), 7.23 (1H, d, J = 9.0 Hz, Ar), 7.34 (1H, t, J = 7.5 Hz, Ar), 7.46 (2H, t, J = 7.5 Hz, Ar), 7.63-7.66 (2H, m, Ar), 7.74 (1H, dd, J_1 = 8.5 Hz, J_2 = 2.5 Hz, Ar), 7.93 (1H, br s), 8.36 (1H, d, J = 2.5 Hz, Ar). HRMS-ESI for $C_{28}H_{35}NO_3$ (m/z): $[M+Na]^+$ calcd, 456.2515; found, 456.2517; $[2M+Na]^+$ calcd, 889.5132; found, 889.5131; $[M-H]^-$ calcd, 432.2537; found, 432.2549.

*General procedure for the synthesis of tosyl compounds **28** and **32-33**.* To a solution of appropriate hydroxy compound among **26**, **29** and **31** (1 mmol, 1 eq) in CH_2Cl_2 (10 mL), TsCl (1.3 eq, 1.3 mmol), and Et_3N (1.3 mmol, 1.3 eq) were added. The resulting mixture was stirred at 0 °C for 4h. The residue mixture was taken up with H_2O (20 mL) and extracted with CH_2Cl_2 (3 x 20 mL). The collected organic layers were dried (Na_2SO_4) and evaporated under vacuum to afford a crude residue which was purified by column chromatography

*2-(2-(2-(((3s,5s,7s)-adamantan-1-yl)carbamoyl)phenoxy)ethoxy)ethyl 4-methylbenzenesulfonate (**28**).* The crude residue was purified by column chromatography using n-Ex/AcOEt 1:1 to obtain a white solid. Yield, 42%. ^{1}H-NMR ($CDCl_3$, 500 MHz) δ: 1.70 (6H, br s, Ad), 2.07 (9H, br s, Ad), 2.37 (3H, s), 3.74 (2H, t, J = 4.5 Hz), 3.84 (2H, t, J = 4.2 Hz), 4.16 (2H, t, J = 4.5 Hz), 4.19 (2H, t, J = 4.7 Hz), 6.88 (1H, d, J = 8.0 Hz, Ar), 7.08 (1H, t, J = 7.7 Hz, Ar), 7.26 (2H, d, J = 8.0 Hz, Ar), 7.39 (1H, t, J = 7.7 Hz, Ar), 7.74 (1H, br s), 7.77 (2H, d, J = 8.0 Hz, Ar), 8.16 (1H, d, J = 8.0 Hz, Ar). HRMS-ESI for $C_{28}H_{35}NO_6S$ (m/z): $[M+Na]^+$ calcd, 536.2083; found, 536.2073; $[M-H]^-$ calcd, 512.2105; found, 512.2095.

*5-(2-(((3s,5s,7s)-adamantan-1-yl)carbamoyl)phenoxy)pentyl 4-methylbenzenesulfonate (**32**).* The crude residue was purified by column chromatography using CH_2Cl_2/AcOEt 8:2 to obtain a white solid. Yield, 87%. ^{1}H-NMR ($CDCl_3$, 500 MHz) δ: 1.52-1.59 (2H, m) 1.60-1.72 (6H, m, Ad), 1.73-1.78 (2H, m), 1.85 (2H, quint, J = 7.5 Hz), 2.04-2.14 (9H, m, Ad), 2.41 (3H, s), 4.03-4.07 (4H, m), 6.88 (1H, d, J = 8.0 Hz), 7.05 (1H, t, J = 8.0 Hz), 7.32 (2H, d, J = 8.0 Hz, Ar), 7.36-7.40 (1H, m, Ar), 7.75-7.80 (3H, m, Ar), 8.14 (1H, dd, J_1 = 7.7 Hz, J_2 = 1.7 Hz, Ar). HRMS-ESI for $C_{29}H_{37}NO_5S$ (m/z): $[M+Na]^+$ calcd, 534.2290; found, 534.2289; $[2M+Na]^+$ calcd, 1045.4682; found, 1045.4684; $[M-H]^-$ calcd, 510.2312; found, 510.2326.

*5-((3-(((3s,5s,7s)-adamantan-1-yl)carbamoyl)-[1,1'-biphenyl]-4-yl)oxy)pentyl 4-methylbenzenesulfonate (**33**)*. The crude residue was purified by column chromatography using CH_2Cl_2/AcOEt 8:2 to obtain a yellow solid. Yield, 66%. ^{1}H-NMR ($CDCl_3$, 500 MHz) δ: 1.60-1.65 (2H, m) 1.72-1.76 (6H, m, Ad), 1.78-1.83 (2H, m), 1.87-1.97 (2H, m), 2.10-2.20 (9H, m, Ad), 2.45 (3H, s), 4.08-4.15 (4H, m), 6.99 (1H, d, J = 8.4 Hz), 7.30-7.37 (3H, m, Ar), 7.39-7.42 (2H, m, Ar), 7.60-7.68 (3H, m, Ar), 7.76-7.84 (3H, m, Ar), 8.47 (1H, d, J = 2.8 Hz, Ar). HRMS-ESI for $C_{35}H_{41}NO_5S$ (m/z): $[M+Na]^+$ calcd, 610.2603; found, 610.2618; $[M-H]^-$ calcd, 586.2625; found, 586.2630.

*N-((3s,5s,7s)-adamantan-1-yl)-2-(2-(2-fluoroethoxy)ethoxy)benzamide (**7**).* To a solution of compound **28** (1 mmol, 1 eq) in CH_3CN (10 mL), K_2CO_3 (1.5 eq, 1.5 mmol), $K_{2.2.2}$ (1.5 eq, 1.5 mmol), and KF (1.5 mmol, 1.5 eq) were added and the resulting mixture was stirred at reflux ON. The resulting mixture was refluxed with stirring ON and then was allowed to cool to room temperature. The solvent was removed under vacuum. The residue was taken up with H_2O (20 mL) and extracted with CH_2Cl_2 (3 x 20 mL). The combined organic layers were dried (Na_2SO_4) and evaporated under vacuum to afford a crude residue which was purified by column chromatography using n-Ex/AcOEt 6:4 to obtain a white solid. Yield, 48%. m.p. 70-72 °C. ^{1}H-NMR ($CDCl_3$, 500 MHz) δ: 1.69-1.75 (6H, m, Ad), 2.10-2.14 (9H, m, Ad), 3.79 (2H, dt, J_F = 29.5 Hz, J = 4.2 Hz), 3.93-3.95 (2H, m), 4.26-4.28 (2H, m), 4.59 (2H, dt, J_F = 48.0 Hz, J = 4.2 Hz), 6.91 (1H, dd, J_1 = 8.2 Hz, J_2 = 0.5 Hz), 7.05-7.08 (1H, m), 7.37-7.40 (1H, m), 7.84 (1H, br s), 8.16 (1H, dd, J_1 = 7.7 Hz, J_2 = 1.7 Hz, Ar). HRMS-ESI for $C_{21}H_{28}FNO_3$ (m/z): $[M+Na]^+$ calcd, 384.1951; found, 384.1951; $[2M+Na]^+$ calcd, 745.4004; found, 745.4005; $[M-H]^-$ calcd, 360.1973; found, 360.1994.

5.12.2. Biological studies

5.12.2.1. Materials

Cell culture reagents were purchased from Celbio s.r.l. (Milano, Italy). CulturePlate 96/wells plates were purchased from PerkinElmer Life Science; GW405833 and (R)-(þ)-WIN 55,212-2 were obtained from TOCRIS (Milan, Italy); Multiscreen HTS filter plates were purchased by Merck Millipore (Ireland). OptiPhase Supermix and [^{3}H]CP55940 were purchased from PerkinElmer Life Science. COSTAR flat black plates were purchased from Sigma Aldrich. FAAH human recombinant enzyme and its substrate 7-amino-4-methyl-2H-1-benzopyran-2-one-5Z,8Z,11Z,14Z-eicosatetraen-amide (AMC-AA) were purchased from Cayman Chemical, Ann Arbor, MI, USA. Ferrozine and NKH 477 were obtained from Sigma-Aldrich-RBI s.r.l. (Milan, Italy). Clear 96-wells microplate was purchased from Greiner Bio-One Italia S.r.l. (Milan, Italy). [^{3}H]RO6957022 (specific activity 82.83 Ci/mmol) was synthesized in-house as previously published [520]. GF/C filter plates (#6055690) and MicroScint-20 scintillation cocktail (#6013621) were purchased from Revvity (Waltham, MA, USA). Bicinchoninic acid (BCA) and BCA protein assay reagent were obtained from Pierce Chemical Company (Rockford, IL, USA). CP55,940 (#C1112) and AM630 (#SML0327) were purchased from Sigma-Aldrich (Saint Louis, MO, USA). Forskolin (FSK, #F701800) was obtained from Toronto Research Chemicals. FuGENE® 6 Transfection Reagent (#E2692), Nano-Glo® Vivazine™ Substrate (#N2581), GloSensor™ cAMP reagent (#E1291) and pGloSensor™-22F cAMP Plasmid (#E2301) were obtained from Promega (Madison, WI, USA) and 96-well solid white flat bottom microplates (#3917) were obtained from Corning (Corning, NY, USA). All buffers and solutions were prepared using Millipore water (deionized using a MilliQ A10 Biocel™ with a 0.22 μm filter) and analytical grade reagents and solvents. Buffers were prepared at RT and stored

at 4 °C, unless stated otherwise.

5.12.2.2. Cell cultures

For [^{3}H]CP55,940 radioligand binding assays, CB2R-HEK293 and CB1R-HEK293 cells were grown in DMEM high glucose supplemented with 10% fetal bovine serum, 2 mM glutamine,100 U/mL penicillin,100 mg/mL streptomycin, 0.1 mg/mL G418, in a humidified incubator at 37 °C with a 5% CO2 atmosphere. Human monocyte THP-1 cells were obtained from ATCC (Manassas, VA) and seeded at 1 x 105 cells/ml for 48 h. To differentiate cells into macrophages, 0.01 μM PMA was added for 48 h. By microscope analysis, in these conditions > 98% cells became adherent. To stimulate THP-1 monocytes and adherent cells, 10 μg/ml of LPS was added for 24 h, according to the protocol of differentiation and activation reported in Dreskin et al. [521]. Cells were cultured in RPMI-1640 medium supplemented with 10% fetal bovine serum, 2 mM glutamine,100 U/mL penicillin,100 mg/mL streptomycin, in a humidified incubator at 37 °C with a 5% CO2 atmosphere [521]. For [3H]RO6957022 radioligand binding assays, Chinese Hamster Ovary (CHO) cells stably expressing hCB2R (CHOK1_hCB2bgal, #93-0706C2, PathHunter EA Parental cell line, female, DiscoverX) were cultured in Ham's F12 Nutrient Mixture supplemented with 10% (v/v) fetal calf serum (FCS), 2 mM Glutamax, 100 IU/ mL penicillin, 100 μg/mL streptomycin, 300 μg/mL hygromycin and 800 μg/mL G418 in a humidified atmosphere at 37 °C and 5% CO2. For Multiplexed cAMP production and β-arrestin-2ß-arrestin-2 recruitment assays, HEK293T cells stably expressing full-length hCB2R-SmBiT and LgBiT- β-arrestin-2 ß-arrestin-2 constructs (HEK293T CB2R-SmBiT LgBiT- β-arrestin-2ß-arrestin-2, a kind gift by Christophe Stove, Ghent University, Belgium) [522] were grown in monolayers and was cultured in Dulbecco's Modified Eagle's Medium supplemented with 10% FCS, 2 mM Glutamax, 100 IU/mL penicillin and 100 μ/mL streptomycin in a humidified atmosphere at 37 °C and 5% CO2. All cells were subcultured twice per week when reaching 80-90% confluence on 10 or 15 cm ø plates by trypsinization and used for further experiments within 20 passages. Caco-2 and MDCK-MDR1 cells were grown in Dulbecco's high-glucose modified eagle medium, composed of 10% fetal bovine serum, 2 mM of glutamine, 100 U/mL of penicillin, and 0.1 mg/mL of streptomycin (all components purchased from Euroclone, Milan, Italy) in a humidified incubator at 37 °C with a 5 % CO2 atmosphere.

5.12.3. *In vitro* CB1R and CB2R Binding Affinities

Membrane preparations for CB1 and CB2 receptors assays. Membranes of HEK293 cells recombinantly expressing the human CB1 receptor subtype, were prepared by scratching the cells off the previously frozen cell culture dishes in PBS (pH 7.4). The cell suspension was centrifuged at 800xg for 15 min and the pellet was resuspended and homogenized on ice for 1 min using a dounce homogenizer, and subsequently spun down for 5 min at 4 °C and 500 g. The supernatant was centrifuged for 20 min at 25,000 g. The obtained membrane pellets were resuspended in buffer A ($NaHCO_3$10 mM, EGTA 10 mM, EDTA 10 mM, protease inhibitors cocktail 1X (Sigma Aldrich), pH 7.4) and centrifuged for 20 min at 25,000 g. The pellet was resuspended in the required amount of Tris-HCl buffer 25mM, $MgCl_2$ 5 mM, EDTA 1mM, pH 7.4. Aliquots of the membrane preparation were stored at -80°C until being used.[63] Membranes of HEK293 cells recombinantly expressing the human CB2 receptor subtypes were prepared by scratching the cells off the previously frozen cell culture dishes in ice-cold hypotonic buffer (Tris-HCl5 mM, EDTA, 2 mM, pH 7.4).

The cell suspension was homogenized on ice for 1 min using an Ultra-Turrax (T25basic, IKALABORTECHNIK, Higashiosaka, Japan) followed by further homogenization for 1 min with a dounce homogenizer, and subsequently spun down for 10 min at 4 °C and 1000 g. The supernatant was centrifuged for 60 min at 48,000 g. The obtained membrane pellets were resuspended and homogenized in the required amount of Tris-HCl 50 mM buffer, pH 7.4. Aliquots of the membrane preparation were stored at -80 °C until being used.

Radioligand competition binding assays at CB2 and CB1 receptors. Competition binding assays were performed as reported in Spinelli *et al* [284]. The membrane preparations of the HEK293 cells stably expressing CB receptor subtype 2 (50 µg protein/well) was used as source for human CB2 receptor and as radioligand the CB agonist [^{3}H](-)-*cis*-3-[2-hydroxy-4-(1,1-dimethylheptyl)phenyl]-*trans*-4-(3-hydroxypropyl)cyclohexanol (CP55,940), PerkinElmer Italia SPA, Milano, Italy). After addition of 25 µL of the test compounds at different concentrations (10^{-12}-10^{-5}M), 25 µL of [^{3}H]-CP55,940 solution in assay buffer (at final concentration of 0.2 nM), and 100 µL of membrane preparation to 100 µL of assay buffer (Tris-HCl 50 mM, EGTA 2.5mM, $MgCl_2$ 5mM, fatty acid fere bovine serum albumine BSA 0.1%, pH 7.4), the suspension was incubated for 90 min at 30 °C. Total binding was determined without the test compounds. Nonspecific binding was determined in the presence of 10 µM GW405833, CB2R reference compound. The incubation was stopped by rapid filtration through a GF/C glass fibre filter (Merck Millipore, Ireland) presoaked for 30 min with 0.05% aq. Polyethyleneimine solution, using a 96-channel cell harvester (Merck Millipore, Ireland). The filter was washed three times with 100 µL ice-cold washing buffer (Tris-HCl 50 mM, EGTA 2.5 mM, $MgCl_2$ 5 mM, BSA 1%, pH 7.4), and then dried for 1.5 h at 50 °C. Radioactivity on the filter was determined in a MicroBeta JET counter (Perkin- Elmer, Boston, MA, USA) after 6 h of preincubation with 100 µl of scintillation cocktail (OptiPhase superMix, Perkin- Elmer). Data were obtained in three independent experiments, performed in triplicates. Data were analyzed using GraphPad Prism Version 7 (San Diego, CA, USA). For the calculation of K_i values, the Cheng-Prusoff equation and a K_D value of 1.5 nM ([^{3}H]-CP55,940 at CB2) were used. Cannabinoid CB1 receptor competition binding experiments were carried out in a polypropilene 96-well plate. In each well 20 µg of membranes from HEK 293-hCB1 cell line, 0.8 nM [^{3}H]-CP55940 (164.9 Ci/mmol, 1 mCi/mL, Perkin Elmer NET1051250UC) and studied and standard compounds were incubated. Non-specific binding was determined in the presence of Surinabant 10 µM. The reaction mixture was incubated at 30 °C for 60 min, 200 µL were transferred to GF/C 96-well plate (Millipore, Madrid, Spain) pretreated with binding buffer (Tris-HCl 50 mM, EDTA 1 mM, $MgCl_2$ 5 mM, BSA 0.5%, pH 7.4), afterwards it was filtered and washed four times with 250 µL wash buffer (Tris-HCl 50 mM, EDTA 1 mM, $MgCl_2$ 5 mM, BSA 0.5%, pH 7.4), before measuring in a microplate beta scintillation counter (Microbeta Trilux, PerkinElmer, Madrid, Spain). Data were obtained in three independent experiments, performed in triplicates.

5.12.4. Binding kinetics at the human CB2R

Membrane preparation. CHOK1_hCB2bgal cells were harvested when reaching 80-90% confluence in 15 cm ø plates after one week subculture at a 1:6 ratio. The cells were detached by scraping into 5 mL phosphate-buffered saline (PBS) and subsequently centrifuged at 2,000 × g for 5 min. Pellets were resuspended in ice-cold Tris buffer (50 mM Tris-HCl, pH 7.4) and homogenized with an Ultra Turrax homogenizer (IKA-Werke GmbH & Co. KG, Staufen, Germany). Cytosolic and membrane fractions were

separated using an Optima LE-80 K ultracentrifuge (Beckman Coulter, Inc., Fullerton, CA) at 100,000 × g for 20 min at 4 °C. The supernatant was discarded and the resuspension, homogenization, and ultracentrifugation steps were repeated. The final pellets were resuspended and homogenized in ice-cold Tris buffer and subsequently aliquoted and stored in 100 µL aliquots at -70 °C. Membrane protein concentrations were determined using a BCA protein determination assay, as described by the manufacturer (Pierce BCA protein assay kit).

5.12.4.1. [^{3}H]RO6957022 displacement and competition association assays

[^{3}H]RO6957022 displacement and competition association assays were performed as previously described to determine binding affinity and kinetics, respectively [517]. In short, the reactions were performed in 100 µL assay buffer ((50 mM Tris-HCl (pH 7.4), 0.1% (w/v) bovine serum albumin (BSA)) containing ~1.5 nM [^{3}H]RO6957022, and 1 µg membrane protein CHOK1_hCB2bgal at 10 °C. Displacement assays were performed with six ranging concentrations (from 0.01 nM to 10 µM) competing compound. The reaction mixtures were incubated for 2 h before termination. Competition associations assays were performed with competing compounds at IC_{50} concentration as obtained from the displacement assays. Competition was initiated by addition of CHOK1_hCB2bgal membrane homogenates at different time points for 2 h, after which incubations were terminated. Nonspecific binding (NSB) was determined using 10 µM AM630 and DMSO concentrations were constant and kept < 1% in all samples. Total radioligand binding (TB) did not exceed 10% of the amount added to prevent ligand depletion. For all assays, incubations were terminated by rapid vacuum filtration with ice-cold assay buffer through Whatman GF/C filters using a Filtermate 96-well harvester (Revvity, Waltham, MA, USA). Filters were dried for at least 30 min at 55 °C and subsequently 25 µL MicroScint-20 was added per well. Filter-bound radioactivity was measured by scintillation spectrometry using a Microbeta2 2450 counter (Revvity, Waltham, MA, USA).

5.12.4.2. Multiplexed cAMP production and β-arrestin-2 recruitment assay

Inhibition of cAMP production and β-arrestin-2 recruitment after CB_2R activation were measured using the GloSensor™ and NanoBiT® technologies, respectively, in a multiplexed manner using HEK293T CB_2R-SmBiT LgBiT-β-arrestin-2 cells as described previously [Bouma, J.; de Koning, E. J. M.; van der Horst, C.; Kumar, S. S.; van den Berg, B. J. W.; Hoare, S. R. J.; Wittwer, M. B.; Guba, W.; Rufer, A. C.; Grether, U.; van der Stelt, M.; Heitman, L. H. Kinetic Multiplex Assay to Assess Biased Signaling of Clinical GPCR Agonists. Pharmacol. Res. 2025, 222, 108021. https://doi.org/10.1016/j.phrs.2025.108021.]. In short, the cells were transfected with 10 µg pGloSensor™-22F cAMP plasmid using FuGENE® 6 transfection in a 3:1 reagent:DNA ratio. The next day, the transfected cells were seeded at a density of 50,000 cells/well in culture medium in a solid white, flat bottom 96-well plate coated with poly-D-lysine, and were incubated for another 24 h at 37 °C with 5%. On assay day, culture medium was replaced by assay medium (CO_2 independent medium + 10% (v/v) FCS)) supplemented with 2% (v/v) GloSensor™ cAMP reagent and 1% (v/v) Vivazine™ substrate. The plate was incubated for 2 h at 25°C in the dark after which baseline levels were measured for 7.5 min. To induce cAMP production, cells were prestimulated with 1 µM forskolin (FSK) until reaching a stable plateau of cAMP production as monitored with the plate reader for 52.5 min. Immediately after, cells were stimulated with ranging concentrations of compound of interest (from 0.01 nM to 10 µM). The maximal response was determined by 1 µM CP55,940 and DMSO concentrations were

constant and kept < 1% in all samples. Luminescence was measured for another 90 min in the plate reader resulting in a total read time of 150 min. The simultaneous luminescence was measured in a Wallac EnVision 2104 Multilabel reader (Revvity, Waltham, MA, USA). The cAMP response and β-arrestin-2 recruitment signals were detected using the Cy3 595 (595/60 nm, barcode 229) and the NanoBRET Blue (460/80 nm, barcode 703) emission filters, respectively, in a dual luminescent manner. Each wavelength was measured for 250 ms/well and the total interval between plate repeats was 90 s.

5.12.5. Calcein-AM experiment

The experiment was carried out as described by Contino et al. with minor modifications [335]. MDCK-MDR1 cell line (30,000 cells per well) was seeded into black CulturePlate 96/wells plate with 100 µL medium and allowed to become confluent overnight. 100 µL of test compounds were solubilized in culture medium and added to monolayers, with final concentrations ranging from 0.1 to 100 mM. 96/Wells plate was incubated at 37 °C for 30 min. Calcein-AM was added in 100 mL of Phosphate Buffered Saline (PBS) to yield a final concentration of 2.5 µM and the plate was incubated for 30 min. Each well was washed 3 times with ice-cold PBS. Saline buffer was added to each well and the plate was read with Victor3 (PerkinElmer) at excitation and emission wavelengths of 485 nm and 535 nm, respectively. In these experimental conditions, Calcein cell accumulation in the absence and in the presence of tested compounds was evaluated and fluorescence basal level was estimated with untreated cells. In treated wells the increase of fluorescence with respect to basal level was measured. EC_{50} values were determined by fitting the fluorescence increase percentage versus log[dose].

5.12.6. Permeability Experiments

The experiment started with the preparation of the Caco-2 monolayer, which occurred by seeding the cells (20,000/well) in Millicell plates (Millipore, Milan, Italy). Its growth was followed for 21 days by changing the medium occasionally and measuring its transepithelial electrical resistance (TEER) daily using an epithelial voltohmmeter (Millicell-ERS) until a TEER value >240 ohms×cm^2 was reached. After 21 days, the plate was washed twice with Hank's balanced salt solution (HBSS) (Invitrogen). After the second wash, the wells were filled with buffer, and the plate was kept at 37 °C for 30 min. After the incubation time, the HBSS buffer was replaced with the solutions of the compounds to be tested at a concentration of 1×10^{-4} M. The plates were placed in an incubator at 37 °C for 120 min. The apparent permeability (Papp), in units of nm/sec, was calculated [335] using the following equation:

$$P_{app} = \left(\frac{V_A}{Area\ x\ time}\right) \times \left(\frac{[drug]_{acceptor}}{[drug]_{initial}}\right)$$

VA = the volume (in mL) in the acceptor well; Area= the surface area of the membrane (0.11cm^2 of the well); time = the total transport time in seconds (7200 s); $[drug]_{acceptor}$= the concentration of the drug measured by U.V. spectroscopy; $[drug]_{initial}$ = the initial drug concentration (1 x10^{-4} M) in the apical or basolateral wells.

5.12.7. Computational studies

Docking simulations for **FR10** and **GR106** were carried out using the standard precision (SP) protocol. Two X-ray crystallographic structures of the CB2R were selected: one bound to an antagonist (PDB ID: 5ZTY [523]) and the other to an agonist (PDB ID: 6KPC [516]). Both 3D models were processed using the "Protein Preparation Workflow" from Schrödinger Suite 2024-3. During preparation, hydrogen atoms were added at pH 7.4 (±2.0), missing side chains were reconstructed, and the most probable protonation states were assigned based on the hydrogen bonding network. A final energy minimization was performed using the S-OPLS (OPLS4 [524]) force field to optimize the protein-ligand complex. Ligands were prepared using the "LigPrep" module of Schrödinger Suite 2024-3, generating all relevant tautomers and conformers at pH 7.4 (± 2.0). Docking was performed using GLIDE [525] with grid-based ligand docking and energy evaluation, keeping the protein rigid while allowing ligand flexibility. The docking grid was centered on the co-crystallized ligand: AM12033 (PDB ID: E3R) for 6KPC and AM10257 (PDB ID: 9JU) for 5ZTY. The inner grid box measured 103 Å³, while the outer boxes were approximately 253 Å³ and 263 Å³, respectively. Default docking parameters were used, including the OPLS_2005 force field and the SP protocol. The docking setup was validated by re-docking the native ligands, yielding RMSD values of 0.299 Å for AM12033 (6KPC) and 0.315 Å for AM10257 (5ZTY).

5.12.8. Radiochemistry

The anhydrous solvents CH_3CN, DMSO and DMF used for the manual radiosynthesis were purchased from sigma-aldrich chemie gmbh, part of merck, taufkirchen, Germany. The $K_{2.2.2.}$ used as a phase transfer catalyst was purchased from Sigma-Aldrich chemie gmbh, part of Merck, Taufkirchen, Germany. The K_2CO_3 was used as an aqueous solution 20 mg/mL and purchased from sigma-aldrich chemie gmbh, part of merck, taufkirchen, Germany.

Radio thin layer chromatography (radio-TLC) was performed on silica gel (polygram® sil g/UV_{254} from machery-nagel, Germany) pre-coated plates with a mixture of ethyl acetate/n-hexane 7/3 (v/v) as eluent. The plates were exposed to storage phosphor screens (bas-ip ms 2025, fujifilm co., Tokyo, Japan) and recorded using the amersham typhoon rgb biomolecular imager (ge healthcare life sciences). Images were quantified with the imagequant tl8.1 software (ge healthcare life sciences).

5.12.8.1. [^{18}F]Fluoride production

No-carrier-added [^{18}F]fluoride was produced via the [^{18}O(p,n)^{18}F] nuclear reaction by irradiation of an [^{18}O]H_2O target (Hyox 18 enriched water, Rotem Industries Ltd, Israel) on a Cyclone 18/9 (iba RadioPharma Solutions, Belgium) with fixed energy proton beam using Nirta [^{18}F]fluoride XL target.

Preconditioning of Chromafix® 30 PS-HCO_3 (45 mg) cartridge (ABX advanced biochemical compounds GmBH, Radeberg, Germany) and Sep-Pak® Accell QMA light cartridge (Waters GmBH, Eschborn, Germany) was done using 10 mL of 0.5 M $NaHCO_3$ followed by 10 mL water. Preconditioning of Sep-Pak® C_{18} light and plus cartridges (Waters GmBH, Eschborn, Germany) was done using 5 ml of EtOH and 20 ml of water.

5.12.8.2. Manual Radiosynthesis of [^{18}F]FM10 and [^{18}F]GR106

The manual synthesis of **[^{18}F]FM10** and **[^{18}F]GR106** began with azeotropically or non-azeotropically dried [^{18}F]fluoride, which was dissolved in the 300 µL of MeCN. Azeotropic removal of water to obtain the anhydrous [^{18}F]fluoride–Kryptofix complex ($K_{2.2.2}$, 5 mg; MeCN, 800 µL; H_2O, 200 µL; K_2CO_3 sol. (20 mg/mL), 15 µL, 20 mg/mL) was performed by microwave heating for 15 min under continuous flow of nitrogen

After activation, the [^{18}F]fluoride–Kryptofix complex was added to a vial containing the tosylate precursor (**32** or **33**) previously dissolved 300 µL of the reaction solvent . For the synthesis of **[^{18}F]FM10**, the reaction was carried out in MeCN at 90 °C, DMSO at 130 °C and DMF at 130 °C. In contrast, for the synthesis of **[^{18}F]GR106**, only MeCN at 90 °C was employed. Following addition of the activated complex, the reaction mixture was stirred for 15 min. To monitor labeling progress, aliquots were withdrawn at 5, 10, and 15 min and analyzed by radio-TLC and, randomly, by radio-HPLC.

Optimized manual procedure for **[^{18}F]FM10** and **[^{18}F]GR106:** the azeotropically dried [^{18}F]fluoride–Kryptofix complex was dissolved in MeCN (300 µL) and **32** (1 mg) or **33** (2 mg), dissolved in MeCN (300 µL), was added. The resulting reaction mixture was stirred at 90 °C for 10 min.

5.12.8.3. Automated Radiosynthesis of [^{18}F]FM10 and [^{18}F]GR106

The optimized manual labeling procedure was successfully transferred to a remote-controlled synthesis module (SynChrom R&D from Elysia-Raytest, Figure S5.2). The [^{18}F]fluoride was trapped on a pre-conditioned Sep-Pak® Accell QMA light cartridge (entry 1, Figure S5.2). The trapped [^{18}F]fluoride was eluted with the Kriptofix-complex (entry 2, Figure S5.2) into the reaction vessel 1 (entry 3, Figure S5.2) and was dried by azeotropic distillation with MeCN (entry 4, Figure S5.2) for 15 min. Then 1 mg of **32** or 2 mg of **33** in 1 mL of MeCN (entry 5, Figure S5.2) was added into reactor 1 (3, reaction vessel 1 (entry 3, Figure S5.2) and stirring for 10 min at 90 °C. The reaction mixture was quenched with 4.1 mL of MeCN/H_2O 1:1 (entry 6, Figure S5.2) and transfered in reactor 2 (entry 7, Figure S5.2).

The resulting mixture containing **[^{18}F]FM10** or **[^{18}F]GR106** was injected in the RP-HPLC column (Reprosil-Pur C_{18}-Aq, 10 mm, 250 x 10 mm column from Dr. Maisch GmbH, entry 9, Figure S5.2) and eluted with a mobile phase of 75% MeCN / 25% aq$AcNH_4$ 20 mM, flow 4.2 mL/min for **[^{18}F]FM10** and 80% MeCN / 20% aq$AcNH_4$ 20 mM, flow 4.0 mL/min for **[^{18}F]GR106**. The radiolabeled products **[^{18}F]FM10** and **[^{18}F]GR106** were isolated (Rt = 21-22 min and Rt = 24-25 min, respectivelly) and directed to a collection vial (entry 10, Figure S5.2) that was previously loaded with 40 mL of water.

The final purification step was achieved through SPE on a Sep-Pak® C_{18} light cartridge, (entry 11, Figure S5.2) followed by washing of the cartridge with 2 mL water (entry 12, Figure S5.2) and successive elution of the radioligand with the 1.2 mL of EtOH (entry 13, Figure S5.2) into the product vial (entry 14, Figure S5.2).

The EtOH solution was transferred out of the hot cell and volume was reduced under a gentle Argon stream at 70 °C to a final volume of 10-25 µL.

Afterwards, the radiotracer was formulated in an isotonic saline solution to obtain a final product containing 10 % EtOH (*v/v*).

For quality control, the final product of the radiotracer was inspected by analytical radio- and UV-HPLC with and without co-injection of the reference compound in isocratic or gradient method with RP-HPLC

(Reprosil-Pur C_{18}-Aq, 10 mm, 250 x 10 mm column from Dr. Maisch GmbH). The isocratic method was 70 % MeCN and 20 mM NH_4OAc aq. for **[^{18}F]FM10** and 80 % MeCN and 20 mM NH_4OAc aq. for **[^{18}F]GR106**, with flow rate of 1 mL/min at maximum absorbing wavelength of 286 nm for **[^{18}F]FM10** and at 260 nm for **[^{18}F]GR106**.

For the determination of A_m of **[^{18}F]FM10** and **[^{18}F]GR106**, an aliquot of the tracer solution (50 µl, 5 - 30 MBq plus 50 µl MeCN/H_2O 1:1) was analyzed by HPLC under isocratic conditions (74% MeCN / 26% 20 mM NH_4OAc aq for **[^{18}F]FM10** and 82% MeCN / 18% 20 mM NH_4OAc aq for **[^{18}F]GR106**) using chromatograms obtained at 286 nm for **[^{18}F]FM10** and at 260 nm for **[^{18}F]GR106** as the wavelength of high absorption. The amount of non-radioactive **FM10** and **GR106** was calculated from calibration curves (Figure S5.10) obtained under the same HPLC conditions.

5.12.9. *In vitro* evaluation of [^{18}F]FM10 and [^{18}F]GR106

5.12.9.1. Experimental determination of lipofilicity

The apparent distribution coefficient ($logD_{7.4}$) value of both **[^{18}F]FM10** and **[^{18}F]GR106** was determined using a shake-flask method by measuring the distribution of the radiotracer between *n*-octanol and PBS (0.05 mol/L, pH = 7.4). The two phases were pre-saturated with each other. A solution of the radiotracer (10 µL, 1.1 MBq) was added to a 15 mL plastic centrifuge tube containing *n*-octanol (3 mL) and PBS (3 mL). The tube was vortexed for 3 min and centrifuged at 3500 rpm for 5 min (Anke TDL80-2B, China). About 50 µL of the *n*-octanol layer and 500 µL of the buffer layer were pipetted in two tared tubes and the activity was measured in an automatic γ-counter (Wallac 2480 Wizard, USA). The $logD_{7.4}$ was determined as the ratio of cpm/mL of the *n*-octanol layer to that of the buffer layer. Samples from the *n*-octanol layer were redistributed until consistent distribution coefficient values were obtained. The measurement was carried out in triplicate and repeated three times.

5.12.9.2. Determination of Binding Affinities by Homogenate Assays

Binding assays were performed as previously reported by Teodoro et al. [496]. In brief, membrane preparations obtained from CHO cell lines stably transfected with human CB_2R (*h*CB2R-CHO; kindly provided by Paul L. Prather, Department of Pharmacology and Toxicology, College of Medicine, University of Arkansas for Medical Sciences, USA) were used for radioligand binding experiments. Membrane homogenates from rat spleen or *h*CB2R-CHO cells were incubated with the corresponding ^{18}F-labeled radiotracers (**[^{18}F]FM10** or **[^{18}F]GR106**) and increasing concentrations of the respective unlabeled compound, following the same general protocol. For **[^{18}F]FM10**, an optimized radiotracer formulation consisting of a 1:2 mixture of Kolliphor EL:DMSO was applied prior to addition to the binding buffer. This replaced the previously used 10% ethanol vehicle (employed in other binding studies with **[^{18}F]GR106** and in autoradiography experiments) to improve solubility and minimize potential aggregation effects. Nonspecific binding was determined by coincubation with CP55,940 (final concentration 10^{-5} M). After incubation, bound radioactivity was measured using a γ-counter (1480 WIZARD, Perkin Elmer, Turku, Finland). Data were normalized to percentage of specific binding and plotted against the logarithm of the competitor concentration. IC_{50} values were determined by nonlinear regression analysis using GraphPad Prism. The K_D values were calculated using the modified Cheng–Prusoff equation.

$$K_D = K_i = \mathrm{IC}_{50} - [\text{radioligand}]$$

allowing direct determination of apparent K_D values from homologous displacement curves.

5.12.9.3. *In Vitro* Metabolism

[^{18}F]FM10 and **[^{18}F]GR106** were incubated with MLM in PBS in the presence of NADPH for 30 min at 37 °C with gentle shaking at 350 rpm (*n = 2*), following a previously published protocol [337] with minor modifications. For all incubation mixtures the total volume was 250 µL. 12.5 µL of MLM (1 mg/mL) was added to 187.5 µL of PBS, followed by 25 µL of **[^{18}F]FM10** or **[^{18}F]GR106** (10–20 MBq). The mixture was pre-incubated at 37 °C with gentle shaking at 350 rpm for 5 min. Subsequently, 25 µL of pre-incubated NADPH (2 mM) was added, and the reaction was incubated at 37 °C with gentle shaking at 350 rpm for 30 min (*n = 3*). Positive control experiments were performed using testosterone as substrate, both in the presence and absence of NADPH (25 µL of testosterone, 12.5 µL of MLM at 1 mg/mL, and either 0 or 25 µL of 2 mM NADPH in 212.5 µL or 187.5 µL of PBS, respectively). In these experiments, incubation was carried out at 37 °C with gentle shaking at 350 rpm for 60 min, corresponding to the time required for complete conversion of testosterone. Negative control experiments were conducted by incubating **[^{18}F]FM10** or **[^{18}F]GR106** either without NADPH (25 µL of **[^{18}F]FM10** or **[^{18}F]GR106** and 12.5 µL of MLM at 1 mg/mL in 212.5 µL of PBS) or in the absence of both MLM and NADPH (25 µL of **[^{18}F]FM10** or **[^{18}F]GR106** in 225 µL of PBS). All negative control incubations were performed at 37 °C with gentle shaking at 350 rpm for 30 min.

After incubation, samples were subjected to protein precipitation. An aliquot of 25 µL from each reaction mixture was added to 100 µL of ice-cold CH_3CN, vortexed for 5 min, and placed on ice for 3 min, followed by centrifugation at 14,000 rpm for 10 min. The supernatant was separated from the pellet and analyzed by radio-HPLC. Efficiencies of the extractions were calculated after activity measurement of aliquots of the supernatants and the corresponding residues by gamma counter using the following equation:

$$\text{Extraction Efficiency (\%)} = \frac{\text{activity}_{\text{supernatant}}}{\text{activity}_{\text{residue}} + \text{activity}_{\text{supernatant}}} \times 100\%$$

Radio-HPLC analysis of **[^{18}F]FM10** and **[^{18}F]GR106** metabolism was performed using a radio-HPLC method and columns different from those employed for quality control after automated synthesis.

Separations were carried out on a RP-HPLC column (ReproSil-Pur 120 C_{18}-AQ, 3 µm, 150 × 3 mm; Dr. Maisch GmbH). For both compounds, the same gradient program was applied: isocratic elution at 5% CH_3CN from 0 to 1.5 min, followed by a linear gradient from 5% to 80% CH_3CN between 1.5 and 10.0 min, isocratic elution at 80% CH_3CN from 10.1 to 12.0 min, and re-equilibration at 5% CH_3CN from 12.1 to 15.0 min. The Rt were 10.0 min for **[^{18}F]FM10** and 11.9 min for **[^{18}F]GR106**.

For testosterone metabolism analysis in positive control experiments, HPLC was performed using an appropriate gradient method with UV detection (λ = 245 nm).

The $t_{1/2}$ determination (Figure S5.11) was performed following a previously published protocol [501] using the following equations:

Equation 5.1. $\ln(intact\ radiotracer\ in\ \%) = \ln 100 - slope \times t$

Equation 5.2. $t_{1/2} = \frac{ln\ 2}{slope}$

5.12.9.4. *In Vitro* Autoradiography

Autoradiography in 10 µm cryosections from rat were thawed, dried, and pre-incubated with incubation buffer for 10 min, dried under an airstream. Subsequently, the incubation buffer containing **[^{18}F]FM10** or **[^{18}F]GR106** was added alone or together with 1 µM reference compound. Additionally, to assess the non-specific binding of the radiotracers to cryosections SR144528 (inverse CB2R agonist) or SR141716A (inverse CB1R agonist) was added instead of the reference compound. After 90 min, cryosections were washed two times for 2 min with ice-cold 50 mM Tris HCl, $pH_{7.4}$ and 10s in ddH_2O and subsequently dried under an airstream. Subsequently, the slides were exposed to a phosphor imager plate. After scanning at high sensitivity and a 12.5 µm resolution with a CR35 Bio image plate scanner (Raytest Isotopenmessgeräte GmbH, Straubenhardt, Germany). The analyses of the autoradiographic images were performed with the AIDA 5.1 software (Elysia-Raytest, Angleur, Belgium).

5.13. Supporting information

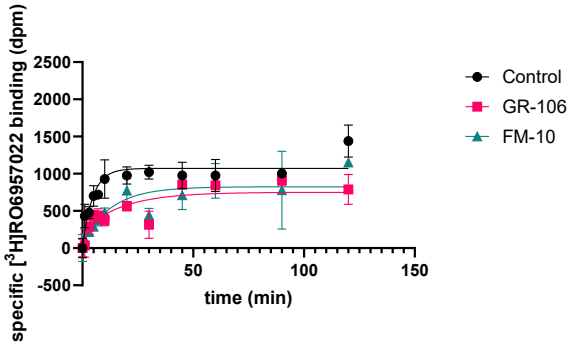

Figure S5.1: Competition association of [^{3}H]RO6957022 (~1.5 nM) binding to CHOK1hCB2_bgal membranes in the presence of the compounds **FM10** and **GR106** at their IC_{50} concentration at 10°C. Represented graphs of one experiment performed in duplicate are shown.

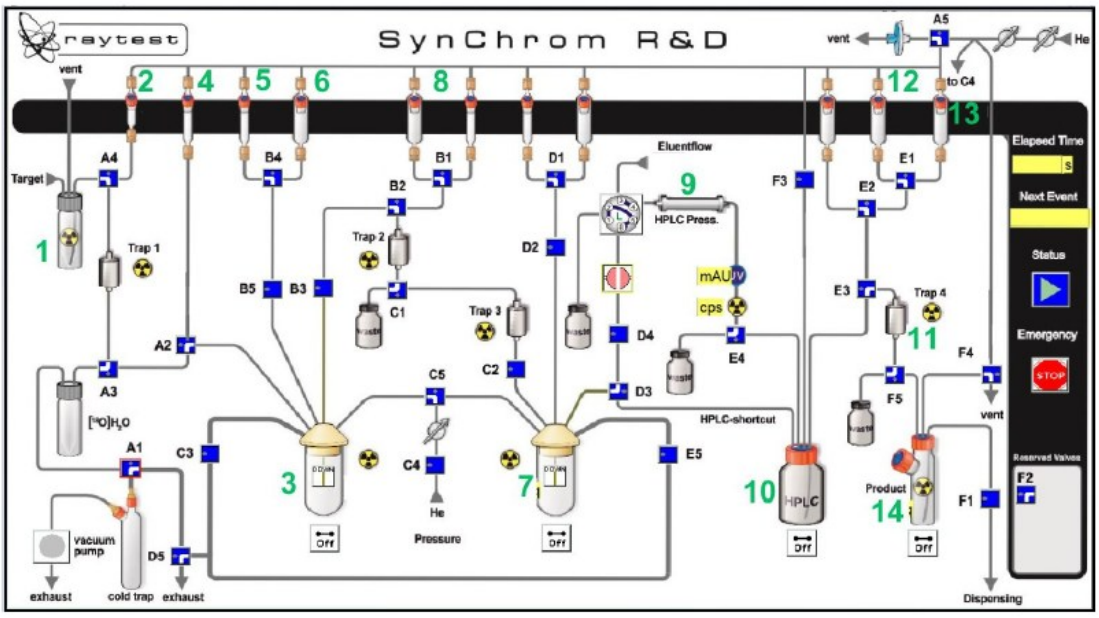

Figure S5.2. Scheme of the Raytest SynChrom R&D synthesis module (Hamburg, Germany) for the automated radiosynthesis of the **[^{18}F]FM10** and **[^{18}F]GR106** with 1) Sep-Pak® Accell Plus QMA Plus Light cartridge; 2) Mixture of 5 mg of $K_{2.2.2.}$, 15 µL K_2CO_3 (20 mg/mL), 800 µL MeCN and 200 µL water; 3) Reactor 1; 4) 1.5 mL MeCN; 5) 1 mg of **32** or 2 mg of **33** in 1 mL of MeCN; 6) 4.1 mL of MeCN/H_2O 1:1; 7) Reactor 2; 8) empty 9) Reprosil-Pur C_{18}-AQ, 10 µm, 250 x 10 mm column from Dr. Maisch GmbH using a mixture of 75% MeCN/ 25% $AcNH_4$ 20 mM flow 4.2 mL/min for **[^{18}F]FM10** and 80% MeCN/ 20% $AcNH_4$ 20 mM flow 4.0 mL/min for **[^{18}F]GR106**; 10) Collecting vial, 40 mL water; 11) Sep-Pak® C_{18} light; 12) 2 mL water; 13) 1.2 mL EtOH; 14) product vial.

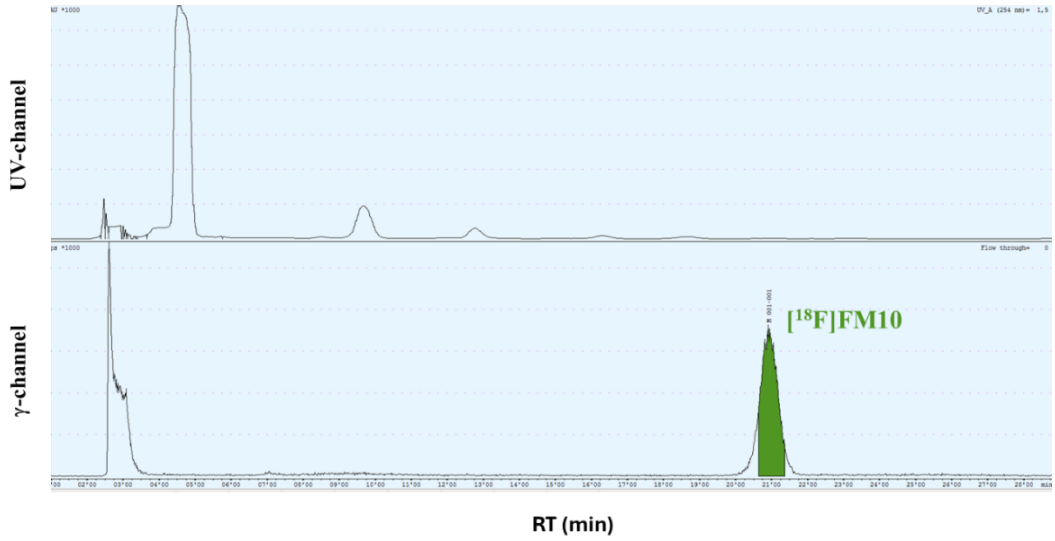

Figure S5.3. Representation of the graphical interface of **[^{18}F]FM10** during purification by semi-preparative HPLC (Reprosil-Pur C_{18}-AQ, 10 µm, 250 x 10 mm column, Dr. Maisch GmbH, Ammerbuch, Germany), eluted with a mobile phase of 75% CH_3CN (20 mM NH_4OAc) at a flow rate of 4.2 mL/min (Rt ≈ 21–22 min).

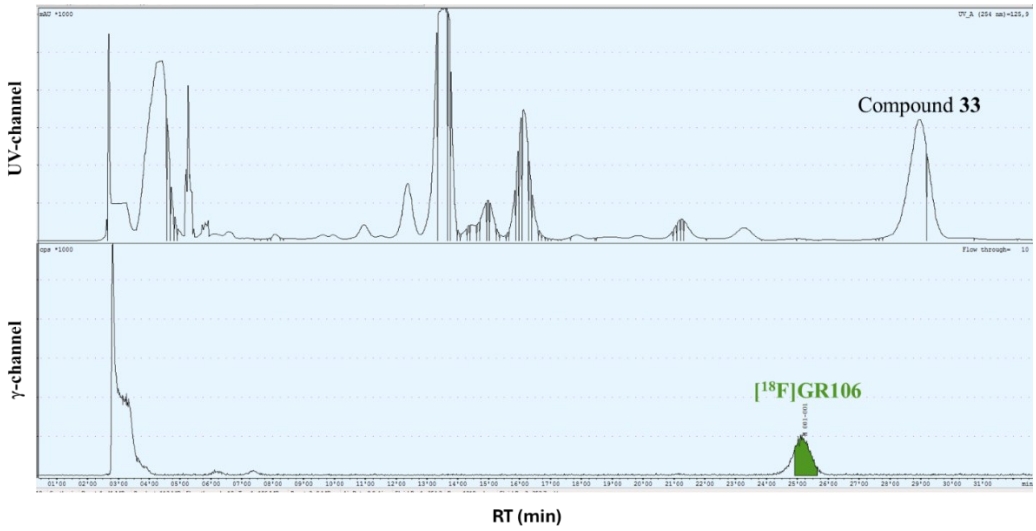

Figure S5.4. Representation of the graphical interface of **[^{18}F]GR106** during purification by semi-preparative HPLC (Reprosil-Pur C_{18}-AQ, 10 µm, 250 x 10 mm column, Dr. Maisch GmbH, Ammerbuch, Germany), eluted with a mobile phase of 80% CH_3CN (20 mM NH_4OAc) at a flow rate of 4.0 mL/min (Rt ≈ 24–25 min).

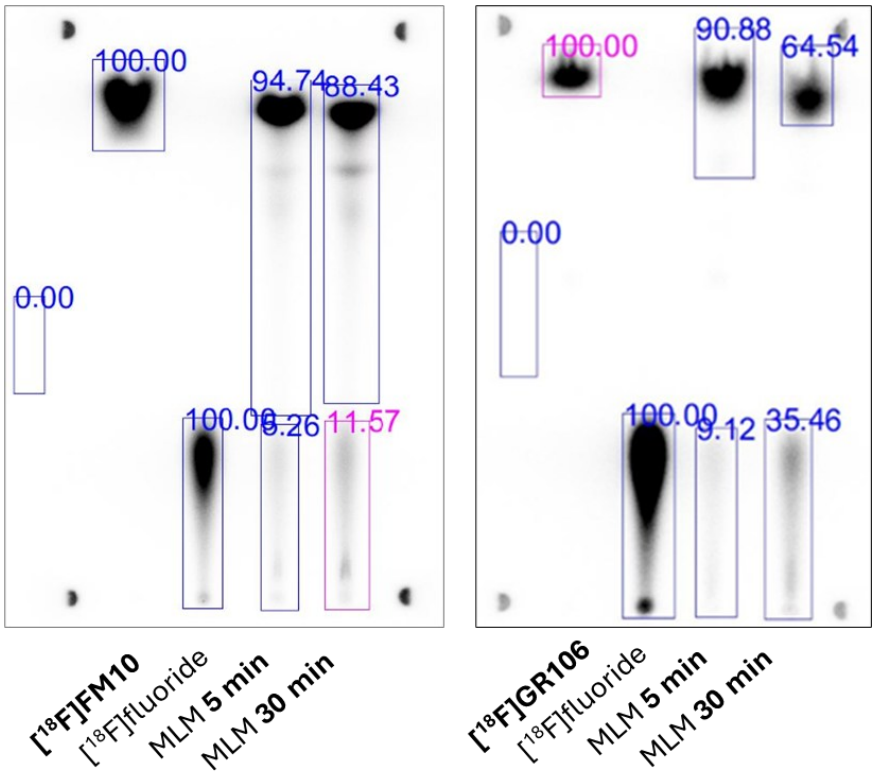

Figure S5.5. Radio-TLC (MeOH / AcOEt / aqAcNH$_4$ (20 mM) 1:1:1).

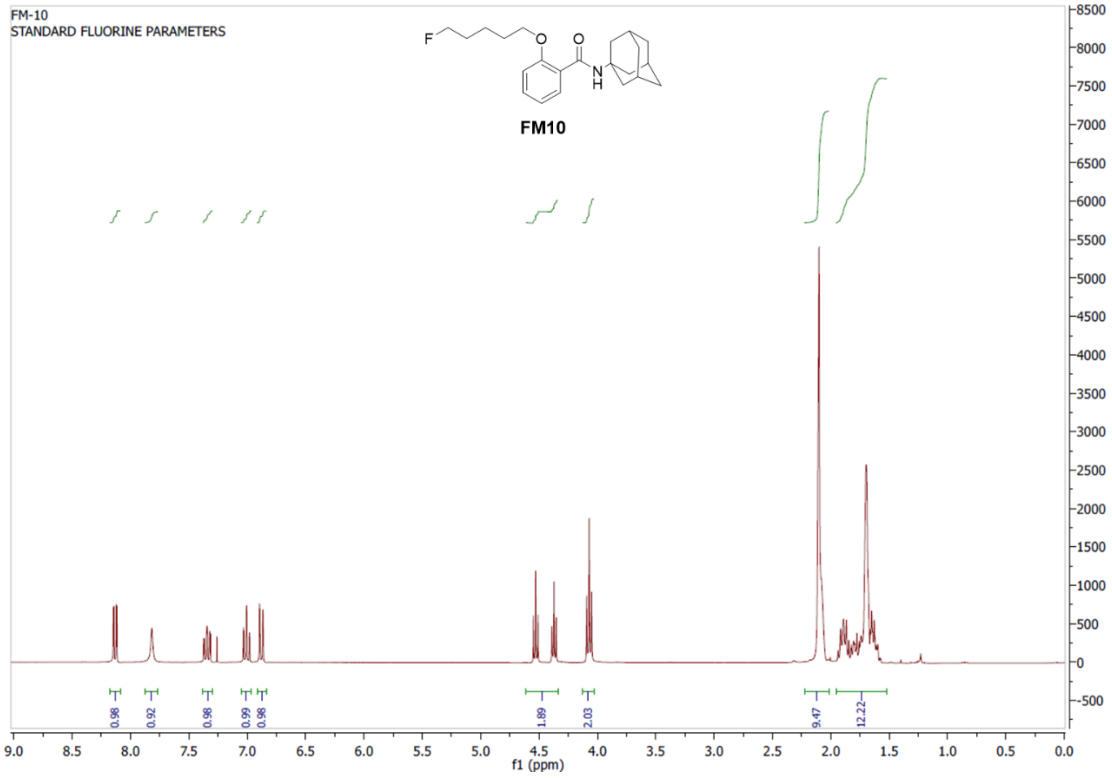

Figure S5.6. ^{1}H-NMR spectrum of **FM10**. $CDCl_3$, 300 MHz, 25 °C.

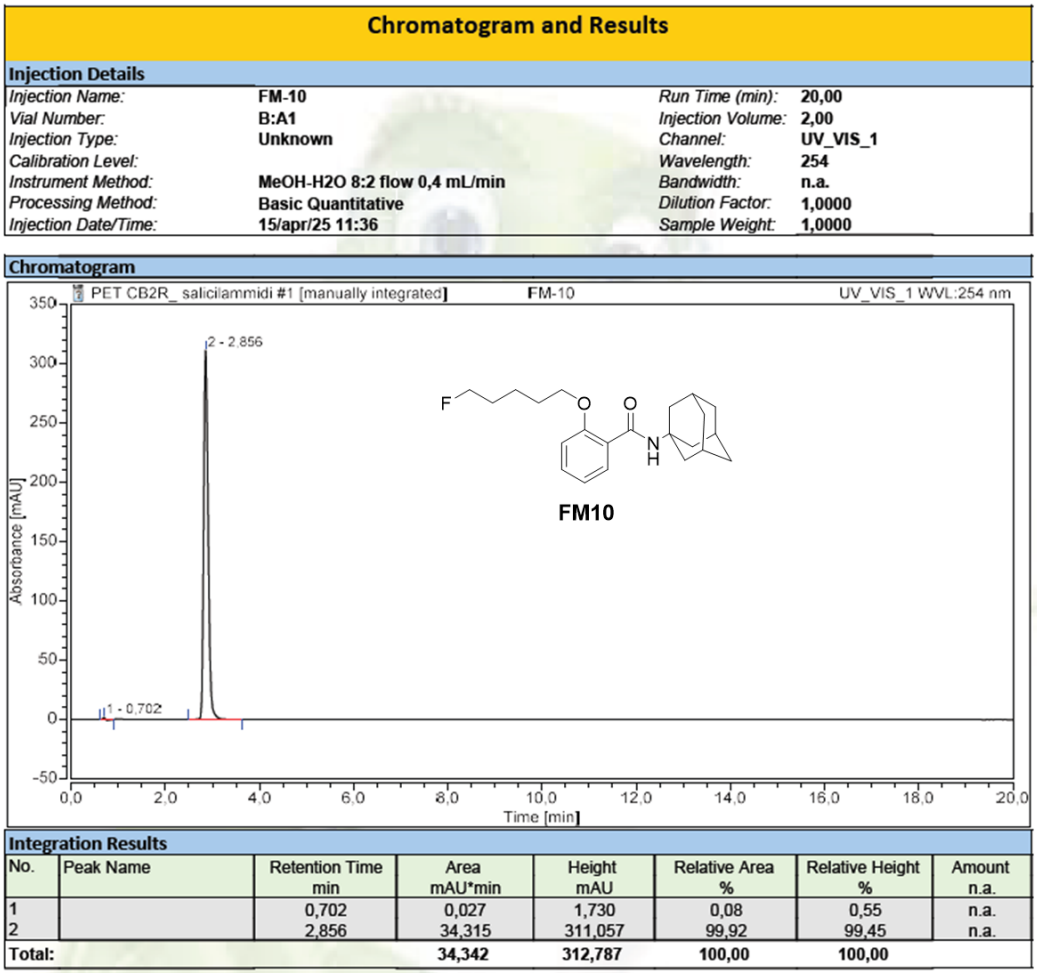

Figure S5.7. HPLC analysis of **FM10**. MeOH-H_2O 8:2, flow 0.4 mL/min. Wavelength, 254 nM..

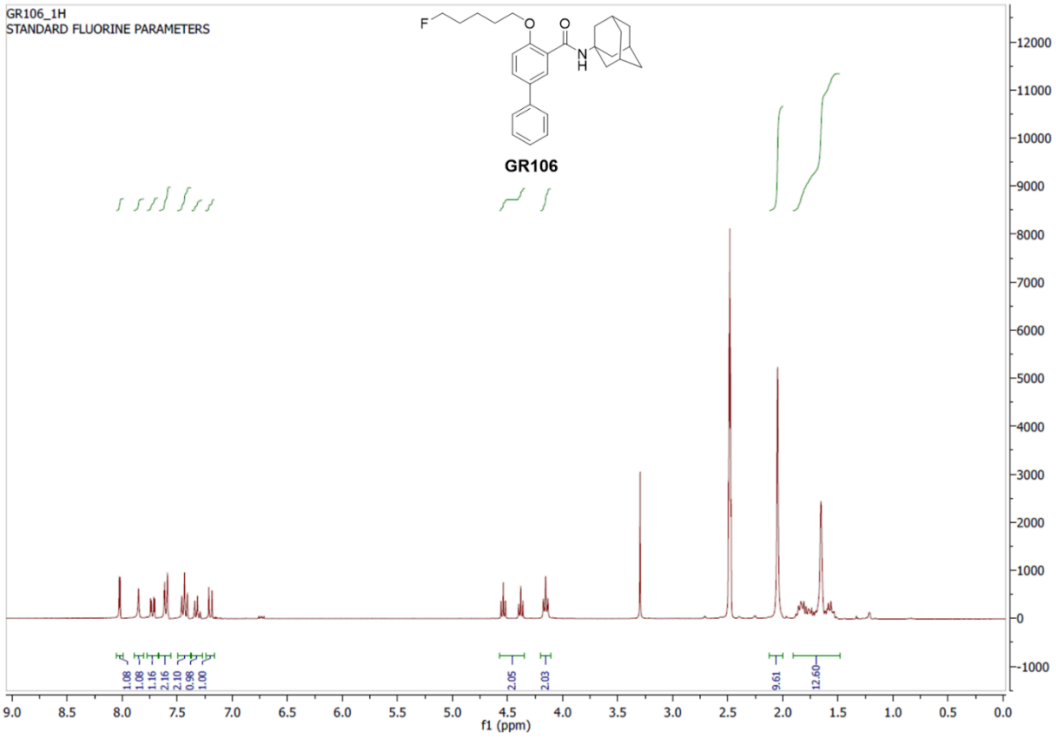

Figure S5.8. ^{1}H-NMR spectrum of **FM10**. DMSO-d_6, 300 MHz, 25 °C.

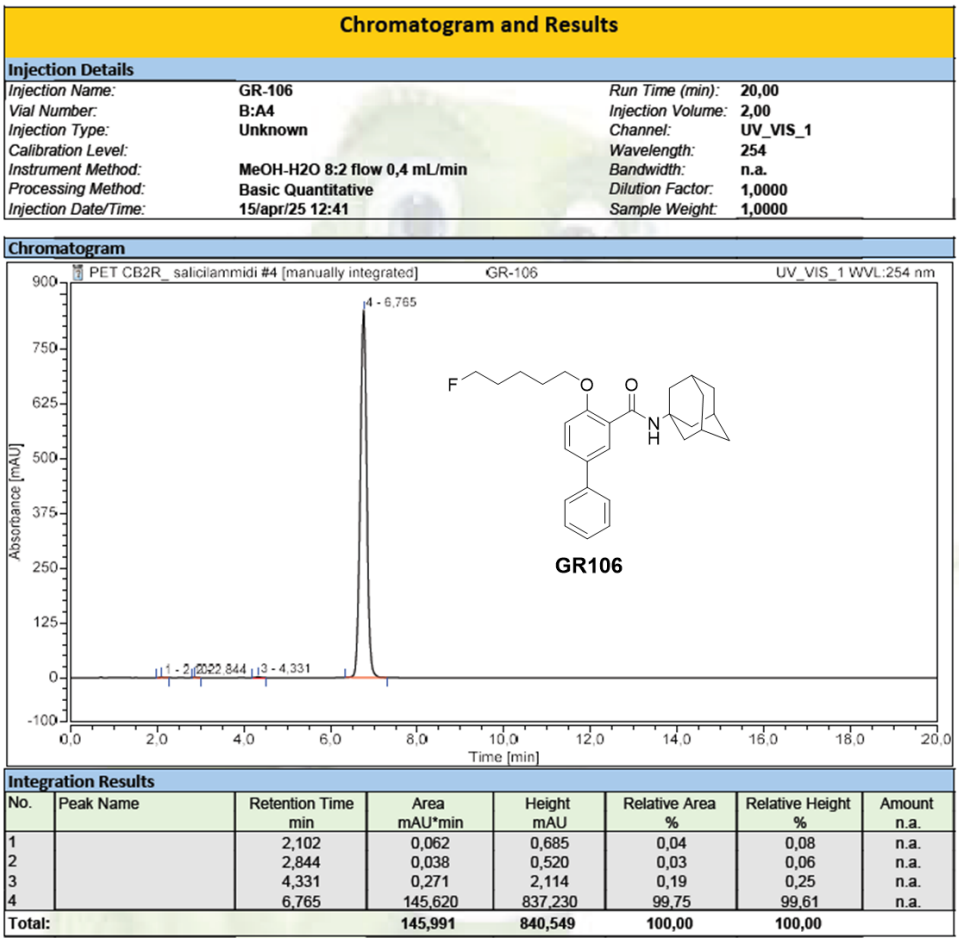

Figure S5.9. HPLC analysis of **GR106**. MeOH-H_2O 8:2, flow 0.4 mL/min. Wavelength, 254 nM..

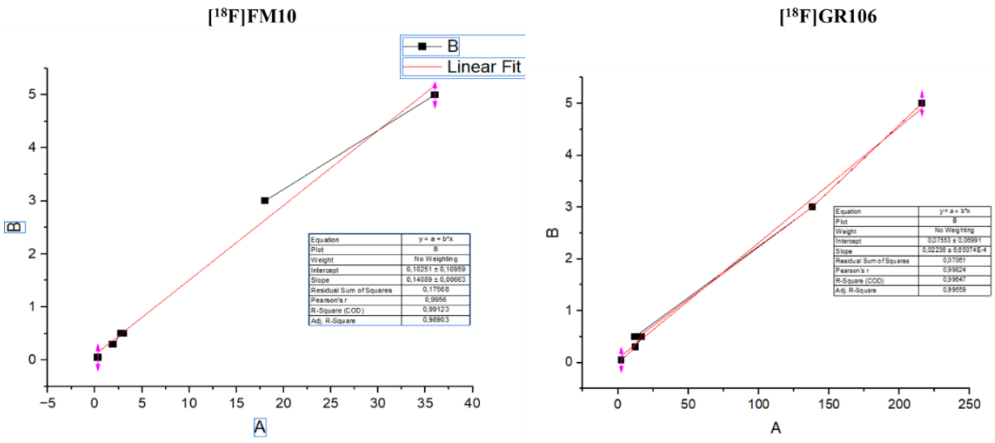

Figure S5.10. Calibration curve for the determination of A_m.

[^{18}F]FM10

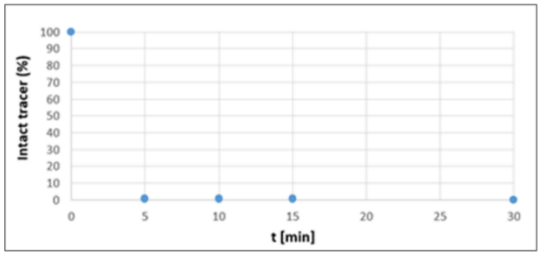

Time course of degradation

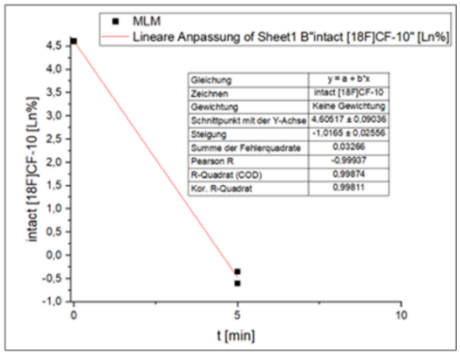

Determination of in vitro half life $t_{1/2}$

[^{18}F]GR106

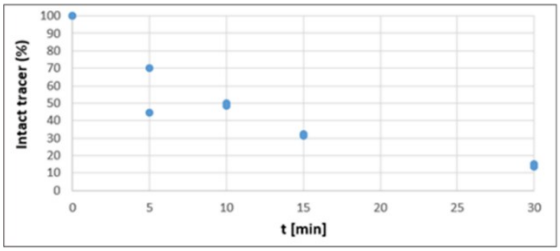

Time course of degradation

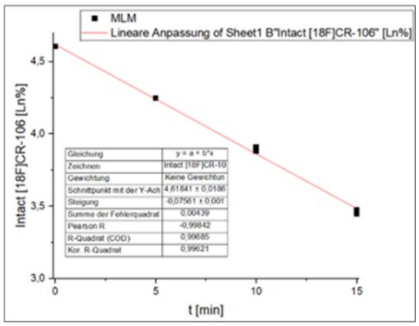

Determination of in vitro half life $t_{1/2}$

Figure S5.11. Graphical analysis of time-dependent depletion of **[^{18}F]FM10** and **[^{18}F]GR106** *in vitro* and linear regression for calculation of *in vitro* $t_{1/2}$ using the following equations: $ln(\text{intact radiotracer in \%}) = ln100 - slope \times t$, and $t_{1/2} = ln2 / slope$.

CHAPTER 6

General conclusions

[^{18}F]MC225, [^{18}F]CF31, [^{18}F]LC2, [^{18}F]FM10 and [^{18}F]GR106: Novel Positron Emission Tomography Radiotracers for Imaging P-Glycoprotein, Sigma-1 and Sigma-2 Receptors, and Cannabinoid subtype 2 receptors in the Central Nervous System

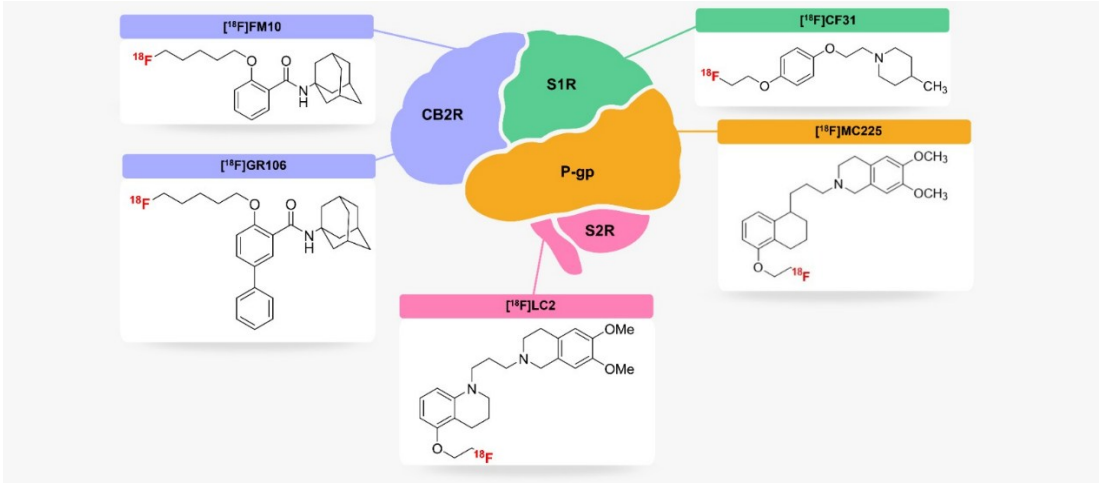

6. General conclusions

The work carried out in this thesis enabled the development and characterization of a series of innovative PET radiotracers for the CNS, aimed at the early diagnosis of neurodegenerative disorders, particularly AD, using P-gp, S1R, S2R, and CB2R as molecular biomarkers.

Regarding P-gp, the first part of the work focused on the development and optimization of **[^{18}F]MC225**, a radiotracer developed in our laboratory and currently under evaluation in two Phase II clinical trials in collaboration with the Department of Nuclear Medicine at the University of Groningen. These studies aim to assess the role of **[^{18}F]MC225** in neurodegenerative disorders, such as PD and AD, and to investigate potential sex-related differences in P-gp expression at the BBB.

The synthesis of the phenolic precursor **FM4**/**MC226** and the cold compound **FM5**/**MC225**, performed in multiple independent batches, demonstrated the robustness and reproducibility of the synthetic process. This provided essential support for obtaining AIFA authorization for a new clinical trial designed to investigate the correlation between P-gp expression and treatment-resistant major depressive disorder. The purity, stability and absence of biological contaminants and residual metals in the precursors were confirmed by an independent accredited laboratory through UPLC analysis and quantitative NMR, in compliance with regulatory requirements and ensuring safety for clinical use. Preliminary results from the clinical trial remain confidential and are therefore not disclosed.

In parallel, the work focused on the development of new potential PET radiotracers through structural simplification of **MC225**. By increasing conformational flexibility and introducing heteroatoms into the molecular structure, lipophilicity was significantly reduced and the chiral center present in **MC225** was eliminated. Subsequent SAfiR analysis identified two promising lead compounds (**ATL22** and **ATL30**), characterized by good P-gp activity (EC_{50} = 1.8 μM and 3.3 μM, respectively), with prospects for future radiolabeling in collaboration with the Policlinico Gemelli using ^{11}C and [^{18}F]-fluoroethoxy groups, following the strategy previously applied for **[^{18}F]MC225**.

The study of sigma receptors represented another major chapter of this thesis. In particular, **CF31**, belonging to the phenoxyethylpiperidine class, emerged as a promising PET candidate for S1R, showing high affinity (K_i S1R = 5.36 nM), excellent selectivity over S2R (K_i S2R = 3009 nM), no interaction with P-gp (EC_{50} > 100 μM) and good BBB permeability. Radiolabeling with ^{18}F was successfully completed, affording good RCY 12–22%, excellent molar activity (A_m 118–194 GBq/μmol), and radiochemical purity >99%. **[^{18}F]CF31** exhibited high chemical stability in biological solutions (>98% after 120 min) and a $logD_{7.4}$ value of 1.24, supporting its potential to cross the BBB. K_D values (1.34–1.36 nM), together with *in vitro* autoradiography performed in the presence and absence of blocking agents, confirmed highly specific binding consistent with S1R distribution in the CNS, supporting future *in vivo* application. However, a major limitation of **[^{18}F]CF31** is its metabolic instability: after 30 min of in v*itro* incubation in MLM, only approximately 5% of the parent radiotracer remained intact, with cleavage of the fluoroethoxy moiety identified as the main metabolic pathway.

Regarding S2R, **LC2**, a radiotracer belonging to the tetralin class and featuring 6,7-dimethoxytetrahydroisoquinoline as the BM, was developed. *In vitro* evaluation of the cold compound revealed high affinity (K_i S2R = 5.87 nM), good selectivity (K_i S1R = 427 nM), and minimal off-target effects assessed across 56 major CNS targets. Interaction with P-gp (EC_{50} = 9.56 μM) could potentially limit CNS penetration. Radiolabeling was performed once (RCY = 7%), and *in vitro* autoradiography

combined with *in vivo* PET imaging demonstrated a rapid but moderate CNS uptake (maximum SUV ≈ 1.4) and equally rapid washout of **[^{18}F]LC2**. The moderate brain penetration may be attributed to P-gp-mediated efflux; therefore, the experiment will be repeated using CsA as a P-gp inhibitor.

Further investigations on S2R involved indole and azaindole derivatives bearing the 3*H*-Spiro[isobenzofuran-1,4′-piperidine] as BM. SAfiR analysis revealed that all compounds exhibited high affinity (K_i 1–5 nM) for both S1R and S2R, and the lack of selectivity precluded their development as PET radiotracers. Additional structural modifications were designed to introduce two methoxy groups to mimic the 6,7-dimethoxytetrahydroisoquinoline scaffold; however, synthetic challenges prevented successful isolation of these molecules. Among the synthesized compounds, **CF7** (K_i S1R = 4.62 nM; K_i S2R = 2.86 nM) emerged as a potential multitarget molecule with a dual S1R/S2R profile, also supported by low cytotoxicity across several cell lines. Further studies are ongoing, particularly to characterize its functional profile at S1R. Potential S2R antagonism combined with S1R agonism could support the development of **CF7** as a neuroprotective agent.

Finally, the thesis addressed the development of new CB2R PET radiotracers belonging to the *N*-adamantyl-salicylamide class. All compounds displayed nanomolar affinity for CB2R and varying degrees of selectivity, demonstrating the robustness of this scaffold. Among the synthesized compounds, two (**FM10** and **GR106**) emerged as particularly promising due to their high affinity (K_i CB2R = 5.7 nM and 1.1 nM, respectively), selectivity (K_i CB1R = 1058 nM and 2% displacement at 1 μM, respectively), moderate interaction with P-gp (EC_{50} = 14.8 μM and 50 μM, respectively), and distinct activity profiles (agonist vs inverse agonist/antagonist), which may for the first time allow investigation of whether intrinsic activity influences CB2R PET imaging.

Radiolabeling of both **FM10** and **GR106** with ^{18}F was successfully achieved, yielding good RCY (32–35% and 7–17%, respectively), satisfactory A_m (79–81 GBq/μmol and 45–61 GBq/μmol, respectively), and radiochemical purity >99%. The $logD_{7.4}$ values (3.41 and 3.64, respectively) support potential CNS penetration. Preliminary autoradiography data suggest higher binding specificity for **[^{18}F]FM10** compared to **[^{18}F]GR106**, possibly related to their different activity profiles; however, optimization of experimental protocols and repetition of the studies are required to confirm these findings. Both compounds exhibited poor *in vitro* metabolic stability: after 30 min of incubation in MLM, only approximately 1% of intact radiotracer remained for **[^{18}F]FM10** and 14% for **[^{18}F]GR106**, with defluorination identified as the main metabolic pathway, particularly for **[^{18}F]GR106**.

SAfiR analysis also identified additional promising compounds (**FM13**, **FM15**, **FM24**, and **FM26**) that were not selected for radiolabeling because they did not meet the predefined criteria (K_i CB2R < 6 nM and ≥100-fold selectivity). These compounds are currently under investigation as potential neuroprotective or antitumor agents.

In summary, the overall results of this thesis confirm the effectiveness of a medicinal chemistry-driven approach for the identification and development of highly specific and selective PET radiotracers. These new tools may enable the investigation of complex molecular systems under both physiological and pathological conditions, offering new opportunities for early diagnosis beyond the currently available approaches. This work represents a significant contribution to translational research and lays the foundation for future preclinical and clinical studies aimed at improving the understanding of pathogenic mechanisms and optimizing therapeutic intervention strategies.

References

1. Steinmetz, J.D.; Seeher, K.M.; Schiess, N.; Nichols, E.; Cao, B.; Servili, C.; Cavallera, V.; Cousin, E.; Hagins, H.; Moberg, M.E.; et al. Global, Regional, and National Burden of Disorders Affecting the Nervous System, 1990–2021: A Systematic Analysis for the Global Burden of Disease Study 2021. *Lancet Neurol.* **2024**, *23*, 344–381, doi:10.1016/S1474-4422(24)00038-3.
2. Feigin, V.L.; Vos, T.; Nichols, E.; Owolabi, M.O.; Carroll, W.M.; Dichgans, M.; Deuschl, G.; Parmar, P.; Brainin, M.; Murray, C. The Global Burden of Neurological Disorders: Translating Evidence into Policy. *Lancet Neurol.* **2020**, *19*, 255–265, doi:10.1016/S1474-4422(19)30411-9.
3. Teleanu, D.M.; Niculescu, A.-G.; Lungu, I.I.; Radu, C.I.; Vladâcenco, O.; Roza, E.; Costăchescu, B.; Grumezescu, A.M.; Teleanu, R.I. An Overview of Oxidative Stress, Neuroinflammation, and Neurodegenerative Diseases. *Int. J. Mol. Sci.* **2022**, *23*, 5938, doi:10.3390/ijms23115938.
4. Van Schependom, J.; D'haeseleer, M. Advances in Neurodegenerative Diseases. *J. Clin. Med.* **2023**, *12*, 1709, doi:10.3390/jcm12051709.
5. Przedborski, S.; Vila, M.; Jackson-Lewis, V. Series Introduction: Neurodegeneration: What Is It and Where Are We? *J. Clin. Invest.* **2003**, *111*, 3–10, doi:10.1172/JCI200317522.
6. Wilson, D.M.; Cookson, M.R.; Van Den Bosch, L.; Zetterberg, H.; Holtzman, D.M.; Dewachter, I. Hallmarks of Neurodegenerative Diseases. *Cell* **2023**, *186*, 693–714, doi:10.1016/j.cell.2022.12.032.
7. Lamptey, R.N.L.; Chaulagain, B.; Trivedi, R.; Gothwal, A.; Layek, B.; Singh, J. A Review of the Common Neurodegenerative Disorders: Current Therapeutic Approaches and the Potential Role of Nanotherapeutics. *Int. J. Mol. Sci.* **2022**, *23*, 1851, doi:10.3390/ijms23031851.
8. DeLegge, M.H.; Smoke, A. Neurodegeneration and Inflammation. *Nutr. Clin. Pract.* **2008**, *23*, 35–41, doi:10.1177/011542650802300135.
9. Abbas, A.K.; Lichtman, A.H.; Pillai, S.; Baker, D.L. *Cellular and Molecular Immunology*; Tenth edition.; Elsevier: Philadelphia, Pennsylvania, 2022; ISBN 978-0-323-75748-5.
10. Medzhitov, R. Origin and Physiological Roles of Inflammation. *Nature* **2008**, *454*, 428–435, doi:10.1038/nature07201.
11. Wickstead, E.S.; Solito, E.; McArthur, S. Promiscuous Receptors and Neuroinflammation: The Formyl Peptide Class. *Life* **2022**, *12*, 2009, doi:10.3390/life12122009.
12. Leng, F.; Edison, P. Neuroinflammation and Microglial Activation in Alzheimer Disease: Where Do We Go from Here? *Nat. Rev. Neurol.* **2021**, *17*, 157–172, doi:10.1038/s41582-020-00435-y.
13. DiSabato, D.J.; Quan, N.; Godbout, J.P. Neuroinflammation: The Devil Is in the Details. *J. Neurochem.* **2016**, *139*, 136–153, doi:10.1111/jnc.13607.
14. Valente, M.; Dentoni, M.; Bellizzi, F.; Kuris, F.; Gigli, G.L. Specialized Pro-Resolving Mediators in Neuroinflammation: Overview of Studies and Perspectives of Clinical Applications. *Molecules* **2022**, *27*, 4836, doi:10.3390/molecules27154836.
15. Cabral, G.A.; Raborn, E.S.; Griffin, L.; Dennis, J.; Marciano-Cabral, F. CB_2 Receptors in the Brain: Role in Central Immune Function. *Br. J. Pharmacol.* **2008**, *153*, 240–251, doi:10.1038/sj.bjp.0707584.
16. Mecha, M.; Carrillo-Salinas, F.J.; Feliú, A.; Mestre, L.; Guaza, C. Microglia Activation States and Cannabinoid System: Therapeutic Implications. *Pharmacol. Ther.* **2016**, *166*, 40–55, doi:10.1016/j.pharmthera.2016.06.011.
17. Bolós, M.; Perea, J.R.; Avila, J. Alzheimer's Disease as an Inflammatory Disease. *Biomol. Concepts* **2017**, *8*, 37–43, doi:10.1515/bmc-2016-0029.
18. Salvi, V.; Sozio, F.; Sozzani, S.; Del Prete, A. Role of Atypical Chemokine Receptors in Microglial Activation and Polarization. *Front. Aging Neurosci.* **2017**, *9*, 148, doi:10.3389/fnagi.2017.00148.
19. Hamilton, T.A.; Adams, D.O. Molecular Mechanisms of Signal Transduction in Macrophages. *Immunol. Today* **1987**, *8*, 151–158, doi:10.1016/0167-5699(87)90145-9.
20. Yang, Z.; Ming, X.-F. Functions of Arginase Isoforms in Macrophage Inflammatory Responses: Impact on Cardiovascular Diseases and Metabolic Disorders. *Front. Immunol.* **2014**, *5*, doi:10.3389/fimmu.2014.00533.
21. Chen, W.-W.; Zhang, X.; Huang, W.-J. Role of Neuroinflammation in Neurodegenerative Diseases (Review). *Mol. Med. Rep.* **2016**, *13*, 3391–3396, doi:10.3892/mmr.2016.4948.
22. Ransohoff, R.M. How Neuroinflammation Contributes to Neurodegeneration. *Science* **2016**, *353*, 777–783, doi:10.1126/science.aag2590.
23. Cassano, T.; Calcagnini, S.; Pace, L.; De Marco, F.; Romano, A.; Gaetani, S. Cannabinoid Receptor 2 Signaling in Neurodegenerative Disorders: From Pathogenesis to a Promising Therapeutic Target. *Front. Neurosci.* **2017**, *11*, doi:10.3389/fnins.2017.00030.
24. Laurent, C.; Dorothée, G.; Hunot, S.; Martin, E.; Monnet, Y.; Duchamp, M.; Dong, Y.; Légeron, F.-P.; Leboucher, A.; Burnouf, S.; et al. Hippocampal T Cell Infiltration Promotes Neuroinflammation and Cognitive Decline in a Mouse Model of Tauopathy. *Brain* **2017**, *140*, 184–200, doi:10.1093/brain/aww270.
25. Mayne, K.; White, J.A.; McMurran, C.E.; Rivera, F.J.; De La Fuente, A.G. Aging and Neurodegenerative Disease: Is the Adaptive Immune System a Friend or Foe? *Front. Aging Neurosci.* **2020**, *12*, 572090, doi:10.3389/fnagi.2020.572090.
26. Takata, F.; Nakagawa, S.; Matsumoto, J.; Dohgu, S. Blood-Brain Barrier Dysfunction Amplifies the Development of Neuroinflammation: Understanding of Cellular Events in Brain Microvascular Endothelial Cells for Prevention and Treatment of BBB Dysfunction. *Front. Cell. Neurosci.* **2021**, *15*, 661838, doi:10.3389/fncel.2021.661838.
27. *Global Status Report on the Public Health Response to Dementia*; 1st ed.; World Health Organization: Geneva, 2021; ISBN 978-92-4-003324-5.

28. Knopman, D.S.; Amieva, H.; Petersen, R.C.; Chételat, G.; Holtzman, D.M.; Hyman, B.T.; Nixon, R.A.; Jones, D.T. Alzheimer Disease. *Nat. Rev. Dis. Primer* **2021**, *7*, 33, doi:10.1038/s41572-021-00269-y.
29. Scheltens, P.; De Strooper, B.; Kivipelto, M.; Holstege, H.; Chételat, G.; Teunissen, C.E.; Cummings, J.; Van Der Flier, W.M. Alzheimer's Disease. *The Lancet* **2021**, *397*, 1577–1590, doi:10.1016/S0140-6736(20)32205-4.
30. Serrano-Pozo, A.; Das, S.; Hyman, B.T. APOE and Alzheimer's Disease: Advances in Genetics, Pathophysiology, and Therapeutic Approaches. *Lancet Neurol.* **2021**, *20*, 68–80, doi:10.1016/S1474-4422(20)30412-9.
31. De-Paula, V.J.; Radanovic, M.; Diniz, B.S.; Forlenza, O.V. Alzheimer's Disease. In *Protein Aggregation and Fibrillogenesis in Cerebral and Systemic Amyloid Disease*; Harris, J.R., Ed.; Subcellular Biochemistry; Springer Netherlands: Dordrecht, 2012; Vol. 65, pp. 329–352 ISBN 978-94-007-5415-7.
32. Jucker, M.; Walker, L.C. Alzheimer's Disease: From Immunotherapy to Immunoprevention. *Cell* **2023**, *186*, 4260–4270, doi:10.1016/j.cell.2023.08.021.
33. Breijyeh, Z.; Karaman, R. Comprehensive Review on Alzheimer's Disease: Causes and Treatment. *Molecules* **2020**, *25*, 5789, doi:10.3390/molecules25245789.
34. Johnson, K.A.; Fox, N.C.; Sperling, R.A.; Klunk, W.E. Brain Imaging in Alzheimer Disease. *Cold Spring Harb. Perspect. Med.* **2012**, *2*, a006213–a006213, doi:10.1101/cshperspect.a006213.
35. Van Oostveen, W.M.; De Lange, E.C.M. Imaging Techniques in Alzheimer's Disease: A Review of Applications in Early Diagnosis and Longitudinal Monitoring. *Int. J. Mol. Sci.* **2021**, *22*, 2110, doi:10.3390/ijms22042110.
36. Rajendran, K.; Krishnan, U.M. Biomarkers in Alzheimer's Disease. *Clin. Chim. Acta* **2024**, *562*, 119857, doi:10.1016/j.cca.2024.119857.
37. Poewe, W.; Seppi, K.; Tanner, C.M.; Halliday, G.M.; Brundin, P.; Volkmann, J.; Schrag, A.-E.; Lang, A.E. Parkinson Disease. *Nat. Rev. Dis. Primer* **2017**, *3*, 17013, doi:10.1038/nrdp.2017.13.
38. Pan, Y.; Nicolazzo, J.A. Impact of Aging, Alzheimer's Disease and Parkinson's Disease on the Blood-Brain Barrier Transport of Therapeutics. *Adv. Drug Deliv. Rev.* **2018**, *135*, 62–74, doi:10.1016/j.addr.2018.04.009.
39. Jankovic, J.; Tan, E.K. Parkinson's Disease: Etiopathogenesis and Treatment. *J. Neurol. Neurosurg. Psychiatry* **2020**, *91*, 795–808, doi:10.1136/jnnp-2019-322338.
40. McColgan, P.; Tabrizi, S.J. Huntington's Disease: A Clinical Review. *Eur. J. Neurol.* **2018**, *25*, 24–34, doi:10.1111/ene.13413.
41. Finkbeiner, S. Huntington's Disease. *Cold Spring Harb. Perspect. Biol.* **2011**, *3*, a007476–a007476, doi:10.1101/cshperspect.a007476.
42. Walker, F.O. Huntington's Disease. *The Lancet* **2007**, *369*, 218–228, doi:10.1016/S0140-6736(07)60111-1.
43. Oh, J.; Vidal-Jordana, A.; Montalban, X. Multiple Sclerosis: Clinical Aspects. *Curr. Opin. Neurol.* **2018**, *31*, 752–759, doi:10.1097/WCO.0000000000000622.
44. Yamout, B.; Alroughani, R. Multiple Sclerosis. *Semin. Neurol.* **2018**, *38*, 212–225, doi:10.1055/s-0038-1649502.
45. Feldman, E.L.; Goutman, S.A.; Petri, S.; Mazzini, L.; Savelieff, M.G.; Shaw, P.J.; Sobue, G. Amyotrophic Lateral Sclerosis. *The Lancet* **2022**, *400*, 1363–1380, doi:10.1016/S0140-6736(22)01272-7.
46. Hardiman, O.; Al-Chalabi, A.; Chio, A.; Corr, E.M.; Logroscino, G.; Robberecht, W.; Shaw, P.J.; Simmons, Z.; Van Den Berg, L.H. Amyotrophic Lateral Sclerosis. *Nat. Rev. Dis. Primer* **2017**, *3*, 17071, doi:10.1038/nrdp.2017.71.
47. Ilieva, H.; Vullaganti, M.; Kwan, J. Advances in Molecular Pathology, Diagnosis, and Treatment of Amyotrophic Lateral Sclerosis. *BMJ* **2023**, *383*, e075037, doi:10.1136/bmj-2023-075037.
48. Brust, P.; Van Den Hoff, J.; Steinbach, J. Development of 18F-Labeled Radiotracers for Neuroreceptor Imaging with Positron Emission Tomography. *Neurosci. Bull.* **2014**, *30*, 777–811, doi:10.1007/s12264-014-1460-6.
49. Matthews, P.M.; Rabiner, E.A.; Passchier, J.; Gunn, R.N. Positron Emission Tomography Molecular Imaging for Drug Development. *Br. J. Clin. Pharmacol.* **2012**, *73*, 175–186, doi:10.1111/j.1365-2125.2011.04085.x.
50. Pichler, B.J.; Judenhofer, M.S.; Pfannenberg, C. Multimodal Imaging Approaches: PET/CT and PET/MRI. In *Molecular Imaging I*; Semmler, W., Schwaiger, M., Eds.; Handbook of Experimental Pharmacology; Springer Berlin Heidelberg: Berlin, Heidelberg, 2008; Vol. 185/1, pp. 109–132 ISBN 978-3-540-72717-0.
51. Schwenck, J.; Sonanini, D.; Cotton, J.M.; Rammensee, H.-G.; La Fougère, C.; Zender, L.; Pichler, B.J. Advances in PET Imaging of Cancer. *Nat. Rev. Cancer* **2023**, *23*, 474–490, doi:10.1038/s41568-023-00576-4.
52. Shukla, A.; Kumar, U. Positron Emission Tomography: An Overview. *J. Med. Phys.* **2006**, *31*, 13, doi:10.4103/0971-6203.25665.
53. Conti, M.; Eriksson, L. Physics of Pure and Non-Pure Positron Emitters for PET: A Review and a Discussion. *EJNMMI Phys.* **2016**, *3*, 8, doi:10.1186/s40658-016-0144-5.
54. Jacobson, O.; Kiesewetter, D.O.; Chen, X. Fluorine-18 Radiochemistry, Labeling Strategies and Synthetic Routes. *Bioconjug. Chem.* **2015**, *26*, 1–18, doi:10.1021/bc500475e.
55. Myburgh, P.J.; Sai, K.K.S. Development and Optimization of ^{11}C-Labeled Radiotracers: A Review of the Modern Quality Control Design Process. *ACS Pharmacol. Transl. Sci.* **2023**, *6*, 1616–1631, doi:10.1021/acsptsci.3c00200.
56. Fan, A.P.; An, H.; Moradi, F.; Rosenberg, J.; Ishii, Y.; Nariai, T.; Okazawa, H.; Zaharchuk, G. Quantification of Brain Oxygen Extraction and Metabolism with [15O]-Gas PET: A Technical Review in the Era of PET/MRI. *NeuroImage* **2020**, *220*, 117136, doi:10.1016/j.neuroimage.2020.117136.
57. Deng, X.; Rong, J.; Wang, L.; Vasdev, N.; Zhang, L.; Josephson, L.; Liang, S.H. Chemistry for Positron Emission Tomography: Recent Advances in^{11}C-,^{18}F-,^{13}N-, and^{15}O-Labeling Reactions. *Angew. Chem. Int. Ed.* **2019**, *58*, 2580–2605, doi:10.1002/anie.201805501.
58. Martiniova, L.; De Palatis, L.; Etchebehere, E.; Ravizzini, G. Gallium-68 in Medical Imaging. *Curr. Radiopharm.* **2016**, *9*, 187–207, doi:10.2174/1874471009666161028150654.
59. Tanwar, K.S.; Pandey, M.K. Gallium-68-Labeled Radiopharmaceuticals: A Review. *Chem. Soc. Rev.* **2025**, *54*, 7421–7483, doi:10.1039/D5CS00392J.
60. Koehler, L.; Gagnon, K.; McQuarrie, S.; Wuest, F. Iodine-124: A Promising Positron Emitter for Organic PET Chemistry. *Molecules* **2010**, *15*, 2686–2718, doi:10.3390/molecules15042686.

61. Luurtsema, G.; Pichler, V.; Bongarzone, S.; Seimbille, Y.; Elsinga, P.; Gee, A.; Vercouillie, J. EANM Guideline for Harmonisation on Molar Activity or Specific Activity of Radiopharmaceuticals: Impact on Safety and Imaging Quality. *EJNMMI Radiopharm. Chem.* **2021**, *6*, 34, doi:10.1186/s41181-021-00149-6.
62. Jacobson, O.; Chen, X. PET Designated Flouride-18 Production and Chemistry. *Curr. Top. Med. Chem.* **2010**, *10*, 1048–1059, doi:10.2174/156802610791384298.
63. Wagner, M.; Wuest, F. The Radiopharmaceutical Chemistry of Fluorine-18: Electrophilic Fluorinations. In *Radiopharmaceutical Chemistry*; Lewis, J.S., Windhorst, A.D., Zeglis, B.M., Eds.; Springer International Publishing: Cham, 2019; pp. 285–295 ISBN 978-3-319-98946-4.
64. Cole, E.; Stewart, M.; Littich, R.; Hoareau, R.; Scott, P. Radiosyntheses Using Fluorine-18: The Art and Science of Late Stage Fluorination. *Curr. Top. Med. Chem.* **2014**, *14*, 875–900, doi:10.2174/1568026614666140202205035.
65. Telu, S.; Chun, J.-H.; Siméon, F.G.; Lu, S.; Pike, V.W. Syntheses of mGluR5 PET Radioligands through the Radiofluorination of Diaryliodonium Tosylates. *Org. Biomol. Chem.* **2011**, *9*, 6629, doi:10.1039/c1ob05555k.
66. Kim, D.W.; Jeong; Lim, S.T.; Sohn, M.-H.; Katzenellenbogen, J.A.; Chi, D.Y. Facile Nucleophilic Fluorination Reactions Using *Tert* -Alcohols as a Reaction Medium: Significantly Enhanced Reactivity of Alkali Metal Fluorides and Improved Selectivity. *J. Org. Chem.* **2008**, *73*, 957–962, doi:10.1021/jo7021229.
67. Coenen, H.H. Fluorine-18 Labeling Methods: Features and Possibilities of Basic Reactions. In *PET Chemistry*; Schubiger, P.A., Lehmann, L., Friebe, M., Eds.; Ernst Schering Research Foundation Workshop; Springer Berlin Heidelberg, 2007; Vol. 64, pp. 15–50 ISBN 978-3-540-32623-6.
68. Ermert, J.; Neumaier, B. The Radiopharmaceutical Chemistry of Fluorine-18: Nucleophilic Fluorinations. In *Radiopharmaceutical Chemistry*; Lewis, J.S., Windhorst, A.D., Zeglis, B.M., Eds.; Springer International Publishing: Cham, 2019; pp. 273–283 ISBN 978-3-319-98946-4.
69. Sanford, M.S.; Scott, P.J.H. Moving Metal-Mediated^{18} F-Fluorination from Concept to Clinic. *ACS Cent. Sci.* **2016**, *2*, 128–130, doi:10.1021/acscentsci.6b00061.
70. Lee, E.; Hooker, J.M.; Ritter, T. Nickel-Mediated Oxidative Fluorination for PET with Aqueous [^{18} F] Fluoride. *J. Am. Chem. Soc.* **2012**, *134*, 17456–17458, doi:10.1021/ja3084797.
71. Lee, E.; Kamlet, A.S.; Powers, D.C.; Neumann, C.N.; Boursalian, G.B.; Furuya, T.; Choi, D.C.; Hooker, J.M.; Ritter, T. A Fluoride-Derived Electrophilic Late-Stage Fluorination Reagent for PET Imaging. *Science* **2011**, *334*, 639–642, doi:10.1126/science.1212625.
72. Tredwell, M.; Preshlock, S.M.; Taylor, N.J.; Gruber, S.; Huiban, M.; Passchier, J.; Mercier, J.; Génicot, C.; Gouverneur, V. A General Copper-Mediated Nucleophilic^{18} F Fluorination of Arenes. *Angew. Chem. Int. Ed.* **2014**, *53*, 7751–7755, doi:10.1002/anie.201404436.
73. Preshlock, S.; Tredwell, M.; Gouverneur, V. ^{18} F-Labeling of Arenes and Heteroarenes for Applications in Positron Emission Tomography. *Chem. Rev.* **2016**, *116*, 719–766, doi:10.1021/acs.chemrev.5b00493.
74. Nerella, S.G.; Singh, P.; Sanam, T.; Digwal, C.S. PET Molecular Imaging in Drug Development: The Imaging and Chemistry Perspective. *Front. Med.* **2022**, *9*, 812270, doi:10.3389/fmed.2022.812270.
75. Pike, V.W. PET Radiotracers: Crossing the Blood–Brain Barrier and Surviving Metabolism. *Trends Pharmacol. Sci.* **2009**, *30*, 431–440, doi:10.1016/j.tips.2009.05.005.
76. Bauer, M.; Tournier, N.; Langer, O. Imaging P-Glycoprotein Function at the Blood–Brain Barrier as a Determinant of the Variability in Response to Central Nervous System Drugs. *Clin. Pharmacol. Ther.* **2019**, *105*, 1061–1064, doi:10.1002/cpt.1402.
77. Waterhouse, R. Determination of Lipophilicity and Its Use as a Predictor of Blood–Brain Barrier Penetration of Molecular Imaging Agents. *Mol. Imaging Biol.* **2003**, *5*, 376–389, doi:10.1016/j.mibio.2003.09.014.
78. Xing, J.; Huang, S.; Heng, Y.; Mei, H.; Pan, X. Computational Insights into Allosteric Conformational Modulation of P-Glycoprotein by Substrate and Inhibitor Binding. *Molecules* **2020**, *25*, 6006, doi:10.3390/molecules25246006.
79. Halder, J.; Pradhan, D.; Kar, B.; Ghosh, G.; Rath, G. Nanotherapeutics Approaches to Overcome P-Glycoprotein-Mediated Multi-Drug Resistance in Cancer. *Nanomedicine Nanotechnol. Biol. Med.* **2022**, *40*, 102494, doi:10.1016/j.nano.2021.102494.
80. Mairinger, S.; Wanek, T.; Kuntner, C.; Doenmez, Y.; Strommer, S.; Stanek, J.; Capparelli, E.; Chiba, P.; Müller, M.; Colabufo, N.A.; et al. Synthesis and Preclinical Evaluation of the Radiolabeled P-Glycoprotein Inhibitor [11C]MC113. *Nucl. Med. Biol.* **2012**, *39*, 1219–1225, doi:10.1016/j.nucmedbio.2012.08.005.
81. Van Waarde, A.; Ramakrishnan, N.K.; Rybczynska, A.A.; Elsinga, P.H.; Berardi, F.; De Jong, J.R.; Kwizera, C.; Perrone, R.; Cantore, M.; Sijbesma, J.W.A.; et al. Synthesis and Preclinical Evaluation of Novel PET Probes for P-Glycoprotein Function and Expression. *J. Med. Chem.* **2009**, *52*, 4524–4532, doi:10.1021/jm900485a.
82. Silva, R.; Vilas-Boas, V.; Carmo, H.; Dinis-Oliveira, R.J.; Carvalho, F.; De Lourdes Bastos, M.; Remião, F. Modulation of P-Glycoprotein Efflux Pump: Induction and Activation as a Therapeutic Strategy. *Pharmacol. Ther.* **2015**, *149*, 1–123, doi:10.1016/j.pharmthera.2014.11.013.
83. Ohashi, R.; Watanabe, R.; Esaki, T.; Taniguchi, T.; Torimoto-Katori, N.; Watanabe, T.; Ogasawara, Y.; Takahashi, T.; Tsukimoto, M.; Mizuguchi, K. Development of Simplified in Vitro P-Glycoprotein Substrate Assay and in Silico Prediction Models To Evaluate Transport Potential of P-Glycoprotein. *Mol. Pharm.* **2019**, *16*, 1851–1863, doi:10.1021/acs.molpharmaceut.8b01143.
84. Nguyen, T.-T.-L.; Duong, V.-A.; Maeng, H.-J. Pharmaceutical Formulations with P-Glycoprotein Inhibitory Effect as Promising Approaches for Enhancing Oral Drug Absorption and Bioavailability. *Pharmaceutics* **2021**, *13*, 1103, doi:10.3390/pharmaceutics13071103.
85. Husain, A.; Makadia, V.; Valicherla, G.R.; Riyazuddin, M.; Gayen, J.R. Approaches to Minimize the Effects of P-glycoprotein in Drug Transport: A Review. *Drug Dev. Res.* **2022**, *83*, 825–841, doi:10.1002/ddr.21918.

86. Staud, F.; Ceckova, M.; Micuda, S.; Pavek, P. Expression and Function of P-Glycoprotein in Normal Tissues: Effect on Pharmacokinetics. In *Multi-Drug Resistance in Cancer*; Zhou, J., Ed.; Methods in Molecular Biology; Humana Press: Totowa, NJ, 2010; Vol. 596, pp. 199–222 ISBN 978-1-60761-415-9.
87. Milojkovic, M.; Milacic, N.; Radovic, J.; Ljubisavljevic, S. MDR1 Gene Polymorphisms and P-Glycoprotein Expression in Respiratory Diseases. *Biomed. Pap.* **2015**, *159*, 341–346, doi:10.5507/bp.2014.032.
88. Mairinger, S.; Hernández-Lozano, I.; Filip, T.; Löbsch, M.; Stanek, J.; Zeitlinger, M.; Hacker, M.; Tournier, N.; Wanek, T.; Ehrhardt, C.; et al. Influence of P-Glycoprotein on Pulmonary Disposition of the Model Substrate [11C]Metoclopramide Assessed by PET Imaging in Rats. *Eur. J. Pharm. Sci.* **2023**, *183*, 106404, doi:10.1016/j.ejps.2023.106404.
89. Al-Jayyoussi, G.; Price, D.F.; Francombe, D.; Taylor, G.; Smith, M.W.; Morris, C.; Edwards, C.D.; Eddershaw, P.; Gumbleton, M. Selectivity in the Impact of P-Glycoprotein upon Pulmonary Absorption of Airway-Dosed Substrates: A Study in Ex Vivo Lung Models Using Chemical Inhibition and Genetic Knockout. *J. Pharm. Sci.* **2013**, *102*, 3382–3394, doi:10.1002/jps.23587.
90. Kozlosky, D.; Barrett, E.; Aleksunes, L.M. Regulation of Placental Efflux Transporters during Pregnancy Complications. *Drug Metab. Dispos.* **2022**, *50*, 1364–1375, doi:10.1124/dmd.121.000449.
91. Gil, S.; Saura, R.; Forestier, F.; Farinotti, R. P-Glycoprotein Expression of the Human Placenta during Pregnancy. *Placenta* **2005**, *26*, 268–270, doi:10.1016/j.placenta.2004.05.013.
92. Eyal, S.; Chung, F.S.; Muzi, M.; Link, J.M.; Mankoff, D.A.; Kaddoumi, A.; O'Sullivan, F.; Hebert, M.F.; Unadkat, J.D. Simultaneous PET Imaging of P-Glycoprotein Inhibition in Multiple Tissues in the Pregnant Nonhuman Primate. *J. Nucl. Med.* **2009**, *50*, 798–806, doi:10.2967/jnumed.108.059360.
93. Liu, W.; Mossel, P.; Schwach, V.; Slart, R.H.J.A.; Luurtsema, G. Cardiac PET Imaging of ATP Binding Cassette (ABC) Transporters: Opportunities and Challenges. *Pharmaceuticals* **2023**, *16*, 1715, doi:10.3390/ph16121715.
94. Solbach, T.; Konig, J.; Fromm, M.; Zolk, O. ATP-Binding Cassette Transporters in the Heart. *Trends Cardiovasc. Med.* **2006**, *16*, 7–15, doi:10.1016/j.tcm.2005.10.001.
95. Mora Lagares, L.; Novič, M. Recent Advances on P-Glycoprotein (ABCB1) Transporter Modelling with In Silico Methods. *Int. J. Mol. Sci.* **2022**, *23*, 14804, doi:10.3390/ijms232314804.
96. Kumar, A.; Jaitak, V. Natural Products as Multidrug Resistance Modulators in Cancer. *Eur. J. Med. Chem.* **2019**, *176*, 268–291, doi:10.1016/j.ejmech.2019.05.027.
97. Mora Lagares, L.; Pérez-Castillo, Y.; Minovski, N.; Novič, M. Structure–Function Relationships in the Human P-Glycoprotein (ABCB1): Insights from Molecular Dynamics Simulations. *Int. J. Mol. Sci.* **2021**, *23*, 362, doi:10.3390/ijms23010362.
98. Ahmed Juvale, I.I.; Abdul Hamid, A.A.; Abd Halim, K.B.; Che Has, A.T. P-Glycoprotein: New Insights into Structure, Physiological Function, Regulation and Alterations in Disease. *Heliyon* **2022**, *8*, e09777, doi:10.1016/j.heliyon.2022.e09777.
99. Aller, S.G.; Yu, J.; Ward, A.; Weng, Y.; Chittaboina, S.; Zhuo, R.; Harrell, P.M.; Trinh, Y.T.; Zhang, Q.; Urbatsch, I.L.; et al. Structure of P-Glycoprotein Reveals a Molecular Basis for Poly-Specific Drug Binding. *Science* **2009**, *323*, 1718–1722, doi:10.1126/science.1168750.
100. Mollazadeh, S.; Sahebkar, A.; Hadizadeh, F.; Behravan, J.; Arabzadeh, S. Structural and Functional Aspects of P-Glycoprotein and Its Inhibitors. *Life Sci.* **2018**, *214*, 118–123, doi:10.1016/j.lfs.2018.10.048.
101. Gil-Martins, E.; Barbosa, D.J.; Silva, V.; Remião, F.; Silva, R. Dysfunction of ABC Transporters at the Blood-Brain Barrier: Role in Neurological Disorders. *Pharmacol. Ther.* **2020**, *213*, 107554, doi:10.1016/j.pharmthera.2020.107554.
102. Qosa, H.; Miller, D.S.; Pasinelli, P.; Trotti, D. Regulation of ABC Efflux Transporters at Blood-Brain Barrier in Health and Neurological Disorders. *Brain Res.* **2015**, *1628*, 298–316, doi:10.1016/j.brainres.2015.07.005.
103. Lam, F.C.; Liu, R.; Lu, P.; Shapiro, A.B.; Renoir, J.; Sharom, F.J.; Reiner, P.B. β-Amyloid Efflux Mediated by P-glycoprotein. *J. Neurochem.* **2001**, *76*, 1121–1128, doi:10.1046/j.1471-4159.2001.00113.x.
104. Bartels, A.L. Blood-Brain Barrier P-Glycoprotein Function in Neurodegenerative Disease. *Curr. Pharm. Des.* **2011**, *17*, 2771–2777, doi:10.2174/138161211797440122.
105. Xing, Z.-K.; Du, L.-S.; Fang, X.; Liang, H.; Zhang, S.-N.; Shi, L.; Kuang, C.-X.; Han, T.-X.; Yang, Q. The Relationship among Amyloid-β Deposition, Sphingomyelin Level, and the Expression and Function of P-Glycoprotein in Alzheimer's Disease Pathological Process. *Neural Regen. Res.* **2023**, *18*, 1300, doi:10.4103/1673-5374.358607.
106. Jeynes, B.; Provias, J. P-Glycoprotein Altered Expression in Alzheimer's Disease: Regional Anatomic Variability. *J. Neurodegener. Dis.* **2013**, *2013*, 1–7, doi:10.1155/2013/257953.
107. Ding, Y.; Zhong, Y.; Baldeshwiler, A.; Abner, E.L.; Bauer, B.; Hartz, A.M.S. Protecting P-Glycoprotein at the Blood–Brain Barrier from Degradation in an Alzheimer's Disease Mouse Model. *Fluids Barriers CNS* **2021**, *18*, 10, doi:10.1186/s12987-021-00245-4.
108. Desai, B.S.; Monahan, A.J.; Carvey, P.M.; Hendey, B. Blood–Brain Barrier Pathology in Alzheimer's and Parkinson's Disease: Implications for Drug Therapy. *Cell Transplant.* **2007**, *16*, 285–299, doi:10.3727/000000007783464731.
109. Pizarro-Galleguillos, B.M.; Kunert, L.; Brüggemann, N.; Prasuhn, J. Neuroinflammation and Mitochondrial Dysfunction in Parkinson's Disease: Connecting Neuroimaging with Pathophysiology. *Antioxidants* **2023**, *12*, 1411, doi:10.3390/antiox12071411.
110. Hou, J.; Liu, Q.; Li, Y.; Sun, H.; Zhang, J. An *In Vivo* Microdialysis Study of FLZ Penetration through the Blood-Brain Barrier in Normal and 6-Hydroxydopamine Induced Parkinson's Disease Model Rats. *BioMed Res. Int.* **2014**, *2014*, 1–11, doi:10.1155/2014/850493.
111. Bartels, A.L.; Van Berckel, B.N.M.; Lubberink, M.; Luurtsema, G.; Lammertsma, A.A.; Leenders, K.L. Blood–Brain Barrier P-Glycoprotein Function Is Not Impaired in Early Parkinson's Disease. *Parkinsonism Relat. Disord.* **2008**, *14*, 505–508, doi:10.1016/j.parkreldis.2007.11.007.

112. Bartels, A.L.; Kortekaas, R.; Bart, J.; Willemsen, A.T.M.; De Klerk, O.L.; De Vries, J.J.; Van Oostrom, J.C.H.; Leenders, K.L. Blood–Brain Barrier P-Glycoprotein Function Decreases in Specific Brain Regions with Aging: A Possible Role in Progressive Neurodegeneration. *Neurobiol. Aging* **2009**, *30*, 1818–1824, doi:10.1016/j.neurobiolaging.2008.02.002.
113. Salk, R.H.; Hyde, J.S.; Abramson, L.Y. Gender Differences in Depression in Representative National Samples: Meta-Analyses of Diagnoses and Symptoms. *Psychol. Bull.* **2017**, *143*, 783–822, doi:10.1037/bul0000102.
114. Van Loo, H.M.; Aggen, S.H.; Gardner, C.O.; Kendler, K.S. Sex Similarities and Differences in Risk Factors for Recurrence of Major Depression. *Psychol. Med.* **2018**, *48*, 1685–1693, doi:10.1017/S0033291717003178.
115. Carvalho Silva, R.; Pisanu, C.; Maffioletti, E.; Menesello, V.; Bortolomasi, M.; Gennarelli, M.; Baune, B.T.; Squassina, A.; Minelli, A. Biological Markers of Sex-Based Differences in Major Depressive Disorder and in Antidepressant Response. *Eur. Neuropsychopharmacol.* **2023**, *76*, 89–107, doi:10.1016/j.euroneuro.2023.07.012.
116. Liu, D.Y.; Thompson, R.J. Selection and Implementation of Emotion Regulation Strategies in Major Depressive Disorder: An Integrative Review. *Clin. Psychol. Rev.* **2017**, *57*, 183–194, doi:10.1016/j.cpr.2017.07.004.
117. Qian, W.; Homma, M.; Itagaki, F.; Tachikawa, H.; Kawanishi, Y.; Mizukami, K.; Asada, T.; Inomata, S.; Honda, K.; Ohkohchi, N.; et al. MDR1 Gene Polymorphism in Japanese Patients with Schizophrenia and Mood Disorders Including Depression. *Biol. Pharm. Bull.* **2006**, *29*, 2446–2450, doi:10.1248/bpb.29.2446.
118. Fujii, T.; Ota, M.; Hori, H.; Sasayama, D.; Hattori, K.; Teraishi, T.; Yamamoto, N.; Hashikura, M.; Tatsumi, M.; Higuchi, T.; et al. Association between the Functional Polymorphism (C3435T) of the Gene Encoding P-Glycoprotein (ABCB1) and Major Depressive Disorder in the Japanese Population. *J. Psychiatr. Res.* **2012**, *46*, 555–559, doi:10.1016/j.jpsychires.2012.01.012.
119. O'Brien, F.E.; Dinan, T.G.; Griffin, B.T.; Cryan, J.F. Interactions between Antidepressants and P-glycoprotein at the Blood–Brain Barrier: Clinical Significance of *in Vitro* and *in Vivo* Findings. *Br. J. Pharmacol.* **2012**, *165*, 289–312, doi:10.1111/j.1476-5381.2011.01557.x.
120. Uhr, M.; Tontsch, A.; Namendorf, C.; Ripke, S.; Lucae, S.; Ising, M.; Dose, T.; Ebinger, M.; Rosenhagen, M.; Kohli, M.; et al. Polymorphisms in the Drug Transporter Gene ABCB1 Predict Antidepressant Treatment Response in Depression. *Neuron* **2008**, *57*, 203–209, doi:10.1016/j.neuron.2007.11.017.
121. Lin, K.-M.; Chiu, Y.-F.; Tsai, I.-J.; Chen, C.-H.; Shen, W.W.; Liu, S.C.; Lu, S.-C.; Liu, C.-Y.; Hsiao, M.-C.; Tang, H.-S.; et al. ABCB1 Gene Polymorphisms Are Associated with the Severity of Major Depressive Disorder and Its Response to Escitalopram Treatment. *Pharmacogenet. Genomics* **2011**, *21*, 163–170, doi:10.1097/FPC.0b013e32833db216.
122. Uhr, M. Penetration of Amitriptyline, but Not of Fluoxetine, into Brain Is Enhanced in Mice with Blood-Brain Barrier Deficiency Due to Mdr1a P-Glycoprotein Gene Disruption. *Neuropsychopharmacology* **2000**, *22*, 380–387, doi:10.1016/S0893-133X(99)00095-0.
123. Weiss, J.; Dormann, S.-M.G.; Martin-Facklam, M.; Kerpen, C.J.; Ketabi-Kiyanvash, N.; Haefeli, W.E. Inhibition of P-Glycoprotein by Newer Antidepressants. *J. Pharmacol. Exp. Ther.* **2003**, *305*, 197–204, doi:10.1124/jpet.102.046532.
124. Singh, A.B.; Bousman, C.A.; Ng, C.H.; Byron, K.; Berk, M. ABCB1 Polymorphism Predicts Escitalopram Dose Needed for Remission in Major Depression. *Transl. Psychiatry* **2012**, *2*, e198–e198, doi:10.1038/tp.2012.115.
125. Chang, H.H.; Chou, C.-H.; Yang, Y.K.; Lee, I.H.; Chen, P.S. Association between *ABCB1* Polymorphisms and Antidepressant Treatment Response in Taiwanese Major Depressive Patients. *Clin. Psychopharmacol. Neurosci.* **2015**, *13*, 250–255, doi:10.9758/cpn.2015.13.3.250.
126. Kao, Y.-H.; Chern, Y.; Yang, H.-T.; Chen, H.-M.; Lin, C.-J. Regulation of P-Glycoprotein Expression in Brain Capillaries in Huntington's Disease and Its Impact on Brain Availability of Antipsychotic Agents Risperidone and Paliperidone. *J. Cereb. Blood Flow Metab.* **2016**, *36*, 1412–1423, doi:10.1177/0271678X15606459.
127. De Klerk, O.L.; Willemsen, A.T.M.; Bosker, F.J.; Bartels, A.L.; Hendrikse, N.H.; Den Boer, J.A.; Dierckx, R.A. Regional Increase in P-Glycoprotein Function in the Blood-Brain Barrier of Patients with Chronic Schizophrenia: *Psychiatry Res. Neuroimaging* **2010**, *183*, 151–156, doi:10.1016/j.pscychresns.2010.05.002.
128. Bukowski, K.; Kciuk, M.; Kontek, R. Mechanisms of Multidrug Resistance in Cancer Chemotherapy. *Int. J. Mol. Sci.* **2020**, *21*, 3233, doi:10.3390/ijms21093233.
129. Wanek, T.; Kuntner, C.; Bankstahl, J.P.; Bankstahl, M.; Stanek, J.; Sauberer, M.; Mairinger, S.; Strommer, S.; Wacheck, V.; Löscher, W.; et al. A Comparative Small-Animal PET Evaluation of [11C]Tariquidar, [11C]Elacridar and (R)-[11C]Verapamil for Detection of P-Glycoprotein-Expressing Murine Breast Cancer. *Eur. J. Nucl. Med. Mol. Imaging* **2012**, *39*, 149–159, doi:10.1007/s00259-011-1941-7.
130. Carocci, A.; Catalano, A.; Turi, F.; Lovece, A.; Cavalluzzi, M.M.; Bruno, C.; Colabufo, N.A.; Contino, M.; Perrone, M.G.; Franchini, C.; et al. Stereoselective Modulation of P-Glycoprotein by Chiral Small Molecules. *ChemMedChem* **2016**, *11*, 93–101, doi:10.1002/cmdc.201500417.
131. Palmeira, A.; Sousa, E.; Helena Vasconcelos, M.; Pinto, M.; X. Fernandes, M. Structure and Ligand-Based Design of P-Glycoprotein Inhibitors: A Historical Perspective. *Curr. Pharm. Des.* **2012**, *18*, 4197–4214, doi:10.2174/138161212802430530.
132. Pettersson, M.; Hou, X.; Kuhn, M.; Wager, T.T.; Kauffman, G.W.; Verhoest, P.R. Quantitative Assessment of the Impact of Fluorine Substitution on P-Glycoprotein (P-Gp) Mediated Efflux, Permeability, Lipophilicity, and Metabolic Stability. *J. Med. Chem.* **2016**, *59*, 5284–5296, doi:10.1021/acs.jmedchem.6b00027.
133. Dong, J.; Qin, Z.; Zhang, W.-D.; Cheng, G.; Yehuda, A.G.; Ashby, C.R.; Chen, Z.-S.; Cheng, X.-D.; Qin, J.-J. Medicinal Chemistry Strategies to Discover P-Glycoprotein Inhibitors: An Update. *Drug Resist. Updat.* **2020**, *49*, 100681, doi:10.1016/j.drup.2020.100681.
134. Syvänen, S.; Eriksson, J. Advances in PET Imaging of P-Glycoprotein Function at the Blood-Brain Barrier. *ACS Chem. Neurosci.* **2013**, *4*, 225–237, doi:10.1021/cn3001729.
135. Vaalburg, W.; Hendrikse, N.; Elsinga, P.; Bart, J.; Vanwaarde, A. P-Glycoprotein Activity and Biological Response. *Toxicol. Appl. Pharmacol.* **2005**, *207*, 257–260, doi:10.1016/j.taap.2005.03.027.

136. Unadkat, J.D.; Ke, B.; Eyal, S. The Impact of the BBB on the Pharmacokinetics of Drugs: Investigations by PET. In *Trends on the Role of PET in Drug Development*; WORLD SCIENTIFIC, 2012; pp. 575–614 ISBN 978-981-4317-73-3.
137. Simony-Lafontaine, J.; Esslimani, M.; Bribes, E.; Gourgou, S.; Lequeux, N.; Lavail, R.; Grenier, J.; Kramar, A.; Casellas, P. Immunocytochemical Assessment of Sigma-1 Receptor and Human Sterol Isomerase in Breast Cancer and Their Relationship with a Series of Prognostic Factors. *Br. J. Cancer* **2000**, *82*, 1958–1966, doi:10.1054/bjoc.2000.1162.
138. Arakawa, R.; Ito, H.; Okumura, M.; Morimoto, T.; Seki, C.; Takahashi, H.; Takano, A.; Suhara, T. No Inhibitory Effect on P-Glycoprotein Function at Blood–Brain Barrier by Clinical Dose of Clarithromycin: A Human PET Study with [11C]Verapamil. *Ann. Nucl. Med.* **2010**, *24*, 83–87, doi:10.1007/s12149-009-0336-3.
139. Hanke, N.; Türk, D.; Selzer, D.; Wiebe, S.; Fernandez, É.; Stopfer, P.; Nock, V.; Lehr, T. A Mechanistic, Enantioselective, Physiologically Based Pharmacokinetic Model of Verapamil and Norverapamil, Built and Evaluated for Drug–Drug Interaction Studies. *Pharmaceutics* **2020**, *12*, 556, doi:10.3390/pharmaceutics12060556.
140. Abrahim, A.; Luurtsema, G.; Bauer, M.; Karch, R.; Lubberink, M.; Pataraia, E.; Joukhadar, C.; Kletter, K.; Lammertsma, A.A.; Baumgartner, C.; et al. Peripheral Metabolism of (R)-[11C]Verapamil in Epilepsy Patients. *Eur. J. Nucl. Med. Mol. Imaging* **2008**, *35*, 116–123, doi:10.1007/s00259-007-0556-5.
141. Toyohara, J.; Okamoto, M.; Aramaki, H.; Zaitsu, Y.; Shimizu, I.; Ishiwata, K. (R)-[11C]Emopamil as a Novel Tracer for Imaging Enhanced P-Glycoprotein Function. *Nucl. Med. Biol.* **2016**, *43*, 52–62, doi:10.1016/j.nucmedbio.2015.09.001.
142. Robinson, M.A.; Mehvar, R. ENANTIOSELECTIVE DISTRIBUTION OF VERAPAMIL AND NORVERAPAMIL INTO HUMAN AND RAT ERYTHROCYTES: THE ROLE OF PLASMA PROTEIN BINDING. *Biopharm. Drug Dispos.* **1996**, *17*, 577–587, doi:10.1002/(SICI)1099-081X(199610)17:7<577::AID-BDD984>3.0.CO;2-P.
143. Waldegger, S.; Niemeyer, G.; Mörike, K.; Wagner, C.A.; Suessbrich, H.; Busch, A.E.; Lang, F.; Eichelbaum, M. Effect of Verapamil Enantiomers and Metabolites on Cardiac K^+ Channels Expressed in *Xenopus* Oocytes. *Cell. Physiol. Biochem.* **1999**, *9*, 81–89, doi:10.1159/000016304.
144. Luurtsema, G.; Molthoff, C.F.M.; Windhorst, A.D.; Smit, J.W.; Keizer, H.; Boellaard, R.; Lammertsma, A.A.; Franssen, E.J.F. (R)- and (S)-[11C]Verapamil as PET-Tracers for Measuring P-Glycoprotein Function: In Vitro and in Vivo Evaluation. *Nucl. Med. Biol.* **2003**, *30*, 747–751, doi:10.1016/S0969-8051(03)00078-7.
145. Takashima, T.; Yokoyama, C.; Mizuma, H.; Yamanaka, H.; Wada, Y.; Onoe, K.; Nagata, H.; Tazawa, S.; Doi, H.; Takahashi, K.; et al. Developmental Changes in P-Glycoprotein Function in the Blood–Brain Barrier of Nonhuman Primates: PET Study with *R* -^{11} C-Verapamil and^{11} C-Oseltamivir. *J. Nucl. Med.* **2011**, *52*, 950–957, doi:10.2967/jnumed.110.083949.
146. Verbeek, J.; Syvänen, S.; Schuit, R.C.; Eriksson, J.; De Lange, E.C.; Windhorst, A.D.; Luurtsema, G.; Lammertsma, A.A. Synthesis and Preclinical Evaluation of [11C]D617, a Metabolite of (R)-[11C]Verapamil. *Nucl. Med. Biol.* **2012**, *39*, 530–539, doi:10.1016/j.nucmedbio.2011.10.017.
147. Lubberink, M.; Luurtsema, G.; Van Berckel, B.N.; Boellaard, R.; Toornvliet, R.; Windhorst, A.D.; Franssen, E.J.; Lammertsma, A.A. Evaluation of Tracer Kinetic Models for Quantification of P-Glycoprotein Function Using (*R*)-[^{11} C]Verapamil and PET. *J. Cereb. Blood Flow Metab.* **2007**, *27*, 424–433, doi:10.1038/sj.jcbfm.9600349.
148. Luurtsema, G.; Molthoff, C.F.M.; Schuit, R.C.; Windhorst, A.D.; Lammertsma, A.A.; Franssen, E.J.F. Evaluation of (R)-[11C]Verapamil as PET Tracer of P-Glycoprotein Function in the Blood–Brain Barrier: Kinetics and Metabolism in the Rat. *Nucl. Med. Biol.* **2005**, *32*, 87–93, doi:10.1016/j.nucmedbio.2004.06.007.
149. Ikoma, Y.; Takano, A.; Ito, H.; Kusuhara, H.; Sugiyama, Y.; Arakawa, R.; Fukumura, T.; Nakao, R.; Suzuki, K.; Suhara, T. Quantitative Analysis of 11C-Verapamil Transfer at the Human Blood-Brain Barrier for Evaluation of P-Glycoprotein Function. *J. Nucl. Med. Off. Publ. Soc. Nucl. Med.* **2006**, *47*, 1531–1537.
150. Lee, Y.-J.; Maeda, J.; Kusuhara, H.; Okauchi, T.; Inaji, M.; Nagai, Y.; Obayashi, S.; Nakao, R.; Suzuki, K.; Sugiyama, Y.; et al. In Vivo Evaluation of P-Glycoprotein Function at the Blood-Brain Barrier in Nonhuman Primates Using [11C]Verapamil. *J. Pharmacol. Exp. Ther.* **2006**, *316*, 647–653, doi:10.1124/jpet.105.088328.
151. Wanek, T.; Mairinger, S.; Langer, O. Radioligands Targeting P-glycoprotein and Other Drug Efflux Proteins at the Blood–Brain Barrier. *J. Label. Compd. Radiopharm.* **2013**, *56*, 68–77, doi:10.1002/jlcr.2993.
152. Bart, J.; Willemsen, A.T.M.; Groen, H.J.M.; Van Der Graaf, W.T.A.; Wegman, T.D.; Vaalburg, W.; De Vries, E.G.E.; Hendrikse, N.H. Quantitative Assessment of P-Glycoprotein Function in the Rat Blood–Brain Barrier by Distribution Volume of [11C]Verapamil Measured with PET. *NeuroImage* **2003**, *20*, 1775–1782, doi:10.1016/S1053-8119(03)00405-1.
153. Sasongko, L.; Link, J.; Muzi, M.; Mankoff, D.; Yang, X.; Collier, A.; Shoner, S.; Unadkat, J. Imaging P-Glycoprotein Transport Activity at the Human Blood-Brain Barrier with Positron Emission Tomography. *Clin. Pharmacol. Ther.* **2005**, *77*, 503–514, doi:10.1016/j.clpt.2005.01.022.
154. Elsinga, P.H.; Tsukada, H.; Harada, N.; Kakiuchi, T.; Kawamura, K.; Vaalburg, W.; Kimura, Y.; Kobayashi, T.; Ishiwata, K. Evaluation of [^{18} F]Fluorinated Sigma Receptor Ligands in the Conscious Monkey Brain. *Synapse* **2004**, *52*, 29–37, doi:10.1002/syn.20001.
155. Toornvliet, R.; Vanberckel, B.; Luurtsema, G.; Lubberink, M.; Geldof, A.; Bosch, T.; Oerlemans, R.; Lammertsma, A.; Franssen, E. Effect of Age on Functional P-Glycoprotein in the Blood-Brain Barrier Measured by Use of (R)-[11C]Verapamil and Positron Emission Tomography. *Clin. Pharmacol. Ther.* **2006**, *79*, 540–548, doi:10.1016/j.clpt.2006.02.004.
156. Takano, A.; Kusuhara, H.; Suhara, T.; Ieiri, I.; Morimoto, T.; Lee, Y.-J.; Maeda, J.; Ikoma, Y.; Ito, H.; Suzuki, K.; et al. Evaluation of in Vivo P-Glycoprotein Function at the Blood-Brain Barrier among MDR1 Gene Polymorphisms by Using 11C-Verapamil. *J. Nucl. Med. Off. Publ. Soc. Nucl. Med.* **2006**, *47*, 1427–1433.

157. Ghosh, K.K.; Padmanabhan, P.; Yang, C.-T.; Mishra, S.; Halldin, C.; Gulyás, B. Dealing with PET Radiometabolites. *EJNMMI Res.* **2020**, *10*, doi:10.1186/s13550-020-00692-4.
158. Raaphorst, R.M.; Luurtsema, G.; Schuit, R.C.; Kooijman, E.J.M.; Elsinga, P.H.; Lammertsma, A.A.; Windhorst, A.D. Synthesis and Evaluation of New Fluorine-18 Labeled Verapamil Analogs To Investigate the Function of P-Glycoprotein in the Blood–Brain Barrier. *ACS Chem. Neurosci.* **2017**, *8*, 1925–1936, doi:10.1021/acschemneuro.7b00086.
159. Raaphorst, R.M.; Luurtsema, G.; Schokker, C.J.; Attia, K.A.; Schuit, R.C.; Elsinga, P.H.; Lammertsma, A.A.; Windhorst, A.D. Improving Metabolic Stability of Fluorine-18 Labeled Verapamil Analogs. *Nucl. Med. Biol.* **2018**, *64–65*, 47–56, doi:10.1016/j.nucmedbio.2018.06.009.
160. Wagner, C.C.; Bauer, M.; Karch, R.; Feurstein, T.; Kopp, S.; Chiba, P.; Kletter, K.; Löscher, W.; Müller, M.; Zeitlinger, M.; et al. A Pilot Study to Assess the Efficacy of Tariquidar to Inhibit P-Glycoprotein at the Human Blood–Brain Barrier with (*R*)-^{11} C-Verapamil and PET. *J. Nucl. Med.* **2009**, *50*, 1954–1961, doi:10.2967/jnumed.109.063289.
161. Bankstahl, J.P.; Kuntner, C.; Abrahim, A.; Karch, R.; Stanek, J.; Wanek, T.; Wadsak, W.; Kletter, K.; Müller, M.; Löscher, W.; et al. Tariquidar-Induced P-Glycoprotein Inhibition at the Rat Blood–Brain Barrier Studied with (*R*)-^{11} C-Verapamil and PET. *J. Nucl. Med.* **2008**, *49*, 1328–1335, doi:10.2967/jnumed.108.051235.
162. Wang, M.; Gao, M.; Zheng, Q.-H. A High-Yield Route to Synthesize the P-Glycoprotein Radioligand [C]N-Desmethyl-Loperamide and Its Parent Radioligand [C]Loperamide. *Bioorg. Med. Chem. Lett.* **2013**, *23*, 5259–5263, doi:10.1016/j.bmcl.2013.08.024.
163. Wandel, C.; Kim, R.; Wood, M.; Wood, A. Interaction of Morphine, Fentanyl, Sufentanil, Alfentanil, and Loperamide with the Efflux Drug Transporter P-Glycoprotein. *Anesthesiology* **2002**, *96*, 913–920, doi:10.1097/00000542-200204000-00019.
164. Kim, K.-A.; Chung, J.; Jung, D.-H.; Park, J.-Y. Identification of Cytochrome P450 Isoforms Involved in the Metabolism of Loperamide in Human Liver Microsomes. *Eur. J. Clin. Pharmacol.* **2004**, *60*, 575–581, doi:10.1007/s00228-004-0815-3.
165. Seneca, N.; Zoghbi, S.S.; Shetty, H.U.; Tuan, E.; Kannan, P.; Taku, A.; Innis, R.B.; Pike, V.W. Effects of Ketoconazole on the Biodistribution and Metabolism of [11C]Loperamide and [11C]N-Desmethyl-Loperamide in Wild-Type and P-Gp Knockout Mice. *Nucl. Med. Biol.* **2010**, *37*, 335–345, doi:10.1016/j.nucmedbio.2009.12.010.
166. Zoghbi, S.S.; Liow, J.-S.; Yasuno, F.; Hong, J.; Tuan, E.; Lazarova, N.; Gladding, R.L.; Pike, V.W.; Innis, R.B. ^{11} C-Loperamide and Its *N* - *Desmethyl* Radiometabolite Are Avid Substrates for Brain Permeability-Glycoprotein Efflux. *J. Nucl. Med.* **2008**, *49*, 649–656, doi:10.2967/jnumed.107.047308.
167. Seneca, N.; Zoghbi, S.S.; Liow, J.-S.; Kreisl, W.; Herscovitch, P.; Jenko, K.; Gladding, R.L.; Taku, A.; Pike, V.W.; Innis, R.B. Human Brain Imaging and Radiation Dosimetry of^{11} C- *N* - *Desmethyl* -Loperamide, a PET Radiotracer to Measure the Function of P-Glycoprotein. *J. Nucl. Med.* **2009**, *50*, 807–813, doi:10.2967/jnumed.108.058453.
168. Lazarova, N.; Zoghbi, S.S.; Hong, J.; Seneca, N.; Tuan, E.; Gladding, R.L.; Liow, J.-S.; Taku, A.; Innis, R.B.; Pike, V.W. Synthesis and Evaluation of [*N*- Methyl-^{11} C] *N* -Desmethyl-Loperamide as a New and Improved PET Radiotracer for Imaging P-Gp Function. *J. Med. Chem.* **2008**, *51*, 6034–6043, doi:10.1021/jm800510m.
169. Kannan, P.; Brimacombe, K.R.; Kreisl, W.C.; Liow, J.-S.; Zoghbi, S.S.; Telu, S.; Zhang, Y.; Pike, V.W.; Halldin, C.; Gottesman, M.M.; et al. Lysosomal Trapping of a Radiolabeled Substrate of P-Glycoprotein as a Mechanism for Signal Amplification in PET. *Proc. Natl. Acad. Sci.* **2011**, *108*, 2593–2598, doi:10.1073/pnas.1014641108.
170. Liow, J.-S.; Kreisl, W.; Zoghbi, S.S.; Lazarova, N.; Seneca, N.; Gladding, R.L.; Taku, A.; Herscovitch, P.; Pike, V.W.; Innis, R.B. P-Glycoprotein Function at the Blood–Brain Barrier Imaged Using^{11} C- *N-Desmethyl* -Loperamide in Monkeys. *J. Nucl. Med.* **2009**, *50*, 108–115, doi:10.2967/jnumed.108.056226.
171. Wanek, T.; Römermann, K.; Mairinger, S.; Stanek, J.; Sauberer, M.; Filip, T.; Traxl, A.; Kuntner, C.; Pahnke, J.; Bauer, F.; et al. Factors Governing P-Glycoprotein-Mediated Drug–Drug Interactions at the Blood–Brain Barrier Measured with Positron Emission Tomography. *Mol. Pharm.* **2015**, *12*, 3214–3225, doi:10.1021/acs.molpharmaceut.5b00168.
172. Kannan, P.; Brimacombe, K.R.; Zoghbi, S.S.; Liow, J.-S.; Morse, C.; Taku, A.K.; Pike, V.W.; Halldin, C.; Innis, R.B.; Gottesman, M.M.; et al. N-Desmethyl-Loperamide Is Selective for P-Glycoprotein among Three ATP-Binding Cassette Transporters at the Blood-Brain Barrier. *Drug Metab. Dispos.* **2010**, *38*, 917–922, doi:10.1124/dmd.109.031161.
173. Moerman, L.; De Naeyer, D.; Boon, P.; De Vos, F. P-Glycoprotein at the Blood-Brain Barrier: Kinetic Modeling of 11C-Desmethylloperamide in Mice Using a 18F-FDG µPET Scan to Determine the Input Function. *EJNMMI Res.* **2011**, *1*, 12, doi:10.1186/2191-219X-1-12.
174. Farwell, M.D.; Chong, D.J.; Iida, Y.; Bae, S.A.; Easwaramoorthy, B.; Ichise, M. Imaging P-Glycoprotein Function in Rats Using [11C]-N-Desmethyl-Loperamide. *Ann. Nucl. Med.* **2013**, *27*, 618–624, doi:10.1007/s12149-013-0725-5.
175. Kreisl, W.C.; Liow, J.-S.; Kimura, N.; Seneca, N.; Zoghbi, S.S.; Morse, C.L.; Herscovitch, P.; Pike, V.W.; Innis, R.B. P-Glycoprotein Function at the Blood–Brain Barrier in Humans Can Be Quantified with the Substrate Radiotracer^{11} C- *N-Desmethyl* -Loperamide. *J. Nucl. Med.* **2010**, *51*, 559–566, doi:10.2967/jnumed.109.070151.
176. Damont, A.; Goutal, S.; Auvity, S.; Valette, H.; Kuhnast, B.; Saba, W.; Tournier, N. Imaging the Impact of Cyclosporin A and Dipyridamole on P-Glycoprotein (ABCB1) Function at the Blood-Brain Barrier: A [11C]-N-Desmethyl-Loperamide PET Study in Nonhuman Primates. *Eur. J. Pharm. Sci.* **2016**, *91*, 98–104, doi:10.1016/j.ejps.2016.06.005.
177. Kreisl, W.C.; Bhatia, R.; Morse, C.L.; Woock, A.E.; Zoghbi, S.S.; Shetty, H.U.; Pike, V.W.; Innis, R.B. Increased Permeability-Glycoprotein Inhibition at the Human Blood–Brain Barrier Can Be Safely Achieved by Performing

PET During Peak Plasma Concentrations of Tariquidar. *J. Nucl. Med.* **2015**, *56*, 82–87, doi:10.2967/jnumed.114.146894.
178. Pichler, V.; Ozenil, M.; Bamminger, K.; Vraka, C.; Hacker, M.; Langer, O.; Wadsak, W. Pitfalls and Solutions of the Fully-Automated Radiosynthesis of [11C]Metoclopramide. *EJNMMI Radiopharm. Chem.* **2019**, *4*, 31, doi:10.1186/s41181-019-0083-2.
179. Livezey, M.R.; Briggs, E.D.; Bolles, A.K.; Nagy, L.D.; Fujiwara, R.; Furge, L.L. Metoclopramide Is Metabolized by CYP2D6 and Is a Reversible Inhibitor, but Not Inactivator, of CYP2D6. *Xenobiotica* **2014**, *44*, 309–319, doi:10.3109/00498254.2013.835885.
180. Breuil, L.; Ziani, N.; Leterrier, S.; Hugon, G.; Caillé, F.; Bouilleret, V.; Truillet, C.; Goislard, M.; El Biali, M.; Bauer, M.; et al. Impact of Cytochrome Induction or Inhibition on the Plasma and Brain Kinetics of [11C]Metoclopramide, a PET Probe for P-Glycoprotein Function at the Blood-Brain Barrier. *Pharmaceutics* **2022**, *14*, 2650, doi:10.3390/pharmaceutics14122650.
181. Caillé, F.; Goutal, S.; Marie, S.; Auvity, S.; Cisternino, S.; Kuhnast, B.; Pottier, G.; Tournier, N. Positron Emission Tomography Imaging Reveals an Importance of Saturable Liver Uptake Transport for the Pharmacokinetics of Metoclopramide. *Contrast Media Mol. Imaging* **2018**, *2018*, 1–8, doi:10.1155/2018/7310146.
182. Pottier, G.; Marie, S.; Goutal, S.; Auvity, S.; Peyronneau, M.-A.; Stute, S.; Boisgard, R.; Dollé, F.; Buvat, I.; Caillé, F.; et al. Imaging the Impact of the P-Glycoprotein (ABCB1) Function on the Brain Kinetics of Metoclopramide. *J. Nucl. Med.* **2016**, *57*, 309–314, doi:10.2967/jnumed.115.164350.
183. Auvity, S.; Tournier, N. Impact of Acute Alcohol Exposure on P-Glycoprotein Function at the Blood-Brain Barrier Assessed Using^{11} C-Metoclopramide PET Imaging. *Clin. Pharmacol. Ther.* **2019**, *105*, 812–813, doi:10.1002/cpt.1266.
184. Auvity, S.; Caillé, F.; Marie, S.; Wimberley, C.; Bauer, M.; Langer, O.; Buvat, I.; Goutal, S.; Tournier, N. P-Glycoprotein (ABCB1) Inhibits the Influx and Increases the Efflux of^{11} C-Metoclopramide Across the Blood–Brain Barrier: A PET Study on Nonhuman Primates. *J. Nucl. Med.* **2018**, *59*, 1609–1615, doi:10.2967/jnumed.118.210104.
185. Tournier, N.; Bauer, M.; Pichler, V.; Nics, L.; Klebermass, E.-M.; Bamminger, K.; Matzneller, P.; Weber, M.; Karch, R.; Caillé, F.; et al. Impact of P-Glycoprotein Function on the Brain Kinetics of the Weak Substrate^{11} C-Metoclopramide Assessed with PET Imaging in Humans. *J. Nucl. Med.* **2019**, *60*, 985–991, doi:10.2967/jnumed.118.219972.
186. Zoufal, V.; Mairinger, S.; Brackhan, M.; Krohn, M.; Filip, T.; Sauberer, M.; Stanek, J.; Wanek, T.; Tournier, N.; Bauer, M.; et al. Imaging P-Glycoprotein Induction at the Blood–Brain Barrier of a β-Amyloidosis Mouse Model with^{11} C-Metoclopramide PET. *J. Nucl. Med.* **2020**, *61*, 1050–1057, doi:10.2967/jnumed.119.237198.
187. Breuil, L.; El Biali, M.; Vodovar, D.; Marie, S.; Auvity, S.; Bauer, M.; Goutal, S.; Rodrigo, S.; Langer, O.; Tournier, N. Parametric Imaging of P-Glycoprotein Function at the Blood–Brain Barrier Using kE,Brain-Maps Generated from [11C]Metoclopramide PET Data in Rats, Nonhuman Primates and Humans. *Mol. Imaging Biol.* **2023**, *25*, 1135–1141, doi:10.1007/s11307-023-01864-z.
188. Bauer, M.; Barna, S.; Blaickner, M.; Prosenz, K.; Bamminger, K.; Pichler, V.; Tournier, N.; Hacker, M.; Zeitlinger, M.; Karanikas, G.; et al. Human Biodistribution and Radiation Dosimetry of the P-Glycoprotein Radiotracer [11C]Metoclopramide. *Mol. Imaging Biol.* **2021**, *23*, 180–185, doi:10.1007/s11307-021-01582-4.
189. Hernández-Lozano, I.; Mairinger, S.; Sauberer, M.; Stanek, J.; Filip, T.; Wanek, T.; Ciarimboli, G.; Tournier, N.; Langer, O. Influence of Cation Transporters (OCTs and MATEs) on the Renal and Hepatobiliary Disposition of [11C]Metoclopramide in Mice. *Pharm. Res.* **2021**, *38*, 127–140, doi:10.1007/s11095-021-03002-2.
190. Goutal, S.; Novell, A.; Leterrier, S.; Breuil, L.; Selingue, E.; Gerstenmayer, M.; Marie, S.; Saubaméa, B.; Caillé, F.; Langer, O.; et al. Imaging the Impact of Blood-Brain Barrier Disruption Induced by Focused Ultrasound on P-Glycoprotein Function. *J. Controlled Release* **2023**, *361*, 483–492, doi:10.1016/j.jconrel.2023.08.012.
191. El Biali, M.; Wölfl-Duchek, M.; Jackwerth, M.; Mairinger, S.; Weber, M.; Bamminger, K.; Poschner, S.; Rausch, I.; Schindler, N.; Lozano, I.H.; et al. St. John's Wort Extract with a High Hyperforin Content Does Not Induce P-glycoprotein Activity at the Human Blood–Brain Barrier. *Clin. Transl. Sci.* **2024**, *17*, e13804, doi:10.1111/cts.13804.
192. Garcia-Varela, L.; Attia, K.; Sembrano, J.C.; Jacquet, O.; Antunes, I.F.; Kwizera, C.; Visser, T.J.; Dierckx, R.A.J.O.; Elsinga, P.H.; Luurtsema, G. A New Approach to Produce [18F]MC225 via One-Step Synthesis, a PET Radiotracer for Measuring P-Gp Function. *EJNMMI Radiopharm. Chem.* **2021**, *6*, 24, doi:10.1186/s41181-021-00139-8.
193. Savolainen, H.; Windhorst, A.D.; Elsinga, P.H.; Cantore, M.; Colabufo, N.A.; Willemsen, A.T.; Luurtsema, G. Evaluation of [^{18} F]MC225 as a PET Radiotracer for Measuring P-Glycoprotein Function at the Blood–Brain Barrier in Rats: Kinetics, Metabolism, and Selectivity. *J. Cereb. Blood Flow Metab.* **2017**, *37*, 1286–1298, doi:10.1177/0271678X16654493.
194. García-Varela, L.; Arif, W.M.; Vállez García, D.; Kakiuchi, T.; Ohba, H.; Harada, N.; Tago, T.; Elsinga, P.H.; Tsukada, H.; Colabufo, N.A.; et al. Pharmacokinetic Modeling of [^{18} F]MC225 for Quantification of the P-Glycoprotein Function at the Blood–Brain Barrier in Non-Human Primates with PET. *Mol. Pharm.* **2020**, *17*, 3477–3486, doi:10.1021/acs.molpharmaceut.0c00514.
195. Savolainen, H.; Cantore, M.; Colabufo, N.A.; Elsinga, P.H.; Windhorst, A.D.; Luurtsema, G. Synthesis and Preclinical Evaluation of Three Novel Fluorine-18 Labeled Radiopharmaceuticals for P-Glycoprotein PET Imaging at the Blood–Brain Barrier. *Mol. Pharm.* **2015**, *12*, 2265–2275, doi:10.1021/mp5008103.
196. García-Varela, L.; Vállez García, D.; Aguiar, P.; Kakiuchi, T.; Ohba, H.; Harada, N.; Nishiyama, S.; Tago, T.; Elsinga, P.H.; Tsukada, H.; et al. Head-to-Head Comparison of (R)-[11C]Verapamil and [18F]MC225 in Non-Human Primates, Tracers for Measuring P-Glycoprotein Function. *Eur. J. Nucl. Med. Mol. Imaging* **2021**, *48*, 4307–4317, doi:10.1007/s00259-021-05411-2.

197. Garcia-Varela, L.; Mossel, P.; Aguiar, P.; Vazquez-Matias, D.A.; Van Waarde, A.; Willemsen, A.T.M.; Bartels, A.L.; Colabufo, N.A.; Dierckx, R.A.J.O.; Elsinga, P.H.; et al. Dose-Response Assessment of Cerebral P-Glycoprotein Inhibition in Vivo with [18F]MC225 and PET. *J. Controlled Release* **2022**, *347*, 500–507, doi:10.1016/j.jconrel.2022.05.026.
198. García-Varela, L.; Rodríguez-Pérez, M.; Custodia, A.; Moraga-Amaro, R.; Colabufo, N.A.; Aguiar, P.; Sobrino, T.; Dierckx, R.A.J.O.; Van Waarde, A.; Elsinga, P.H.; et al. *In Vivo* Induction of P-Glycoprotein Function Can Be Measured with [^{18} F]MC225 and PET. *Mol. Pharm.* **2021**, *18*, 3073–3085, doi:10.1021/acs.molpharmaceut.1c00302.
199. Muzi, M.; Mankoff, D.A.; Link, J.M.; Shoner, S.; Collier, A.C.; Sasongko, L.; Unadkat, J.D. Imaging of Cyclosporine Inhibition of P-Glycoprotein Activity Using^{11} C-Verapamil in the Brain: Studies of Healthy Humans. *J. Nucl. Med.* **2009**, *50*, 1267–1275, doi:10.2967/jnumed.108.059162.
200. Mossel, P.; Garcia Varela, L.; Arif, W.M.; Van Der Weijden, C.W.J.; Boersma, H.H.; Willemsen, A.T.M.; Boellaard, R.; Elsinga, P.H.; Borra, R.J.H.; Colabufo, N.A.; et al. Evaluation of P-Glycoprotein Function at the Blood–Brain Barrier Using [18F]MC225-PET. *Eur. J. Nucl. Med. Mol. Imaging* **2021**, *48*, 4105–4106, doi:10.1007/s00259-021-05419-8.
201. Fusi, F.; Durante, M.; Gorelli, B.; Perrone, M.G.; Colabufo, N.A.; Saponara, S. MC225, a Novel Probe for P-Glycoprotein PET Imaging at the Blood–Brain Barrier: In Vitro Cardiovascular Safety Evaluation. *J. Cardiovasc. Pharmacol.* **2017**, *70*, 405–410, doi:10.1097/FJC.0000000000000536.
202. Toyohara, J.; Sakata, M.; Tago, T.; Colabufo, N.A.; Luurtsema, G. Automated Synthesis, Preclinical Toxicity, and Radiation Dosimetry of [18F]MC225 for Clinical Use: A Tracer for Measuring P-Glycoprotein Function at the Blood-Brain Barrier. *EJNMMI Res.* **2020**, *10*, 84, doi:10.1186/s13550-020-00674-6.
203. Toyohara, J.; Sakata, M.; Ishibashi, K.; Mossel, P.; Imai, M.; Wagatsuma, K.; Tago, T.; Imabayashi, E.; Colabufo, N.A.; Luurtsema, G.; et al. First Clinical Assessment of [18F]MC225, a Novel Fluorine-18 Labelled PET Tracer for Measuring Functional P-Glycoprotein at the Blood–Brain Barrier. *Ann. Nucl. Med.* **2021**, *35*, 1240–1252, doi:10.1007/s12149-021-01666-9.
204. Mossel, P.; Arif, W.M.; De Souza, G.S.; Varela, L.G.; Van Der Weijden, C.W.J.; Boersma, H.H.; Willemsen, A.T.M.; Boellaard, R.; Elsinga, P.H.; Borra, R.J.H.; et al. Quantification of P-Glycoprotein Function at the Human Blood-Brain Barrier Using [18F]MC225 and PET. *Eur. J. Nucl. Med. Mol. Imaging* **2023**, *50*, 3917–3927, doi:10.1007/s00259-023-06363-5.
205. Savolainen, H.; Meerlo, P.; Elsinga, P.H.; Windhorst, A.D.; Dierckx, R.A.J.O.; Colabufo, N.A.; Van Waarde, A.; Luurtsema, G. P-Glycoprotein Function in the Rodent Brain Displays a Daily Rhythm, a Quantitative In Vivo PET Study. *AAPS J.* **2016**, *18*, 1524–1531, doi:10.1208/s12248-016-9973-3.
206. García-Varela, L.; Vállez García, D.; Rodríguez-Pérez, M.; Van Waarde, A.; Sijbesma, J.W.A.; Schildt, A.; Kwizera, C.; Aguiar, P.; Sobrino, T.; Dierckx, R.A.J.O.; et al. Test–Retest Repeatability of [^{18} F]MC225-PET in Rodents: A Tracer for Imaging of P-Gp Function. *ACS Chem. Neurosci.* **2020**, *11*, 648–658, doi:10.1021/acschemneuro.9b00682.
207. Kurdziel, K.A.; Kalen, J.D.; Hirsch, J.I.; Wilson, J.D.; Agarwal, R.; Barrett, D.; Bear, H.D.; McCumiskey, J.F. Imaging Multidrug Resistance with 4-[18F]Fluoropaclitaxel. *Nucl. Med. Biol.* **2007**, *34*, 823–831, doi:10.1016/j.nucmedbio.2007.04.011.
208. Bauer, F.; Kuntner, C.; Bankstahl, J.P.; Wanek, T.; Bankstahl, M.; Stanek, J.; Mairinger, S.; Dörner, B.; Löscher, W.; Müller, M.; et al. Synthesis and in Vivo Evaluation of [11C]Tariquidar, a Positron Emission Tomography Radiotracer Based on a Third-Generation P-Glycoprotein Inhibitor. *Bioorg. Med. Chem.* **2010**, *18*, 5489–5497, doi:10.1016/j.bmc.2010.06.057.
209. Dörner, B.; Kuntner, C.; Bankstahl, J.P.; Bankstahl, M.; Stanek, J.; Wanek, T.; Stundner, G.; Mairinger, S.; Löscher, W.; Müller, M.; et al. Synthesis and Small-Animal Positron Emission Tomography Evaluation of [^{11} C]-Elacridar As a Radiotracer to Assess the Distribution of P-Glycoprotein at the Blood−Brain Barrier. *J. Med. Chem.* **2009**, *52*, 6073–6082, doi:10.1021/jm900940f.
210. Dörner, B.; Kuntner, C.; Bankstahl, J.P.; Wanek, T.; Bankstahl, M.; Stanek, J.; Müllauer, J.; Bauer, F.; Mairinger, S.; Löscher, W.; et al. Radiosynthesis and in Vivo Evaluation of 1-[18F]Fluoroelacridar as a Positron Emission Tomography Tracer for P-Glycoprotein and Breast Cancer Resistance Protein. *Bioorg. Med. Chem.* **2011**, *19*, 2190–2198, doi:10.1016/j.bmc.2011.02.039.
211. Müllauer, J.; Karch, R.; Bankstahl, J.P.; Bankstahl, M.; Stanek, J.; Wanek, T.; Mairinger, S.; Müller, M.; Löscher, W.; Langer, O.; et al. Assessment of Cerebral P-Glycoprotein Expression and Function with PET by Combined [11C]Inhibitor and [11C]Substrate Scans in Rats. *Nucl. Med. Biol.* **2013**, *40*, 755–763, doi:10.1016/j.nucmedbio.2013.05.005.
212. Bauer, M.; Blaickner, M.; Philippe, C.; Wadsak, W.; Hacker, M.; Zeitlinger, M.; Langer, O. Whole-Body Distribution and Radiation Dosimetry of^{11} C-Elacridar and^{11} C-Tariquidar in Humans. *J. Nucl. Med.* **2016**, *57*, 1265–1268, doi:10.2967/jnumed.116.175182.
213. Hernández Lozano, I.; Bauer, M.; Wulkersdorfer, B.; Traxl, A.; Philippe, C.; Weber, M.; Häusler, S.; Stieger, B.; Jäger, W.; Mairinger, S.; et al. Measurement of Hepatic ABCB1 and ABCG2 Transport Activity with [^{11} C]Tariquidar and PET in Humans and Mice. *Mol. Pharm.* **2020**, *17*, 316–326, doi:10.1021/acs.molpharmaceut.9b01060.
214. Luurtsema, G.; Schuit, R.C.; Klok, R.P.; Verbeek, J.; Leysen, J.E.; Lammertsma, A.A.; Windhorst, A.D. Evaluation of [11C]Laniquidar as a Tracer of P-Glycoprotein: Radiosynthesis and Biodistribution in Rats. *Nucl. Med. Biol.* **2009**, *36*, 643–649, doi:10.1016/j.nucmedbio.2009.03.004.
215. Froklage, F.E.; Boellaard, R.; Bakker, E.; Hendrikse, N.H.; Reijneveld, J.C.; Schuit, R.C.; Windhorst, A.D.; Schober, P.; Van Berckel, B.N.M.; Lammertsma, A.A.; et al. Quantification of^{11} C-Laniquidar Kinetics in the Brain. *J. Nucl. Med.* **2015**, *56*, 1730–1735, doi:10.2967/jnumed.115.157586.

216. Postnov, A.; Froklage, F.E.; Van Lingen, A.; Reijneveld, J.C.; Hendrikse, N.H.; Windhorst, A.D.; Schuit, R.C.; Eriksson, J.; Lammertsma, A.A.; Huisman, M.C. Radiation Dose of the P-Glycoprotein Tracer[11] C-Laniquidar. *J. Nucl. Med.* **2013**, *54*, 2101–2103, doi:10.2967/jnumed.113.120857.
217. Schmidt, H.R.; Zheng, S.; Gurpinar, E.; Koehl, A.; Manglik, A.; Kruse, A.C. Crystal Structure of the Human Σ1 Receptor. *Nature* **2016**, *532*, 527–530, doi:10.1038/nature17391.
218. Schmidt, H.R.; Kruse, A.C. The Molecular Function of σ Receptors: Past, Present, and Future. *Trends Pharmacol. Sci.* **2019**, *40*, 636–654, doi:10.1016/j.tips.2019.07.006.
219. Alon, A.; Lyu, J.; Braz, J.M.; Tummino, T.A.; Craik, V.; O'Meara, M.J.; Webb, C.M.; Radchenko, D.S.; Moroz, Y.S.; Huang, X.-P.; et al. Structures of the Σ2 Receptor Enable Docking for Bioactive Ligand Discovery. *Nature* **2021**, *600*, 759–764, doi:10.1038/s41586-021-04175-x.
220. Lizama, B.N.; Kahle, J.; Catalano, S.M.; Caggiano, A.O.; Grundman, M.; Hamby, M.E. Sigma-2 Receptors—From Basic Biology to Therapeutic Target: A Focus on Age-Related Degenerative Diseases. *Int. J. Mol. Sci.* **2023**, *24*, 6251, doi:10.3390/ijms24076251.
221. Chu, U.B.; Ruoho, A.E. Biochemical Pharmacology of the Sigma-1 Receptor. *Mol. Pharmacol.* **2016**, *89*, 142–153, doi:10.1124/mol.115.101170.
222. Aishwarya, R.; Abdullah, C.S.; Morshed, M.; Remex, N.S.; Bhuiyan, Md.S. Sigmar1's Molecular, Cellular, and Biological Functions in Regulating Cellular Pathophysiology. *Front. Physiol.* **2021**, *12*, 705575, doi:10.3389/fphys.2021.705575.
223. Su, T.-P.; Su, T.-C.; Nakamura, Y.; Tsai, S.-Y. The Sigma-1 Receptor as a Pluripotent Modulator in Living Systems. *Trends Pharmacol. Sci.* **2016**, *37*, 262–278, doi:10.1016/j.tips.2016.01.003.
224. Alonso, G.; Phan, V.-L.; Guillemain, I.; Saunier, M.; Legrand, A.; Anoal, M.; Maurice, T. Immunocytochemical Localization of the Sigma1 Receptor in the Adult Rat Central Nervous System. *Neuroscience* **2000**, *97*, 155–170, doi:10.1016/S0306-4522(00)00014-2.
225. Su, T.-P.; Wu, X.-Z. Guinea Pig Vas Deferens Contains ρ but Not Phencyclidine Receptors. *Neurosci. Lett.* **1990**, *108*, 341–345, doi:10.1016/0304-3940(90)90664-U.
226. Hellewell, S.B.; Bruce, A.; Feinstein, G.; Orringer, J.; Williams, W.; Bowen, W.D. Rat Liver and Kidney Contain High Densities of Σ1 and Σ2 Receptors: Characterization by Ligand Binding and Photoaffinity Labeling. *Eur. J. Pharmacol. Mol. Pharmacol.* **1994**, *268*, 9–18, doi:10.1016/0922-4106(94)90115-5.
227. Wolfe, S.A.; Culp, S.G.; De Souza, E.B. σ-Receptors in Endocrine Organs: Identification, Characterization, and Autoradiographic Localization in Rat Pituitary, Adrenal, Testis, and Ovary. *Endocrinology* **1989**, *124*, 1160–1172, doi:10.1210/endo-124-3-1160.
228. Sharma, N.; Patel, C.; Shenkman, M.; Kessel, A.; Ben-Tal, N.; Lederkremer, G.Z. The Sigma-1 Receptor Is an ER-Localized Type II Membrane Protein. *J. Biol. Chem.* **2021**, *297*, 101299, doi:10.1016/j.jbc.2021.101299.
229. Hayashi, T.; Su, T.-P. Sigma-1 Receptor Chaperones at the ER- Mitochondrion Interface Regulate Ca2+ Signaling and Cell Survival. *Cell* **2007**, *131*, 596–610, doi:10.1016/j.cell.2007.08.036.
230. Hanner, M.; Moebius, F.F.; Flandorfer, A.; Knaus, H.G.; Striessnig, J.; Kempner, E.; Glossmann, H. Purification, Molecular Cloning, and Expression of the Mammalian Sigma1-Binding Site. *Proc. Natl. Acad. Sci.* **1996**, *93*, 8072–8077, doi:10.1073/pnas.93.15.8072.
231. Schmidt, H.R.; Betz, R.M.; Dror, R.O.; Kruse, A.C. Structural Basis for Σ1 Receptor Ligand Recognition. *Nat. Struct. Mol. Biol.* **2018**, *25*, 981–987, doi:10.1038/s41594-018-0137-2.
232. Glennon, R. Pharmacophore Identification for Sigma-1 (σ1) Receptor Binding: Application of the "Deconstruction - Reconstruction - Elaboration" Approach. *Mini-Rev. Med. Chem.* **2005**, *5*, 927–940, doi:10.2174/138955705774329519.
233. Mastropasqua, F.; Ludwig, F.-A.; Abate, C. A Full-Spectrum Evaluation of Sigma-1 Receptor (S1R) Positron Emission Tomography (PET) Radioligands from Binding Affinity to Clinical Imaging. *Molecules* **2025**, *30*, 4296, doi:10.3390/molecules30214296.
234. Weng, T.-Y.; Tsai, S.-Y.A.; Su, T.-P. Roles of Sigma-1 Receptors on Mitochondrial Functions Relevant to Neurodegenerative Diseases. *J. Biomed. Sci.* **2017**, *24*, 74, doi:10.1186/s12929-017-0380-6.
235. Kruse, A. Structural Insights into Sigma1 Function. In *Sigma Proteins: Evolution of the Concept of Sigma Receptors*; Kim, F.J., Pasternak, G.W., Eds.; Handbook of Experimental Pharmacology; Springer International Publishing: Cham, 2016; Vol. 244, pp. 13–25 ISBN 978-3-319-65851-3.
236. Gasparre, G.; Abate, C.; Carlucci, R.; Berardi, F.; Cassano, G. The Σ1 Receptor Agonist (+)-Pentazocine Increases Store-Operated Ca2+ Entry in MCF7σ1 and SK-N-SH Cell Lines. *Pharmacol. Rep.* **2017**, *69*, 542–545, doi:10.1016/j.pharep.2017.01.022.
237. Vela, J.M. Repurposing Sigma-1 Receptor Ligands for COVID-19 Therapy? *Front. Pharmacol.* **2020**, *11*, 582310, doi:10.3389/fphar.2020.582310.
238. Gordon, D.E.; Hiatt, J.; Bouhaddou, M.; Rezelj, V.V.; Ulferts, S.; Braberg, H.; Jureka, A.S.; Obernier, K.; Guo, J.Z.; Batra, J.; et al. Comparative Host-Coronavirus Protein Interaction Networks Reveal Pan-Viral Disease Mechanisms. *Science* **2020**, *370*, eabe9403, doi:10.1126/science.abe9403.
239. Abate, C.; Niso, M.; Abatematteo, F.S.; Contino, M.; Colabufo, N.A.; Berardi, F. PB28, the Sigma-1 and Sigma-2 Receptors Modulator With Potent Anti–SARS-CoV-2 Activity: A Review About Its Pharmacological Properties and Structure Affinity Relationships. *Front. Pharmacol.* **2020**, *11*, 589810, doi:10.3389/fphar.2020.589810.
240. Hashimoto, K. Repurposing of CNS Drugs to Treat COVID-19 Infection: Targeting the Sigma-1 Receptor. *Eur. Arch. Psychiatry Clin. Neurosci.* **2021**, *271*, 249–258, doi:10.1007/s00406-020-01231-x.
241. Mishra, A.K.; Mavlyutov, T.; Singh, D.R.; Biener, G.; Yang, J.; Oliver, J.A.; Ruoho, A.; Raicu, V. The Sigma-1 Receptors Are Present in Monomeric and Oligomeric Forms in Living Cells in the Presence and Absence of Ligands. *Biochem. J.* **2015**, *466*, 263–271, doi:10.1042/BJ20141321.
242. Albayrak, Y.; Hashimoto, K. Sigma-1 Receptor Agonists and Their Clinical Implications in Neuropsychiatric Disorders. In *Sigma Receptors: Their Role in Disease and as Therapeutic Targets*; Smith, S.B., Su, T.-P., Eds.;

Advances in Experimental Medicine and Biology; Springer International Publishing: Cham, 2017; Vol. 964, pp. 153–161 ISBN 978-3-319-50172-7.
243. Ferris, R.M.; Tang, F.L.M.; Chang, K.-J.; Russell, A. Evidence That the Potential Antipsychotic Agent Rimcazole (BW 234U) Is a Specific, Competitive Antagonist of Sigma Sites in Brain. *Life Sci.* **1986**, *38*, 2329–2337, doi:10.1016/0024-3205(86)90640-5.
244. Schoenwald, R.D.; Barfknecht, C.F.; Shirolkar, S.; Xia, E. The Effects of Sigma Ligands on Protein Release from Lacrimal Acinar Cells: A Potential Agonist/Antagonist Assay. *Life Sci.* **1995**, *56*, 1275–1285, doi:10.1016/0024-3205(95)00073-9.
245. Yano, H.; Bonifazi, A.; Xu, M.; Guthrie, D.A.; Schneck, S.N.; Abramyan, A.M.; Fant, A.D.; Hong, W.C.; Newman, A.H.; Shi, L. Pharmacological Profiling of Sigma 1 Receptor Ligands by Novel Receptor Homomer Assays. *Neuropharmacology* **2018**, *133*, 264–275, doi:10.1016/j.neuropharm.2018.01.042.
246. Gómez-Soler, M.; Fernández-Dueñas, V.; Portillo-Salido, E.; Pérez, P.; Zamanillo, D.; Vela, J.M.; Burgueño, J.; Ciruela, F. Predicting the Antinociceptive Efficacy of σ1 Receptor Ligands by a Novel Receptor Fluorescence Resonance Energy Transfer (FRET) Based Biosensor. *J. Med. Chem.* **2014**, *57*, 238–242, doi:10.1021/jm401529t.
247. Borbély, E.; Varga, V.; Szögi, T.; Schuster, I.; Bozsó, Z.; Penke, B.; Fülöp, L. Impact of Two Neuronal Sigma-1 Receptor Modulators, PRE084 and DMT, on Neurogenesis and Neuroinflammation in an Aβ1–42-Injected, Wild-Type Mouse Model of AD. *Int. J. Mol. Sci.* **2022**, *23*, 2514, doi:10.3390/ijms23052514.
248. Freyssin, A.; Carles, A.; Guehairia, S.; Rubinstenn, G.; Maurice, T. Fluoroethylnormemantine (FENM) Shows Synergistic Protection in Combination with a Sigma-1 Receptor Agonist in a Mouse Model of Alzheimer's Disease. *Neuropharmacology* **2024**, *242*, 109733, doi:10.1016/j.neuropharm.2023.109733.
249. Maurice, T.; Lockhart, B.P.; Privat, A. Amnesia Induced in Mice by Centrally Administered β-Amyloid Peptides Involves Cholinergic Dysfunction. *Brain Res.* **1996**, *706*, 181–193, doi:10.1016/0006-8993(95)01032-7.
250. Huang, Y.; Zheng, L.; Halliday, G.; Dobson-Stone, C.; Wang, Y.; Tang, H.-D.; Cao, L.; Deng, Y.-L.; Wang, G.; Zhang, Y.-M.; et al. Genetic Polymorphisms in Sigma-1 Receptor and Apolipoprotein E Interact to Influence the Severity of Alzheimers Disease. *Curr. Alzheimer Res.* **2011**, *8*, 765–770, doi:10.2174/156720511797633232.
251. Lenoir, S.; Lahaye, R.A.; Vitet, H.; Scaramuzzino, C.; Virlogeux, A.; Capellano, L.; Genoux, A.; Gershoni-Emek, N.; Geva, M.; Hayden, M.R.; et al. Pridopidine Rescues BDNF/TrkB Trafficking Dynamics and Synapse Homeostasis in a Huntington Disease Brain-on-a-Chip Model. *Neurobiol. Dis.* **2022**, *173*, 105857, doi:10.1016/j.nbd.2022.105857.
252. Mavlyutov, T.A.; Baker, E.M.; Losenegger, T.M.; Kim, J.R.; Torres, B.; Epstein, M.L.; Ruoho, A.E. The Sigma-1 Receptor–A Therapeutic Target for the Treatment of ALS? In *Sigma Receptors: Their Role in Disease and as Therapeutic Targets*; Smith, S.B., Su, T.-P., Eds.; Advances in Experimental Medicine and Biology; Springer International Publishing: Cham, 2017; Vol. 964, pp. 255–265 ISBN 978-3-319-50172-7.
253. Kawamura, K.; Ishiwata, K.; Shimada, Y.; Kimura, Y.; Kobayashi, T.; Matsuno, K.; Homma, Y.; Senda, M. Preclinical Evaluation of [11C]SA4503: Radiation Dosimetry,in Vivo Selectivity and PET Imaging of Sigma1 Receptors in the Cat Brain. *Ann. Nucl. Med.* **2000**, *14*, 285–292, doi:10.1007/BF02988211.
254. Kawamura, K.; Ishiwata, K.; Tajima, H.; Ishii, S.-I.; Matsuno, K.; Homma, Y.; Senda, M. In Vivo Evaluation of [11C]SA4503 as a PET Ligand for Mapping CNS Sigma1 Receptors. *Nucl. Med. Biol.* **2000**, *27*, 255–261, doi:10.1016/S0969-8051(00)00081-0.
255. Elsinga, P.H.; Kawamura, K.; Kobayashi, T.; Tsukada, H.; Senda, M.; Vaalburg, W.; Ishiwata, K. Synthesis and Evaluation of [^{18} F]Fluoroethyl SA4503 as a PET Ligand for the Sigma Receptor. *Synapse* **2002**, *43*, 259–267, doi:10.1002/syn.10045.
256. Kawamura, K.; Tsukada, H.; Shiba, K.; Tsuji, C.; Harada, N.; Kimura, Y.; Ishiwata, K. Synthesis and Evaluation of Fluorine-18-Labeled SA4503 as a Selective Sigma1 Receptor Ligand for Positron Emission Tomography. *Nucl. Med. Biol.* **2007**, *34*, 571–577, doi:10.1016/j.nucmedbio.2007.03.009.
257. Ishiwata, K.; Tsukada, H.; Kawamura, K.; Kimura, Y.; Nishiyama, S.; Kobayashi, T.; Matsuno, K.; Senda, M. Mapping of CNS Sigma1 Receptors in the Conscious Monkey: Preliminary PET Study with [^{11} C]SA4503. *Synapse* **2001**, *40*, 235–237, doi:10.1002/syn.1046.
258. Ye, J.; Wang, L.; Deuther-Conrad, W.; Chen, Y.; Zhang, X.; Zhang, J.; Huang, Y.; Brust, P.; Jia, H. ^{18}F-Labeled Benzylpiperazine Derivatives as Highly Selective Ligands for Imaging σ1 Receptor with Positron Emission Tomography. *J. Label. Compd. Radiopharm.* **2019**, *62*, 425–437, doi:10.1002/jlcr.3738.
259. Wang, X.; Li, Y.; Deuther-Conrad, W.; Xie, F.; Chen, X.; Cui, M.-C.; Zhang, X.-J.; Zhang, J.-M.; Steinbach, J.; Brust, P.; et al. Synthesis and Biological Evaluation of 18F Labeled Fluoro-Oligo-Ethoxylated 4-Benzylpiperazine Derivatives for Sigma-1 Receptor Imaging. *Bioorg. Med. Chem.* **2013**, *21*, 215–222, doi:10.1016/j.bmc.2012.10.038.
260. Lepelletier, F.-X.; Vandesquille, M.; Asselin, M.-C.; Prenant, C.; Robinson, A.C.; Mann, D.M.A.; Green, M.; Barnett, E.; Banister, S.D.; Mottinelli, M.; et al. Evaluation of ^{18}F-IAM6067 as a Sigma-1 Receptor PET Tracer for Neurodegeneration *in Vivo* in Rodents and in Human Tissue. *Theranostics* **2020**, *10*, 7938–7955, doi:10.7150/thno.47585.
261. Moussa, I.A.; Banister, S.D.; Giboureau, N.; Meikle, S.R.; Kassiou, M. Synthesis and in Vivo Evaluation of [18F]N-(2-Benzofuranylmethyl)-N′-[4-(2-Fluoroethoxy)Benzyl]Piperazine, a Novel Σ1 Receptor PET Imaging Agent. *Bioorg. Med. Chem. Lett.* **2011**, *21*, 6820–6823, doi:10.1016/j.bmcl.2011.09.028.
262. He, Y.; Xie, F.; Ye, J.; Deuther-Conrad, W.; Cui, B.; Wang, L.; Lu, J.; Steinbach, J.; Brust, P.; Huang, Y.; et al. 1-(4-[^{18}F]Fluorobenzyl)-4-[(Tetrahydrofuran-2-Yl)Methyl]Piperazine: A Novel Suitable Radioligand with Low Lipophilicity for Imaging σ1 Receptors in the Brain. *J. Med. Chem.* **2017**, *60*, 4161–4172, doi:10.1021/acs.jmedchem.6b01723.
263. Große Maestrup, E.; Fischer, S.; Wiese, C.; Schepmann, D.; Hiller, A.; Deuther-Conrad, W.; Steinbach, J.; Wünsch, B.; Brust, P. Evaluation of Spirocyclic 3-(3-Fluoropropyl)-2-Benzofurans as σ1 Receptor Ligands for

Neuroimaging with Positron Emission Tomography. *J. Med. Chem.* **2009**, *52*, 6062–6072, doi:10.1021/jm900909e.
264. Fisher, A.; Bezprozvanny, I.; Wu, L.; Ryskamp, D.A.; Bar-Ner, N.; Natan, N.; Brandeis, R.; Elkon, H.; Nahum, V.; Gershonov, E.; et al. AF710B, a Novel M1/Σ1 Agonist with Therapeutic Efficacy in Animal Models of Alzheimer's Disease. *Neurodegener. Dis.* **2016**, *16*, 95–110, doi:10.1159/000440864.
265. Li, Y.; Wang, X.; Zhang, J.; Deuther-Conrad, W.; Xie, F.; Zhang, X.; Liu, J.; Qiao, J.; Cui, M.; Steinbach, J.; et al. Synthesis and Evaluation of Novel^{18}F-Labeled Spirocyclic Piperidine Derivatives as σ$_1$Receptor Ligands for Positron Emission Tomography Imaging. *J. Med. Chem.* **2013**, *56*, 3478–3491, doi:10.1021/jm301734g.
266. Chen, Y.-Y.; Wang, X.; Zhang, J.-M.; Deuther-Conrad, W.; Zhang, X.-J.; Huang, Y.; Li, Y.; Ye, J.-J.; Cui, M.-C.; Steinbach, J.; et al. Synthesis and Evaluation of a 18F-Labeled Spirocyclic Piperidine Derivative as Promising Σ1 Receptor Imaging Agent. *Bioorg. Med. Chem.* **2014**, *22*, 5270–5278, doi:10.1016/j.bmc.2014.08.003.
267. Baum, E.; Cai, Z.; Bois, F.; Holden, D.; Lin, S.; Lara-Jaime, T.; Kapinos, M.; Chen, Y.; Deuther-Conrad, W.; Fischer, S.; et al. PET Imaging Evaluation of Four σ$_1$ Radiotracers in Nonhuman Primates. *J. Nucl. Med.* **2017**, *58*, 982–988, doi:10.2967/jnumed.116.188052.
268. Xie, F.; Bergmann, R.; Kniess, T.; Deuther-Conrad, W.; Mamat, C.; Neuber, C.; Liu, B.; Steinbach, J.; Brust, P.; Pietzsch, J.; et al. ^{18}F-Labeled 1,4-Dioxa-8-Azaspiro[4.5]Decane Derivative: Synthesis and Biological Evaluation of a σ$_1$Receptor Radioligand with Low Lipophilicity as Potent Tumor Imaging Agent. *J. Med. Chem.* **2015**, *58*, 5395–5407, doi:10.1021/acs.jmedchem.5b00593.
269. Tian, J.; He, Y.; Deuther-Conrad, W.; Fu, H.; Xie, F.; Zhang, Y.; Wang, T.; Zhang, X.; Zhang, J.; Brust, P.; et al. Synthesis and Evaluation of New 1-Oxa-8-Azaspiro[4.5]Decane Derivatives as Candidate Radioligands for Sigma-1 Receptors. *Bioorg. Med. Chem.* **2020**, *28*, 115560, doi:10.1016/j.bmc.2020.115560.
270. James, M.L.; Shen, B.; Zavaleta, C.L.; Nielsen, C.H.; Mesangeau, C.; Vuppala, P.K.; Chan, C.; Avery, B.A.; Fishback, J.A.; Matsumoto, R.R.; et al. New Positron Emission Tomography (PET) Radioligand for Imaging σ-1 Receptors in Living Subjects. *J. Med. Chem.* **2012**, *55*, 8272–8282, doi:10.1021/jm300371c.
271. James, M.L.; Shen, B.; Nielsen, C.H.; Behera, D.; Buckmaster, C.L.; Mesangeau, C.; Zavaleta, C.; Vuppala, P.K.; Jamalapuram, S.; Avery, B.A.; et al. Evaluation of σ-1 Receptor Radioligand^{18} F-FTC-146 in Rats and Squirrel Monkeys Using PET. *J. Nucl. Med.* **2014**, *55*, 147–153, doi:10.2967/jnumed.113.120261.
272. Waterhouse, R.N.; Lee Collier, T. In Vivo Evaluation of [18F]1-(3-Fluoropropyl)-4-(4-Cyanophenoxymethyl)Piperidine: A Selective Sigma-1 Receptor Radioligand for PET. *Nucl. Med. Biol.* **1997**, *24*, 127–134, doi:10.1016/s0969-8051(96)00184-9.
273. Waterhouse, R.N.; Stabin, M.G.; Page, J.G. Preclinical Acute Toxicity Studies and Rodent-Based Dosimetry Estimates of the Novel Sigma-1 Receptor Radiotracer [18F]FPS. *Nucl. Med. Biol.* **2003**, *30*, 555–563, doi:10.1016/s0969-8051(03)00020-9.
274. Waterhouse, R.N.; Chang, R.C.; Zhao, J.; Carambot, P.E. In Vivo Evaluation in Rats of [18F]1-(2-Fluoroethyl)-4-[(4-Cyanophenoxy)Methyl]Piperidine as a Potential Radiotracer for PET Assessment of CNS Sigma-1 Receptors. *Nucl. Med. Biol.* **2006**, *33*, 211–215, doi:10.1016/j.nucmedbio.2005.10.007.
275. Jin, H.; Fan, J.; Zhang, X.; Li, J.; Flores, H.P.; Perlmutter, J.S.; Parsons, S.M.; Tu, Z. Radiosynthesis and*in Vivo*Evaluation of a Novel σ$_1$Selective PET Ligand. *MedChemComm* **2014**, *5*, 1669–1677, doi:10.1039/c4md00240g.
276. Yue, X.; Jin, H.; Luo, Z.; Liu, H.; Zhang, X.; McSpadden, E.D.; Tian, L.; Flores, H.P.; Perlmutter, J.S.; Parsons, S.M.; et al. Chiral Resolution of Serial Potent and Selective Σ1 Ligands and Biological Evaluation of (−)-[18F]TZ3108 in Rodent and the Nonhuman Primate Brain. *Bioorg. Med. Chem.* **2017**, *25*, 1533–1542, doi:10.1016/j.bmc.2017.01.017.
277. Soda, A.K.; Huang, T.; Zhou, W.; Chen, H.; Jiang, H.; Jadhav, S.B.; Xing, Z.; Yu, Y.; Tian, L.; Wong, D.F.; et al. Synthesis and in Vivo Biological Characterization of Six Carbon-11 Sigma-1 Receptor Radiotracers in Rodent and Nonhuman Primate. *Bioorg. Med. Chem.* **2025**, *126*, 118218, doi:10.1016/j.bmc.2025.118218.
278. Lan, Y.; Bai, P.; Chen, Z.; Neelamegam, R.; Placzek, M.S.; Wang, H.; Fiedler, S.A.; Yang, J.; Yuan, G.; Qu, X.; et al. Novel Radioligands for Imaging Sigma-1 Receptor in Brain Using Positron Emission Tomography (PET). *Acta Pharm. Sin. B* **2019**, *9*, 1204–1215, doi:10.1016/j.apsb.2019.07.002.
279. Bai, P.; Bagdasarian, F.A.; Xu, Y.; Wang, Y.; Wang, Y.; Gomm, A.; Zhou, Y.; Wu, R.; Wey, H.-Y.; Tanzi, R.E.; et al. Molecular Imaging of Alzheimer's Disease-Related Sigma-1 Receptor in the Brain ***via*** a Novel Ru-Mediated Aromatic ^{18}F-Deoxyfluorination Probe. *J. Med. Chem.* **2024**, *67*, 6207–6217, doi:10.1021/acs.jmedchem.3c02178.
280. Zhang, M.-R.; Haradahira, T.; Maeda, J.; Okauchi, T.; Kawabe, K.; Kida, T.; Suzuki, K.; Suhara, T. Synthesis and Evaluation of 3-(4-Chlorobenzyl)-8-[11C]Methoxy-1,2,3,4-Tetrahydrochromeno[3,4-c]Pyridin-5-One: A PET Tracer for Imaging Sigma1 Receptors. *Nucl. Med. Biol.* **2002**, *29*, 469–476, doi:10.1016/s0969-8051(02)00293-7.
281. Dahl, K.; Halldin, C.; Schou, M. New Methodologies for the Preparation of Carbon-11 Labeled Radiopharmaceuticals. *Clin. Transl. Imaging* **2017**, *5*, 275–289, doi:10.1007/s40336-017-0223-1.
282. Gangangari, K.K.; Váradi, A.; Majumdar, S.; Larson, S.M.; Pasternak, G.W.; Pillarsetty, N.K. Imaging Sigma-1 Receptor (S1R) Expression Using Iodine-124-Labeled 1-(4-Iodophenyl)-3-(2-Adamantyl)Guanidine ([124I]IPAG). *Mol. Imaging Biol.* **2020**, *22*, 358–366, doi:10.1007/s11307-019-01369-8.
283. Colabufo, N.A.; Abate, C.; Contino, M.; Inglese, C.; Niso, M.; Berardi, F.; Perrone, R. PB183, a Sigma Receptor Ligand, as a Potential PET Probe for the Imaging of Prostate Adenocarcinoma. *Bioorg. Med. Chem. Lett.* **2008**, *18*, 1990–1993, doi:10.1016/j.bmcl.2008.01.109.
284. Spinelli, F.; Haider, A.; Toscano, A.; Pati, M.L.; Keller, C.; Berardi, F.; Colabufo, N.A.; Abate, C.; Ametamey, S. Synthesis, Radiolabelling, and Evaluation of [11C]PB212 as a Radioligand for Imaging Sigma-1 Receptors Using PET. *8*, 32–40.

285. Yang, D.; Comeau, A.; Bowen, W.D.; Mach, R.H.; Ross, B.D.; Hong, H.; Van Dort, M.E. Design and Investigation of a [^{18}F]-Labeled Benzamide Derivative as a High Affinity Dual Sigma Receptor Subtype Radioligand for Prostate Tumor Imaging. *Mol. Pharm.* **2017**, *14*, 770–780, doi:10.1021/acs.molpharmaceut.6b01020.
286. Bergstrom, M. Autoradiography with Positron Emitting Isotopes in Positron Emission Tomography Tracer Discovery. *Mol. Imaging Biol.* **2003**, *5*, 390–396, doi:10.1016/j.mibio.2003.09.004.
287. Schmidt, K.C.; Smith, C.B. Resolution, Sensitivity and Precision with Autoradiography and Small Animal Positron Emission Tomography: Implications for Functional Brain Imaging in Animal Research. *Nucl. Med. Biol.* **2005**, *32*, 719–725, doi:10.1016/j.nucmedbio.2005.04.020.
288. Ishiwata, K.; Kawamura, K.; Yajima, K.; QingGeLeTu; Mori, H.; Shiba, K. Evaluation of (+)-p-[11C]Methylvesamicol for Mapping Sigma1 Receptors: A Comparison with [11C]SA4503. *Nucl. Med. Biol.* **2006**, *33*, 543–548, doi:10.1016/j.nucmedbio.2006.01.008.
289. Ramakrishnan, N.K.; Rybczynska, A.A.; Visser, A.K.D.; Marosi, K.; Nyakas, C.J.; Kwizera, C.; Sijbesma, J.W.A.; Elsinga, P.H.; Ishiwata, K.; Pruim, J.; et al. Small-Animal PET with a σ-Ligand,^{11} C-SA4503, Detects Spontaneous Pituitary Tumors in Aged Rats. *J. Nucl. Med.* **2013**, *54*, 1377–1383, doi:10.2967/jnumed.112.115931.
290. Wang, T.; Zhang, Y.; Zhang, X.; Chen, L.; Zheng, M.; Zhang, J.; Brust, P.; Deuther-Conrad, W.; Huang, Y.; Jia, H. Synthesis and Characterization of the Two Enantiomers of a Chiral Sigma-1 Receptor Radioligand: (S)-(+)- and (R)-(-)-[18F]FBFP. *Chin. Chem. Lett.* **2022**, *33*, 3543–3548, doi:10.1016/j.cclet.2022.03.099.
291. Wiese, C.; Maestrup, E.G.; Schepmann, D.; Grimme, S.; Humpf, H.; Brust, P.; Wünsch, B. Enantioselective σ_1 Receptor Binding and Biotransformation of the Spirocyclic PET Tracer 1′-benzyl-3-(3-fluoropropyl)-3 *H* -spiro[[2]Benzofuran-1,4′-piperidine]. *Chirality* **2011**, *23*, 148–154, doi:10.1002/chir.20893.
292. Holl, K.; Falck, E.; Köhler, J.; Schepmann, D.; Humpf, H.; Brust, P.; Wünsch, B. Synthesis, Characterization, and Metabolism Studies of Fluspidine Enantiomers. *ChemMedChem* **2013**, *8*, 2047–2056, doi:10.1002/cmdc.201300322.
293. Brust, P.; Deuther-Conrad, W.; Becker, G.; Patt, M.; Donat, C.K.; Stittsworth, S.; Fischer, S.; Hiller, A.; Wenzel, B.; Dukic-Stefanovic, S.; et al. Distinctive In Vivo Kinetics of the New σ_1 Receptor Ligands (*R*)-(+)- and (*S*)-(–)-^{18} F-Fluspidine in Porcine Brain. *J. Nucl. Med.* **2014**, *55*, 1730–1736, doi:10.2967/jnumed.114.137562.
294. Ludwig, F.-A.; Fischer, S.; Houska, R.; Hoepping, A.; Deuther-Conrad, W.; Schepmann, D.; Patt, M.; Meyer, P.M.; Hesse, S.; Becker, G.-A.; et al. In Vitro and in Vivo Human Metabolism of (S)-[18F]Fluspidine – A Radioligand for Imaging Σ1 Receptors With Positron Emission Tomography (PET). *Front. Pharmacol.* **2019**, *10*, 534, doi:10.3389/fphar.2019.00534.
295. Hjørnevik, T.; Cipriano, P.W.; Shen, B.; Park, J.H.; Gulaka, P.; Holley, D.; Gandhi, H.; Yoon, D.; Mittra, E.S.; Zaharchuk, G.; et al. Biodistribution and Radiation Dosimetry of^{18} F-FTC-146 in Humans. *J. Nucl. Med.* **2017**, *58*, 2004–2009, doi:10.2967/jnumed.117.192641.
296. Pantel, A.R.; Viswanath, V.; Muzi, M.; Doot, R.K.; Mankoff, D.A. Principles of Tracer Kinetic Analysis in Oncology, Part I: Principles and Overview of Methodology. *J. Nucl. Med.* **2022**, *63*, 342–352, doi:10.2967/jnumed.121.263518.
297. Dimitrakopoulou-Strauss, A.; Pan, L.; Sachpekidis, C. Kinetic Modeling and Parametric Imaging with Dynamic PET for Oncological Applications: General Considerations, Current Clinical Applications, and Future Perspectives. *Eur. J. Nucl. Med. Mol. Imaging* **2021**, *48*, 21–39, doi:10.1007/s00259-020-04843-6.
298. Kimura, Y.; Naganawa, M.; Shidahara, M.; Ikoma, Y.; Watabe, H. PET Kinetic Analysis —Pitfalls and a Solution for the Logan Plot. *Ann. Nucl. Med.* **2007**, *21*, 1–8, doi:10.1007/BF03033993.
299. Zhou, Y.; Ye, W.; Brašić, J.R.; Crabb, A.H.; Hilton, J.; Wong, D.F. A Consistent and Efficient Graphical Analysis Method to Improve the Quantification of Reversible Tracer Binding in Radioligand Receptor Dynamic PET Studies. *NeuroImage* **2009**, *44*, 661–670, doi:10.1016/j.neuroimage.2008.09.021.
300. Sakata, M.; Kimura, Y.; Naganawa, M.; Oda, K.; Ishii, K.; Chihara, K.; Ishiwata, K. Mapping of Human Cerebral Sigma1 Receptors Using Positron Emission Tomography and [11C]SA4503. *NeuroImage* **2007**, *35*, 1–8, doi:10.1016/j.neuroimage.2006.11.055.
301. Kawamura, K.; Elsinga, P.H.; Kobayashi, T.; Ishii, S.; Wang, W.-F.; Matsuno, K.; Vaalburg, W.; Ishiwata, K. Synthesis and Evaluation of 11C- and 18F-Labeled 1-[2-(4-Alkoxy-3-Methoxyphenyl)Ethyl]-4-(3-Phenylpropyl)Piperazines as Sigma Receptor Ligands for Positron Emission Tomography Studies. *Nucl. Med. Biol.* **2003**, *30*, 273–284, doi:10.1016/S0969-8051(02)00439-0.
302. Preface, Executive Summary and Glossary. *Ann. ICRP* **2007**, *37*, 9–34, doi:10.1016/j.icrp.2007.10.003.
303. Jackson, I.M.; Lee, S.J.; Sowa, A.R.; Rodnick, M.E.; Bruton, L.; Clark, M.; Preshlock, S.; Rothley, J.; Rogers, V.E.; Botti, L.E.; et al. Use of 55 PET Radiotracers under Approval of a Radioactive Drug Research Committee (RDRC). *EJNMMI Radiopharm. Chem.* **2020**, *5*, doi:10.1186/s41181-020-00110-z.
304. Ishiwata, K.; Ishii, K.; Kimura, Y.; Kawamura, K.; Oda, K.; Sasaki, T.; Sakata, M.; Senda, M. Successive Positron Emission Tomography Measurement of Cerebral Blood Flow and Neuroreceptors in the Human Brain: An 11C-SA4503 Study. *Ann. Nucl. Med.* **2008**, *22*, 411–416, doi:10.1007/s12149-008-0133-4.
305. Kranz, M.; Sattler, B.; Wüst, N.; Deuther-Conrad, W.; Patt, M.; Meyer, P.; Fischer, S.; Donat, C.; Wünsch, B.; Hesse, S.; et al. Evaluation of the Enantiomer Specific Biokinetics and Radiation Doses of [18F]Fluspidine—A New Tracer in Clinical Translation for Imaging of Σ1 Receptors. *Molecules* **2016**, *21*, 1164, doi:10.3390/molecules21091164.
306. Shen, B.; James, M.L.; Andrews, L.; Lau, C.; Chen, S.; Palner, M.; Miao, Z.; Arksey, N.C.; Shuhendler, A.J.; Scatliffe, S.; et al. Further Validation to Support Clinical Translation of [18F]FTC-146 for Imaging Sigma-1 Receptors. *EJNMMI Res.* **2015**, *5*, 49, doi:10.1186/s13550-015-0122-2.

307. Waterhouse, R.N.; Zhao, J.; Stabin, M.G.; Ng, H.; Schindler-Horvat, J.; Chang, R.C.; Mirsalis, J.C. Preclinical Acute Toxicity Studies and Dosimetry Estimates of the Novel Sigma-1 Receptor Radiotracer, [18F]SFE. *Mol. Imaging Biol.* **2006**, *8*, 284–291, doi:10.1007/s11307-006-0056-1.
308. Ishikawa, M.; Sakata, M.; Ishii, K.; Kimura, Y.; Oda, K.; Toyohara, J.; Wu, J.; Ishiwata, K.; Iyo, M.; Hashimoto, K. High Occupancy of Σ1 Receptors in the Human Brain after Single Oral Administration of Donepezil: A Positron Emission Tomography Study Using [11C]SA4503. *Int. J. Neuropsychopharmacol.* **2009**, *12*, 1127, doi:10.1017/S1461145709990204.
309. Ishikawa, M.; Ishiwata, K.; Ishii, K.; Kimura, Y.; Sakata, M.; Naganawa, M.; Oda, K.; Miyatake, R.; Fujisaki, M.; Shimizu, E.; et al. High Occupancy of Sigma-1 Receptors in the Human Brain after Single Oral Administration of Fluvoxamine: A Positron Emission Tomography Study Using [11C]SA4503. *Biol. Psychiatry* **2007**, *62*, 878–883, doi:10.1016/j.biopsych.2007.04.001.
310. Wang, W.-F.; Ishiwata, K.; Kiyosawa, M.; Kawamura, K.; Oda, K.; Kobayashi, T.; Matsuno, K.; Mochizuki, M. Visualization of Sigma1 Receptors in Eyes by Ex Vivo Autoradiography and in Vivo Positron Emission Tomography. *Exp. Eye Res.* **2002**, *75*, 723–730, doi:10.1006/exer.2002.2048.
311. Toyohara, J.; Kobayashi, T.; Mita, S.; Ishiwata, K. Application of [11C]SA4503 to Selection of Novel Σ1 Selective Agonists. *Nucl. Med. Biol.* **2012**, *39*, 1117–1121, doi:10.1016/j.nucmedbio.2012.06.004.
312. Kortekaas, R.; Maguire, R.P.; Van Waarde, A.; Leenders, K.L.; Elsinga, P.H. Despite Irreversible Binding, PET Tracer [11C]-SA5845 Is Suitable for Imaging of Drug Competition at Sigma Receptors—The Cases of Ketamine and Haloperidol. *Neurochem. Int.* **2008**, *53*, 45–50, doi:10.1016/j.neuint.2008.04.010.
313. Meyer, P.; Strauss, M.; Becker, G.; Hesse, S.; Bednasch, K.; Ettrich, B.; Zientek, F.; Rullmann, M.; Wilke, S.; Luthardt, J.; et al. Increased Sigma-1 Receptor (Sig-1R) Binding in the Brain of Unmedicated Patients with Acute Major Depressive Disorder (MDD) Using the Novel Sig-1R-Specific Radioligand (-)-[^{18}F]Fluspidine and PET. *J. Nucl. Med.* **2018**, *59*, 551.
314. Toussaint, M.; Deuther-Conrad, W.; Kranz, M.; Fischer, S.; Ludwig, F.-A.; Juratli, T.A.; Patt, M.; Wünsch, B.; Schackert, G.; Sabri, O.; et al. Sigma-1 Receptor Positron Emission Tomography: A New Molecular Imaging Approach Using (S)-(−)-[18F]Fluspidine in Glioblastoma. *Molecules* **2020**, *25*, 2170, doi:10.3390/molecules25092170.
315. Grachev, I.D.; Meyer, P.M.; Becker, G.A.; Bronzel, M.; Marsteller, D.; Pastino, G.; Voges, O.; Rabinovich, L.; Knebel, H.; Zientek, F.; et al. Sigma-1 and Dopamine D2/D3 Receptor Occupancy of Pridopidine in Healthy Volunteers and Patients with Huntington Disease: A [18F] Fluspidine and [18F] Fallypride PET Study. *Eur. J. Nucl. Med. Mol. Imaging* **2021**, *48*, 1103–1115, doi:10.1007/s00259-020-05030-3.
316. Shen, B.; Behera, D.; James, M.L.; Reyes, S.T.; Andrews, L.; Cipriano, P.W.; Klukinov, M.; Lutz, A.B.; Mavlyutov, T.; Rosenberg, J.; et al. Visualizing Nerve Injury in a Neuropathic Pain Model with [^{18} F]FTC-146 PET/MRI. *Theranostics* **2017**, *7*, 2794–2805, doi:10.7150/thno.19378.
317. Yoon, D.; Fast, A.M.; Cipriano, P.; Shen, B.; Castillo, J.B.; McCurdy, C.R.; Mari Aparici, C.; Lum, D.; Biswal, S. Sigma-1 Receptor Changes Observed in Chronic Pelvic Pain Patients: A Pilot PET/MRI Study. *Front. Pain Res.* **2021**, *2*, 711748, doi:10.3389/fpain.2021.711748.
318. Reyes, S.T.; Deacon, R.M.J.; Guo, S.G.; Altimiras, F.J.; Castillo, J.B.; Van Der Wildt, B.; Morales, A.P.; Park, J.H.; Klamer, D.; Rosenberg, J.; et al. Effects of the Sigma-1 Receptor Agonist Blarcamesine in a Murine Model of Fragile X Syndrome: Neurobehavioral Phenotypes and Receptor Occupancy. *Sci. Rep.* **2021**, *11*, 17150, doi:10.1038/s41598-021-94079-7.
319. Waterhouse, R.N.; Chang, R.C.; Atuehene, N.; Collier, T.L. In Vitro and in Vivo Binding of Neuroactive Steroids to the Sigma-1 Receptor as Measured with the Positron Emission Tomography Radioligand [^{18}F]FPS. *Synapse* **2007**, *61*, 540–546, doi:10.1002/syn.20369.
320. Huang, P.; Li, Z.; Peng, T.; Yang, J.; Bi, L.; Huang, G.; Qiu, Y.; Yang, M.; Ye, P.; Huang, M.; et al. Evaluation of [18F]F-TZ3108 for PET Imaging of Metabolic-Associated Fatty Liver Disease. *Mol. Imaging Biol.* **2022**, *24*, 909–919, doi:10.1007/s11307-022-01740-2.
321. Han, Z.; Yang, M.; Bi, L.; Ye, P.; Liu, Y.; He, P.; Huang, G.; Jin, H.; Xia, J. Quantitative Imaging Using [18F]F-TZ3108 to Assess Metabolic-Associated Fatty Liver Disease Progression and Low-Carbohydrate Diet Efficacy. *Nucl. Med. Biol.* **2025**, *144–145*, 108997, doi:10.1016/j.nucmedbio.2025.108997.
322. Siddiqui, T.; Bhatt, L.K. Targeting Sigma-1 Receptor: A Promising Strategy in the Treatment of Parkinson's Disease. *Neurochem. Res.* **2023**, *48*, 2925–2935, doi:10.1007/s11064-023-03960-6.
323. Ye, N.; Qin, W.; Tian, S.; Xu, Q.; Wold, E.A.; Zhou, J.; Zhen, X.-C. Small Molecules Selectively Targeting Sigma-1 Receptor for the Treatment of Neurological Diseases. *J. Med. Chem.* **2020**, *63*, 15187–15217, doi:10.1021/acs.jmedchem.0c01192.
324. Berardi, F.; Ferorelli, S.; Abate, C.; Pedone, M.P.; Colabufo, N.A.; Contino, M.; Perrone, R. Methyl Substitution on the Piperidine Ring of *N* -[ω-(6-Methoxynaphthalen-1-Yl)Alkyl] Derivatives as a Probe for Selective Binding and Activity at the σ_1 Receptor. *J. Med. Chem.* **2005**, *48*, 8237–8244, doi:10.1021/jm050654o.
325. Berardi, F.; Loiodice, F.; Fracchiolla, G.; Colabufo, N.A.; Perrone, R.; Tortorella, V. Synthesis of Chiral 1-[ω-(4-Chlorophenoxy)Alkyl]-4-Methylpiperidines and Their Biological Evaluation at σ_1 , σ_2 , and Sterol Δ_8 $-\Delta_7$ Isomerase Sites. *J. Med. Chem.* **2003**, *46*, 2117–2124, doi:10.1021/jm021014d.
326. Abatematteo, F.S.; Mosier, P.D.; Niso, M.; Brunetti, L.; Berardi, F.; Loiodice, F.; Contino, M.; Delprat, B.; Maurice, T.; Laghezza, A.; et al. Development of Novel Phenoxyalkylpiperidines as High-Affinity Sigma-1 (Σ1) Receptor Ligands with Potent Anti-Amnesic Effect. *Eur. J. Med. Chem.* **2022**, *228*, 114038, doi:10.1016/j.ejmech.2021.114038.
327. Mastropasqua, F.; Lisi, A.T.; Crouzier, L.; Musillo, G.R.; Abatematteo, F.S.; Niso, M.; Delprat, B.; Colabufo, N.A.; Nanna, V.; Mangiatordi, G.F.; et al. Development of Second-Generation Phenoxyethylpiperidines as Potent Sigma-1 Receptor Agonists with Neuroprotective Potential for Alzheimer's Disease. *J. Med. Chem.* **2026**, acs.jmedchem.5c03240, doi:10.1021/acs.jmedchem.5c03240.

328. Eissa Mohammed, Y.H.; Thirusangu, P.; Zabiulla; V, V.; B.T, P.; Khanum, S.A. The Anti-Invasive Role of Novel Synthesized Pyridazine Hydrazide Appended Phenoxy Acetic Acid against Neoplastic Development Targeting Matrix Metallo Proteases. *Biomed. Pharmacother.* **2017**, *95*, 375–386, doi:10.1016/j.biopha.2017.08.105.
329. Wang, T.; Wang, W.; Peng, H.; He, H. Synthesis and Biological Activity of 1-(Substituted Phenoxyacetoxy)-1-(Pyridin-2-yl or Thien-2-yl)Methylphosphonates. *J. Heterocycl. Chem.* **2015**, *52*, 173–179, doi:10.1002/jhet.1944.
330. Martin, M.W.; Newcomb, J.; Nunes, J.J.; Boucher, C.; Chai, L.; Epstein, L.F.; Faust, T.; Flores, S.; Gallant, P.; Gore, A.; et al. Structure-Based Design of Novel 2-Amino-6-Phenyl-Pyrimido[5′,4′:5,6]Pyrimido[1,2- *a*]Benzimidazol-5(6 *H*)-Ones as Potent and Orally Active Inhibitors of Lymphocyte Specific Kinase (Lck): Synthesis, SAR, and In Vivo Anti-Inflammatory Activity. *J. Med. Chem.* **2008**, *51*, 1637–1648, doi:10.1021/jm701095m.
331. Sakamuri, S.; Enyedy, I.J.; Zaman, W.A.; Tella, S.R.; Kozikowski, A.P.; Flippen-Anderson, J.L.; Farkas, T.; Johnson, K.M.; Wang, S. 2,3-Disubstituted Quinuclidines as a Novel Class of Dopamine Transporter Inhibitors. *Bioorg. Med. Chem.* **2003**, *11*, 1123–1136, doi:10.1016/S0968-0896(02)00450-9.
332. Alford, V.M.; Kamath, A.; Ren, X.; Kumar, K.; Gan, Q.; Awwa, M.; Tong, M.; Seeliger, M.A.; Cao, J.; Ojima, I.; et al. Targeting the Hemopexin-like Domain of Latent Matrix Metalloproteinase-9 (proMMP-9) with a Small Molecule Inhibitor Prevents the Formation of Focal Adhesion Junctions. *ACS Chem. Biol.* **2017**, *12*, 2788–2803, doi:10.1021/acschembio.7b00758.
333. Deuther-Conrad, W.; Diez-Iriepa, D.; Iriepa, I.; López-Muñoz, F.; Martínez-Grau, M.A.; Gütschow, M.; Marco-Contelles, J. Studies on the Affinity of 6-[(*n* -(Cyclo)Aminoalkyl)Oxy]-4 *H* -Chromen-4-Ones for Sigma 1/2 Receptors. *RSC Med. Chem.* **2021**, *12*, 1000–1004, doi:10.1039/D1MD00105A.
334. Mastropasqua, F.; Luurtsema, G.; Filosa, C.; Colabufo, N.A. Designing a Small Molecule for PET Radiotracing: [18F]MC225 in Human Trials for Early Diagnosis in CNS Pathologies. *Molecules* **2025**, *30*, 3696, doi:10.3390/molecules30183696.
335. Contino, M.; Guglielmo, S.; Riganti, C.; Antonello, G.; Perrone, M.G.; Giampietro, R.; Rolando, B.; Fruttero, R.; Colabufo, N.A. One Molecule Two Goals: A Selective P-Glycoprotein Modulator Increases Drug Transport across Gastro-Intestinal Barrier and Recovers Doxorubicin Toxicity in Multidrug Resistant Cancer Cells. *Eur. J. Med. Chem.* **2020**, *208*, 112843, doi:10.1016/j.ejmech.2020.112843.
336. Ritawidya, R.; Ludwig, F.-A.; Briel, D.; Brust, P.; Scheunemann, M. Synthesis and In Vitro Evaluation of 8-Pyridinyl-Substituted Benzo[e]Imidazo[2,1-c][1,2,4]Triazines as Phosphodiesterase 2A Inhibitors. *Molecules* **2019**, *24*, 2791, doi:10.3390/molecules24152791.
337. Ludwig, F.-A.; Smits, R.; Fischer, S.; Donat, C.; Hoepping, A.; Brust, P.; Steinbach, J. LC-MS Supported Studies on the in Vitro Metabolism of Both Enantiomers of Flubatine and the in Vivo Metabolism of (+)-[18F]Flubatine—A Positron Emission Tomography Radioligand for Imaging A4β2 Nicotinic Acetylcholine Receptors. *Molecules* **2016**, *21*, 1200, doi:10.3390/molecules21091200.
338. Schröder, S.; Lai, T.H.; Toussaint, M.; Kranz, M.; Chovsepian, A.; Shang, Q.; Dukić-Stefanović, S.; Deuther-Conrad, W.; Teodoro, R.; Wenzel, B.; et al. PET Imaging of the Adenosine A2A Receptor in the Rotenone-Based Mouse Model of Parkinson's Disease with [18F]FESCH Synthesized by a Simplified Two-Step One-Pot Radiolabeling Strategy. *Molecules* **2020**, *25*, 1633, doi:10.3390/molecules25071633.
339. Zoghbi, S.S.; Shetty, H.U.; Ichise, M.; Fujita, M.; Imaizumi, M.; Liow, J.-S.; Shah, J.; Musachio, J.L.; Pike, V.W.; Innis, R.B. PET Imaging of the Dopamine Transporter with 18F-FECNT: A Polar Radiometabolite Confounds Brain Radioligand Measurements. *J. Nucl. Med. Off. Publ. Soc. Nucl. Med.* **2006**, *47*, 520–527.
340. Evens, N.; Vandeputte, C.; Muccioli, G.G.; Lambert, D.M.; Baekelandt, V.; Verbruggen, A.M.; Debyser, Z.; Van Laere, K.; Bormans, G.M. Synthesis, in Vitro and in Vivo Evaluation of Fluorine-18 Labelled FE-GW405833 as a PET Tracer for Type 2 Cannabinoid Receptor Imaging. *Bioorg. Med. Chem.* **2011**, *19*, 4499–4505, doi:10.1016/j.bmc.2011.06.033.
341. Phan, V. Preserved Sigma1 (Σ1) Receptor Expression and Behavioral Efficacy in the Aged C57BL/6 Mouse. *Neurobiol. Aging* **2003**, *24*, 865–881, doi:10.1016/S0197-4580(02)00231-2.
342. Hellewell, S.B.; Bowen, W.D. A Sigma-like Binding Site in Rat Pheochromocytoma (PC12) Cells: Decreased Affinity for (+)-Benzomorphans and Lower Molecular Weight Suggest a Different Sigma Receptor Form from That of Guinea Pig Brain. *Brain Res.* **1990**, *527*, 244–253, doi:10.1016/0006-8993(90)91143-5.
343. Xu, J.; Zeng, C.; Chu, W.; Pan, F.; Rothfuss, J.M.; Zhang, F.; Tu, Z.; Zhou, D.; Zeng, D.; Vangveravong, S.; et al. Identification of the PGRMC1 Protein Complex as the Putative Sigma-2 Receptor Binding Site. *Nat. Commun.* **2011**, *2*, 380, doi:10.1038/ncomms1386.
344. Pati, M.L.; Groza, D.; Riganti, C.; Kopecka, J.; Niso, M.; Berardi, F.; Hager, S.; Heffeter, P.; Hirai, M.; Tsugawa, H.; et al. Sigma-2 Receptor and Progesterone Receptor Membrane Component 1 (PGRMC1) Are Two Different Proteins: Proofs by Fluorescent Labeling and Binding of Sigma-2 Receptor Ligands to PGRMC1. *Pharmacol. Res.* **2017**, *117*, 67–74, doi:10.1016/j.phrs.2016.12.023.
345. Abate, C.; Niso, M.; Infantino, V.; Menga, A.; Berardi, F. Elements in Support of the 'Non-Identity' of the PGRMC1 Protein with the Σ2 Receptor. *Eur. J. Pharmacol.* **2015**, *758*, 16–23, doi:10.1016/j.ejphar.2015.03.067.
346. Alon, A.; Schmidt, H.R.; Wood, M.D.; Sahn, J.J.; Martin, S.F.; Kruse, A.C. Identification of the Gene That Codes for the σ_2 Receptor. *Proc. Natl. Acad. Sci.* **2017**, *114*, 7160–7165, doi:10.1073/pnas.1705154114.
347. Alon, A.; Lyu, J.; Braz, J.M.; Tummino, T.A.; Craik, V.; O'Meara, M.J.; Webb, C.M.; Radchenko, D.S.; Moroz, Y.S.; Huang, X.-P.; et al. Structures of the Σ2 Receptor Enable Docking for Bioactive Ligand Discovery. *Nature* **2021**, *600*, 759–764, doi:10.1038/s41586-021-04175-x.
348. Vilner, B.J.; Bowen, W.D. Modulation of Cellular Calcium by Sigma-2 Receptors: Release from Intracellular Stores in Human SK-N-SH Neuroblastoma Cells. *J. Pharmacol. Exp. Ther.* **2000**, *292*, 900–911.
349. Zhang, H.; Cuevas, J. Sigma Receptors Inhibit High-Voltage–Activated Calcium Channels in Rat Sympathetic and Parasympathetic Neurons. *J. Neurophysiol.* **2002**, *87*, 2867–2879, doi:10.1152/jn.2002.87.6.2867.

350. Cassano, G.; Gasparre, G.; Contino, M.; Niso, M.; Berardi, F.; Perrone, R.; Colabufo, N.A. The Sigma-2 Receptor Agonist PB28 Inhibits Calcium Release from the Endoplasmic Reticulum of SK-N-SH Neuroblastoma Cells. *Cell Calcium* **2006**, *40*, 23–28, doi:10.1016/j.ceca.2006.03.004.
351. Weatherspoon, J.K.; Werling, L.L. Modulation of Amphetamine-Stimulated [3H]Dopamine Release from Rat Pheochromocytoma (PC12) Cells by Sigma Type 2 Receptors. *J. Pharmacol. Exp. Ther.* **1999**, *289*, 278–284.
352. Ostenfeld, M.S.; Høyer-Hansen, M.; Bastholm, L.; Fehrenbacher, N.; Olsen, O.D.; Groth-Pedersen, L.; Puustinen, P.; Kirkegaard-Sørensen, T.; Nylandsted, J.; Farkas, T.; et al. Anti-Cancer Agent Siramesine Is a Lysosomotropic Detergent That Induces Cytoprotective Autophagosome Accumulation. *Autophagy* **2008**, *4*, 487–499, doi:10.4161/auto.5774.
353. Hornick, J.R.; Vangveravong, S.; Spitzer, D.; Abate, C.; Berardi, F.; Goedegebuure, P.; Mach, R.H.; Hawkins, W.G. Lysosomal Membrane Permeabilization Is an Early Event in Sigma-2 Receptor Ligand Mediated Cell Death in Pancreatic Cancer. *J. Exp. Clin. Cancer Res.* **2012**, *31*, 41, doi:10.1186/1756-9966-31-41.
354. Colgan, S.M.; Al-Hashimi, A.A.; Austin, R.C. Endoplasmic Reticulum Stress and Lipid Dysregulation. *Expert Rev. Mol. Med.* **2011**, *13*, e4, doi:10.1017/S1462399410001742.
355. Mach, R.H.; Zeng, C.; Hawkins, W.G. The σ_2 Receptor: A Novel Protein for the Imaging and Treatment of Cancer. *J. Med. Chem.* **2013**, *56*, 7137–7160, doi:10.1021/jm301545c.
356. Cantonero, C.; Camello, P.J.; Abate, C.; Berardi, F.; Salido, G.M.; Rosado, J.A.; Redondo, P.C. NO1, a New Sigma 2 Receptor/TMEM97 Fluorescent Ligand, Downregulates SOCE and Promotes Apoptosis in the Triple Negative Breast Cancer Cell Lines. *Cancers* **2020**, *12*, 257, doi:10.3390/cancers12020257.
357. Pati, M.L.; Hornick, J.R.; Niso, M.; Berardi, F.; Spitzer, D.; Abate, C.; Hawkins, W. Sigma-2 Receptor Agonist Derivatives of 1-Cyclohexyl-4-[3-(5-Methoxy-1,2,3,4-Tetrahydronaphthalen-1-Yl)Propyl]Piperazine (PB28) Induce Cell Death via Mitochondrial Superoxide Production and Caspase Activation in Pancreatic Cancer. *BMC Cancer* **2017**, *17*, 51, doi:10.1186/s12885-016-3040-4.
358. Crawford, K.W.; Bowen, W.D. Sigma-2 Receptor Agonists Activate a Novel Apoptotic Pathway and Potentiate Antineoplastic Drugs in Breast Tumor Cell Lines. *Cancer Res.* **2002**, *62*, 313–322.
359. Zeng, C.; Weng, C.-C.; Schneider, M.E.; Puentes, L.; Riad, A.; Xu, K.; Makvandi, M.; Jin, L.; Hawkins, W.G.; Mach, R.H. TMEM97 and PGRMC1 Do Not Mediate Sigma-2 Ligand-Induced Cell Death. *Cell Death Discov.* **2019**, *5*, 58, doi:10.1038/s41420-019-0141-2.
360. Fontanilla, D.; Johannessen, M.; Hajipour, A.R.; Cozzi, N.V.; Jackson, M.B.; Ruoho, A.E. The Hallucinogen *N,N* -Dimethyltryptamine (DMT) Is an Endogenous Sigma-1 Receptor Regulator. *Science* **2009**, *323*, 934–937, doi:10.1126/science.1166127.
361. Izzo, N.J.; Colom-Cadena, M.; Riad, A.A.; Xu, J.; Singh, M.; Abate, C.; Cahill, M.A.; Spires-Jones, T.L.; Bowen, W.D.; Mach, R.H.; et al. Proceedings from the Fourth International Symposium on σ-2 Receptors: Role in Health and Disease. *eneuro* **2020**, *7*, ENEURO.0317-20.2020, doi:10.1523/ENEURO.0317-20.2020.
362. Izzo, N.J.; Xu, J.; Zeng, C.; Kirk, M.J.; Mozzoni, K.; Silky, C.; Rehak, C.; Yurko, R.; Look, G.; Rishton, G.; et al. Alzheimer's Therapeutics Targeting Amyloid Beta 1–42 Oligomers II: Sigma-2/PGRMC1 Receptors Mediate Abeta 42 Oligomer Binding and Synaptotoxicity. *PLoS ONE* **2014**, *9*, e111899, doi:10.1371/journal.pone.0111899.
363. Yi, B.; Sahn, J.J.; Ardestani, P.M.; Evans, A.K.; Scott, L.L.; Chan, J.Z.; Iyer, S.; Crisp, A.; Zuniga, G.; Pierce, J.T.; et al. Small Molecule Modulator of Sigma 2 Receptor Is Neuroprotective and Reduces Cognitive Deficits and Neuroinflammation in Experimental Models of Alzheimer's Disease. *J. Neurochem.* **2017**, *140*, 561–575, doi:10.1111/jnc.13917.
364. Izzo, N.J.; Yuede, C.M.; LaBarbera, K.M.; Limegrover, C.S.; Rehak, C.; Yurko, R.; Waybright, L.; Look, G.; Rishton, G.; Safferstein, H.; et al. Preclinical and Clinical Biomarker Studies of CT1812: A Novel Approach to Alzheimer's Disease Modification. *Alzheimers Dement.* **2021**, *17*, 1365–1382, doi:10.1002/alz.12302.
365. Kocher, A.; Stamm, T. Commentary on the Article: Hughes M & Pauling JD. Exploring the Patient Experience of Digital Ulcers in Systemic Sclerosis. Semin Arthritis Rheum. 2018 Aug 11. Pii: S0049-0172(18)30354-8. Doi: 10.1016/j.Semarthrit.2018.08.001. [Epub Ahead of Print] Review. *Semin. Arthritis Rheum.* **2019**, *49*, e9, doi:10.1016/j.semarthrit.2018.12.005.
366. Kaur, G.; Dar, Z.A.; Bajpai, A.; Singh, R.; Bansal, R. Clinical Update on an Anti-Alzheimer Drug Candidate CT1812: A Sigma-2 Receptor Antagonist. *Clin. Ther.* **2024**, *46*, e21–e28, doi:10.1016/j.clinthera.2024.08.013.
367. Tu, Z.; Dence, C.S.; Ponde, D.E.; Jones, L.; Wheeler, K.T.; Welch, M.J.; Mach, R.H. Carbon-11 Labeled Σ2 Receptor Ligands for Imaging Breast Cancer. *Nucl. Med. Biol.* **2005**, *32*, 423–430, doi:10.1016/j.nucmedbio.2005.03.008.
368. Rowland, D.J.; Tu, Z.; Xu, J.; Ponde, D.; Mach, R.H.; Welch, M.J. Synthesis and in Vivo Evaluation of 2 High-Affinity 76Br-Labeled Sigma2-Receptor Ligands. *J. Nucl. Med. Off. Publ. Soc. Nucl. Med.* **2006**, *47*, 1041–1048.
369. Xu, J.; Tu, Z.; Jones, L.A.; Vangveravong, S.; Wheeler, K.T.; Mach, R.H. [3H]N-[4-(3,4-Dihydro-6,7-Dimethoxyisoquinolin-2(1H)-Yl)Butyl]-2-Methoxy-5-Methylbenzamide: A Novel Sigma-2 Receptor Probe. *Eur. J. Pharmacol.* **2005**, *525*, 8–17, doi:10.1016/j.ejphar.2005.09.063.
370. Tu, Z.; Xu, J.; Jones, L.A.; Li, S.; Dumstorff, C.; Vangveravong, S.; Chen, D.L.; Wheeler, K.T.; Welch, M.J.; Mach, R.H. Fluorine-18-Labeled Benzamide Analogues for Imaging the σ_2 Receptor Status of Solid Tumors with Positron Emission Tomography. *J. Med. Chem.* **2007**, *50*, 3194–3204, doi:10.1021/jm0614883.
371. Tu, Z.; Xu, J.; Jones, L.A.; Li, S.; Zeng, D.; Kung, M.-P.; Kung, H.F.; Mach, R.H. Radiosynthesis and Biological Evaluation of a Promising Σ2-Receptor Ligand Radiolabeled with Fluorine-18 or Iodine-125 as a PET/SPECT Probe for Imaging Breast Cancer. *Appl. Radiat. Isot.* **2010**, *68*, 2268–2273, doi:10.1016/j.apradiso.2010.06.004.
372. Dehdashti, F.; Laforest, R.; Gao, F.; Shoghi, K.I.; Aft, R.L.; Nussenbaum, B.; Kreisel, F.H.; Bartlett, N.L.; Cashen, A.; Wagner-Johnson, N.; et al. Assessment of Cellular Proliferation in Tumors by PET Using^{18} F-ISO-1. *J. Nucl. Med.* **2013**, *54*, 350–357, doi:10.2967/jnumed.112.111948.

373. McDonald, E.S.; Doot, R.K.; Young, A.J.; Schubert, E.K.; Tchou, J.; Pryma, D.A.; Farwell, M.D.; Nayak, A.; Ziober, A.; Feldman, M.D.; et al. Breast Cancer^{18} F-ISO-1 Uptake as a Marker of Proliferation Status. *J. Nucl. Med.* **2020**, *61*, 665–670, doi:10.2967/jnumed.119.232363.
374. Shoghi, K.I.; Xu, J.; Su, Y.; He, J.; Rowland, D.; Yan, Y.; Garbow, J.R.; Tu, Z.; Jones, L.A.; Higashikubo, R.; et al. Quantitative Receptor-Based Imaging of Tumor Proliferation with the Sigma-2 Ligand [18F]ISO-1. *PLoS ONE* **2013**, *8*, e74188, doi:10.1371/journal.pone.0074188.
375. Wang, L.; Ye, J.; He, Y.; Deuther-Conrad, W.; Zhang, J.; Zhang, X.; Cui, M.; Steinbach, J.; Huang, Y.; Brust, P.; et al. 18F-Labeled Indole-Based Analogs as Highly Selective Radioligands for Imaging Sigma-2 Receptors in the Brain. *Bioorg. Med. Chem.* **2017**, *25*, 3792–3802, doi:10.1016/j.bmc.2017.05.019.
376. Zhang, Y.; Wang, T.; Zhang, X.; Deuther-Conrad, W.; Fu, H.; Cui, M.; Zhang, J.; Brust, P.; Huang, Y.; Jia, H. Discovery and Development of Brain-Penetrant 18F-Labeled Radioligands for Neuroimaging of the Sigma-2 Receptors. *Acta Pharm. Sin. B* **2022**, *12*, 1406–1415, doi:10.1016/j.apsb.2021.08.029.
377. Alluri, S.R.; Zheng, M.; Holden, D.; Zhang, Y.; Zhang, L.; Felchner, Z.; Li, S.; Ropchan, J.; Carson, R.; Jia, H.; et al. Evaluation of a First PET Tracer Suitable for Imaging the Sigma-2 Receptor in the Brain of Nonhuman Primates. *Mol. Pharm.* **2024**, *21*, 194–200, doi:10.1021/acs.molpharmaceut.3c00750.
378. Moldovan, R.-P.; Gündel, D.; Teodoro, R.; Ludwig, F.-A.; Fischer, S.; Toussaint, M.; Schepmann, D.; Wünsch, B.; Brust, P.; Deuther-Conrad, W. Design, Radiosynthesis and Preliminary Biological Evaluation in Mice of a Brain-Penetrant 18F-Labelled Σ2 Receptor Ligand. *Int. J. Mol. Sci.* **2021**, *22*, 5447, doi:10.3390/ijms22115447.
379. Abate, C.; Selivanova, S.V.; Müller, A.; Krämer, S.D.; Schibli, R.; Marottoli, R.; Perrone, R.; Berardi, F.; Niso, M.; Ametamey, S.M. Development of 3,4-Dihydroisoquinolin-1(2H)-One Derivatives for the Positron Emission Tomography (PET) Imaging of Σ2 Receptors. *Eur. J. Med. Chem.* **2013**, *69*, 920–930, doi:10.1016/j.ejmech.2013.09.018.
380. Kim, H.Y.; Lee, J.Y.; Hsieh, C.-J.; Riad, A.; Izzo, N.J.; Catalano, S.M.; Graham, T.J.A.; Mach, R.H. Screening of σ_2 Receptor Ligands and *In Vivo* Evaluation of^{11} C-Labeled 6,7-Dimethoxy-2-[4-(4-Methoxyphenyl)Butan-2-Yl]-1,2,3,4-Tetrahydroisoquinoline for Potential Use as a σ_2 Receptor Brain PET Tracer. *J. Med. Chem.* **2022**, *65*, 6261–6272, doi:10.1021/acs.jmedchem.2c00191.
381. Wang, T.; Wang, J.; Chen, L.; Zhang, X.; Mou, T.; An, X.; Zhang, J.; Zhang, X.; Deuther-Conrad, W.; Huang, Y.; et al. Development of a Highly Specific^{18} F-Labeled Radioligand for Imaging of the Sigma-2 Receptor in Brain Tumors. *J. Med. Chem.* **2023**, *66*, 12840–12857, doi:10.1021/acs.jmedchem.3c00735.
382. Kassiou, M.; Dannals, R.F.; Liu, X.; Wong, D.F.; Ravert, H.T.; Scheffel, U.A. Synthesis and in Vivo Evaluation of a New PET Radioligand for Studying Sigma-2 Receptors. *Bioorg. Med. Chem.* **2005**, *13*, 3623–3626, doi:10.1016/j.bmc.2005.03.039.
383. Selivanova, S.V.; Toscano, A.; Abate, C.; Berardi, F.; Müller, A.; Krämer, S.D.; Schibli, R.; Ametamey, S.M. Synthesis and Pharmacological Evaluation of 11C-Labeled Piperazine Derivative as a PET Probe for Sigma-2 Receptor Imaging. *Nucl. Med. Biol.* **2015**, *42*, 399–405, doi:10.1016/j.nucmedbio.2014.12.018.
384. Chu, W.; Xu, J.; Zhou, D.; Zhang, F.; Jones, L.A.; Wheeler, K.T.; Mach, R.H. New N-Substituted 9-Azabicyclo[3.3.1]Nonan-3α-Yl Phenylcarbamate Analogs as Σ2 Receptor Ligands: Synthesis, in Vitro Characterization, and Evaluation as PET Imaging and Chemosensitization Agents. *Bioorg. Med. Chem.* **2009**, *17*, 1222–1231, doi:10.1016/j.bmc.2008.12.025.
385. Abate, C.; Niso, M.; Lacivita, E.; Mosier, P.D.; Toscano, A.; Perrone, R. Analogues of σ Receptor Ligand 1-Cyclohexyl-4-[3-(5-Methoxy-1,2,3,4-Tetrahydronaphthalen-1-Yl)Propyl]Piperazine (PB28) with Added Polar Functionality and Reduced Lipophilicity for Potential Use as Positron Emission Tomography Radiotracers. *J. Med. Chem.* **2011**, *54*, 1022–1032, doi:10.1021/jm1013133.
386. Abate, C.; Ferorelli, S.; Niso, M.; Lovicario, C.; Infantino, V.; Convertini, P.; Perrone, R.; Berardi, F. 2-Aminopyridine Derivatives as Potential σ_2 Receptor Antagonists. *ChemMedChem* **2012**, *7*, 1847–1857, doi:10.1002/cmdc.201200246.
387. Barbanente, A.; Kopecka, J.; Vitone, D.; Niso, M.; Rizzi, R.; Cuocci, C.; Abatematteo, F.S.; Mastropasqua, F.; Colabufo, N.A.; Margiotta, N.; et al. First-In-Class Thiosemicarbazone Metal Complexes Targeting the Sigma-2 Receptor (S2R) as an Innovative Strategy against Pancreatic Cancer. *J. Med. Chem.* **2024**, *67*, 20118–20134, doi:10.1021/acs.jmedchem.4c01410.
388. Niso, M.; Riganti, C.; Pati, M.L.; Ghigo, D.; Berardi, F.; Abate, C. Novel and Selective Fluorescent σ_2 -Receptor Ligand with a 3,4-Dihydroisoquinolin-1-one Scaffold: A Tool to Study σ_2 Receptors in Living Cells. *ChemBioChem* **2015**, *16*, 1078–1083, doi:10.1002/cbic.201402712.
389. Abate, C.; Hornick, J.R.; Spitzer, D.; Hawkins, W.G.; Niso, M.; Perrone, R.; Berardi, F. Fluorescent Derivatives of σ Receptor Ligand 1-Cyclohexyl-4-[3-(5-Methoxy-1,2,3,4-Tetrahydronaphthalen-1-Yl)Propyl]Piperazine (PB28) as a Tool for Uptake and Cellular Localization Studies in Pancreatic Tumor Cells. *J. Med. Chem.* **2011**, *54*, 5858–5867, doi:10.1021/jm200591t.
390. Abate, C.; Niso, M.; Marottoli, R.; Riganti, C.; Ghigo, D.; Ferorelli, S.; Ossato, G.; Perrone, R.; Lacivita, E.; Lamb, D.C.; et al. Novel Derivatives of 1-Cyclohexyl-4-[3-(5-Methoxy-1,2,3,4-Tetrahydronaphthalen-1-Yl)Propyl]Piperazine (PB28) with Improved Fluorescent and σ Receptors Binding Properties. *J. Med. Chem.* **2014**, *57*, 3314–3323, doi:10.1021/jm401874n.
391. Niso, M.; Pati, M.L.; Berardi, F.; Abate, C. Rigid versus Flexible Anilines or Anilides Confirm the Bicyclic Ring as the Hydrophobic Portion for Optimal σ_2 Receptor Binding and Provide Novel Tools for the Development of Future σ_2 Receptor PET Radiotracers. *RSC Adv.* **2016**, *6*, 88508–88518, doi:10.1039/C6RA15783A.
392. Linkens, K.; Schmidt, H.R.; Sahn, J.J.; Kruse, A.C.; Martin, S.F. Investigating Isoindoline, Tetrahydroisoquinoline, and Tetrahydrobenzazepine Scaffolds for Their Sigma Receptor Binding Properties. *Eur. J. Med. Chem.* **2018**, *151*, 557–567, doi:10.1016/j.ejmech.2018.02.024.

393. Anobile, D.P.; Niso, M.; Puerta, A.; Fraga Rodrigues, S.M.; Abatematteo, F.S.; Avan, A.; Abate, C.; Riganti, C.; Giovannetti, E. New Pharmacological Strategies against Pancreatic Adenocarcinoma: The Multifunctional Thiosemicarbazone FA4. *Molecules* **2022**, *27*, 1682, doi:10.3390/molecules27051682.
394. Niso, M.; Kopecka, J.; Abatematteo, F.S.; Berardi, F.; Riganti, C.; Abate, C. Multifunctional Thiosemicarbazones Targeting Sigma Receptors: In Vitro and in Vivo Antitumor Activities in Pancreatic Cancer Models. *Cell. Oncol.* **2021**, *44*, 1307–1323, doi:10.1007/s13402-021-00638-5.
395. Chiarugi, A.; Meli, E.; Calvani, M.; Picca, R.; Baronti, R.; Camaioni, E.; Costantino, G.; Marinozzi, M.; Pellegrini-Giampietro, D.E.; Pellicciari, R.; et al. Novel Isoquinolinone-Derived Inhibitors of Poly(ADP-Ribose) Polymerase-1: Pharmacological Characterization and Neuroprotective Effects in an in Vitro Model of Cerebral Ischemia. *J. Pharmacol. Exp. Ther.* **2003**, *305*, 943–949, doi:10.1124/jpet.103.048934.
396. Roth, Bryan L. *National Institute of Mental Health Psychoactive Drug Screening Program (NIMH PDSP): Assay Protocol Book. Version III*; University of North Carolina at Chapel Hill: Chapel Hill, NC, 2018;
397. Colabufo, N.A.; Berardi, F.; Cantore, M.; Perrone, M.G.; Contino, M.; Inglese, C.; Niso, M.; Perrone, R.; Azzariti, A.; Simone, G.M.; et al. 4-Biphenyl and 2-Naphthyl Substituted 6,7-Dimethoxytetrahydroisoquinoline Derivatives as Potent P-Gp Modulators. *Bioorg. Med. Chem.* **2008**, *16*, 3732–3743, doi:10.1016/j.bmc.2008.01.055.
398. Schoultz, B.; Reed, B.; Marton, J.; Willoch, F.; Henriksen, G. A Fully Automated Radiosynthesis of [18F]Fluoroethyl-Diprenorphine on a Single Module by Use of SPE Cartridges for Preparation of High Quality 2-[18F]Fluoroethyl Tosylate. *Molecules* **2013**, *18*, 7271–7278, doi:10.3390/molecules18067271.
399. Song, Z.; Li, Y.; Dahl, K.; Sun, Z.; Chen, J.; Zhou, X.; Gao, Y.; Rong, J.; Zhao, C.; Yuan, K.; et al. Development and Preclinical Characterization of [^{18} F]H3-2406 and [^{18} F]H3-2407 for Positron Emission Tomography Imaging of the Histamine Subtype-3 Receptor. *J. Med. Chem.* **2025**, *68*, 15372–15385, doi:10.1021/acs.jmedchem.4c02924.
400. Loraine, A.; Farr, S.A.; Niehoff, M.L.; Larrea, I.G.; Ganev, Y.; Samanta, J.; Rahman, K.; Crider, A.M.; Sandoval, K.; Witt, K.A. Dual Sigma Receptor 1 and 2 Modulator Improves Memory Behavior in Mouse Model of Age-Related Cognitive Decline. *J. Pharmacol. Exp. Ther.* **2026**, *393*, 103795, doi:10.1016/j.jpet.2025.103795.
401. Basavarajappa, B.S.; Subbanna, S. Molecular Insights into Epigenetics and Cannabinoid Receptors. *Biomolecules* **2022**, *12*, 1560, doi:10.3390/biom12111560.
402. Lowe, H.; Toyang, N.; Steele, B.; Bryant, J.; Ngwa, W. The Endocannabinoid System: A Potential Target for the Treatment of Various Diseases. *Int. J. Mol. Sci.* **2021**, *22*, 9472, doi:10.3390/ijms22179472.
403. De Petrocellis, L.; Di Marzo, V. Non-CB1, Non-CB2 Receptors for Endocannabinoids, Plant Cannabinoids, and Synthetic Cannabimimetics: Focus on G-Protein-Coupled Receptors and Transient Receptor Potential Channels. *J. Neuroimmune Pharmacol.* **2010**, *5*, 103–121, doi:10.1007/s11481-009-9177-z.
404. Lu, H.-C.; Mackie, K. An Introduction to the Endogenous Cannabinoid System. *Biol. Psychiatry* **2016**, *79*, 516–525, doi:10.1016/j.biopsych.2015.07.028.
405. Cascio, M.G.; Marini, P. Biosynthesis and Fate of Endocannabinoids. In *Endocannabinoids*; Pertwee, R.G., Ed.; Handbook of Experimental Pharmacology; Springer International Publishing: Cham, 2015; Vol. 231, pp. 39–58 ISBN 978-3-319-20824-4.
406. Schurman, L.D.; Lu, D.; Kendall, D.A.; Howlett, A.C.; Lichtman, A.H. Molecular Mechanism and Cannabinoid Pharmacology. In *Substance Use Disorders*; Nader, M.A., Hurd, Y.L., Eds.; Handbook of Experimental Pharmacology; Springer International Publishing: Cham, 2019; Vol. 258, pp. 323–353 ISBN 978-3-030-33678-3.
407. Marzo, V.D.; Bifulco, M.; Petrocellis, L.D. The Endocannabinoid System and Its Therapeutic Exploitation. *Nat. Rev. Drug Discov.* **2004**, *3*, 771–784, doi:10.1038/nrd1495.
408. Howlett, A.C.; Abood, M.E. CB 1 and CB 2 Receptor Pharmacology. In *Advances in Pharmacology*; Elsevier, 2017; Vol. 80, pp. 169–206 ISBN 978-0-12-811232-8.
409. Rezende, B.; Alencar, A.K.N.; De Bem, G.F.; Fontes-Dantas, F.L.; Montes, G.C. Endocannabinoid System: Chemical Characteristics and Biological Activity. *Pharmaceuticals* **2023**, *16*, 148, doi:10.3390/ph16020148.
410. Zou, S.; Kumar, U. Cannabinoid Receptors and the Endocannabinoid System: Signaling and Function in the Central Nervous System. *Int. J. Mol. Sci.* **2018**, *19*, 833, doi:10.3390/ijms19030833.
411. Stella, N. Cannabinoid and Cannabinoid-like Receptors in Microglia, Astrocytes, and Astrocytomas. *Glia* **2010**, *58*, 1017–1030, doi:10.1002/glia.20983.
412. Cristino, L.; Bisogno, T.; Di Marzo, V. Cannabinoids and the Expanded Endocannabinoid System in Neurological Disorders. *Nat. Rev. Neurol.* **2020**, *16*, 9–29, doi:10.1038/s41582-019-0284-z.
413. Rodriguez-Arias, M.; Navarrete, F.; Daza-Losada, M.; Navarro, D.; Aguilar, M.A.; Berbel, P.; Miñarro, J.; Manzanares, J. CB1 Cannabinoid Receptor-Mediated Aggressive Behavior. *Neuropharmacology* **2013**, *75*, 172–180, doi:10.1016/j.neuropharm.2013.07.013.
414. Gado, F.; Digiacomo, M.; Macchia, M.; Bertini, S.; Manera, C. Traditional Uses of Cannabinoids and New Perspectives in the Treatment of Multiple Sclerosis. *Medicines* **2018**, *5*, 91, doi:10.3390/medicines5030091.
415. Xing, C.; Zhuang, Y.; Xu, T.-H.; Feng, Z.; Zhou, X.E.; Chen, M.; Wang, L.; Meng, X.; Xue, Y.; Wang, J.; et al. Cryo-EM Structure of the Human Cannabinoid Receptor CB2-Gi Signaling Complex. *Cell* **2020**, *180*, 645-654.e13, doi:10.1016/j.cell.2020.01.007.
416. Atwood, B.K.; Mackie, K. CB_2 : A Cannabinoid Receptor with an Identity Crisis. *Br. J. Pharmacol.* **2010**, *160*, 467–479, doi:10.1111/j.1476-5381.2010.00729.x.
417. Bie, B.; Wu, J.; Foss, J.F.; Naguib, M. An Overview of the Cannabinoid Type 2 Receptor System and Its Therapeutic Potential. *Curr. Opin. Anaesthesiol.* **2018**, *31*, 407–414, doi:10.1097/ACO.0000000000000616.
418. Skaper, S.D.; Buriani, A.; Dal Toso, R.; Petrelli, L.; Romanello, S.; Facci, L.; Leon, A. The ALIAmide Palmitoylethanolamide and Cannabinoids, but Not Anandamide, Are Protective in a Delayed Postglutamate

Paradigm of Excitotoxic Death in Cerebellar Granule Neurons. *Proc. Natl. Acad. Sci.* **1996**, *93*, 3984–3989, doi:10.1073/pnas.93.9.3984.
419. Gong, J.-P.; Onaivi, E.S.; Ishiguro, H.; Liu, Q.-R.; Tagliaferro, P.A.; Brusco, A.; Uhl, G.R. Cannabinoid CB2 Receptors: Immunohistochemical Localization in Rat Brain. *Brain Res.* **2006**, *1071*, 10–23, doi:10.1016/j.brainres.2005.11.035.
420. Brusco, A.; Tagliaferro, P.; Saez, T.; Onaivi, E.S. Postsynaptic Localization of CB2 Cannabinoid Receptors in the Rat Hippocampus. *Synapse* **2008**, *62*, 944–949, doi:10.1002/syn.20569.
421. Van Sickle, M.D.; Duncan, M.; Kingsley, P.J.; Mouihate, A.; Urbani, P.; Mackie, K.; Stella, N.; Makriyannis, A.; Piomelli, D.; Davison, J.S.; et al. Identification and Functional Characterization of Brainstem Cannabinoid CB_2 Receptors. *Science* **2005**, *310*, 329–332, doi:10.1126/science.1115740.
422. Zhang, H.-Y.; Gao, M.; Liu, Q.-R.; Bi, G.-H.; Li, X.; Yang, H.-J.; Gardner, E.L.; Wu, J.; Xi, Z.-X. Cannabinoid CB_2 Receptors Modulate Midbrain Dopamine Neuronal Activity and Dopamine-Related Behavior in Mice. *Proc. Natl. Acad. Sci.* **2014**, *111*, doi:10.1073/pnas.1413210111.
423. Zhang, H.-Y.; Bi, G.-H.; Li, X.; Li, J.; Qu, H.; Zhang, S.-J.; Li, C.-Y.; Onaivi, E.S.; Gardner, E.L.; Xi, Z.-X.; et al. Species Differences in Cannabinoid Receptor 2 and Receptor Responses to Cocaine Self-Administration in Mice and Rats. *Neuropsychopharmacology* **2015**, *40*, 1037–1051, doi:10.1038/npp.2014.297.
424. Stempel, A.V.; Stumpf, A.; Zhang, H.-Y.; Özdoğan, T.; Pannasch, U.; Theis, A.-K.; Otte, D.-M.; Wojtalla, A.; Rácz, I.; Ponomarenko, A.; et al. Cannabinoid Type 2 Receptors Mediate a Cell Type-Specific Plasticity in the Hippocampus. *Neuron* **2016**, *90*, 795–809, doi:10.1016/j.neuron.2016.03.034.
425. Zoratti, C.; Kipmen-Korgun, D.; Osibow, K.; Malli, R.; Graier, W.F. Anandamide Initiates Ca^{2+} Signaling *via* CB_2 Receptor Linked to Phospholipase C in Calf Pulmonary Endothelial Cells. *Br. J. Pharmacol.* **2003**, *140*, 1351–1362, doi:10.1038/sj.bjp.0705529.
426. Grimaldi, P.; Orlando, P.; Di Siena, S.; Lolicato, F.; Petrosino, S.; Bisogno, T.; Geremia, R.; De Petrocellis, L.; Di Marzo, V. The Endocannabinoid System and Pivotal Role of the CB_2 Receptor in Mouse Spermatogenesis. *Proc. Natl. Acad. Sci.* **2009**, *106*, 11131–11136, doi:10.1073/pnas.0812789106.
427. Maccarrone, M. CB_2 Receptors in Reproduction. *Br. J. Pharmacol.* **2008**, *153*, 189–198, doi:10.1038/sj.bjp.0707444.
428. Storr, M.; Gaffal, E.; Saur, D.; Schusdziarra, V.; Allescher, H.D. Effect of Cannabinoids on Neural Transmission in Rat Gastric Fundus. *Can. J. Physiol. Pharmacol.* **2002**, *80*, 67–76, doi:10.1139/y02-005.
429. Duncan, M.; Mouihate, A.; Mackie, K.; Keenan, C.M.; Buckley, N.E.; Davison, J.S.; Patel, K.D.; Pittman, Q.J.; Sharkey, K.A. Cannabinoid CB_2 Receptors in the Enteric Nervous System Modulate Gastrointestinal Contractility in Lipopolysaccharide-Treated Rats. *Am. J. Physiol.-Gastrointest. Liver Physiol.* **2008**, *295*, G78–G87, doi:10.1152/ajpgi.90285.2008.
430. Zhong, L.; Geng, L.; Njie, Y.; Feng, W.; Song, Z.-H. CB2 Cannabinoid Receptors in Trabecular Meshwork Cells Mediate JWH015-Induced Enhancement of Aqueous Humor Outflow Facility. *Investig. Opthalmology Vis. Sci.* **2005**, *46*, 1988, doi:10.1167/iovs.04-0651.
431. Roche, R.; Hoareau, L.; Bes-Houtmann, S.; Gonthier, M.-P.; Laborde, C.; Baron, J.-F.; Haffaf, Y.; Cesari, M.; Festy, F. Presence of the Cannabinoid Receptors, CB1 and CB2, in Human Omental and Subcutaneous Adipocytes. *Histochem. Cell Biol.* **2006**, *126*, 177–187, doi:10.1007/s00418-005-0127-4.
432. Cabral, G.A.; Griffin-Thomas, L. Emerging Role of the Cannabinoid Receptor CB_2 in Immune Regulation: Therapeutic Prospects for Neuroinflammation. *Expert Rev. Mol. Med.* **2009**, *11*, e3, doi:10.1017/S1462399409000957.
433. Turcotte, C.; Chouinard, F.; Lefebvre, J.S.; Flamand, N. Regulation of Inflammation by Cannabinoids, the Endocannabinoids 2-Arachidonoyl-Glycerol and Arachidonoyl-Ethanolamide, and Their Metabolites. *J. Leukoc. Biol.* **2015**, *97*, 1049–1070, doi:10.1189/jlb.3RU0115-021R.
434. Hanuš, L.; Breuer, A.; Tchilibon, S.; Shiloah, S.; Goldenberg, D.; Horowitz, M.; Pertwee, R.G.; Ross, R.A.; Mechoulam, R.; Fride, E. HU-308: A Specific Agonist for CB_2 , a Peripheral Cannabinoid Receptor. *Proc. Natl. Acad. Sci.* **1999**, *96*, 14228–14233, doi:10.1073/pnas.96.25.14228.
435. Consroe, P. Brain Cannabinoid Systems as Targets for the Therapy of Neurological Disorders. *Neurobiol. Dis.* **1998**, *5*, 534–551, doi:10.1006/nbdi.1998.0220.
436. Beltramo, M.; Grundy, R.I.; Rabuffetti, M. Cannabinoids and Neuroprotection. *Mol. Neurobiol.* **2001**, *24*, 029–052, doi:10.1385/MN:24:1-3:029.
437. Fernández-Ruiz, J.; Moro, M.A.; Martínez-Orgado, J. Cannabinoids in Neurodegenerative Disorders and Stroke/Brain Trauma: From Preclinical Models to Clinical Applications. *Neurotherapeutics* **2015**, *12*, 793–806, doi:10.1007/s13311-015-0381-7.
438. Basavarajappa, B.S.; Shivakumar, M.; Joshi, V.; Subbanna, S. Endocannabinoid System in Neurodegenerative Disorders. *J. Neurochem.* **2017**, *142*, 624–648, doi:10.1111/jnc.14098.
439. Chiarlone, A.; Bellocchio, L.; Blázquez, C.; Resel, E.; Soria-Gómez, E.; Cannich, A.; Ferrero, J.J.; Sagredo, O.; Benito, C.; Romero, J.; et al. A Restricted Population of CB_1 Cannabinoid Receptors with Neuroprotective Activity. *Proc. Natl. Acad. Sci.* **2014**, *111*, 8257–8262, doi:10.1073/pnas.1400988111.
440. Smith, S.R.; Terminelli, C.; Denhardt, G. Effects of Cannabinoid Receptor Agonist and Antagonist Ligands on Production of Inflammatory Cytokines and Anti-Inflammatory Interleukin-10 in Endotoxemic Mice. *J. Pharmacol. Exp. Ther.* **2000**, *293*, 136–150.
441. Chen, Y.; McCarron, R.M.; Ohara, Y.; Bembry, J.; Azzam, N.; Lenz, F.A.; Shohami, E.; Mechoulam, R.; Spatz, M. Human Brain Capillary Endothelium: 2-Arachidonoglycerol (Endocannabinoid) Interacts With Endothelin-1. *Circ. Res.* **2000**, *87*, 323–327, doi:10.1161/01.RES.87.4.323.
442. Benito, C.; Núñez, E.; Tolón, R.M.; Carrier, E.J.; Rábano, A.; Hillard, C.J.; Romero, J. Cannabinoid CB_2 Receptors and Fatty Acid Amide Hydrolase Are Selectively Overexpressed in Neuritic Plaque-Associated Glia in Alzheimer's Disease Brains. *J. Neurosci.* **2003**, *23*, 11136–11141, doi:10.1523/JNEUROSCI.23-35-11136.2003.

443. Ramírez, B.G.; Blázquez, C.; Del Pulgar, T.G.; Guzmán, M.; De Ceballos, M.L. Prevention of Alzheimer's Disease Pathology by Cannabinoids: Neuroprotection Mediated by Blockade of Microglial Activation. *J. Neurosci.* **2005**, *25*, 1904–1913, doi:10.1523/JNEUROSCI.4540-04.2005.
444. Price, D.A.; Martinez, A.A.; Seillier, A.; Koek, W.; Acosta, Y.; Fernandez, E.; Strong, R.; Lutz, B.; Marsicano, G.; Roberts, J.L.; et al. WIN55,212-2, a Cannabinoid Receptor Agonist, Protects against Nigrostriatal Cell Loss in the 1-methyl-4-phenyl-1,2,3,6-tetrahydropyridine Mouse Model of Parkinson's Disease. *Eur. J. Neurosci.* **2009**, *29*, 2177–2186, doi:10.1111/j.1460-9568.2009.06764.x.
445. Concannon, R.M.; Okine, B.N.; Finn, D.P.; Dowd, E. Differential Upregulation of the Cannabinoid CB2 Receptor in Neurotoxic and Inflammation-Driven Rat Models of Parkinson's Disease. *Exp. Neurol.* **2015**, *269*, 133–141, doi:10.1016/j.expneurol.2015.04.007.
446. Concannon, R.M.; Okine, B.N.; Finn, D.P.; Dowd, E. Upregulation of the Cannabinoid CB2 Receptor in Environmental and Viral Inflammation-Driven Rat Models of Parkinson's Disease. *Exp. Neurol.* **2016**, *283*, 204–212, doi:10.1016/j.expneurol.2016.06.014.
447. Palazuelos, J.; Aguado, T.; Pazos, M.R.; Julien, B.; Carrasco, C.; Resel, E.; Sagredo, O.; Benito, C.; Romero, J.; Azcoitia, I.; et al. Microglial CB2 Cannabinoid Receptors Are Neuroprotective in Huntington's Disease Excitotoxicity. *Brain* **2009**, *132*, 3152–3164, doi:10.1093/brain/awp239.
448. Haider, A.; Spinelli, F.; Herde, A.M.; Mu, B.; Keller, C.; Margelisch, M.; Weber, M.; Schibli, R.; Mu, L.; Ametamey, S.M. Evaluation of 4-Oxo-Quinoline-Based CB2 PET Radioligands in R6/2 Chorea Huntington Mouse Model and Human ALS Spinal Cord Tissue. *Eur. J. Med. Chem.* **2018**, *145*, 746–759, doi:10.1016/j.ejmech.2017.12.097.
449. Shoemaker, J.L.; Seely, K.A.; Reed, R.L.; Crow, J.P.; Prather, P.L. The CB2 Cannabinoid Agonist AM-1241 Prolongs Survival in a Transgenic Mouse Model of Amyotrophic Lateral Sclerosis When Initiated at Symptom Onset. *J. Neurochem.* **2007**, *101*, 87–98, doi:10.1111/j.1471-4159.2006.04346.x.
450. Moreno-Martet, M.; Espejo-Porras, F.; Fernández-Ruiz, J.; De Lago, E. Changes in Endocannabinoid Receptors and Enzymes in the Spinal Cord of SOD 1^{G93A} Transgenic Mice and Evaluation of a Sativex® -like Combination of Phytocannabinoids: Interest for Future Therapies in Amyotrophic Lateral Sclerosis. *CNS Neurosci. Ther.* **2014**, *20*, 809–815, doi:10.1111/cns.12262.
451. Gómez-Gálvez, Y.; Palomo-Garo, C.; Fernández-Ruiz, J.; García, C. Potential of the Cannabinoid CB2 Receptor as a Pharmacological Target against Inflammation in Parkinson's Disease. *Prog. Neuropsychopharmacol. Biol. Psychiatry* **2016**, *64*, 200–208, doi:10.1016/j.pnpbp.2015.03.017.
452. Yiangou, Y.; Facer, P.; Durrenberger, P.; Chessell, I.P.; Naylor, A.; Bountra, C.; Banati, R.R.; Anand, P. COX-2, CB2 and P2X7-Immunoreactivities Are Increased in Activated Microglial Cells/Macrophages of Multiple Sclerosis and Amyotrophic Lateral Sclerosis Spinal Cord. *BMC Neurol.* **2006**, *6*, 12, doi:10.1186/1471-2377-6-12.
453. Aso, E.; Ferrer, I. CB2 Cannabinoid Receptor As Potential Target against Alzheimer's Disease. *Front. Neurosci.* **2016**, *10*, doi:10.3389/fnins.2016.00243.
454. Spinelli, F.; Capparelli, E.; Abate, C.; Colabufo, N.A.; Contino, M. Perspectives of Cannabinoid Type 2 Receptor (CB2R) Ligands in Neurodegenerative Disorders: Structure–Affinity Relationship (SAfiR) and Structure–Activity Relationship (SAR) Studies: Miniperspective. *J. Med. Chem.* **2017**, *60*, 9913–9931, doi:10.1021/acs.jmedchem.7b00155.
455. Wu, J.; Bie, B.; Yang, H.; Xu, J.J.; Brown, D.L.; Naguib, M. Activation of the CB2 Receptor System Reverses Amyloid-Induced Memory Deficiency. *Neurobiol. Aging* **2013**, *34*, 791–804, doi:10.1016/j.neurobiolaging.2012.06.011.
456. Chen, R.; Zhang, J.; Fan, N.; Teng, Z.; Wu, Y.; Yang, H.; Tang, Y.; Sun, H.; Song, Y.; Chen, C. Δ9-THC-Caused Synaptic and Memory Impairments Are Mediated through COX-2 Signaling. *Cell* **2013**, *155*, 1154–1165, doi:10.1016/j.cell.2013.10.042.
457. Martín-Moreno, A.M.; Brera, B.; Spuch, C.; Carro, E.; García-García, L.; Delgado, M.; Pozo, M.A.; Innamorato, N.G.; Cuadrado, A.; De Ceballos, M.L. Prolonged Oral Cannabinoid Administration Prevents Neuroinflammation, Lowers β-Amyloid Levels and Improves Cognitive Performance in Tg APP 2576 Mice. *J. Neuroinflammation* **2012**, *9*, 8, doi:10.1186/1742-2094-9-8.
458. Concannon, R.; Finn, D.P.; Dowd, E. Cannabinoids in Parkinson's Disease. In *Cannabinoids in Neurologic and Mental Disease*; Elsevier, 2015; pp. 35–59 ISBN 978-0-12-417041-4.
459. Han, Q.-W.; Yuan, Y.-H.; Chen, N.-H. The Therapeutic Role of Cannabinoid Receptors and Its Agonists or Antagonists in Parkinson's Disease. *Prog. Neuropsychopharmacol. Biol. Psychiatry* **2020**, *96*, 109745, doi:10.1016/j.pnpbp.2019.109745.
460. Aso, E.; Juvés, S.; Maldonado, R.; Ferrer, I. CB_2 Cannabinoid Receptor Agonist Ameliorates Alzheimer-Like Phenotype in AβPP/PS1 Mice. *J. Alzheimer's Dis.* **2013**, *35*, 847–858, doi:10.3233/JAD-130137.
461. Frankel, J.P.; Hughes, A.; Lees, A.J.; Stern, G.M. Marijuana for Parkinsonian Tremor. *J. Neurol. Neurosurg. Psychiatry* **1990**, *53*, 436–436, doi:10.1136/jnnp.53.5.436.
462. García, C.; Palomo-Garo, C.; García-Arencibia, M.; Ramos, J.; Pertwee, R.; Fernández-Ruiz, J. Symptom-relieving and Neuroprotective Effects of the Phytocannabinoid Δ^9 -THCV in Animal Models of Parkinson's Disease. *Br. J. Pharmacol.* **2011**, *163*, 1495–1506, doi:10.1111/j.1476-5381.2011.01278.x.
463. Xin, Q.; Xu, F.; Taylor, D.H.; Zhao, J.; Wu, J. The Impact of Cannabinoid Type 2 Receptors (CB2Rs) in Neuroprotection against Neurological Disorders. *Acta Pharmacol. Sin.* **2020**, *41*, 1507–1518, doi:10.1038/s41401-020-00530-2.
464. Bouchard, J.; Truong, J.; Bouchard, K.; Dunkelberger, D.; Desrayaud, S.; Moussaoui, S.; Tabrizi, S.J.; Stella, N.; Muchowski, P.J. Cannabinoid Receptor 2 Signaling in Peripheral Immune Cells Modulates Disease Onset and Severity in Mouse Models of Huntington's Disease. *J. Neurosci.* **2012**, *32*, 18259–18268, doi:10.1523/JNEUROSCI.4008-12.2012.

465. Fu, W.; Taylor, B.K. Activation of Cannabinoid CB2 Receptors Reduces Hyperalgesia in an Experimental Autoimmune Encephalomyelitis Mouse Model of Multiple Sclerosis. *Neurosci. Lett.* **2015**, *595*, 1–6, doi:10.1016/j.neulet.2015.04.002.
466. Munson, A.E.; Harris, L.S.; Friedman, M.A.; Dewey, W.L.; Carchman, R.A. Antineoplastic Activity of Cannabinoids2. *JNCI J. Natl. Cancer Inst.* **1975**, *55*, 597–602, doi:10.1093/jnci/55.3.597.
467. Hermanson, D.J.; Marnett, L.J. Cannabinoids, Endocannabinoids, and Cancer. *Cancer Metastasis Rev.* **2011**, *30*, 599–612, doi:10.1007/s10555-011-9318-8.
468. Chakravarti, B.; Ravi, J.; Ganju, R.K. Cannabinoids as Therapeutic Agents in Cancer: Current Status and Future Implications. *Oncotarget* **2014**, *5*, 5852–5872, doi:10.18632/oncotarget.2233.
469. Caffarel, M.M.; Andradas, C.; Mira, E.; Pérez-Gómez, E.; Cerutti, C.; Moreno-Bueno, G.; Flores, J.M.; García-Real, I.; Palacios, J.; Mañes, S.; et al. Cannabinoids Reduce ErbB2-Driven Breast Cancer Progression through Akt Inhibition. *Mol. Cancer* **2010**, *9*, 196, doi:10.1186/1476-4598-9-196.
470. Olea-Herrero, N.; Vara, D.; Malagarie-Cazenave, S.; Díaz-Laviada, I. The Cannabinoid R(+)Methanandamide Induces IL-6 Secretion by Prostate Cancer PC3 Cells. *J. Immunotoxicol.* **2009**, *6*, 249–256, doi:10.3109/15476910903241696.
471. Qamri, Z.; Preet, A.; Nasser, M.W.; Bass, C.E.; Leone, G.; Barsky, S.H.; Ganju, R.K. Synthetic Cannabinoid Receptor Agonists Inhibit Tumor Growth and Metastasis of Breast Cancer. *Mol. Cancer Ther.* **2009**, *8*, 3117–3129, doi:10.1158/1535-7163.MCT-09-0448.
472. Sánchez, C.; de Ceballos, M.L.; Gomez del Pulgar, T.; Rueda, D.; Corbacho, C.; Velasco, G.; Galve-Roperh, I.; Huffman, J.W.; Ramón y Cajal, S.; Guzmán, M. Inhibition of Glioma Growth in Vivo by Selective Activation of the CB(2) Cannabinoid Receptor. *Cancer Res.* **2001**, *61*, 5784–5789.
473. Casanova, M.L.; Blázquez, C.; Martínez-Palacio, J.; Villanueva, C.; Fernández-Aceñero, M.J.; Huffman, J.W.; Jorcano, J.L.; Guzmán, M. Inhibition of Skin Tumor Growth and Angiogenesis in Vivo by Activation of Cannabinoid Receptors. *J. Clin. Invest.* **2003**, *111*, 43–50, doi:10.1172/JCI200316116.
474. Gómez Del Pulgar, T.; Velasco, G.; Guzmán, M. The CB1 Cannabinoid Receptor Is Coupled to the Activation of Protein Kinase B/Akt. *Biochem. J.* **2000**, *347*, 369–373, doi:10.1042/bj3470369.
475. Velasco, G.; Hernández-Tiedra, S.; Dávila, D.; Lorente, M. The Use of Cannabinoids as Anticancer Agents. *Prog. Neuropsychopharmacol. Biol. Psychiatry* **2016**, *64*, 259–266, doi:10.1016/j.pnpbp.2015.05.010.
476. Twelves, C.; Short, S.; Wright, S.; Cannabinoid in Recurrent Glioma Study Group A Two-Part Safety and Exploratory Efficacy Randomized Double-Blind, Placebo-Controlled Study of a 1:1 Ratio of the Cannabinoids Cannabidiol and Delta-9-Tetrahydrocannabinol (CBD:THC) plus Dose-Intense Temozolomide in Patients with Recurrent Glioblastoma Multiforme (GBM). *J. Clin. Oncol.* **2017**, *35*, 2046–2046, doi:10.1200/JCO.2017.35.15_suppl.2046.
477. Guzmán, M.; Duarte, M.J.; Blázquez, C.; Ravina, J.; Rosa, M.C.; Galve-Roperh, I.; Sánchez, C.; Velasco, G.; González-Feria, L. A Pilot Clinical Study of Δ9-Tetrahydrocannabinol in Patients with Recurrent Glioblastoma Multiforme. *Br. J. Cancer* **2006**, *95*, 197–203, doi:10.1038/sj.bjc.6603236.
478. Hou, L.; Rong, J.; Haider, A.; Ogasawara, D.; Varlow, C.; Schafroth, M.A.; Mu, L.; Gan, J.; Xu, H.; Fowler, C.J.; et al. Positron Emission Tomography Imaging of the Endocannabinoid System: Opportunities and Challenges in Radiotracer Development. *J. Med. Chem.* **2021**, *64*, 123–149, doi:10.1021/acs.jmedchem.0c01459.
479. Ni, R.; Mu, L.; Ametamey, S. Positron Emission Tomography of Type 2 Cannabinoid Receptors for Detecting Inflammation in the Central Nervous System. *Acta Pharmacol. Sin.* **2019**, *40*, 351–357, doi:10.1038/s41401-018-0035-5.
480. Basagni, F.; Rosini, M.; Decker, M. Functionalized Cannabinoid Subtype 2 Receptor Ligands: Fluorescent, PET, Photochromic and Covalent Molecular Probes. *ChemMedChem* **2020**, *15*, 1374–1389, doi:10.1002/cmdc.202000298.
481. Evens, N.; Muccioli, G.G.; Houbrechts, N.; Lambert, D.M.; Verbruggen, A.M.; Van Laere, K.; Bormans, G.M. Synthesis and Biological Evaluation of Carbon-11- and Fluorine-18-Labeled 2-Oxoquinoline Derivatives for Type 2 Cannabinoid Receptor Positron Emission Tomography Imaging. *Nucl. Med. Biol.* **2009**, *36*, 455–465, doi:10.1016/j.nucmedbio.2009.01.009.
482. Evens, N.; Vandeputte, C.; Coolen, C.; Janssen, P.; Sciot, R.; Baekelandt, V.; Verbruggen, A.M.; Debyser, Z.; Van Laere, K.; Bormans, G.M. Preclinical Evaluation of [11C]NE40, a Type 2 Cannabinoid Receptor PET Tracer. *Nucl. Med. Biol.* **2012**, *39*, 389–399, doi:10.1016/j.nucmedbio.2011.09.005.
483. Ahmad, R.; Koole, M.; Evens, N.; Serdons, K.; Verbruggen, A.; Bormans, G.; Van Laere, K. Whole-Body Biodistribution and Radiation Dosimetry of the Cannabinoid Type 2 Receptor Ligand [11C]-NE40 in Healthy Subjects. *Mol. Imaging Biol.* **2013**, *15*, 384–390, doi:10.1007/s11307-013-0626-y.
484. Ahmad, R.; Postnov, A.; Bormans, G.; Versijpt, J.; Vandenbulcke, M.; Van Laere, K. Decreased in Vivo Availability of the Cannabinoid Type 2 Receptor in Alzheimer's Disease. *Eur. J. Nucl. Med. Mol. Imaging* **2016**, *43*, 2219–2227, doi:10.1007/s00259-016-3457-7.
485. Mu, L.; Slavik, R.; Müller, A.; Popaj, K.; Čermak, S.; Weber, M.; Schibli, R.; Krämer, S.; Ametamey, S. Synthesis and Preliminary Evaluation of a 2-Oxoquinoline Carboxylic Acid Derivative for PET Imaging the Cannabinoid Type 2 Receptor. *Pharmaceuticals* **2014**, *7*, 339–352, doi:10.3390/ph7030339.
486. Mu, L.; Bieri, D.; Slavik, R.; Drandarov, K.; Müller, A.; Čermak, S.; Weber, M.; Schibli, R.; Krämer, S.D.; Ametamey, S.M. Radiolabeling and *in Vitro* / *in Vivo* Evaluation of N-(1-adamantyl)-8-methoxy-4-oxo-1-phenyl-1,4-dihydroquinoline-3-carboxamide as a PET Probe for Imaging Cannabinoid Type 2 Receptor. *J. Neurochem.* **2013**, *126*, 616–624, doi:10.1111/jnc.12354.
487. Slavik, R.; Herde, A.M.; Bieri, D.; Weber, M.; Schibli, R.; Krämer, S.D.; Ametamey, S.M.; Mu, L. Synthesis, Radiolabeling and Evaluation of Novel 4-Oxo-Quinoline Derivatives as PET Tracers for Imaging Cannabinoid Type 2 Receptor. *Eur. J. Med. Chem.* **2015**, *92*, 554–564, doi:10.1016/j.ejmech.2015.01.028.

488. Slavik, R.; Müller Herde, A.; Haider, A.; Krämer, S.D.; Weber, M.; Schibli, R.; Ametamey, S.M.; Mu, L. Discovery of a Fluorinated 4-oxo-quinoline Derivative as a Potential Positron Emission Tomography Radiotracer for Imaging Cannabinoid Receptor Type 2. *J. Neurochem.* **2016**, *138*, 874–886, doi:10.1111/jnc.13716.
489. Teodoro, R.; Gündel, D.; Deuther-Conrad, W.; Ueberham, L.; Toussaint, M.; Bormans, G.; Brust, P.; Moldovan, R.-P. Development of [18F]LU14 for PET Imaging of Cannabinoid Receptor Type 2 in the Brain. *Int. J. Mol. Sci.* **2021**, *22*, 8051, doi:10.3390/ijms22158051.
490. Gündel, D.; Deuther-Conrad, W.; Ueberham, L.; Kaur, S.; Otikova, E.; Teodoro, R.; Toussaint, M.; Lai, T.H.; Clauß, O.; Scheunemann, M.; et al. Structure-Based Design, Optimization, and Development of [^{18} F]LU13: A Novel Radioligand for Cannabinoid Receptor Type 2 Imaging in the Brain with PET. *J. Med. Chem.* **2022**, *65*, 9034–9049, doi:10.1021/acs.jmedchem.2c00256.
491. Slavik, R.; Grether, U.; Müller Herde, A.; Gobbi, L.; Fingerle, J.; Ullmer, C.; Krämer, S.D.; Schibli, R.; Mu, L.; Ametamey, S.M. Discovery of a High Affinity and Selective Pyridine Analog as a Potential Positron Emission Tomography Imaging Agent for Cannabinoid Type 2 Receptor. *J. Med. Chem.* **2015**, *58*, 4266–4277, doi:10.1021/acs.jmedchem.5b00283.
492. Haider, A.; Kretz, J.; Gobbi, L.; Ahmed, H.; Atz, K.; Bürkler, M.; Bartelmus, C.; Fingerle, J.; Guba, W.; Ullmer, C.; et al. Structure–Activity Relationship Studies of Pyridine-Based Ligands and Identification of a Fluorinated Derivative for Positron Emission Tomography Imaging of Cannabinoid Type 2 Receptors. *J. Med. Chem.* **2019**, *62*, 11165–11181, doi:10.1021/acs.jmedchem.9b01280.
493. Ni, R.; Müller Herde, A.; Haider, A.; Keller, C.; Louloudis, G.; Vaas, M.; Schibli, R.; Ametamey, S.M.; Klohs, J.; Mu, L. In Vivo Imaging of Cannabinoid Type 2 Receptors: Functional and Structural Alterations in Mouse Model of Cerebral Ischemia by PET and MRI. *Mol. Imaging Biol.* **2022**, *24*, 700–709, doi:10.1007/s11307-021-01655-4.
494. Vandeputte, C.; Evens, N.; Toelen, J.; Deroose, C.M.; Bosier, B.; Ibrahimi, A.; Van Der Perren, A.; Gijsbers, R.; Janssen, P.; Lambert, D.M.; et al. A PET Brain Reporter Gene System Based on Type 2 Cannabinoid Receptors. *J. Nucl. Med.* **2011**, *52*, 1102–1109, doi:10.2967/jnumed.110.084426.
495. Modemann, D.J.; Mahardhika, A.B.; Yamoune, S.; Kreyenschmidt, A.-K.; Maaß, F.; Kremers, S.; Breunig, C.; Sahlmann, C.-O.; Bucerius, J.; Stalke, D.; et al. Development of High-Affinity Fluorinated Ligands for Cannabinoid Subtype 2 Receptor, and in Vitro Evaluation of a Radioactive Tracer for Imaging. *Eur. J. Med. Chem.* **2022**, *232*, 114138, doi:10.1016/j.ejmech.2022.114138.
496. Teodoro, R.; Gündel, D.; Deuther-Conrad, W.; Kazimir, A.; Toussaint, M.; Wenzel, B.; Bormans, G.; Hey-Hawkins, E.; Kopka, K.; Brust, P.; et al. Synthesis, Structure–Activity Relationships, Radiofluorination, and Biological Evaluation of [^{18} F]RM365, a Novel Radioligand for Imaging the Human Cannabinoid Receptor Type 2 (CB2R) in the Brain with PET. *J. Med. Chem.* **2023**, *66*, 13991–14010, doi:10.1021/acs.jmedchem.3c01035.
497. Horti, A.G.; Gao, Y.; Ravert, H.T.; Finley, P.; Valentine, H.; Wong, D.F.; Endres, C.J.; Savonenko, A.V.; Dannals, R.F. Synthesis and Biodistribution of [11C]A-836339, a New Potential Radioligand for PET Imaging of Cannabinoid Type 2 Receptors (CB2). *Bioorg. Med. Chem.* **2010**, *18*, 5202–5207, doi:10.1016/j.bmc.2010.05.058.
498. Savonenko, A.V.; Melnikova, T.; Wang, Y.; Ravert, H.; Gao, Y.; Koppel, J.; Lee, D.; Pletnikova, O.; Cho, E.; Sayyida, N.; et al. Cannabinoid CB2 Receptors in a Mouse Model of Aβ Amyloidosis: Immunohistochemical Analysis and Suitability as a PET Biomarker of Neuroinflammation. *PLOS ONE* **2015**, *10*, e0129618, doi:10.1371/journal.pone.0129618.
499. Pottier, G.; Gómez-Vallejo, V.; Padro, D.; Boisgard, R.; Dollé, F.; Llop, J.; Winkeler, A.; Martín, A. PET Imaging of Cannabinoid Type 2 Receptors with [^{11} C]A-836339 Did Not Evidence Changes Following Neuroinflammation in Rats. *J. Cereb. Blood Flow Metab.* **2017**, *37*, 1163–1178, doi:10.1177/0271678X16685105.
500. Moldovan, R.-P.; Teodoro, R.; Gao, Y.; Deuther-Conrad, W.; Kranz, M.; Wang, Y.; Kuwabara, H.; Nakano, M.; Valentine, H.; Fischer, S.; et al. Development of a High-Affinity PET Radioligand for Imaging Cannabinoid Subtype 2 Receptor. *J. Med. Chem.* **2016**, *59*, 7840–7855, doi:10.1021/acs.jmedchem.6b00554.
501. Gündel, D.; Maqbool, M.; Teodoro, R.; Ludwig, F.-A.; Heerklotz, A.; Toussaint, M.; Deuther-Conrad, W.; Bormans, G.; Brust, P.; Kopka, K.; et al. Development and Evaluation of Deuterated [18F]JHU94620 Isotopologues for the Non-Invasive Assessment of the Cannabinoid Type 2 Receptor in Brain. *EJNMMI Radiopharm. Chem.* **2024**, *9*, 91, doi:10.1186/s41181-024-00319-2.
502. Caillé, F.; Cacheux, F.; Peyronneau, M.-A.; Jego, B.; Jaumain, E.; Pottier, G.; Ullmer, C.; Grether, U.; Winkeler, A.; Dollé, F.; et al. From Structure–Activity Relationships on Thiazole Derivatives to the *In Vivo* Evaluation of a New Radiotracer for Cannabinoid Subtype 2 PET Imaging. *Mol. Pharm.* **2017**, *14*, 4064–4078, doi:10.1021/acs.molpharmaceut.7b00746.
503. Auvity, S.; Attili, B.; Caillé, F.; Goislard, M.; Cayla, J.; Hinnen, F.; Demphel, S.; Brulon, V.; Bottlaender, M.; Leroy, C.; et al. Translational Preclinical PET Imaging and Metabolic Evaluation of a New Cannabinoid 2 Receptor (CB_2 R) Radioligand, (*Z*)- *N* -(3-(2-(2-[^{18} F]Fluoroethoxy)Ethyl)-4,5-Dimethylthiazol-2(3 *H*)-Ylidene)-2,2,3,3-Tetramethylcyclopropane-1-Carboxamide. *ACS Pharmacol. Transl. Sci.* **2024**, *7*, 3144–3154, doi:10.1021/acsptsci.4c00348.
504. Ueberham, L.; Gündel, D.; Kellert, M.; Deuther-Conrad, W.; Ludwig, F.-A.; Lönnecke, P.; Kazimir, A.; Kopka, K.; Brust, P.; Moldovan, R.-P.; et al. Development of the High-Affinity Carborane-Based Cannabinoid Receptor Type 2 PET Ligand [^{18} F]LUZ5- d_8. *J. Med. Chem.* **2023**, *66*, 5242–5260, doi:10.1021/acs.jmedchem.3c00195.
505. Haider, A.; Müller Herde, A.; Slavik, R.; Weber, M.; Mugnaini, C.; Ligresti, A.; Schibli, R.; Mu, L.; Mensah Ametamey, S. Synthesis and Biological Evaluation of Thiophene-Based Cannabinoid Receptor Type 2 Radiotracers for PET Imaging. *Front. Neurosci.* **2016**, *10*, 350, doi:10.3389/fnins.2016.00350.
506. Teodoro, R.; Moldovan, R.-P.; Lueg, C.; Günther, R.; Donat, C.K.; Ludwig, F.-A.; Fischer, S.; Deuther-Conrad, W.; Wünsch, B.; Brust, P. Radiofluorination and Biological Evaluation of N-Aryl-Oxadiazolyl-Propionamides as

Potential Radioligands for PET Imaging of Cannabinoid CB2 Receptors. *Org. Med. Chem. Lett.* **2013**, *3*, 11, doi:10.1186/2191-2858-3-11.
507. Ahamed, M.; Van Veghel, D.; Ullmer, C.; Van Laere, K.; Verbruggen, A.; Bormans, G.M. Synthesis, Biodistribution and In Vitro Evaluation of Brain Permeable High Affinity Type 2 Cannabinoid Receptor Agonists [11C]MA2 and [18F]MA3. *Front. Neurosci.* **2016**, *10*, doi:10.3389/fnins.2016.00431.
508. Attili, B.; Celen, S.; Ahamed, M.; Koole, M.; Haute, C.V.D.; Vanduffel, W.; Bormans, G. Preclinical Evaluation of [^{18} F]MA3: A CB_2 Receptor Agonist Radiotracer for PET. *Br. J. Pharmacol.* **2019**, *176*, 1481–1491, doi:10.1111/bph.14564.
509. Solas, M.; Francis, P.T.; Franco, R.; Ramirez, M.J. CB2 Receptor and Amyloid Pathology in Frontal Cortex of Alzheimer's Disease Patients. *Neurobiol. Aging* **2013**, *34*, 805–808, doi:10.1016/j.neurobiolaging.2012.06.005.
510. Intranuovo, F.; Brunetti, L.; DelRe, P.; Mangiatordi, G.F.; Stefanachi, A.; Laghezza, A.; Niso, M.; Leonetti, F.; Loiodice, F.; Ligresti, A.; et al. Development of *N* -(1-Adamantyl)Benzamides as Novel Anti-Inflammatory Multitarget Agents Acting as Dual Modulators of the Cannabinoid CB2 Receptor and Fatty Acid Amide Hydrolase. *J. Med. Chem.* **2023**, *66*, 235–250, doi:10.1021/acs.jmedchem.2c01084.
511. Lucchesi, V.; Parkkari, T.; Savinainen, J.R.; Malfitano, A.M.; Allarà, M.; Bertini, S.; Castelli, F.; Del Carlo, S.; Laezza, C.; Ligresti, A.; et al. 1,2-Dihydro-2-Oxopyridine-3-Carboxamides: The C-5 Substituent Is Responsible for Functionality Switch at CB2 Cannabinoid Receptor. *Eur. J. Med. Chem.* **2014**, *74*, 524–532, doi:10.1016/j.ejmech.2013.10.070.
512. Schirizzi, A.; Renna, N.; De Leonardis, G.; Montanaro, R.; Mastropasqua, F.; Graziano, G.; Riganti, C.; Pisano, I.; Laghezza, A.; Abate, C.; et al. CC48 a New CB2R Agonist/FAAH Inhibitor Dual Drug Blocks Gastric Cancer Progression and Overcomes Paclitaxel Resistance. *J. Exp. Clin. Cancer Res.* **2025**, *44*, 209, doi:10.1186/s13046-025-03476-7.
513. Graziano, G; Crouzier, L.; Mastropasqua, F.; van Horst, C.; Meunier, J.; Delprat, B.; Perrone M.G.; Mammone M.; Brera J.; Loza M.I.; et al. Dual-Targeting CB2R Agonists and FAAH Inhibitors as A Promising Strategy Against Alzheimer's Disease (Manuscript Submitted to Biological Research) 2026.
514. Graziano, G.; Delre, P.; Carofiglio, F.; Brea, J.; Ligresti, A.; Kostrzewa, M.; Riganti, C.; Gioè-Gallo, C.; Majellaro, M.; Nicolotti, O.; et al. N-Adamantyl-Anthranil Amide Derivatives: New Selective Ligands for the Cannabinoid Receptor Subtype 2 (CB2R). *Eur. J. Med. Chem.* **2023**, *248*, 115109, doi:10.1016/j.ejmech.2023.115109.
515. Graziano, G; Mastropasqua, F.; Fanizzi A.; Papadopoulos M.G.E.; Laghezza A.; Mammone M.; Mangiatordi G.F.; Esposito D.; Brera J.; Loza M.I.; et al. Design and Development of New Dual Target Agents, Cannabinoid Subtype 2 Receptor (CB2R) Agonists and Fatty Acid Amide Hydrolase (FAAH) Inhibitors Against Neurodegeneration (Manuscript Submitted to Journal of Medicinal Chemistry) 2026.
516. Li, X.; Chang, H.; Bouma, J.; De Paus, L.V.; Mukhopadhyay, P.; Paloczi, J.; Mustafa, M.; Van Der Horst, C.; Kumar, S.S.; Wu, L.; et al. Structural Basis of Selective Cannabinoid CB2 Receptor Activation. *Nat. Commun.* **2023**, *14*, 1447, doi:10.1038/s41467-023-37112-9.
517. Bouma, J.; De Koning, E.J.M.; Van Der Horst, C.; Kumar, S.S.; Van Den Berg, B.J.W.; Hoare, S.R.J.; Wittwer, M.B.; Guba, W.; Rufer, A.C.; Grether, U.; et al. Kinetic Multiplex Assay to Assess Biased Signaling of Clinical GPCR Agonists. *Pharmacol. Res.* **2025**, *222*, 108021, doi:10.1016/j.phrs.2025.108021.
518. Rinaldi-Carmona, M.; Barth, F.; Millan, J.; Derocq, J.-M.; Casellas, P.; Congy, C.; Oustric, D.; Sarran, M.; Bouaboula, M.; Calandra, B.; et al. SR 144528, the First Potent and Selective Antagonist of the CB2 Cannabinoid Receptor. *J. Pharmacol. Exp. Ther.* **1998**, *284*, 644–650, doi:10.1016/S0022-3565(24)37266-0.
519. Rinaldi-Carmona, M.; Barth, F.; Héaulme, M.; Shire, D.; Calandra, B.; Congy, C.; Martinez, S.; Maruani, J.; Néliat, G.; Caput, D.; et al. SR141716A, a Potent and Selective Antagonist of the Brain Cannabinoid Receptor. *FEBS Lett.* **1994**, *350*, 240–244, doi:10.1016/0014-5793(94)00773-X.
520. Martella, A.; Sijben, H.; Rufer, A.C.; Grether, U.; Fingerle, J.; Ullmer, C.; Hartung, T.; IJzerman, A.P.; Van Der Stelt, M.; Heitman, L.H. A Novel Selective Inverse Agonist of the CB2 Receptor as a Radiolabeled Tool Compound for Kinetic Binding Studies. *Mol. Pharmacol.* **2017**, *92*, 389–400, doi:10.1124/mol.117.108605.
521. Darden, T.; York, D.; Pedersen, L. Particle Mesh Ewald: An $N \cdot \log(N)$ Method for Ewald Sums in Large Systems. *J. Chem. Phys.* **1993**, *98*, 10089–10092, doi:10.1063/1.464397.
522. Cannaert, A.; Franz, F.; Auwärter, V.; Stove, C.P. Activity-Based Detection of Consumption of Synthetic Cannabinoids in Authentic Urine Samples Using a Stable Cannabinoid Reporter System. *Anal. Chem.* **2017**, *89*, 9527–9536, doi:10.1021/acs.analchem.7b02552.
523. Li, X.; Hua, T.; Vemuri, K.; Ho, J.-H.; Wu, Y.; Wu, L.; Popov, P.; Benchama, O.; Zvonok, N.; Locke, K.; et al. Crystal Structure of the Human Cannabinoid Receptor CB2. *Cell* **2019**, *176*, 459-467.e13, doi:10.1016/j.cell.2018.12.011.
524. Lu, C.; Wu, C.; Ghoreishi, D.; Chen, W.; Wang, L.; Damm, W.; Ross, G.A.; Dahlgren, M.K.; Russell, E.; Von Bargen, C.D.; et al. OPLS4: Improving Force Field Accuracy on Challenging Regimes of Chemical Space. *J. Chem. Theory Comput.* **2021**, *17*, 4291–4300, doi:10.1021/acs.jctc.1c00302.
525. Halgren, T.A.; Murphy, R.B.; Friesner, R.A.; Beard, H.S.; Frye, L.L.; Pollard, W.T.; Banks, J.L. Glide: A New Approach for Rapid, Accurate Docking and Scoring. 2. Enrichment Factors in Database Screening. *J. Med. Chem.* **2004**, *47*, 1750–1759, doi:10.1021/jm030644s.

List of abbreviations

Positron emission tomography (PET); Central nervous system (CNS); P-glycoprotein (P-gp); Sigma-1 (S1R); Sigma-2 (S2R); Endocannabinoid receptor subtype 2 (CB2R); Structure–affinity relationship (SAfiR).

Helmholtz-Zentrum Dresden-Rossendorf (HZDR); NEXTGENERATIONEU (NGEU); Ministry of University and Research (MUR); National Recovery and Resilience Plan (NRRP); *A Multiscale Integrated Approach to the Study of the Nervous System in Health and Disease* (MNESYS); National Research Council (CNR); European Cooperation in Science and Technology (COST); Short-Term Scientific Mission (STSM).

Alzheimer's disease (AD); Parkinson's disease (PD); Peripheral nervous system (PNS); Neurodegenerative diseases (NDs); amyotrophic lateral sclerosis (ALS); Huntington's disease (HD); Multiple sclerosis (MS); Toll-like receptors (TLRs); NOD-like receptors (NLRs); Polymorphonuclear neutrophils (PMNs); Reactive oxygen species (ROS); Reactive nitrogen species (RNS); Specialized Pro-Resolving Mediators (SPMs); Interleukin (IL); Tumor necrosis factor (TNF); Nitric oxide (NO); Lipopolysaccharides (LPS); Blood–brain barrier (BBB); World Health Organization (WHO); β-amyloid (Aβ); Amyloid precursor protein (APP); Beta-secretase (BACE-1); Neurofibrillary tangles (NFTs); Paired helical filaments (PHFs); Computed tomography (CT); Magnetic resonance imaging (MRI); Substantia nigra (SN); Disseminated in space (DIS); Disseminated in time (DIT); Clinically isolated syndrome (CIS); positron (β^+), Electron neutrino (ν_e); Carbon-11 (^{11}C); Fluorine-18 (^{18}F); Gallium-68 (^{68}Ga); Nitrogen-13 (^{13}N); Oxigen-15 (^{15}O); Iodine-124 (^{124}I); Molar activity (A_m); Radiochemical yield (RCY); Nucleophilic substitution (SN); Aromatic nucleophilic substitution (SN_{Ar}); Phase-transfer catalyst (PTC); Kryptofix2.2.2 ($K_{2.2.2.}$); Tetraethylammonium bicarbonate (TEAF); Tetrabutylammonium bicarbonate (TBAF); Acetonitrile (CH_3CN); Dimethyl sulfoxide (DMSO); Dimethylformamide (DMF); Trifluoromethanesulfonate (triflate); 1-nitrobenzenesulfonate (nosylate); Methanesulfonate (mesylate); 4-methylbenzenesulfonate (tosylate); Electron-withdrawing groups (EWGs); Palladium (Pd); Nickel (Ni); Copper (Cu); Copper-mediated radiofluorination (CMRF); Topological polar surface area (TPSA).

ATP-binding cassette transporter (ABC); Chronic obstructive pulmonary disease (COPD); Surface of syncytiotrophoblasts (STBs); Cyclosporin A (CsA); Transmembrane domains (TMDs); Nucleotide-binding cytosolic regions (NBD); Protein kinase C (PKC); Drug-binding domains (DBSs); Main binding cavity (MBC); Other binding sites (OBSs); Multidrug resistance (MDR); Intracellular coupling helices (CHs); human amyloid precursor protein (hAPP); Major depressive disorder (MDD); Single nucleotide polymorphisms (SNPs); Serotonin–norepinephrine reuptake inhibitors (SNRIs); Area under the $curve_{cereb}$ (AUC_{cereb}); [^{11}C]-*N*-desmethyl-loperamide ([^{11}C]dLop); Tariquidar (TQ); Brain influx rate constant (K1); Extraction fraction (E); Antiepileptic drugs (AEDs); non-human primates (NHPs); Basal ganglia (BG); St. John's Wort extract (SJW); Interindividual variability (CV); Thin layer chromatography (TLC); Melting points (mp); singlet (s); doublet (d); triplet (t); quartet (q); quintet (quint); multiplet (m); doublet of doublets (dd); triplet of doublets (td); broad signal (br); coupling constant (*J*); Dichloromethane (CH_2Cl_2); Gas Chromatography–Mass Spectrometry (GC-MS); Nuclear Magnetic Resonance (NMR); Ethanol (EtOH); Ethyl acetate (AcOEt); Tetrahydrofuran (THF); Basic Moiety (BM); Methanol (MeOH); Ethyl ether (Et_2O);

Room Temperature (RT); Overnight (ON); High-Resolution Mass Spectrometry- Electrospray Ionization (HRMS-ESI); Good Laboratory Practice (GLP); Structure–activity relationship (SAR);
Sigma receptors (SRs); Sigma-1 receptor (S1R); Sigma-2 receptor (S2R); Endoplasmic reticulum (ER); Mitochondria-associated membranes (MAM); Sterol-binding domain-like (SBDL); Binding Immunoglobulin Protein (BiP); inositol 1,4,5-trisphosphate receptor (IP_3R); store-operated calcium entry (SOCE); inositol-requiring enzyme 1 (IRE1); B-cell lymphoma 2 (Bcl-2); Nuclear factor erythroid 2–related factor 2 (Nrf2); Severe acute respiratory syndrome coronavirus 2 (SARS-CoV-2); Knockout (KO); Knockdown (KD); Protein–protein interactions (PPIs); Fluorescence resonance energy transfer (FRET); Bioluminescence resonance energy transfer (BRET); Standardized Uptake Value (SUV) ; Wild-type (WT); Autoradiography (ARG); Senescence-accelerated prone (SAMP8); Post-injection (p.i.); Total distribution volume (V_t); Distribution volume ratio (DVR); Binding potential (BP_{ND}); International Conference on Harmonization (ICH); Effective Dose (ED); Food and Drug Administration (FDA); Radioactive Drug Research Committee (RDRC); regional cerebral blood flow (rCBF); Metabolic-associated fatty liver disease (MAFLD); 1,1′-carbonyldiimidazole (CDI); Borane–methyl sulfide complex (BMS); 1-ethyl-3-(3-dimethylaminopropyl)carbodiimide (EDC); Inhibition constants (K_i); Selectivity (SI); permeability coefficients (P_{app}); Tosyl chloride (TsCl); High Performance Liquid Chromatography (HPLC); Ammonium acetate (NH_4OAc); reversed-phase (RP); Phosphate-buffered saline (PBS); Dissociation constant (K_D); Maximal binding capacity (B_{max}); Mouse liver microsomes (MLM); Nicotinamide adenine dinucleotide phosphate (NADPH); TransEpithelial Electrical Resistance (TEER); Radio thin layer chromatography (radio-TLC).
Progesterone receptor membrane component 1 (PGRMC1); Sarcoplasmic/endoplasmic reticulum calcium ATPase (SERCA); Low-density lipoprotein receptor (LDLR); Single Photon Emission Computed Tomography (SPECT); *N*-methyl-*N*-nitrosourea (MNU); Time–activity curves (TACs); [^{18}F]fluoroethyltosylate ([^{18}F]FETos); Psychoactive Drug Screening Program (PDSP); Tetrabutylammonium bromide (TBABr); Human neuroblastoma cells (SH-SY5Y); human embryonic kidney cells (HEK293); Human osteosarcoma cells (U2OS); human pancreatic ductal adenocarcinoma cells (PANC-1); Multi-Target Directed Agents (MTDA).
Endocannabinoid system (ECS); Transient receptor potential (TRP); Peroxisome proliferator-activated receptors (PPARs); Anandamide (AEA); 2-arachidonoyl glycerol (2-AG); Transient Receptor Potential Vanilloid 1 (TRPV1); G protein-coupled receptor 55 (GPR55); 2-arachidonylglyceryl ether (2-AGE); *N*-arachidonoyl dopamine (NADA); *O*-arachidonoyl ethanolamine (*O*-AEA); G protein–coupled receptors (GPCRs); Second extracellular loop (ECL2); Cyclic adenosine monophosphate (cAMP); Protein kinase A (PKA); Mitogen-activated protein kinases (MAPKs); Mitochondrial CB1Rs (mtCB1Rs); c-Jun *N*-terminal kinase (JNK); Brain-derived neurotrophic factor (BDNF); Δ^9-tetrahydrocannabinol (Δ^9-THC); Levodopa-induced dyskinesias (LID); Fatty acid amide hydrolase (FAAH); Extracellular signal-regulated kinase (ERK); Time-activity curves (CT scans); Multi-target directed ligand (MTDL); Principal component analysis (PCA); *O*-benzotriazol-1-yl-*N*,*N*,*N*′,*N*′-tetramethyluronium hexafluorophosphate (HBTU); diisopropylethylamine (DIPEA); Microwave (MW); Radiochemical conversions (RCC); Half-life ($t_{1/2}$); Standard precision (SP); Protein data bank (PDB); Chinese Hamster Ovary (CHO); fetal calf serum (FCS).

List of publications

- **Mastropasqua, F.**, Lisi, A. T., Crouzier, L., Musillo, G. R., Abatematteo, F. S., Niso, M., ... Laghezza, A.* & Abate, C.* (**2026**). Development of Second-Generation Phenoxyethylpiperidines as Potent Sigma-1 Receptor Agonists with Neuroprotective Potential for Alzheimer's Disease. *Journal of Medicinal Chemistry*.
- **Mastropasqua, F.***, Ludwig, F. A.*, & Abate, C. (**2025**). A Full-Spectrum Evaluation of Sigma-1 Receptor (S1R) Positron Emission Tomography (PET) Radioligands from Binding Affinity to Clinical Imaging. *Molecules*, *30*(21), 4296.
- **Mastropasqua, F.***, Luurtsema, G., Filosa, C.*, & Colabufo, N. A. (**2025**). Designing a Small Molecule for PET Radiotracing: [^{18}F]MC225 in Human Trials for Early Diagnosis in CNS Pathologies. *Molecules*, *30*(18), 3696.
- Schirizzi, A., Renna, N., De Leonardis, G., Montanaro, R., **Mastropasqua, F.**, Graziano, G., ... Contino, M.* & D'Alessandro, R.* (**2025**). CC48 a new CB2R agonist/FAAH inhibitor dual drug blocks gastric cancer progression and overcomes paclitaxel resistance. *Journal of Experimental & Clinical Cancer Research*, *44*(1), 209.
- Barbanente, A., Kopecka, J., Vitone, D., Niso, M., Rizzi, R., Cuocci, C., Abatematteo, F.S, **Mastropasqua, F.**, ... Riganti, C.* & Abate, C.* (**2024**). First-In-Class thiosemicarbazone metal complexes targeting the Sigma-2 Receptor (S2R) as an innovative strategy against pancreatic cancer. *Journal of medicinal chemistry*, *67*(22), 20118-20134.
- Intranuovo, F., Majellaro, M., **Mastropasqua, F.**, Delre, P., Abatematteo, F. S., Mangiatordi, G. F., ... Abate, C.* & Contino, M.* (**2024**). N-adamantyl-1-alkyl-4-oxo-1, 4-dihydroquinoline-3-carboxamide derivatives as fluorescent probes to detect microglia activation through the imaging of cannabinoid receptor subtype 2 (CB2R). *Journal of Medicinal Chemistry*, *67*(13), 11003-11023.
- Graziano, G.,[#] **Mastropasqua, F.**,[#] Fanizzi A., Papadopoulos M.G.E., Laghezza A., Mammone M., Mangiatordi G.F., Esposito D., Brera J., Loza M.I., … & Contino, M. Design and Development of New Dual Target Agents, Cannabinoid Subtype 2 Receptor (CB2R) Agonists and Fatty Acid Amide Hydrolase (FAAH) Inhibitors Against Neurodegeneration. *Journal of Medicinal Chemistry* (**Submitted**).
- Graziano, G., Crouzier, L., **Mastropasqua, F.**, van Horst, C., Meunier, J., Delprat, B., Perrone M.G., Mammone M., Brera J., Loza M.I., ... & Contino, M.* Dual-Targeting CB2R Agonists and FAAH Inhibitors as A Promising Strategy Against Alzheimer's Disease. *Biological Research* (**Submitted**).
- Lisi, A.T., **Mastropasqua, F.**, Abate, C., Contino, M. Perrone, M.G., Graziano, G., ... & Di Giuuda, D. From ^{18}F-MC225 to conformationally free derivatives. Potent and promising PET tracers to detect P-glycoprotein at BBB with aryloxy-(thio)-alkyl fragment. *ACS Omega* (**Submitted**).

List of Conferences

- 2nd Meeting of the Italian GPCR Network (IT-GPCR). Bari, February 20, 2026. **Oral communication.**
- 2nd Cannabinoid Translational Science Symposium. Online, February 11,18 and 25, 2026. **Flash poster presentation.**
- 5th Edition of "Chimica sotto l'albero". Bari, December 18-19, 2025. **Oral communication.**
- 5th European Symposium / 1st Meeting of the European Network for Sigma-1 Receptor as a Therapeutic Opportunity (SIGMA-1EUROPE – Physiopathology of Sigma-1 Receptors). Granada, June 25-27, 2025. **Poster presentation**.
- First Meeting of the Italian GCPCR Network (IT-GPCR). Bari, February 14, 2025. **Poster presentation**.
- 4th Edition of "Chimica sotto l'albero". Bari, December 19-20, 2024. **Oral communication.**
- XXVIII EFMC International Symposium on Medicinal Chemistry (EFMC-ISMC 2024). Rome, September 1-5, 2024. **Poster presentation**.
- 43th European School of Medicinal Chemistry (ESMEC). Urbino, June 30 – July 4, 2024. **Poster presentation**.
- 3th Edition of "Chimica sotto l'albero". Bari, December 18-19, 2023. **Flash communication.**
- 4th European Symposium On Sigma-1 Receptor. Montpellier, September 28-29, 2023. **Oral communication.**
- XXVIII National Meeting of Medicinal Chemistry. Chieti, September 17-20, 2023. **Poster presentation**.